Interaction of piezoelectric transducer excited ultrasonic pulsed beams with a fluid-embedded viscoelastic plate

Finite element modeling, angular spectrum modeling and measurements

Magne Aanes

Dissertation for the degree philosophiae doctor (PhD)

at the University of Bergen,

Department of Physics and Technology.

December 2013

Preface

This work is the result of a 4-year PhD project financed by the University of Bergen, under the supervision of Professor Per Lunde and Associate Professor Magne Vestrheim at the Department of Physics and Technology, in cooperation with Professor Tor Arne Johansen at the Department of Earth Science and the Michelsen Centre for Industrial Measurement Science and Technology. I have chosen to write this thesis as a monograph instead of a collection of articles, because the form chosen here allows for a more complete and systematic analysis of the topics considered. However, parts of the present work have been presented at international conferences, cf. list of publications.

Firstly, I would like to sincerely thank my supervisors for their guidance and support. Throughout this work, they have been available for discussions whenever necessary or at the weekly meetings held between the supervisors and the candidate. It has been a delight working with you!

A special thanks is directed towards Scientist and PhD-candidate Kjetil Daae Lohne at Christian Michelsen Research for helpfull advice regarding the design of the experimental setup, an introduction to the angular spectrum method, lending me his steel plate, and fruitfull cooperation in relation to several sientific papers and the work leading up to them. PhD-candidate Espen Storheim also deserves a special thank for the close cooperation and several discussions over the years. Fruitfull discussions and talks, both academically and socially, making these 4 years very enjoyable, have been provided by members of the Acoustic Group at the department.

Finally, I would like to thank my family and friends for their endless support, and last but not least my most heartfelt personal thanks goes to my beloved wife Line and our son Håvard. You have been my rock!

Yours truly,

Bergen, December 20, 2013

List of publications

1. M. Aanes, J. Kocbach and M. Vestrheim. "Modal and direct harmonic solution methods in FE modeling of piezoceramic disks", in *Proc. 33rd Scand. Symp. Phys. Acoust.*, Geilo, Norway, 7-10 February 2010.

2. E. Storheim, M. Aanes, M. Vestrheim and P. Lunde. "Ultrasonic piezoceramic transducers for air, -finite element analysis and measurements", in *Proc. 33rd Scand. Symp. Phys. Acoust.*, Geilo, Norway, 7-10 February 2010.

3. M. Aanes, E. Storheim, M. Vestrheim and P. Lunde. "Finite element analysis and measurements of ultrasonic piezoceramic transducers in air and water", in *Proc. Baltic-Nordic Acoust. Meeting*, Bergen, Norway, 10-12 May 2010.

4. M. Aanes, K. D. Lohne, P. Lunde and M. Vestrheim. "Finite element analysis of acoustic beam interactions with a plate at normal incidence. Comparison with a 3D angular spectrum method and measurements", in *Proc. 34th Scand. Symp. Phys. Acoust.*, Geilo, Norway, 30 January - 2 February 2011.

5. Ø. S. Amundsen, M. Aanes, J. Kocbach and M. Vestrheim. "'Generalized Permittivity' and Source Sensitivity of Piezoelectric Ceramic Disks", in *Proc. 34th Scand. Symp. Phys. Acoust.*, Geilo, Norway, 30 January - 2 February 2011.

6. M. Aanes, K. D. Lohne, P. Lunde and M. Vestrheim. "Normal incidence ultrasonic beam transmission through a water-immersed plate using a piezoelectric transducer. Finite element modeling, angular spectrum method and measurements", in *Proc. 19th Int. Congr. Sound and Vib.*, Vilnius, Lithuania, 8-12 July 2012.

7. M. Aanes, K. D. Lohne, P. Lunde and M. Vestrheim. "Ultrasonic beam transmission through a water-immersed plate at oblique incidence using a piezoelectric source transducer. Finite element - angular spectrum modeling and measurements", in *IEEE Int. Ultrason. Symp. Proc.*, Dresden, Germany, 7-10 October 2012.

8. M. Aanes, P. Lunde and M. Vestrheim. "Ultrasonic beam transmission through a steel plate at oblique incidence. Uniform piston vs. piezoelectric transducer", in *Proc. 36th Scand. Symp. Phys. Acoust.*, Geilo, Norway, 3-6 February 2013.

Summary

Non-invasive ultrasonic technology for media contained by plane walls or pipes is of interest for various applications, such as flow metering, hydrate detection, non-destructive testing and evaluation, crack detection, corrosion and sand monitoring, etc. As such methodologies may involve rather complex ultrasonic waveguide propagation (leaky Lamb modes), accurate modeling tools can significantly aid in the development and optimization of such measurement methods. Fundamental understanding and control with the generation, reflection, transmission and reception of the ultrasonic pulsed signals propagating in a pipe wall/plate and the surrounding fluids, are important to achieve effective measurement solutions. This include the exploitation of leaky Lamb mode suited for the application at hand. Properties of importance in this respect include signal level and waveform, bandwidth of the pulse and signal-to-noise ratio. The parameters influencing the transmission are e.g. the vibration pattern, beam pattern, frequency response and operation frequency of the transmitting transducer, in addition to the angle of beam incidence, the material parameters and the thickness of the pipe wall/plate.

For description of sound generation and propagation in viscoelastic plates and surrounding fluids various theoretical approaches have been used in the literature. This include the plane-wave theory, two-dimensonal (2D) Cartesian angular spectrum method (ASM) employing a 2D Gaussian beam, three-dimensional (3D) ASM using a 3D Gaussian beam or a 3D beam from a circular, baffled and uniformly vibrating piston source, 2D finite element modeling (FEM) and 3D FEM approaches, and a distributed point source method (DPSM). In the aforementioned descriptions the source transducer itself may not be accounted for, and a simplified radiated sound field is used as an approximation of the real beam pattern of the measurement transducer. The transducer construction and properties are of critical importance for excitation of the desired waveguide. The transmitting transducer should therefore be accounted for in the modeling for a more complete description of the signal chain through the system.

The objective of this thesis is to investigate theoretically and experimentally the interaction of piezoelectric transducer-excited ultrasonic pulsed beams with a fluid-embedded viscoelastic plate. Two modeling approaches are used to simulate the 3D signal propagation through the measurement system: **i)** A finite element method approach, and **ii)** a hybrid approach, involving finite element modeling combined with an angular spectrum method at normal and arbitrary angles of beam incidence, respectively. The presented work extends earlier descriptions by including the 3D signal propagation through the transducer, its vibration, including the effect of the electrical loading of the signal generator, excitation of

leaky Lamb modes in the viscoelastic plate, and the sound field transmitted through the plate. Since use of a commercial transducer does not provide sufficient information concerning the transducer construction, dimensions and materials involved, and material data, a piezoelectric transducer has been designed, constructed, characterized and used for measurements and FEM simulations. Calculations of the transducer's input voltage to transmitted sound pressure transfer function, and transmitted sound pressure signal waveforms, are compared to measurements. Comparisons are made at a given distance between the transducer and the plate for given angles of orientation of the transducer with respect to the plate and for given receiver positions. The comparisons include signal frequencies close to excited leaky Lamb modes in the plate and in-between such modes. Discussions with respect to optimization of acoustic and electroacoustic properties mentioned above are made. Thus, this work extends current theoretical descriptions of bounded beam interaction with fluid-plates and halfspaces. This includes the 3D electro-acoustical coupling in the transducer, accounting for a more realistic beam pattern of the measurement transducer in the theoretical description, and its influence on leaky Lamb mode propagation in the plate, in addition to a quantitative description of the measurement system described.

Contents

Chapter 1

Introduction

The objective of this thesis is to investigate theoretically and experimentally the interaction of piezoelectric transducer-excited ultrasonic pulsed beams with a fluid-embedded viscoelastic plate. The three-dimensional (3D) theoretical description includes the signal propagation through a piezoelectric source transducer and its vibration, the effect of the electrical loading of the signal generator, the radiated sound pressure field, excitation of leaky Lamb modes (guided waves) in the viscoelastic plate, and the sound field transmitted through the plate[1].

In this chapter the background and motivation for the current thesis is presented in Sect. 1.1, and the objectives are further formulated in Sect. 1.2. A review of previous work with relevance to the current work is presented in Sect. 1.3. The structure of the thesis is described in Sect. 1.4.

1.1 Background and motivation

Non-invasive ultrasonic technology for media contained by pipes or plane walls is of interest for various applications, such as pipeline deposit detection of e.g. sand-, wax- or hydrate-formation e.g. [1, 2, 3, 4], non-destructive testing and evaluation (NDT& E) of defects, cracks, corrosion, etc in pipes, e.g. [5, 6, 7, 8, 9, 10], flow metering e.g. [11, 12, 13], etc. As such methodologies may involve rather complex ultrasonic waveguide propagation, accurate modeling tools can significantly aid in the development and optimization of the measurement methods. Fundamental understanding and control with the generation, reflection, transmission and reception of the ultrasonic pulsed signals propagating in the pipe wall/plate and the surrounding fluids, are important to achieve effective measurement solutions. Li and Rose [14] presented dispersion curve comparison between hollow-cylinder guided waves and guided waves in infinite plates (cf. Lamb waves[2]), for different $2R/h$ (pipe diameter/wall thickness) ratios, see Fig. 3 in [14]. They concluded that the non-axisymmetric guided waves in the pipe wall can be treated as Lamb waves in an elastic plate when the wall thickness h is far less than the cylinder diameter $2R$. Velichko and Wilcox [17] concluded that for a wall thickness h much less than the pipe

[1] This thesis focuses on sound transmission through the plate, but reflected beams from the plate are included in the description, but are not shown.

[2] Another common notation for these waves are "Rayleigh-Lamb waves" [15, 16].

radius R, and the wavelength λ of the guided wave much less than the pipe circumference the effect of the curvature of the pipe on wave propagation becomes negligibly small. Thus, the isotropic elastic pipe wall can formally be represented as a plate given

$$h << R \text{ and } \lambda << 2\pi R, \tag{1.1}$$

respectively.

Sound reflection from, transmission through, and propagation in isotropic elastic and viscoelastic fluid-embedded plates is then relevant and useful in the work to enhance our understanding of guided wave propagation and mechanisms involved in non-invasive ultrasonic technology. This includes the exploitation of leaky Lamb mode suited for the application at hand. Properties of importance in this respect include signal level and waveform, bandwidth of the signal and signal-to-noise ratio. The parameters influencing the transmission are e.g. the vibration pattern, beam pattern, frequency response and operation frequency of the source transducer, in addition to the angle of beam incidence, the material parameters, and the thickness of the plate.

Theoretical and numerical modeling and experimental studies involving fluid-embedded elastic plates have been extensively investigated in the literature using various approaches, cf. Sect. 1.3. In many of these descriptions the source transducer itself may not be accounted for, and simplified radiated sound pressure fields are used as approximations for the real beam pattern of the measurement transducer. The transducer construction, properties and operation are of critical importance for the excitation of the desired waveguide and the total transmission through the system. It would be advantageous to provide a three-dimensional (3D) theoretical description of ultrasonic pulsed beam transmission through a system consisting of a piezoelectric source transducer and a viscoelasic plate, including the electroacoustical coupling in the transducer, the real beam pattern of the transducer, and their effect on guided wave propagation in the elastic plate. By doing so, a quantitative description of such measurement systems can be acheived, useful to explain and optimize the signal propagation through the system with respect to non-invasive ultrasonic technology and its challenges, and optimization of acoustic and electroacoustic properties.

1.2 Objectives

The objective of this thesis is to extend the theoretical description of ultrasonic non-invasive measurement systems by including the signal propagation through a piezoelectric source transducer and its vibration, the effect of the electrical loading of the signal generator, the radiated sound pressure field, excitation of leaky Lamb modes (guided waves) in the viscoelastic plate, and the sound field transmitted through the plate. The piezoelectric source transducer is to be included in the 3D theoretical description using the finite element method (FEM), thereby accounting for the electroacoustial coupling in the transducer, a more realistic beam pattern of the transducer than more simplified transducer models, and their influence on leaky Lamb mode excitation in the plate. Since use of a commerical transducer does not provide sufficient information regarding the transducer construction, dimensions and materi-

als involved, and material data, a piezoelectric transducer is to be designed, constructed, characterized and used for measurements and FEM simulations. This will enable a quantitative description of the measurement system, from input voltage to the transducer - to the transmitted sound pressure through the plate. The effect of accounting for a more realistic beam pattern, in comparison to more simplified models for beam excitation, is to be investigated based upon transmission through the plate and the excitation of leaky Lamb modes. The simplified model of a uniformly vibrating planar and circular piston mounted in a rigid baffle of infinite extent is here of interest, since this model seems to be extensionally used in the literature. For convenience, this source is here referred to as the "baffled piston model". Important properties such as signal level, bandwidth of the transmitted signal, and waveform is sought, and discussed based upon optimization of transmission through the total system, and with respect to non-invasive ultrasonic technology.

1.3 Literature

This section presents a summary review of some earlier work which are of relevance for this thesis. The literature study focuses on ultrasonic beam interaction with a fluid-embedded elastic plate, with emphasis on the theoretical description of the imposed incident acoustic beam and its feasibility to account for the real beam pattern of the measurement transducer. Bounded beam interaction with an immersed solid half-space is also of interest, due to its historical and theoretical similarity to the elastic plate. A vast number of related articles have been published utilizing guided waves for NDT purposes, with the main objective to detect areas within the plate affected by defects, cracks, corrosion, etc. The finite element method has been used for piezoelectric transducer characterization and design, by e.g. [18, 19, 20], etc. It is not within the scope of this thesis to give a full review on these matters, but rather focus on relevant work which utilizes finite beams to excite the guided waves.

The theory for symmetric and anti-symmetric Lamb modes in a free (vacuum-embedded) solid plate was formulated by Rayleigh [21] and Lamb [22] in 1889, and Lamb [23] in 1917, respectively. In 1938 Reissner [24] presented a solution for the transmission of a plane-wave through a solid plate immersed in a single fluid medium, as a function of incidence angle, frequency and plate thickness. Levi and Nath [25] gave an equivalent solution the same year, Osborne and Hart [26] in 1945 (focused on the eigenmodes), and Schoch [27] in 1952. Transmission measurements were performed by Sanders [28], Osborne and Hart [29], Smyth and Lindsay [30], and Fay and Fortier [31], all showing evidence for diffraction effects of the source. Fay and Fortier [31] pointed out that the radiation pattern of the transmitter sound field may be of importance, since the impinging sound does not entirely consist of plane-wave motion. In 1950, for a liquid-solid (L/S) interface, Schoch [32] discussed how a reflected beam is displaced laterally from the position prescribed by geometrical acoustics. In 1952 Weinstein [33] pointed out the failure of plane-wave theory to predict the reflection of a narrow ultrasonic beam, since the rays of which the beam is composed will all be incident at slighly different incidence angles. Both Fay and Fortier, and Weinstein made no attempt to account for a diffracted beam in their simulations.

A series of experiments on a (L/S) interface made by Neubauer [34] in 1973 gave insight to reflection effects that occur for incidence at or near the Rayleigh angle, which could not be explained by Schoch's beam-displacement theory. In addition to specular reflection, a Rayleigh wave was generated by the incident beam and radiated continously into the fluid. This effect was called the Rayleigh angle phenomena. Later that year, Bertoni and Tamir [35] used an asymptotic analysis and presented a unified theory for the Rayleigh angle phenomena, by accounting for the bounded character of the acoustic beam. They explained the reflected field for incidence at or near the Rayleigh angle as a superposition of a geometrical-acoustic component and a leaky Rayleigh-wave field. Bertoni and Tamir made use of plane waves in terms of a two-dimensional (2D) Cartesian angular spectrum method (ASM), using rather idealized 2D Gaussian beams, with no description of sidelobes in the transducer beam pattern, and with the beam extending to infinity in one plate dimension. Neubauer and Dragonette [36] presented in 1974 measurements of Rayleigh phase velocity and shear speed estimation near or at the Rayleigh angle, in agreement with the theoretical model of Bertoni and Tamir. Plona *et al.* [37] showed in 1975 that the simple expressions for Rayleigh waves and Lamb modes for a vacuum-embedded plate could approximate the behaviour of solids and plates loaded by a liquid, provided that the densities of the two substances were quite different. In 1976 Pitts *et al.* [38] presented theoretical results that showed that the Rayleigh mode is a special type of Lamb mode vibration, and that the physical properties of a thick solid plate will show some resemblance to that of an infinite half space. Breazeale *et al.* [39] measured in 1977 the reflected beams for different materials using a specially manufactured transducer providing a near Gaussian beam, presenting fair agreement with the theory of Bertoni and Tamir. While the measurements where performed in 3D, the theory used was for a 2D field.

Reflection and transmission of an ultrasonic bounded beam at oblique incidence to a solid plate was treated by Plona [40] and Pitts [41] in 1976 and 1977, using an angular spectrum method with 2D Gaussian beams. They concluded that the non-geometric effects which were present for both the reflected and transmitted beams in a liquid-solid-liquid (L/S/L) interface when the incident angle corresponds to the excitation of a leaky Lamb mode, were consistent with the same effects at or near the Rayleigh angle for a (L/S) interface, explained by Bertoni and Tamir. In 1979 Fiorito and Madigosky [42, 43] investigated a plane-wave resonance theory for sound transmission and reflection from a fluid-embedded solid plate for oblique incidence angles, representing the transmission maxima as poles and zeroes in terms of the expanded transmission coefficient. Ngoc and Mayer [44] extended in 1980 the earlier limitations by using the complete reflection coefficient in relation to the asymptotic representation, thereby enabling a theoretical model to study the reflected field from a (L/S) interface for any incident angles. Ngoc and Mayer used 2D Gaussian beams to create the incident sound pressure field. Ng *et al.* [45] extended in 1981 the theory of Bertoni and Tamir to fluid-loaded solid plate using 2D Gaussian beams, taking into account all existing poles, and in 1982 Claeys and Leroy [46] presented the reflection and transmission of 2D bounded beams on half-spaces and through plates using exact transmission coefficients and inhomogenous plane waves to form the incident beam.

In 1984 Pott and Harris [47] used a complex source-point method with an asymptotic analysis to model incident 3D Gaussian beams on a L/S interface. Their work showed that the incident beam is spec-

ularly reflected except at or near the critical angles. Schmidt and Jensen [48] studied reflection from a vertical line-array source (almost Gaussian) at a (L/S) interface near the Rayleigh angle in 1985, which included full wavefield solutions for both continous and pulsed ultrasonic beams. Rousseau and Gatignol [49] discovered in 1986 that the incident beam is specularly reflected except at or near the critical angles for a (L/S/L) interface, with an asymptotic analysis utilizing 2D Gaussian beams. They concluded that the nongeometrical effects of the reflected field depends cojointly of the excited Lamb waves at a specific frequency. In 1988 Ng *et al.* [50] measured the non-specular reflection phenomena for an ultrasonic bounded beam reflected from a solid plate, and found close agreement with 2D angular spectrum method using a Gaussian beam. That same year, a study of the reflection of bounded beams on layered half-spaces and plates was carried out by Kundu [51]. There, the incident beams were approximated by Gaussian beams, and the Thomson-Haskell matrix was used to solve the problem. In 1991 Lunde [52] studied interference effects in sound fields transmitted at fluid-solid interfaces using the full-wave simulation model CAPROS [53]. The model enabled 3D sound fields composed of arbitrarily distrubuted point sources to model a 2D horizontal source array. In 1992 Zeroug and Felsen [54] used the complex source point method to model nonspecular reflection in a liquid-solid interface, using collimated 2D Gaussian beams.

Matikas *et al.* [55] presented in 1993 reflection studies from a focused Gaussian beam from a fluid-solid interface, by decomposition using the Fourier integral representation, for any angle of incidence. The same year presented Abeele and Leroy [56] a study of bounded beam on arbitrary layered media using heterogeneous plane waves. Dechamps and Chevèe [57] studied reflection and transmission of 2D transient Gaussian beams on viscoelastic and orthotropic plates in water using Debye's series to describe reflection/refraction coefficients. For comparing simulated and measured responses, both are normalized by the amplitude at a specific position. Due to scanning limitations, only the region with relatively high transmission through the plates was measured. Chimenti *et al.* [58] presented similar work as Rousseau and Gatignol [49] in 1994, but included also other elastic stuctures like half-spaces and solid cylinders. They compared measured and simulated data of the reflected field from a plate as a function of position parallell to the plate. That same year, Zeroug and Felsen [59] investigated 3D Gaussian incident beam interaction with fluid-loaded plane layered elastic structures, combining the complex source-point technique with an asymptotic solution for the reflection coefficients. Anderson *et al.* [60] used a 3D baffled piston model for transmission calculations through a solid plate in air using ASM and exact plane-wave pressure transmission coefficient in 1995. The model showed that the incidence of a three-dimensional beam onto an elastic plate exhibits behaviour which is significantly different than the case of two-dimensional models, concluding the need for 3D modelling. E.g. the 3D transmitted field has a characteristic width in the transverse direction that is on the order of the transducer diameter, leaky attenuation in the sagittal plane observed in the 3D case appears to be higher than what is expected using 2D. This transducer-model provided a more realistic and accurate description of the sound field radiated by a real source than 2D or 3D Gaussian beams, when properly accounting for sidelobes of a finite dimensional transducer. In 1996 Zeroug and Stanke [61] presented both theory and experiment for ultrasonic pulsed beam transmission through a fluid-embedded elastic plate, using the complete reflection coefficient and using a series of complex source-point monopoles to

account for a quasi-Gaussian 3D diffraction (symmetric 3D beam with a quasi-Gaussian amplitude).

In 1996 Lobkis *et al.* [62, 63] studied 3D bounded beam reflection from a fluid-loaded plate. This study permits the inclusion of the transducer diffraction effects for both the transmitter and receiver, using both baffled piston and Gaussian sources. They concluded that for two identical transducers, the beam shape, and near- and far-field conditions had a relatively minor impact on the receiver voltage, which was calculated using Auld's reciprocity formulas. The same year, Castaings and Cawley [64] studied the generation, propagation and detection of Lamb waves in plates using air-coupled transducers. The transducers radiated fields were approximated as 2D collimated beams, and the pressure distribution are applied to the 2D plate modelled using finite elements (FE). The plate itself was assumed to vibrate in vacuum, so fluid loading was not accounted for. In 1997 Cawley and Hosten [65] investigated the possibility to better determine elastic constants of a plate by fitting the experimental results to the predictions of plane-wave theory. They concluded that bounded beam effects were large at low frequencies, and used large transducers to minize the bounded beam effect on measurements. Moulin *et al.* [66, 67] used a coupled 2D finite element-normal modes expansion approach in 1999 and 2000, respectively, to account for a piezoelectric element and its influence to Lamb mode excitation. The piezoelectric elements where bonded onto a vacuum-embedded plate, and the surface stresses where calculated using FEM and used in the normal modes expansion. One assumption was that the propagating normal modes in the plate where not alterned too much by the presence of the surface-mounted elements.

In 1997 and 2001 Landsberger and Hamilton [68, 69] investigated the second-harmonic generation in sound beams reflected and transmitted through elastic solids, by using a 3D angular spectrum method to model the incident field from a baffled piston source, thus accounting for effects of sidelobes in the transmission of the beam pattern through the solid, and finite extent of the beam pattern, in both plate dimensions. Younghouse [70] extended the work of Landsberger in 2002 by considering a plate rather than a thick solids, by using the complete plane-wave reflection/transmission coefficients. Both work accounted for fluid loading. Vandeputte *et al.* [71] studied in 2003 the influence of planar cracks in plates on reflected and transmitted pressure fields utilizing 2D Gaussian beams. They presented results for incident angles near critical angles of L/S/L and L/S/V(vacuum) interfaces. That same year, Vanaverbeke *et al.* [72] studied the interaction of 2D Gaussian beam on a thin inclusion in a fluid-loaded plate.

Duquenne *et al.* [73] extended in 2004 the 2D coupled finite element-normal mode expansion technique by Moulin to account for transient excitation and lossy materials. They assumed that the resonance of a thin piezoelectric element coupled to the plate was significantly damped, hence its frequency response was smoothed. Then, the frequency dependence of the surface traction on the plate could be approximated to be the spectrum of the excitation signal. In 2005 presented Potel *et al.* [74] a study of Lamb waves in anisotropic multilayered media, by a monochromatic incident 3D beam, using an asymptotic approach. An analytical expression for particle displacement on the emitter was used to excite Lamb waves. The same year, Declercq *et al.* [75] gave a historical survey of the development

of inhomogeneous wave theory, and its impact on reflection/transmission phenomena. Bezdek *et al.* [11] investigated in 2005 a 3D simulation of a transit-time ultrasonic flowmeter based upon a coupled FEM-HIRM (Helmholtz-Integral-Raytracing method) approach. A piezoelectric element and its structure-borne coupling to the surrounding pipe wall was simulated using FEM, and the fluid-borne acoustic was simulated using the HIRM. In 2006 Kazys *et al.* [76] used finite-difference to detect and visualize inhomogeneties in composite materials using air-coupled transducers, running 2D simulations and using a strip-like source to excite the Lamb modes in the elastic structure. Bouzidi and Schmitt [77] modelled a large ultrasonic bounded pulse transducer for use in acoustic transmission goniometry in 2006, where the observed bounded acoustic pulse at $z = 2$ cm was used to model the incident field towards the plate, and appropriate transmission coefficients were used at both interfaces of the thick plate. Banerjee and Kundu [78] used in 2007 a distributed point source method (DPSM) to calculate the 3D ultrasonic field in a solid plate immersed in a fluid, where the incident beam was generated by a finite dimensional transducer modelled as a piston source. The DPSM models the vibration pattern on the front surface of the transducer by a finite number of point sources. Qualitative agreement between theoretical and experimental results is shown. That same year, Banerjee *et al.* also used the DPSM for a near fluid-solid interface [79]. They showed visual images of the critical reflection phenomenon, showing the incident and reflected beam.

Jocker and Smeulders [80] investigated methods for minimization of finite beam effects for determining reflection and transmission coefficients of an elastic layer in 2007. They proposed a spectral decomposition of a finite beam to determine the reflection and transmission coefficient for each plane wave, and concluded that the method would also work for thin plates where the wavelength was larger than the plate thickness. Lamkanfi *et al.* [81] studied the same year the transmission of leaky Rayleigh waves near the edges of a fluid-loaded elastic plate using finite elements. They used a 2D Gaussian beam to simulate the incident pressure field, and showed that leaky Rayleigh waves on the horizontal surface of the plate travel around the corner of the plate. In 2007, Bezdek *et al.* [12] further developed the hybrid FEM-HIRM approach, focused on flow measurement and used Snell's law to calculate the nominal beam path and the axial sensor distance. As pointed out in that work, this does not include the effect of e.g leaky Lamb mode propagation in the pipe, and its effect on the actual nominal beam path. The next year a book on the subject was released [13]. That same year, Bezdek and Tittman [82] used finite element modeling to describe guided wave propagation excited by a piezoelectric element mounted on a wedge, attached to a three-layered elastic plate structure. In this 2D simulation study the piezoelectric element and the beam pattern was extending to infinity in one plate dimension. The DPSM was further used by Das *et al.* [83] in 2007 to study the interaction between a 3D finite bounded beam and corrugated plates.

In 2008 Bouzidi and Schmitt [84] used the phase advance technique to study a bounded acoustic beam interacting with a water-loaded plate, being able to model both the stationary monofrequency beam wavefield and the temporally bounded pulse using Gaussian beams. In 2008 Hosten and Biateau [85] predicted the absolute values of the pressure field generated by guided waves propagating in a plate-structure, excited by air-coupled transducers. The plate and surrounding air regions were modeled

using 2D FEM, and the transducer's beam by volume pressure excitation equal to the measured pressure (magnitude only) from the transducers. In a 3D FEM study of sound propagation in an air-coupled NDT system by Ke *et al.* [86] in 2009, the local pressure distribution produced by the source transducer was used as normal-stress excitation on the plate surface, using 2D Gaussian window to define the pressure distribution on the surface of the transducer. The plate itself was assumed to vibrate in vacuum, so fluid loading was not accounted for. That same year, Dao *et al.* [87] studied the wave propagation in a fluid wedge over a solid half-space using the DPSM method, and comparison with measurement showed that the DPSM computation were qualitatively in line with the experimental results. Partially immersed and fully submerged solid half-spaces were compared. In 2010 Masmoudi *et al.* [88] extended the work by [85] to include 3D FEM for the plate, and showed comparison (absolute level) between simulations and measurements, where they assumed that the transducer radiated as an unbaffled rigid piston. In a 2D FEM study in 2010 Delrue *et al.* [89] investigated single-sided air-coupled technique for non-destructive testing. In this work the elastic steel plate was immersed in air, where 2D Gaussian beam is used. Whereas Landsberger and Younghouse focused on nonlinear effects, Lohne *et al.* in the years 2008-2013 [90, 91, 92, 93, 94, 95] studied the transmission through a water-immersed plate using the exact plane-wave pressure transmission coefficient in both frequency and time domains, using pulsed piston-generated 3D beams. Comparisons to measurements were made. Lohne *et al.* observed a frequency shift of the S_1 mode at normal incidence in [90], and explained the shift in [91, 92] as beam diffraction effects. Waag *et al.* [96] studied thickness measurements of steel plates using half-wave resonances in air, using the baffled piston model to account for a finite dimensional transducer in 2012. Simulations and measurements showed a similar frequency shift as observed and discussed by Lohne *et al.* in [90, 91], respectively. [88] was extended by Masmoudi and Castaings in 2012 [97], to study material anisotrophy on the purity of the guided wave modes. In both cases comparison were made with measurements.

The presented work in this thesis is partly based on the work by Lohne *et al.* [90, 91, 92]. Earlier work based on radiation from a directive baffled piston source, or Gaussian beams, is extended to account for the piezoelectric transducer in the description of 3D sound transmission through a viscoelastic plate, which includes the transducer's frequency response, vibration and beam pattern, and its electroacoustical coupling. Axisymmetric finite elements are used to simulate the signal propagation through a system consisting of a piezoelectric source transducer and a water-embedded viscoelastic plate at normal beam incidence, denoted the FEM approach. This approach is extended to account for oblique angles of beam incidence using a hybrid FEM-ASM approach. In this approach the transducer's voltage-to-pressure response and the radiated free-field sound pressure are simulated using the FEM. This FEM-simulated sound pressure field is further propagated through the viscoelastic plate and the surrounding fluid using an ASM and the exact plane-wave pressure transmission coefficient. Since use of a commercial transducer does not provide sufficient information and control concerning the transducer construction, dimensions, materials and material data involved, a piezoelectric source transducer is designed, constructed, characterized, and used for measurements and FE simulations. This enables quantitative simulations of the measurement system, from input voltage to the transducer, to the transmitted pressure through the plate, in addition to a more realistic beam pattern representation

than earlier work based on simplified beam models. The two approaches are compared to measurement results.

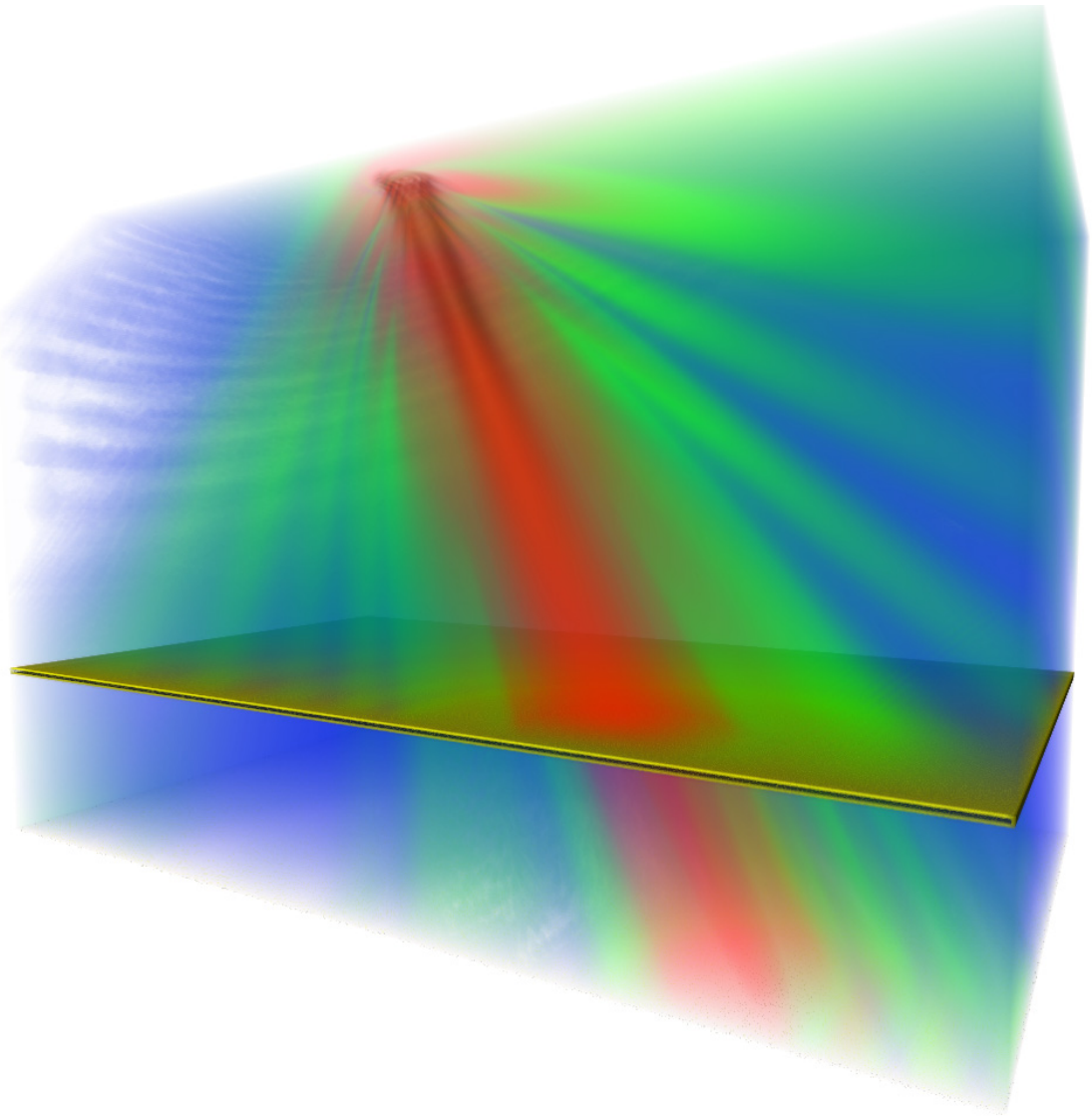

Fig 1.1. Hybrid FEM-ASM simulated free-field sound pressure field radiated by the piezoelectric source transducer at a frequency of 446 kHz (near the S_0 mode), titled towards the steel plate (thickness of 6.05 mm) (yellow) at a 25° beam incidence angle, and simulated transmitted pressure field below the steel plate. Dag Magne Ulvang at Christian Michelsen Research, Bergen, Norway, visualized the simulated sound pressure data using VOLUMESHOP (`http://www.cg.tuwien.ac.at/volumeshop`)(October 28, 2013). 3D volume. For pressure spectra and pressure waveforms as function of e.g. frequency, receiver position for the following case refer to Figs. 7.30 to 7.33.

Fig. 1.1 exemplifies the 3D signal transmission through the measurement system, showing the hybrid FEM-ASM simulated free-field pressure sound field radiated by the piezoelectric source transducer at a frequency of 446 kHz (near the S_0 mode), tilted towards the steel plate (thickness of 6.05 mm) (yellow) at a 25° beam incidence angle, and simulated transmitted pressure field below the steel plate, propagated through the plate using the plane-wave pressure transmission coefficient. In the figure, the reflected sound pressure field is not displayed. Pressure spectra and pressure waveforms, as function of

e.g. frequency, beam incidence, receiver position, are simulated and compared to measurement results in Chap. 7, for the following case refer to Figs. 7.30 to 7.33.

Earlier work, e.g. [91, 98], have shown that for relevant transducer dimensions and frequencies, a plane-wave approach is not sufficient for accurate description of guided waves in the solid plate and the associated leaky Lamb modes. [60, 91, 92, 93, 94, 95] have shown that accounting for the source transducer's 3D beam pattern is important, even at normal incidence. Previous work, e.g [60, 91, 92, 93, 68, 69, 70], on description of 3D beam transmission through elastic plate at normal and oblique angles of beam incidence have been based on approximating the incident field radiated by the piezoelectric transducer with the simplified field of a baffled piston source having the same -3 dB beamwidth. In the description of such measurement systems, there is therefore the question of the importance of accounting for the real beam pattern of the transducer. The errors introduced by using such a baffled piston model approach can now be evaluated.

1.4 Outline of the thesis

The theory for the 3D signal propagation through the measurement system is presented in Chapter 2, using the FEM and hybrid FEM-ASM approaches. For the FEM approach the analysis is formulated in the time- and frequency-domain, using finite elements to describe the signal propagation through the measurement system. For the hybrid FEM-ASM approach the analysis is formulated also in the frequency-wavenumber domain, using finite elements to describe the signal propagation through the source transducer and surrounding fluid, calculating the incident free field sound pressure at the upper surface of the plate (when the plate is absent). Then, the signal is propagated through the plate using the exact plane-wave pressure transmission coefficient based on the leaky Lamb dispersion equations. For that reason, the plane-wave pressure transmission and reflection coefficients are derived, arguments for this are given in Sect. 2.2.1.

The experimental setup and measurement methods are presented in Chapter 3, including the hydrophone calibration scheme, measurements of the piezoelectric transducer properties and transmission measurements through the system. A method for determining the sound velocities in the plate [91] is described and used, and extended to approximate the corresponding loss factors (Q-factors).

The simulation setup of the FEM and hybrid FEM-ASM approaches are presented in Chapter 4, in addition to the FE simulations of the piezoelectric source transducer and the baffled piston source. An example of FEM convergence tests for the hybrid FEM-ASM approach is also presented.

Chapter 5 presents the piezoelectric source transducer construction, including the transducer design and the construction process. Results for the FEM calculated piezoelectric source transducer are presented and compared to measurements.

The importance of accounting for the real beam pattern of the measurement transducer is addressed

in Chapter 6, comparing transmission through the plate using FEM transducer-excited vs. piston-generated beams and plane waves at different angles of beam incidence, to measurements. The results include the measurement of the sound velocities in the plate with corresponding loss factors.

In Chapter 7 the results for the quantitative description of the signal transmission through the measurement system are reported, using the FEM and hybrid FEM-ASM approaches at different angles of beam incidence. Results are shown for the voltage-to-pressure transfer function in the frequency domain, and for pressure waveforms in the time domain, for given voltage excitation to the transducer, in comparison with measurements. The overall findings of the work is discussed in relation to the objectives and relevant literature.

Chapter 8 presents the major conclusions of the thesis. Finally, topics for future work are discussed. A list of references follows the conclusions, listed in the order they are referred. The FEM baffled, FEM piezoelectric transducer and FEM approach project-codes are listed in Appendices A, B, C, respectively. In Appendix D the program code for calculation of FEM incident fields is listed, while the ASM-part of the hybrid approach program code is listed in Appendix E. The time domain signal calculation program code is listed in Appendix F. Various program codes for the measurement setup and stage control are listed in Appendix G.

Chapter 2

Theory

2.1 Introduction

This chapter presents the theoretical description of the measurement system described in Chap. 3, consisting of a piezoelectric source transducer and a fluid-embedded viscoelastic isotropic plate, see Fig. 2.1, assuming a linear system. The 3D description includes the signal propagation through the piezoelectric transducer and its vibration, including the effect of the electrical loading of the signal generator, the radiated sound pressure field, excitation of leaky Lamb modes (guided waves) in the viscoelastic plate, and the sound field transmitted through the plate. The analysis is formulated as a series of transfer functions, each describing the sound propagation through a part of the total system. Axisymmetric finite elements are used to simulate the signal propagation through the measurement system at normal beam incidence, denoted the FEM approach. This approach is extended to account for oblique angles of beam incidence using a hybrid approach, involving axisymmetric finite elements to describe the transducer's voltage-to-pressure response and the radiated free-field sound pressure. A coordinate transformation is then used to calculate the incident free-field pressure on the surface of the plate for a given beam incidence, and further propagate this through the plate and the surrounding fluid using the angular spectrum method, and the plane-wave pressure transmission coefficient. This approach is denoted the hybrid FEM-ASM approach. The analysis for both approaches is formulated in the time- and frequency-domains, and for the hybrid FEM-ASM approach, also in the frequency-wavenumber domain.

The 3D signal propagation through the measurement system is described in Sect. 2.2, with the hybrid FEM-ASM approach described in Sect. 2.2.1, and the FEM approach in Sect. 2.2.2. Since no information is available for the sound transmission through the transducer using the simplified baffled piston model, a transfer function for comparison of the FEM transducer model vs. the baffled piston model for plate transmission is derived in Sect. 2.2.3. A short description of the FEM, its use, and the finite element program used in this thesis, is given in Sect. 2.3. The Lamb frequency equations for a solid plate in vaccum are formulated in Sect. 2.4.1, and extended in Sect. 2.4.2 to include the leaky Lamb frequency equations for a solid fluid-embedded plate. The plane-wave pressure transmission and

reflection coefficients for a solid plate immersed in a single-fluid are formulated in Sect. 2.4.3.

2.2 Signal transmission through the system

Figs. 2.1, 3.1(a) and 3.1(b) show the system consisting of a piezoelectric source transducer connected to a signal generator, radiating at a beam incidence θ towards an assumed infinite water-embedded viscoelastic steel plate of thickness $2L$. A cylindrical coordinate system (r', z'), or (x', y', z') (where $x' = r' \cos\phi'$, $y' = r' \sin\phi'$, and $\phi' \in [0, 2\pi]$, where ϕ' is the angle between $r-$ and the $x-$axis), is used to describe the axisymmetric source transducer and the incident pressure field in the water between the transducer and the steel plate. A 3D Cartesian coordinate system (x, y, z) is used to describe the sound field in the water-immersed steel plate and the lower adjacent water region. Both coordinate systems have origin located at the center of the transducer's front surface; z' and z are directly normal to the transducer's front surface and the plate, respectively.[1] The relationship between the two coordinate systems is

$$\begin{aligned} x &= \cos\theta x' - \sin\theta z', \\ y &= y', \\ z &= \sin\theta x' + \cos\theta z'. \end{aligned} \tag{2.1}$$

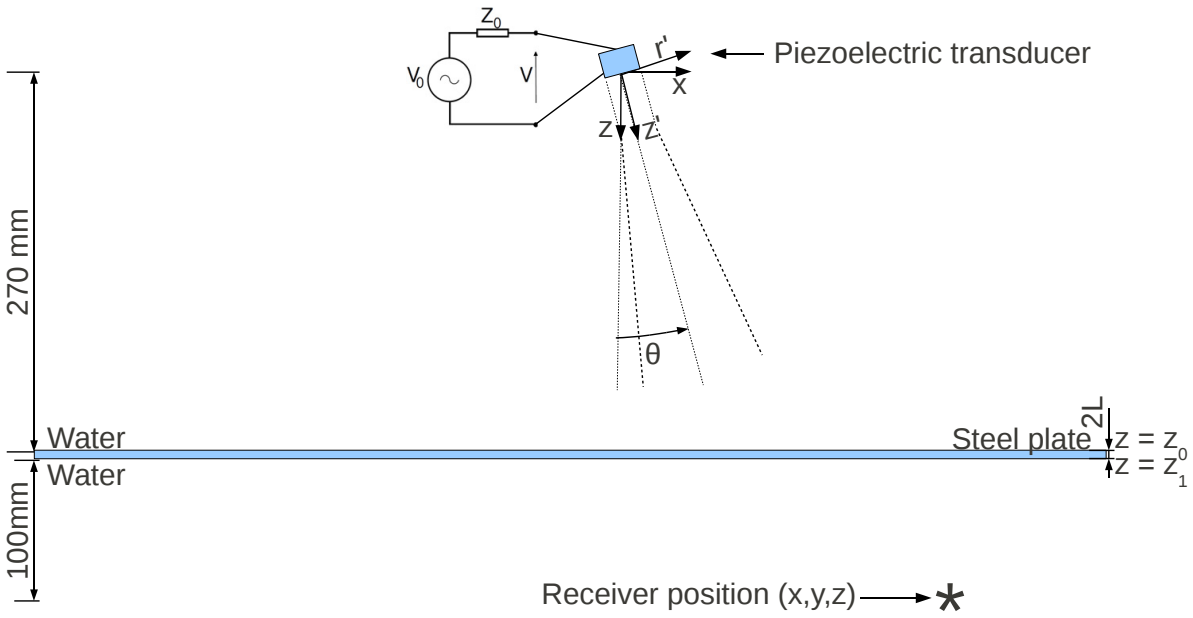

Fig 2.1. An illustration of an acoustic beam, generated by a piezoelectric transducer at an angle of beam incidence θ, interacting with a water-immersed viscoelastic steel plate. y is directed out of the paper.

θ is the angle between the two coordinate systems (in the xz-plane), i.e. the angle between the transducer and the plate; θ is therefore the angle of beam incidence, relative to the z-axis. Hence, the

[1] For measurements in Chap. 3 the coordinate system is directed horizontally, i.e. $z-$axis is horizontal, where in the theoretical description the $z-$axis is directed vertically.

tranducer tilts in the xz-plane, and not in the yz-plane. A time dependency of $e^{i\omega t}$ is assumed and used throughout the entire thesis. $\omega = 2\pi f$ is the angular frequency, and f is the frequency.

A pulsed voltage waveform $v_0(t)$, representing the electromotive force of the signal generator, is used to excite the piezoelectric source transducer. Due to the generator's internal impedance, Z_0, and the electrical connection to the transducer, a voltage reduction appears across the transducer. The resulting voltage waveform transmitted to the piezoelectric transducer is denoted $v(t)$. The pulsed ultrasonic beam interacts with the water-immersed steel plate with upper surface located at $z = z_0$, and lower surface located at $z = z_1 \equiv z_0 + 2L$. The pressure waveform is transmitted through the plate, exciting leaky Lamb modes, and into the adjacent water region and detected at various receiver positions indicated by '$*$' in Fig. 2.1. $p_t(x, y, z, t)$ is the transmitted pressure waveform at a given receiver position $(x, y, z)|_{z \geq z_1}$ below the steel plate.

The electrical loading of the signal generator is simulated using the Thévenin model (Fig. 2.1), given by the transfer function

$$H_{VV}(f) = \frac{V(f)}{V_0(f)} = \frac{Z_T(f)}{Z_T(f) + Z_0}, \tag{2.2}$$

where $Z_T(f)$ is the electrical input impedance of the piezoelectric transducer and Z_0 is the internal (output) impedance of the signal generator. The voltage frequency spectra of $v_0(t)$ and $v(t)$, $V_0(f)$ and $V(f)$, are given by the temporal Fourier transform [99] as

$$V_0(f) = \int_{-\infty}^{\infty} v_0(t) e^{-i2\pi f t} dt, \tag{2.3}$$

$$V(f) = \int_{-\infty}^{\infty} v(t) e^{-i2\pi f t} dt, \tag{2.4}$$

respectively. The signal transmission through the system is modeled using the hybrid FEM-ASM and the FEM approaches. The hybrid FEM-ASM approach is presented in Sect. 2.2.1, and describes the signal transmission for normal and oblique beam incidence between the transducer and the steel plate. The FEM approach is presented in Sect. 2.2.2, and describes the signal transmission for normal beam incidence between the transducer and the steel plate, due to the axisymmetric finite elements.

2.2.1 The hybrid FEM-ASM approach

The hybrid FEM-ASM approach is used to simulate the signal propagation through the system at an arbitary angle of beam incidence, but the angle is limited by the numerical capabilities of the simulation computer. The transducer's voltage-to-pressure response and the radiated free-field sound pressure field in water at the upper surface of the plate are simulated using the FEM. This FEM-simulated sound pressure field is further propagated through the plate and the surrounding fluid medium using the ASM, for given angles of orientation of the transducer with respect to the plate (angle of beam incidence), and for given receiver positions. The ASM models the propagation of an ultrasonic beam by representing the wave field as an integration over plane waves [100]. The method propagates a known pressure field

at a 2D reference plane $z = \text{const.}$ to another parallell plane in the frequency-wavenumber domain using the spatial Fourier transform, Eq. (2.6). Our ASM approach includes the plane-wave pressure transmission coefficient $\mathscr{T}$ to describe the propagation through the steel plate, Eqs. (2.7) or (2.104), and the plane wave propagator to propagate the transmitted pressure frequency-wavenumber spectrum $\mathbf{P}_1(h_{f,x}, h_{f,y}, z_0 + 2L, f)$ to the receiver depth, Eq. (2.8).

The signal propagation through the transducer and into the adjacent water region is described by the transducer's voltage-to-pressure transfer function

$$\frac{P_0(r', z', f)}{V(f)}, \tag{2.5}$$

where $P_0(r', z', f)$ is the free-field sound pressure frequency spectrum in the water radiated by the transducer. The coordinate relationship of Eq. (2.1) gives the relationship between the transducer's axisymmetric sound field and the 3D coordinate system (x, y, z), for a given angle of beam incidence, θ. Thus, the sound pressure as a function of (x, y, z) is calculated from the axisymmetric sound pressure, given as function of (r', z'), for a known angle θ. Interpolating $P_0(r', z', f)$, cf. Chap. 4 for detailed description of the interpolation, over the plane (x, y, z_0) gives $P_0(x, y, z_0, f)$ where $z_0 = \text{const.}$, which is the incident free-field sound pressure frequency spectrum in water at the upper surface of the steel plate when the plate is absent. $P_0(x, y, z_0, f)$ is transformed into the frequency-wavenumber domain by the 2D spatial Fourier transform [100] with respect to (x, y), giving

$$\mathbf{P}_0(h_{f,x}, h_{f,y}, z_0, f) = \iint_{-\infty}^{\infty} P_0(x, y, z_0, f) e^{i(h_{f,x}x + h_{f,y}y)} dx dy, \tag{2.6}$$

where $\mathbf{P}_0(h_{f,x}, h_{f,y}, z_0, f)$ is the incident free-field sound pressure frequency-wavenumber spectrum in water at the upper surface of the steel plate when the plate is absent.

The signal propagation through the steel plate is described by the plane-wave pressure transmission coefficient $\mathscr{T}$, given as [80, 98, 95]

$$\mathscr{T}(h_{f,x}, h_{f,y}, L, f) = \frac{\mathbf{P}_1(h_{f,x}, h_{f,y}, z_0 + 2L, f)}{\mathbf{P}_0(h_{f,x}, h_{f,y}, z_0, f)} = \frac{-iY(A + S)}{(S + iY)(A - iY)}, \tag{2.7}$$

where $\mathbf{P}_1(h_{f,x}, h_{f,y}, z_0 + 2L, f)$ is the transmitted pressure frequency-wavenumber spectrum in water at the lower surface of the steel plate, and S, A and Y are defined in Eqs. (2.49), (2.50) and (2.91) respectively[2]. The derivation of the plane-wave pressure transmission coefficient $\mathscr{T}$ is given in Sect. 2.4.3 as a function of horizontal wavenumber, derived from the Lamb and leaky Lamb dispersion equations given in Sects. 2.4.1 and 2.4.2, respectively. These relations are well known and have been derived by e.g. [27, 101, 102, 80]. In these and related works, the derivation is often incomplete (skips multiple derivations), formulated as a function of incident angle, or uses another time dependency. As the plane-wave pressure transmission coefficient is an important part of this thesis, a complete derivation

[2]Here, it is assumed that each plane-wave component of the 3D beam has no particle motion perpendicular to its direction.

as a function of horizontal wavenumber was deemed necessary.

The signal propagation through the lower adjacent water region to the receiver plane at depth z is described by the plane-wave propagator transfer function [100] as

$$\frac{\mathbf{P}_t(h_{f,x}, h_{f,y}, z, f)}{\mathbf{P}_1(h_{f,x}, h_{f,y}, z_0 + 2L, f)} = e^{-ih_{f,z}(z-(z_0+2L))}, \tag{2.8}$$

where $\mathbf{P}_t(h_{f,x}, h_{f,y}, z, f)$ is the transmitted sound pressure frequency-wavenumber spectrum at the receiver depth. This spectrum is transformed into the frequency-space domain by the inverse 2D spatial Fourier transform [100], giving

$$P_t(x, y, z, f) = \frac{1}{(2\pi)^2} \iint_{-\infty}^{\infty} \mathbf{P}_t(h_{f,x}, h_{f,y}, z, f) e^{-i(h_{f,x}x + h_{f,y}y)} dh_{f,x} dh_{f,y}, \tag{2.9}$$

where $P_t(x, y, z, f)$ is the transmitted sound pressure frequency spectrum at the receiver depth.

In the frequency-space domain, the total signal propagation through the transducer-water-plate system is then governed by the voltage-to-pressure transfer function

$$H_{VP}(x, y, z, f) = \frac{P_t(x, y, z, f)}{V(f)}, \qquad \text{for } z \geq z_1. \tag{2.10}$$

Finally, the transmitted pressure waveform, $p_t(x, y, z, t)$ at the receiver position (x, y, z), is given by the inverse temporal Fourier transform [99] as

$$p_t(x, y, z, t) = \int_{-\infty}^{\infty} P_t(x, y, z, f) e^{i2\pi ft} df, \tag{2.11}$$

$$= \mathscr{F}_t^{-1} \left[V_0(f) \cdot H_{VV}(f) \cdot H_{VP}(x, y, z, f) \right], \tag{2.12}$$

where $\mathscr{F}_t^{-1}$ denotes the inverse temporal Fourier transform in Eq. (2.11).

2.2.2 The FEM approach

The FEM approach is used to simulate the signal propagation through the measurement system using axisymmetric finite elements (due to limitations in computer capabilities), hence its limitation to normal beam incidence. For normal beam incidence to the plate, the 3D Cartesian coordinate system (x, y, z) which governs the steel plate and the lower adjacent water region is coincident with the cylindrical coordinate system (r', z'), and the cylindrical coordinate system is therefore used. The circular piezoelectric source transducer transmits an ultrasonic beam towards the steel plate, which is represented as a circular elastic plate with thickness $2L$ and radius R, cf. Sect. 2.3 regarding the modelling of infinite fluid and elastic regions. Using a frequency domain implementation (cf. Sect. 2.3), standing waves appear between the transducer and the upper surface of the steel plate. This standing wave pattern influences the voltage-to-pressure transfer function, preventing comparisons with measurements and the hybrid FEM-ASM approach. $P_t(x, y, z, f)_{cw}$[3] is simulated directly and used to

[3] Subscript *cw* (continuous waves) denotes that a standing wave pattern is present.

calculate $H_{VP}(x, y, z_2, f)_{cw}$ using Eq. (2.10). The temporal Fourier transform described in Eqs. (2.3) and (2.11) is used to enable separation of the first arrival and successive echoes in time. $p_t(x, y, z, t)$ is determined to be the first arrival, and $P_t(x, y, z, f)$ is determined from that waveform's steady state region using Fourier analysis. See Sect. 4.2 for a detailed description of this method.

2.2.3 Transfer function for simulated piston generated beams

A circular, baffled and uniformly vibrating piston model has been used in the literature [60, 68, 69, 70, 91, 92, 98, 93] to approximate the incident pressure field from a real transducer. By using such a simplified model, no information is available for the sound transmission through the transducer. For that reason $H_{VP}(x, y, z, f)$ can not be used for comparison of the FEM transducer and the baffled piston models. To enable such a comparison a pressure-to-pressure transfer function, which governs the signal propagation through the steel plate and water, is defined as

$$H_{PP}(x, y, z, f) = \frac{P_t(x, y, z, f)}{P_0(0, 0, z_0, f)\ |_{\theta=0^\circ}}, \tag{2.13}$$

where $P_0(x, y, z_0, f)|_{\theta=0^\circ}$ is the incident free-field sound pressure frequency spectrum in water at the upper surface of the steel plate when the plate is absent, for transducer or piston radiation at normal beam incidence, i.e. $\theta = 0^\circ$. Eq. (2.13) is defined similarly as in [91, 98, 93, 94]. This transfer function is used here to compare simulated piezoelectric transducer vs. piston-generated transmission of sound through the plate at normal and oblique angles of beam incidence. It is also used to measure the sound velocities in the plate using the method described in Sect. 3.3.

2.3 Finite element method (FEM)

The finite element (FE) equations for a piezoelectric structure vibrating in a fluid are presented for both K-form and H-form, by e.g. [103, 104, 105] as

$$-\omega^2 \begin{bmatrix} M_{uu} & 0 & 0 \\ 0 & 0 & 0 \\ 0 & 0 & -M_{\psi\psi} \end{bmatrix} \begin{Bmatrix} \hat{u} \\ \hat{\beta} \\ \hat{\psi} \end{Bmatrix} + i\omega \begin{Bmatrix} 0 & 0 & C_{u\psi} \\ 0 & 0 & 0 \\ C_{\psi u} & 0 & 0 \end{Bmatrix} \begin{Bmatrix} \hat{u} \\ \hat{\beta} \\ \hat{\psi} \end{Bmatrix} \begin{bmatrix} K_{uu} & K_{u\beta} & 0 \\ K_{\beta u} & K_{\beta\beta} & 0 \\ 0 & 0 & -K_{\psi\psi} \end{bmatrix} \begin{Bmatrix} \hat{u} \\ \hat{\beta} \\ \hat{\psi} \end{Bmatrix} = \begin{bmatrix} 0 \\ -Q \\ 0 \end{bmatrix}, \tag{2.14}$$

and

$$-\omega^2 \begin{bmatrix} M_{uu} & 0 & 0 \\ 0 & 0 & 0 \\ 0 & 0 & -M_{\psi\psi} \end{bmatrix} \begin{Bmatrix} \hat{u} \\ V \\ \hat{\psi} \end{Bmatrix} + i\omega \begin{Bmatrix} 0 & 0 & C_{u\psi} \\ 0 & 0 & 0 \\ C_{\psi u} & 0 & 0 \end{Bmatrix} \begin{Bmatrix} \hat{u} \\ V \\ \hat{\psi} \end{Bmatrix} \begin{bmatrix} H_{uu} & H_{u\beta} & 0 \\ H_{\beta u} & H_{\beta\beta} & 0 \\ 0 & 0 & -K_{\psi\psi} \end{bmatrix} \begin{Bmatrix} \hat{u} \\ V \\ \hat{\psi} \end{Bmatrix} = \begin{bmatrix} 0 \\ -I/(i\omega) \\ 0 \end{bmatrix}, \tag{2.15}$$

where the variables are defined in Tab. 2.1.

TABLE 2.1. Definition of the variables used in Eq. (2.14).

$[M_{uu}]$	global mass matrix
$[M_{\psi\psi}]$	global fluid mass matrix
$\{\hat{u}\}$	displacement vector
$\left\{\hat{\beta}\right\}$	electric potential vector
$\left\{\hat{\psi}\right\}$	velocity potential vector
$[C_{u\psi}]$	global fluid/structure coupling matrix
$[C_{\psi u}]$	global fluid/structure coupling matrix
$[K_{uu}]$	global stiffness matrix
$[K_{\beta u}]$	global piezoelectric stiffness matrix
$[K_{u\beta}]$	global piezoelectric stiffness matrix
$[K_{\beta\beta}]$	global dielectric stiffness matrix
$[K_{\psi\psi}]$	global fluid stiffness matrix
$\{Q\}$	global charge vector

The value of any variable A defined in each node of the structure is written as $\hat{A}$. The K-form gives the relations between the displacement, electrical potential, velocity potential and the electrical charge. The transition from K- to H-form is described in [103, 106]. H-form gives the relations between displacement, electrical voltage V, velocity potential, and the electrical current I. From Eq. (2.15) the equations for the velocity potential $\psi(r', z', f)$, sound pressure $P(r', z', f)$, electrical admittance $Y_T(f)$, source sensitivity $S_V(f)$ and beam pattern $D(f, \phi)$ are as following:

$$\{\hat{\psi}\} = -i\omega \left(-\left[K_{\psi\psi}\right] + \omega^2 \left[M_{\psi\psi}\right]\right)^{-1} \left[C_{\psi u}\right] \{\hat{u}\}, \tag{2.16}$$

$$P(r', z', f) = -i\omega\rho_f \psi(r', z', f), \tag{2.17}$$

$$Y_T(f) = i\omega \left[\{H_{u\beta}\}^T [D]^{-1} \{H_{u\beta}\} - H_{\beta\beta}\right], \tag{2.18}$$

where $[D] = [H_{uu}] - \omega^2 [M_{uu}] + \omega^2 [C_{u\psi}] \left(-\left[K_{\psi\psi}\right] + \omega^2 \left[M_{\psi\psi}\right]\right)^{-1} [C_{\psi u}]$,

$$S_V(f) = \frac{P(0, d = d_0 = 1\text{m}, f)}{V(f)}, \tag{2.19}$$

$$D(f, \phi) = \frac{P(r', d, f)}{P(0, d, f)}, \tag{2.20}$$

where ρ_f is the density of the fluid, d_0 and d are distances from the front surface of the transducer to the sound pressure $P(r', z', f)$, assuming far field conditions at these distances.

The 3D finite element model used in the present thesis is the FEMP 5.0 program (runs on MATLAB), which is a frequency domain implementation [103, 106, 107, 108, 109] developed in a cooperation between the University of Bergen and Christian Michelsen Research. This program has seen extensive

use, and has been successfully compared to measurement results, e.g. [18, 110, 111, 112, 113, 114, 115], and other FEM codes such as ABAQUS and ANSYS [103]. The losses in the piezoelectric and elastic regions are represented by the imaginary parts of the complex constants as used in [116], see the discussion on material data in Sect. 5.2.1. Lossless fluid is assumed. For an axisymmetric simulation this implementation uses 8 node isoparametric finite elements for both the fluid, elastic and piezoelectric regions [103]. For modeling infinite fluid regions infinite elements [103] or perfectly matched layers (PMLs) [108, 117, 118, 119] can be used. The PML method can be interpreted as a coordinate streching in the frequency domain through a complex change of variables. In the direction x, where x denotes either r' or z', the coordinate transformation is

$$\frac{\partial}{\partial x} \rightarrow \frac{\partial}{\partial x`} = \frac{1}{\gamma_x}\frac{\partial}{\partial x}, \tag{2.21}$$

where γ_x is defined by

$$\gamma_x = 1 + \frac{i}{\omega}\sigma_x(x) \qquad , x \geq x^* \tag{2.22}$$

$$\gamma_x = 1 \qquad , x < x^*. \tag{2.23}$$

The damping function σ used in this thesis is an 'optimal' damping function introduced by [118]

$$\sigma = \frac{c_l}{x^* - x}, \tag{2.24}$$

where x^* is truncation of the normal fluid region in the x direction, and c_f is the compressional sound velocity in the fluid. In the FE implementation used, there is no possibility for having frequency dependent mass- and stiffness matrices [108]. In order to get rid of the frequency dependency in Eq. (2.22) a σ^* is defined as $\sigma^* = \sigma\omega/\omega_0$ [108] and used for σ_x

$$\gamma_x = 1 + \frac{i}{\omega_0}\sigma(x) \qquad , x \geq x^*. \tag{2.25}$$

For modelling an infinite elastic medium without end reflections (such as for the plate) a "decreasing Q_M" method [108, 112] has been employed here, because PML for an elastic region have not been implemented yet for the current version of FEMP 5. This "decreasing Q_M" method reduce the loss factor Q_M exponentially inside a region of an elastic medium to approximately zero, thus reducing the reflections from the endfaces of that region. Use of this method forces the losses associated with the compressional and shear waves in the plate to be equal.

2.4 Plane waves in layered media

Planes waves in layered elastic media have been formulated and derived by many, e.g [15, 27, 101, 120, 121] etc. The Lamb modes for a vacuum-embedded elastic plate are formulated in Sect. 2.4.1, and extended to account for fluid loading in Sect. 2.4.2, where the leaky Lamb modes for a fluid-embedded plate are given. The plane-wave pressure transmission and reflection coefficients for a single-fluid immersed elastic plate are derived in Sect. 2.4.3.

In the derivation that follows it is assumed that the plate is infinite in both $x-$ and $y-$directions, and a Cartesian coordinate system (x, z) is chosen. The components of the particle motion are confined to these directions, and it is assumed that no Lamb modes have particle motion in the $y-$direction, thus SH-modes (shear-horizontal) are excluded, this is consistent with e.g. [16, 58, 60, 70, 90, 120]. The thickness of the elastic plate is $2L$. In this section, for the sake of simplicity in the derivation, the plate is centered around $z = 0$.

2.4.1 Lamb modes in a vacuum-embedded plate

The derivation of the symmetrical and anti-symmetrical Lamb modes in a vacuum-embedded elastic plate follows [90], but there a time dependency of $e^{-i\omega t}$ is used. The linearized displacement equation of motion for an isotropic elastic, homogeneous, solid medium is given as

$$(\lambda_S + 2\mu_S)\nabla(\nabla \cdot \underline{u}) - \mu_S \left[\nabla \times (\nabla \times \underline{u})\right] = \rho_S \frac{\partial^2 \underline{u}}{\partial t^2}, \tag{2.26}$$

where $\underline{u}$ is the the displacement, λ_S and μ_S are the Láme parameters, ρ_S is the density of the medium and t is time [16]. Eq. (2.26) can be decomposed into two expressions by introducing longitudinal and shear wave velocities [16]. By the Helmholtz decomposition, the displacement vector can be expressed by a scalar potential, Φ, and a vector potential, $\underline{\Psi}$, i.e. $\underline{u} = \nabla\Phi + \nabla \times \underline{\Psi}$. This yields the two equations [16],

$$\left(\nabla^2 - \frac{1}{c_L^2}\frac{\partial^2}{\partial t^2}\right)\Phi = 0, \qquad \text{and} \qquad \left(\nabla^2 - \frac{1}{c_S^2}\frac{\partial^2}{\partial t^2}\right)\underline{\Psi} = 0, \tag{2.27}$$

for longitudinal and shear waves respectively. The longitudinal and shear wave velocities, c_L and c_S, in a solid medium are defined as

$$c_L = \sqrt{\frac{\lambda_S + 2\mu_S}{\rho_S}}, \qquad \text{and} \qquad c_S = \sqrt{\frac{\mu_S}{\rho_S}}, \tag{2.28}$$

respectively. The horizontal and vertical displacements, u_x and u_z, and the normal and shear stresses, T_{zz} and T_{xz}, for an elastic medium are given in [16] Eqs. (2.29) and (2.30). Without loss of generality, the waves can propagate in the $x-$direction, making Φ and Ψ independent from y, thus $\frac{\partial}{\partial y} = 0$.

$$u_x = \frac{\partial\Phi}{\partial x} + \frac{\partial\Psi_z}{\partial y} - \frac{\partial\Psi_y}{\partial z}, \qquad u_z = \frac{\partial\Phi}{\partial z} + \frac{\partial\Psi_y}{\partial x} - \frac{\partial\Psi_x}{\partial y}, \tag{2.29}$$

$$T_{zz} = (\lambda_S + 2\mu_S)\left(\frac{\partial u_z}{\partial z}\right) + \lambda_S\left(\frac{\partial u_x}{\partial x} + \frac{\partial u_y}{\partial y}\right), \qquad T_{xz} = \mu_S\left(\frac{\partial u_x}{\partial z} + \frac{\partial u_z}{\partial x}\right), \tag{2.30}$$

respectively. By separation of variables, the solution for the scalar and vector potential are then given as

$$\Phi = \left(A_2^- e^{ih_z z} + A_2^+ e^{-ih_z z}\right) e^{i(\omega t - \eta x)} \qquad \text{and} \qquad \Psi_y = \left(B_2^- e^{ik_z z} + B_2^+ e^{-ik_z z}\right) e^{i(\omega t - \eta x)}. \tag{2.31}$$

The amplitudes A_2^+ and B_2^+ represent longitudinal and shear waves propagating in the positive z-direction, and the amplitudes A_2^- and B_2^- represent longitudinal and shear waves propagating in the

negative z-direction, as shown in Fig. 2.2. Subscript 2 indicate layer (2). The wavenumbers for the longitudinal and shear waves are given as $h = \omega/c_L$ and $k = \omega/c_S$, respectively.

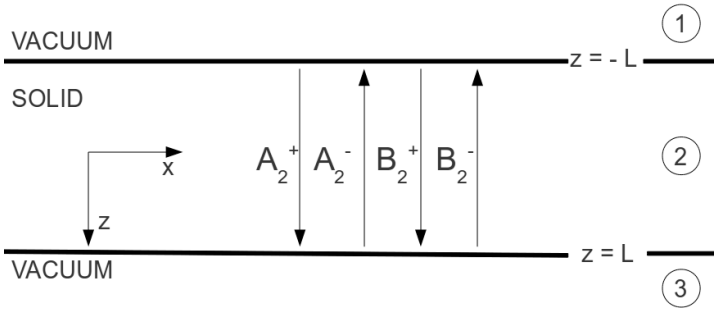

Fig 2.2. An elastic plate with thickness $2L$ in vacuum. y is directed out of the paper.

The boundary conditions for an isotropic elastic plate in vacuum are zero normal and shear stresses at the surfaces, given as

$$T_{zz} = 0 \text{ at } z = \pm L, \tag{2.32}$$

$$T_{xz} = 0 \text{ at } z = \pm L, \tag{2.33}$$

respectively. The vertical wavenumbers for longitudinal and shear waves, h_z and k_z, and the horizontal wavenumber η, in Eq. (2.31) are defined as (including evanescent waves) [100]

$$h_z = \begin{cases} \sqrt{h^2 - \eta^2} \text{ for } \eta \leq h \\ i\sqrt{\eta^2 - h^2} \text{ for } \eta > h \end{cases}, \tag{2.34}$$

$$k_z = \begin{cases} \sqrt{k^2 - \eta^2} \text{ for } \eta \leq k \\ i\sqrt{\eta^2 - k^2} \text{ for } \eta > k \end{cases}. \tag{2.35}$$

Derived from the boundary conditions, the two waves must have the same phase velocity on the surfaces, giving $\eta = h_x = k_x$ when $h_y = k_y = 0$, i.e.

$$\eta = \sqrt{h_x^2 + h_y^2} = \sqrt{k_x^2 + k_y^2} \Rightarrow \eta = h_x = k_x. \tag{2.36}$$

The horizontal phase velocity c_{ph} in the plate is given as

$$c_{ph} = \frac{\omega}{\eta}, \tag{2.37}$$

which represents the phase velocity for the waves in the plate in the $x-$direction. From now on, the term $e^{i(\omega t - \eta x)}$ is suppressed [16]. By introducing trigonometric functions, Eq. (2.31) can be formulated as

$$\Phi = \left[A_{2,1}\cos(h_z z) + iA_{2,2}\sin(h_z z)\right], \qquad \Psi_y = \left[B_{2,1}\cos(k_z z) + iB_{2,2}\sin(k_z z)\right], \tag{2.38}$$

where $A_{2,1} = A_2^+ + A_2^-$, $A_{2,2} = -A_2^+ + A_2^-$, $B_{2,1} = B_2^+ + B_2^-$ and $B_{2,2} = -B_2^+ + B_2^-$.

The displacements and stresses can be obtained by using Eq. (2.38) and Eqs. (2.29-2.30) giving

$$u_x = -i\eta \left[A_{2,1}\cos(h_z z) + iA_{2,2}\sin(h_z z)\right] + k_z \left[B_{2,1}\sin(k_z z) - iB_{2,2}\cos(k_z z)\right] \tag{2.39}$$

$$u_z = -h_z \left[A_{2,1}\sin(h_z z) - iA_{2,2}\cos(h_z z)\right] - i\eta \left[B_{2,1}\cos(k_z z) + iB_{2,2}\sin(k_z z)\right] \tag{2.40}$$

$$\begin{aligned} T_{zz} &= \lambda_S \left[-\eta^2\{A_{2,1}\cos(h_z z) + iA_{2,2}\sin(h_z z)\} - i\eta k_z\{B_{2,1}\sin(k_z z) - iB_{2,2}\cos(k_z z)\}\right] \\ &\quad + (\lambda_S + 2\mu_S)\left[-h_z^2\{A_{2,1}\cos(h_z z) + iA_{2,2}\sin(h_z z)\} + i\eta k_z\{B_{2,1}\sin(k_z z) - iB_{2,2}\cos(k_z z)\}\right] \\ &= \left[A_{2,1}\cos(h_z z) + iA_{2,2}\sin(h_z z)\right](-\eta^2\lambda_S - h_z^2(\lambda_S + 2\mu_S)) \\ &\quad + \left[B_{2,1}\sin(k_z z) - iB_{2,2}\cos(k_z z)\right](-i\eta k_z\lambda_S + i\eta k_z(\lambda_S + 2\mu_S)) \\ &= \mu_S(2\eta^2 - k^2)\left[A_{2,1}\cos(h_z z)) + iA_{2,2}\sin(h_z z)\right] + i2\mu_S\eta k_z\left[B_{2,1}\sin(k_z z) - iB_{2,2}\cos(k_z z)\right] \end{aligned} \tag{2.41}$$

$$\begin{aligned} T_{xz} &= \mu_S[i\eta h_z\{A_{2,1}\sin(h_z z) - iA_{2,2}\cos(h_z z)\} + k_z^2\{B_{2,1}\cos(k_z z) + iB_{2,2}\sin(k_z z)\} \\ &\quad + ih_z\eta\{A_{2,1}\sin(h_z z) - iA_{2,2}\cos(h_z z)\} - \eta^2\{B_{2,1}\cos(k_z z) + iB_{2,2}\sin(k_z z)\}] \\ &= i2\mu_S\eta h_z\left[A_{2,1}\sin(h_z z) - iA_{2,2}\cos(hz_z)\right] - \mu_S(2\eta^2 - k^2)\left[B_{2,1}\cos(k_z z) + iB_{2,2}\sin(k_z z)\right] \end{aligned} \tag{2.42}$$

Using the boundary conditions at $z = \pm L$ in Eqs. (2.41) and (2.42) gives

$$\begin{bmatrix} T_{zz}(L) \\ T_{xz}(L) \\ T_{zz}(-L) \\ T_{xz}(-L) \end{bmatrix} = \begin{bmatrix} \cos(h_z L) & \frac{2\eta k_z}{(2\eta^2-k^2)}\cos(k_z L) & i\sin(h_z L) & \frac{i2\eta k_z}{(2\eta^2-k^2)}\sin(k_z L) \\ \frac{i2\eta h_z}{(2\eta^2-k^2)}\sin(h_z L) & -i\sin(k_z L) & \frac{2\eta h_z}{(2\eta^2-k^2)}\cos(h_z L) & -\cos(k_z L) \\ \cos(h_z L) & \frac{2\eta k_z}{(2\eta^2-k^2)}\cos(k_z L) & -i\sin(h_z L) & \frac{-i2\eta k_z}{(2\eta^2-k^2)}\sin(k_z L) \\ \frac{-i2\eta h_z}{(2\eta^2-k^2)}\sin(h_z L) & i\sin(k_z L) & \frac{2\eta h_z}{(2\eta^2-k^2)}\cos(h_z L) & -\cos(k_z L) \end{bmatrix} \begin{bmatrix} A_{2,1} \\ B_{2,2} \\ A_{2,2} \\ B_{2,1} \end{bmatrix} = \begin{bmatrix} 0 \\ 0 \\ 0 \\ 0 \end{bmatrix} \tag{2.43}$$

By Gaussian elimination, adding -1 times row 1 to row 3 and dividing by 2, adding +1 times row 2 to row 4 and dividing by 2, then adding +1 times row 3 to row 1 and -1 times row 4 to row 2, gives the matrix

$$\begin{bmatrix} \cos(h_z L) & \frac{2\eta k_z}{(2\eta^2-k^2)}\cos(k_z L) & 0 & 0 \\ \frac{i2\eta h_z}{(2\eta^2-k^2)}\sin(h_z L) & -i\sin(k_z L) & 0 & 0 \\ 0 & 0 & -i\sin(h_z L) & \frac{-i2\eta k_z}{(2\eta^2-k^2)}\sin(k_z L) \\ 0 & 0 & \frac{2\eta h_z}{(2\eta^2-k^2)}\cos(h_z L) & -\cos(k_z L) \end{bmatrix}. \tag{2.44}$$

Setting the determinant of this matrix to zero gives the dispersion relations for symmetric and anti-symmetric Lamb modes for a solid plate in vacuum. The determinant of this matrix is zero if one or both of Eqs. (2.45) and (2.46) are zero

$$-i\cos(h_z L)\sin(k_z L) - \frac{i4\eta^2 h_z k_z}{(2\eta^2 - k^2)^2}\cos(k_z L)\sin(h_z L) = 0, \tag{2.45}$$

$$i\sin(h_z L)\cos(k_z L) + \frac{i4\eta^2 h_z k_z}{(2\eta^2 - k^2)^2}\cos(h_z L)\sin(k_z L) = 0, \tag{2.46}$$

defining the symmetric and antisymmetric Lamb modes for a vacuum-embedded elastic plate, e.g. [15, 120], as

$$\text{Symmetric: } \frac{-4\eta^2 h_z k_z}{(2\eta^2 - k^2)^2} = \frac{\tan(k_z L)}{\tan(h_z L)}, \tag{2.47}$$

$$\text{Anti-symmetric: } \frac{-4\eta^2 h_z k_z}{(2\eta^2 - k^2)^2} = \frac{\tan(h_z L)}{\tan(k_z L)}. \tag{2.48}$$

For later use one introduces the Lamb characteristic functions for the symmetric (S) and antisymmetric (A) plate modes as

$$S = (2\eta^2 - k^2)^2 \frac{1}{\tan(h_z L)} + 4\eta^2 h_z k_z \frac{1}{\tan(k_z L)}, \tag{2.49}$$

$$A = (2\eta^2 - k^2)^2 \tan(h_z L) + 4\eta^2 h_z k_z \tan(k_z L). \tag{2.50}$$

2.4.1.1 Cut-off frequencies

For certain frequencies standing compressional and shear waves are present across the thickness of the plate [92, 120]. These frequencies occur when the phase velocity of the generated Lamb waves approach infinity [122], and can be calculated letting the horizontal wavenumber η approach zero [90, 92, 122]. Letting the horizontal wavenumber approach zero in Eqs. (2.47) and (2.48) gives

$$\text{Symmetric: } \frac{\tan(kL)}{\tan(hL)} = 0, \tag{2.51}$$

$$\text{Anti-symmetric: } \frac{\tan(hL)}{\tan(kL)} = 0. \tag{2.52}$$

These equations are zero if the numerator becomes zero, or the denominator becomes infinity. For Eqs. (2.51) and (2.52) this happens when

$$\lim_{x \to n\pi} \tan(x) = 0 \text{ or } \lim_{x \to \frac{n\pi}{2}} \tan(x) = \infty, \tag{2.53}$$

where $x = hL$ or $x = kL$ and $n = 1, 2, 3...$. The cut-off frequencies for symmetric Lamb modes from Eq. (2.51) are given as

$$f_{tn}^S = \frac{2nc_S}{4L}, n = 1, 2, 3, ... \text{ and } f_{ln}^S = \frac{(2n-1)c_L}{4L}, n = 1, 2, 3, ..., \tag{2.54}$$

where f_{tn}^S and f_{ln}^S are the corresponding frequencies for the symmetrical TS (thickness-shear) and TE (thickness-extensional) modes respectively. The cut-off frequencies for anti-symmetric Lamb modes from Eq. (2.52) are given as

$$f_{ln}^A = \frac{2nc_L}{4L}, n = 1, 2, 3, ... \text{ and } f_{tn}^A = \frac{(2n-1)c_S}{4L}, m = 1, 2, 3, ..., \tag{2.55}$$

where f_{ln}^A and f_{tn}^A are the corresponding frequencies for the antisymmetrical TE and TS modes respectively.

2.4.2 Leaky Lamb modes in a fluid-embedded plate

[4]If the plate is immersed in a single fluid with compressional sound velocity c_f, and wavenumber $h_f = \omega/c_f$, the guided waves inside the plate can leak energy into the surrounding fluid. Such waves are named leaky Lamb waves. This means that longitudinal waves in the fluid are generated when guided waves propagates inside the plate, see Fig. 2.3. In the upper semi-infinite fluid half-space (layer (1)) there exists an applied incident plane wave A_1^+, coming from $z = -\infty$, and one reflected plane wave A_1^-, propagating towards $z = -\infty$. In the lower semi-infinite fluid half-space (layer (3)) one transmitted plane wave A_3^+ is propagating towards $z = \infty$. The sound pressure in the fluid layers (1) and (3) can be written as (where subscript denotes layer no.)

$$\Phi_1 = A_1^+ e^{-ih_{f,z}z} + A_1^- e^{ih_{f,z}z}. \tag{2.56}$$

$$\Phi_3 = A_3^+ e^{-ih_{f,z}z}, \tag{2.57}$$

respectively [27, 90].

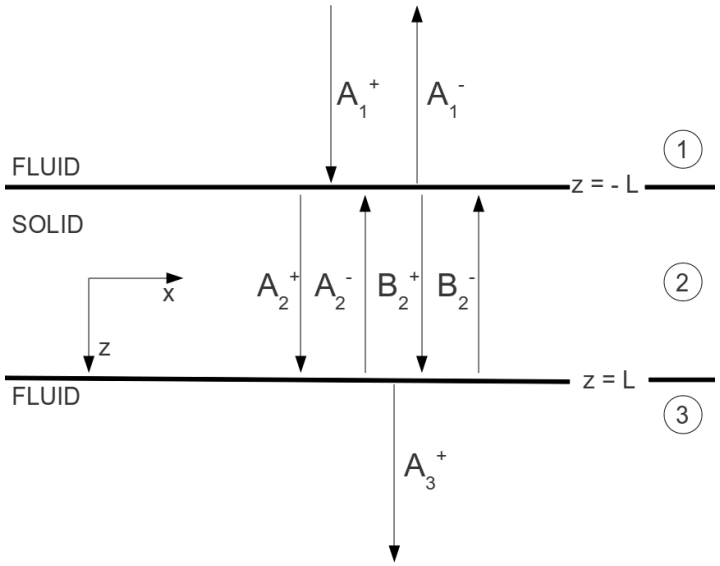

Fig 2.3. An elastic plate with thickness $2L$ immersed in a single fluid. y is directed out of the paper.

The boundary conditions for an infinite isotropic plate fully immersed in a single fluid are continuity of normal displacement u_z, normal stress T_{zz} and vanishing shear stress T_{xz}, given as [90]

$$u_{z,n} = u_{z,n+1} \text{ at } z = \pm L, \tag{2.58}$$

$$T_{zz,n} = T_{zz,n+1} \text{ at } z = \pm L, \tag{2.59}$$

$$T_{xz} = 0 \text{ at } z = \pm L, \tag{2.60}$$

[4]This derivation continues from Sect. 2.4.1 and follows [90] until Tab. (2.73), the matrix calculations thereafter have been made independently.

where n denotes layer no. The vertical wavenumber for the fluid is defined as

$$h_{f,z} = \begin{cases} \sqrt{h_f^2 - \eta^2} \text{ for } \eta \leq \omega/c_f \\ i\sqrt{\eta^2 - h_f^2} \text{ for } \eta > \omega/c_f. \end{cases} \tag{2.61}$$

The horizontal/normal displacement and normal stress in the fluid layers ($n = 1, 3$) can now be calculated as

$$u_x = \frac{\partial \Phi}{\partial x} \qquad u_z = \frac{\partial \Phi}{\partial z} \tag{2.62}$$

$$T_{zz} = -p = \lambda_f \left(\frac{\partial u_x}{\partial x} + \frac{\partial u_z}{\partial z} \right), \tag{2.63}$$

where p is the sound pressure, $c_f = \sqrt{\frac{\lambda_f}{\rho_f}}$, λ_f is the Lamé parameter, and ρ_f is the fluid density.

For layer (1) in Fig. 2.3 this gives

$$u_z = -ih_{f,z} \left[A_1^+ e^{-ih_{f,z}z} - A_1^- e^{ih_{f,z}z} \right], \tag{2.64}$$

$$T_{zz} = -p = -\rho_f \omega^2 \left[A_1^+ e^{-ih_{f,z}z} + A_1^- e^{ih_{f,z}z} \right]. \tag{2.65}$$

For layer (3) in Fig. 2.3 this gives

$$u_z = -ih_{f,z} A_3^+ e^{-ih_{f,z}z}, \tag{2.66}$$

$$\begin{aligned} T_{zz} = -p &= \lambda_f (0 - h_{f,z}^2 A_3^+ e^{-ih_{f,z}z}) \\ &= -\rho_f \omega^2 A_3^+ e^{-ih_{f,z}z}. \end{aligned} \tag{2.67}$$

Using the boundary conditions at $z = \pm L$, combining Eqs. (2.40) and (2.41) and the above equations, gives the displacement u_z and T_{zz} as

$$\begin{aligned} u_z(L) = &-h_z \left[A_{2,1} \sin(h_z L) - iA_{2,2} \cos(h_z L) \right] - i\eta \left[B_{2,1} \cos(k_z L) + iB_{2,2} \sin(k_z L) \right] \\ &+ ih_{f,z} A_3^+ e^{-ih_{f,z}L} = 0, \end{aligned} \tag{2.68}$$

$$\begin{aligned} u_z(-L) = &-h_z \left[-A_{2,1} \sin(h_z L) - iA_{2,2} \cos(h_z L) \right] - i\eta \left[B_{2,1} \cos(k_z L) - iB_{2,2} \sin(k_z L) \right] \\ &- ih_{f,z} A_1^- e^{-ih_{f,z}L} + ih_{f,z} A_1^+ e^{ih_{f,z}L} = 0, \end{aligned} \tag{2.69}$$

$$\begin{aligned} T_{zz}(L) = &\mu_S (2\eta^2 - k^2) \left[A_{2,1} \cos(h_z L) + iA_{2,2} \sin(h_z L) \right] + i2\mu_S \eta k_z \left[B_{2,1} \sin(k_z L) - iB_{2,2} \cos(k_z L) \right] \\ &+ \rho_f \omega^2 A_3^+ e^{-ih_{f,z}L} = 0, \end{aligned} \tag{2.70}$$

$$\begin{aligned} T_{zz}(-L) = &\mu_S (2\eta^2 - k^2) \left[A_{2,1} \cos(h_z L) - iA_{2,2} \sin(h_z L) \right] + i2\mu_S \eta k_z \left[-B_{2,1} \sin(k_z L) - iB_{2,2} \cos(k_z L) \right] \\ &+ \rho_f \omega^2 A_1^- e^{-ih_{f,z}L} + \rho_f \omega^2 A_1^+ e^{ih_{f,z}L} = 0, \end{aligned} \tag{2.71}$$

where T_{xz} at $z = \pm L$ is given in Eqs. (2.41) and (2.42). Arranging these equations into a matrix as

$$\begin{bmatrix} u_z(-L) \\ T_{zz}(-L) \\ T_{xz}(-L) \\ u_z(L) \\ T_{zz}(L) \\ T_{xz}(L) \end{bmatrix} \begin{bmatrix} -a_{11} & a_{12} & -a_{13} & a_{14} & -a_{15} & 0 \\ a_{21} & a_{22} & -a_{23} & a_{24} & -a_{25} & 0 \\ 0 & a_{32} & -a_{33} & a_{34} & -a_{35} & 0 \\ 0 & -a_{12} & a_{13} & a_{14} & -a_{15} & a_{16} \\ 0 & a_{22} & -a_{23} & -a_{24} & a_{25} & a_{26} \\ 0 & -a_{32} & a_{33} & a_{34} & -a_{35} & 0 \end{bmatrix} \begin{bmatrix} A_1^- \\ A_{2,1} \\ B_{2,2} \\ A_{2,2} \\ B_{2,1} \\ A_3^+ \end{bmatrix} = \begin{bmatrix} -ih_{f,z}A_1^+ e^{ih_{f,z}L} \\ -\rho_f\omega^2 A_1^+ e^{ih_{f,z}L} \\ 0 \\ 0 \\ 0 \\ 0 \end{bmatrix}, \tag{2.72}$$

where the constants are defined as

$$\begin{aligned} a_{11} &= ih_{f,z}e^{-ih_{f,z}L} & a_{24} &= -i\mu_S(2\eta^2 - k^2)\sin(h_zL) \\ a_{12} &= h_z\sin(h_zL) & a_{25} &= i2\mu_S\eta k_z\sin(k_zL) \\ a_{13} &= \eta\sin(k_zL) & a_{32} &= -i2\eta h_z\sin(h_zL) \\ a_{14} &= ih_z\cos(h_zL) & a_{33} &= -i(2\eta^2 - k^2)\sin(k_zL) \\ a_{15} &= i\eta\cos(k_zL) & a_{34} &= 2\eta h_z\cos(h_zL) \\ a_{21} &= \rho_f\omega^2 e^{-ih_{f,z}L} & a_{35} &= (2\eta^2 - k^2)\cos(k_zL) \\ a_{22} &= \mu_S(2\eta^2 - k^2)\cos(h_zL) & a_{16} &= ih_{f,z}e^{-ih_{f,z}L} \\ a_{23} &= -2\mu_S\eta k_z\cos(k_zL) & a_{26} &= \rho_f\omega^2 e^{-ih_{f,z}L}. \end{aligned} \tag{2.73}$$

This is in agreement with [90], although appropriate signs due to the chosen time dependency are different. The 6×6 matrix in Eq. (2.72) is now denoted **A**. Dispersion relations for symmetric and antisymmetric leaky Lamb waves can be found setting the determinant of this matrix to zero. The determinant of this 6×6 matrix is calculated using the cofactor expansion, thus the determinant can be calculated by the weighted sum of the determinants of sub-matrices.

$$\det|\mathbf{A}| = -a_{11}\begin{vmatrix} a_{22} & -a_{23} & a_{24} & -a_{25} & 0 \\ a_{32} & -a_{33} & a_{34} & -a_{35} & 0 \\ -a_{12} & a_{13} & a_{14} & -a_{15} & a_{16} \\ a_{22} & -a_{23} & -a_{24} & a_{25} & a_{26} \\ -a_{32} & a_{33} & a_{34} & -a_{35} & 0 \end{vmatrix} - a_{21}\begin{vmatrix} a_{12} & -a_{13} & a_{14} & -a_{15} & 0 \\ a_{32} & -a_{33} & a_{34} & -a_{35} & 0 \\ -a_{12} & a_{13} & a_{14} & -a_{15} & a_{16} \\ a_{22} & -a_{23} & -a_{24} & a_{25} & a_{26} \\ -a_{32} & a_{33} & a_{34} & -a_{35} & 0 \end{vmatrix}. \tag{2.74}$$

From Tab. 2.73, identify $a_{16} = a_{11}$ and $a_{26} = a_{21}$ and further reduce these two 5×5 matrix determinants to four 4×4 matrix determinants as

$$\det|\mathbf{A}| = -a_{11}a_{11}\begin{vmatrix} a_{22} & -a_{23} & a_{24} & -a_{25} \\ a_{32} & -a_{33} & a_{34} & -a_{35} \\ a_{22} & -a_{23} & -a_{24} & a_{25} \\ -a_{32} & a_{33} & a_{34} & -a_{35} \end{vmatrix} + a_{11}a_{21}\begin{vmatrix} a_{22} & -a_{23} & a_{24} & -a_{25} \\ a_{32} & -a_{33} & a_{34} & -a_{35} \\ -a_{12} & a_{13} & a_{14} & -a_{15} \\ -a_{32} & a_{33} & a_{34} & -a_{35} \end{vmatrix}$$

$$-a_{21}a_{11}\begin{vmatrix} a_{12} & -a_{13} & a_{14} & -a_{15} \\ a_{32} & -a_{33} & a_{34} & -a_{35} \\ a_{22} & -a_{23} & -a_{24} & a_{25} \\ -a_{32} & a_{33} & a_{34} & -a_{35} \end{vmatrix} + a_{21}a_{21}\begin{vmatrix} a_{12} & -a_{13} & a_{14} & -a_{15} \\ a_{32} & -a_{33} & a_{34} & -a_{35} \\ -a_{12} & a_{13} & a_{14} & -a_{15} \\ -a_{32} & a_{33} & a_{34} & -a_{35} \end{vmatrix}. \tag{2.75}$$

Denote these four 4×4 matrix determinants as $\boxed{1}$, $\boxed{2}$, $\boxed{3}$ and $\boxed{4}$ respectively, writing Eq. (2.75) as

$$\det|\mathbf{A}| = -a_{11}^2\boxed{1} + a_{11}a_{21}\boxed{2} - a_{21}a_{11}\boxed{3} + a_{21}^2\boxed{4}. \tag{2.76}$$

Calculating now the determinant of each of these four matrix determinants:

$\boxed{1}$:

$$\begin{aligned}
\begin{vmatrix} a_{22} & -a_{23} & a_{24} & -a_{25} \\ a_{32} & -a_{33} & a_{34} & -a_{35} \\ a_{22} & -a_{23} & -a_{24} & a_{25} \\ -a_{32} & a_{33} & a_{34} & -a_{35} \end{vmatrix} &= a_{22}\begin{vmatrix} -a_{33} & a_{34} & -a_{35} \\ -a_{23} & -a_{24} & a_{25} \\ a_{33} & a_{34} & -a_{35} \end{vmatrix} - (-a_{23})\begin{vmatrix} a_{32} & a_{34} & -a_{35} \\ a_{22} & -a_{24} & a_{25} \\ -a_{32} & a_{34} & -a_{35} \end{vmatrix} \\
&\quad + a_{24}\begin{vmatrix} a_{32} & -a_{33} & -a_{35} \\ a_{22} & -a_{23} & a_{25} \\ -a_{32} & a_{33} & -a_{35} \end{vmatrix} - (-a_{25})\begin{vmatrix} a_{32} & -a_{33} & a_{34} \\ a_{22} & -a_{23} & -a_{24} \\ -a_{32} & a_{33} & a_{34} \end{vmatrix} \\
&= a_{22}\left[-a_{33}(a_{24}a_{35} - a_{25}a_{34}) - a_{34}(a_{23}a_{35} - a_{33}a_{25}) - a_{35}(-a_{23}a_{34} + a_{33}a_{24})\right] \\
&\quad + a_{23}\left[a_{32}(a_{24}a_{35} - a_{34}a_{25}) - a_{34}(a_{22}(-a_{35}) + a_{32}a_{25}) - a_{35}(a_{22}a_{34} - a_{32}a_{24})\right] \\
&\quad + a_{24}\left[a_{32}(a_{23}a_{35} - a_{33}a_{25}) + a_{33}(a_{22}(-a_{35}) + a_{25}a_{32}) - a_{35}(a_{22}a_{33} - a_{32}a_{23})\right] \\
&\quad + a_{25}\left[a_{32}(-a_{23}a_{34} + a_{33}a_{24}) + a_{33}(a_{22}a_{34} - a_{24}a_{32}) + a_{34}(a_{22}a_{33} - a_{32}a_{23})\right] \\
&= 4(a_{22}a_{33}a_{25}a_{34} + a_{23}a_{32}a_{24}a_{35} - a_{22}a_{33}a_{24}a_{35} - a_{25}a_{32}a_{23}a_{34})
\end{aligned} \tag{2.77}$$

$\boxed{2}$:

$$\begin{vmatrix} a_{22} & -a_{23} & a_{24} & -a_{25} \\ a_{32} & -a_{33} & a_{34} & -a_{35} \\ -a_{12} & a_{13} & a_{14} & -a_{15} \\ -a_{32} & a_{33} & a_{34} & -a_{35} \end{vmatrix} = a_{22} \begin{vmatrix} -a_{33} & a_{34} & -a_{35} \\ a_{13} & a_{14} & -a_{15} \\ a_{33} & a_{34} & -a_{35} \end{vmatrix} - (-a_{23}) \begin{vmatrix} a_{32} & a_{34} & -a_{35} \\ -a_{12} & a_{14} & -a_{15} \\ -a_{32} & a_{34} & -a_{35} \end{vmatrix}$$
$$+a_{24} \begin{vmatrix} a_{32} & -a_{33} & -a_{35} \\ -a_{12} & a_{13} & -a_{15} \\ -a_{32} & a_{33} & -a_{35} \end{vmatrix} - (-a_{25}) \begin{vmatrix} a_{32} & -a_{33} & a_{34} \\ -a_{12} & a_{13} & a_{14} \\ -a_{32} & a_{33} & a_{34} \end{vmatrix}$$
$$\begin{aligned} &= a_{22}\left[-a_{33}(a_{14}(-a_{35}) + a_{15}a_{34}) - a_{34}(a_{13}(-a_{35}) + a_{33}a_{15}) - a_{35}(a_{13}a_{34} - a_{33}a_{14})\right] \\ &\quad + a_{23}\left[a_{32}(a_{14}(-a_{35}) + a_{34}a_{15}) - a_{34}(a_{12}a_{35} - a_{32}a_{15}) - a_{35}(-a_{12}a_{34} + a_{32}a_{14})\right] \\ &\quad + a_{24}\left[a_{32}(a_{13}(-a_{35}) + a_{33}a_{15}) + a_{33}(a_{12}a_{35} - a_{15}a_{32}) - a_{35}(-a_{12}a_{33} + a_{32}a_{13})\right] \\ &\quad + a_{25}\left[a_{32}(a_{13}a_{34} - a_{33}a_{14}) + a_{33}(-a_{12}a_{34} + a_{14}a_{32}) + a_{34}(-a_{12}a_{33} + a_{32}a_{13})\right] \\ &= 2(a_{22}a_{33}a_{14}a_{35} - a_{22}a_{33}a_{15}a_{34} - a_{23}a_{32}a_{14}a_{35} + a_{23}a_{32}a_{34}a_{15} \\ &\quad - a_{24}a_{32}a_{13}a_{35} + a_{24}a_{33}a_{12}a_{35} + a_{25}a_{32}a_{13}a_{34} - a_{25}a_{33}a_{12}a_{34}) \end{aligned} \tag{2.78}$$

$\boxed{3}$:

$$\begin{vmatrix} a_{12} & -a_{13} & a_{14} & -a_{15} \\ a_{32} & -a_{33} & a_{34} & -a_{35} \\ a_{22} & -a_{23} & -a_{24} & a_{25} \\ -a_{32} & a_{33} & a_{34} & -a_{35} \end{vmatrix} = a_{12} \begin{vmatrix} -a_{33} & a_{34} & -a_{35} \\ -a_{23} & -a_{24} & a_{25} \\ a_{33} & a_{34} & -a_{35} \end{vmatrix} + a_{13} \begin{vmatrix} a_{32} & a_{34} & -a_{35} \\ a_{22} & -a_{24} & a_{25} \\ -a_{32} & a_{34} & -a_{35} \end{vmatrix}$$
$$+a_{14} \begin{vmatrix} a_{32} & -a_{33} & -a_{35} \\ a_{22} & -a_{23} & a_{25} \\ -a_{32} & a_{33} & -a_{35} \end{vmatrix} + a_{15} \begin{vmatrix} a_{32} & -a_{33} & a_{34} \\ a_{22} & -a_{23} & -a_{24} \\ -a_{32} & a_{33} & a_{34} \end{vmatrix}$$
$$\begin{aligned} &= a_{12}\left[-a_{33}(a_{24}a_{35} - a_{25}a_{34}) - a_{34}(a_{23}a_{35} - a_{33}a_{25}) - a_{35}(-a_{23}a_{34} + a_{33}a_{24})\right] \\ &\quad + a_{13}\left[a_{32}(a_{24}a_{35} - a_{34}a_{25}) - a_{34}(a_{22}(-a_{35}) + a_{32}a_{25}) - a_{35}(a_{22}a_{34} - a_{32}a_{24})\right] \\ &\quad + a_{14}\left[a_{32}(a_{23}a_{35} - a_{33}a_{25}) + a_{33}(-a_{22}a_{35} + a_{25}a_{32}) - a_{35}(a_{22}a_{33} - a_{32}a_{23})\right] \\ &\quad + a_{15}\left[a_{32}(-a_{23}a_{34} + a_{33}a_{24}) + a_{33}(a_{22}a_{34} - a_{24}a_{32}) + a_{34}(a_{22}a_{33} - a_{32}a_{23})\right] \\ &= 2(a_{12}a_{33}a_{25}a_{34} + a_{13}a_{32}a_{24}a_{35} - a_{13}a_{32}a_{34}a_{25} - a_{14}a_{33}a_{35}a_{22} \\ &\quad - a_{15}a_{32}a_{23}a_{34} + a_{15}a_{34}a_{22}a_{33} + a_{14}a_{35}a_{32}a_{23} - a_{12}a_{33}a_{24}a_{35}) \end{aligned} \tag{2.79}$$

$\boxed{4}$**:**

$$\begin{vmatrix} a_{12} & -a_{13} & a_{14} & -a_{15} \\ a_{32} & -a_{33} & a_{34} & -a_{35} \\ -a_{12} & a_{13} & a_{14} & -a_{15} \\ -a_{32} & a_{33} & a_{34} & -a_{35} \end{vmatrix} = a_{12} \begin{vmatrix} -a_{33} & a_{34} & -a_{35} \\ a_{13} & a_{14} & -a_{15} \\ a_{33} & a_{34} & -a_{35} \end{vmatrix} + a_{13} \begin{vmatrix} a_{32} & a_{34} & -a_{35} \\ -a_{12} & a_{14} & -a_{15} \\ -a_{32} & a_{34} & -a_{35} \end{vmatrix}$$

$$+a_{14} \begin{vmatrix} a_{32} & -a_{33} & -a_{35} \\ -a_{12} & a_{13} & -a_{15} \\ -a_{32} & a_{33} & -a_{35} \end{vmatrix} + a_{15} \begin{vmatrix} a_{32} & -a_{33} & a_{34} \\ -a_{12} & a_{13} & a_{14} \\ -a_{32} & a_{33} & a_{34} \end{vmatrix}$$

$$\begin{aligned} &= a_{12}\left[-a_{33}(-a_{14}a_{35} + a_{15}a_{34}) - a_{34}(-a_{13}a_{35} + a_{33}a_{15}) - a_{35}(a_{13}a_{34} - a_{33}a_{14})\right] \\ &\quad + a_{13}\left[a_{32}(-a_{14}a_{35} + a_{34}a_{15}) - a_{34}(a_{12}a_{35} - a_{32}a_{15}) - a_{35}(-a_{12}a_{34} + a_{32}a_{14})\right] \\ &\quad + a_{14}\left[a_{32}(-a_{13}a_{35} + a_{33}a_{15}) + a_{33}(a_{12}a_{35} - a_{15}a_{32}) - a_{35}(-a_{12}a_{33} + a_{32}a_{13})\right] \\ &\quad + a_{15}\left[a_{32}(a_{13}a_{34} - a_{33}a_{14}) + a_{33}(-a_{12}a_{34} + a_{14}a_{32}) + a_{34}(-a_{12}a_{33} + a_{32}a_{13})\right] \\ &= 4(a_{12}a_{33}a_{35}a_{14} + a_{13}a_{32}a_{34}a_{15} - a_{12}a_{33}a_{34}a_{15} - a_{13}a_{32}a_{35}a_{14}) \end{aligned} \tag{2.80}$$

Simplifying Eq. (2.76) as

$$\det|\mathbf{A}| = -a_{11}^2\boxed{1} + a_{11}a_{21}(\boxed{2} - \boxed{3}) + a_{21}^2\boxed{4}, \tag{2.81}$$

it becomes apparent that $\boxed{2}$ minus $\boxed{3}$ must be calculated.

Using Eqs. (2.78) and (2.79) this gives

$$\begin{aligned} \boxed{2} - \boxed{3} = 4(&a_{22}a_{33}a_{14}a_{35} + a_{23}a_{32}a_{34}a_{15} + a_{24}a_{33}a_{12}a_{35} + a_{25}a_{32}a_{13}a_{34} \\ &- a_{22}a_{33}a_{15}a_{34} - a_{23}a_{32}a_{14}a_{35} - a_{24}a_{32}a_{13}a_{35} - a_{25}a_{33}a_{12}a_{34}.) \end{aligned} \tag{2.82}$$

Inserting now the constants from Tab. 2.73 for each of the variables in $\boxed{1}$, $\boxed{2}$, $\boxed{3}$ and $\boxed{4}$ gives

$$
\begin{aligned}
\boxed{1} &= 4(a_{22}a_{33}a_{25}a_{34} + a_{23}a_{32}a_{24}a_{35} - a_{22}a_{33}a_{24}a_{35} - a_{25}a_{32}a_{23}a_{34}) \\
&= 4[\mu_S(2\eta^2-k^2)\cos(h_zL) - i(2\eta^2-k^2)\sin(k_zL)i2\mu_S\eta k_z\sin(k_zL)2\eta h_z\cos(h_zL) \\
&\quad - 2\mu_S\eta k_z\cos(k_zL)(-i)2\eta h_z\sin(h_zL)(-i)\mu_S(2\eta^2-k^2)\sin(h_zL)(2\eta^2-k^2)\cos(k_zL) \\
&\quad - \mu_S(2\eta^2-k^2)\cos(h_zL)(-i)(2\eta^2-k^2)\sin(k_zL)(-i)\mu_S(2\eta^2-k^2)\sin(h_zL)(2\eta^2-k^2)\cos(k_zL) \\
&\quad - i2\mu_S\eta k_z\sin(k_zL)(-i)2\eta h_z\sin(h_zL)(-2)\mu_S\eta k_z\cos(k_zL)2\eta h_z\cos(h_zL)] \\
&= 4[4\mu_S^2\eta^2h_zk_z(2\eta^2-k^2)^2\cos^2(h_zL)\sin^2(k_zL) + 4\mu_S^2\eta^2h_zk_z(2\eta^2-k^2)^2\sin^2(h_zL)\cos^2(k_zL) \\
&\quad + \mu_S^2(2\eta^2-k^2)^4\sin(k_zL)\cos(k_zL)\sin(h_zL)\cos(h_zL) \\
&\quad + 16\mu_S^2\eta^4h_z^2k_z^2\sin(k_zL)\cos(k_zL)\sin(h_zL)\cos(h_zL)]. \\
&= [\sin(k_zL)\cos(k_zL)\sin(h_zL)\cos(h_zL)] \\
&\quad 4[4\mu_S^2\eta^2h_zk_z(2\eta^2-k^2)^2\frac{\tan(k_zL)}{\tan(h_zL)} + 4\mu_S^2\eta^2h_zk_z(2\eta^2-k^2)^2\frac{\tan(h_zL)}{\tan(k_zL)} \\
&\quad + \mu_S^2(2\eta^2-k^2)^4 + 16\mu_S^2\eta^4h_z^2k_z^2] \\
&= [\sin(k_zL)\cos(k_zL)\sin(h_zL)\cos(h_zL)]\,4\mu_S^2AS. \qquad (2.83)
\end{aligned}
$$

$$
\begin{aligned}
\boxed{2} - \boxed{3} &= 4[\mu_S(2\eta^2-k^2)\cos(h_zL)(-i)(2\eta^2-k^2)\sin(k_zL)ih_z\cos(h_zL)(2\eta^2-k^2)\cos(k_zL) \\
&\quad - 2\mu_S\eta k_z\cos(k_zL)(-i)2\eta h_z\sin(h_zL)2\eta h_z\cos(h_zL)i\eta\cos(k_zL) \\
&\quad - i\mu_S(2\eta^2-k^2)\sin(h_zL)(-i)(2\eta^2-k^2)\sin(k_zL)h_z\sin(h_zL)(2\eta^2-k^2)\cos(k_zL) \\
&\quad + i2\mu_S\eta k_z\sin(k_zL)(-i)2\eta h_z\sin(h_zL)\eta\sin(k_zL)2\eta h_z\cos(h_zL) \\
&\quad - \mu_S(2\eta^2-k^2)\cos(h_zL)(-i)(2\eta^2-k^2)\sin(k_zL)i\eta\cos(k_zL)2\eta h_z\cos(h_zL) \\
&\quad + 2\mu_S\eta k_z\cos(k_zL)(-i)2\eta h_z\sin(h_zL)ih_z\cos(h_zL)(2\eta^2-k^2)\cos(k_zL) \\
&\quad + i\mu_S(2\eta^2-k^2)\sin(h_zL)(-i)2\eta h_z\sin(h_zL)\eta\sin(k_zL)(2\eta^2-k^2)\cos(k_zL) \\
&\quad - i2\mu_S\eta k_z\sin(k_zL)(-i)(2\eta^2-k^2)\sin(k_zL)h_z\sin(h_zL)2\eta h_z\cos(k_zL)]. \qquad (2.84)
\end{aligned}
$$

Setting the term $[\sin(k_zL)\cos(k_zL)\sin(h_zL)\cos(h_zL)]$ outside the brackets provides

$$
\begin{aligned}
&4[\mu_Sh_z(2\eta^2-k^2)^3\frac{1}{\tan(h_zL)} - 8\mu_S\eta^4h_z^2k_z\frac{1}{\tan(k_zL)} - \mu_Sh_z(2\eta^2-k^2)^3\tan(h_zL) + 8\mu_S\eta^4h_z^2k_z\tan(k_zL) \\
&- 2\mu_S\eta^2h_z(2\eta^2-k^2)^2\frac{1}{\tan(h_zL)} + 4\mu_S\eta^2h_z^2k_z(2\eta^2-k^2)\frac{1}{\tan(k_zL)} + 2\mu_S\eta^2h_z(2\eta^2-k^2)^2\tan(h_zL) \\
&- 4\mu_S\eta^2h_z^2k_z(2\eta^2-k^2)\tan(k_zL)] \\
&= 4[\mu_Sh_z[\frac{1}{\tan(h_zL)}[(2\eta^2-k^2)^2(-k^2)] + \frac{1}{\tan(k_zL)}[-4\eta^2k^2h_zk_z] \\
&+ [\tan(h_zL)[2\eta^2-k^2)^2(k^2)] + \tan(k_zL)[4\eta^2k^2h_zk_z] \\
&= -4k^2\mu_Sh_z\left[\left\{(2\eta^2-k^2)^2\frac{1}{\tan(h_zL)} + 4\eta^2h_zk_z\frac{1}{\tan(k_zL)}\right\} - (2\eta^2-k^2)^2\tan(h_zL) - 4\eta^2h_zk_z\tan(k_zL))\right] \qquad (2.85)
\end{aligned}
$$

Identifying S and A from Eqs. (2.49) and (2.50) this gives

$$\boxed{2} - \boxed{3} = [\sin(k_z L)\cos(k_z L)\sin(h_z L)\cos(h_z L)] \times [-4k^2\mu_S h_z(S-A)]. \tag{2.86}$$

$$\begin{aligned}
\boxed{4} &= 4(a_{12}a_{33}a_{35}a_{14} + a_{13}a_{32}a_{34}a_{15} - a_{12}a_{33}a_{34}a_{15} - a_{13}a_{32}a_{35}a_{14}) \\
&= 4[h_z \sin(h_z L)(-i)(2\eta^2 - k^2)\sin(k_z L)(2\eta^2 - k^2)^2\cos(k_z L) i h_z \cos(h_z L) \\
&\quad + \eta \sin(k_z L)(-i)2\eta h_z \sin(h_z L) 2\eta h_z \cos(h_z L) i\eta \cos(k_z L) \\
&\quad - h_z \sin(h_z L)(-i)(2\eta^2 - k^2)\sin(k_z L) 2\eta h_z \cos(h_z L) i\eta \cos(k_z L) \\
&\quad - \eta \sin(k_z L)(-i)2\eta h_z \sin(h_z L)(2\eta^2 - k^2)\cos(k_z L) i h_z \cos(h_z L) \\
&= [\sin(k_z L)\cos(k_z L)\sin(h_z L)\cos(h_z L)] \times \\
&\quad 4h_z^2[(2\eta^2 - k^2)^2 + 4\eta^4 - 4\eta^2(2\eta^2 - k^2)] \\
&= [\sin(k_z L)\cos(k_z L)\sin(h_z L)\cos(h_z L)]\, 4h_z^2 k^4
\end{aligned} \tag{2.87}$$

Gather now the terms to calculate $\det|\mathbf{A}|$ as

$$\begin{aligned}
\det|\mathbf{A}| &= -a_{11}^2\boxed{1} + a_{11}a_{21}(\boxed{2} - \boxed{3}) + a_{21}^2\boxed{4} \\
&= [\sin(k_z L)\cos(k_z L)\sin(h_z L)\cos(h_z L)] \times \\
&\quad e^{-i2h_{f,z}L}\left[h_{f,z}^2 4\mu_S^2 AS - i h_{f,z}\rho_f\omega^2 4k^2\mu_S h_z(S-A) + \rho_f^2\omega^4 4h_z^2 k^4\right]
\end{aligned} \tag{2.88}$$

The dispersion relations for the symmetrical and antisymmetrical leaky Lamb modes are derived by setting the determinant in Eq. (2.88) to zero as

$$h_{f,z}^2 4\mu_S^2 AS - i h_{f,z}\rho_f\omega^2 4k^2\mu_S h_z(S-A) + \rho_f^2\omega^4 4h_z^2 k^4 = 0 \tag{2.89}$$

Setting the term $h_{f,z}^2 4\mu_S^2$ outside the brackets, and using $\mu_S = c_S^2\rho_S$ and $\omega = kc_S$, provides

$$AS - i\frac{\rho_f h_z}{\rho_S h_{f,z}}k^4(S-A) + \frac{\rho_f^2 h_z^2}{\rho_S^2 h_{f,z}^2}k^8 = (S+iY)(A-iY) \tag{2.90}$$

where,

$$Y = \frac{\rho_f h_z}{\rho_S h_{f,z}}k^4, \tag{2.91}$$

and S and A are defined in Eqs. (2.49) and (2.50). This defines the dispersion relations for leaky Lamb modes in a single fluid-embedded plate as

$$S + iY = 0, \tag{2.92}$$

and

$$A - iY = 0, \tag{2.93}$$

for symmetrical and antisymmetrical modes, respectively.

2.4.3 Plane-wave reflection and transmission from a fluid-embedded plate

[5]The plane-wave pressure reflection and transmission coefficients, $\mathscr{R}(h_{f,x}, h_{f,y}, L, f)$ and $\mathscr{T}(h_{f,x}, h_{f,y}, L, f)$ respectively, can be calculated by setting the incident wave amplitude in Eq. (2.72) to unity, i.e. $A_1^+ = 1$ in

$$\mathscr{R}(h_{f,x}, h_{f,y}, L, f) = \frac{A_1^-}{A_1^+} e^{-i2h_{f,z}L}, \qquad \mathscr{T}(h_{f,x}, h_{f,y}, L, f) = \frac{A_3^+}{A_1^+} e^{-i2h_{f,z}L}. \tag{2.94}$$

By using Cramer's rule A_1^- and A_3^+ can be calculated as

$$A_1^- = \frac{\det \begin{bmatrix} -ih_{f,z}A_1^+ e^{ih_{f,z}L} & a_{12} & -a_{13} & a_{14} & -a_{15} & 0 \\ -\rho_f \omega^2 A_1^+ e^{ih_{f,z}L} & a_{22} & -a_{23} & a_{24} & -a_{25} & 0 \\ 0 & a_{32} & -a_{33} & a_{34} & -a_{35} & 0 \\ 0 & -a_{12} & a_{13} & a_{14} & -a_{15} & a_{16} \\ 0 & a_{22} & -a_{23} & -a_{24} & a_{25} & a_{26} \\ 0 & -a_{32} & a_{33} & a_{34} & -a_{35} & 0 \end{bmatrix}}{\det \begin{bmatrix} -a_{11} & a_{12} & -a_{13} & a_{14} & -a_{15} & 0 \\ a_{21} & a_{22} & -a_{23} & a_{24} & -a_{25} & 0 \\ 0 & a_{32} & -a_{33} & a_{34} & -a_{35} & 0 \\ 0 & -a_{12} & a_{13} & a_{14} & -a_{15} & a_{16} \\ 0 & a_{22} & -a_{23} & -a_{24} & a_{25} & a_{26} \\ 0 & -a_{32} & a_{33} & a_{34} & -a_{35} & 0 \end{bmatrix}} \tag{2.95}$$

and

$$A_3^+ = \frac{\det \begin{bmatrix} -a_{11} & a_{12} & -a_{13} & a_{14} & -a_{15} & -ih_{f,z}A_1^+ e^{ih_{f,z}L} \\ a_{21} & a_{22} & -a_{23} & a_{24} & -a_{25} & -\rho_f \omega^2 A_1^+ e^{ih_{f,z}L} \\ 0 & a_{32} & -a_{33} & a_{34} & -a_{35} & 0 \\ 0 & -a_{12} & a_{13} & a_{14} & -a_{15} & 0 \\ 0 & a_{22} & -a_{23} & -a_{24} & a_{25} & 0 \\ 0 & -a_{32} & a_{33} & a_{34} & -a_{35} & 0 \end{bmatrix}}{\det \begin{bmatrix} -a_{11} & a_{12} & -a_{13} & a_{14} & -a_{15} & 0 \\ a_{21} & a_{22} & -a_{23} & a_{24} & -a_{25} & 0 \\ 0 & a_{32} & -a_{33} & a_{34} & -a_{35} & 0 \\ 0 & -a_{12} & a_{13} & a_{14} & -a_{15} & a_{16} \\ 0 & a_{22} & -a_{23} & -a_{24} & a_{25} & a_{26} \\ 0 & -a_{32} & a_{33} & a_{34} & -a_{35} & 0 \end{bmatrix}}. \tag{2.96}$$

Recall that, the determinant to the denominator matrix, called **A** in Sec. 2.4.2, has been calculated in Eq. (2.88). Thus, in order to calculate the plane-wave pressure reflection and transmission coefficients

[5]The present derivation continues from the derivation of the leaky Lamb modes in Sect. 2.4.2 using a $e^{i\omega t}$ time dependency, and expresses the plane-wave pressure coefficients as a function of horizontal wavenumber.

the determinants of the numerator matrices above must be calculated.

Calculation of the plane-wave pressure reflection coefficient, $\mathscr{R}(h_{f,x}, h_{f,y}, L, f)$
Denote the numerator matrix in Eq. (2.95) for $A_1^- m$. Calculating the determinant of this matrix by cofactor expansion, recall the matrix determinant calculation in Sect. 2.4.2. Each of the four 4×4 matrix determinants are the same, so by cofactor expansion the determinant is given as

$$\begin{aligned}\det A_1^- m &= -ih_{f,z}e^{ih_{f,z}L}\left(a_{11}\boxed{1} - a_{21}\boxed{2}\right) + \rho_f\omega^2 e^{ih_{f,z}L}\left(a_{11}\boxed{3} - a_{21}\boxed{4}\right) \\ &= e^{ih_{f,z}L}\left(-ih_{f,z}a_{11}\boxed{1} + e^{-ih_{f,z}L}ih_{f,z}\rho_f\omega^2\left(\boxed{2}+\boxed{3}\right) - \rho_f\omega^2 a_{21}\boxed{4}\right), \end{aligned} \tag{2.97}$$

where $a_{16} = a_{11}$, and $a_{26} = a_{21}$, see Tab. (2.73). The determinants $\boxed{1}$, $\boxed{2}$, $\boxed{3}$ and $\boxed{4}$ are defined in Sec. 2.4.2 in Eqs. (2.77), (2.78), (2.79) and (2.80), respectively. From Eqs. (2.78) and (2.79), $\boxed{2} + \boxed{3}$ is zero. Then

$$\begin{aligned}\det A_1^- m &= e^{ih_{f,z}L}\left(-ih_{f,z}a_{11}\boxed{1} - \rho_f\omega^2 a_{21}\boxed{4}\right) \\ &= h_{f,z}^2\boxed{1} - \rho_f^2\omega^4\boxed{4} \\ &= \left[\sin(k_z L)\cos(k_z L)\sin(h_z L)\cos(h_z L)\right]\left[4\mu_S^2 h_{f,z}^2 AS - 4\rho_f^2\omega^4 h_z^2 k^4\right]. \end{aligned} \tag{2.98}$$

Using Eq. (2.95), A_1^- is calculated as

$$A_1^- = \frac{\det A_1^- m}{\det A}.$$

Substituting this for A_1^- in Eq. (2.94) and setting $A_1^+ = 1$, the plane-wave pressure reflection coefficient is formulated as

$$\begin{aligned}\mathscr{R}(h_{f,x}, h_{f,y}, L, f) &= \frac{\det A_1^- m}{\det A} e^{-i2h_{z,f}L} \\ &= e^{-i2h_{f,z}L}\left[\frac{4\mu_S^2 h_{f,z}^2 AS - 4\rho_f^2\omega^4 h_z^2 k^4}{e^{-i2h_{f,z}L}\left(4h_z^2\mu_S^2 AS - i4h_{f,z}\rho_f\omega^2 k^2\mu_s h_z(S-A) + 4\rho_f^2\omega^4 h_z^2 k^4\right)}\right]. \end{aligned}$$

Utilizing $\mu_S = c_S^2\rho_S$ and $\omega = kc_S$ gives

$$\mathscr{R}(h_{f,x}, h_{f,y}, L, f) = \frac{AS - \frac{\rho_f^2\omega^4 h_z^2 k^4}{\mu_S^2 h_{f,z}^2}}{AS - i\frac{\mu_S h_z k^2 h_{f,z}\rho_f\omega^2}{\mu_S^2 h_{f,z}^2}(S-A) + \frac{\rho_f^2\omega^4 h_z^2 k^4}{\mu_S^2 h_{z,f}^2}}. \tag{2.99}$$

Identifying Y in Eq. (2.91) this gives

$$\begin{aligned}\mathscr{R}(h_{f,x}, h_{f,y}, L, f) &= \frac{AS - Y^2}{AS - iY(S-A) + Y^2} \\ &= \frac{AS - Y^2}{(S+iY)(A-iY)}. \end{aligned} \tag{2.100}$$

Eq. (2.100) is identical to the plane-wave pressure reflection coefficient formulated by [80], and similar to [58] (with opposite sign in front of i due to the different time dependency). The plane-wave pressure reflection coefficient is not used further in this thesis, but is included in the calculations.

Calculation of the transmission coefficient, $\mathscr{T}(h_{f,x}, h_{f,y}, L, f)$

Denote the numerator matrix in Eq. (2.96) for $A_3^+ m$. Calculating the determinant of this matrix by cofactor expansion gives

$$\begin{aligned}
\det A_3^+ m &= ih_{f,z}e^{ih_{f,z}L}\begin{vmatrix} a_{21} & a_{22} & -a_{23} & a_{24} & -a_{25} \\ 0 & a_{32} & -a_{33} & a_{34} & -a_{35} \\ 0 & -a_{12} & a_{13} & a_{14} & -a_{15} \\ 0 & a_{22} & -a_{23} & -a_{24} & a_{25} \\ 0 & -a_{32} & a_{33} & a_{34} & -a_{35} \end{vmatrix} - \rho_f\omega^2 e^{ih_{f,z}L}\begin{vmatrix} -a_{11} & a_{12} & -a_{13} & a_{14} & -a_{15} \\ 0 & a_{32} & -a_{33} & a_{34} & -a_{35} \\ 0 & -a_{12} & a_{13} & a_{14} & -a_{15} \\ 0 & a_{22} & -a_{23} & -a_{24} & a_{25} \\ 0 & -a_{32} & a_{33} & a_{34} & -a_{35} \end{vmatrix} \\
&= ih_{f,z}e^{ih_{f,z}L}a_{21}\begin{vmatrix} a_{32} & -a_{33} & a_{34} & -a_{35} \\ -a_{12} & a_{13} & a_{14} & -a_{15} \\ a_{22} & -a_{23} & -a_{24} & a_{25} \\ -a_{32} & a_{33} & a_{34} & -a_{35} \end{vmatrix} + \rho_f\omega^2 e^{ih_{f,z}L}a_{11}\begin{vmatrix} a_{32} & -a_{33} & a_{34} & -a_{35} \\ -a_{12} & a_{13} & a_{14} & -a_{15} \\ a_{22} & -a_{23} & -a_{24} & a_{25} \\ -a_{32} & a_{33} & a_{34} & -a_{35} \end{vmatrix} \\
&= \left(ih_{f,z}e^{ih_{f,z}L}a_{21} + \rho_f\omega^2 e^{ih_{f,z}L}a_{11}\right)\begin{vmatrix} a_{32} & -a_{33} & a_{34} & -a_{35} \\ -a_{12} & a_{13} & a_{14} & -a_{15} \\ a_{22} & -a_{23} & -a_{24} & a_{25} \\ -a_{32} & a_{33} & a_{34} & -a_{35} \end{vmatrix}. \qquad (2.101)
\end{aligned}$$

Denote the matrix determinant of Eq. (2.101) as $\boxed{5}$.

$\boxed{5}$**:**

$$\begin{aligned}
\begin{vmatrix} a_{32} & -a_{33} & a_{34} & -a_{35} \\ -a_{12} & a_{13} & a_{14} & -a_{15} \\ a_{22} & -a_{23} & -a_{24} & a_{25} \\ -a_{32} & a_{33} & a_{34} & -a_{35} \end{vmatrix} &= a_{32}\begin{vmatrix} a_{13} & a_{14} & -a_{15} \\ -a_{23} & -a_{24} & a_{25} \\ a_{33} & a_{34} & -a_{35} \end{vmatrix} + a_{33}\begin{vmatrix} -a_{12} & a_{14} & -a_{15} \\ a_{22} & -a_{24} & a_{25} \\ -a_{32} & a_{34} & -a_{35} \end{vmatrix} \\
&\quad + a_{34}\begin{vmatrix} -a_{12} & a_{13} & -a_{15} \\ a_{22} & -a_{23} & a_{25} \\ -a_{32} & a_{33} & -a_{35} \end{vmatrix} + a_{35}\begin{vmatrix} -a_{12} & a_{13} & a_{14} \\ a_{22} & -a_{23} & -a_{24} \\ -a_{32} & a_{33} & a_{34} \end{vmatrix} \\
&= a_{32}\left[a_{13}(a_{24}a_{35} - a_{34}a_{25}) - a_{14}(a_{23}a_{35} - a_{33}a_{25}) - a_{15}(-a_{23}a_{34} + a_{33}a_{24})\right] \\
&\quad + a_{33}\left[-a_{12}(a_{24}a_{35} - a_{34}a_{25}) - a_{14}(-a_{22}a_{35} + a_{32}a_{25}) - a_{15}(a_{22}a_{34} - a_{32}a_{24})\right] \\
&\quad + a_{34}\left[-a_{12}(a_{23}a_{35} - a_{33}a_{25}) - a_{13}(-a_{22}a_{35} + a_{32}a_{25}) - a_{15}(a_{22}a_{33} - a_{32}a_{23})\right] \\
&\quad + a_{35}\left[-a_{12}(-a_{23}a_{34} + a_{33}a_{24}) - a_{13}(a_{22}a_{34} - a_{32}a_{24}) + a_{14}(a_{22}a_{33} - a_{32}a_{23})\right] \\
&= 2(a_{32}a_{15}a_{23}a_{34} + a_{32}a_{13}a_{24}a_{35} + a_{33}a_{14}a_{22}a_{35} + a_{33}a_{12}a_{34}a_{25} \\
&\quad - a_{32}a_{13}a_{34}a_{25} - a_{32}a_{14}a_{23}a_{35} - a_{33}a_{12}a_{24}a_{35} - a_{33}a_{15}a_{22}a_{34}) \qquad (2.102)
\end{aligned}$$

Inserting now constants from Tab. 2.73 for each variable in $\boxed{5}$ gives

$$
\begin{aligned}
\boxed{5} =& 2[-i2\eta h_z \sin(h_z L) i\eta \cos(k_z L)(-2)\mu_S \eta k_z \cos(k_z L) 2\eta h_z \cos(h_z L) \\
& - i2\eta h_z \sin(h_z L)\eta \sin(k_z L)(-i)\mu_S (2\eta^2 - k^2)\sin(h_z L)(2\eta^2 - k^2)\cos(k_z L) \\
& - i(2\eta^2 - k^2)\sin(k_z L) i h_z \cos(h_z L)\mu_S (2\eta^2 - k^2)\cos(h_z L)(2\eta^2 - k^2)\cos(k_z L) \\
& - i(2\eta^2 - k^2)\sin(k_z L) h_z \sin(h_z L) 2\eta h_z \cos(h_z L) i2\mu_S \eta k_z \sin(k_z L) \\
& + i2\eta h_z \sin(h_z L)\eta \sin(k_z L) 2\eta h_z \cos(h_z L) i2\mu_S \eta k_z \sin(k_z L) \\
& + 2\eta h_z \sin(h_z L) i h_z \cos(h_z L)(-2)\mu_S \eta k_z \cos(k_z L)(2\eta^2 - k^2)\cos(k_z L) \\
& + i(2\eta^2 - k^2)\sin(k_z L) h_z \sin(h_z L)(-i)\mu_S (2\eta^2 - k^2)\sin(h_z L)(2\eta^2 - k^2)\cos(k_z L) \\
& + i(2\eta^2 - k^2)\sin(k_z L) i\eta \cos(k_z L)\mu_S (2\eta^2 - k^2)\cos(h_z L) 2\eta h_z \cos(h_z L)] \\
=& [\sin(k_z L)\cos(k_z L)\sin(h_z L)\cos(h_z L)]\,(\\
& 2[-8\mu_S \eta^4 h_z^2 k_z \frac{1}{\tan(k_z L)} - 2\mu_S \eta^2 h_z (2\eta^2 - k^2)^2 \tan(h_z L) + \mu_S h_z (2\eta^2 - k^2)^3 \frac{1}{\tan(h_z L)} \\
& + 4\mu_S \eta^2 h_z^2 k_z (2\eta^2 - k^2)\tan(k_z L) - 8\mu_S \eta^4 h_z^2 k_z \tan(k_z L) + 4\mu_S \eta^2 h_z^2 k_z (2\eta^2 - k^2)\frac{1}{\tan(k_z L)} \\
& + \mu_S h_z (2\eta^2 - k^2)^3 \tan(h_z L) - 2\mu_S \eta^2 h_z (2\eta^2 - k^2)^2 \frac{1}{\tan(h_z L)}]) \\
=& [\sin(k_z L)\cos(k_z L)\sin(h_z L)\cos(h_z L)]\,(\\
& 2[\mu_S h_z [\tan(k_z L)[4\eta^2 h_z k_z (2\eta^2 - k^2) - 8\eta^4 h_z k_z] + \frac{1}{\tan(k_z L)}[4\eta^2 h_z k_z (2\eta^2 - k^2) - 8\eta^4 h_z k_z] \\
& + \tan(h_z L)[(2\eta^2 - k^2)^2(-k^2)] + \frac{1}{\tan(h_z L)}[(2\eta^2 - k^2)^2(-k^2)]]) \\
=& [\sin(k_z L)\cos(k_z L)\sin(h_z L)\cos(h_z L)]\,(\\
& - 2k^2 \mu_S h_z \left[(2\eta^2 - k^2)\tan(h_z L) + 4\eta^2 h_z k_z \tan(k_z L) + \left\{(2\eta^2 - k^2)\frac{1}{\tan(h_z L)} + 4\eta^2 h_z k_z \frac{1}{\tan(k_z L)}\right\}\right]) \\
=& [\sin(k_z L)\cos(k_z L)\sin(h_z L)\cos(h_z L)]\left[-2k^2 \mu_S h_z (A + S)\right]. \qquad (2.103)
\end{aligned}
$$

Substituting this in Eq. (2.101), and for a_{21} and a_{11} using Tab. 2.73,

$$
\begin{aligned}
\det A_3^+ m &= \left(i h_{f,z} \rho_f \omega^2 + \rho_f \omega^2 i h_{f,z}\right)\boxed{5} \\
&= 2i h_{f,z} \rho_f \omega^2 \boxed{5} \\
&= [\sin(k_z L)\cos(k_z L)\sin(h_z L)\cos(h_z L)] \times \left[-i4\mu_S h_z k^2 h_{f,z} \rho_f \omega^2 (A + S)\right],
\end{aligned}
$$

utilizing $\mu_S = \rho_S c_S^2$ and $\omega = k c_S$. Using Eq. (2.96), A_3^+ is calculated as

$$
A_3^+ = \frac{\det A_3^+ m}{\det A}.
$$

Substituting this in Eq. (2.94) and setting $A_1^+ = 1$, the plane-wave pressure transmission coefficient is calculated as

$$\mathscr{T}(h_{f,x}, h_{f,y}, L, f) = \frac{\det A_3^+ m}{\det A} e^{-i2h_{f,z}L}$$
$$= e^{-i2h_{f,z}L} \left[\frac{-i4\mu_S h_z k^2 h_{f,z} \rho_f \omega^2 (A+S)}{e^{-i2h_{f,z}L} \left(4h_z^2 \mu_S^2 AS - i4h_{f,z}\rho_f \omega^2 k^2 \mu_S h_z (S-A) + 4\rho_f^2 \omega^4 h_z^2 k^4 \right)} \right].$$

Utilizing $\mu_S = c_S^2 \rho_S$ and $\omega = k c_S$ gives

$$\mathscr{T}(h_{f,x}, h_{f,y}, L, f) = \frac{-i\frac{\rho_f h_z}{\rho_S h_{f,z}} k^4 (A+S)}{AS - i\frac{\mu_S h_z k^2 h_{f,z} \rho_f \omega^2}{\mu_S^2 h_{f,z}^2}(S-A) + \frac{\rho_f^2 \omega^4 h_z^2 k^4}{\mu_S^2 h_{f,z}^2}}.$$

Identifying Y in Eq. (2.91) this gives

$$\mathscr{T}(h_{f,x}, h_{f,y}, L, f) = \frac{-iY(A+S)}{AS - iY(S-A) + Y^2}$$
$$= \frac{-iY(A+S)}{(S+iY)(A-iY)}. \tag{2.104}$$

Eq. (2.104) is identical to the plane-wave transmission coefficient formulated by [80].

Chapter 3

Experimental setup and measurement methods

3.1 Introduction

This chapter presents the experimental arrangement for sound transmission measurements of a system consisting of a piezoelectric source transducer and a water-embedded viscoelastic plate, see Chap. 2 for the theoretical description of this measurement system. In addition, measurements of the properties for the piezoelectric source immersion transducer described in Chap. 5 is presented. The experimental arrangement of the measurement system, used to measure the transmission through the water-embedded steel plate using the piezoelectric source transducer as transmitter, and a needle hydrophone as a receiver, is given in Sect. 3.2, together with a method [91, 92] for determining the sound velocities in the steel plate and the corresponding Q-factors (cf. Sect. 3.3). For quantitative measurements of the system, a calibration of the needle hydrophone is needed and described in Sect. 3.5, using a 2-transducer (cf. Sect. 3.5.2) and a 3-transducer (cf. Sect. 3.5.3) calibration scheme. The experimental setup for measuring the piezoelectric transducer properties are given in Sect. 3.6, for the electrical admittance Y_T (cf. Sect. 3.6.1), the source sensitivity $S_V(f)$ (cf. Sect. 3.6.2) and the beam pattern $D(\phi, f)$ (cf. Sect. 3.6.3). The program codes for the data acquisition, motor control and calculation of measured transfer functions are listed in App. F.

3.2 Transmission measurements

A $2L = 6.05$ mm thick, 500 mm wide and 760 mm long hot rolled[1] AISI 316L stainless steel plate is immersed in a water tank with dimensions (60 - 75 - 160) cm^3 (height,y - width,x - length,z), see Figs. 3.1(a) and 3.1(b). A computer controlled HP 33120A [123] signal generator set up a 10 V peak-to-peak (130 μs duration) sine burst, $v_0(t)$, and transmits the resulting waveform $v(t)$ (affected by the electrical loading, see Sect. 2.2) to a piezoelectric transducer (Figs. 3.1(d) and 5.14), at a distance of 270 mm from the steel plate, i.e. the upper surface of the steel plate is located at $z = z_0 \equiv 270$

[1] The significance of hot rolled vs. cold rolled steel is briefly reported in Sect. 6.2.2.

mm. Measurements are made over the frequency range 350 kHz - 1 MHz. The distance was chosen so that comparisons to the works by [90, 91, 92] were possible. The frequency range was chosen due to the excitation of the leaky Lamb modes in that frequency range. The in-house constructed 36.1 mm diameter piezoelectric transducer has been designed, constructed, characterized and used for measurements and FEM simulations, cf. Chap. 5. A 1 mm PVDF needle hydrophone [124] with a specially made 100 mm probe length (serial no. 1820) (Fig. 3.1(c)) is connected to a preamplifier (serial no. PA110078) and a DC coupler (serial no. DCPS223)(Precision Acoustics Ltd. (PA)) and is used to detect the transmitted signal in a plane at $z_2 = 376.05$ mm, 100 mm from the steel plate. The signal is terminated with 50 Ω load in parallell with the input of a high impedance (1 MΩ) Femto HVA-10M-60-F amplifier [125] by a RG-58 coaxial cable from the DC coupler, before the signal is filtered using a Krohn-Hite type 3202 bandpass filter [126](20 kHz - 2 MHz) and digitized using a Tektronix DPO3012 oscilloscope [127]. The oscilloscope uses 8-bit vertical resolution, temporal settings are adjusted to 100 000 samples in the 400 μs windows, which results in a sample rate of 250 MHz. An average of 256 bursts are used in the measurements presented. The hydrophone has been calibrated by PA and the National Physical Laboratory (NPL) UK, and has also been calibrated in-house over the frequency range using a 3-transducer reciprocity calibration scheme, cf. Sect. 3.5.3. The transmitted sound pressure $p_t(x, y, z_2, t)$ is measured at given receiver positions, '*' in Fig. 2.1. The measured waveforms are converted from voltage to sound pressure, using the magnitude of the probe hydrophone receiver sensitivity at the centre frequency of each waveform, i.e. the phase response of the probe has not been available and used for correction of measured waveforms. $P_t(x, y, z_2, f)$ is calculated using the Fourier transform, defining the transmitted peak-to-peak pressure as the maximum frequency spectrum amplitude of the steady state region in $p_t(x, y, z_2, t)$. Utilizing MATLAB and the function `fft`, the frequency spectrum is two-sided, i.e. the spectrum is displayed for both negative and positive frequencies. For a real time response, the frequency spectrum is symmetrical around the DC-component. Thus, only half of the energy is contained at the maximum positive frequency spectrum amplitude. Hence, to calculate the peak-to-peak amplitude, a factor of 2×2 is needed.

For transmission measurements, a sine burst $v_0(t)$ with a 130 μs duration was needed in order to reach the steady state region of the transmitted waveforms $p_t(x, y, z_2, t)$ in the frequency range 350 kHz - 1 MHz. A Precision Acoustics Ltd (PA) PVDF 1 mm needle hydrophone (standard probe length) [124] was used for measurements at first, but, using this hydrophone, one experienced fluctations in the steady state region of the transmitted waveform. Applying a 130 μs long burst the source of these fluctations were reflections from the transition region between the probe and the preamplifier of the hydrophone, due to the length ($\approx$ 35 mm) of the probe. This was confirmed by applying a shorter pulse, reducing the fluctations to approximately zero. The experimental setup here is based on the experimental setup by Lohne [90, 91, 92]. Lohne used the same type of hydrophone, and reduced the fluctations implementing a normalization method. This method cannot be used here, since the goal is to make quantitative measurements including the piezoelectric source transducer response. In order to limit the fluctations, the reflected sound must either be scattered and/or absorbed. A sound aborber provided by PA was inserted just before the transition region with limited success, similar to the one used by [92]. A copper cone was inserted just before the transition region with no improvement, and

for some frequencies even worsening the fluctations. A new 1 mm needle hydrophone with a probe length of 100 mm was then ordered from PA, so that the reflections from the transition region would not affect the steady state region, applying a 130 μs long burst.

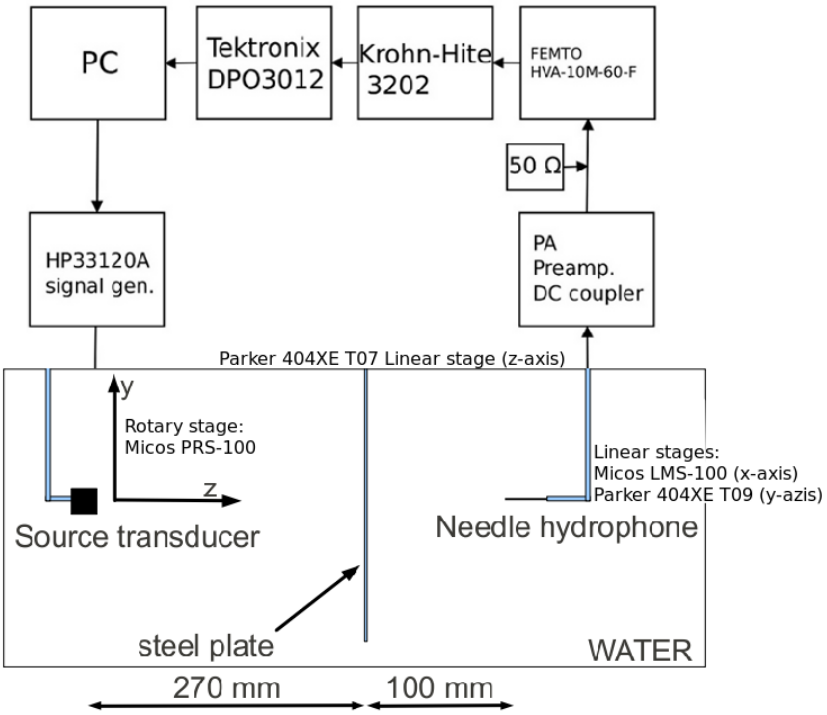

(a)

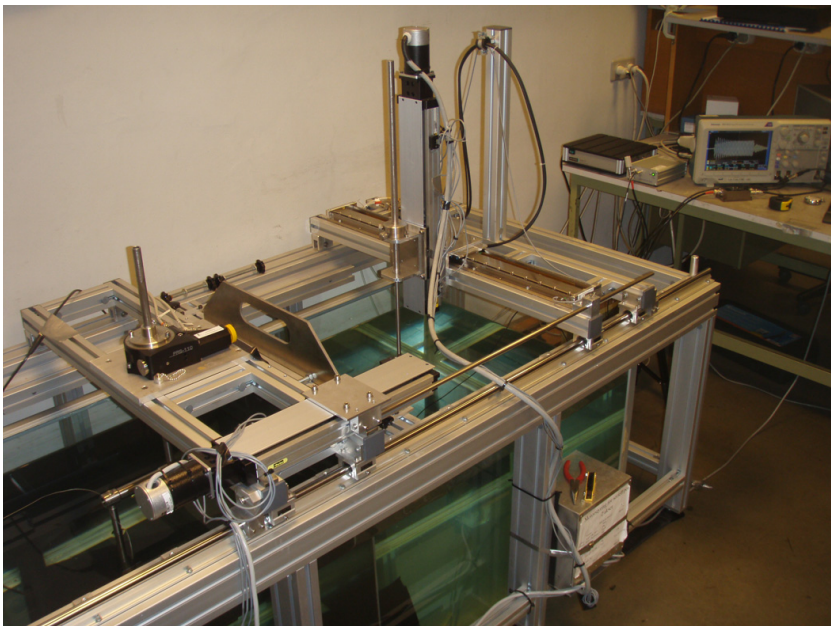

(b)

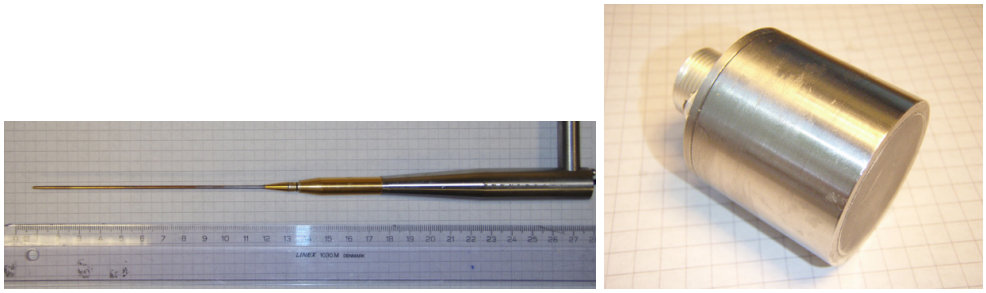

(c) (d)

Fig 3.1. Experimental measurement setup. **a)** Principle sketch of the measurement setup, with coordinate system (x, y, z). x into the paper. **b)** Photograph of the measurement tank with the steel plate immersed in water. **c)** Photograph of the PA needle hydrophone with 100 mm probe length. **d)** Photograph of the in-house constructed piezoelectric transducer used as source.

3.2.1 Frequency response of the electronic equipment

To correctly determine the transmitted signal $p_t(x, y, z_2, f)$ through the measurement system, the frequency response for the FEMTO amplifier, together with the frequency response for the Krohn-Hite filter, must be determined. The amplification factor for the instruments is given as

$$\frac{|V(f)_{\text{out}}|}{|V(f)_{\text{in}}|}, \tag{3.1}$$

where $V(f)_{\text{in}}$ and $V(f)_{\text{out}}$ are the input/output voltages to and from the instrument as function of frequency, respectively. In this study one neglects the electrical loading of the cables.

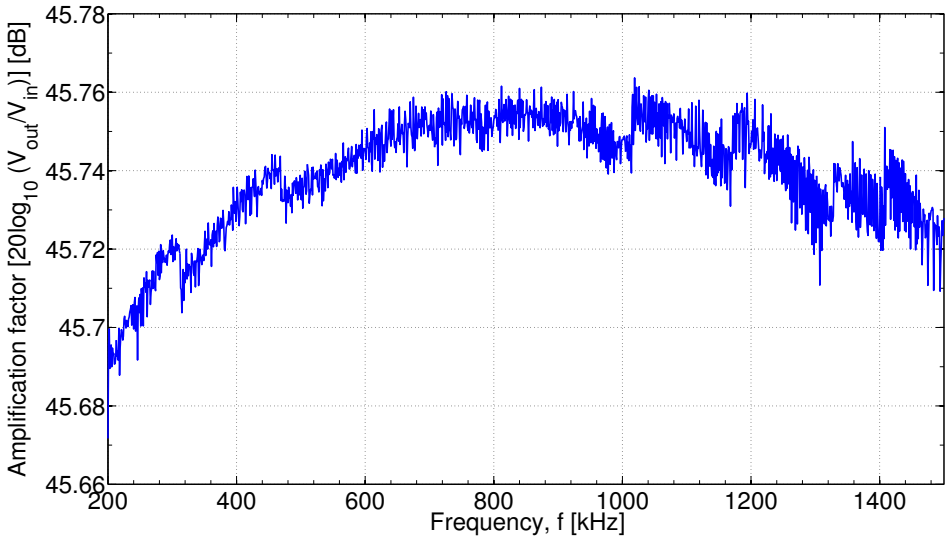

FIG 3.2. Measured amplification factor of the FEMTO HVA-10M-60-F amplifier in the frequency range 200 kHz - 1.5 MHz. The amplifier is operating in 40 dB mode.

Fig. 3.2 shows the measured amplification factor for the FEMTO HVA-10M-60-F amplifier as a function of frequency, operating in 40 dB mode. In accordance with its usage in the total measurement

system, the amplification factor is measured using the signal generator with a 50 Ω output impedance to generate V_{in}, and using the oscilloscope with a 1 MΩ||11.5pF input impedance to measure V_{out}. The input and output impedance of the FEMTO amplifier is 1 MΩ||15pF and 50 Ω, respectively. Fig. 3.2 shows that the frequency response of the amplification factor is relatively flat in the frequency range, 350 kHz to 1 MHz, and therefore a constant amplification factor of 45.74 dB is used throughout the frequency range when conducting measurements.

Fig. 3.3 shows the measured amplification factor for the Krohn-Hite filter as a function of frequency, operating as a bandbass filter in the range 20 kHz - 2 MHz. In accordance with its usage in the total measurement system, where the input and output impedance of the Krohn-Hite filter is 100 kΩ||50 pF and 50 Ω, respectively, the same measurement setup is used as for the measurement of the amplification factor for the FEMTO amplifier. Fig. 3.3 shows that the frequency response of the amplification factor varies up to 1 dB in the frequency range, hence it is taken into account when conducting measurements.

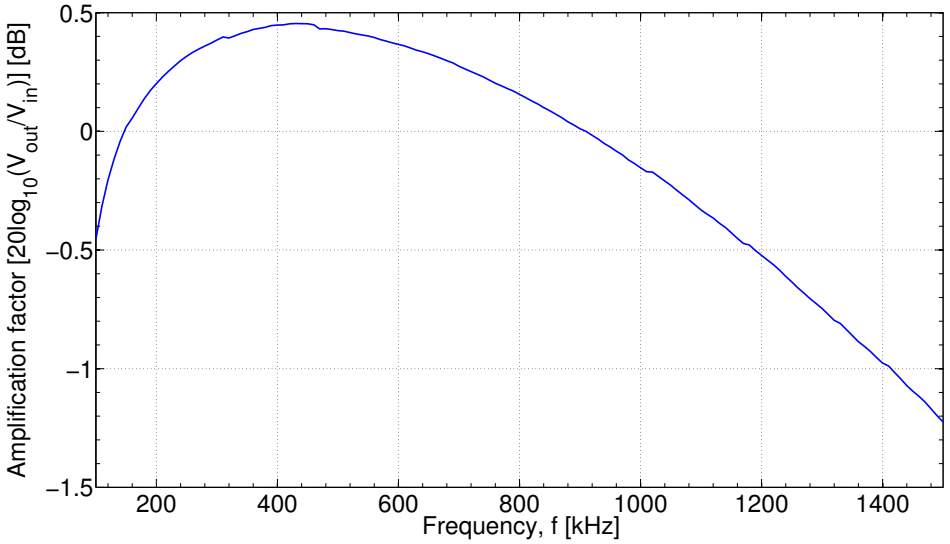

FIG 3.3. Measured amplification factor of the Krohn-Hite bandpass filter (20 kHz - 2 MHz) in the frequency range 100 kHz - 1.5 MHz.

3.2.2 Alignment and distance measurements

The piezoelectric source transducer is connected through a mounting rack to a Micos precision rotary stage PRS-110 [128], which rotates about the transducer's front surface, such that z_0 do not change with the beam incidence θ. This rotary stage is mounted on a carriage able to move in parallell to the z-direction, see Fig. 3.1(a) and Fig. 3.1(b). On this carriage, a Parker 404XE T07 [129] linear stage is positioned, making it possible to step in the $z-$direction, and connected through a rod to a carriage on the other side of the steel plate, which supports the needle hydrophone. On this carriage, a system consisting of a Micos LMS-100 [130](in the x-direction) and a Parker 404EX T09 [131] (in the y-direction) linear stage is mounted, which in turn supports the needle hydrophone. Thus, making the measurement system able to make 3D scans.

Alignment of the transducer and needle hydrophone is carried out using a cross laser to determine that the transmitter and the receiver is on-axis with respect to each other. Fine-tuning is done acoustically, finding the maximum sound pressure at a high frequency where the transducer's main lobe is narrow. The distance between the transmitter and receiver is determined measuring the transit time of a pulse, knowing the sound velocity c_f in water. The sound velocity of water is measured by a two-distance method using time arrivals. At a given distance between the transmitter and receiver the time arrival t_1 of a pulse is determined. Using the Parker 404XE T07 motor stage the receiver is driven to another position along the acoustical axis, where δz is the relative distance between the two positions. Here, another time arrival t_2 is determined. Knowing the time arrivals and the relative distance between the two positions, the sound velocity in water c_f can be calculated as

$$c_f = \frac{\delta z}{t_2 - t_1}. \tag{3.2}$$

The distance between the transmitter and the steel plate for transmission measurements is fixed using a reference rod with a length of 270 mm.

3.3 Method for determining c_L and c_S, and the corresponding Q-factors

A method [91, 92] relates the transmission of sound through the plate at normal beam incidence to the cut-off frequencies for a solid plate in vaccum (Eqs. (2.54) and (2.55)) to determine the sound velocities, c_L and c_S, for the steel plate. For a solid plate immersed in a fluid, where the density of the fluid is much less than the density of the plate, the frequencies that corresponds to maximum transmission through the plate is almost equal to the excitation frequencies of Lamb modes for the same plate in vacuum [37]. The cut-off frequencies can then be found from plane-wave transmission when the incident ultrasonic plane-wave approaches the normal incident angle [91].

The sound velocities for the water-embedded steel plate is found by measuring $H_{PP}(0, 0, z_2, f)$ (Eq. (2.13)) for a normal beam incidence, where the frequencies of maximum transmission are used as the cut-off frequencies in Eqs (2.54) and (2.55). The method assumes a normal incident plane-wave, and care must be taken to ensure negligible beam effects in transmission measurements. This will be further discussed in Sect. 6.2.2.

This method is here extended to approximate the corresponding loss factors (Q_M^L and Q_M^S) for the compressional and shear sound velocities, respectively. After the sound velocities in the plate are determined, hybrid FEM-ASM simulations of $H_{PP}(0, 0, z_2, f)$ at normal beam incidence are compared to transmission measurements, and simulated loss factors are varied until agreement is found. Results are reported in Sect. 6.2.2.

3.4 Measurements for the transducer front layer

In order to facilitate FEM simulations of the measurement transducer described in Chap. 5, the material data for the components of the transducer design must be determined. From Chap. 5, the material data for the other components in the transducer design than the front layer were either taken from other sources, or determined in a different way, e.g. adjustment of piezoelectric material data, cf. Sect. 5.2. This section describes the methods for determining the density (cf. Sect. 3.4.1) and the sound velocities (cf. Sect. 3.4.2) of the front layer used in the piezoelectric source transducer.

3.4.1 Density measurements

The front layer material[2] was delivered by the manufacturer in the form of a plate (height $\times$ width $\times$ thickness of 306 $\times$ 306 $\times$ 7 mm). The density of the front layer was determined by measuring the weight and the volume of this plate. The weight was measured using a AND EK-2000i [132], measurement uncertainty of 0.1 g. The length and width of the plate were measured using a Kobra(Mauser) [133] 300 mm caliper, where the thickness was measured using a Tesa Digit mircometer [134], measurement uncertainty of 5 μm.

3.4.2 Sound velocities measurements

The same setup as in Sect. 3.2 is used, where two V301 Olympus transducers [135] are used as transmitter and receiver positioned a distance d apart, and on-axis with respect to each other. The sound velocities for the front layer material are measured by determining the time-of-flight difference between the signals received by the receiver V301 of the two cases; with the inserted plate with thickness t_m, and that witout the plate[136]. The compressional sound velocity is then calculated as

$$c_{m,l} = \frac{c_f}{1 - \Delta t_l c_f / d}, \tag{3.3}$$

where Δt_l is the time-of-flight difference at normal beam incidence towards the plate. The shear sound velocity is then calculated as

$$c_{m,s} = \frac{c_f}{1 - \Delta t_s c_f / d}, \tag{3.4}$$

where Δt_s is the time-of-flight difference at an angle above the critical angle towards the plate, given as

$$\theta_c = \sin^{-1}(c_f / c_{m,l}), \tag{3.5}$$

assuming that the travel distance through the plate corresponded to the plate thickness. This method assums that the phase velocity is approximately equal to the group velocity.

[2] See Sect. 5.2.2 for the discussion regarding the choice of material.

3.5 Hydrophone calibration

3.5.1 Introduction

In order to facilitate quantitative assessment of the measurement system, the receiver hydrophone has been calibrated by Precision Acoustics (PA)[124] in the frequency range 1 - 20 MHz, with 1 MHz increments, and by the National Physical Laboratory (NPL)[137] in the frequency range of 100 kHz to 1 MHz, with 10 kHz increments, providing a level of confidence of approximately 95%. The end-of-cable loaded sensitivity is calculated, which is the combined receiver sensitivity of the needle hydrophone, preamplifier and the DC coupler, when the DC coupler is terminated with a 50 Ω load in parallell with a high impedance amplifier. In order to assess whether the NPL calibration can be used in the measurement system described in Sect. 3.2, an in-house calibration is made. In Sect. 3.5.2 and 3.5.3 two reciprocity calibration schemes [138] are used to determine the end-of-cable loaded receiver sensitivity of the hydrophone in the frequency range 100 kHz - 1.5 MHz, with increments of 5 kHz. The needle hydrophone with serial no. 1820, preamplifier with serial no. PA110078 and a DC coupler with serial no. DCPS223 are calibrated, denoted receiver R, using two V301 immersion transducers by Olympus [135], denoted S (serial no. 654220) and T (serial no. 654055).

In the following derivation one assume that the measurements are preformed under ideal conditions, i.e. free field, far field, no losses in fluid, no loss due to cables. The theoretical derivation takes into account the phase responses, but for measurement results, only the magnitude is used. Measurement results are not corrected for absorption, since it can be neglected in frequency ranges up to 1 MHz for calibration in fresh water [138]. As absorption increases with frequency and distance, the worst case scenario at 1 MHz, i.e. maximum frequency for transmission measurements, with a maximum distance of 376.05 mm is examined. For the following case, absorption corresponded to 0.086 dB.

3.5.2 2-transducer calibration scheme

This calibration method assumes that the two V301 transducers, denoted S and T, are equal and reciprocal. Two measurements must be completed to calibrate the unknown receiver sensitivity of the hydrophone, where the first measurement determines the open circuit voltage source sensitivity of the transmitting transducer and the second measurement determines the end-of-cable loaded receiver sensitivity of the hydrophone. Since the end-of-cable loaded receiver sensitivity for the needle hydrophone is to be calculated, the hydrophone in measurement B (source S $\rightarrow$ receiver R) is terminated with 50 Ω, whereas transducer T in measurement A (source S $\rightarrow$ transducer T) is terminated with 1 MΩ to determine the open circuit voltage source sensivitiy.

Measurement A): Source S $\rightarrow$ Transducer T
A voltage $V_S^{(1)}$ is delivered to source S. This provides the on-axis free-field sound pressure P_T at transducer T as

$$P_T = \frac{S_S^V V_S^{(1)} d_0}{d_1} e^{ik(d_0 - d_1)}, \tag{3.6}$$

where d_1 is the distance between the source and the transducer, S_S^V is the open circuit voltage source

sensitivity of source S at $d_0 = 1$ m. $k = \omega/c$, where c is the sound velocity in water.

The open circuit output voltage V_{ST} of transducer T is given as

$$V_{ST} = M_T^V P_T = \frac{M_T^V S_S^V V_S^{(1)} d_0}{d_1} e^{ik(d_0 - d_1)}, \tag{3.7}$$

where M_T^V is the open circuit voltage receiver sensitivity of T.

A reciprocal transducer must be linear, passive and reversible. If one assumes that transducer T is reciprocal, then

$$\frac{M_T^V}{S_T^I} = J, \tag{3.8}$$

where S_T^I is the open circuit current source sensitivity of T. J is the spherical reciprocity factor [138, 139], given as

$$J = \frac{M_T^V}{Z_T S_T^V} = \frac{2d_0}{\rho f} e^{ikd_0}, \tag{3.9}$$

where Z_T is the electrical input impedance of transducer T, S_T^V is the open circuit voltage source sensitivity of T, and ρ is the density of the surrounding fluid.

Inserting for M_T^V in Eq. (3.7) gives

$$V_{ST} = \frac{J S_T^V Z_T S_S^V V_S^{(1)} d_0}{d_1} e^{ik(d_0 - d_1)}. \tag{3.10}$$

If now source S and transducer T are equal then

$$S_T^V = S_S^V, \tag{3.11}$$

and the voltage source sensitivity of the source S can be calculated as

$$S_S^V = \sqrt{\frac{V_{ST}}{V_S^{(1)}} \frac{d_1}{d_0} \frac{1}{J Z_T} e^{ik(d_1 - d_0)}}. \tag{3.12}$$

Measurement B): Source S $\rightarrow$ Receiver R
A voltage $V_S^{(2)}$ is delivered to source S. This provides the on-axis sound pressure P_R at receiver R as

$$P_R = \frac{S_S^V V_S^{(2)} d_0}{d_2} e^{ik(d_0 - d_2)}, \tag{3.13}$$

where d_2 is the distance between the source and the receiver.

The end-of-cable loaded voltage V_{SR} out of receiver R is given as

$$V_{SR} = M_R^V P_R = \frac{M_R^V S_S^V V_S^{(2)} d_0}{d_2} e^{ik(d_0 - d_2)}, \tag{3.14}$$

where M_R^V is the end-of-cable loaded voltage receiver sensitivity of R.

Inserting Eq. (3.12) for the source sensitivity of S in Eq. (3.14), the end-of-cable loaded voltage receiver sensitivity of R is calculated as

$$M_V^R = \frac{V_{SR}}{V_S^{(2)}} \frac{d_2}{d_0} \frac{1}{\sqrt{\frac{V_{ST}}{V_S^{(1)}} \frac{d_1}{d_0} \frac{1}{JZ_T} e^{ik(d_1-d_0)}}} e^{ik(d_2-d_0)}. \tag{3.15}$$

The electrical conductance for the two V301 transducers used as source S and transducer T is presented in Fig. 3.4 to verify that the two transducers have approximately the same electrical response. Below 300 kHz, there exists some deviations between the two transducers, but these were disregarded due to the measurement range set in Sect. 3.2. See Sect. 3.6.1 for the experimental setup for the electrical measurements.

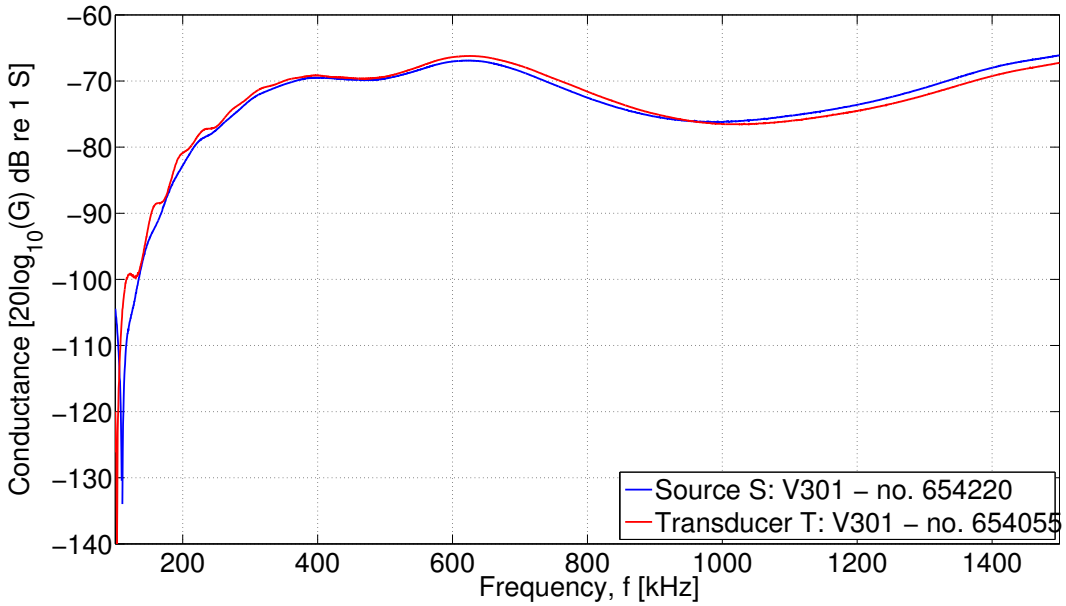

Fig 3.4. The electrical conductance for the V301 transducers, source S (no. 654220) (blue line) and transducer T (no. 654055) (red line), used in the two-transducer calibration scheme.

Carrying out measurement A), the open circuit voltage source sensitivity for the source S is calculated and presented in Fig. 3.5(a), using a distance of 1.167 m between the source and transducer. The corresponding open circuit voltage receiver sensitivity for the source S is calculated using Eq. (3.8), and presented in Fig. 3.5(b). Concluding measurement B), the end-of-cable loaded receiver sensitivity of the 1 mm needle hydrophone (probe length 100 mm) (red line) is determined and presented in Fig. 3.6 using a distance of 0.9109 m between the source and receiver, terminated with a 50 Ω load in parallell to the high impedance amplifier in comparison with the end-of-cable loaded sensitivity measured by NPL (blue line). During the NPL calibration the separation distance between the hydrophone and the source was 1 m. The two stipulated black lines is the measurement uncertainty of the NPL calibration, level of confidence of approximately 95%. From Figs. 3.5(a) and 3.5(b), the V301 transducer can not be used in the region 1.1 - 1.2 MHz. This means that the reciprocity calibration in this region, see Fig. 3.6 can not be used.

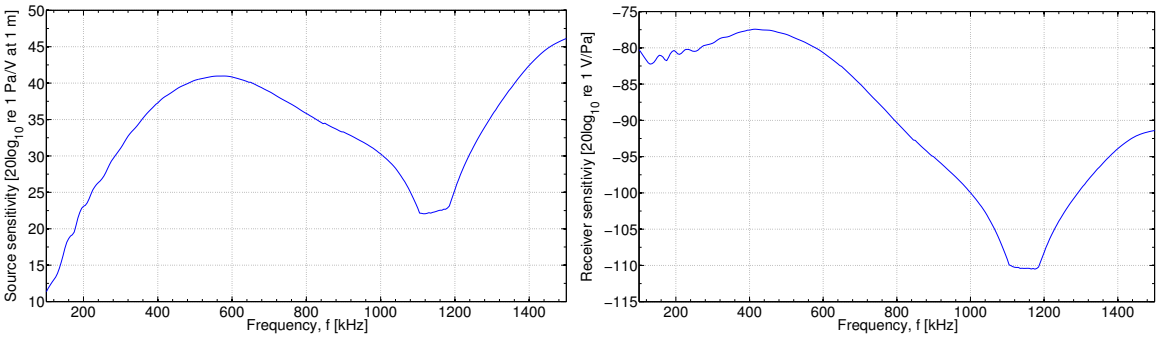

(a) (b)

Fig 3.5. Open circuit voltage **a)** source sensitivity $S_V(f)$ and **b)** receiver sensitivity of the V301 transducr used as source S, calculated assuming reciprocity.

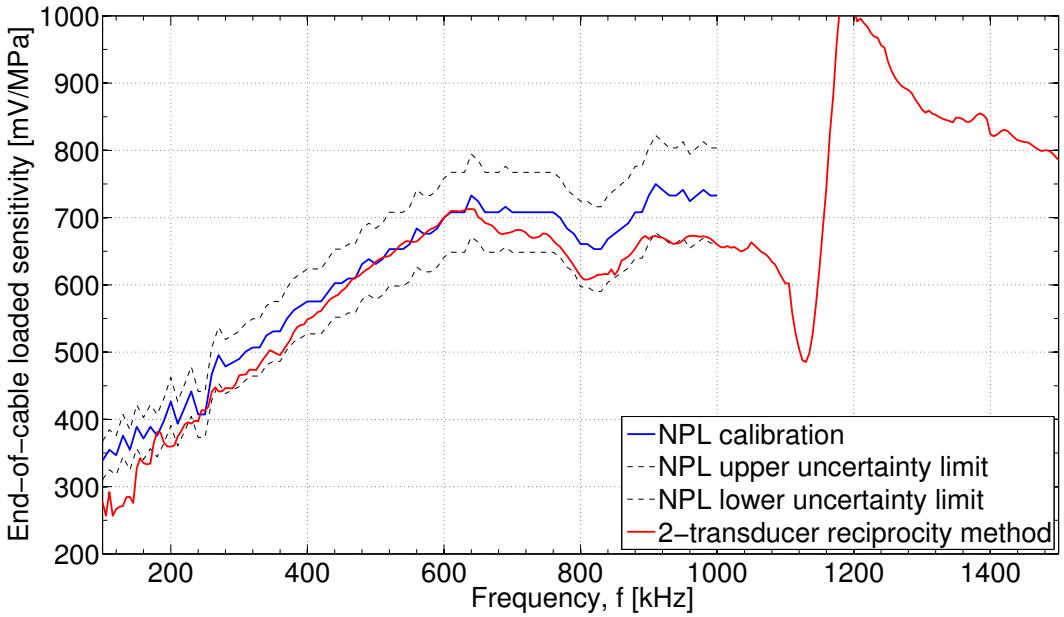

Fig 3.6. In-house end-of-cable receiver sensitivity of the PA 1 mm needle hydrophone (probe length 100 mm) (red line) in comparison with the NPL calibration (blue line) with uncertainty limits (dotted black lines).

3.5.3 3-transducer calibration scheme

In this calibration method two transducers are used to determine the receiver sensitivity of a receiver, a source S, transducer T and receiver R. The difference from the 2-transducer method is that one does not need to assume two equal transducers to determine the receiver sensitivity. Four measurements must be completed to calibrate the unknown receiver sensitivity, where three measurements are needed to actually determine the sensitivity, and the fourth measurement is completed in order to test if transducer T is reciprocal. Since the end-of-cable loaded receiver sensitivity for the needle hydrophone is to be calculated, the hydrophone in measurement A (source S $\rightarrow$ receiver R) and C (transducer T $\rightarrow$ receiver R) is terminated with 50 Ω, whereas measurement B and D is made under open circuit conditions (terminated with 1 MΩ). The same distances as in Sect. 3.5.2 between source S, transducer

T and receiver R is used.

Measurement A): Source S $\rightarrow$ Receiver R
A voltage $V_S^{(1)}$ is delivered to source S. This provides the on-axis free field sound pressure P_R at the receiver R as

$$P_R = \frac{S_S^V V_S^{(1)} d_0}{d_1} e^{ik(d_0 - d_1)}, \tag{3.16}$$

where d_1 is the distance between the receiver and the source, , S_S^V is the open circuit voltage source sensitivity of source S at $d_0 = 1$ m. $k = \omega/c$, where c is the sound velocity in water.

The end-of-cable loaded voltage V_{SR} out of receiver R is given as

$$V_{SR} = M_R^V P_R = \frac{M_R^V S_S^V V_S^{(1)} d_0}{d_1} e^{ik(d_0 - d_1)}, \tag{3.17}$$

where M_R^V is the end-of-cable loaded voltage receiver sensitivity of R.

Measurement B): Source S $\rightarrow$ Transducer T
A voltage $V_S^{(2)}$ is delivered to source S. This provides the on-axis free field sound pressure P_T at the transducer T as

$$P_T = \frac{S_S^V V_S^{(2)} d_0}{d_2} e^{ik(d_0 - d_2)}, \tag{3.18}$$

where d_2 is the distance between the transducer and the source.

The open circuit voltage V_{ST} out of transducer T is given as

$$V_{ST} = M_T^V P_T = \frac{M_T^V S_S^V V_S^{(2)} d_0}{d_2} e^{ik(d_0 - d_2)}, \tag{3.19}$$

where M_T^V is the open circuit receiver sensitivity of T with respect to voltage.

Dividing the voltage V_{SR} in Eq. (3.17) with voltage V_{ST} in Eq. (3.19) gives

$$\frac{V_{SR}}{V_{ST}} = \frac{M_R^V}{M_T^V} \frac{d_2}{d_1} \frac{V_S^{(1)}}{V_S^{(2)}} e^{ik(d_2 - d_1)}. \tag{3.20}$$

A reciprocal transducer must be linear, passive and reversible. If one assumes that transducer T is reciprocal, then

$$\frac{M_T^V}{S_T^I} = J, \tag{3.21}$$

where S_T^I is the current source sensitivity of T. J is the spherical reciprocity factor [138, 139], given as

$$J = \frac{M_T^V}{Z_T S_T^V} = \frac{2d_0}{\rho f} e^{ikd_0}, \tag{3.22}$$

where Z_T is the electrical input impedance of transducer T, S_T^V is the open circuit voltage source sensitivity of T, and ρ is the density of the surrounding fluid.

From Eq. (3.20), the end-of-cable loaded receiver sensitivity of R is given as

$$M_R^V = \frac{V_S^{(2)}}{V_S^{(1)}} \frac{V_{SR}}{V_{ST}} \frac{d_1}{d_2} M_T^V e^{ik(d_1-d_2)}. \tag{3.23}$$

Using the spherical reciprocity factor in Eq. (3.22) gives

$$M_R^V = \frac{V_S^{(2)}}{V_S^{(1)}} \frac{V_{SR}}{V_{ST}} \frac{d_1}{d_2} S_T^V J Z_T e^{ik(d_1-d_2)}. \tag{3.24}$$

Measurement C): Transducer T $\rightarrow$ Receiver R

A voltage $V_T^{(1)}$ is delivered to transducer T. This provides the on-axis free field sound pressure P_R at the receiver R as

$$P_R = \frac{S_T^V V_T^{(1)} d_0}{d_3} e^{ik(d_0-d_3)}, \tag{3.25}$$

where d_3 is the distance between the transducer and the receiver.

The end-of-cable loaded voltage V_{TR} out of receiver R is given as

$$V_{TR} = M_R^V P_R = \frac{M_R^V S_T^V V_T^{(1)} d_0}{d_3} e^{ik(d_0-d_3)}. \tag{3.26}$$

From Eq. (3.26) the open circuit voltage source sensitivity of T is then given as

$$S_T^V = \frac{V_{TR}}{V_T^{(1)}} \frac{d_3}{d_0} \frac{1}{M_R^V} e^{ik(d_3-d_0)}. \tag{3.27}$$

The end-of-cable loaded receiver voltage sensitivity of receiver R can be calculated inserting Eq. (3.27) into Eq. (3.24), giving

$$M_R^V = \frac{V_S^{(2)}}{V_S^{(1)}} \frac{V_{SR}}{V_{ST}} \frac{d_1}{d_2} \frac{V_{TR}}{V_T^{(1)}} \frac{d_3}{d_0} \frac{1}{M_R^V} J Z_T e^{ik(d_1-d_2+d_3-d_0)}, \tag{3.28}$$

which becomes

$$M_R^V = \sqrt{\frac{V_S^{(2)}}{V_S^{(1)}} \frac{V_{SR}}{V_{ST}} \frac{d_1}{d_2} \frac{V_{TR}}{V_T^{(1)}} \frac{d_3}{d_0} J Z_T e^{ik(d_1-d_2+d_3-d_0)}}. \tag{3.29}$$

Using the spherical reciprocity factor given in Eq. (3.22), this can be rewritten as

$$M_R^V = \sqrt{\frac{V_S^{(2)}}{V_S^{(1)}} \frac{V_{SR}}{V_{ST}} \frac{d_1}{d_2} \frac{V_{TR}}{V_T^{(1)}} \frac{d_3}{d_0} \frac{2d_0}{\rho f} Z_T e^{ik(d_1-d_2+d_3)}}. \tag{3.30}$$

Measurement D:) Transducer T $\rightarrow$ Source S

This measurement is conducted to test if transducer T is reciprocal. After completing measurement B), the transducers are kept in their positions, and a voltage $V_T^{(2)}$ is applied to the transducer T, resulting in a measured voltage V_{TS}. This test will actually check if the system 'transducer T – source S' is reciprocal, but if that is the case, then most likely will transducer T also be reciprocal. The system will be reciprocal if

$$\frac{V_{ST}}{I_S} = \frac{V_{TS}}{I_T}, \tag{3.31}$$

where $I_S = V_S^{(2)}/Z_S$ and $I_T = V_T^{(2)}/Z_T$, and Z_S is the input impedance of source S.

Measurements A), B) and C) are conducted to calculate the end-of-cable loaded receiver sensitivity, using the same tranducers as in Sect. 3.5.2 for source S and transducer T. Fig. 3.7 shows the end-of-cable loaded receiver sensitivity of the hydrophone (100 mm probe length) for the 2- (blue line) and 3-transducer (red line) reciprocity methods. There is up to approximately 280 mV/MPa difference between the two methods in the frequency range. For the same reason as for the 2-transducer reciprocity calibration scheme, the 3-transducer method can not be used in the frequency range 1.1-1.2 MHz, but the 3-transducer calibration curve shows an improved continuity before 1.1 MHz, and after 1.2 MHz.

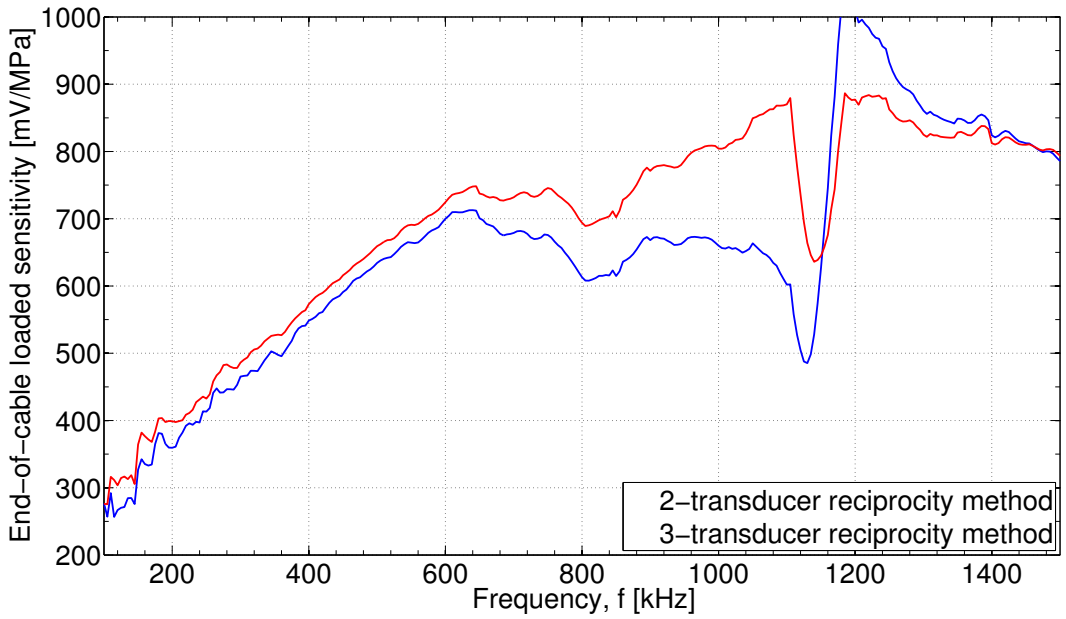

Fig 3.7. End-of-cable loaded receiver sensitivity of the PA 1 mm needle hydrophone (100 mm probe length). Comparison of the 2-transducer (blue line) and 3-transducer (red line) reciprocity calibration methods.

In Fig. 3.8 the end-of-cable loaded receiver sensitivity calculated using the 3-transducer reciprocity calibration method (red line) is compared to the calibration provided by NPL (blue line). A closer agreement can be observed than for the 2-transducer reciprocity method in Fig. 3.6 because one does not need to assume that the two V301 transducers are equal.

In Fig. 3.9 the ratio between the two fractions of Eq. (3.31) is presented. The ratio is approximately unity (exception 1.1-1.2 MHz region), confirming that the system 'transducer T – source S' is nearly reciprocal, and that the 3-transducer reciprocity method can be used to calibrate the hydrophone. If not stated otherwise, the NPL calibration is used for piezoelectric transducer properties and transmission measurements throughout this thesis.

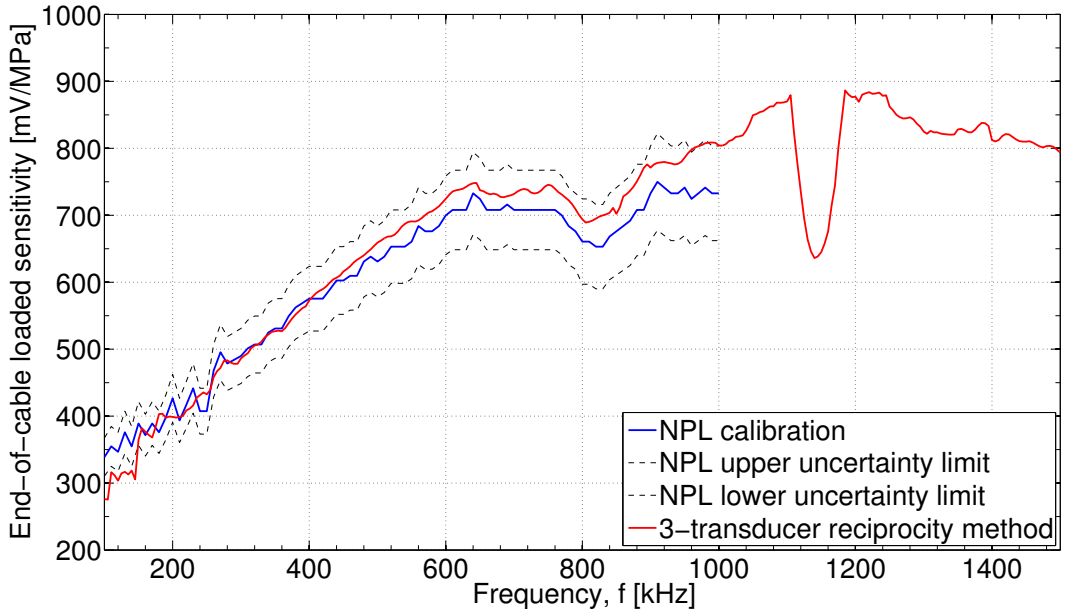

Fig 3.8. In-house end-of-cable receiver sensitivity of the PA 1 mm needle hydrophone (probe length 100 mm) (red line) in comparison with the NPL calibration (blue line) with uncertainty limits (dotted black lines).

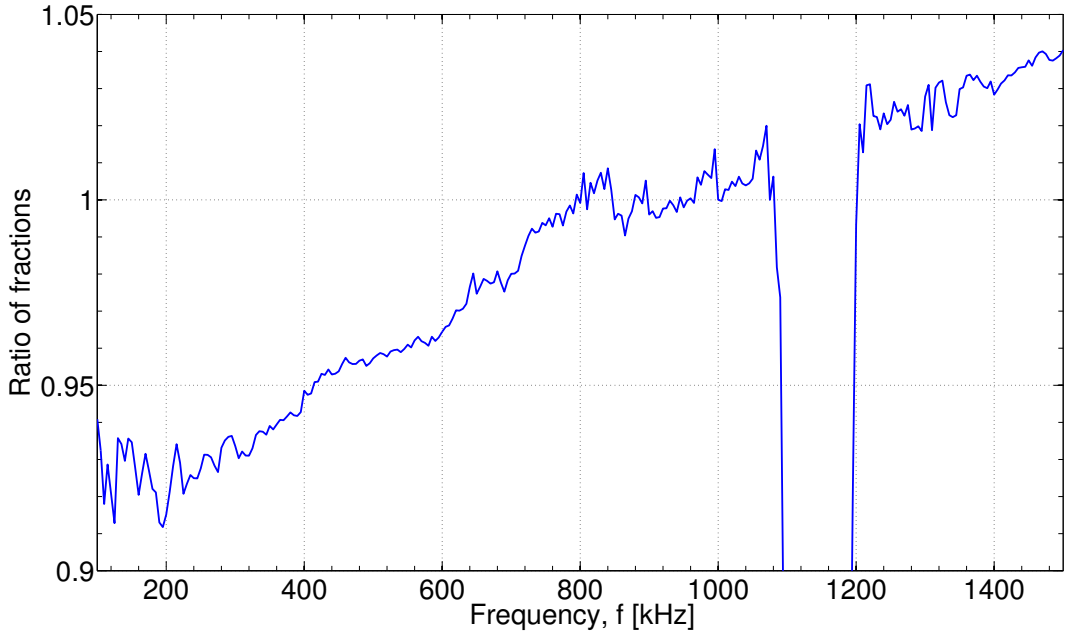

Fig 3.9. The ratio between the two fractions of Eq. (3.31), confirming that the system 'transducer T – source S' is nearly reciprocal.

3.6 Measurements of piezoelectric transducer properties

In this section the measurement setup for the piezoelectric transducer properties are given. For acoustical measurements the measurement setup described in Sect. 3.2 is used, with the steel plate absent.

The experimental setup for measuring the electrical admittance is given in Sect. 3.6.1, the source sensitivity in Sect. 3.6.2 and the beam pattern in Sect. 3.6.3.

3.6.1 Electrical admittance, $Y(f)$

The electrical measurements are carried out using a HP4192A Impedance analyzer [140], connected to a PC through a GPIB cable. Fig. 3.10 shows the impedance analyzer, with a holder of polystyrene to reduce reflections from the piezoelectric transducer structure used for measuring the electrical admittance $Y(f)$ for the structure in air, where $Y(f) = \frac{1}{Z(f)}$. When the transducer radiates in water, a RG-58 coaxial cable is used to connect the transducer to the instrument. In order to minimize effects of the measurement equipment, including cables, the instrument and cables are zero-adjusted [140] before each measurement.

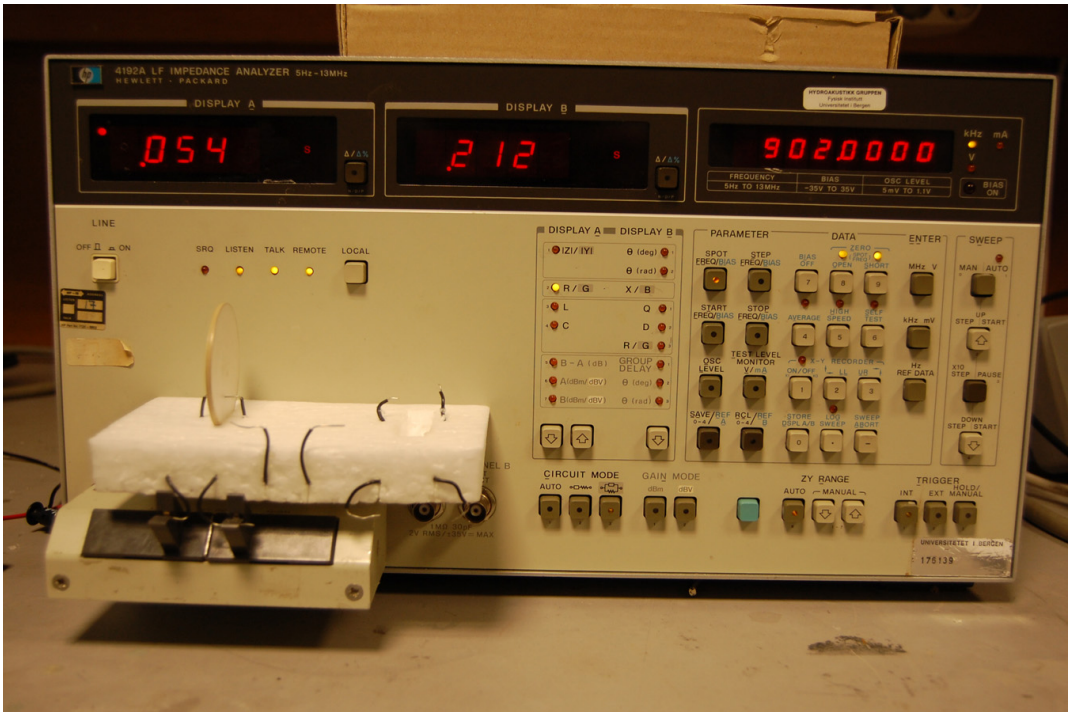

Fig 3.10. HP4192A Impedance analyzer used to measure the electrical admittance $Y(f)$.

3.6.2 Source sensitivity, $S_V(f)$

The source sensitivity is defined e.g. [138, 141] as

$$S_V(f) = \frac{P(0, d = d_0 = 1\text{m}, f)}{V(f)}, \tag{3.32}$$

where $V(f)$ is the input voltage to the transducer, $P(0, d = d_0 = 1\text{m}, f)$ is the free-field on-axis sound pressure at a distance $d_0 = 1$ m, assuming far field conditions at this distance. A distance of $d = 0.9065$ m between the transducer and receiver is used for the results reported in Chap. 5. The rayleigh distance for the prototype transducer (cf. Chap. 5) is shown in Fig. 3.11 using the radius of the front layer (blue line) and piezoelectric disk (red line), respectively.

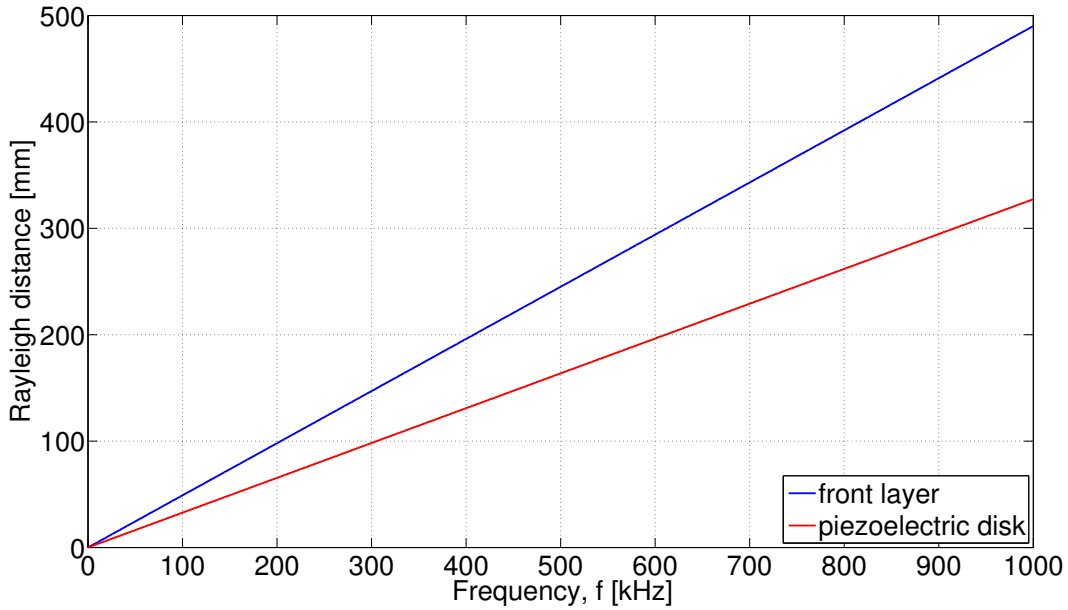

Fig 3.11. Rayleigh distance of the prototype transducer in water (c_f = 1485 m/s) using the radius of the front layer (blue line) and the piezoelectric disk (red line), respectively.

3.6.3 Beam pattern, $D(\phi, f)$

The beam pattern is defined [141] as

$$D(f, \phi) = \frac{P(d, f, \phi)}{P(d, f, 0)}, \tag{3.33}$$

where $\phi = \tan(r'/z')$ in Fig. 2.1 in Chap. 2, $p(d, f, \phi)$ is the sound pressure at a distance d, assuming far field conditions at this distance, with an angle ϕ from the on-axis. The hydrophone is positioned at $(x, y, z) = (0, 0, z)$, and the piezoelectric source transducer is positioned at $(x, y, z) = (0, 0, 0)$, and is rotated around the $y-$axis by the Micos PRS-110 rotary stage to conduct the measurements. A distance of $d = 0.63$ m between the transducer and receiver is used for the results reported in Chap. 5.

Chapter 4

Simulation setup

4.1 Introduction

This chapter presents the simulation setup for sound transmission simulations of the system described in Chaps. 2 and 3 for the FEM and hybrid FEM-ASM approaches, in Sects. 4.2 and 4.3 respectively. The piezoelectric source transducer model used to excite the measurement system is described in Sect. 4.5, at various steps in the construction process (cf. Sect. 4.5.1), and for the finished prototype in Sect. 4.5.2. The baffled piston source, used in comparison with the piezoelectric transducer, is described in Sect. 4.5.3. The material data for materials in the piezoelectric source transducer and the surrounding water is listed in Chap. 5, and the material data for the steel plate are listed in Chap. 6. For the accuracy of FEM simulations, refer to FEM convergence tests in Sect. 4.4.

4.2 The FEM approach

For normal beam incidence, a FEM approach is used to calculate the voltage-to-pressure transfer function $H_{VP}(x, y, z_2, f)_{cw}$, Eq. (2.10). A decimated mesh of the FE simulations is shown in Fig. 4.1, in order to visualize the meshing of the transducer, steel plate and water regions, refer to Chap. 6 for material type and data for the steel plate. The fluid PML (grey regions) thickness is set to 30 mm in all directions. Different distances to the PMLs, in addition to PML thicknesses were tested to ensure minimal reflections from these regions. The steel plate with a radius of 450 mm is indicated in green with the "decreasing Q_M" method (cf. Sect. 2.3) implemented from $r' = 220$ mm to the endface of the steel plate to reduce end reflections. In this region the Q_M for the steel plate is reduced exponentially from Q_M to 0.001. The frequency range is 300 kHz - 1.2 MHz, using non-frequency dependent damping function (cf. Sect. 2.3) for the PMLs calculations at 750 kHz, with a step frequency of $\Delta f = 500$ Hz. On a 16 x 3.60 GHz processor and 192 GB RAM the simulation took approx. 2.5 weeks to complete. 3 elements per shear wavelength at 1.2 MHz is used as the element division in the piezoelectric disk and in the other elastic regions, whereas 3 elements per compressional wavelength is used in water. The electrical loading of the signal generator is included as described in Chap. 2.

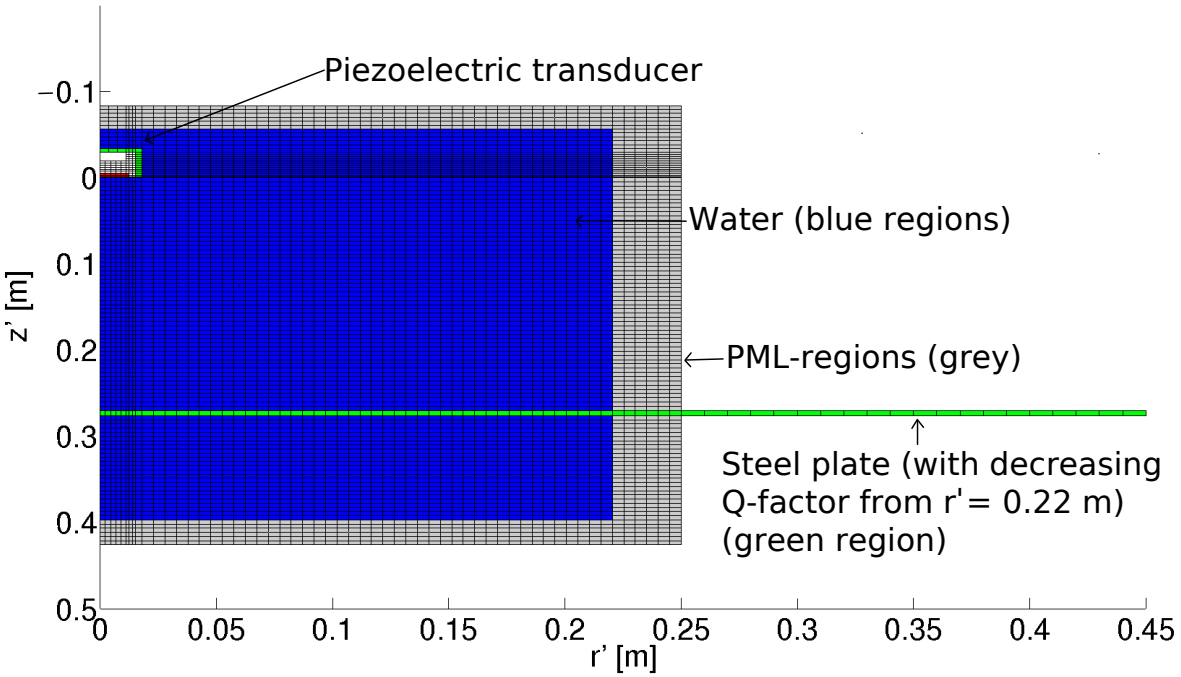

Fig 4.1. A decimated mesh of the axisymmetric FE simulation of the piezoelectric source transducer and the water-immersed steel plate (green region) at normal beam incidence. PMLs and the "decreasing Q_M" method have been utilized to simulate unbounded water regions and non-reflecting endfaces of the steel plate, respectively.

Using a frequency domain implementation, standing waves will appear between the transducer and the steel plate. For separating successive arrivals in time for a given frequency, a 80000 points, 100 period long, signal waveform $v(t)$ with the given centre frequency is used to excite the piezoelectric transducer. A sampling frequency of 40 MHz is used, giving $\Delta t = 0.0250$ μs and $\Delta f = 500$ Hz, equal to the FEM approach simulations. The waveform is transformed into the frequency domain using Eq. (2.4) giving $V(f)$ and multiplied with the voltage-to-pressure transfer function $H_{VP}(x, y, z_2, f)_{cw}$[1] calculated directly from the FE simulations. As the frequency range is 300 kHz - 1.2 MHz, $H_{VP}(x, y, z_2, f)_{cw}$ and the transducer's admittance $Y(f)_{cw}$ is set to zero elsewhere (for $f < 300$ kHz and $f > 1.2$ MHz), see justification in the next paragraph. The combined frequency spectrum of $P_t(x, y, z_2, f)_{cw}$ and $V(f)$ is then transformed back into the time domain using Eq. (2.12), e.g. Fig. 4.11(b) for a 60 period long 457 kHz tone burst. The first arrival is determined by time-gating as $p_t(x, y, z_2, t)$, and its steady state region is determined. From this region the Fourier transform is used to calculate $P_t(x, z, z_2, f)$ in a similar manner as in Sect. 3.2. The voltage-to-pressure transfer function $H_{VP}(x, y, z_2, f)$ is then calculated by completing the above steps for all frequencies in the range 350 kHz - 1 MHz.

The amount of aliasing introduced by using a bandlimited voltage-to-pressure transfer function is dictated by the bandwidth of the sinc-function (frequency spectrum of $V(f)$), and the behaviour of the transfer function at the end-frequencies. First, minimal aliasing due to using a bandlimited transfer function is introduced by smoothly ending $H_{VP}(x, y, z_2, f)_{cw}$ at the end-frequencies. The FEM transducer described in Chap. 5 is built for operating at frequencies around 400-600 kHz. For transducer

[1]Subscript cw denotes that the standing wave pattern is present.

characteristics, e.g. electrical conductance and source sensitivity (Figs. 5.26(a) and 5.26(b)) the source sensitivity has a low value at 300 kHz (approx. 44 dB re 1 Pa/V down from maximum), and in the range 1.1-1.2 MHz (approx. 57 dB re 1 Pa/V at 1.2 MHz down from maximum), and the frequencies are therefore chosen as the end-frequencies to smoothly confine our transfer function. Second, aliasing introduced by not representing the combined spectrum of $V(f)$ and $H_{VP}(x, y, z_2, f)_{cw}$ correctly, increases as the centre frequency of $v(t)$ reaches the end-frequencies of the transfer function, since greater parts of the frequency spectrum of $V(f)$ (sinc-function) is multiplied with zeroes. But, by using 100 period long tone bursts, the narrow bandwidth of $V(f)$ makes it possible to represent frequency spectra of $P_t(x, y, z_2, f)_{cw}$ in the frequency range 350 kHz - 1 MHz without introducing significant numerical errors due to this. The same conclusion can be made for simulating transmitted waveforms using either the FEM or hybrid FEM-ASM approach. The difference there is that the number of periods is changed, which effects the bandwidth of the sinc-function (less than 100 periods – wider bandwidth, more than 100 periods – narrower bandwidth). But, the centre frequencies of the simulating waveforms are located in the middle of the frequency range, hence the bandwidth of the given sinc-function plays a less important role.

To minimize numerical errors due to folding in the time domain, it is important to use a time trace that does include all significant echoes, since echoes that does arrive later will be folded into our time window. Due to the large acoustic impedance-ratio of water and steel, including the losses in the steel plate, and geometrical distrubution in water, successive arrivals in time will be dampen accordingly. Using the time window above, all significant echoes are represented (e.g. Fig. 4.11(b)), and minimal folding occurs.

4.3 The hybrid FEM-ASM approach

For normal and oblique angles of beam incidence, a hybrid FEM-ASM approach is used to calculate the voltage-to-pressure transfer function $H_{VP}(x, y, z, f)$, Eq. (2.10). The FEM is used to calculate the free-field sound pressure frequency spectrum $P_0(r', z', f)$ from the piezoelectric source transducer in the fluid nodes of the unbounded water region, when the plate is absent, see Fig. 4.2(a). The frequency range is 300 kHz - 1.2 MHz, using non-frequency dependent damping function for the PMLs calculations at 750 kHz, with a step frequency of $\Delta f = 1$ kHz. On a 16 x 3.60 GHz processor and 192 GB RAM the simulation took approx. 3 weeks to complete (dividing the frequency range and running two parallell simulations). 3 elements per shear wavelength at 1.2 MHz is used as the element division in the piezoelectric disk and in the other elastic regions, whereas 3 elements per compressional wavelength is used in water. The fluid PML (grey regions) thickness is set to 30 mm in all directions. A larger water region in front of the transducer than the FEM approach is used, with max $(r', z') = (450, 430)$ mm (incl. PMLs), making it possible to calculate the free-field sound pressure field for angles of beam incidence in the region $0 - 30°$. Convergence tests for the FEM calculations are reported in Sect. 4.4. The coordinate relationship of Eq. (2.1) gives the relationship between the transducer's axisymmetric sound field and the 3D coordinate system (x, y, z), for a given beam incidence θ. Thus, the sound pressure as a function of (x, y, z) can be calculated from the axisymmetric sound pressure, given as

function of (r', z'), for a known beam incidence θ, cf. Chap. 2. 2D linear interpolation of $P_0(r', z', f)$ over the plane (x, y, z_0) gives $P_0(x, y, z_0, f)$. Interpolation is used to fit the axisymmetric data to a grid of $[x_{min}, x_{max}, y_{min}, y_{max}] = [-300, 300, -300, 300]$ mm with $N_x \times N_y = 1024 \times 1024$ points, giving the spatial sampling interval $\Delta x = \Delta y = 0.586$ mm. The maximal horizontal wavenumber $h_{f,x}^{max}$ and $h_{f,y}^{max}$ are calculated as

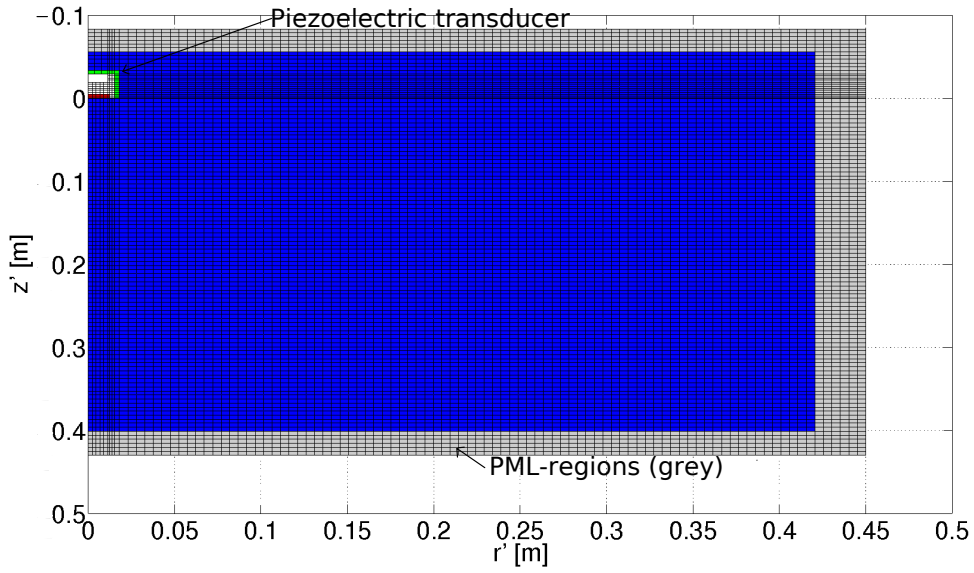

(a)

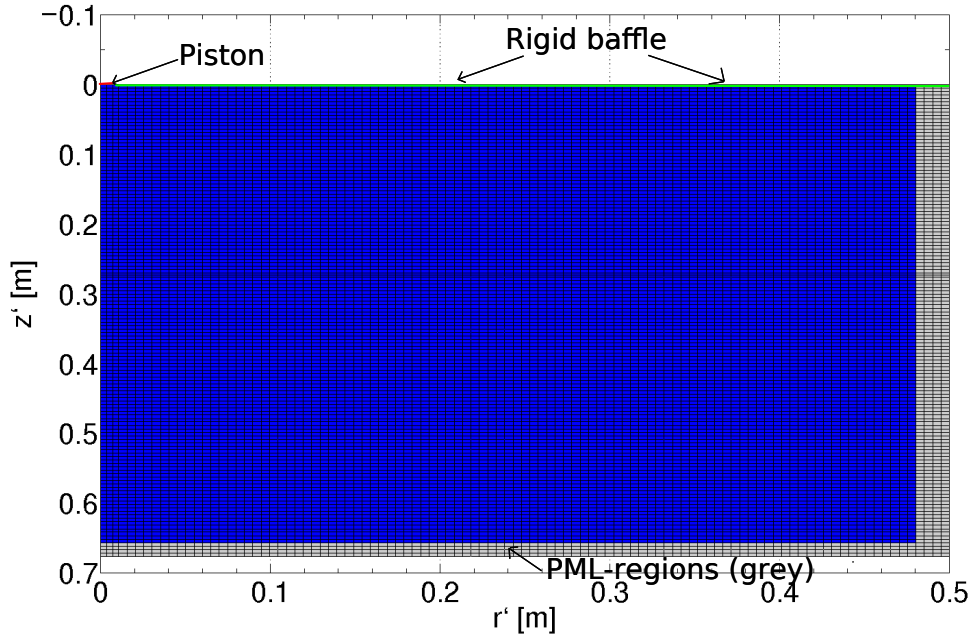

(b)

Fig 4.2. A decimated mesh of the FE simulations used in the hybrid FEM-ASM to calculate $P_0(r', z', f)$. **a)** For the piezoelectric transducer, **b)** For the piston source. Water regions in blue, with fluid PMLs (grey regions) to simulate an unbounded medium.

$$h_{f,x}^{max} = \frac{\pi}{\Delta x} = h_{f,y}^{max} = \frac{\pi}{\Delta y} = 5362 \text{ rad/m}. \tag{4.1}$$

The wavenumber sampling interval $\Delta h_{f,x} = \Delta h_{f,y}$ is then given as

$$\Delta h_{f,x} = \frac{2h_{f,x}^{max}}{N_x} = \Delta h_{f,y} = \frac{2h_{f,y}^{max}}{N_y} = 10.47 \text{ rad/m}. \tag{4.2}$$

The relationship between the real horizontal wavenumber η and the plane-wave incident angle θ_P is given as

$$\theta_P = \sin^{-1}\left(\frac{c_f \eta}{2\pi f}\right). \tag{4.3}$$

The Fourier transform in Eq. (2.6) is used to transform $P_0(x, y, z_0, f)$ into the frequency-wavenumber domain giving $\mathbf{P}_0(h_{f,x}, h_{f,y}, z_0, f)$, using the Fast Fourier transform (FFT) algorithm. The sound pressure is then propagated through the steel plate using the plane-wave pressure transmission coefficient $\mathscr{T}$ given by Eq. (2.7).

The plane wave propagator given by Eq. (2.8) is then used to propagate $\mathbf{P}_1(h_{f,x}, h_{f,y}, z_0 + 2L, f)$ to the receiver depth z_2. $\mathbf{P}_t(h_{f,x}, h_{f,y}, z_2, f)$ is then transformed into the frequency-space domain using Eq. (2.9), using the Fast Fourier transform (FFT) algorithm. Evanescent waves are included in the propagation through the steel plate and lower adjacent water region by Eqs. (2.61), (2.34) and (2.35). The electrical loading of the signal generator is included as described in Chap. 2.

The hybrid FEM-ASM approach is also used to simulate the signal propagation through the system using a simplified piston-generated beam, in order to assess the deviations introduced using a piston model in relation to the piezoelectric transducer. FEM is used to calculate the free-field sound pressure frequency spectrum $P_0(r', z')$ from a piston source in the fluid nodes of the unbounded water region, replacing the transducer. The FEM simulation simulates both near- and far-field sound pressure from the piston, in relation to [60, 68, 69, 70, 91, 92] which only used the far-field solution. A coarse decimated mesh is shown in Fig. 4.2(b). If not stated otherwise, the same setup as in Sect. 4.2 is used. Further information regarding the piston source is located in Sect. 4.5.3. Fluid PMLs (grey regions), with 20 mm thickness in all directions, are used to simulate an unbounded medium in front, and to the sides, of the piston in a water column with size $(r', z') = (500, 676.05)$ mm (including PMLs). The frequency range is 300 - 1 MHz[2], where 3 elements per compressional wavelength at 1 MHz is used as the element division in the water column, and using non-frequency dependent damping function for the PMLs calculations (cf. Sect. 2.3) at 650 kHz. A rigid baffle is specified along the r'-axis, at $z' = 0$ mm.

[2]This simulation is not used to calculate time domain waveforms, hence only including frequencies up to 1 MHz.

4.3.1 Signal transmission exemplified, for propagation of a 457 kHz tone burst at normal beam incidence

In the following section the signal propagation through the system at normal beam incidence using the hybrid FEM-ASM approach is exemplified, for propagation of a 457 kHz tone burst at normal beam incidence using the piezoelectric transducer as source. This is done to illustrate the signal transmission in the hybrid approach, in addition to the time domain calculations in the hybrid FEM-ASM and FEM approaches. Fig. 4.3(a) shows the 80000 points long signal waveform of the electromotive force $v_0(t)$, with a center frequency of $f = 457$ kHz. Using Eq. (2.3) the pulsed waveform is transformed into the frequency domain, giving $|V_0(f)|$ as shown in Fig. 4.3(b). A sampling frequency of 80 MHz is used, giving $\Delta t = 0.0125$ μs and $\Delta f = 1$kHz, equal to the hybrid FEM-ASM simulations.

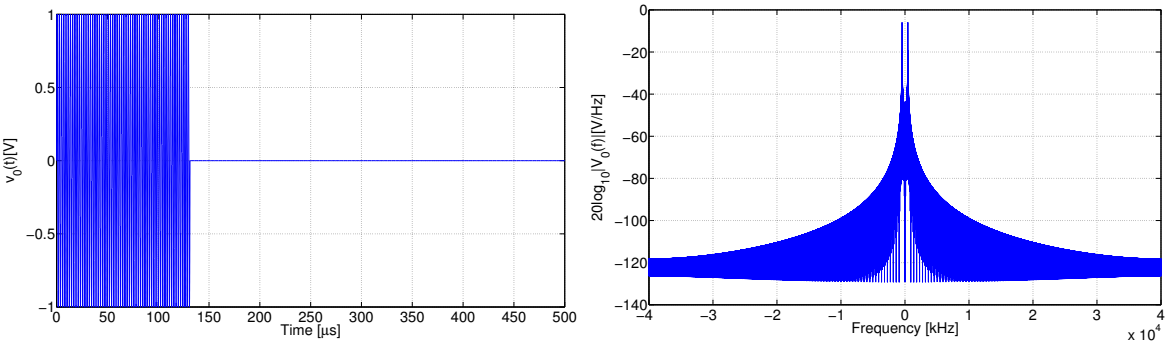

(a) (b)

Fig 4.3. **a)** The electromotive force waveform (tone burst) $v_0(t)$. **b)** Magnitude of the frequency spectrum $V_0(f)$ of $v_0(t)$.

The electrical loading of the signal generator is simulated using the Thévenin model in Eq. (2.2). Fig. 4.4(a) shows the resulting voltage waveform $v(t)$ transmitted to the transducer (representing the electrical input voltage to the piezoelectric transducer). The magnitude of the corresponding frequency spectrum $V(f)$ is given in Fig. 4.4(b). The electrical impedance of the piezoelectric transducer, $Z_T(f)$, is simulated from 300 kHz to 1.2 MHz. $Z_T(f)$ is set to zero elsewhere, cf. Fig. 5.26(a) in Sect. 5.4.3.

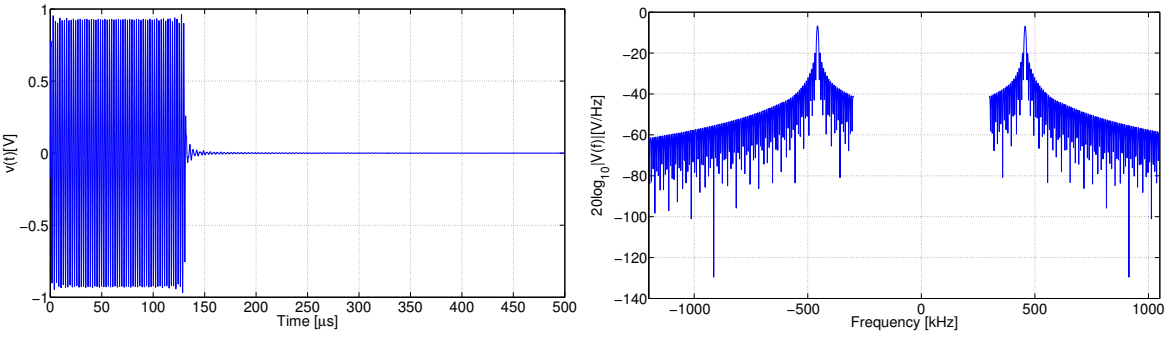

(a) (b)

Fig 4.4. **a)** The electrical input voltage waveform to the piezoelectric transducer, $v(t)$. **b)** Magnitude of the frequency spectrum $V(f)$ of $v(t)$.

Fig. 4.5(a) shows the magnitude of the FEM calculated and interpolated incident free-field pressure frequency spectrum $P_0(x, y, z_0, 457\text{kHz})$ at the plate's upper surface, when the plate is absent. In Fig. 4.5(b) the FEM calculated magnitude of the free-field pressure frequency spectrum $|P_0(x, 0, z_0, 457\text{kHz})|$ at $y = 0$ mm is shown (blue line) and compared to the FEM pressure at the nodes along the surface (red line - before interpolation). At normal incidence $z' = z$, and only interpolation over the (x, y, z_0) grid is needed to calculate $P_0(x, y, z_0, f)$. The axisymmetric FEM incident free-field pressure frequency spectrum is presented in Fig. 4.5(b) from x = 0 mm to x = 300 mm.

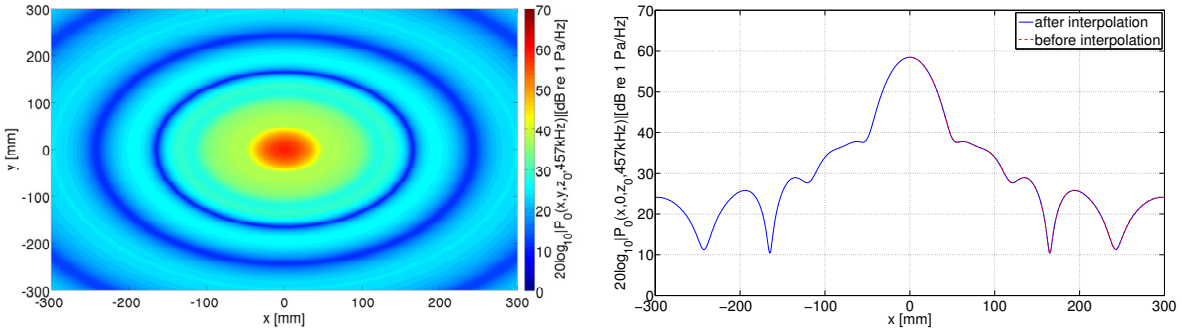

(a) (b)

Fig 4.5. At normal beam incidence $\theta = 0°$: Magnitude of the incident free-field pressure frequency spectrum at the plate's upper surface in absence of the plate, shown as a function of (x, y). **a)** $|P_0(x, y, z_0, 457\text{kHz})|$, **b)** $|P_0(x, 0, z_0, 457\text{kHz})|$, extracted from Fig. 4.5(a) (blue line) and compared to the axisymmetric FEM pressure at the nodes along the surface (red line – before interpolation).

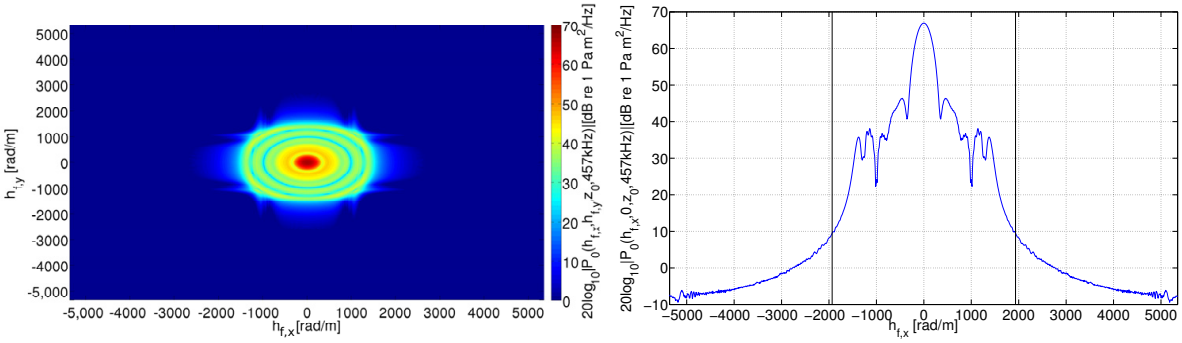

(a) (b)

Fig 4.6. At normal beam incidence ($\theta = 0°$): Magnitude of the 457 kHz component of the incident free-field pressure frequency-wavenumber spectrum at the plate's upper surface in absence of the plate, shown as a function of $h_{f,x}$ and $h_{f,y}$. **a)** $|\mathbf{P}_0(h_{f,x}, h_{f,y}, z_0, 457\text{kHz})|$, **b)** $|\mathbf{P}_0(h_{f,x}, 0, z_0, 457\text{kHz})|$ extracted from Fig. 4.6(a). The transitions from propagating to evanescent regions are marked with black vertical lines.

The incident sound pressure frequency spectrum $P_0(x, y, z_0, 457\text{kHz})$ in Fig. 4.5(a) is transformed into the frequency-wavenumber domain using the Fourier transform of Eq. (2.6), giving $\mathbf{P}_0(h_{f,x}, h_{f,y}, z_0, 457\text{kHz})$ shown in Fig. 4.6(a). The incident free-field pressure $|\mathbf{P}_0(h_{f,x}, 0, z_0, 457\text{kHz})|$ at $h_{f,y} = 0$ rad/m in Fig. 4.6(a) is shown in Fig. 4.6(b). The transitions between the propagating and the evanescent regions are marked with black vertical lines, corresponding to an incident angle of 90°, equal to 1933.6 rad/m

using Eq. (4.3). In the propagating region, Eq. (4.3) can be used to calculate the incident angle of each plane-wave component.

To describe the transmission of sound through the water-immersed steel plate the plane-wave pressure transmission coefficient $\mathscr{T}(h_{f,x}, h_{f,y}, L, f)$, described by Eq. (2.7), is used. The magnitude of the plane-wave pressure transmission coefficent $\mathscr{T}$ at $f = 457$ kHz and $h_{f,y} = 0$ rad/m, $|\mathscr{T}(h_{f,x}, 0, L, 457\text{kHz})|$, is shown in Fig. 4.7(a). This figure demonstrates the transmission of each plane-wave component through the water-immersed steel plate at 457 kHz. Black vertical lines indicate the transitions to the evanescent region. A close up of Fig. 4.7(a) is given in Fig. 4.7(b). Regions where the transmission is relatively high corresponds to the excitation of leaky Lamb modes, closely related to Fig. 6.5. In addition, (the plane-wave pressure transmission coefficient) $\mathscr{T}(h_{f,x}, h_{f,y}, L, f)$ can be considered as a lowpass filter, cutting higher wavenumbers due to little to none transmission of sound at an angle above the excitation of the A_0 mode, i.e. $\approx 32.43°$ at 457 kHz, see Fig. 6.4. Using Eq. (4.3) this corresponds to $h_{f,x} \approx 1037$ rad/m. With regard to the numerical implementation of the angular spectrum method, the plane-wave pressure transmission coefficient thus reduces possible aliasing from higher wavenumbers in $\mathbf{P}_0(h_{f,x}, h_{f,y}, z_0, f)$. Fig. 4.7(b) shows the various leaky Lamb modes excited in the water-immersed steel plate at 457 kHz, see Chap. 6.

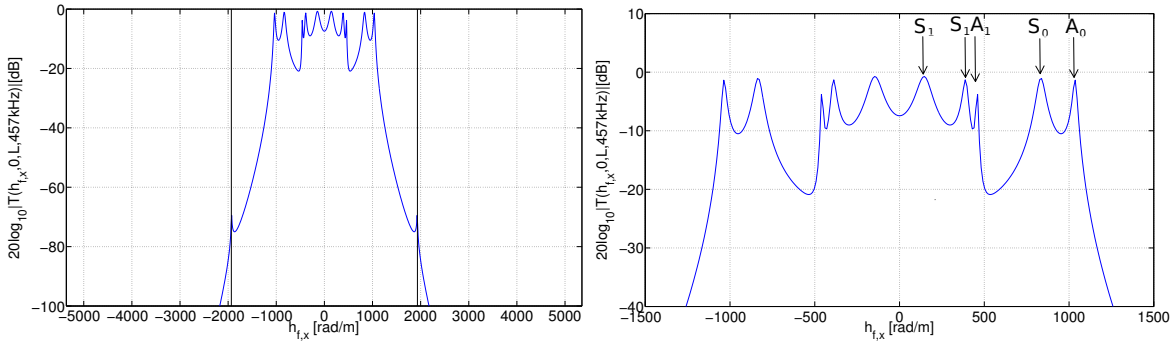

(a) (b)

Fig 4.7. Magnitude of the 457 kHz component of the plane-wave transmission coefficent of the viscoelastic steel plate, $|\mathscr{T}(h_{f,x}, 0, L, 457\text{kHz})|$ at $h_{f,y} = 0$ rad/m. **a)** The transitions from propagating to evanescent regions are marked with black vertical lines, **b)** A close up of Fig. 4.7(a), highlighting the various leaky Lamb modes in the steel plate.

$\mathbf{P}_0(h_{f,x}, h_{f,y}, z_0, 457\text{kHz})$ is now multiplied with the plane-wave pressure transmission coefficient $\mathscr{T}(h_{f,x}, h_{f,y}, L, 457\text{kHz})$ using Eq. (2.8), giving the transmitted free-field pressure frequency-wavenumber spectrum at the lower surface of the steel plate, $\mathbf{P}_1(h_{f,x}, h_{f,y}, z_0 + 2L, 457\text{kHz})$, shown in Fig. 4.8(a). The magnitude of the (transmitted pressure frequency-wavenumber spectrum) $|\mathbf{P}_1(h_{f,x}, 0, z_0{+}2L, 457\text{kHz})|$ at $h_{f,y} = 0$ rad/m in Fig. 4.8(a) is extracted and shown in Fig. 4.8(b). The transitions to the evanescent region are marked with black vertical lines. As a result of the multiplication with the plane-wave pressure transmission coefficient, all plane waves transmitted through the steel plate have been modified, and higher wavenumbers filtered out.

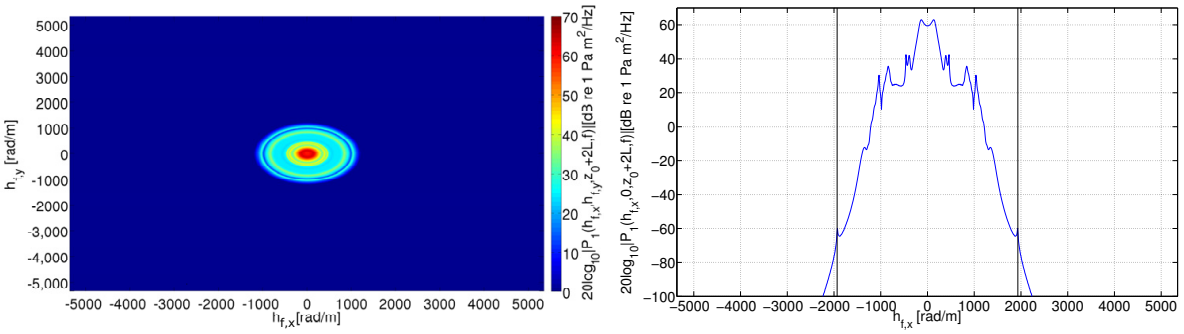

(a) (b)

Fig 4.8. At normal beam incidence ($\theta = 0°$): Magnitude of the 457 kHz component of the transmitted free-field pressure frequency-wavenumber spectrum at the plate's lower surface, shown as a function of wavenumber components $h_{f,x}$ and $h_{f,y}$. **a)** $|\mathbf{P}_1(h_{f,x}, h_{f,y}, z_0 + 2L, 457\text{kHz})|$, **b)** $|\mathbf{P}_1(h_{f,x}, 0, z_0 + 2L, 457\text{kHz})|$ extracted from Fig. 4.8(a). The transitions to the evanescent regions are marked with black vertical lines.

$\mathbf{P}_1(h_{f,x}, h_{f,y}, z_0+2L, 457\text{kHz})$ is now propagated to the receiver depth $z_2 = 376.05$ mm using the plane wave propagator given in Eq. (2.8), giving $\mathbf{P}_t(h_{f,x}, h_{f,y}, z_2, 457\text{kHz})$, the magnitude is shown in Fig. 4.9(a). The magnitude of the transmitted pressure frequency-wavenumber spectrum $|\mathbf{P}_t(h_{f,x}, 0, z_2, 457\text{kHz})|$ at $h_{f,y} = 0$ rad/m in Fig. 4.9(a) is extracted and shown in Fig. 4.9(b). The evanescent waves in Fig. 4.8(b) are suppressed due to a propagation distance of 100 mm, see Fig. 4.9(b).

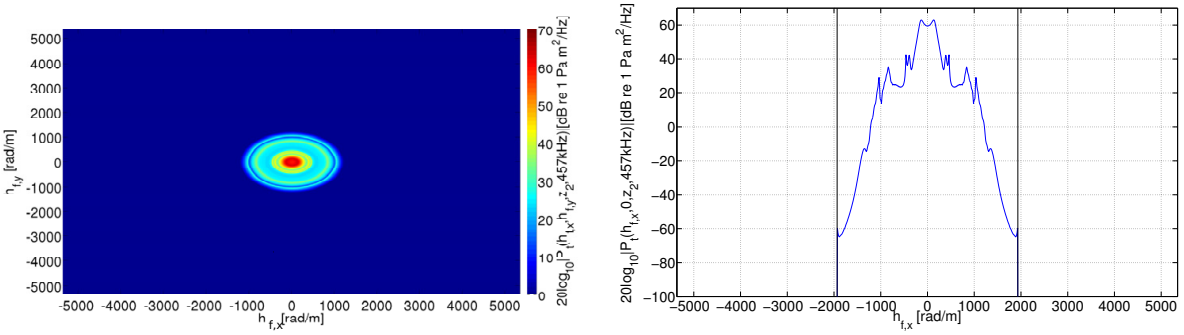

(a) (b)

Fig 4.9. At normal beam incidence ($\theta = 0°$): Magnitude of 457 kHz component of the transmitted pressure frequency-wavenumber spectrum at the receiver depth z_2, i.e. '*' in Fig. 2.1. **a)** $|\mathbf{P}_t(h_{f,x}, h_{f,y}, z_2, 457\text{kHz})|$, **b)** $|\mathbf{P}_t(h_{f,x}, 0, z_2, 457\text{kHz})|$ extracted from Fig. 4.9(a). The transitions to the evanescent regions are marked with black vertical lines.

The transmitted pressure frequency-wavenumber spectrum $\mathbf{P}_t(h_{f,x}, h_{f,y}, z_2, 457\text{kHz})$ is transformed into the spatial domain using the inverse Fourier transform, Eq. (2.9), giving $P_t(x, y, z_2, 457\text{kHz})$, the magnitude presented in Fig. 4.10(a). The magnitude of the transmitted pressure $|P_t(x, 0, z_2, 457\text{kHz})|$ at $y = 0$ mm in Fig. 4.10(a) is extracted and shown (blue line) in Fig. 4.10(b), in comparison with $|P_t(x, 0, z_2, 457\text{kHz})|$ calculated using the FEM approach (red line) discussed in Sect. 4.2. Above $x = 220$ mm the figure shows some deviations between the two approaches, due to the PML region for $x > 220$ mm, in the FEM approach, see Sect. 4.2.

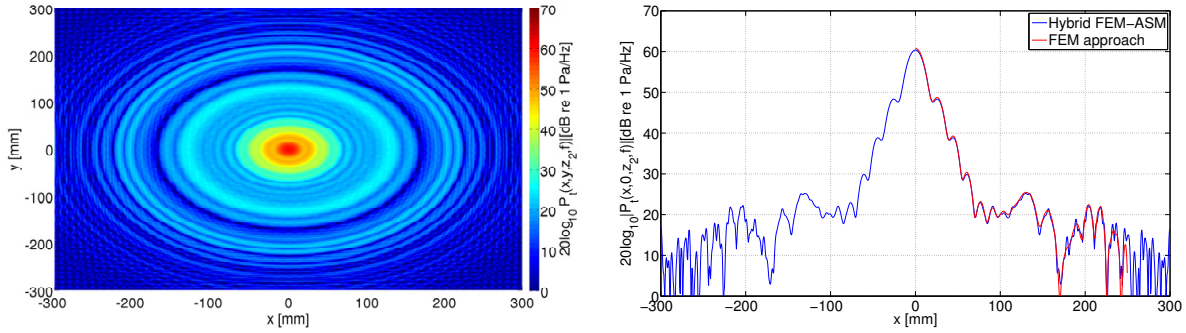

(a) (b)

Fig 4.10. At normal beam incidence ($\theta = 0°$): Magnitude of transmitted pressure frequency spectrum at the receiver depth z_2, i.e. at the depth of '$*$' in Fig. 2.1). **a)** $|P_t(x, y, z_2, 457\text{kHz})|$, **b)** $|P_t(x, 0, z_2, 457\text{kHz})|$, extracted from Fig. 4.9(a), and in comparison with $|P_t(x, 0, z_2, 457\text{kHz})|$ calculated using the FEM approach (red line) discussed in Sect. 4.2.

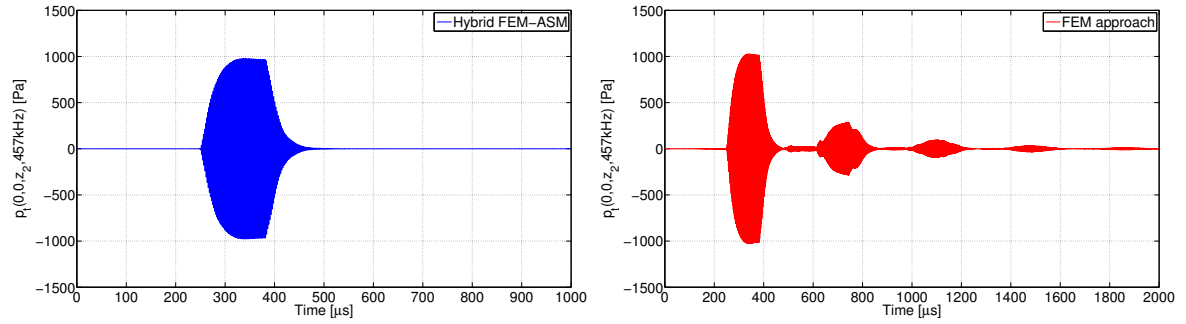

(a) (b)

Fig 4.11. At normal beam incidence ($\theta = 0°$): **a)** The transmitted pressure waveform $p_t(0, 0, z_2, t)$ calculated using the hybrid FEM-ASM approach. **b)** The transmitted pressure waveform $p_t(0, 0, z_2, t)_{cw}$ using the FEM approach.

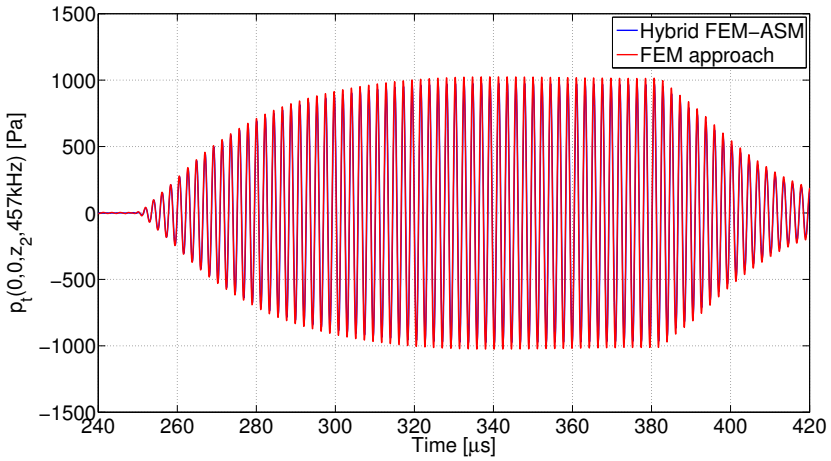

Fig 4.12. At normal beam incidence ($\theta = 0°$): The transmitted pressure waveform $p_t(0, 0, z_2, t)$ calculated using the hybrid FEM-ASM approach (blue line) and the FEM approach (red line).

At a given (x, y, z_2)-position the transmitted pressure $P_t(x, y, z_2, 457\text{kHz})$ is transformed into the time domain using Eq. (2.12), giving $p_t(x, y, z_2, t)$. The hybrid FEM-ASM transmitted pressure waveform $p_t(0, 0, z_2, t)$ is shown in Fig. 4.11(a) in comparison with the transmitted pressure waveform calculated using the FEM approach given in Fig. 4.11(b), see Sect. 4.2. As a step frequency of 500 Hz is used for the FEM approach, the time trace is doubled in relation to the hybrid FEM-ASM approach. In addition, as a consequence of the standing wave pattern in the FEM approach, a first and successive (echoes) pulse arrivals are present. Fig. 4.12 shows the first arrival, and the comparison of the hybrid FEM-ASM (blue line) and FEM (red line) calculated waveform. A phase difference of approximately 11° between the two approaches is observed. As one can observe from Fig. 4.11(b), a fifth echo may coinside with the first arrival, interfering with the signal, which can be one of the reasons for the phase difference between the two approaches. Between the first arrival and echo, there exists some aliasing, probably due e.g. the frequency sampling, reflections from the end faces, PML reflections, etc.

4.4 FEM convergence

In general it is necessary to conduct convergence tests to confirm that a fine enough element discretization has been used for the finite element model. This section reports FEM convergence tests for the hybrid FEM-ASM approach, examining the accuracy of the on-axis pressure $P_0(0, 0, z_0, 457\text{kHz})$ at normal beam incidence ($\theta = 0°$) as a function of elements per wavelength. They are also representative for the FEM approach and the FE simulations in Sect. 4.5. FEM convergence tests of the program FEMP 5.0 and earlier versions have been made by e.g. [103, 109, 111, 142, 143, 144] and the convergence tests made in this section are intended as complementary to those. Note that earlier works only examined the magnitude of given parameters, while the corresponding phase convergence is here also examined.

Convergence tests examines the relative change in FEM simulations as a function of e.g. elements per wavelength, in relation to an assumed converged (very densed meshed) simulation. The error is given in parts-per-million in relation to the highest element division given by Eqs. (4.4) and (4.5) as

$$\text{relative error in } |P_0(0,0,z_0,457\text{kHz})|[\text{ppm}] = 10^6 \left(\frac{|P_0(0,0,z_0,457\text{kHz})_\text{n}| - |P_0(0,0,z_0,457\text{kHz})_\text{conv}|}{|P_0(0,0,z_0,457\text{kHz})_\text{conv}|} \right), \tag{4.4}$$

and

$$\text{relative error in } \angle P_0(0,0,z_0,457\text{kHz})[\text{ppm}] = 10^6 \left(\frac{\angle P_0(0,0,z_0,457\text{kHz})_\text{n} - \angle P_0(0,0,z_0,457\text{kHz})_\text{conv}}{\angle P_0(0,0,z_0,457\text{kHz})_\text{conv}} \right), \tag{4.5}$$

for calculation of magnitude and phase respectively. The subscripts $_\text{n}$ and $_\text{conv}$ denotes that the parameter has been calculated using n elements per wavelength or calculated from the assumed converged simulation, respectively.

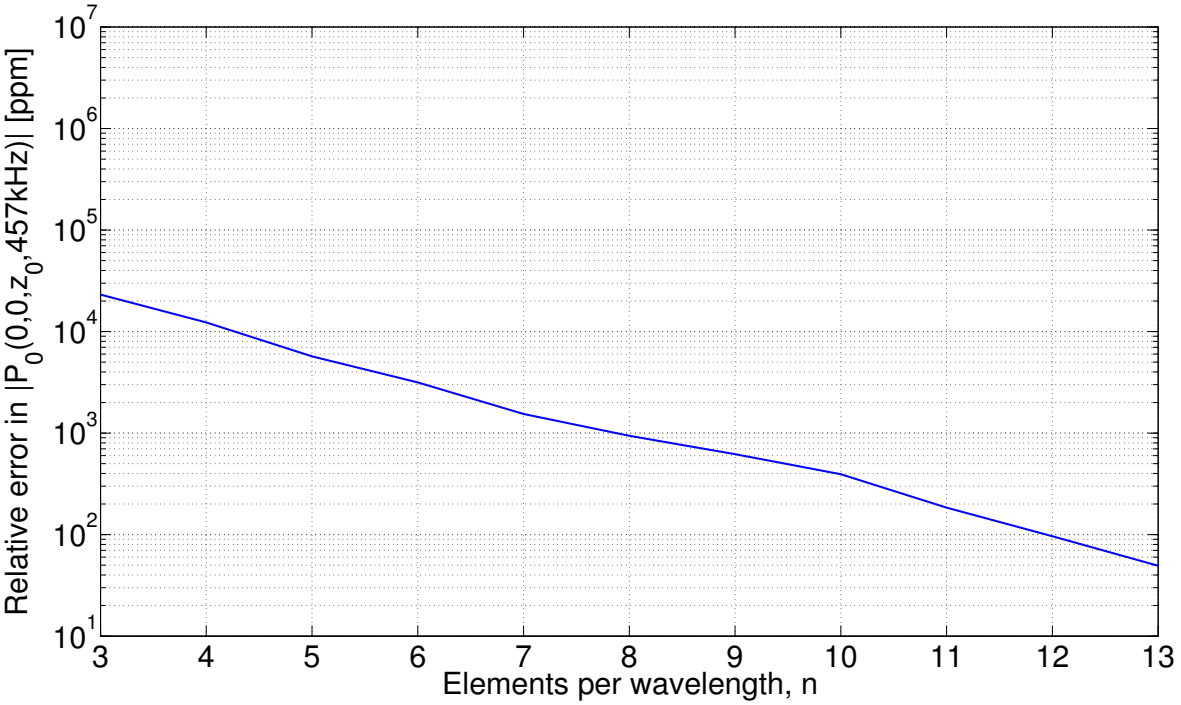
Relative error in |P0(0,0,z0,457kHz)| [ppm]
Elements per wavelength, n

(a)

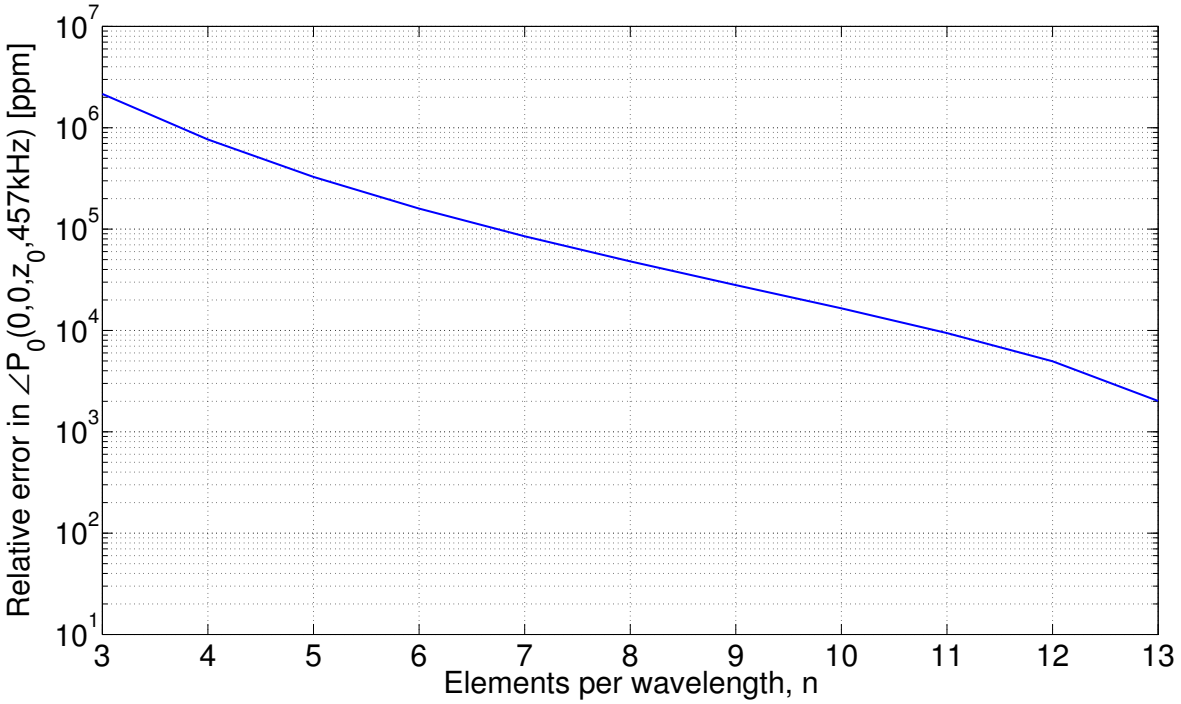
Relative error in ∠P0(0,0,z0,457kHz) [ppm]
Elements per wavelength, n

(b)

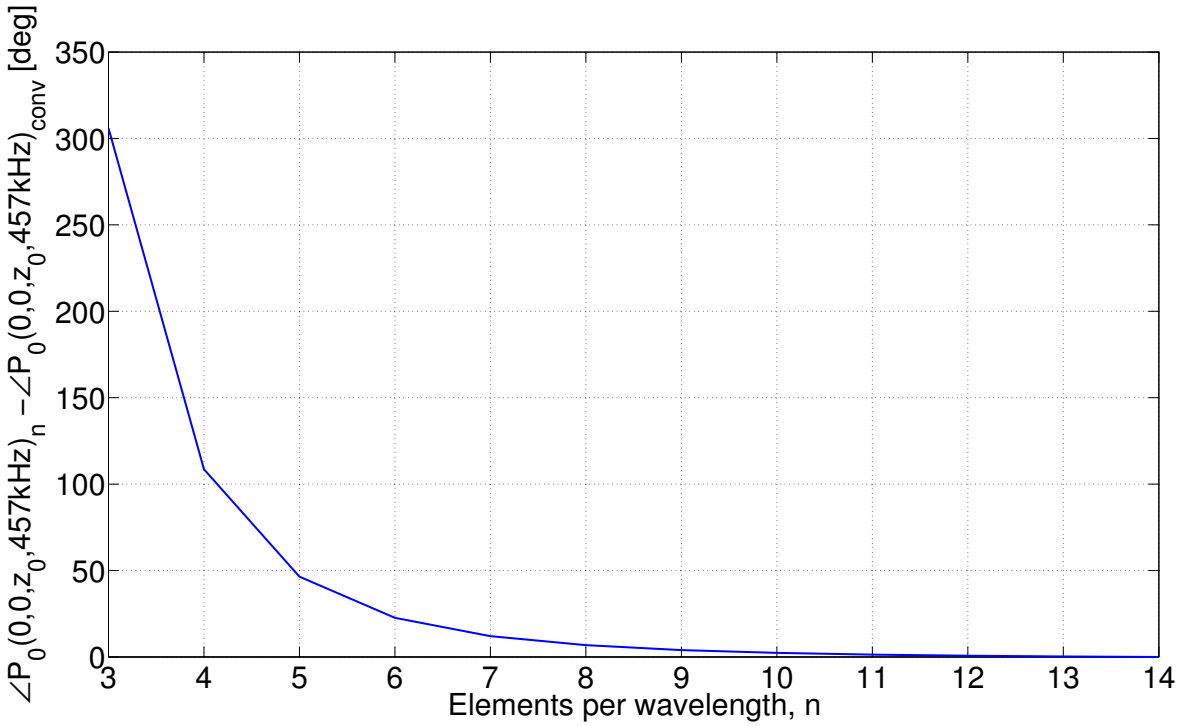

(c)

Fig 4.13. FEM convergence for **a)** the magnitude, and **b)** the phase of $P_0(0,0,z_0,457\text{kHz})$ using the FEM-ASM approach, as a function of elements per wavelength. **c)** Phase difference of $P_0(0,0,z_0,457\text{kHz})_\text{n}$ in relation to $P_0(0,0,z_0,457\text{kHz})_\text{conv}$ (in degrees).

Tab. 4.1 and Fig. 4.13 show the convergence of the magnitude ($||$) and phase ($\angle$) of the incident pressure $P_0(0,0,z_0,457\text{kHz})$ using the hybrid FEM-ASM approach, in relation to the assumed converged solution using 14 elements per wavelength. For FE simulations using less than 3 elements per wavelength, the element division is too coarse, and the error introduced is on a different scale as compared to the level of precision in the thesis otherwise, and is therefore not shown. Fig. 4.13(a) shows a steady convergence of the magnitude of $P_0(0,0,z_0,457\text{kHz})_\text{n}$ towards $|P_0(0,0,z_0,457\text{kHz})_\text{conv}|$ as the number of elements per wavelength, n, increases. Fig. 4.13(b) shows the corresponding phase convergence as a function of elements per wavelength. Fig. 4.13(c) shows the phase difference of $P_0(0,0,z_0,457\text{kHz})_\text{n}$ in relation to $P_0(0,0,z_0,457\text{kHz})_\text{conv}$ as a function of degrees. Since Eq. (4.5) does not take into account differences above one period in the phase, and given the trend in Fig. 4.13(c), the phase difference using 3 elements per wavelength is assumed to be the sum of the calculated phase difference and 1 period. The figures also show a delayed convergence of phase in relation to the convergence of magnitude, as a higher number of elements per wavelength is needed in phase convergence, as opposed to magnitude convergence, to provide a certain level of accuracy. E.g. 6 elements per wavelength is needed to ensure no more than approx. 3‰ error in magnitude, whereas 12 elements is needed to provide the same level of confidence in phase convergence. This is most likely due to the fact that a given phase response is expected to vary more frequently than the corresponding magnitude response.

TABLE 4.1. Convergence for $|P_0(0,0,z_0,457\text{kHz})_\text{n}|$ and $\angle P_0(0,0,z_0,457\text{kHz})_\text{n}$ using the hybrid FEM-ASM approach. Relative error in ppm in relation to the converged solution.

Elements per wavelength	Relative error $\|P_0(0,0,z_2,457\text{kHz})\|_\text{n}$	Relative error $\angle P_0(0,0,z_2,457\text{kHz})_\text{n}$
3	23127 (2.3%)	2157300 (216%)
4	12301 (1.2%)	765800 (76.9%)
5	5695 (0.57%)	327410 (32.7%)
6	3155 (0.3%)	159600 (16%)
7	1543 (0.15%)	84995 (8.4%)
8	940.3 (0.94‰)	48045 (4.8%)
9	619.5 (0.62‰)	28047 (2.8%)
10	393.4 (0.39‰)	16522 (1.65%)
11	184.3 (0.18‰)	9421 (0.94%)
12	96.4 (0.1‰)	4966 (0.5%)
13	49.4 (0.05‰)	2016 (0.2%)
14	0	0

Fig. 4.13(a) asserts the level of convergence for the magnitude of the FEM calculated transducer transfer functions presented in Chap. 5, and the magnitude of the FEM calculated transfer functions for the measurement system presented in Chap. 6 and 7. For simulated sound pressure waveforms in Chap. 7, Fig. 4.13(c), in addition to Figs. 4.13(b) and 4.13(a) asserts the level of convergence. For the results presented in Chap. 5, an element division of 3 elements per wavelength is used at 1 MHz (cf. Sect. 4.5). Hence, we have 4 elements at 750 kHz, 5 elements at 600 kHz, 6 elements at 500 kHz, 7 elements at 428 kHz and 8 elements at 375 kHz. For the results presented in Chap. 6 and 7, an element division of 3 elements per wavelength is used at 1.2 MHz (cf. Sects. 4.2 and 4.3). Hence, we have 4 elements at 900 kHz, 5 elements at 720 kHz, 6 elements at 600 kHz and 7 elements at 515 kHz, 8 elements at 450 kHz, 9 elements at 400 kHz and 10 elements at 360 kHz. The representative numerical errors introduced at these frequencies in the FE simulations used, in relation to the assumed fully converged solution, can be extracted from Table. 4.1.

4.5 The piezoelectric source transducer

For the description of the measurement system, from the excitation voltage signal to the transducer, to the received pressure signal transmitted through the plate, the piezoelectric source transducer is to be included in the FEM. For commercial transducers, constructional details, materials involved and material data are usually not available at the level required for accurate modeling. A piezoelectric transducer is designed and constructed for use in measurement and modeling, and reported in Chap. 5 in Sects. 5.2 and 5.3, respectively. In this section the FE simulation of the piezoelectric source transducer is presented in Sect. 4.5.2, in addition to FE simulations of the transducer at various steps in the construction process in Sect. 4.5.1. Refer to Chap. 5 for the transducer design and construction, in addition to material type, data and dimensions. Axisymmetric (about the $z-$axis) FEM is used throughout this section. For the sake of simplicity, in Sect. 4.5.1 the lower surface of

the piezoelectric disk is located at $z' = 0$, and in Sect. 4.5.2 the piezoelectric source transducer is positioned symmetrically around $z' = 0$. This has been done to ease implementation and the use of infinite fluid elements to simulate an unbounded water region, where the infinite elements must be applied at a fixed radius around the center of the transducer.

4.5.1 Simulation of various steps in the construction process

This section presents the FE simulations of the transducer at early stages in the construction process, starting with a circular piezoelectric disk in vacuum (Sect. 4.5.1.1), and gradually introducing front and adhesive layers (Sect. 4.5.1.2). For FE simulations of backing and encapsulation layers, these are included in the simulations of the piezoelectric transducer in Sect. 4.5.2.

4.5.1.1 Piezoelectric disk in vacuum

Fig. 4.14 shows a decimated mesh of a circular piezoelectric disk (yellow region) vibrating in vaccum. For piezoelectric transducer properties simulations of electrical admittance $Y(f)$, a frequency range of 0 - 1 MHz is utilized, with a step frequency of 1 kHz. 3 elements per shear wavelength at 1 MHz is used as the element division for the piezoelectric element. This setup is used to adjust material data for the piezoelectric disk used as basis for the transducer construction, cf. Sect. 5.2.1.

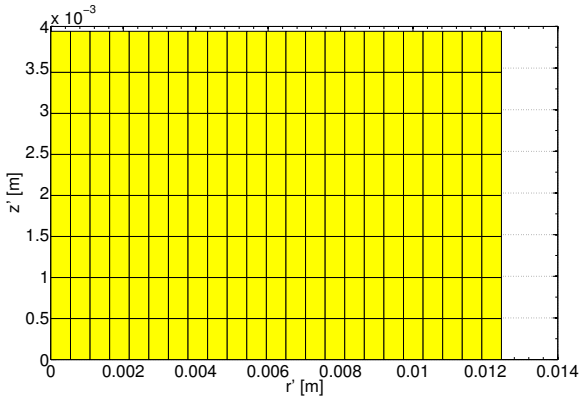

FIG 4.14. A decimated mesh of the axisymmetric FE simulation of a circular piezoelectric disk (yellow regions) vibrating in vacuum.

4.5.1.2 Piezoelectric disk with a front layer in vacuum

Figs. 4.15(a) and 4.15(b) show a decimated mesh of a piezoelectric disk (yellow region) with front layer (green region) vibrating in vacuum, simulated without and with an adhesive layer (blue region) added between the disk and front layer, respectively. For piezoelectric transducer properties simulations of electrical admittance $Y(f)$, the same frequency range as in Sect. 4.5.1.1 is used. 5 elements per shear wavelength specified at 1 MHz for the piezoelectric disk is used as the element division for the piezoelectric disk, the front and the adhesive layers. This setup is used to adjust material data for the electrical conductive adhesive in the transducer design, cf. Sects. 5.4.1 and 5.4.2.

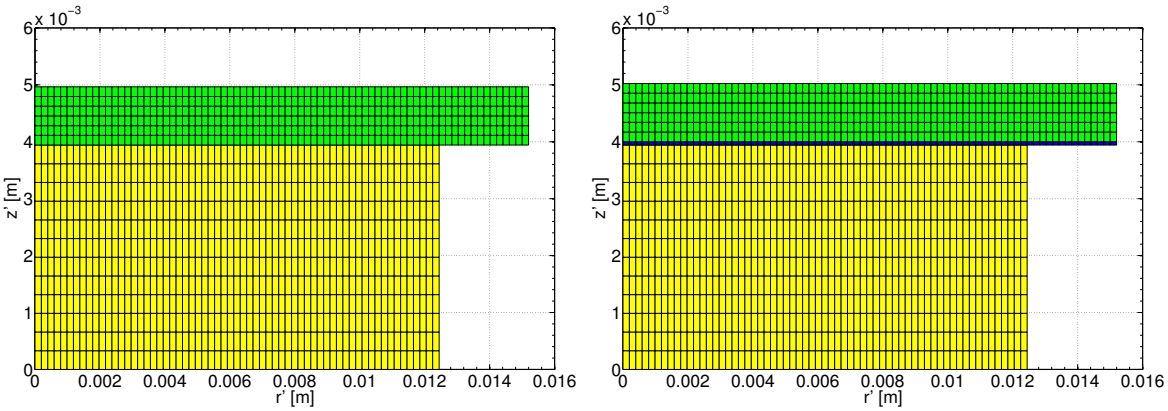

(a) Piezoelectric disk with front layer.

(b) Piezoelectric disk with front and adhesive layers.

Fig 4.15. A decimated mesh of the axisymmetric FE simulation of a piezoelectric disk (yellow region) with front layer (green region), without and with an adhesive layer (blue region), vibrating in vaccum.

4.5.2 Prototype transducer

Fig. 4.16 shows a decimated mesh of the piezoelectric source transducer vibrating in vacuum. The prototype transducer consists of a piezoelectric disk (yellow region) attached to a front layer (green region) with an adhesive layer. A casing (red region) encloses a backing layer (blue region), which supports the piezoelectric disk. The cone of air in the transducer design (cf. Sect. 5.2) is simulated as a rectangle of vaccum. For the piezoelectric transducer properties simulations of electrical admittance $Y(f)$, a frequency range of 0 - 1 MHz with a 1 kHz step frequency is utilized. 3 elements per shear wavelength specified at 1 MHz for the piezoelectric disk is used as the element division for the

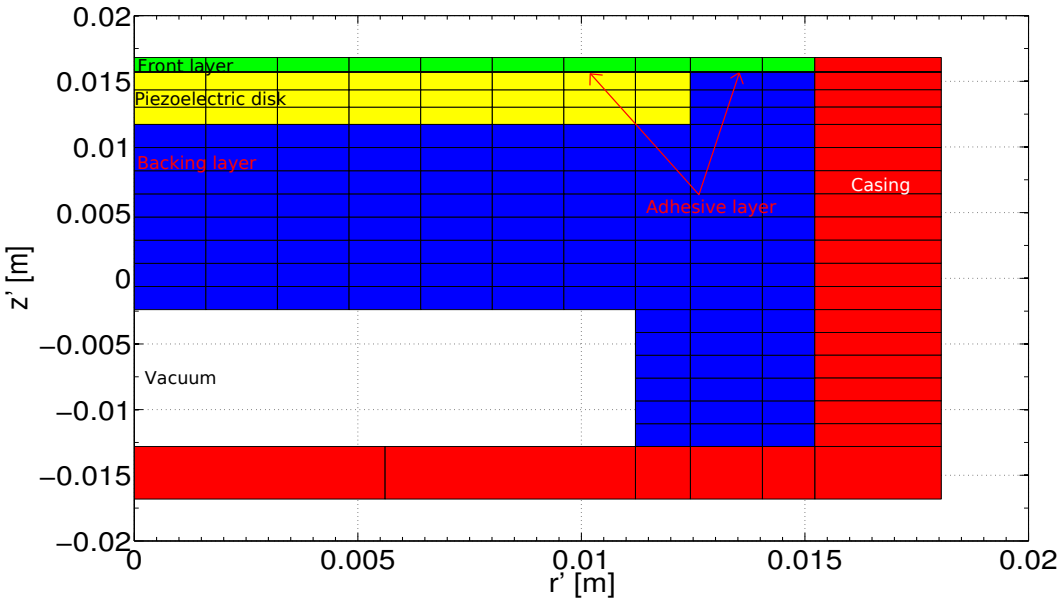

FIG 4.16. A decimated mesh of the axisymmetric piezoelectric source transducer vibrating in vacuum. The transducer consists of a piezoelectric disk (yellow region) with a front layer (green region), with an adhesive layer inbetween. A casing (red region) encloses a backing layer (blue region), which supports the piezoelectric disk.

piezoelectric and elastic regions. This setup is used to compare the prototype transducer to electrical measurements in air. For piezoelectric transducer properties simulations of electrical admittance $Y(f)$, source sensitivity $S_V(f)$ and beam pattern $D(\phi, f)$ in water, 12th order infinite fluid elements [103], with radius $R_{inf} = 80$ mm, have been used to simulate an unbounded fluid medium. [103] examined the influence of R_{inf} on the accuracy of the on-axis pressure, see Fig. 4.14 in [103]. Fig. 4.17 shows a decimated mesh of the piezoelectric source transducer radiating in water using finite (white region) and infinite fluid elements (light blue region). A frequency range of 0 - 1 MHz is used, with a 1 kHz step frequency. The same element division as for the tranducer in vacuum is used, whereas 3 elements per compressional wavelength specified at 1 MHz is used as the element division for the water region. This setup is used to compare and characterize the prototype transducer to electrical and acoustical measurements in water.

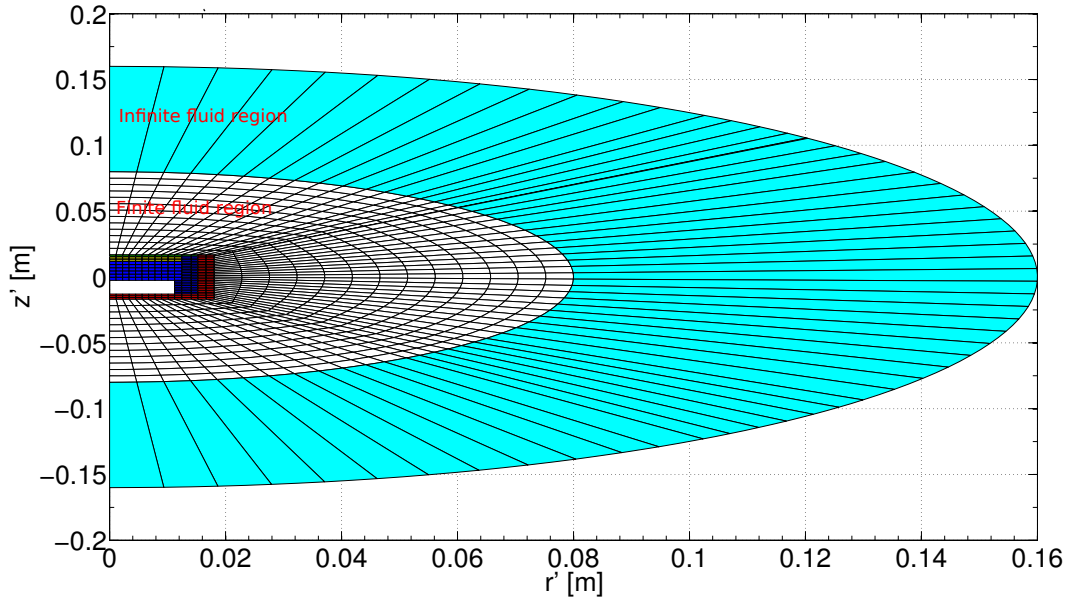

Fig 4.17. A decimated mesh of the axisymmetric piezoelectric source transducer radiating in an unbounded fluid medium using 12th order infinite elements.

4.5.3 The baffled piston source model

Fig. 4.18 shows the decimated mesh of the baffled piston source radiating in water using 12th order infinite fluid elements [107] with radius $R_{inf} = 100$ mm. This simulation is used to compare the baffled piston source to piezoelectric transducer properties in Chap. 5. The effective radius of the piston is calculated to $a_{eff} = 10.55$ mm using the FEM simulated transducer's beam pattern and the -3 dB angle (θ_{-3dB}) of the main lobe at the frequency corresponding to maximum source sensitivity, $f = 575$ kHz, see Figs. 5.25 and 5.27(d). The effective radius is determined from the baffled piston beam pattern, expressed as [141]

$$D(\alpha) = \frac{2J_1(ka_{eff}\sin(\alpha)}{ka_{eff}\sin(\alpha)} = \frac{2J_1(x)}{x}, \tag{4.6}$$

where J_1 is a Bessel function. When the function $D(\alpha)$ is equal to $\sqrt{2}/2$, this corresponds approximately to -3 dB. The value of x which gives $D(\alpha) = \sqrt{2}/2$ is approx. 1.6137. The effective radius a_{eff} is then calculated as

$$a_{eff} = \frac{1.6137}{k \sin(\theta_{-3dB})}. \tag{4.7}$$

The piston source is simulated with a thickness of 0.01 mm. The center of the piston surface is situated at $(r', z') = (0, 0)$, applied with a forced displacement with an amplitude of 1×10^{-6} mm (1 nm) along the r'-axis over the entire piston front surface for each simulated frequency. The frequency range is set to 0 - 1 MHz, where 3 elements per compressional wavelength at 1 MHz is used as the element divison in the water. A rigid baffle is specified along the r'-axis, at $z' = 0$ mm, for $r' > a_{eff}$.

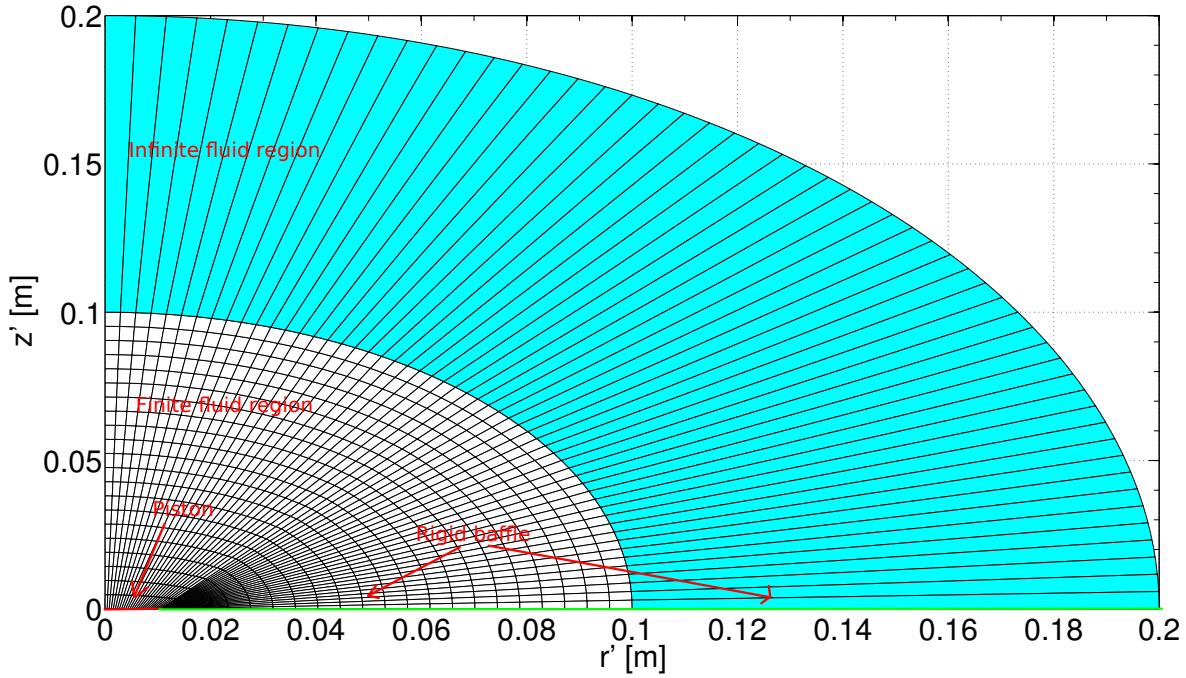

Fig 4.18. A decimated mesh of the axisymmetric baffled piston source radiating in an unbounded fluid medium using 12th order infinite elements.

Chapter 5

Piezoelectric transducer construction

5.1 Introduction

This chapter presents the design and construction of the piezoelectric source transducer used in the measurement system. Since use of a commercial transducer does not provide sufficient information and control concerning the transducer construction, dimensions, materials and material data involved, a piezoelectric source transducer is designed, constructed, characterized, and used for measurements and simulations. The in-house design and construction provides then sufficent knowledge on material types, dimensions and data, enabling the inclusion of the source transducer into the theoretical description of the measurement system using the FEM, thereby accounting for a more realistic beam pattern of the transducer than simplified models, and its influence on leaky Lamb mode excitation in the plate. In addition, this allows for a quantitative description of the system, from input voltage to the transducer - to transmitted sound pressure through the plate (incl. phase response), vital in the optimization of important system properties, such as signal level, bandwidth of transmitted signal, waveform, etc.

The transducer design, consisting of a piezoelectric disk, front layer, backing layer and casing, is presented in Sect. 5.2. In Sect. 5.3 the construction process is documented, explaining the step-by-step process from electrically wiring the piezoelectric disk, to making the transducer waterproof. Three finished prototype transducers with dimensions are presented in Sect. 5.4, including the FEM simulation of them in comparison with measurement results.

5.2 Transducer design

The design of the piezoelectric source transducer is presented in this section. The dimensions for the transducer have been determined after multiple FEM simulations with different radius/thickness of the front, backing and casing layers, with respect to optimization of transducer properties, such as bandwidth and source sensitivity. A Mitutoyo MDH-25M [145] digital micrometer, with measurement uncertainty of 0.5 μm, is used for dimension measurements. Each component is described in detail in the following subsections, the piezoceramic material in Sect. 5.2.1, the front layer in Sect. 5.2.2, the

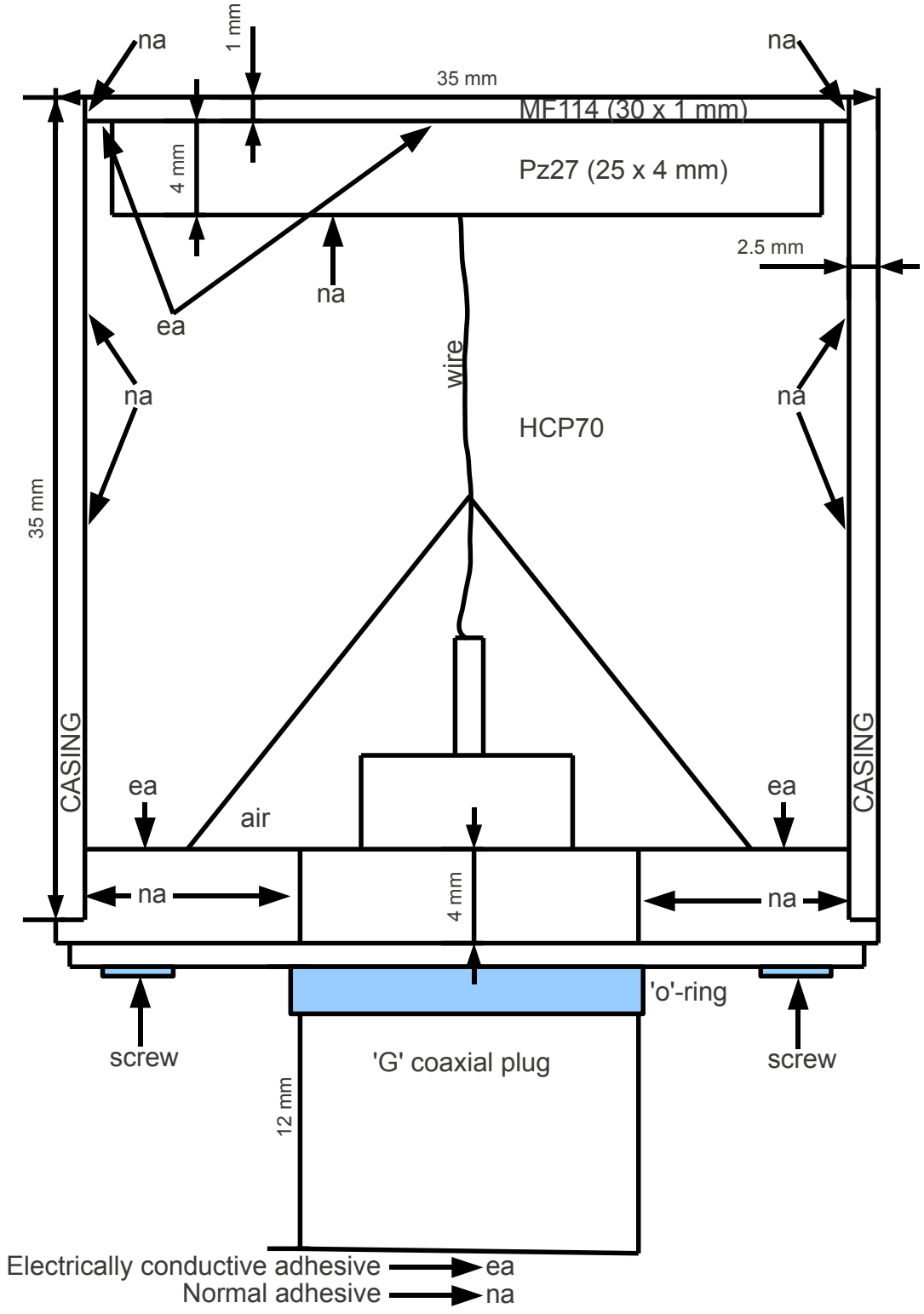

FIG 5.1. Design of the piezoelectric source transducer. Nominally dimensions for the transducer design, where the dimensions of each prototype are listed in Sect. 5.4. A photograph of a prototype transducer can be seen in Fig. 5.14.

backing layer in Sect. 5.2.3 and the waterproof casing in Sect. 5.2.4.

Fig. 5.1 shows the transducer design with representative dimensions, where the dimensions for each prototype are listed in Sect.5.4. The transducer design starts with a Ferroperm Pz27 [146] piezoelectric disk with diameter × thickness (D×T) of nominally 25 × 4 mm. The disk is electrically connected to a 'G' coaxial plug with a wire. An Eccosorb MF114 [147] front layer with (D×T) of nominally 30 × 1 mm is attached to the front surface of the piezoceramic disk, and again attached to the steel casing. A Divinycell HCP70 [148] backing layer is inserted behind the piezoceramic disk, supporting it, and keeping the element electrically isolated from the casing. An electrically conductive adhesive, marked 'ea' in Fig. 5.1, is used to connect the front electrode of the piezoceramic disk to the front layer, and then to the steel casing. It is also used to electrically ground the casing to the coaxial plug. A normal adhesive, marked 'na' in Fig. 5.1, is used to attach surfaces which do not require to conduct electricity. The mechanical workshop at the Department of Physics and Technology, UoB, cut and made the different components in the transducer construction.

5.2.1 Piezoelectric material

The lead zirconate titanate piezoceramic material Pz27 manufactured by Meggitt Ferroperm Piezoceramics [146] is chosen as the starting point for the transducer structure. The Acoustic Group at the Department of Physics and Technology, University of Bergen, has worked with this material beforehand, e.g. [20, 110, 111, 114, 115, 142, 149, 150, 151, 152], with respect to material data and use in the FEM for transducer constructions. A circular disk with diameter × thickness of nominally 25 × 4 mm and D/T = 6.25 (see Fig. 5.2) is chosen, such that the first thickness extensional mode, $f_{TE}^{1} \approx 500$ kHz, is situated in the middle of the measurement frequency range, cf. Chap. 3.

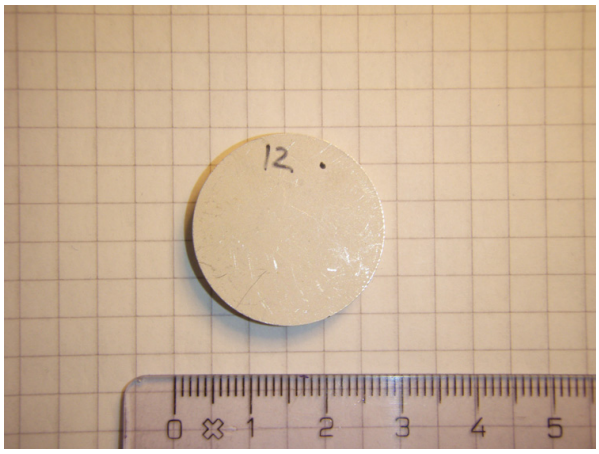

FIG 5.2. A photograph of one of the Pz27 disks (marked element no. 12) used in the prototype transducers, with diameter D = 24.888 mm and thickness T = 3.942 mm, resulting in a D/T = 6.31.

Material data:

With the development of accurate transducer modeling tools such as the FEM, material data supplied by the manufacturer may not provide the optimal comparison between simulations and measurements. The standarized methods [153] for determining material data also may not provide acceptable precision

since the requirements of these methods, based on one-dimensional models, are not sufficiently met for any D/T-ratios [143, 144]. Other methods have been utilized to adjust material data to measurements, e.g. an iterative inversion scheme [19, 154, 155], based upon three-dimensional finite element simulations.

In 2005, Lohne [114] calculated a new set of material constants for a circular Pz27 disk with D/T (20 × 1 mm) = 20 by applying methods described by Sherrit [156, 157], and then adjusting them to electrical measurements in air using the sensitivity analysis provided by [111]. The material constants that could not be calculated using these one-dimensional methods, such as the c_{44}^E, e_{15} and ϵ_{11}^S were taken from the material data provided by the manufacturer of the piezoelectric material PZT-5A [158]. Knappskog [115] further adjusted these material constants by comparing measurements and finite element simulations of Pz27 disks with D/T (20 × 2 mm) = 10, based upon the sensitivity analysis in [111]. In this thesis, the material set given by Lohne/Knappskog is further adjusted to provide an improved agreement with electrical measurements in air on the Pz27 disks used in this work. In Tab. 5.1 the adjusted material data (Lohne/Knappskog/Aanes) for Pz27 is presented, and compared to the material data for Pz27 given by the manufacturer, alongside the adjusted Lohne/Knappskog material set. The constants from Meggitt Ferroperm A/S does not include loss factors for each constant, but two loss factors, one elastic and one dielectric loss constant, Q_M and $\tan\delta$, respectively. The losses in the adjusted sets are represented by the imaginary part of the complex constants as used in [116]. A reservation concerning this method is taken, since it is only based on measurements of one type of Pz27 elements. The material constants can be misleading or erronoeus, especially for the corresponding loss factors.

TABLE 5.1. Material data for Pz27. Material data from the manufacturer and adjusted from electrical measurements in air. Terminology as used in [153].

	Adjusted(Lohne/Knappskog)	Ferroperm	Adjusted(Lohne/Knappskog/Aanes)
$c_{11}^E[10^{10}\ \mathrm{N/m^2}]$	11.875(1 + i/95.75)	14.7	12.025(1 + i/96)
$c_{12}^E[10^{10}\ \mathrm{N/m^2}]$	7.430(1 + i/71.24)	10.5	7.62(1 + i/70)
$c_{13}^E[10^{10}\ \mathrm{N/m^2}]$	7.425(1 + i/120.19)	9.37	7.42(1 + i/120)
$c_{33}^E[10^{10}\ \mathrm{N/m^2}]$	11.205(1 + i/177.99)	11.3	11.005(1 + i/190)
$c_{44}^E[10^{10}\ \mathrm{N/m^2}]$	2.110(1 + i/75)	2.3	2.11(1 + i/75)
$e_{31}[\mathrm{C/m^2}]$	-5.4(1 - i/166)	-3.09	-5.4(1 - i/166)
$e_{33}[\mathrm{C/m^2}]$	16.0389(1 - i/323.77)	16.0	17.0(1 - i/324)
$e_{15}[\mathrm{C/m^2}]$	11.20(1 - i/200)	11.64	11.20(1 - i/200)
$\epsilon_{11}^S[10^{-9}\mathrm{F/m}]$	8.110436208(1 - i/50)	10.005	8.11044/(1 - i/50)
$\epsilon_{33}^S[10^{-9}\mathrm{F/m}]$	8.14585296(1 - i/86.28)	8.0927	8.14585(1 - i/130)
$\rho[\mathrm{kg/m^3}]$	7700	7700	7700
Q_M	0	74	0
$\tan\delta$	0	0.017	0

Fig. 5.3 shows the measurement of the electrical conductance in air for the circular Pz27 disk in Fig. 5.2, (marked no. 12 – blue line). Comparing this measurement to FEM calculated conductance employing

the setup in Sect. 4.5.1.1, using the different material data provided in Tab. 5.1, shows a closer agreement with the adjusted (Lohne/Knappskog/Aanes) set (red line), than with the manufacturer's (dashed black line) and Lohne/Knappskog's (green line) material sets.

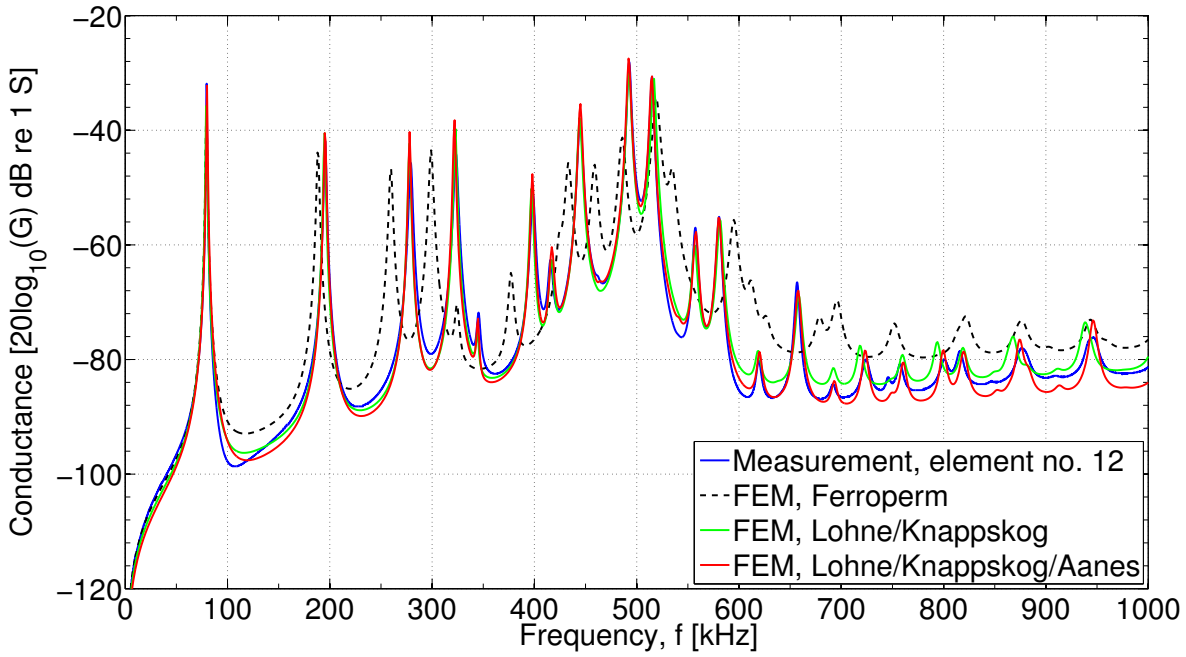

FIG 5.3. Measurements in air of the electrical conductance for the Pz27 no. 12 disk with D/T = 6.31 (blue line), compared to FEM calculated conductance with the different material data given in Tab. 5.1. FEM simulations with material data from, Ferroperm (dashed black line), Lohne/Knappskog (green line), and Lohne/Knappskog/Aanes (red line).

5.2.2 Quarter-wave front layer

To increase the bandwidth and source sensitivity of the transducer a front layer is added to the piezoelectric element. One frequently used method is quarter-wave matching, where the thickness of the matching layer is given as [141, 149, 159]

$$l_m = \frac{\lambda_{m,l}}{4} = \frac{c_{m,l}}{4f}, \tag{5.1}$$

where subscript m denotes matching layer, $c_{m,l}$ and $\lambda_{m,l}$ are the compressional sound velocity, and corresponding wavelength, in the matching layer, respectively. A consequence of this is that the ideal characteristic acoustic impedance for the matching layer, $z_m = \rho_m c_{m,l}$, where ρ_m is the density, between a piezoelectric element and the fluid in which it radiates, is given as

$$z_m = \sqrt{z_p z_f}, \tag{5.2}$$

where

$$z_p = \sqrt{c_{33}^D \rho_p}. \tag{5.3}$$

$z_p = \text{real}(c_p)\rho_p$, where $c_p = \sqrt{c_{33}^D/\rho_p}$ [159] (conversion from c_{33}^E to c_{33}^D is given by e.g. [160]), and $z_f = \rho_f c_f$ is the characteristic acoustic impedances of the piezoelectric element and fluid, respec-

tively. For the case of a Pz27 disk radiating in water using material data in Tabs. 5.1 (adjusted - Lohne/Knappskog/Aanes) and 5.5, the ideal characteristic acoustic impedance of the matching layer is approximately 6.5 Mrayl.

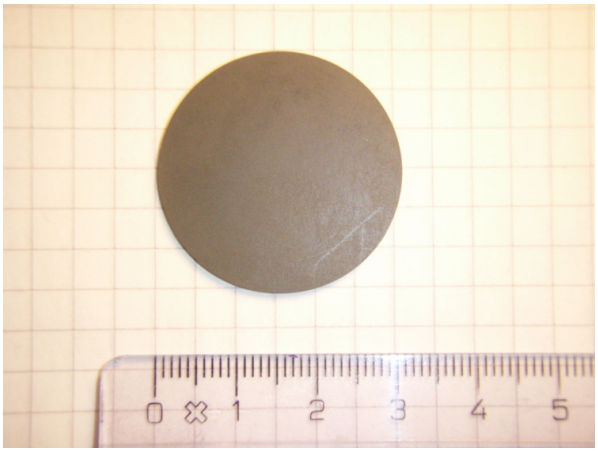

FIG 5.4. A photograph of one of the MF114 front layers used in the prototype transducers, with diameter = 30.396 mm and thickness = 1.023 mm.

The material Eccosorb MF114, see Fig. 5.4, manufactured by Laird Technologies - Emerson & Cuming [147], is chosen as the front layer of the transducer since the characteristic impedance is close to the geometric mean between water and the Pz27 disk, $z_m = 6.4$ Mrayl, using the material data in Tabs. 5.1 and 5.2. This material is classified by the manufacturer as a high loss load absorber for the microwave industry. The manufacturer provided a compressional sound velocity $c_{m,l}$ of 2290 m/s, and a density ρ_m of 2900 kg/m^3 [147]. In the laboratory, the density is measured to be 2850 kg/m^3 using the method given in Sect. 3.4.1. The sound velocities are measured using the method given in Sect. 3.4.2. At normal incidence, the compressional sound velocity $c_{m,l}$ is measured to be 2250 m/s, and at an incidence angle above the critical angle, $\theta_c \approx 41°$ using Eq. (3.5), the shear sound velocity $c_{m,s}$ is measured to be 1000 m/s. A loss factor Q_M^m of 20 is chosen based upon adjusting FEM simulations to electrical measurements. The material data for MF114 used for FE simulations is listed in Tab. 5.2.

TABLE 5.2. Measured material data for Eccosorb MF114.

$c_{m,l}$[m/s]	2250
$c_{m,s}$[m/s]	1000
ρ_m[kg/m^3]	2850
Q_M^m	20

5.2.3 Backing layer

A backing layer is bonded (see Sect. 5.3.1 for the type of adhesive used) to the piezoelectric element to increase scattering and attenuation of sound waves travelling towards the back of the transducer, thus reducing reflections from the stainless steel casing, cf. Sect. 5.2.4. The material Divinycell HCP70, manufactured by DIAB Group [148], is chosen as the backing layer for the transducer as it is easy

to shape, and since Knappskog [115] has prior experience with it, providing the material data needed for FE simulations. The material data for HCP70 is listed in Tab. 5.3. A thin sheet of Divinycell HCP70 was provided by the manufacturer, so, in order to provide the wanted thickness of the backing layer, two layers, denoted backing no. 1 and backing no. 2 is to be carved and mounted together (see Sect. 5.3.4 for specifics) to form the total thickness. Fig. 5.5(a) shows the backing layer no. 1, which supports the Pz27 disk, and keep the element electrically isolated from the casing. Fig. 5.5(b) shows the backing layer no. 2, which is coned in order to scatter waves travelling towards the back of the tranducer.

TABLE 5.3. Material data for HCP70 from [115].

c_L[m/s]	1605.5
c_S[m/s]	826
ρ[kg/m^3]	300
Q_M	25

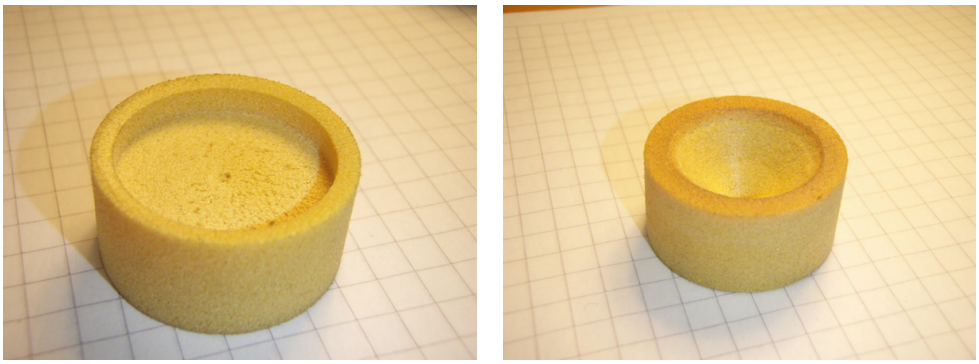

(a) (b)

FIG 5.5. A photograph of the HCP70 backing layer. Both backing layers are used in the construction. **a)** Backing layer no. 1 towards the front of the transducer is formed to hold the Pz27 disk. **b)** Backing layer no. 2 towards the end of the transducer is coned to scatter sound waves travelling towards the back of the transducer.

5.2.4 Water-proof casing

Since the transducer is to operate in water, the transducer's casing is constructed in stainless steel, see Fig. 5.6. Material data from [90] for AISI 316L stainless steel is used for the steel casing, and is listed in Tab. 5.4 (Q_M^c is taken from Tab. 6.5). The inside of the steel casing is mechanically ribbed (μm in the order of magnitude) in order to scatter any sound waves hitting the inside of the wall. These are not taken into account in the FEM simulations of the transducer in Chap. 4.

Fig. 5.7 shows the backside of the transducer, and its electrical connection to a water-proof RG-58 coaxial cable. A thin circular steel plate supports a 'G' coaxial plug, to electrically connect the transducer. The front end of the coaxial plug is grinded down, and an 'o'-ring is inserted to ensure waterproofing towards the coaxial cable. The coaxial plug is grounded to the steel casing via the screws

shown in Fig. 5.1.

TABLE 5.4. Material data for the steel casing from [90].

$c_{c,l}$[m/s]	5780
$c_{c,s}$[m/s]	3050
ρ_c[kg/m^3]	8000
Q_M^c	1000

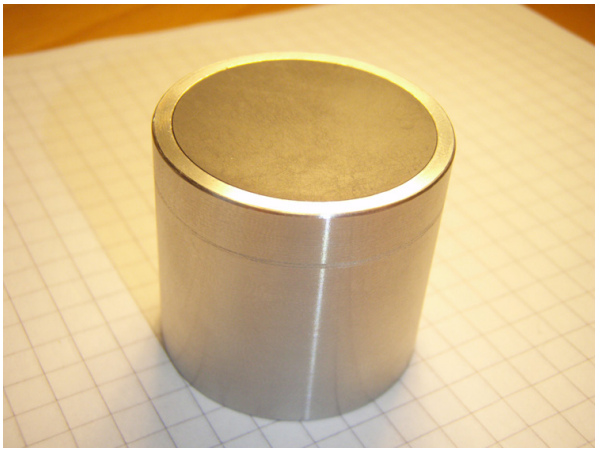

FIG 5.6. The stainless steel casing with the MF114 front layer attached.

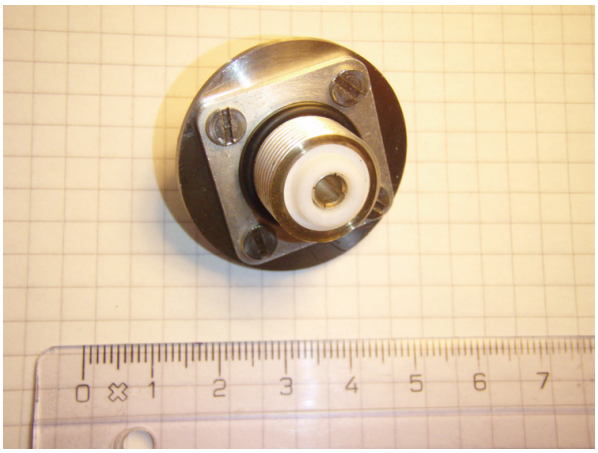

FIG 5.7. The backside of the tranducer, with the coaxial plug.

5.2.4.1 Material data for water

The material data used for water in the simulations is listed in Tab. 5.5. The water density is taken to be 1000 kg/m^3 and the compressional velocity c_f is measured to be 1485 m/s at room temperature using the method in Sect. 3.2.2. Lossless water, where the absorption coefficient α_f is zero, is assmued. Since the measurements have been conducted over a wide time span, this room temperature can vary, resulting in a faster or slower sound velocity in water for the measurements, than that used in the

simulations. This will have an impact on comparisons, especially regarding waveforms and time-of-flight measurements. From [141], a temperature change of 1° C corresponds approximately to a change in the sound velocity in water of 3 m/s. For waveforms in the measurements, which travels 370 mm in water, this corresponds to approx. 0.5 μs difference in the time-of-flight. The time-of-flight measurements reported in Chap. 7 must be considered in light of this.

TABLE 5.5. Material data for water.

c_f[m/s]	1485
ρ_f[kg/m^3]	1000
α_f [dB/m]	0

5.3 Construction process

This section describes the construction process of the piezoelectric transducer, based upon the tranducer design in Sect. 5.2, see Fig. 5.1, and the materials chosen. The step-by-step process in the construction is explained. Fig. 5.8 shows all mechanical parts of the transducer, which include the steel casing, the coaxial plug, the front layer, the backing layer and the piezoelectric disk.

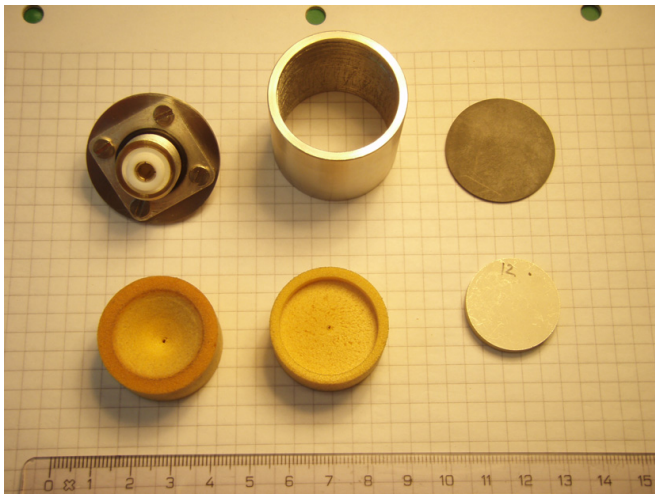

FIG 5.8. All mechanical parts of the piezoelectric transducer. Second row, from left to right: the casing plug, the casing and the front layer. First row, from left to right: the backing layer no. 2 (towards the back of the transducer), the backing layer no. 1 (towards the Pz27 disk) and the Pz27 disk.

The electrical connection of the piezoelectric disk is explained in Sect. 5.3.1. In Sect. 5.3.2 the attachment of the front layer to the piezoelectric disk is described. Then, the casing is attached in Sect. 5.3.3, before the backing layer is inserted in Sect. 5.3.4. At the end, the water-proofing and electrically wiring the coaxial connector is presented in Sect. 5.3.5.

5.3.1 Electrically connecting the piezoelectric disk

Firstly, one has to consider how to electrically connect the piezoelectric disk to the coaxial plug in Fig. 5.7. It is chosen, see Fig. 5.1, that a wire should run through a channel in the HCP70 layers from

the coaxial plug to the back electrode of the Pz27 disk, and attach it by soldering. A hole is drilled in the center of the HCP70 layers, see Fig. 5.5. The wire is soldered to the back electrode such that the direction of polarisation is towards the back of the transducer (side with the "dot"). Per Heraldstveit at the Department of Physics and Technology, UoB, did the soldering, preheating the Pz27 disk to 175 ° C, then soldering the wire to the element at 270° C, below the Curie temperature of the material at 350° C [146]. Fig. 5.9 shows the measured electrical conductance in air for the Pz27 disk no. 12 before (blue line) and after (red line) soldering (including a electrical wire, approx. length 10 cm).

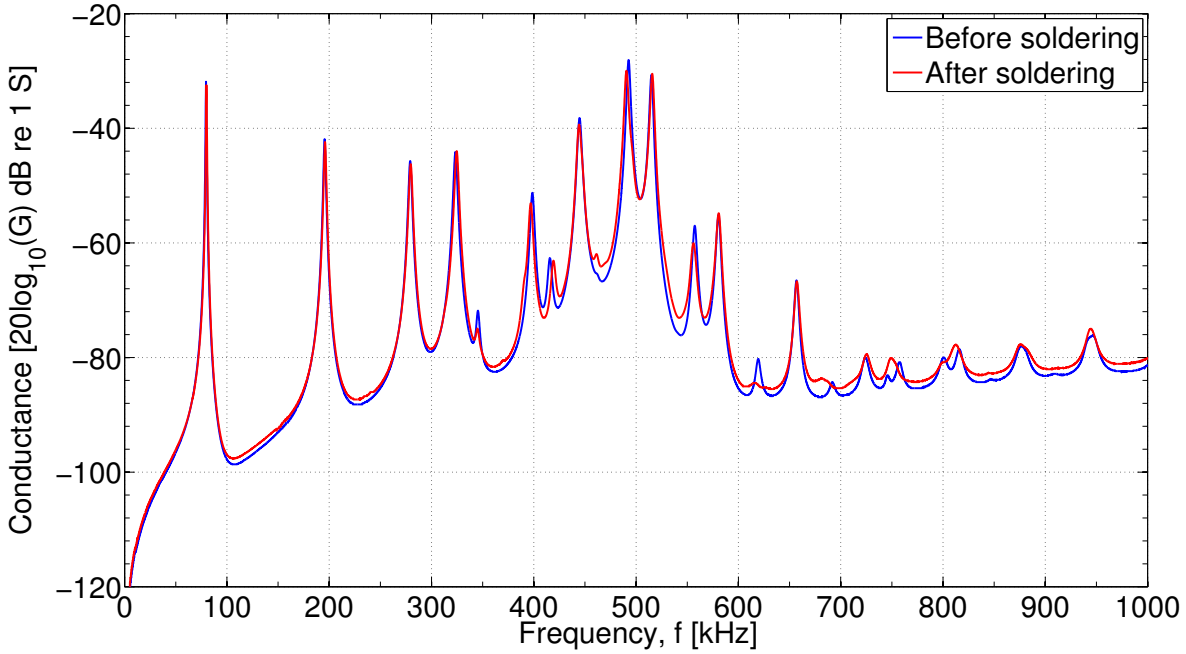

FIG 5.9. Measured electrical conductance in air for the Pz27 disk no. 12 before (blue line) and after (red line) soldering.

In the process of electrically grounding the front surface electrode of the Pz27 disk, several choices were considered. One choice is to solder a second wire to the front electrode, run it downwards, sandwiched between the steel casing and the backing layer, before attaching it to the bottom of the steel casing. This initial proposal was abandoned, since the solder would create a small bump at the upper electrode, either making the front layer not parallell to the Pz27 disk, or removing a small part of the front layer. Since the piezoelectric disk and the front layer is an essensial part of the transducer such procedures could affect its preformance. In addition, such deformations can not be modeled using axisymmetric FE simulations, see Chap. 4.

The preferred design was attaching the front electrode to the steel casing by using an electrically conductive adhesive, cf. Sect. 5.3.2. That way, the Pz27 disk and the front layer would be parallell, and the structure of those materials would be intact. A problem with this method is that such an adhesive would at best only provide a voltage drop, but worst case be non-conductive. In addition, these adhesives are known not to provide the best adhesive properties with respect to normal adhesives. For the case of connecting non-conductive materials, a standard 2-component epoxy Loctite Power Epoxy Extra Time [161] is used.

5.3.2 Attaching the quarter-wave front layer

A Silver Conductive Epoxy 2-component electrically conductive adhesive (silver conductive epoxy) from MG Chemicals [162] is used to connect the Pz27 and MF114 disks, in addition to connect them electrically to the steel casing, see Fig. 5.1. The manufacturer specified the densities of the uncured two-components to be 2470 and 2200 kg/m^3, respectively, but no information were available regarding the sound velocities or corresponding loss factors. This is further discussed in Sect. 5.4.2. This adhesive is also used in order to connect the casing cylinder to the casing plug, see Figs. 5.1 and 5.13. The conductive adhesive was tested on similar materials, and proved to provide a strong bond. The mechanical workshop at the Department of Physics and Technology made a plastic form used in the gluing process to align the center of the piezoelectric disk with the center of the front layer. After the piezoelectric disk and the front layer are bonded together, see Fig. 5.10(b), new electrical measurements in air were compared to FE simulations of the Pz27 and MF114 disks in vacuum, see Sect. 5.4.

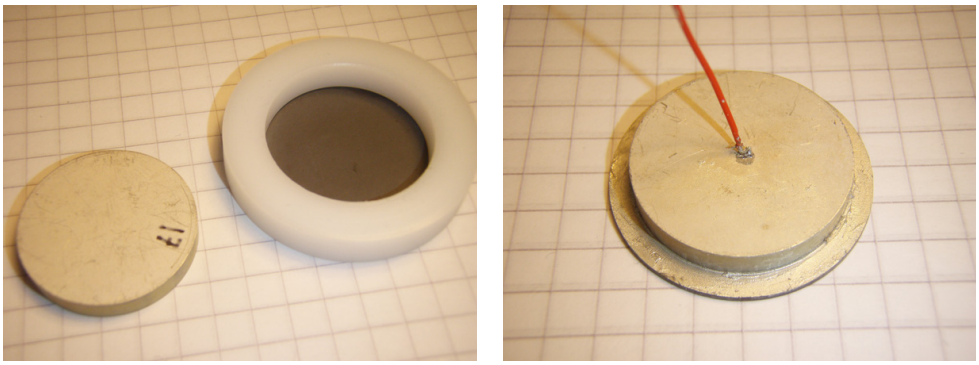

(a) (b)

FIG 5.10. a) The piezoelectric element, and the plastic form used in the gluing process. b) Pz27 disk no. 12 with the MF114 front layer attached. The electrically conductive adhesive is also used in the outer ring of the front layer, around the Pz27 disk, to connect it electrically to the steel casing.

5.3.3 Attaching the casing

The electrically conductive adhesive is left to cure for 24 hours in room temperature before the casing is attached to the front layer using the normal adhesive, see Figs. 5.1 and 5.11. After the curing is complete, the electrical conductivity between the steel casing and the silver epoxy is tested. The electrical resistance at DC was at best about 50 Ω, reduced to approx. 7.3 Ω when a small layer of the electrically conductive adhesive was added to ensure a good contact.

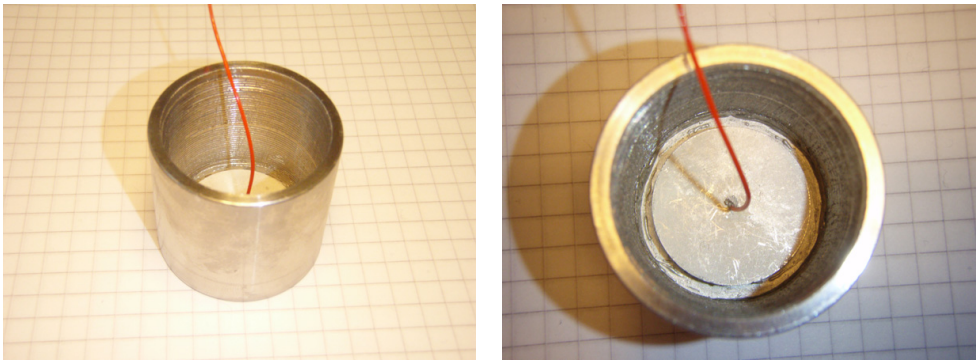

(a) (b)

FIG 5.11. The Pz27 disk no. 12 with the MF114 front layer attached to the stainless steel casing. **a)** from the side, **b)** from above.

5.3.4 Attaching the backing layer

The next step is then to attach the backing layer to the structure, see Figs. 5.1 and 5.12. On the surface of backing layer no. 1 (Fig. 5.5(a)) directed towards the Pz27 disk, the normal adhesive is used to ensure that the backing layer is firmly attached to the Pz27 disk. Small amounts of adhesive is also lubricated alongside the inner wall of the casing to ensure that the backing layer stays in place. Then backing layer no. 2 (Fig. 5.5(b)) is attached the same way as the backing layer no. 1, but only using the normal adhesive towards the steel casing, and not towards backing layer no. 1. The two backing layers are pressed firmly against each other, to minimize the air gap inbetween them, and following reflections.

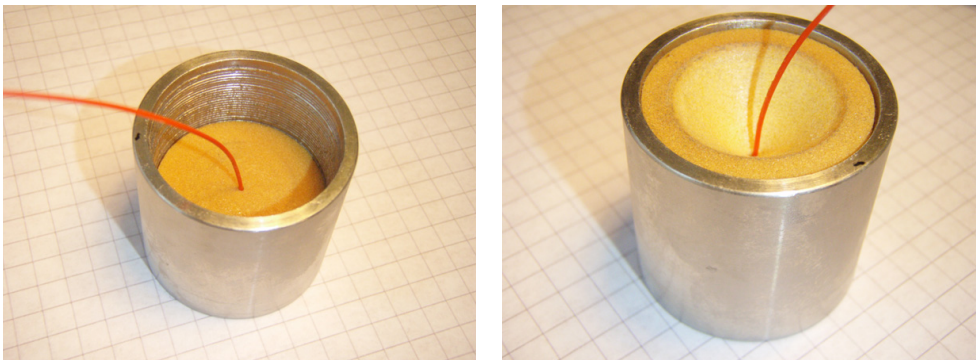

(a) (b)

FIG 5.12. Attaching the backing layer to the structure, **a)** backing layer no. 1, **b)** backing later no. 2.

5.3.5 Waterproofing and electrically wiring a coaxial connector

At the end, the plug-casing (Fig. 5.7) is attached to the steel casing using the normal adhesive, see Figs. 5.1 and 5.13(b). The electrically conductive adhesive is attached to the outer ring of backing layer no. 2 in order to ensure electrical connection between the cylinder and the backside of the steel casing, see Fig. 5.13(a).

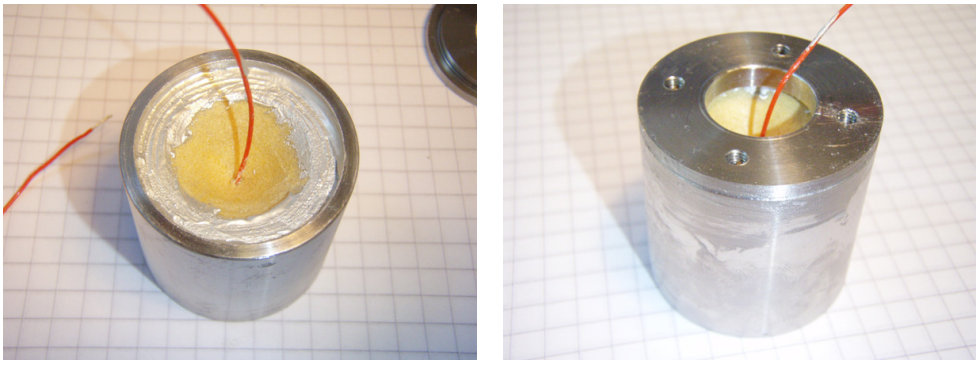

(a) (b)

FIG 5.13. Attaching the backside of the stainless steel casing. **a)** Ensuring electrical connection using the conductive adhesive. **b)** Connecting the backside of the stainless steel casing using the normal adhesive.

The wire is then cut to an appropriate length before soldering to the coaxial plug. The coaxial plug is then inserted into the backside casing, and the normal adhesive is used to ensure that the connection becomes water-proof. Four screws into the backside casing ensures electrical connection to the coaxial plug. An 'o'-ring, see Fig. 5.1 and 5.14(b), is inserted onto the coaxial plug in order to isolate the electrical signal from water. A photograph of one of the finished prototypes is presented in Fig. 5.14. A total of three prototypes were made, but only two of them provided reasonable agreement between FE simulations and measurements, see Sect. 5.4.

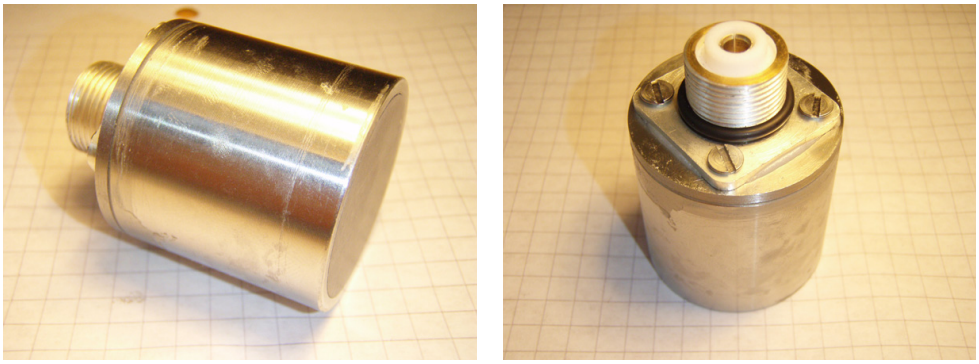

(a) (b)

FIG 5.14. A finished prototype transducer. **a)** from the side, **b)** from the back.

5.4 Piezoelectric transducer properties

In this section the finished prototypes are presented, alongside the measured dimensions used in the FE simulations of them. Measurement and simulation results underway in the construction are also presented. Material data for each material is listed in Sect. 5.2. Three prototypes are made, presenting prototype no. 1, no. 2 and no. 3 in Sects. 5.4.1, 5.4.2 and 5.4.3, respectively. The FE simulation setup for the prototype transducers is given in Sect. 4.5.2, and in Sect. 4.5.1 for FE simulations of various steps in the construction. FEM calculated electrical conductance for the attached Pz27 and

MF114 disks, in addition to finished prototypes, in vacuum and water, are compared to electrical measurements. For prototypes no. 2 and 3, FEM calculated source sensitivity and the beam pattern (for no. 3) are also compared to acoustical measurements. Prototype no. 3 is used for transmission results presented in Chap. 6 and Chap. 7.

5.4.1 Prototype no. 1

For prototype no. 1 the Pz27 disk no. 12 with a $(D_p \times T_p)$ of 24.888 × 3.942 mm is chosen. A front layer with $(D_f \times T_f)$ of 30.396 × 1.023 mm is used. The thickness of the HCP70 backing layer no. 1, T_{b1}, is 14.23 mm, and the backing layer no. 2, T_{b2}, is 15.04 mm. The casing thickness, T_{c1}, is 2.35 mm, and the thickness of the back casing (supporting the coaxial plug), T_{c2}, is 4.02 mm. The total length of the casing, L_c, is 34.53 mm. The thickness of the electrically conductive adhesive, T_{ea}, is 0.058 mm, measuring the total thickness of the Pz27 and MF114 front layer after attachment, and substracting those thicknesses from the total thickness. The air cone thickness and radius, T_{ac} and R_{ac}, is set to 10.42 and 4.01 mm, respectively. The dimensions are listed in Tab. 5.6.

TABLE 5.6. Dimensions for prototype no. 1.

D_p[mm]	24.888	T_{b2}[mm]	15.04
T_p[mm]	3.942	T_{c1}[mm]	2.35
D_f[mm]	30.396	T_{c2}[mm]	4.02
T_f[mm]	1.023	L_c[mm]	34.53
T_{b1}[mm]	14.23	T_{ea}[mm]	0.058
T_{ac}[mm]	10.42	R_{ac}[mm]	4.01

Fig. 5.15 shows the measured electrical conductance, $G(f)$, in air (blue line) for the piezoelectric disk and front layer, see Fig. 5.10(b). This measurement is compared to the FEM calculated conductance, see Sect. 4.5.1.2, of the Pz27 and MF114 disks (blue line), where deviations are observed, especially in the region around the first thickness extensional (TE1) mode. The peak in the proximity of 600 kHz is shifted upwards in frequency in the simulations with respect to measurements. To improve comparison, a layer of the electrically conductive adhesive was added inbetween the Pz27 and MF114 disks in the FE simulations (black line).

The material data for the electrically conductive adhesive is presented in Sect. 5.4.2. A closer agreement to measurements can be observed after including the epoxy layer, but there are still variations in the measurements which are not present in the FE simulations. After multiple simulations of different epoxy layer thicknesses, epoxy material data, and air pockets inside the epoxy layer, it was concluded that most likely small air pockets got trapped in between the front layer and Pz27 disk during curing of the adhesive. The construction continued in order to provide experience for additional prototypes to come, but no effort were made to compare measurements to FE simulations. Fig. 5.16 shows the measured electrical conductance in air (blue line) and water (red line) for the finished prototype.

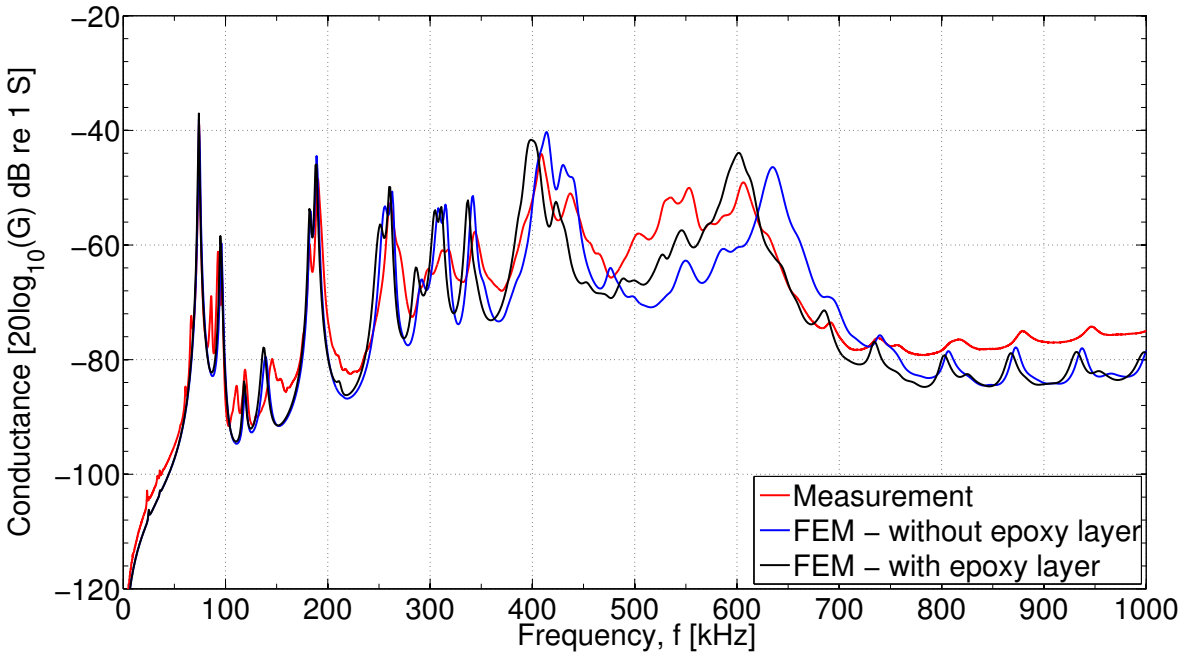

FIG 5.15. Measured electrical conductance $G(f)$ in air (red line) for the attached piezoelectric disk and front layer (see Fig. 5.10(b)), compared to FEM calculated conductance with (black line), and without (blue line) the conductive epoxy layer in the FE simulations.

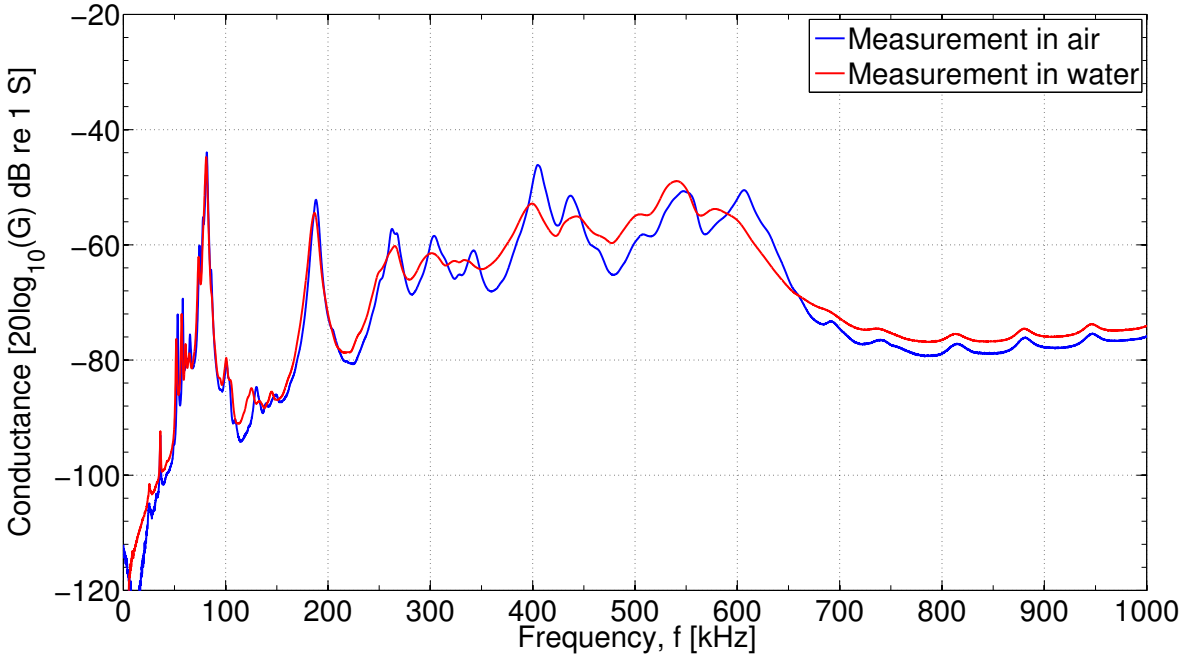

FIG 5.16. Measured electrical conductance in air (blue line) and water (red line) for prototype no. 1.

5.4.2 Prototype no. 2

For prototype no. 2 a Pz27 disk with a ($D_p \times T_p$) of 24.894 × 3.936 mm is chosen. A front layer with ($D_f \times T_f$) of 30.460 × 1.054 mm is used. The thickness of the HCP70 backing layer no. 1, T_{b1}, is 13.45 mm, and the backing layer no. 2, T_{b2}, is 15.01 mm. The casing thickness, T_{c1}, is 2.64 mm, and the thickness of the back casing (supporting the coaxial plug), T_{c2}, is 4.11 mm. The total length of the casing, L_c, is 34.32 mm. The thickness of the electrically conductive adhesive, T_{ea}, is 0.074 mm. The air cone thickness and radius, T_{ac} and R_{ac}, is set to 10.42 and 4.01 mm, respectively. The dimensions are listed in Tab. 5.7.

TABLE 5.7. Dimensions for prototype no. 2.

D_p[mm]	24.894	T_{b2}[mm]	15.01
T_p[mm]	3.936	T_{c1}[mm]	2.64
D_f[mm]	30.460	T_{c2}[mm]	4.11
T_f[mm]	1.054	L_c[mm]	34.32
T_{b1}[mm]	13.45	T_{ea}[mm]	0.074
T_{ac}[mm]	10.42	R_{ac}[mm]	4.01

Based upon experience with prototype no. 1, the electrically conductive adhesive layer was added in the FE simulations of the piezoelectric disk with the front layer, see Sect. 4.5.1.2. Fig. 5.18 shows the measured electrical conductance in air for the Pz27 and MF114 disks (see Fig. 5.10(b)), compared to FEM calculated conductance with the epoxy layer included. Recall from Sect. 5.3.1 that the manufacturer only provided the density, ρ_{ea}, for the epoxy, not the sound velocities. The compressional and shear sound velocities, c_{Lea} and c_{Sea}, of the epoxy, respectively, and the corresponding loss factor, Q_{Mea}, were varied to adjust the FE simulations to the measurements. The material data used for FE simulations of the electrically conductive adhesive is listed in Tab. 5.8.

TABLE 5.8. Material data used for the electrically conductive adhesive.

c_{Lea}[m/s]	1700
c_{Sea}[m/s]	1000
ρ_{ea}[kg/m^3]	2340
Q_{Mea}	50

The construction continued following the procedures in Sect. 5.3. Figs. 5.17 and 5.18 show the FEM simulated (red line) electrical conductance in comparison to electrical measurements (blue line) in air, excluding and including the electrically conductive adhesive in the FE simulations, respectively. Above 700 kHz the simulated electrical conductance shows some deviations from the measurements. Fig. 5.19 shows the measured (blue line) and FEM calculated (red line) electrical conductance in air for prototype no. 2. Fig. 5.20 shows the measured (blue line) and FEM calculated (red line) electrical conductance in water for prototype no. 2. As for Figs. 5.17, 5.18 and 5.19, a deviation can be observed above 700 kHz. Fig. 5.21 shows the measured (blue line) and the FEM calculated (red line) source sensitivity in water for prototype no. 2. Whereas the electrical conductance shows deviations above

700 kHz, the voltage source sensitivity does not show the same deviations.

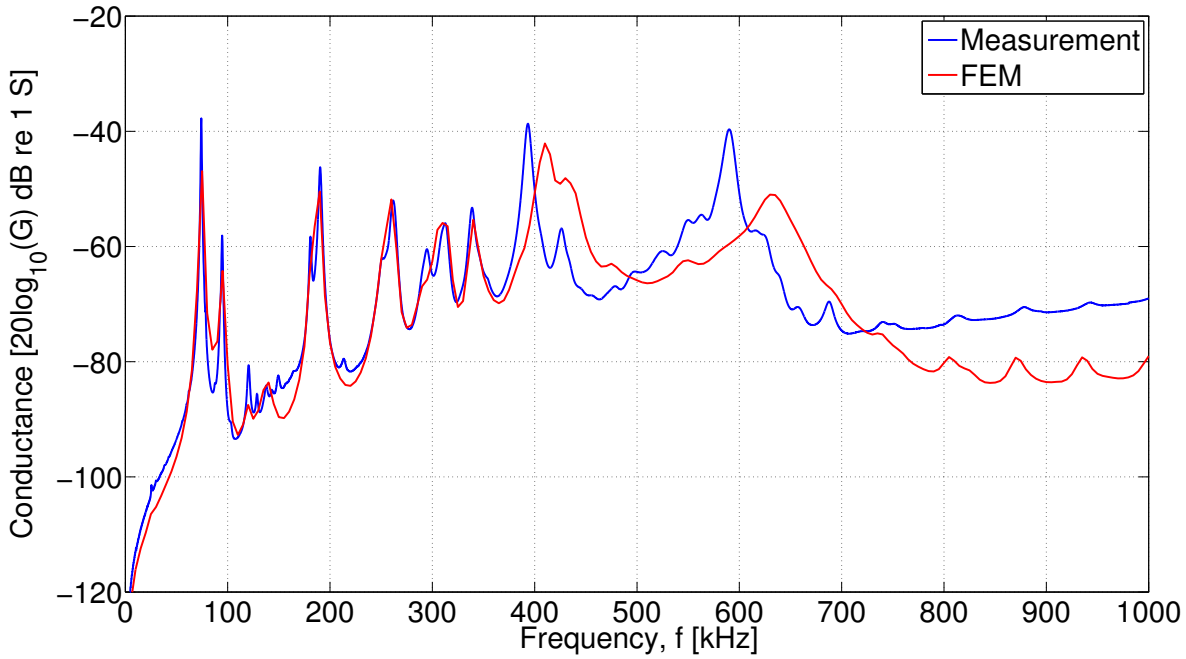

FIG 5.17. Electrical conductance in air for the attached Pz27 disk with front layer (blue line), compared to FEM calculated conductance (red line) with the electrically epoxy adhesive layer excluded.

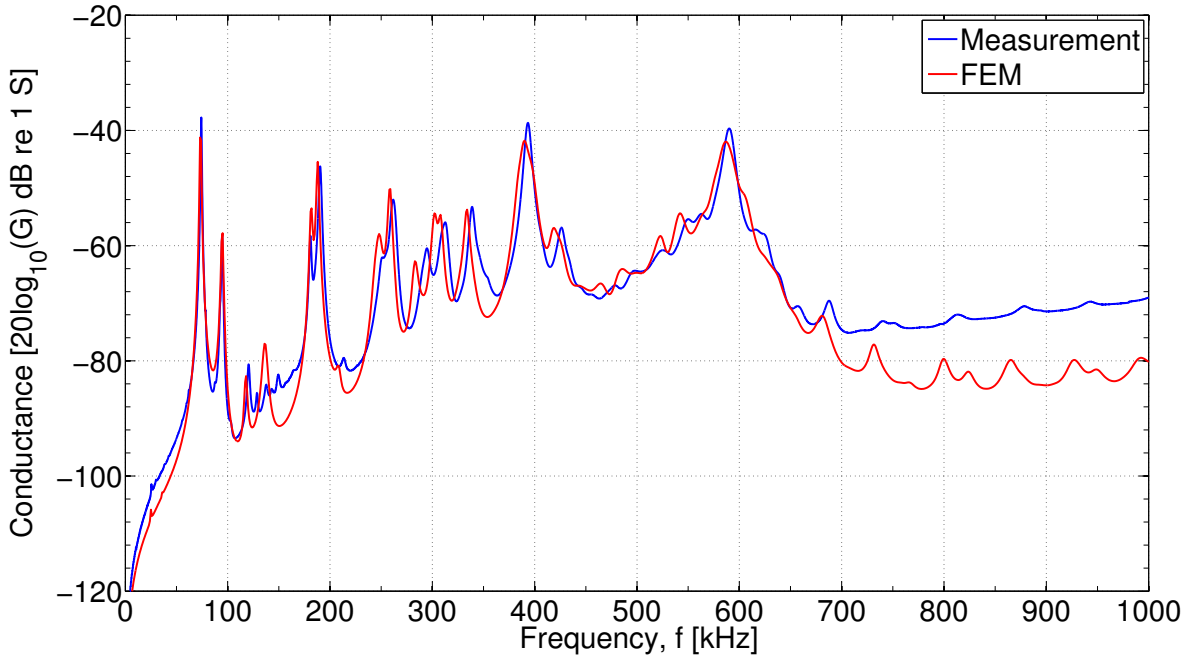

FIG 5.18. Electrical conductance in air for the attached Pz27 disk with front layer (blue line), compared to FEM calculated conductance (red line) with the electrically epoxy adhesive layer included.

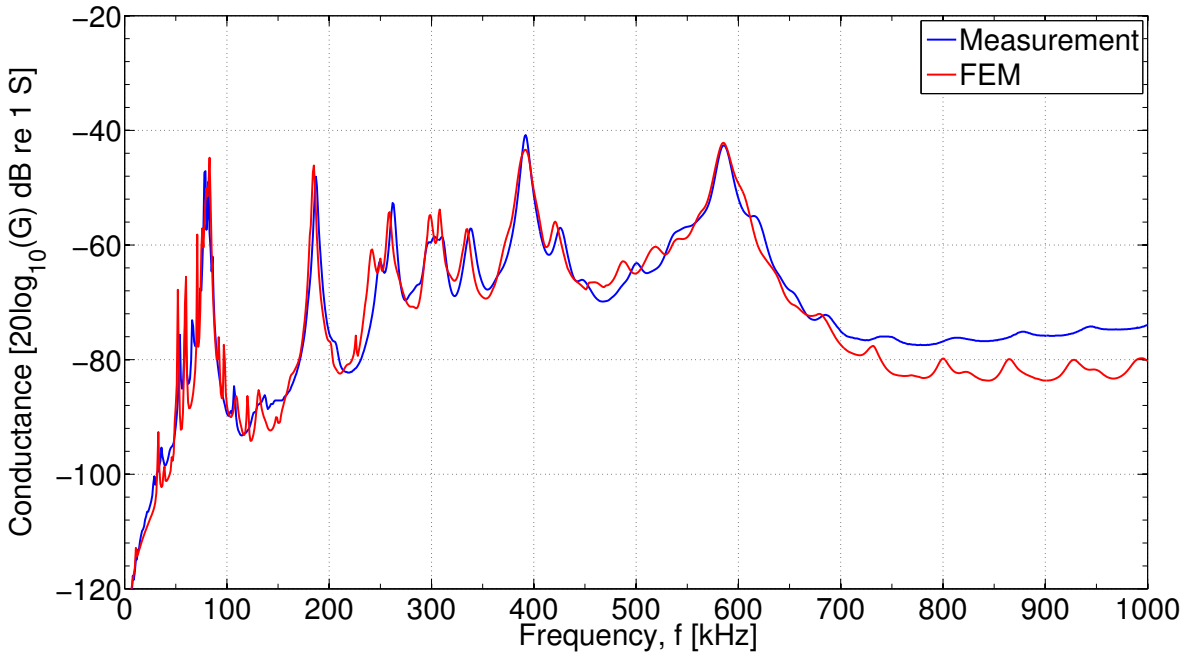

FIG 5.19. Measured (blue line) electrical conductance in air for prototype no. 2, compared to the FEM calculated (red line).

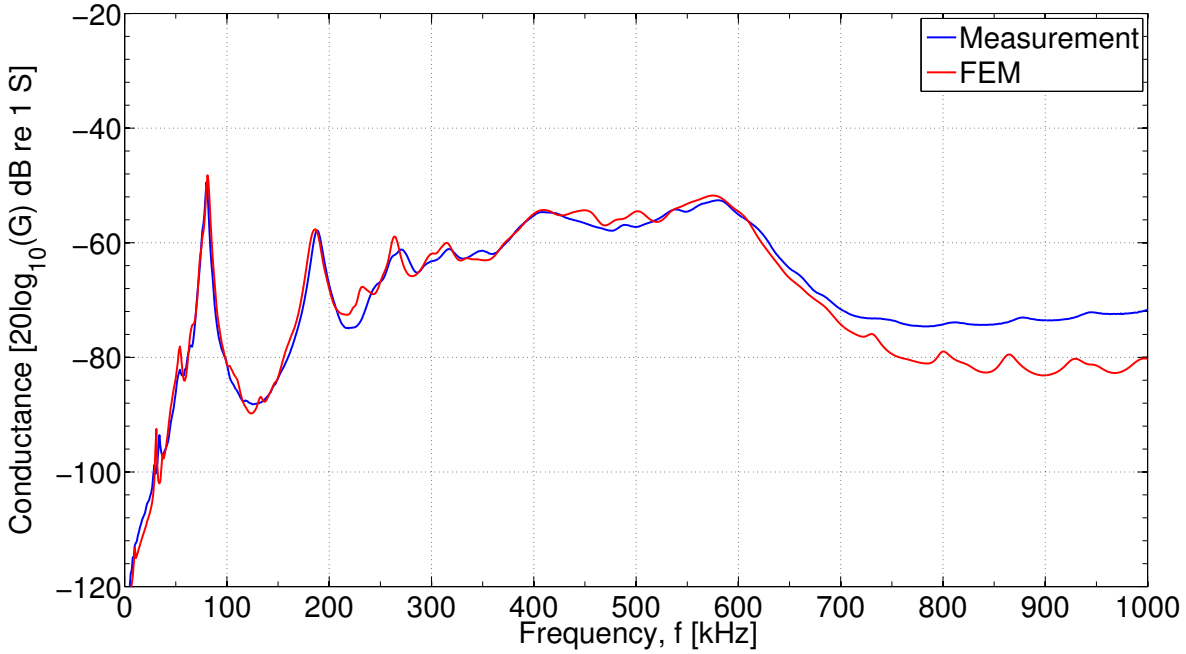

FIG 5.20. Measured (blue line) electrical conductance in water for prototype no. 2, compared to the FEM calculated (red line).

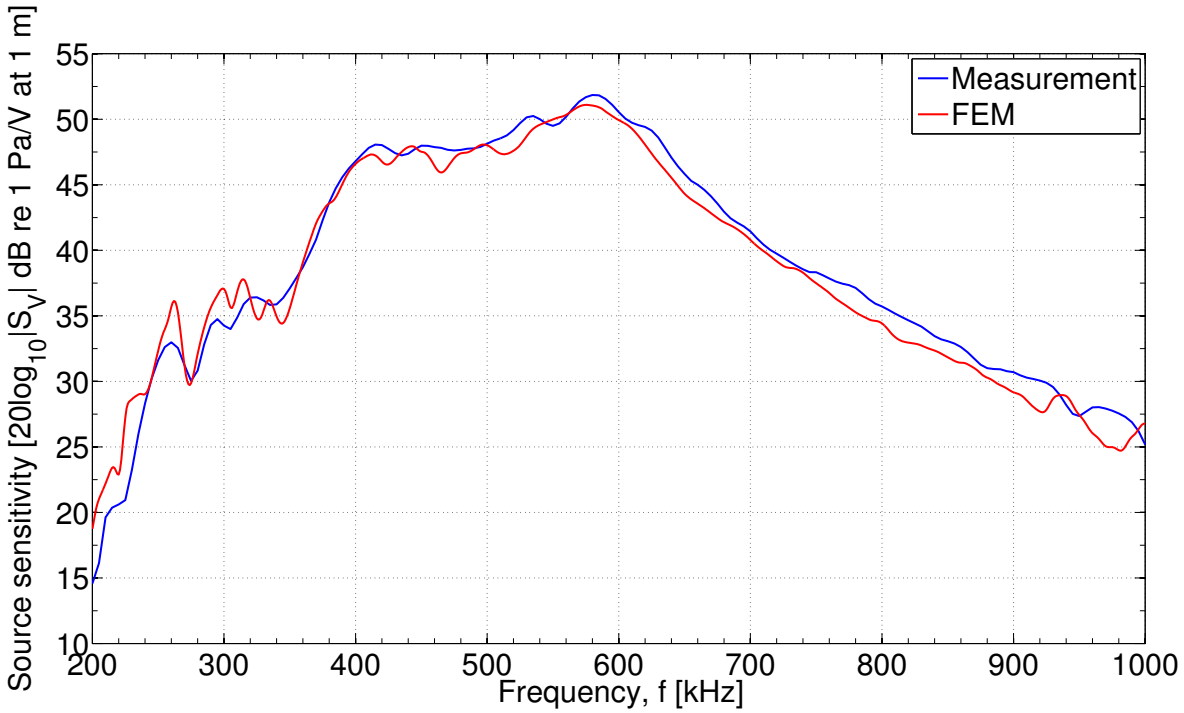

FIG 5.21. Measured (blue line) voltage source sensitivity in water for prototype no. 2, compared to the FEM calculated (red line).

5.4.3 Prototype no. 3

A third prototype is produced to test the reproducibility of the tranducer design, and material data for the electrically conductive adhesive. For prototype no. 3 a Pz27 disk with $(D_p \times T_p)$ of 24.877 × 3.956 mm is used. A front layer with $(D_f \times T_f)$ of 30.440 × 1.065 mm is used. The thickness of the HCP backing layer no. 1, T_{b1}, is 15.12 mm, and the backing layer no. 2, T_{b2}, is 13.64 mm. The casing thickness, T_{c1}, is 2.83 mm, and the thickness of the back casing (supporting the coaxial plug), T_{c2}, is 3.96 mm. The total length of the casing, L_c, is 34.42 mm. The thickness of the electrically conductive adhesive, T_{ea}, is 0.07125 mm. The air cone thickness and radius, T_{ac} and R_{ac}, is set to 10.42 and 4.01 mm, respectively. The dimensions are listed in Tab. 5.9.

TABLE 5.9. Dimensions for prototype no. 3.

D_p[mm]	24.877	T_{b2}[mm]	13.64
T_p[mm]	3.956	T_{c1}[mm]	2.83
D_f[mm]	30.440	T_{c2}[mm]	3.96
T_f[mm]	1.065	L_c[mm]	34.42
T_{b1}[mm]	15.12	T_{ea}[mm]	0.07125
T_{ac}[mm]	10.42	R_{ac}[mm]	4.01

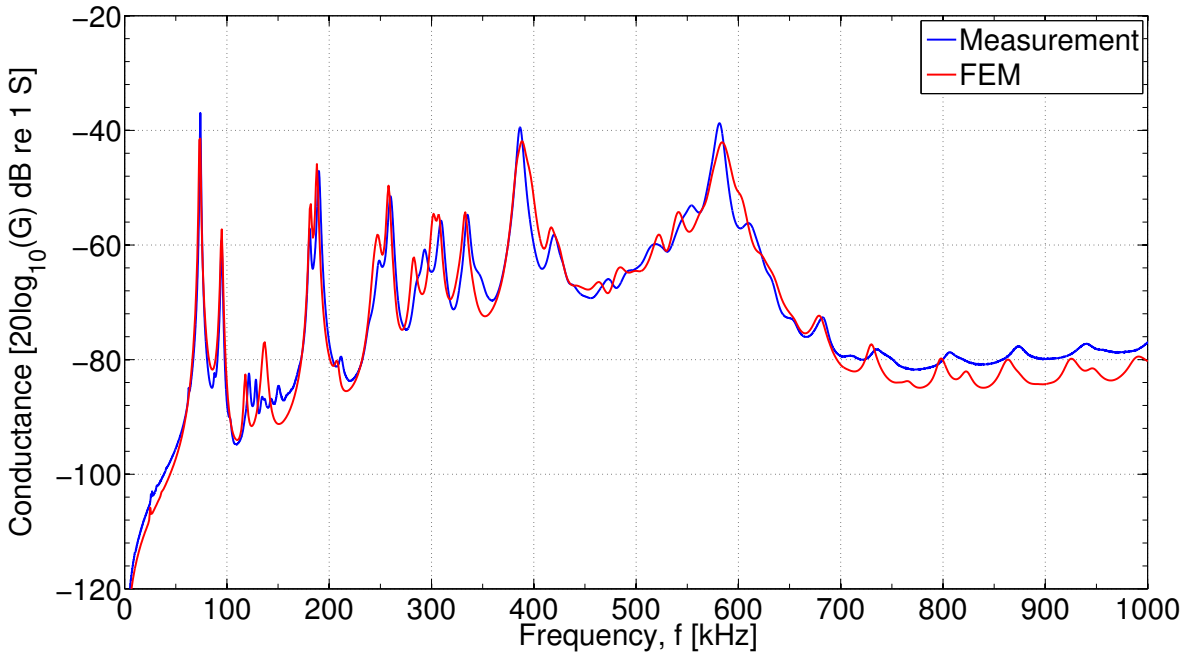

FIG 5.22. Electrical conductance in air for the attached Pz27 disk with front layer (blue line), compared to FEM calculated conductance (red line) with the epoxy layer included.

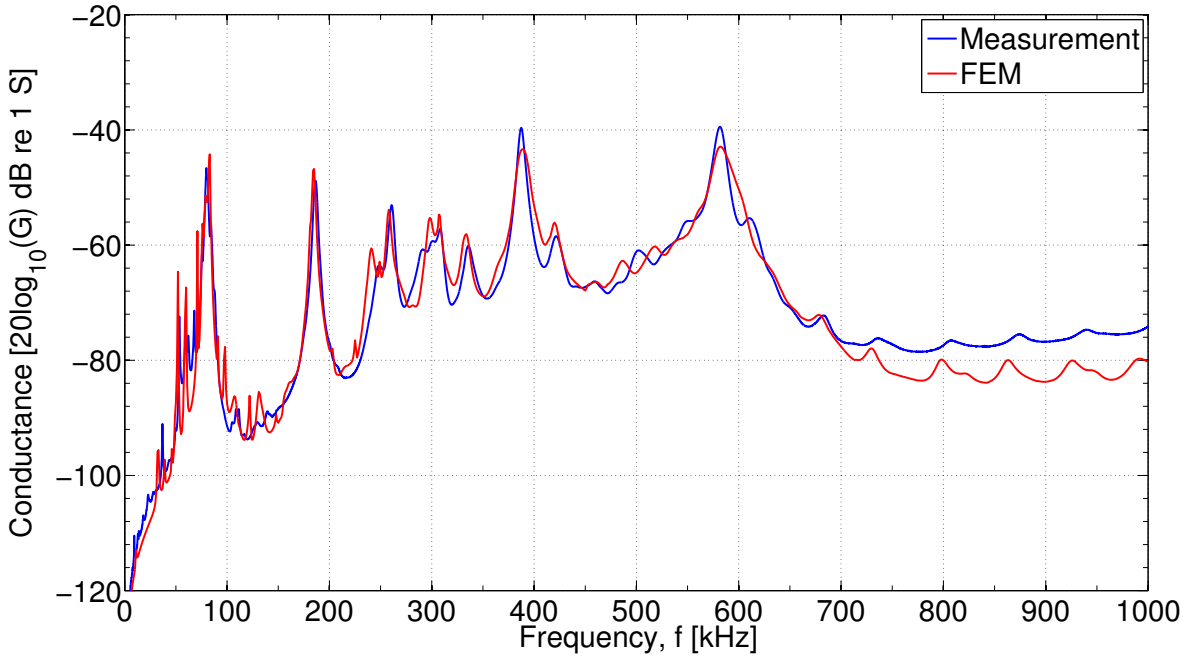

FIG 5.23. Measured (blue line) electrical conductance in air for prototype no. 3, compared to the FEM calculated (red line).

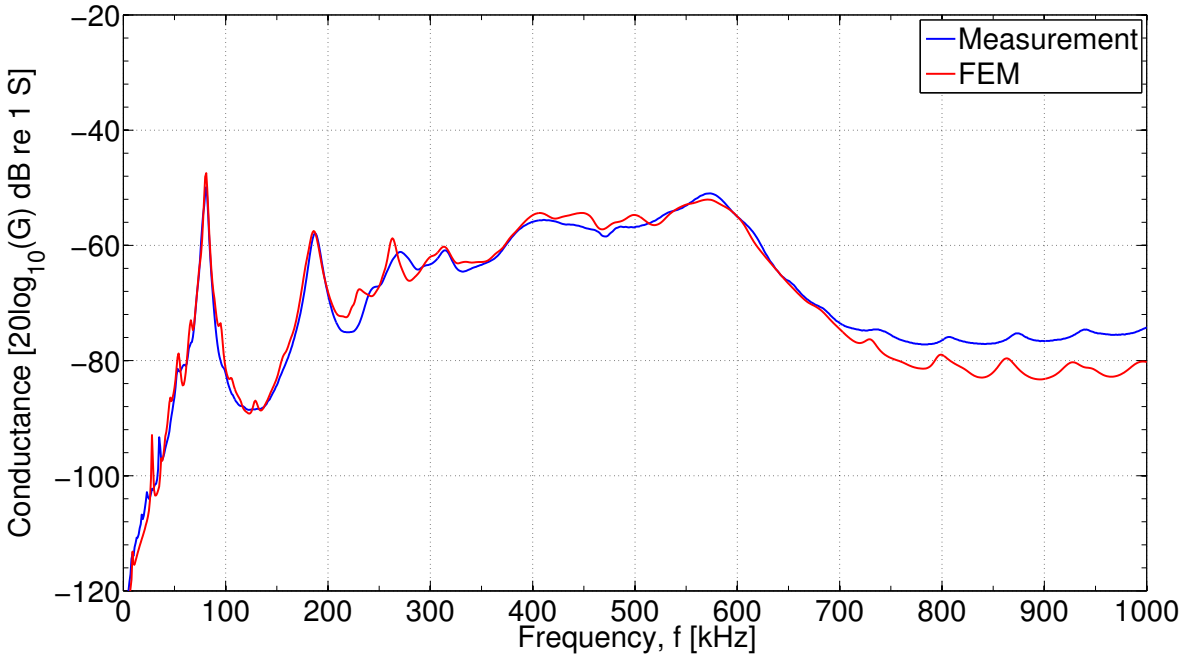

FIG 5.24. Measured (blue line) electrical conductance in water for prototype no. 3, compared to the FEM calculated (red line).

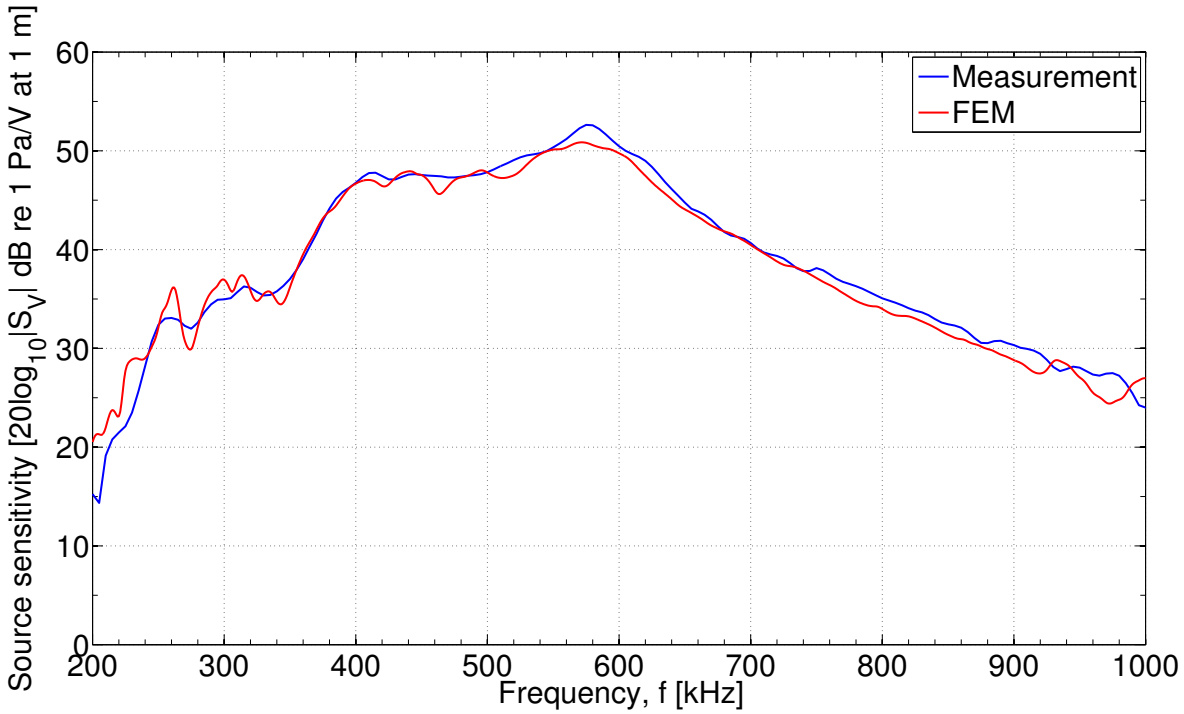

FIG 5.25. Measured (blue line) voltage source sensitivity in water for prototype no. 3, compared to the FEM calculated (red line).

Fig. 5.22 shows the measured (blue line) and FEM calculated (red line) electrical conductance in air for the attached Pz27 disk and front layer, including the electrically conductive epoxy layer in the FE simulations. The construction continued following the procedures in Sect. 5.3. Fig. 5.23 shows the measured (blue line) and FEM calculated (red line) electrical conductance in air for prototype no. 3. Fig. 5.24 shows the measured (blue line) and FEM calculated (red line) electrical conductance in water for prototype no. 3. Fig. 5.25 shows the measured (blue line) and FEM calculated (red line) voltage source sensitivity in water for prototype no. 3. The same deviations above 700 kHz as for Figs. 5.19, 5.20 and 5.23 are observed, but is less apparent here. Figs. 5.26(a) and 5.26(b) show the electrical conductance and the source sensitivity of prototype no. 3 in the frequency range 0 - 1.5 MHz (dotted blue lines), respectively, compared to FEM results (red lines) shown in Figs. 5.24 and 5.25 and measurements (green lines). The in-house 3-transducer reciprocity calibration is used since measurements have been conducted up to 1.5 MHz (NPL calibration was available up to 1 MHz, cf. Sect. 3.5). The FEM setup as described in Sect. 4.5.2 is used, but 3 elements per shear wavelength at 1.5 MHz (instead of at 1 MHz) is used as the element division. A frequency step of 10 kHz is used (instead of 1 kHz). These figures are here presented for the discussion in Sect. 4.2 regarding the limited frequency range of FE simulations, and are also used to confirm that the FEM results presented in this chapter have adequately converged for use in measurement comparisons.

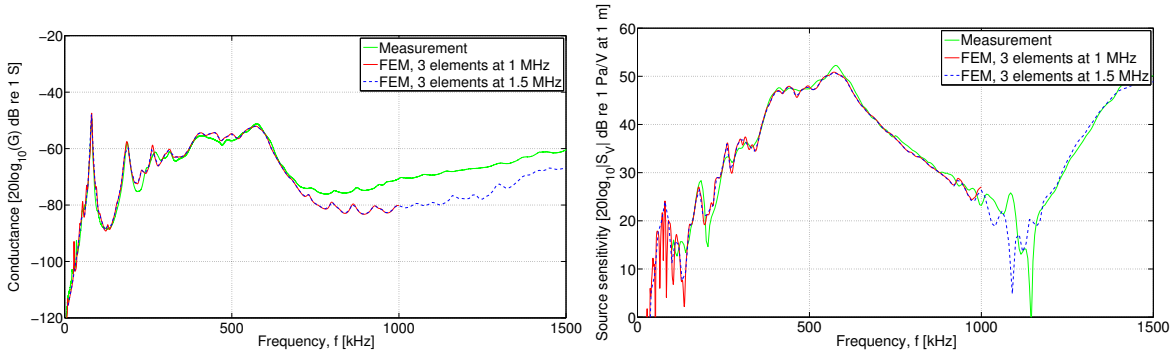

(a) (b)

Fig 5.26. FEM simulated **a)** electrical conductance and **b)** source sensitivity for prototype no. 3 in the frequency range 0 - 1.5 MHz in comparison to measurements (green lines).

Fig. 5.27 shows the measured (blue line) and FEM calculated (red line) magnitude of the beam pattern $|D(\phi)|$ for prototype no. 3, at specific frequencies within the frequency range of interest. Beyond the first side lobe the FEM simulated beam pattern $|D(\phi)|$ show some deviations from measurements, except for the beam patterns at 370 kHz, 420 kHz and 1 MHz, where the deviations occur beyond the main lobe. As the frequency increases, the main lobe of the transducer becomes narrower, thus increasing the effect the higher order side lobes will have on the transmission of sound through the steel plate. From this, one expects that deviations between the simulated $P_t(x, y, z, f)$ compared to measurements will increase both with frequency and position from $z' = 0$. Provided more accurate material data become available, improved agreement beyond the first side lobe may also be possible to obtain for the FEM calculated transducer source.

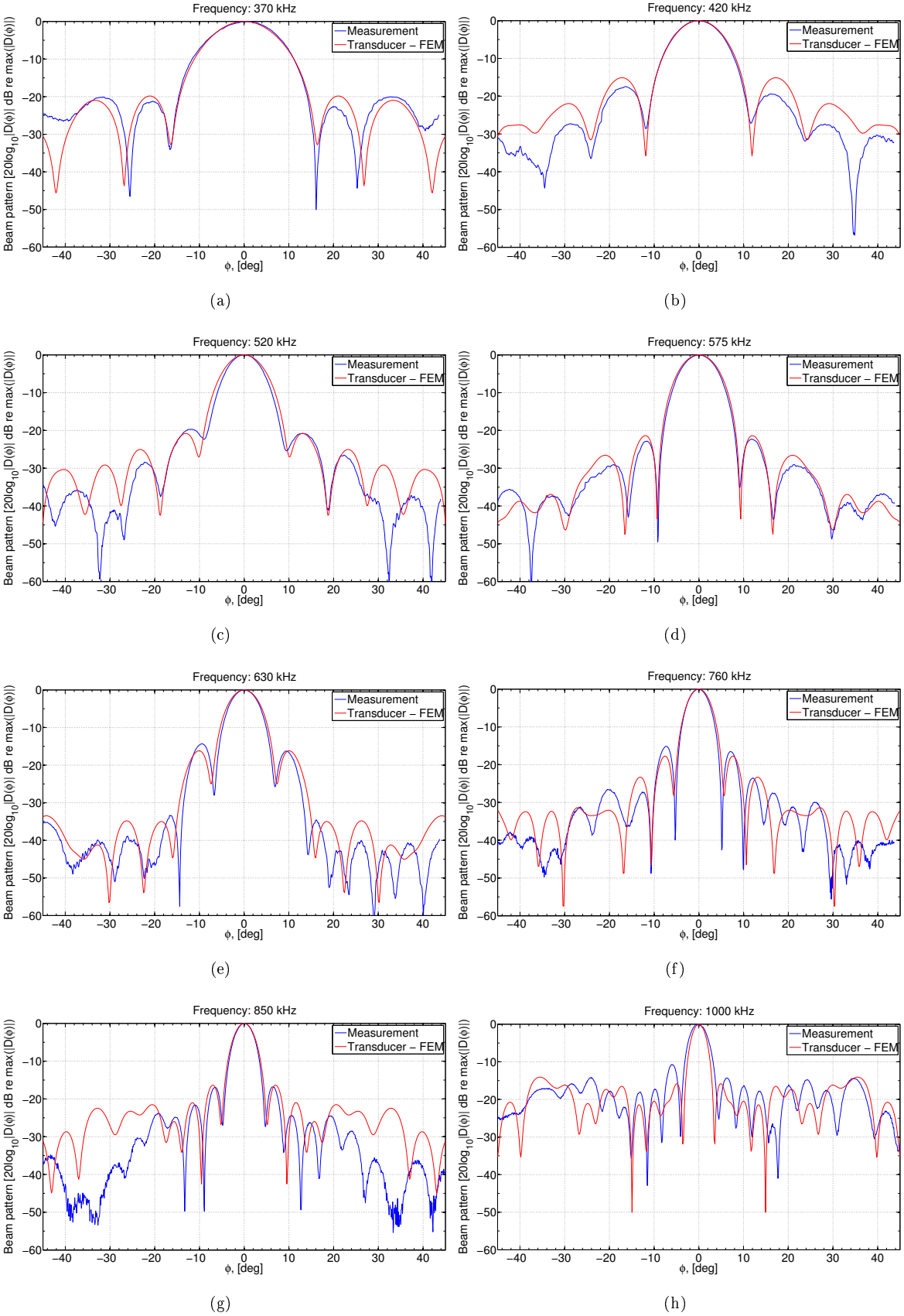

Fig 5.27. FEM simulated (blue line) and measured (red line) magnitude beam pattern $|D(\phi)|$ for the piezoelectric source transducer at specific frequencies, in the range 370 - 1000 kHz.

5.5 Summary and discussion

This chapter presented the design and construction for the piezoelectric source transducer to be used in the measurement system. Electrical and acoustical measurements in water and air, and FE simulations are compared at several steps of the construction process, starting with a circular piezoelectric ceramic disk and gradually introducing matching, backing and encapsulation layers/materials, involving the challenges of obtaining accurate material data. Characterization results in water are compared with simulations of transducer properties such as electrical admittance response, and source sensitivity response and beam pattern, including radial modes and the fundamental thickness-extensional mode of the transducer. The results demonstrates sufficient agreement for use of the transducer in a system modeling approach (with description of signal propagation in time and frequency domain) using FEM. Provided more accurate material data become available, improved agreement to measurements are expected. Figs. 5.26(a) and 5.26(b) show that the FEM results presented in this chapter have adequately converged for use in measurement comparisons, see also the discusssion conserning convergence in Sect. 4.4.

Chapter 6

Ultrasonic beam transmission through fluid-embedded steel plate

6.1 Introduction

This chapter compares the results for the signal transmission through the plate and water, using the piezoelectric transducer, baffled piston and plane-wave theory. Transmission results through the plate are presented in Sect. 6.2.1, comparing 3D beams vs. plane-waves using the FEM approach, with respect to beam effects introduced by using a finite dimensional transducer. Sect. 6.2.2 presents the measurement results for determination of the sound velocities in the plate, and the corresponding Q-factors, based upon the method described in Sect. 3.3 [91, 92]. The assessment of the deviations using the piezoelectric tranducer model vs. the baffled piston model as source to the measurement system is discussed in Sect. 6.3, based upon hybrid FEM-ASM results for transmission of sound through the steel plate and water. Comparison of simulated piezoelectric transducer vs. baffled piston results at different angles of beam incidence are discussed, in relation to the measured beam pattern of the transducer and its influence on leaky Lamb mode excitation in the plate.

6.2 Signal transmission through the plate

In this section the beam effects of using a finite dimensional transducer for transmission measurements are discussed based upon a comparison of 3D beams, using the FEM approach, and plane-wave theory results in Sect. 6.2.1. Further on, the measurement of the sound velocities with corresponding Q-factors for the steel plate is reported in Sect. 6.2.2, using the method described in Sect. 3.3 [91, 92, 150]. With regard to sound velocity measurements, a brief documentation of cold rolled vs. hot rolled steel and its effect on the shear sound velocity is given in Sect. 6.2.2.1.

6.2.1 3D beams vs. plane-waves

In Fig. 6.1 the Lamb dispersion curves for the steel plate in vacuum are shown as a function of horizontal wavenumber η (in the range 0-2500 rad/m) and frequency, calculated from Eqs. (2.47) and (2.48). The dispersion curves defines the symmetrical and antisymmetrical Lamb modes in the steel plate, given in Tab. 6.1 at $\eta = 0$ rad/m. The zero order symmetrical, S_0^v, and zero order antisymmetrical, A_0^v, are defined from Fig. 6.1[1]. The sound velocities in the plate are marked with red lines. In Fig. 6.2 the Lamb dispersion curves for the steel plate in vacuum are shown as a function of phase velocity (in the range 0-2.5) and frequency.

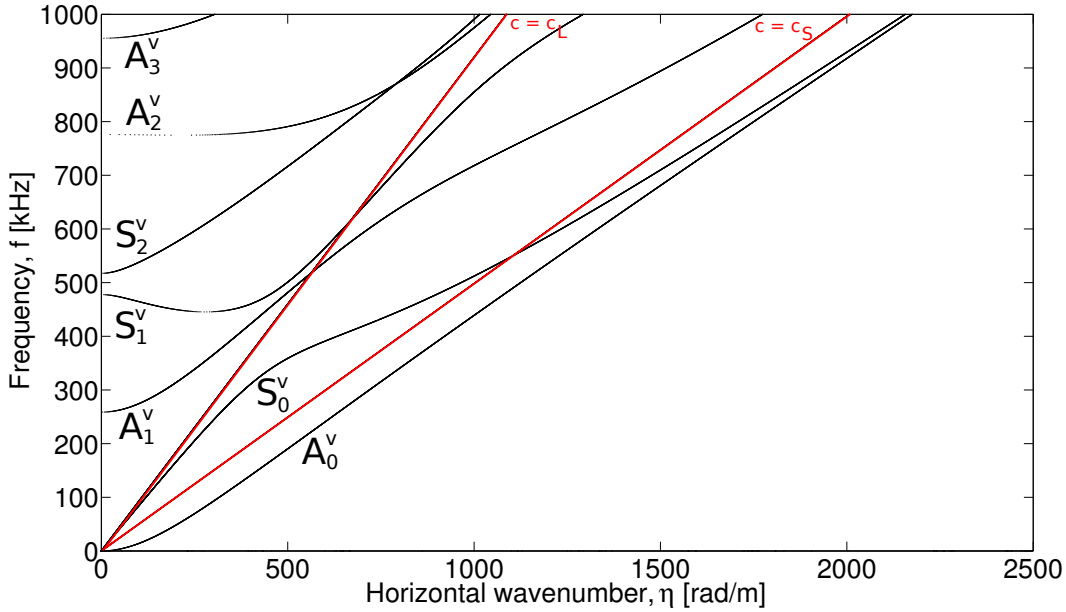

Fig 6.1. Dispersion curves for the steel plate in vacuum as a function of horizontal wavenumber η and frequency. The material data is given in Tab. 6.5. The sound velocities in the plate are marked with red lines.

TABLE 6.1. Vacuum-embedded steel plate at $\eta = 0$ rad/m. Material data for the steel plate is listed in Tab. 6.5.

Symbol	Frequency [kHz]	(S)ymm/(A)ntisymm	Type mode
$f_{t1}^{A,v}$	258.7	A_1^v	TS
$f_{l1}^{S,v}$	477.6	S_1^v	TE
$f_{t1}^{S,v}$	517.4	S_2^v	TS
$f_{t2}^{A,v}$	776.0	A_2^v	TS
$f_{l1}^{A,v}$	955.4	A_3^v	TE

Fig. 6.3 shows the leaky Lamb dispersion curves for the steel plate in water as a function of phase velocity (in the range 0-2.5) and frequency, calculated from Eqs. (2.92) and (2.93). The dispersion curves defines the symmetrical and antisymmetrical leaky Lamb modes in the steel plate, given in Tab.

[1]For references to the plane-wave theory in Chaps. 6 and 7, the leaky Lamb modes are used. For the sake of simplicity in notation, the leaky Lamb modes are therefore denoted without any superscript, and the Lamb modes with the superscript v, e.g. S_0^v and S_0 is the zero order symmetrical Lamb and leaky Lamb mode, respectively.

6.2 at $h_{f,x} = 0$ rad/m, e.g. $\theta_P = 0°$. The zero order symmetrical, S_0, and zero order antisymmetrical, A_0, are defined from Fig. 6.3. Two Scholte-Stoneley waves exists for a single fluid-embedded immersed plate [163], denoted the (S)ymmetrical and (A)ntisymmetrical Scholte-Stoneley wave. The dispersion curves algorithm utilized here is used with permission from Kjetil Daae Lohne [90], refer to this work for discussion regarding numerical difficulties tracing the A_0 mode correctly for low frequencies.

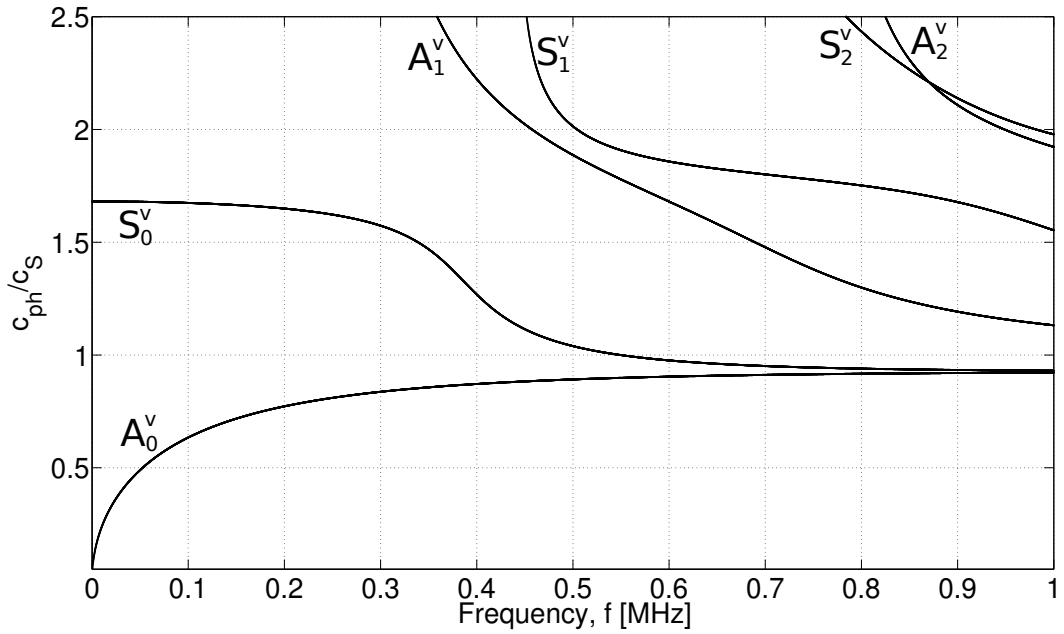

Fig 6.2. Dispersion curves for the steel plate in vacuum as a function of phase velocity and frequency. The material data is given in Tab. 6.5.

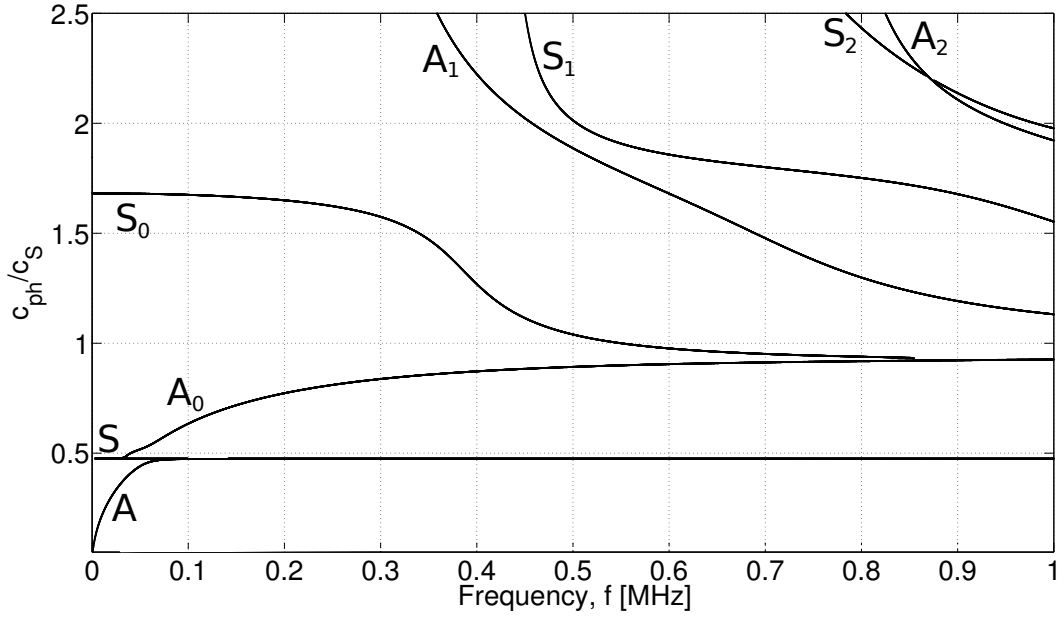

Fig 6.3. Dispersion curves for the steel plate in water as a function of phase velocity and frequency. The material data are given in Tabs. 6.5 and 5.5.

TABLE 6.2. Water-embedded steel plate at normal incidence $\theta_P = 0°$. The $*$ indicates a 1° incidence angle with the steel plate. Material data for the steel plate is listed in Tab. 6.5.

Symbol	Frequency [kHz]	(S)ymm/(A)ntisymm	Type mode
f_{t1}^{A}	260.0$*$	A_1	TS
f_{l1}^{S}	477.7	S_1	TE
f_{t1}^{S}	517.5$*$	S_2	TS
f_{t2}^{A}	774.5$*$	A_2	TS
f_{l1}^{A}	955.4	A_3	TE

In Fig. 6.4 the magnitude of the plane-wave transmission coefficient $\mathscr{T}$ for the steel plate in water is shown as a function of phase velocity c_{ph} (normalized to the shear velocity c_S) (in the range 0-6) and frequency, calculated using Eq. (2.104) and Eq. (2.37) for $h_{f,y} = 0$. The maxima of $|\mathscr{T}|$ corresponds to the symmetrical (S) and antisymmetrical (A) leaky Lamb modes in the steel plate, showing the dispersion curves for leaky Lamb modes (cf. Fig. 6.3) at maxima of the plane-wave pressure transmission coefficient. Material data for the steel plate and water are listed in Tabs. 6.5 and 5.5, respectively. In Fig. 6.5 the magnitude of the plane-wave pressure transmission coefficient $\mathscr{T}$ for the steel plate in water is shown as a function of horizontal wavenumber $h_{f,x}$ (in the range 0-2500 rad/m) and frequency, calculated using Eq. (2.104) for $h_{f,y} = 0$. In Fig. 6.6 the magnitude of the plane-wave transmission coefficient $\mathscr{T}$ for the steel plate in water is shown as a function of plane-wave incidence angle θ_P (in the range 0-60°) and frequency, calculated using Eq. (2.104) and Eq. (4.3) for $h_{f,y} = 0$. Recall Eq. (2.37) that states that $\eta \propto \frac{1}{c_{ph}}$, so as the horizontal phase velocity increase, the horizontal wavenumber approach zero, i.e. the plane-wave incident angle approach normal incidence.

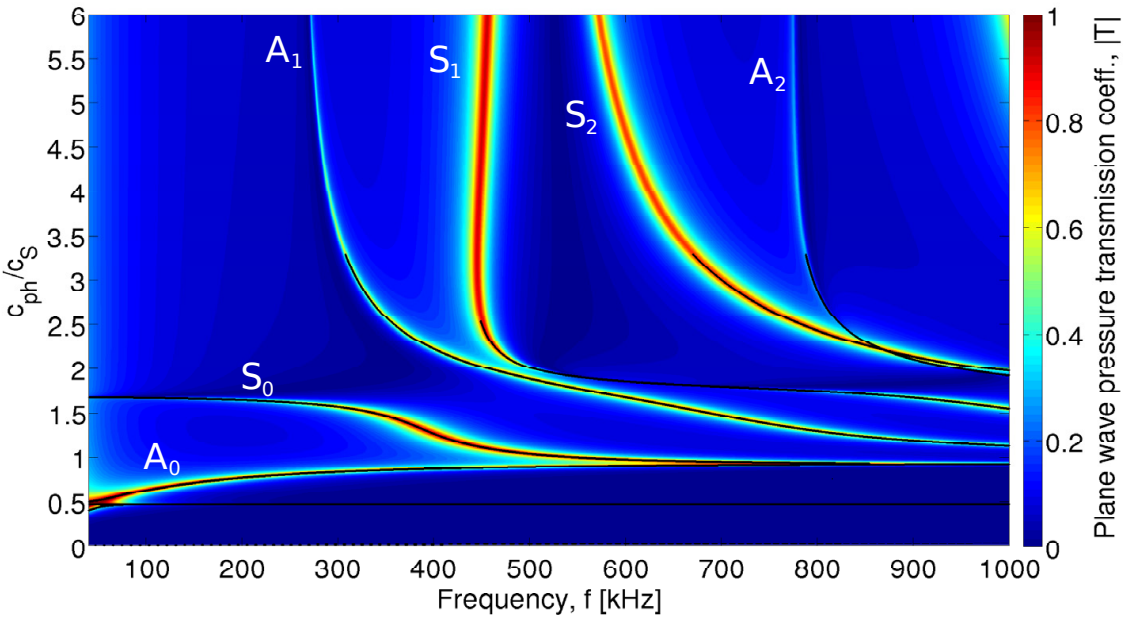

Fig 6.4. Magnitude of the plane-wave pressure transmission coefficient, $|\mathscr{T}|$ as a function of phase velocity and frequency, including leaky Lamb modes in the water-immersed steel plate. The material data are given in Tabs. 6.5 and 5.5.

Similar plots as Figs. 6.5, 6.4 and 6.6 can be found in e.g. [164, 74, 94, 95, 98, 92, 91], but in many of these only the dispersion curves of the (leaky) Lamb modes are given.

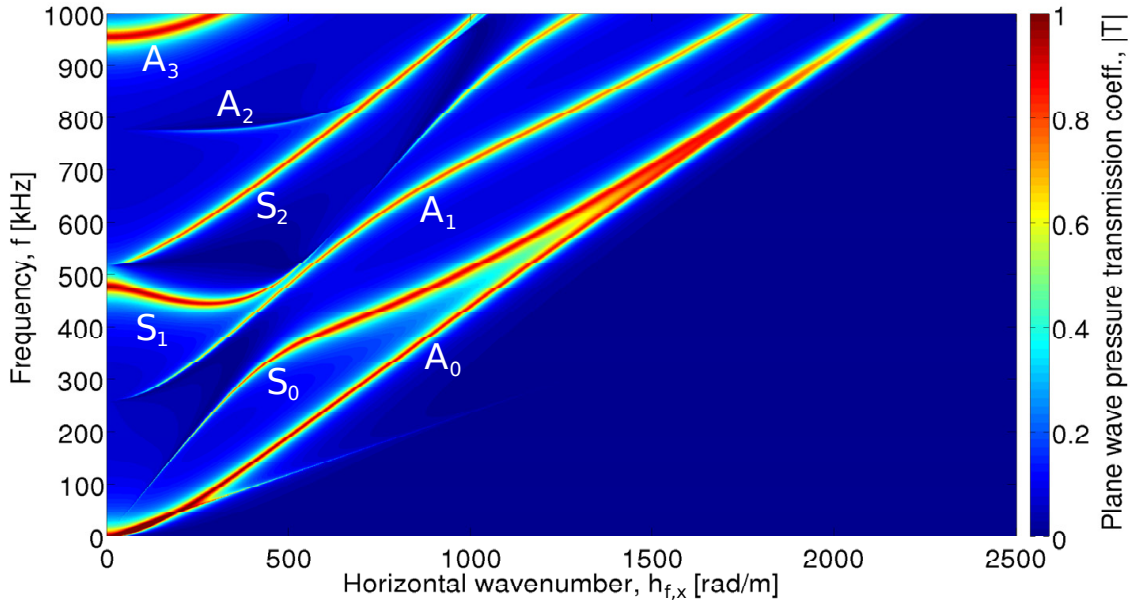

Fig 6.5. Magnitude of the plane-wave pressure transmission coefficient, $|\mathscr{T}|$ as a function of horizontal wavenumber and frequency, including leaky Lamb modes in the water-immersed steel plate. The material data are given in Tabs. 6.5 and 5.5.

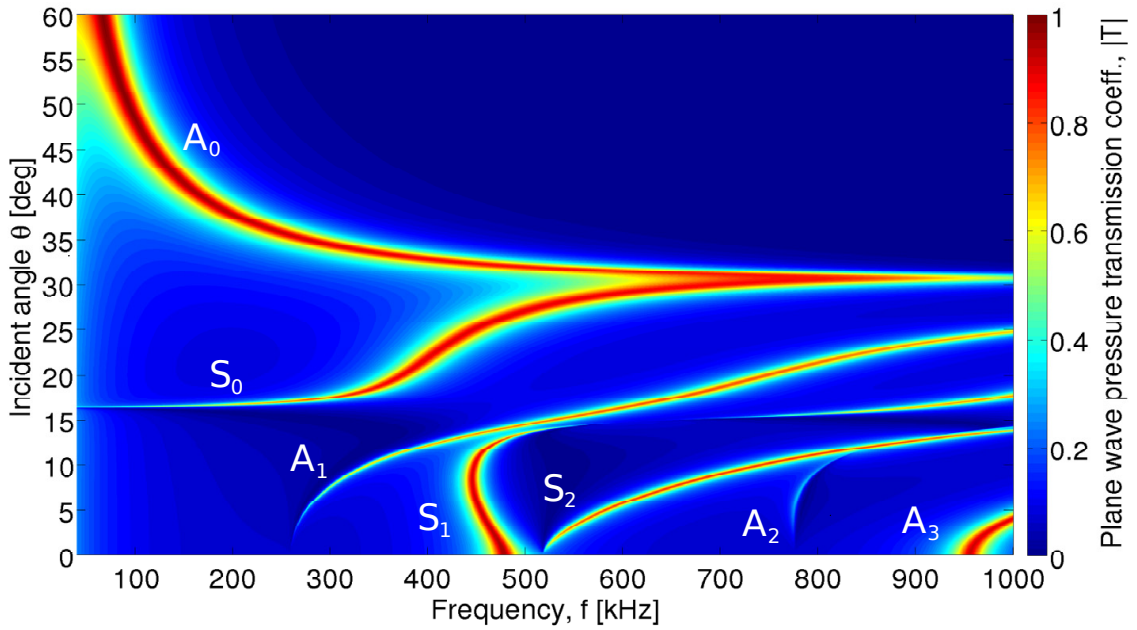

Fig 6.6. Magnitude of the plane-wave pressure transmission coefficient, $|\mathscr{T}|$ as a function of incidence angle and frequency, including leaky Lamb modes in the water-immersed steel plate. The material data are given in Tabs. 6.5 and 5.5.

In Fig. 6.7(a) the black curve shows the magnitude of the plane-wave pressure transmission coefficient $\mathscr{T}$ for plane waves at normal incidence $\theta_p = 0$, cf. Fig. 6.6, presented as a function of frequency. As the plane-wave angle of incidence approaches zero, the symmetrical and antisymmetrical leaky Lamb modes in the plate approach the cut-off frequencies, creating standing waves (thickness-extensional (TE) and thickness-shear (TS) modes, respectively) across the thickness of the steel plate. Since a plane-wave at normal incidence only generates compressional displacement in the plate, only compressional waves appear inside the plate, exciting the S_1 and A_3 modes. For that reason a plane-wave at normal incidence cannot excite TS modes in the plate, and the leaky Lamb modes corresponding to these modes, the S_2 and A_2 modes, will vanish as the incident angle of the imposed plane-wave approaches zero. In Fig. 6.7(a) the plane-wave pressure transmission coefficient at normal incidence is compared to the FEM calculated ratio $|P_1(0,0,z_0+2L,f)/P_0(0,0,z_0,f)|$, using the piezoelectric transducer as source at normal incidence of the beam ($\theta = 0°$). Since the FEM approach impose the transducer's directive beam across the surface of the steel plate, displacements in both the thickness and radial direction will occur at normal incidence of the beam. Both compressional and shear waves are thus set up in the plate, thereby exciting all four leaky Lamb modes in the frequency range at normal beam incidence. The transducer beam can be represented as an integration over an angular spectrum of plane-waves with various incidence angles with respect to the on-axis (z'-axis), scaled according to the wavenumber spectrum of the sound pressure distrubution on the upper surface of the steel plate (when the plate is absent) at the given frequency. Most of the energy transferred from the transducer into the water is transmitted through the main lobe. Thus, plane-waves outside this region will only give a small contribution to the total transmission at that frequency, or none at all. So, at a given frequency and beam incidence, the transducer beam will excite all available leaky Lamb modes at that frequency. But, the main contribution to the overall transmission will be given by leaky Lamb modes excited in the vicinity of the beam incidence (inside the main lobe).

In Fig. 6.7(b), the plane-wave pressure transmission coefficient at 1° incidence angle is compared to the same FEM calculated ratio $|P_1(0,0,z_2+2L,f)/P_0(0,0,z_0,f)|$ as in Fig. 6.7(a), using the piezoelectric transducer as source at normal beam incidence. Here, the S_2 and A_2 modes are excited, together with the S_1 and A_3 mode. The frequencies corresponding to the S_2 and A_2 modes correspond approximately to the frequencies where the TS modes are present across the thickness of the plate [91, 98, 93].

By using the transducer at normal beam incidence it is found that the region with relatively high transmission around the S_1 mode is shifted downwards in frequency, in relation to the use of a plane-wave at normal incidence. This shift will affect the measurement of c_L in the plate using the method described in Sect. 6.2.2. This frequency shift is observed in [90], and explained in [91, 92] using $H_{PP}(0,0,z_2,f)$, and with the ratio $|P_1(0,0,z_0+2L,f)/P_0(0,0,z_0,f)|$ in [98]. In addition, it is observed in [91, 93] and discussed in [98] that $H_{PP}(0,0,z_2,f)$ and the ratio $|P_1(0,0,z_0+2L,f)/P_0(0,0,z_0,f)|$ also exceeds unity in this region, where, the pressure transmission coefficient $\mathscr{T}$ never exceeds unity. For small plane-wave incidence angles, the S_1 mode is excited at lower frequencies than at normal incidence (cf. Fig. 6.6). At these frequencies, the FEM transducer's θ_{-3dB} is approx. 5°. Then, the non-zero incident plane-wave components of the beam will excite the S_1 mode at a lower frequency

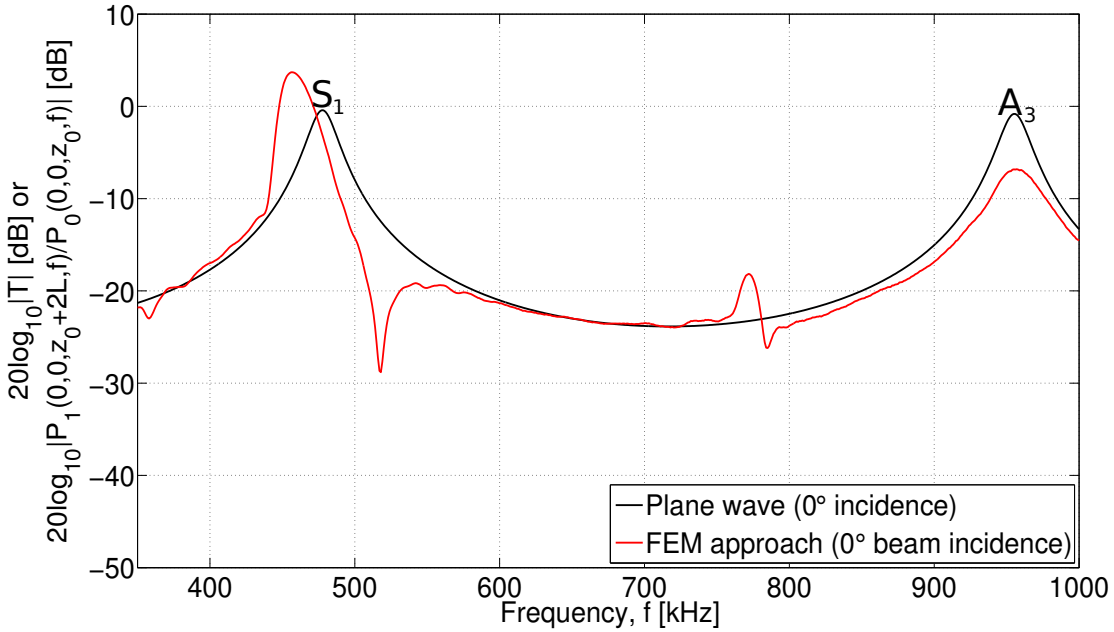

(a)

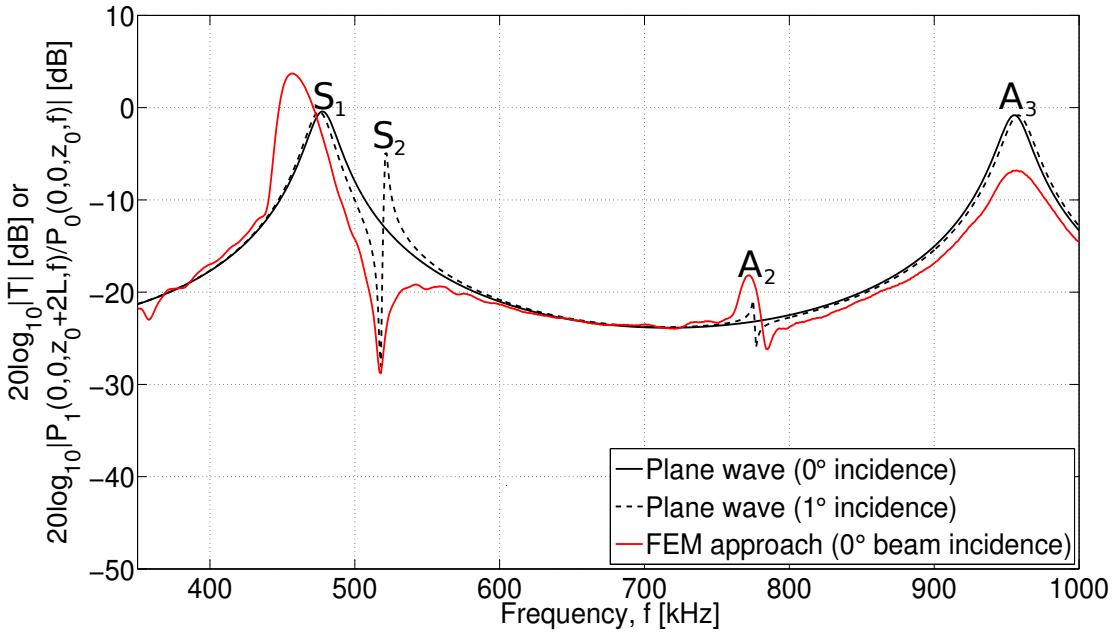

(b)

Fig 6.7. The magnitude of the plane-wave pressure transmission coeff., $|\mathscr{T}|$, for **a)** plane waves at normal incidence ($\theta_p = 0°$), **b)** plane waves at 0° and 1° incidence. Both **a)** and **b)** include comparison with the ratio $|P_1(0,0,z_0+2L,f)/P_0(0,0,z_0,f)|$ for the transducer source field calculated using the FEM approach.

than a normal incident plane-wave (cf. Fig. 6.7(a)), causing the relatively high transmission to be shifted downwards in frequency in relation to plane-wave theory. The ratio $|P_1(0,0,z_0{+}2L,f)/P_0(0,0,z_0,f)|$ represents the beam transmission through the plate, where $P_0(0,0,z_0,f)$ and $P_1(0,0,z_0+2L,f)$ can be represented as an integration of incident and transmitted plane-wave components, respectively. As

$P_0(0,0,z_0,f)$ is located at the centre of the main lobe, it contains a small number of incidence plane-wave components. The leaky Lamb modes can be regarded as very narrow bandpass filters in the frequency-wavenumber domain, depending on the mechanical losses, allowing only a small number of incident plane-wave components through the plate at a given frequency. So, the ratio can for most cases be regarded as a small number of transmitted over incident plane-wave components. But, due to the behaviour of the S_1 mode at low incident angles, this mode allows a wider range of incident plane-wave components to pass through the plate at given frequencies. Given that the conditions a suitable, i.e. wide transducer beam covering this incident plane-wave range, the S_1 mode is excited by a wide range of incident plane-wave components of the beam. Take the example of a normal incidence 457 kHz beam using the hybrid FEM-ASM approach, the wavenumber spectra of $P_0(x,y,z_0,f)$ and $P_1(x,y,z_0+2L,f)$ for that frequency are shown in Figs. 4.6(b) and 4.8(b). Here, no individual plane-wave component of $\mathbf{P}_1(h_{f,x},h_{f,y},z_0+2L,f)$ have increased due to the transmission through the steel plate in relation to the corresponding plane-wave component of $\mathbf{P}_0(h_{f,x},h_{f,y},z_0,f)$, but due to superposition of the plane-wave components, $P_t(0,0,z_2,f)$ in Fig. 4.10(b) has increased in relation to $P_0(0,0,z_0,f)$ in Fig. 4.5(b). This explains why the ratio exceeds unity.

The transmission around the S_2 mode is different for the 3D beam in relation to the plane-wave theory, except at frequencies just below the S_2 mode, where both methods show a minimum. As this minimum is very close in frequency to the S_2 mode, it is later used for measuring the shear sound velocity in the plate using the method described in Sect. 6.2.2. Around the A_2 mode the FEM approach indicates a much wider region where the transmission of sound is relatively high in relation to the plane-wave theory. The 3D beam gives a wider region of relatively high transmission around the A_2 mode in relation to the plane-wave theory. Due to the behaviour of the transmission in this region, the frequency of maximum transmission using 3D beams is slightly less in relation to a 1° incident plane-wave.

Around the A_3 mode the overall transmission of sound through the plate is lowered using the transducer's beam, see Fig. 6.7(a), in relation to plane-wave theory. Only a minor upward frequency shift is observed in relation to the beam excitation of the S_1 mode, although the A_3 mode displays a similar behaviour at small plane-wave incidence angles, where it is excited at higher frequencies than at normal incidence. This is most likely due to the highly directive transducer at these frequencies (see Fig. 5.27(h)). This shift will affect the measurement of c_L at A_3 using the method described in Sect. 6.2.2.

The magnitude of the plane-wave transmission coefficient $\mathscr{T}$, and $|H_{PP}(0,0,z_2,f)|$ calculated using the FEM and hybrid FEM-ASM approaches are presented in Fig. 6.8, based upon the material data in Tab. 6.5 and compared to measurement results. Tab. 6.3 presents the frequencies extracted from local maxima or minima in $|H_{PP}(0,0,z_2,f)|$, corresponding to the (leaky) Lamb modes defined in Tabs. 6.1 and 6.2, respectively. Recall that $|H_{PP}(0,0,z_2,f)|$ is calculated and measured at a distance of 100 mm below the lower surface of the steel plate. If the transmitted pressure at the receiver depth is extrapolated to the lower surface of the steel plate assuming spherical waves, the pressure amplitude is inversely proportional to the range (a distance of 100 mm), an increase of the transmitted pressure of approximately 3.16 dB will be experienced, see [93]. The frequency step for measurements, the hybrid

FEM-ASM approach and the FEM approach are 1 kHz, 1 kHz and 500 Hz, respectively.

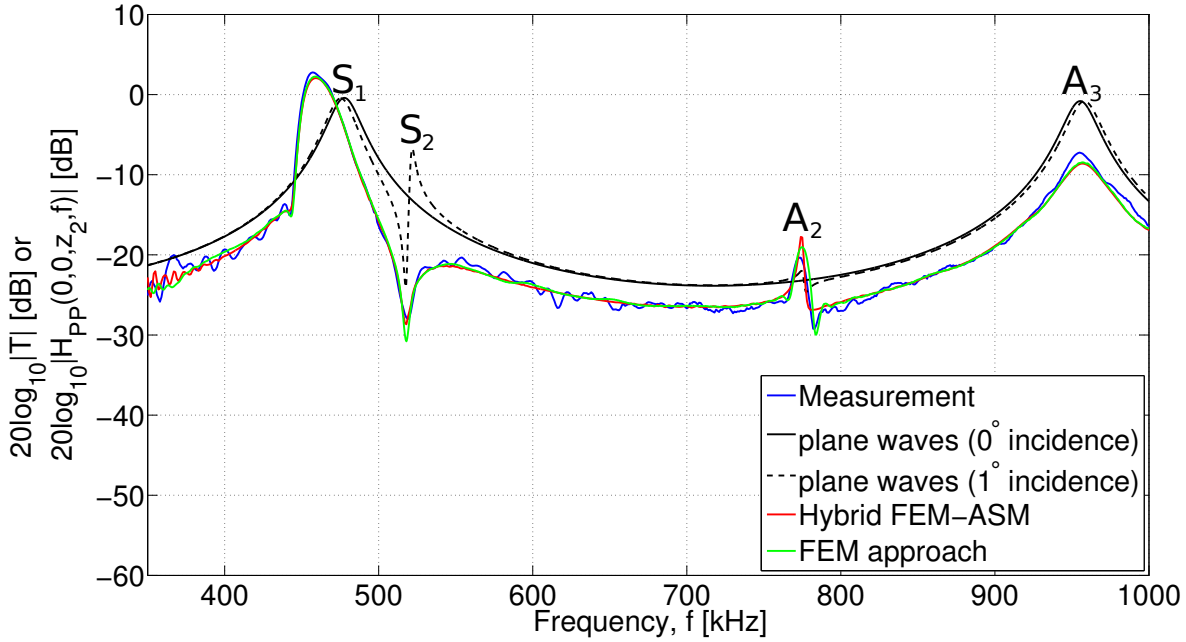

Fig 6.8. At normal beam incidence ($\theta = 0°$): Measured (blue line), in comparison to hybrid FEM-ASM (red line) and FEM (green line) calculated magnitude of the pressure-to-pressure transfer function $|H_{PP}(0,0,z_2,f)|$ and the plane-wave pressure transmission coefficient $|\mathscr{T}|$ (black lines).

TABLE 6.3. Water-embedded steel plate at normal beam incidence $\theta = 0°$. Material data for the steel plate is listed in Tab. 6.5. Frequencies extracted from Fig. 6.8. A_1^{beam} is not determined due to the frequency range used.

Symbol	Frequency [kHz]			(S)ymm/(A)ntisymm	Type mode
	Measured	Simulated (FEM)	Simulated (Hybrid)		
$f_{t1}^{A,\text{beam}}$	-	-	-	A_1^{beam}	TS
$f_{l1}^{S,\text{beam}}$	457	459.0	459	S_1^{beam}	TE
$f_{t1}^{S,\text{beam}}$	519	518.0	518	S_2^{beam}	TS
$f_{t2}^{A,\text{beam}}$	774	774.5	774	A_2^{beam}	TS
$f_{l1}^{A,\text{beam}}$	955	956.5	957	A_3^{beam}	TE

6.2.2 Measurement of c_L and c_S, with corresponding Q-factors

The method described in Sect. 3.3 is here used to measure the sound velocities [91, 92, 93] and corresponding Q-factors in the steel plate. In Fig. 6.9 the measured magnitude of the pressure-to-pressure transfer function $|H_{PP}(0,0,z_2,f)|$ for the steel plate with thickness $2L = 6.05$ mm is presented. The frequencies of maximum and minimum transmission in $|H_{PP}(0,0,z_2,f)|$ is used as approximations of the cut-off frequencies in Sect. 2.4.1. The frequencies are listed in Tab. 6.4 together with the associated mode and the corresponding wave velocity calculated using Eqs. (2.54) and (2.55). The method assumes near plane-wave conditions, which for a finite dimensional transducer does not necessarily exists, cf. discussion in Sect. 6.2.1, and minimal effects due to the loading of the water.

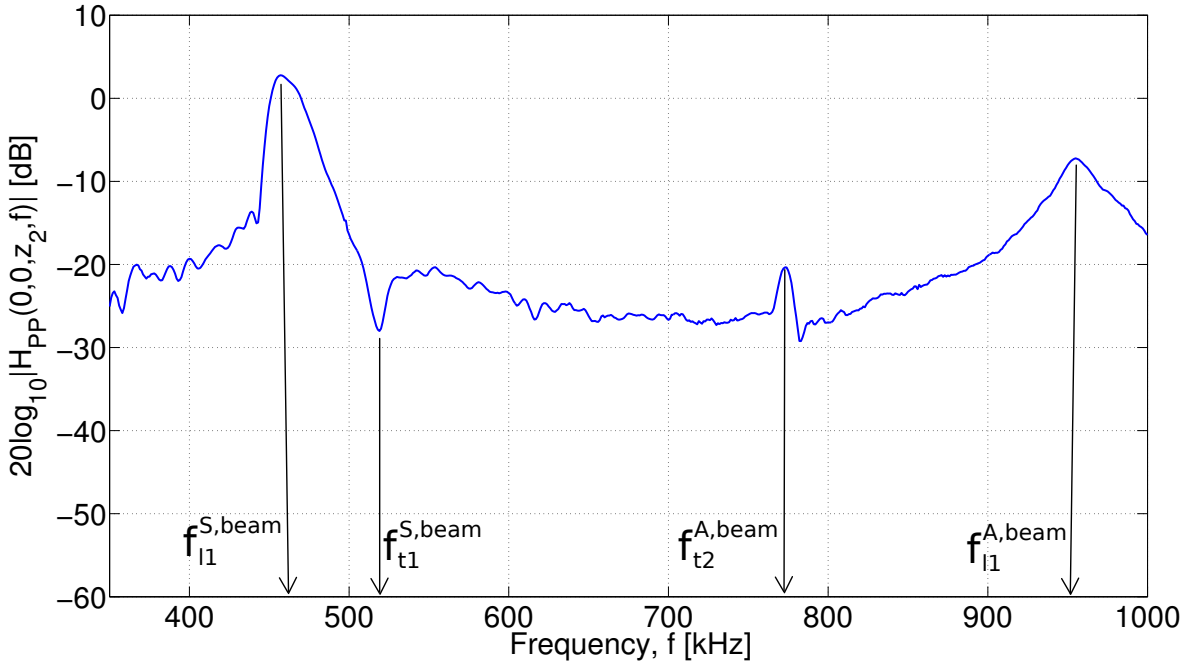

Fig 6.9. At normal beam incidence ($\theta = 0°$): Measured magnitude of the pressure-to-pressure transfer function $|H_{PP}(0, 0, z_2, f)|$.

TABLE 6.4. Calculations of the compressional c_L and shear wave c_S velocity, using Eqs. (2.54) and (2.55), by approximating the frequencies of maximum and minimum transmission in the measured $|H_{PP}(0, 0, z_2, f)|$ in Fig. 6.9 as the cut-off frequencies of the Lamb modes in Sect. 2.4.1.

Symbol	(S)ymm/(A)ntisymm	Frequency [kHz]	c_L [m/s]	c_S [m/s]
$f_{l1}^{S,\text{beam}}$	S_1^{beam}	457	5530	-
$f_{t1}^{S,\text{beam}}$	S_2^{beam}	519	-	3140
$f_{t2}^{A,\text{beam}}$	A_2^{beam}	774	-	3121
$f_{l1}^{A,\text{beam}}$	A_3^{beam}	955	5778	-

The sound velocity determined from the frequency close to the S_1 mode is ignored, cf. S_1 mode discussion in Sect. 6.2.1. The shear velocity determined from the minimum accociated with the S_2 mode is underestimated with respect to the excitation frequency of the S_2 mode, cf. S_2 mode discussion in Sect. 6.2.1. The same argument is made for the shear velocity determination around the A_2 modes, cf. A_2 mode discussion in Sect. 6.2.1. For the determination of the compressional sound velocity using the maximum accociated with the A_3 mode, the frequency is slightly overestimated, cf. A_3 mode discussion in Sect. 6.2.1. The corresponding Q-factors for the compressional and shear wave velocity, Q_M^L and Q_M^S, respectively, are estimated by fitting the hybrid FEM-ASM simulated $|H_{PP}(0, 0, z_2, f)|$ to the measurements in Fig. 6.9, by varying the Q-factors. In Fig. 6.10(a) a $Q_M^L = 1000$ is estimated by fitting the hybrid FEM-ASM simulated $|H_{PP}(0, 0, z_2, f)|$ to measurements around the S_1 mode. In Fig. 6.10(b) a $Q_M^S = 500$ is estimated by fitting the hybrid FEM-ASM simulated $|H_{PP}(0, 0, z_2, f)|$ to measurements around the S_2 mode. This method is only intended to provide a rough estimate of the Q-factors (within $\pm$ 100), and one must take this into consideration using them.

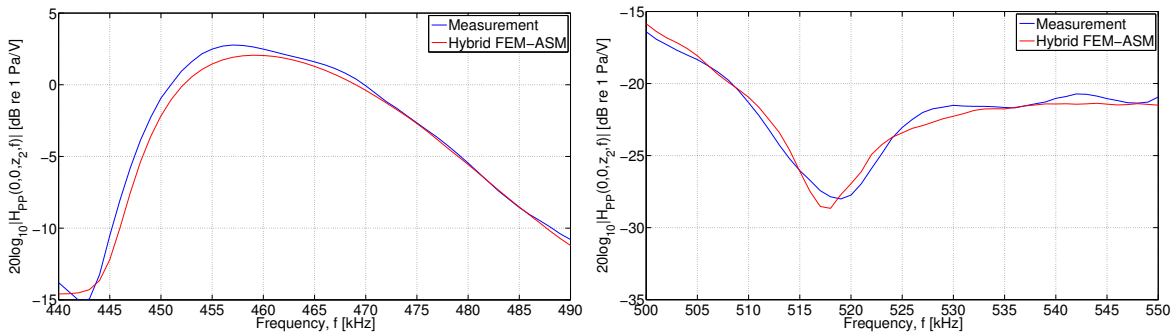

(a) (b)

Fig 6.10. At normal beam incidence ($\theta = 0°$): Fitting the hybrid FEM-ASM simulated pressure-to-pressure transfer function $|H_{PP}(0, 0, z_2, f)|$ with varying Q_M^L and Q_M^S to measurements (red line) around **a)** the S_1 mode for determining Q_M^L, **b)** the S_2 mode for determining Q_M^S.

The material data for the steel plate used for simulations is listed in Tab. 6.5, based upon measurements by [91] and estimations made here. The Q_M^L is used for the Q_M in the FEM approach. The density is taken from Tab. 5.4. From arguments made in Sect. 6.2.1 and in the paragraph above regarding beam effects, the material data listed could most likely be refined.

TABLE 6.5. Material data used in simulations for the steel plate. $Q_M^L = Q_M$ in the FEM approach.

c_L [m/s]	5780
c_S [m/s]	3130
ρ_c[kg/m^3]	8000
Q_M^L	1000
Q_M^S	500

6.2.2.1 Cold rolled vs. hot rolled steel

The AISI 316L steel plate used in the measurement system is hot rolled, cf. Sect. 3.2, which means that the plate is rolled to its thickness using a temperature above the recrystallization temperature of the material [165]. Cold rolling or strain hardening occurs at a temperature below the material's recrystallization temperature. Problems with the use of Lamb waves inspection of cold rolled steel has been investigated by e.g. [166, 167]. In Fig. 6.11 the pressure-to-pressure transfer function $|H_{PP}(0, 0, z_2, f)|$ for a AISI 316L cold rolled steel plate with thickness $2L = 5.9$ mm is presented. Comparing this figure to Fig. 6.9 two mimimas appears around the shear modes S_2 and A_2, which indicates the existence of two shear velocities in the plate. This is most likely due to the anisotropy induced by the cold rolling. [167] found similar results, measuring two different shear velocities in cold rolled AISI 314/6L steel plates, which were reduced to one velocity by heat treatment.

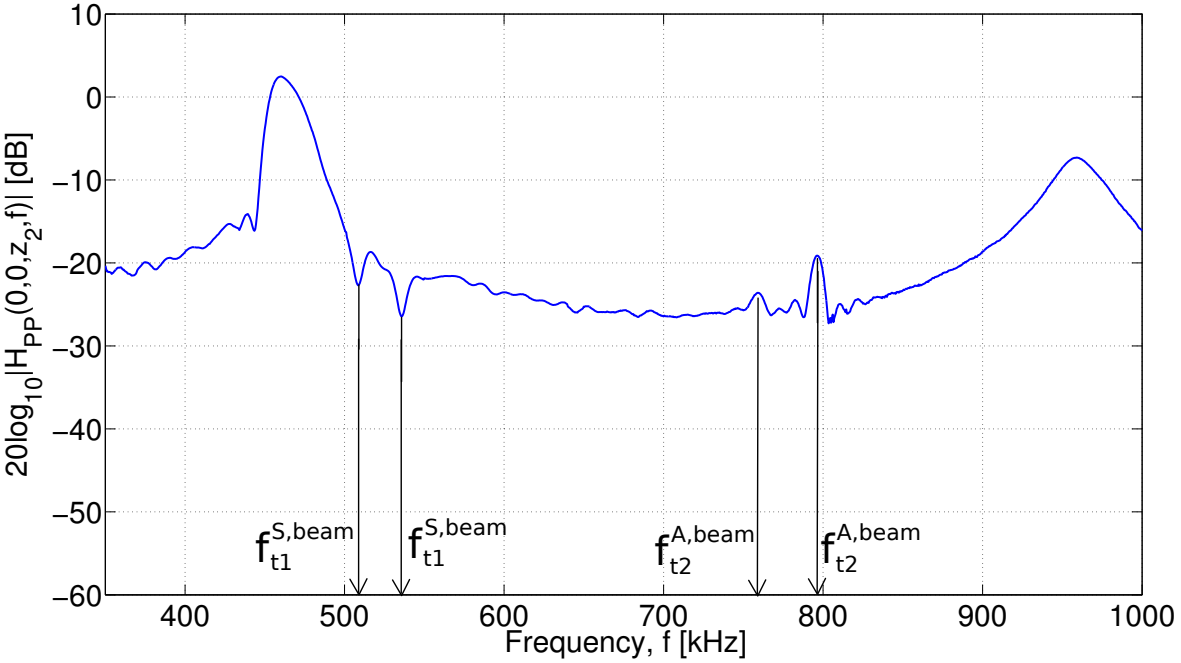

Fig 6.11. At normal beam incidence ($\theta = 0°$): Measured magnitude of the pressure-to-pressure transfer function $|H_{PP}(0, 0, z_2, f)|$ for a cold-rolled AISI 316L stainless steel plate with thickness $2L = 5.9$ mm.

6.3 Piezoelectric transducer model vs. baffled piston model

This section compares the signal transmission through the plate using the piezoelectric source transducer and the baffled piston models, based upon comparison of measured and simulated pressure-to-pressure transfer function $H_{PP}(x, y, z_2, f)$ using the hybrid FEM-ASM approach. The deviations using the simulated piezoelectric transducer vs. the piston source model in the system description are discussed, based upon hybrid FEM-ASM results for transmission of sound through the steel plate and water, and measurements. Transmission studies for beam incidence angles $\theta = 0°, 5°, 10°, 15°, 20°, 25°$ and $30°$ are shown in the following subsections. The listed frequencies for the leaky Lamb modes in this section have been calculated from the plane-wave pressure transmission coefficient given in Fig. 6.6.

Fig. 6.12 shows the FEM calculated (red lines) and measured (blue lines) magnitude of the beam pattern $|D(\phi, f)|$ for the piezoelectric source transducer as shown in Chap. 5, in comparison with the beam pattern of the piston source (dashed black lines). The piston radius is adapted to the FEM transducer's -3 dB angle at 575 kHz, cf. Sect. 4.5.3. The beam pattern at that frequency is presented in Fig. 6.12(d), where the piston source correctly models the transducer main lobe, but none of the higher order side lobes. At a frequency lower than 575 kHz, the piston's main lobe becomes narrower than the main lobe of the FEM calculated piezoelectric transducer and measurements. At a frequency higher than 575 kHz, the piston's main lobe becomes wider than the main lobe of the FEM calculated piezoelectric transducer and measurements. Agreement is shown close to the $z'-$axis (near the centre of the source's main lobe).

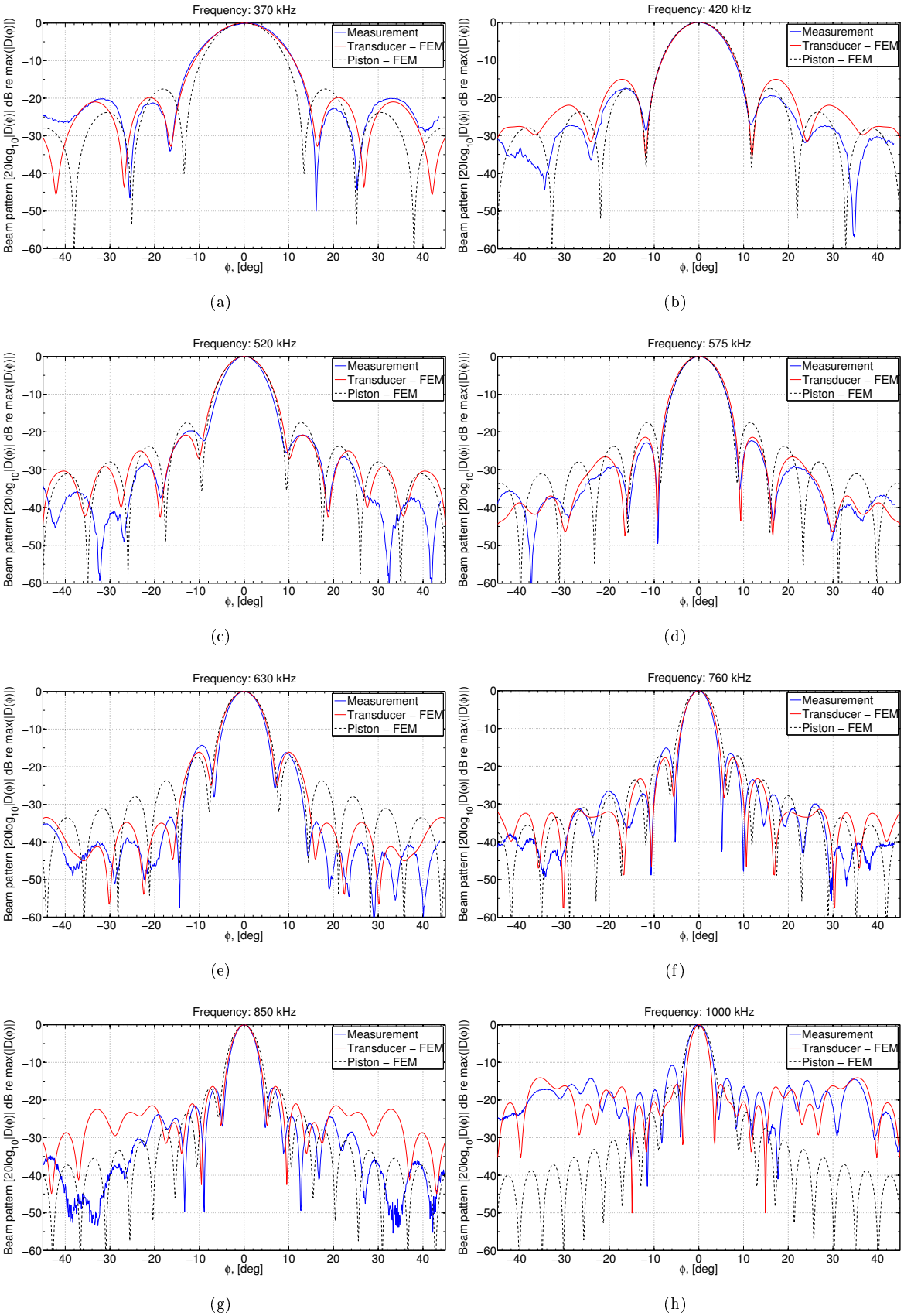

Fig 6.12. FEM simulated (blue line) and measured (red line) magnitude beam pattern $|D(\phi, f)|$ for the piezoelectric source transducer at specific frequencies, in the range 370 - 1000 kHz, together with the simulated beam pattern for the adapted piston source (dashed black). The distance used in the measurements is given in Sect. 3.6.3.

As the baffled piston source is only a valid model to the measurement transducer around the centre of the main lobe, the spatial region where this model can be used for transmission simulations will decrease as a function of frequency, due to a narrowing of the main lobe. And, approaching the edge of the main lobe and moving into the first side lobe, the piston source fails to model the piezoelectric source transducer's beam pattern. Thus, the FEM calculated transducer models the real transducer more correctly.

6.3.1 Normal beam incidence

In Figs. 6.13(a) and 6.13(b) the simulated $|H_{PP}(x, 0, z_2, f)|$ is shown for 0° beam incidence angle, as a function of frequency and x-position, at the receiver depth z_2, using the piezoelectric transducer and piston sources, respectively. The maxima are in the vicinity of the leaky Lamb modes, and demonstrate regions in space and frequency where the transmission of sound through the plate is relatively high. Figs. 6.13(a) and 6.13(b) are qualitatively similar, but quantatively different, which becomes apparent moving beyond the region ($x-$axis) affected by the source's main lobe. The frequencies corresponding to the leaky Lamb modes S_1, S_2, A_2 and A_3 for a plane-wave incident angle $\theta_P = 0°$ cf. Fig. 6.6 are 477.7 kHz, 517.5$*$ kHz, 774.5$*$ kHz and 955.4 kHz respectively, indicated at $x = 0$ mm in Fig. 6.13. The $*$ indicates a 1° incidence angle with the steel plate.

The simulated pressure-to-pressure transfer function $|H_{PP}(x, 0, z_2, f)|$ at $x = 0$, $x = 20$ and $x = 40$ mm in Fig. 6.13 (marked with vertical lines) using the piezoelectric transducer (blue lines) and the piston (red lines) as source, are shown in Figs. 6.14(a), 6.14(b) and 6.14(c) as a function of frequency, respectively, and compared to measurement results (green lines). Maxima are in the vicinity of leaky Lamb mode excitation in the plate. Fig. 6.14(a) for $x = 0$ mm is similar to Figs. 6.8 and 6.9 used for determining the sound velocities in the steel plate. An agreement within 1.2 dB (0.8 dB around S_1^{beam}) is shown for both transducer models to measurements, with some exceptions, including around the A_2 mode. This is approx. within the measurement uncertainty for the calibration of the needle hydrophone at 0.8 dB. The deviations around the A_2 mode for the hybrid approach is also experienced in Fig. 6.8, but not for the FEM approach. This is further discussed in Sect. 7.2. The deviations between the two transducer models are negligible with respect to measurements for this $x-$position. For $x = 20$ mm in Fig. 6.14(b) an agreement within 0.8 dB between simulations and measurements is shown up to approx. 600 kHz. Around the A_2 mode and above, the deviations to measurements are greater, approx. 2 dB with respect to the transducer, and 4 dB with respect to the baffled piston. For $x = 40$ mm in Fig. 6.14(c) an agreement within 2.4 dB between simulations and measurements is shown up to 600 kHz, except at the minimum around 500 kHz. Above 600 kHz, the deviations are greater, but simulations for the transducer are closer to measurements than the baffled piston. For off-axis positions at $x = 20, 40$ mm, as frequency increases, these positions are not covered by the source's main lobe, and one expects deviations to grow, in accordance with the deviations in the beam patterns in Fig. 6.12. As the simulated beam pattern of the source transducer follows the measured beam pattern for a wider range than the baffled piston source, one expects the baffled piston to deviate from measurements at a lower frequency than the source transducer. This is apparent in Fig. 6.14(c).

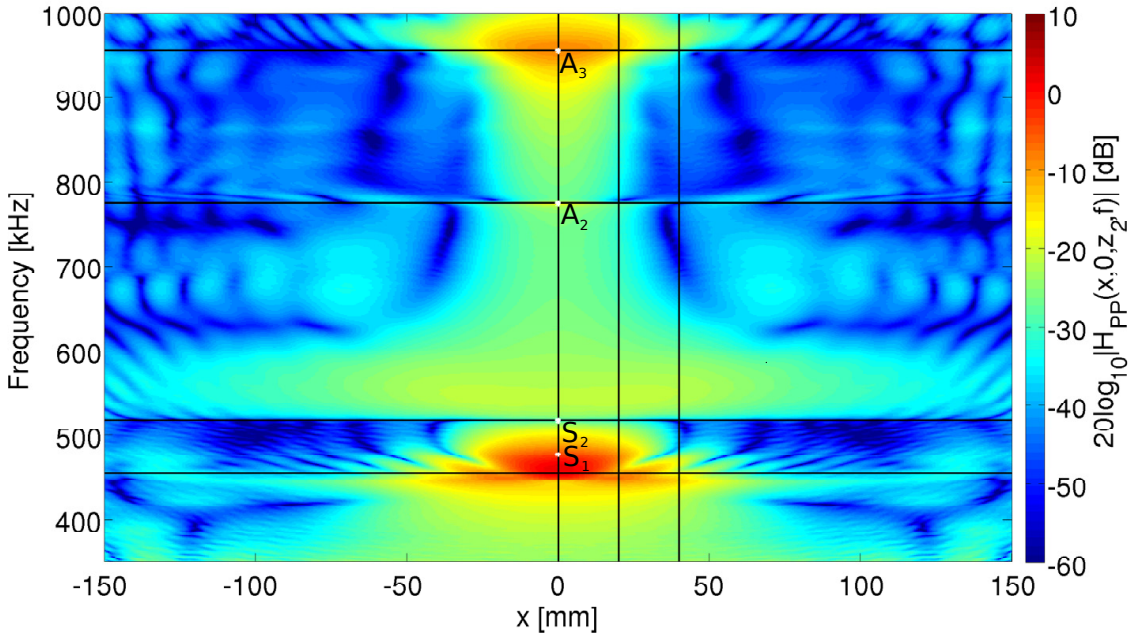

(a)

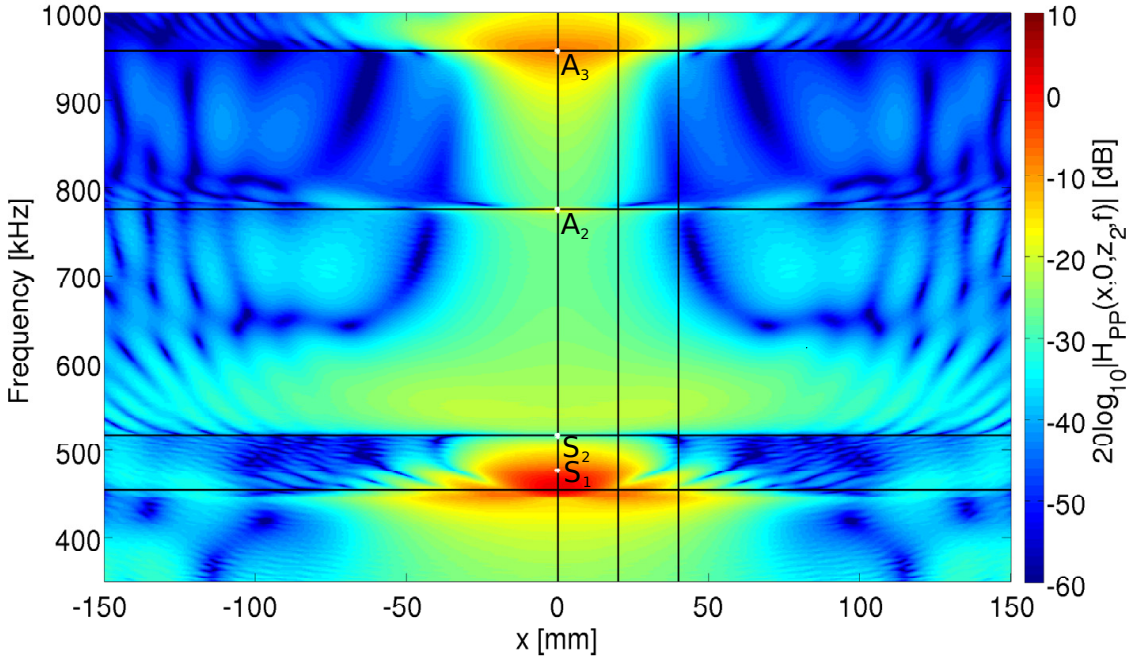

(b)

Fig 6.13. At normal beam incidence ($\theta = 0°$): Simulated magnitude of the pressure-to-pressure transfer function $|H_{PP}(x, 0, z_2, f)|$ using the hybrid FEM-ASM approach, for **a)** the piezoelectric transducer and **b)** the baffled piston source. Solid lines indicate the $x-$distances and frequencies addressed in Figs. 6.14 and 6.15, respectively. Leaky Lamb modes for a plane-wave incident angle $\theta_P = 0°$ are indicated at their respective frequencies at $x = 0$ mm. The leaky Lamb modes S_2 and A_2 have been calculated using a 1° incidence angle.

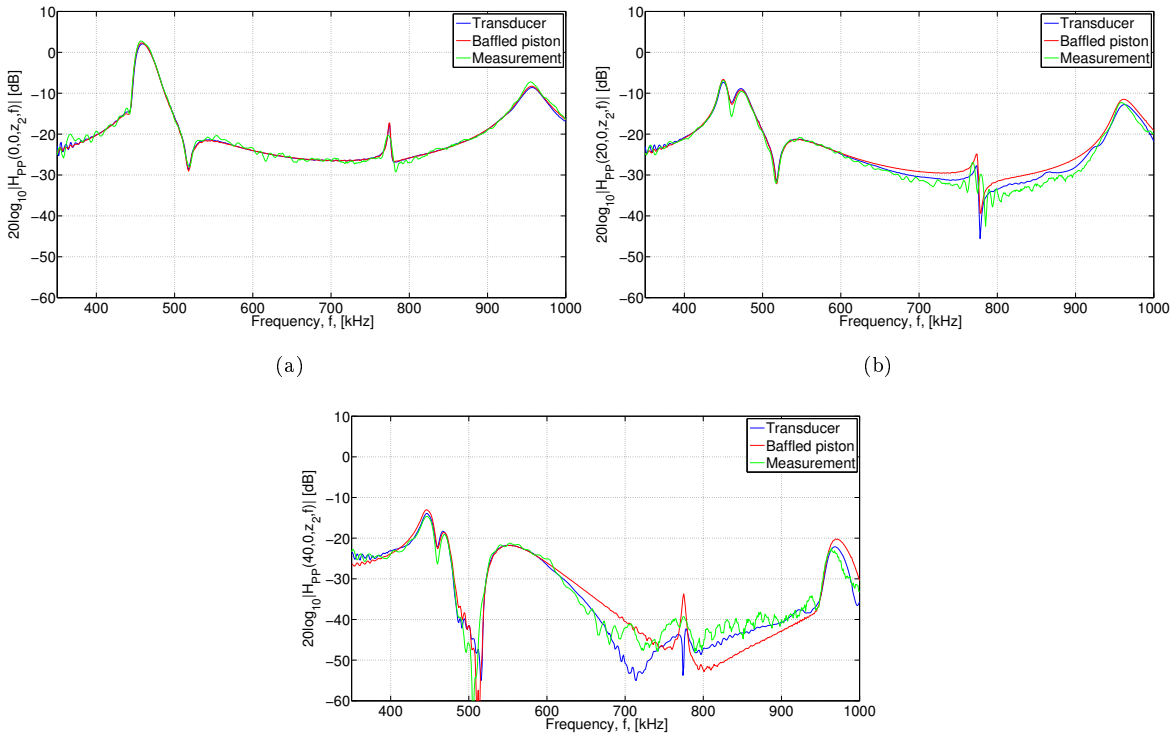

(a) (b)

(c)

Fig 6.14. At normal beam incidence ($\theta = 0°$): Simulated magnitude of the pressure-to-pressure transfer function $|H_{PP}(x, 0, z_2, f)|$ using the hybrid FEM-ASM approach for the piezoelectric transducer (blue line) and baffled piston (red line), in comparison with measurements (green line) for **a)** $x = 0$ mm, **b)** $x = 20$ mm and **c)** $x = 40$ mm. The frequency spectra at the three $x-$distances are indicated with solid lines in Fig. 6.13.

The simulated pressure-to-pressure transfer function $|H_{PP}(x, 0, z_2, f)|$ for $f = 457$ kHz, $f = 518$ kHz, $f = 775$ kHz and $f = 956$ kHz in Fig. 6.13 (marked with horizontal lines) using the piezoelectric transducer (blue lines) and the piston (red lines) as source, are shown in Figs. 6.15(a), 6.15(b), 6.15(c) and 6.15(d) as a function of $x-$position respectively, and compared to measurement results (green lines). For $f = 457$ kHz (below the S_1 mode, cf. discussion in Sect. 6.2.1) in Fig. 6.15(a) there is agreement within 3.3 dB between the simulations and measurements up to approx $x = 50$ mm. $x-$positions below this is covered by the source's main lobe. For $f = 518$ kHz (near the S_2 mode) in

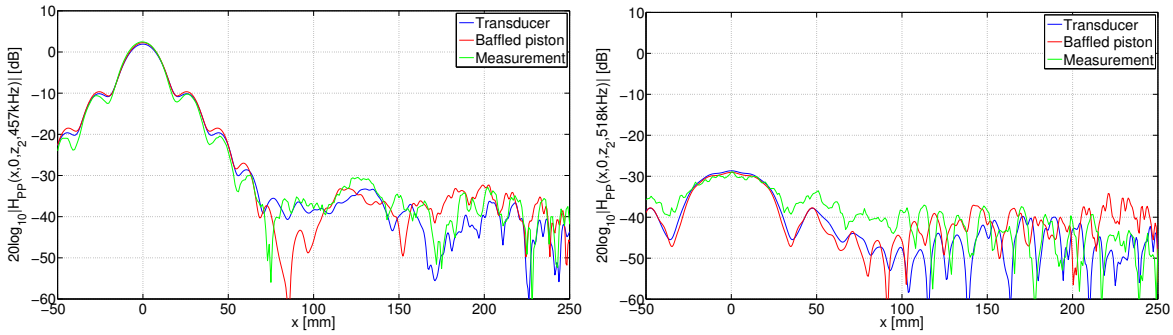

(a) (b)

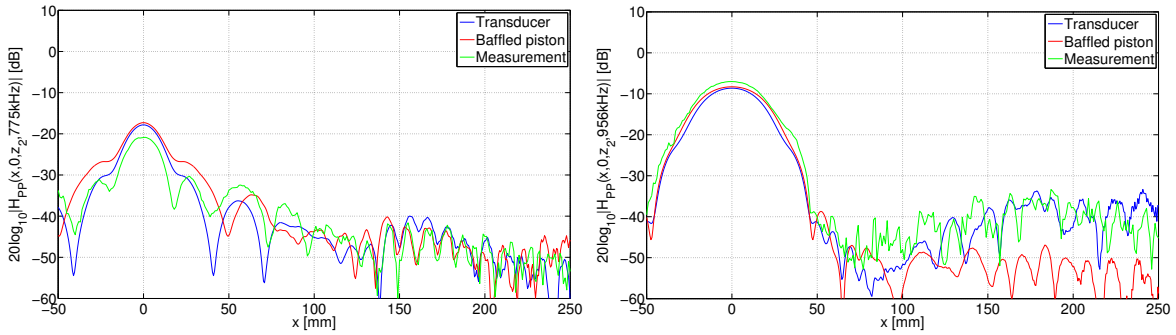

Fig 6.15. At normal beam incidence ($\theta = 0°$): Simulated magnitude of the pressure-to-pressure transfer function $|H_{PP}(x, 0, z_2, f)|$ using the hybrid FEM-ASM approach for the piezoelectric transducer (blue line) and baffled piston (red line), in comparison with measurements (green line) for **a)** $f = 457$ kHz, **b)** $f = 518$ kHz, **c)** $f = 775$ kHz and **d)** $f = 956$ kHz.

Fig. 6.15(b) agreement within 2 dB exists up to $x = 25$ mm. As the transmission through the plate is low in relation to e.g. Fig. 6.15(a), noise in measurements can influence the measurement results. There are larger deviations between simulations and measurement for $f = 775$ kHz (near the A_2 mode) in Fig. 6.15(c) due to the deviations in Fig. 6.14(a), see Sect. 7.2. For $f = 954$ kHz (near the A_3 mode) in Fig. 6.15(d) there is agreement within 4.5 dB between measurements and simulations up to approx. $x = 50$ mm. The same conclusion as for Fig. 6.15(a) can be applied here.

6.3.2 $\theta = 5°$ beam incidence

In Figs. 6.16(a) and 6.16(b) the simulated $|H_{PP}(x, 0, z_2, f)|$ is shown for 5° beam incidence angle, as a function of frequency and x-position, at the receiver depth z_2, using the piezoelectric transducer and piston sources, respectively. As for normal incidence, the maxima are in the vicinity of the leaky Lamb modes, and demonstrates regions in space and frequency where the transmission of sound through the plate is relatively high. Figs. 6.16(a) and 6.16(b) are qualitatively similar, but quantatively different. The frequencies corresponding to the leaky Lamb modes S_1, S_2 and A_2 for a plane-wave incident angle $\theta_P = 5°$ cf. Fig. 6.6 are 453.8 kHz, 581.1 kHz and 774.9 kHz, respectively, indicated at $x = 20$ mm in Fig. 6.16.

The simulated pressure-to-pressure transfer function $|H_{PP}(x, 0, z_2, f)|$ at $x = 0$ mm, $x = 20$ mm, $x = 40$ mm and $x = 80$ mm in Fig. 6.16 (marked with lines) using the piezoelectric transducer (blue lines) and the piston (red lines) as source, are shown in Figs. 6.17(a), 6.17(b), 6.17(c) and 6.17(d) as a function of frequency, respectively, and compared to measurement results (green lines). For $x = 0$ mm in Fig. 6.17(a) an agreement within 2.1 dB for the two sources to measurements are shown up to 600 kHz, and deviations between the simulations are negliable in that respect. But, over 600 kHz the transducer shows a closer agreement to meaurements than the baffled piston. For $x = 20$ mm in Fig. 6.17(b) an agreement within 0.9 dB is shown for the entire frequency range between simulations and measurements, except around the A_2 mode and at high frequency, see discussion in Sect. 7.2. As $x = 20$ mm is positioned within the main lobe of the sources for the whole frequency range, the

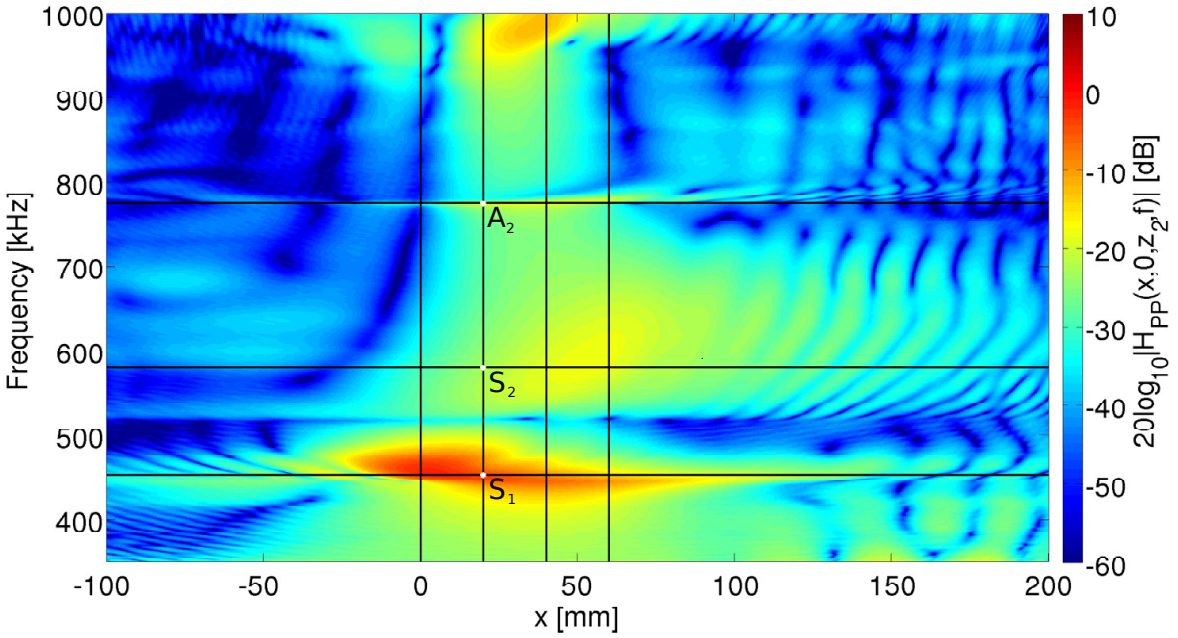

(a)

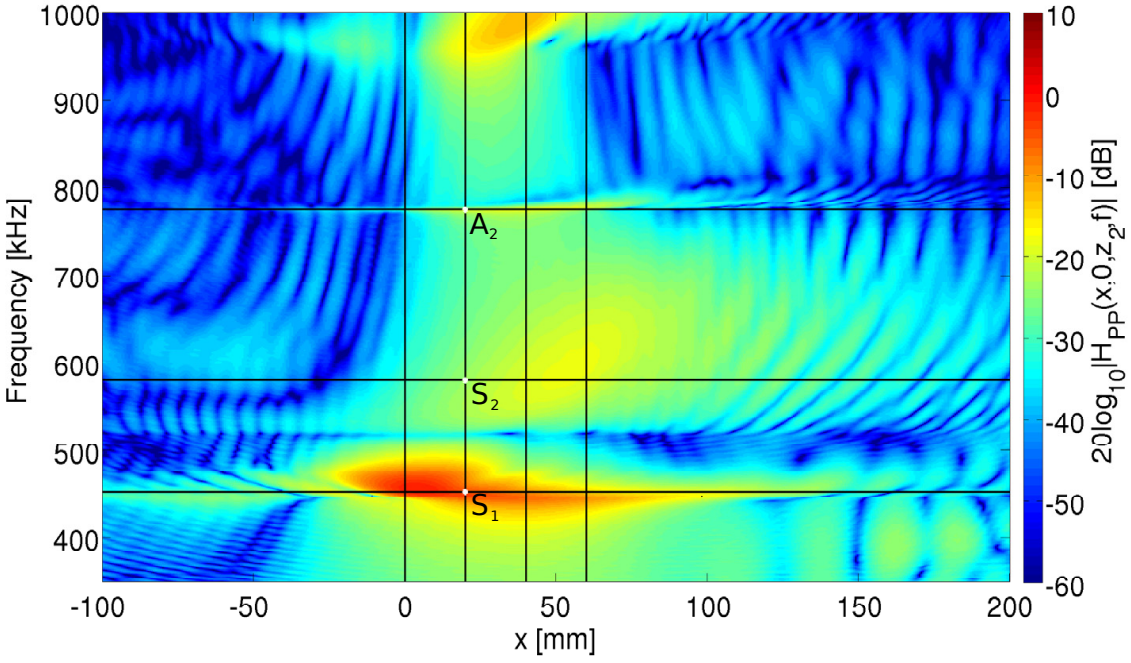

(b)

Fig 6.16. At $\theta = 5°$ beam incidence: Simulated magnitude of the pressure-to-pressure transfer function $|H_{PP}(x, 0, z_2, f)|$ using the hybrid FEM-ASM approach, for **a)** the piezoelectric transducer and **b)** the piston source. Solid lines indicate the $x-$distances and frequencies addressed in Figs. 6.17 and 6.18, respectively. Leaky Lamb modes for a plane-wave incident angle $\theta_P = 5°$ are indicated at their respective frequencies at $x = 20$ mm.

deviations between the transducer and baffled piston are negligible. A similar conclusion can be made for $x = 40$ mm in Fig. 6.17(d). But, for $x = 60$ mm in Fig.6.17(d) one moves to a position not covered by the source's main lobe at high frequencies, above 750 kHz, and deviations occur. Again, the transducer is closer to measurements than the piston model.

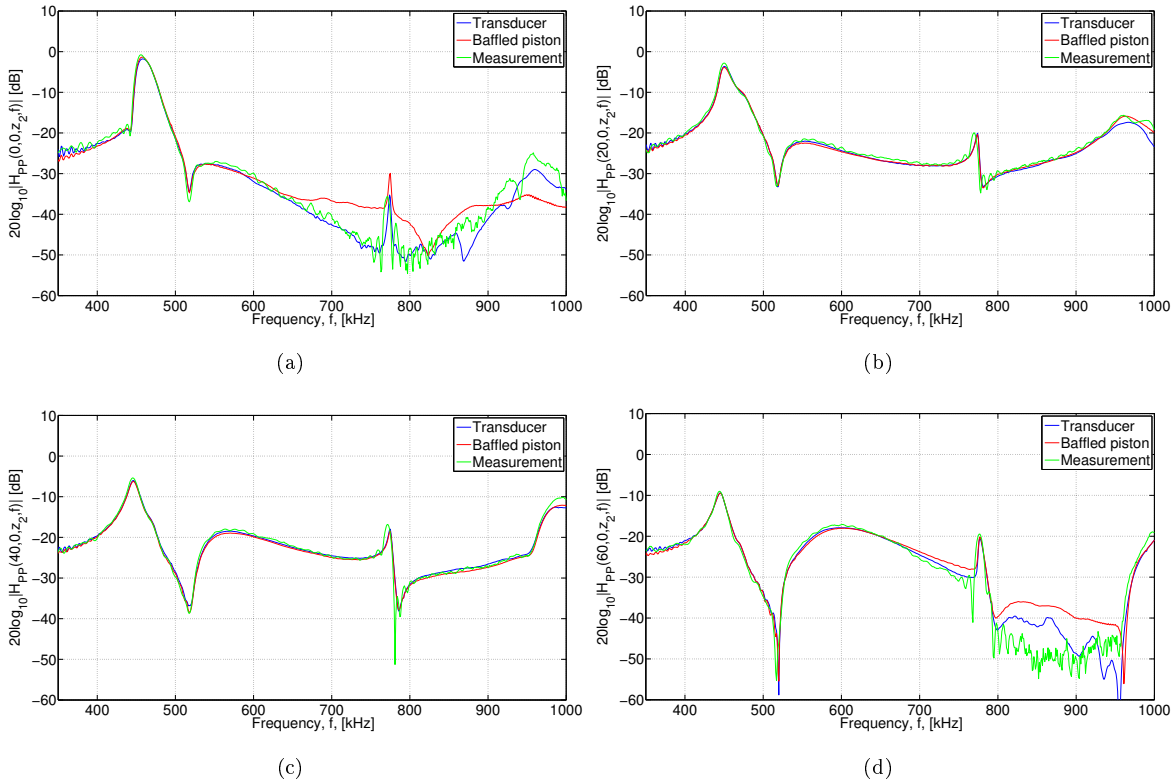

Fig 6.17. At $\theta = 5°$ beam incidence: Simulated magnitude of the pressure-to-pressure transfer function $|H_{PP}(x, 0, z_2, f)|$ using the hybrid FEM-ASM approach for the piezoelectric transducer (blue line) and piston (red line), in comparison with measurements (green line) for **a)** $x = 0$ mm, **b)** $x = 20$, **c)** $x = 40$ mm and **d)** $x = 60$ mm. The frequency spectra at the four $x-$distances are indicated with solid lines in Fig. 6.16.

The simulated pressure-to-pressure transfer function $|H_{PP}(x, 0, z_2, f)|$ for $f = 454$ kHz, $f = 581$ kHz and $f = 775$ kHz in Fig. 6.16 (marked with horizontal lines) using the piezoelectric transducer (blue

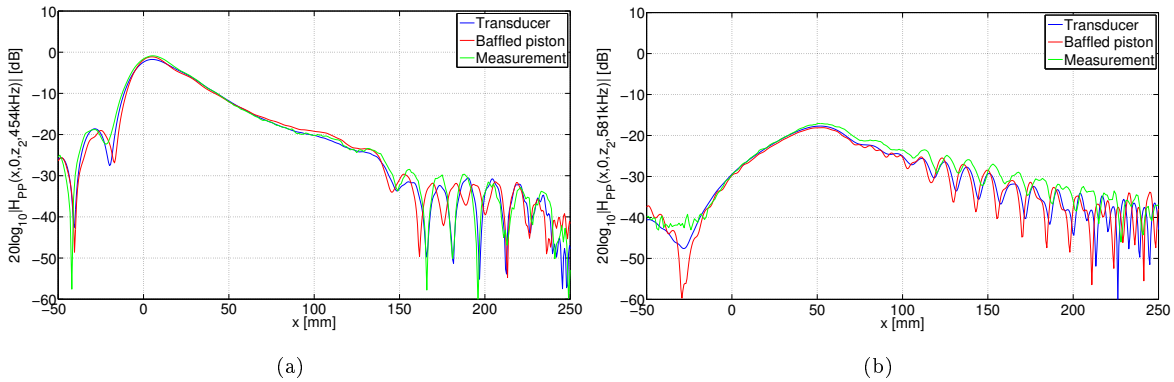

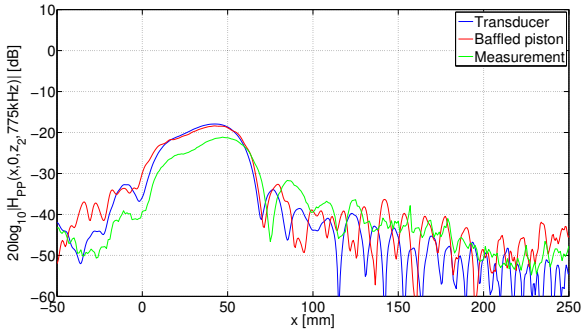

(c)

Fig 6.18. At $\theta = 5°$ beam incidence: Simulated magnitude of the pressure-to-pressure transfer function $|H_{PP}(x, 0, z_2, f)|$ using the hybrid FEM-ASM approach for the piezoelectric transducer (blue line) and baffled piston (red line), in comparison with measurements (green line) for **a)** $f = 454$ kHz, **b)** $f = 581$ kHz and **c)** $f = 775$ kHz.

lines) and the piston (red lines) as source, are shown in Figs. 6.18(a), 6.18(b) and 6.18(c) as a function of $x-$positions respectively, and compared to measurement results (green lines). For $f = 454$ kHz (near the S_1 mode) in Fig. 6.18(a) a closer agreement between the transducer and measurements is shown, than between the baffled piston and measurements, and the transducer correctly models the interference pattern in the region $x = 150 - 200$ mm. The interference pattern will be further discussed in Chap. 7. For $f = 581$ kHz (near the S_2 mode) in Fig. 6.18(b) an agreement within 1 dB between simulations and measurements is observed in the region $x = -20 - 60$ mm, but the measured interference pattern beyond $x = 100$ mm is slightly shifted in frequency in comparison to simulations. For $f = 775$ kHz (near the A_2 mode) in Fig. 6.18(c) the deviations between simulations and measurements are greater, discussed further in Sect. 7.3. From Fig. 6.16, the variations in frequency and position are large in this region, so possible alignment error in measurements will produce large deviations from simulations.

6.3.3 $\theta = 10°$ beam incidence

In Figs. 6.19(a) and 6.19(b) the simulated $|H_{PP}(x, 0, z_2, f)|$ is shown for 10° beam incidence angle, as a function of frequency and x-position, at the receiver depth z_2, using the piezoelectric transducer and piston sources, respectively. As for 0° and 5° incidence, the maxima are in the vicinity of the leaky Lamb modes. Figs. 6.19(a) and 6.19(b) are qualitatively similar, but quantatively different. The frequencies corresponding to the leaky Lamb modes S_1, S_2 and A_2 for a plane-wave incident angle $\theta_P = 10°$ cf. Fig. 6.6 are 447.3 kHz, 738.6 kHz and 806.1 kHz, respectively, indicated at $x = 60$ mm in Fig. 6.19.

The simulated pressure-to-pressure transfer function $|H_{PP}(x, 0, z_2, f)|$ at $x = 40$ mm, $x = 60$ mm, $x = 80$ mm and $x = 100$ mm in Fig. 6.19 (marked with lines) using the piezoelectric transducer (blue lines) and the piston (red lines) as source, are shown in Figs. 6.20(a), 6.20(b), 6.20(c) and 6.20(d) as a function of frequency, respectively, and compared to measurement results (green lines). For $x = 40$ mm in Fig. 6.20(a) an agreement within 2 dB up to and above the A_2 mode between the transducer and measurements is observed, whereas the same level of agreement between the baffled piston and measurements exists only up to the A_2 mode. Above the A_2 mode, $x = 40$ mm is positioned outside

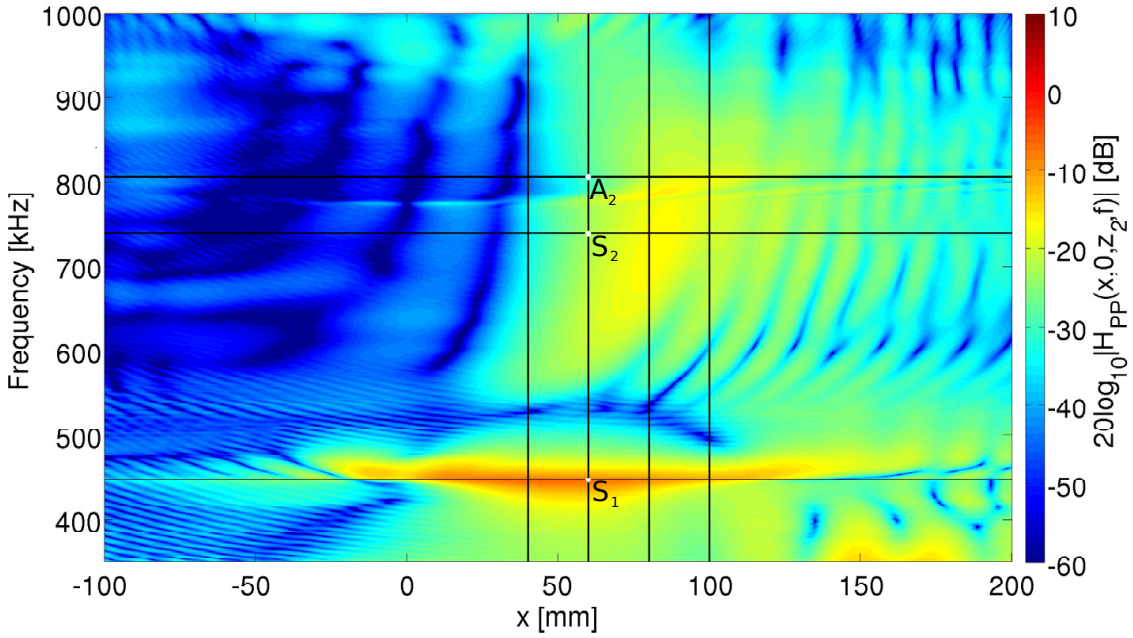

(a)

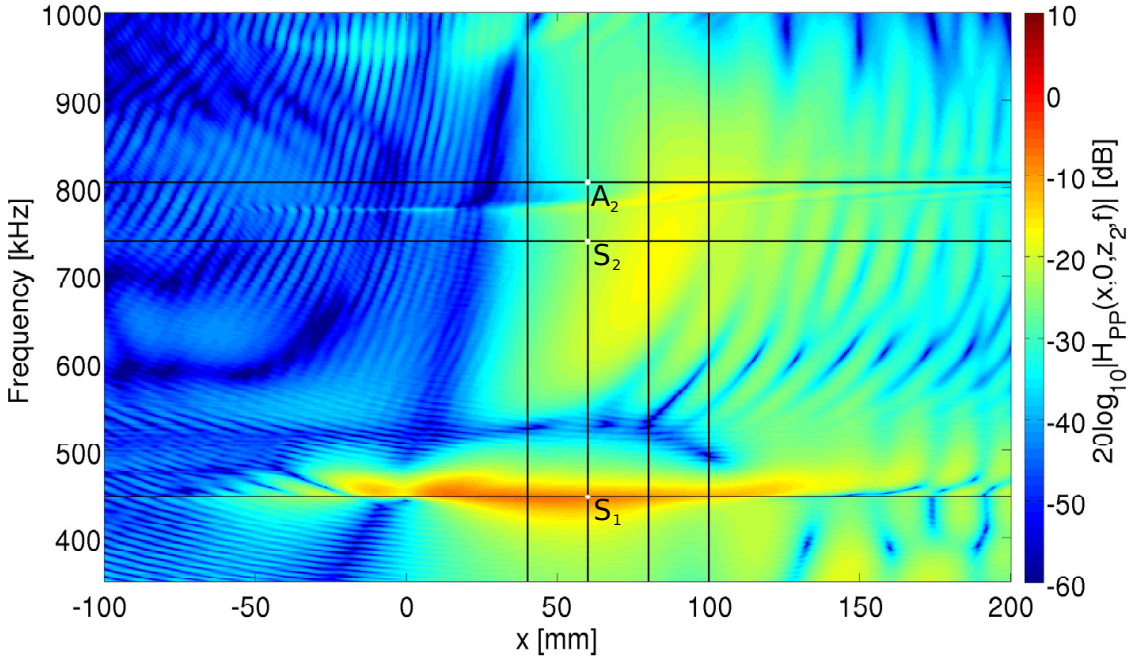

(b)

Fig 6.19. At $\theta = 10°$ beam incidence: Simulated magnitude of the pressure-to-pressure transfer function $|H_{PP}(x, 0, z_2, f)|$ using the hybrid FEM-ASM approach, for **a)** the piezoelectric transducer and **b)** the piston source. Solid lines indicate the $x-$distances and frequencies addressed in Figs. 6.20 and 6.21, respectively. Leaky Lamb modes for a plane-wave incident angle $\theta_P = 5°$ are indicated at their respective frequencies at $x = 60$ mm.

the main lobe of the measurement transducer, hence the FEM transducer model follows the behaviour of the measurements better than the baffled piston, cf. Fig. 6.12. For positions $x = 60, 80, 100$ mm (Figs. 6.20(b), 6.20(c) and 6.20(d)) both transducer models show an agreement within 3 dB to measurements for approximately the entire frequency range, except at certain frequencies. Both simulation models show agreement with the measurement transducer's transmitted pressure, but at $x = 100$ mm for high frequencies the transducer source is closer to measurements than the baffled piston.

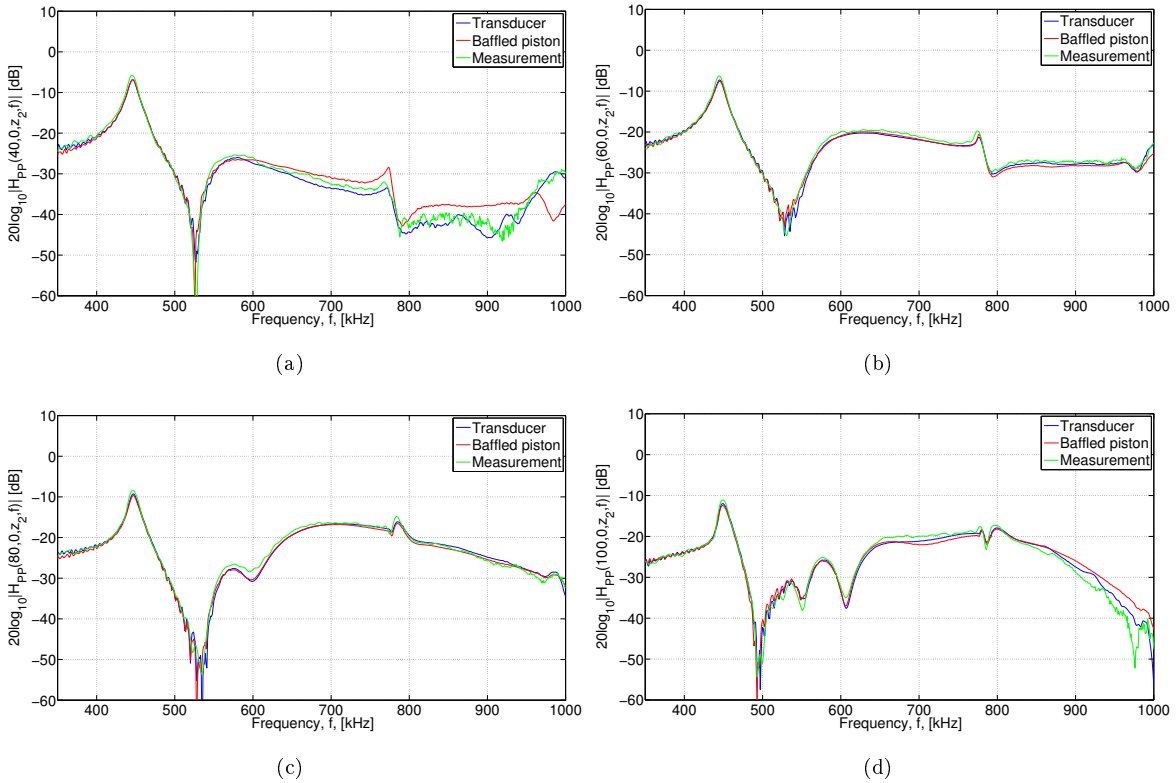

Fig 6.20. At $\theta = 10°$ beam incidence: Simulated magnitude of the pressure-to-pressure transfer function $|H_{PP}(x, 0, z_2, f)|$ using the hybrid FEM-ASM approach for the piezoelectric transducer (blue line) and piston (red line), in comparison with measurements (green line) for **a)** $x = 40$ mm, **b)** $x = 60$ mm, **c)** $x = 60$ mm and **d)** $x = 100$ mm. The frequency spectra at the four $x-$distances are indicated with solid lines in Fig. 6.19.

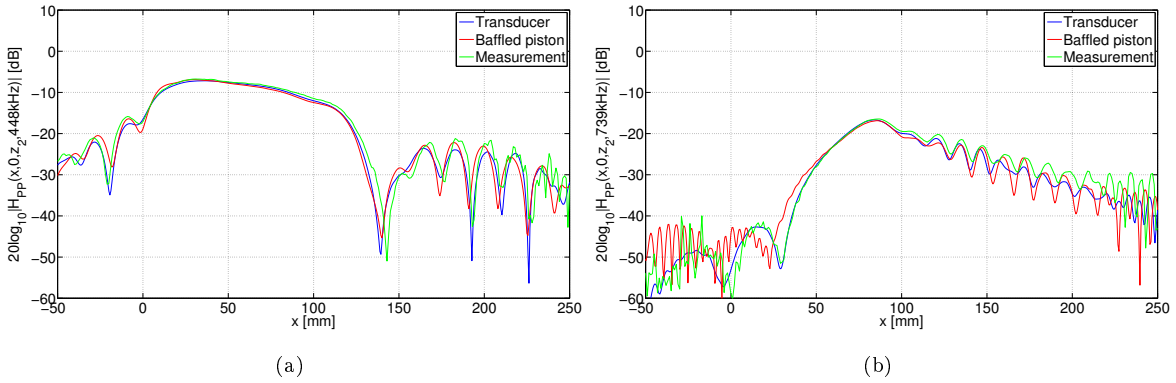

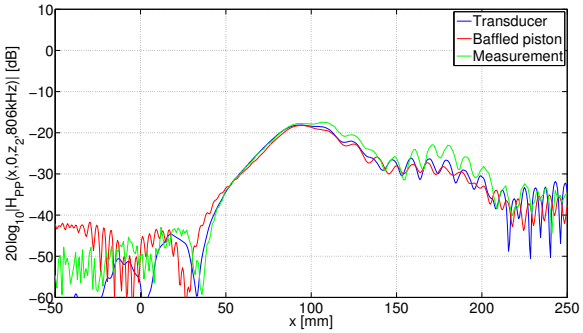

(c)

Fig 6.21. At $\theta = 10°$ beam incidence: Simulated magnitude of the pressure-to-pressure transfer function $|H_{PP}(x, 0, z_2, f)|$ using the hybrid FEM-ASM approach for the piezoelectric transducer (blue line) and baffled piston (red line), in comparison with measurements (green line) for **a)** $f = 448$ kHz, **b)** $f = 739$ kHz and **c)** $f = 806$ kHz.

The simulated pressure-to-pressure transfer function $|H_{PP}(x, 0, z_2, f)|$ for $f = 448$ kHz, $f = 739$ kHz and $f = 806$ kHz in Fig. 6.19 (marked with horizontal lines) using the piezoelectric transducer (blue lines) and the piston (red lines) as source, are shown in Figs. 6.21(a), 6.21(b) and 6.21(c) as a function of $x-$position respectively, and compared to measurement results (green lines). For $f = 448$ kHz (near the S_1 mode) in Fig. 6.21(a) an agreement within 1.2 dB for both models to measurements is observed in the region $x = 0 - 100$ mm, measurements follows (with a frequency shift) the interference pattern (discussed in Chap. 7). For $f = 739$ kHz (near the S_2 mode) in Fig. 6.21(b) the FEM transducer model follows measurements more closely than the baffled piston, especially in the region $x = -50 - 50$ mm. The same conclusions can be made for $f = 806$ kHz (near the A_2 mode) in Fig. 6.21(c), but noise in measurements is more prominent here.

6.3.4 $\theta = 15°$ beam incidence

In Figs. 6.22(a) and 6.22(b) the simulated $|H_{PP}(x, 0, z_2, f)|$ is shown for 15° beam incidence angle, as a function of frequency and x-position, at the receiver depth z_2, using the piezoelectric transducer and piston sources, respectively. The frequencies corresponding to the leaky Lamb modes A_1 and S_1 for a plane-wave incident angle $\theta_P = 15°$ cf. Fig. 6.6 are 523.9 kHz and 631.9 kHz, respectively, indicated at $x = 120$ mm in Fig. 6.22.

The simulated pressure-to-pressure transfer function $|H_{PP}(x, 0, z_2, f)|$ at $x = 100$ mm, $x = 120$ mm and $x = 140$ mm in Fig. 6.22 (marked with lines) using the piezoelectric transducer (blue lines) and the piston (red lines) as source, are shown in Figs. 6.23(a), 6.23(b) and 6.23(c) as a function of frequency, respectively, and compared to measurement results (green lines). For $x = 100$ mm in Fig. 6.23(a), an agreement within 1.3 dB between measurements and the FEM transducer model is shown, while there exists larger deviations to the baffled piston, especially in the region 600-900 kHz. The same conclusions can be made for $x = 120$ mm in Fig. 6.23(b), but the deviations are not as prominent as in Fig. 6.23(a). For $x = 140$ mm in Fig. 6.23(c), the FEM transducer model still exceeds the baffled piston model with regards to agreement to measurements, especially at the minimum around 770 kHz, where the baffled piston incorrectly simulates the minimum at a frequency higher than given by the

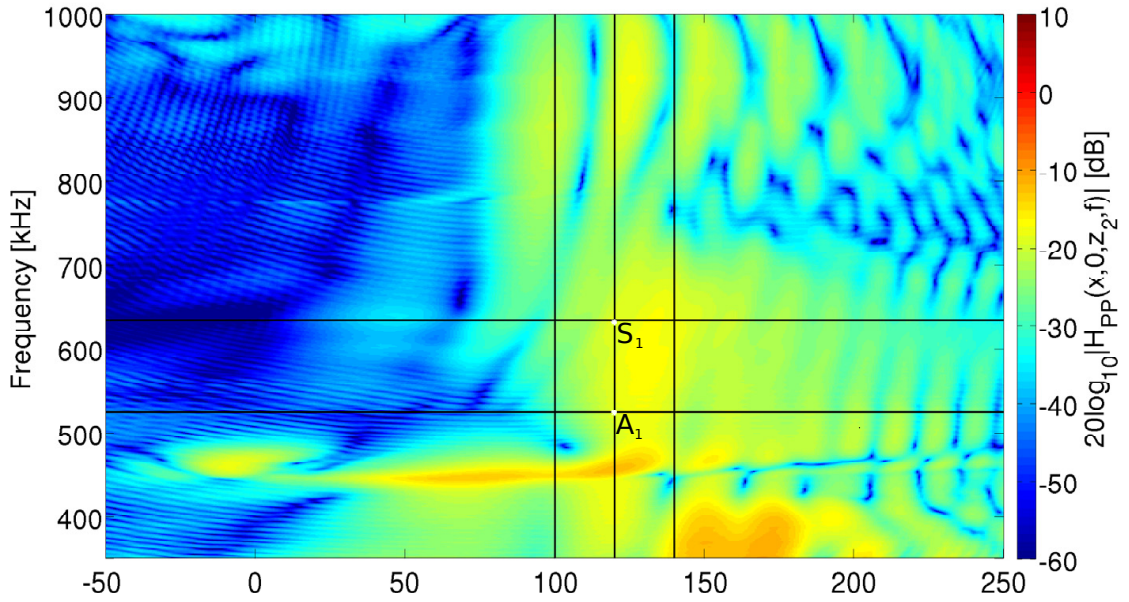

(a)

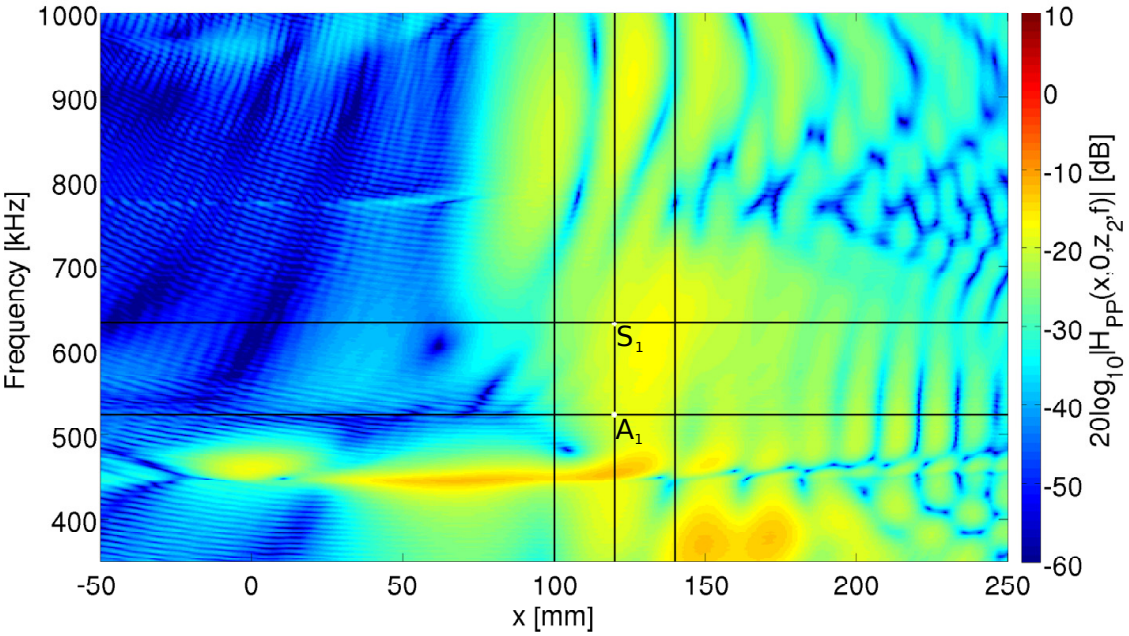

(b)

Fig 6.22. At $\theta = 15°$ beam incidence: Simulated magnitude of the pressure-to-pressure transfer function $|H_{PP}(x, 0, z_2, f)|$ using the hybrid FEM-ASM approach, for **a)** the piezoelectric transducer and **b)** the piston source. Solid lines indicate the $x-$distances and frequencies addressed in Figs. 6.23 and 6.24, respectively. Leaky Lamb modes for a plane-wave incident angle $\theta_P = 15°$ are indicated at their respective frequencies at $x = 120$ mm.

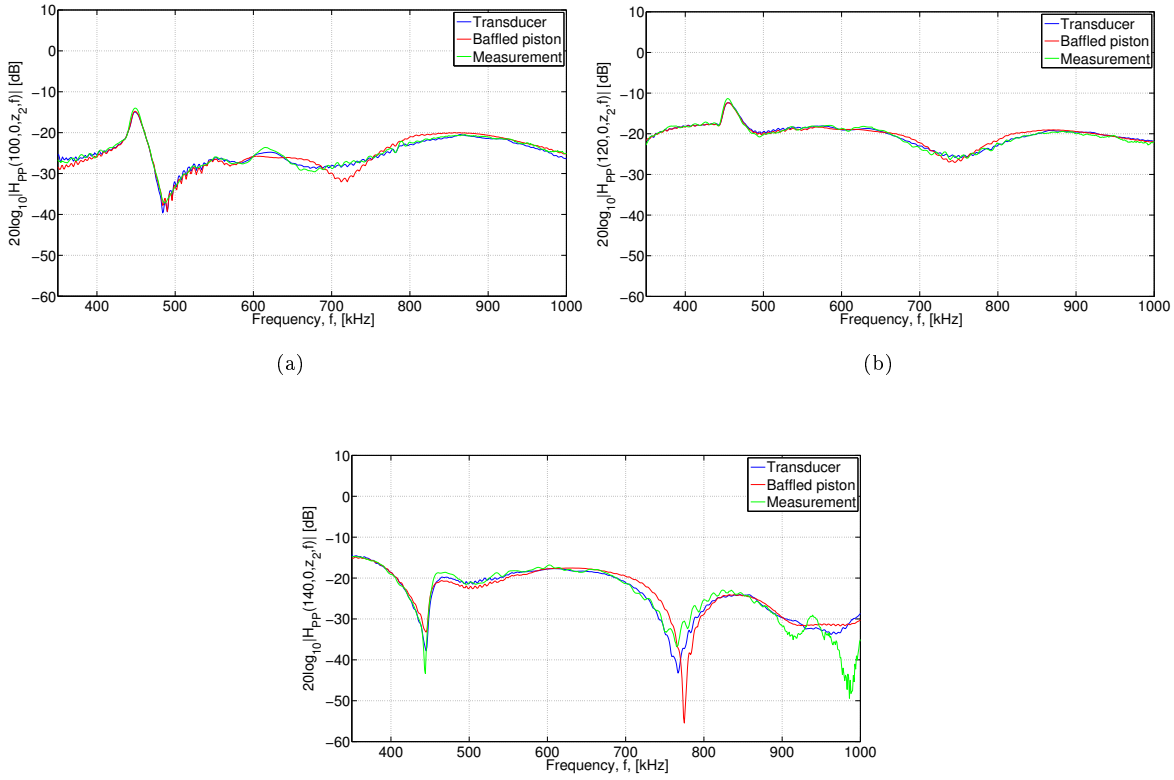

(a) (b)

(c)

Fig 6.23. At $\theta = 15°$ beam incidence: Simulated magnitude of the pressure-to-pressure transfer function $|H_{PP}(x, 0, z_2, f)|$ using the hybrid FEM-ASM approach for the piezoelectric transducer (blue line) and piston (red line), in comparison with measurements (green line) for **a)** $x = 100$ mm, **b)** $x = 120$ mm and **c)** $x = 140$ mm. The frequency spectra at the three $x-$distances are indicated with solid lines in Fig. 6.22.

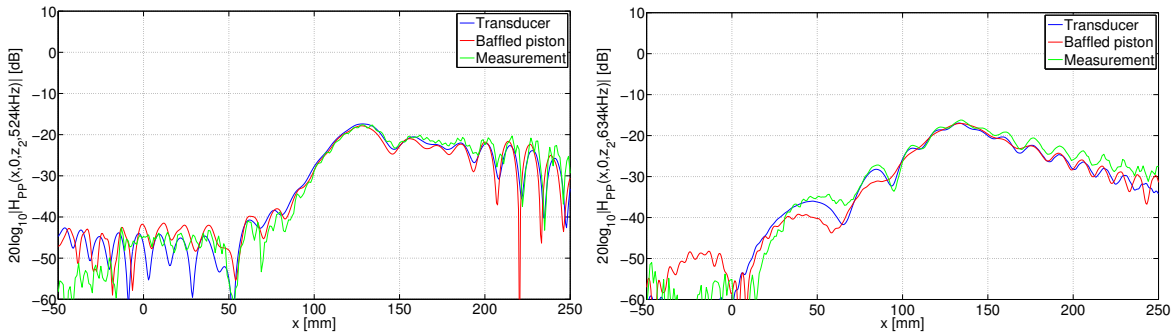

(a) (b)

Fig 6.24. At $\theta = 15°$ beam incidence: Simulated magnitude of the pressure-to-pressure transfer function $|H_{PP}(x, 0, z_2, f)|$ using the hybrid FEM-ASM approach for the piezoelectric transducer (blue line) and baffled piston (red line), in comparison with measurements (green line) for **a)** $f = 524$ kHz and **b)** $f = 634$ kHz.

measurements. There are some issues regarding the measurements at high frequencies, which may be related to alignment issues discussed in Sect. 3.2.2.

The simulated pressure-to-pressure transfer function $|H_{PP}(x, 0, z_2, f)|$ for $f = 524$ kHz and $f = 634$ kHz in Fig. 6.22 (marked with horizontal lines) using the piezoelectric transducer (blue lines) and the piston (red lines) as source, are shown in Figs. 6.24(a) and 6.24(b) as a function of $x-$position respectively, and compared to measurement results (green lines). For $f = 524$ kHz (near the A_1 mode) in Fig. 6.24(a), agreement within 3.4 dB is shown between the simulation models and measurements in the region $x = 100 - 250$ mm, including the interference pattern. For $f = 634$ kHz (near the S_1 mode), agreement within 2.1 dB is shown between the FEM transducer model and measurements in the region $x = 75 - 200$ mm, whereas the baffled piston model shows the same agreement in the region $x = 100 - 200$ mm.

6.3.5 $\theta = 20°$ beam incidence

In Figs. 6.25(a) and 6.25(b) the simulated $|H_{PP}(x, 0, z_2, f)|$ is shown for 20° beam incidence angle, as a function of frequency and $x-$position, at the receiver depth z_2, using the piezoelectric transducer and piston sources, respectively. The frequencies corresponding to the leaky Lamb modes S_0 and A_1 for a plane-wave incident angle $\theta_P = 20°$ cf. Fig. 6.6 are 372.6 kHz and 746.0 kHz, respectively, indicated at $x = 150$ mm in Fig. 6.25.

The simulated pressure-to-pressure transfer function $|H_{PP}(x, 0, z_2, f)|$ at $x = 120$ mm, $x = 150$ mm and $x = 180$ mm in Fig. 6.25 (marked with lines) using the piezoelectric transducer (blue lines) and the piston (red lines) as source, are shown in Figs. 6.26(a), 6.26(b) and 6.26(c), respectively, and compared to measurement results (green lines). For $x = 120$ mm in Fig. 6.26(a), an agreement within 1.5 dB between measurements and the simulation models are shown for the entire frequency range, except above 950 kHz. For $x = 150$ mm in Fig. 6.26(b), an agreement within 2.6 dB for both models to measurements is shown up to 900 kHz (exception around the minimum at 570 kHz). The first minimum around 580 kHz is simulated accurately with respect to frequency, but not the second minimum around 960 kHz. From Fig. 6.25, the second minimum increases with frequency as one moves to higher $x-$positions, so the measurements here is most likely conducted at a position slightly higher than $x = 150$ mm. For $x = 180$ mm in Fig. 6.26(c), agreement within 1.9 dB is shown up to 900 kHz for the transducer, and 850 kHz for the baffled piston. Above this region, greater deviations are shown to measurements for both simulation models, especially the baffled piston. As for the other $x-$positions, alignment of the hydrophone is crucial for accurate measurements at these frequencies.

The simulated pressure-to-pressure transfer function $|H_{PP}(x, 0, z_2, f)|$ for $f = 373$ kHz and $f = 746$ kHz in Fig. 6.25 (marked with horizontal lines) using the piezoelectric transducer (blue lines) and the piston (red lines) as source, are shown in Figs. 6.27(a) and 6.27(b) as a function of $x-$position respectively, and compared to measurement results (green lines). For $f = 373$ kHz (near the S_0 mode) in Fig. 6.27(a) an agreement within 4.2 dB is shown for the transducer in relation to measurements in the region $x = 50 - 250$ mm, except at the beginning of this region where measurement noise is clearly present. For $f = 746$ kHz (near the A_1 mode) in Fig. 6.27(b), agreement within 2 dB for the FEM transducer model to measurement is shown for $x = 75 - 180$ mm, and for the baffled piston model to measurements for $x = 125 - 180$ mm. For the region below $x = 75$ mm, noise is a dominant part of

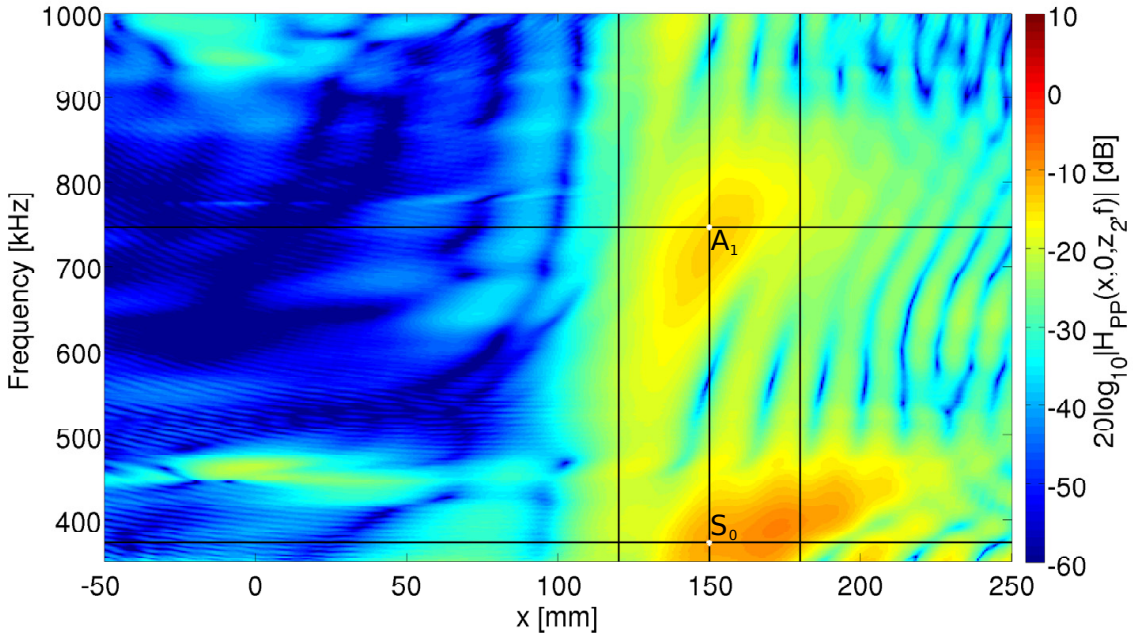

(a)

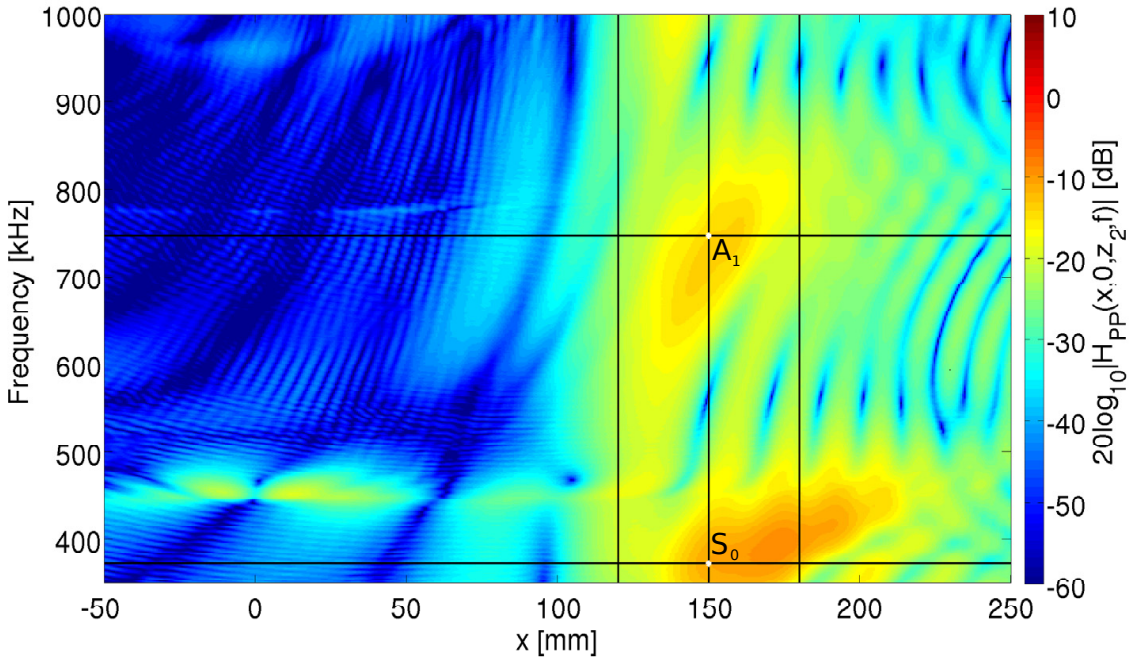

(b)

Fig 6.25. At $\theta = 20°$ beam incidence: Simulated magnitude of the pressure-to-pressure transfer function $|H_{PP}(x, 0, z_2, f)|$ using the hybrid FEM-ASM approach, for **a)** the piezoelectric transducer and **b)** the piston source. Solid lines indicate the $x-$distances and frequencies addressed in Figs. 6.26 and 6.27, respectively. Leaky Lamb modes for a plane-wave incident angle $\theta_P = 20°$ are indicated at their respective frequencies at $x = 150$ mm.

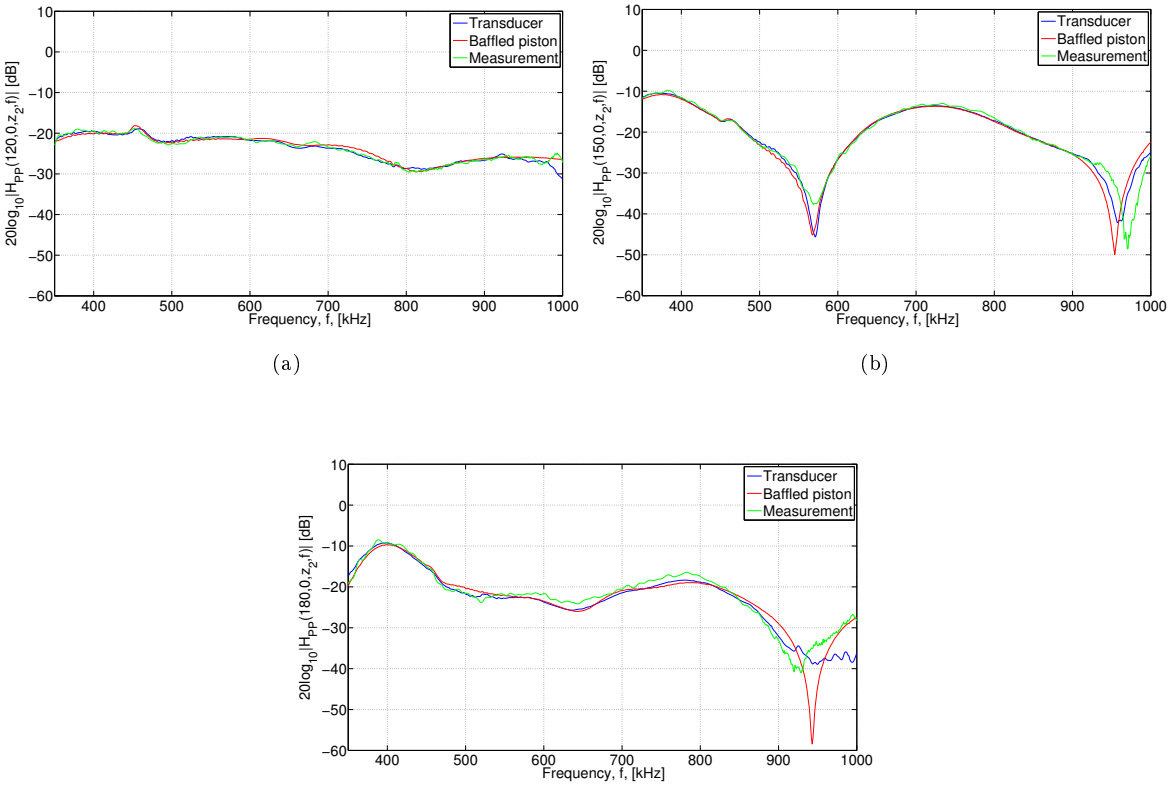

(a) (b)

(c)

Fig 6.26. At $\theta = 20°$ beam incidence: Simulated magnitude of the pressure-to-pressure transfer function $|H_{PP}(x, 0, z_2, f)|$ using the hybrid FEM-ASM approach for the piezoelectric transducer (blue line) and piston (red line), in comparison with measurements (green line) for **a)** $x = 120$ mm, **b)** $x = 150$ mm and **c)** $x = 180$ mm. The frequency spectra at the three $x-$distances are indicated with solid lines in Fig. 6.25.

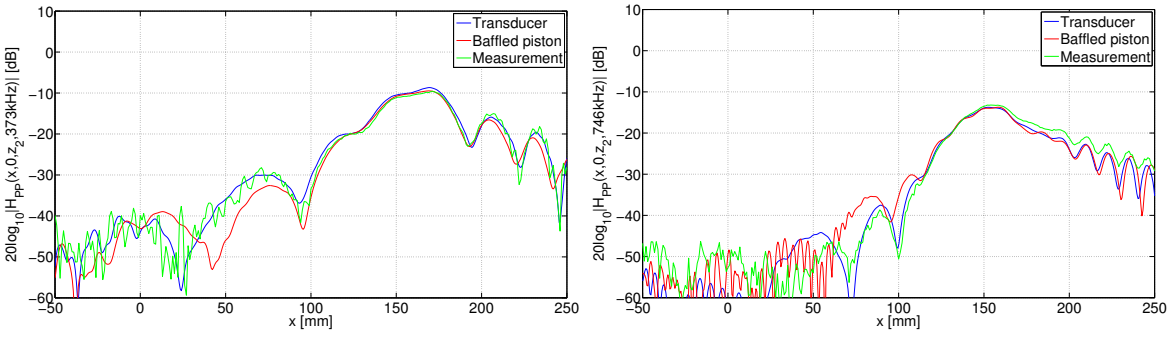

(a) (b)

Fig 6.27. At $\theta = 20°$ beam incidence: Simulated magnitude of the pressure-to-pressure transfer function $|H_{PP}(x, 0, z_2, f)|$ using the hybrid FEM-ASM approach for the piezoelectric transducer (blue line) and baffled piston (red line), in comparison with measurements (green line) for **a)** $f = 373$ kHz and **b)** $f = 746$ kHz.

the measurement results.

6.3.6 $\theta = 25°$ beam incidence

In Figs. 6.28(a) and 6.28(b) the simulated $|H_{PP}(x, 0, z_2, f)|$ is shown for 25° beam incidence angle, as a function of frequency and $x-$position, at the receiver depth z_2, using the piezoelectric transducer and piston source, respectively. The frequency corresponding to the leaky Lamb mode S_0 for a plane-wave incident angle $\theta_P = 25°$ cf. Fig. 6.6 is 446.0 kHz, indicated at $x = 200$ mm in Fig. 6.28.

The simulated pressure-to-pressure transfer function $|H_{PP}(x, 0, z_2, f)|$ at $x = 180$ mm, $x = 200$ mm and $x = 220$ mm in Fig. 6.28 (marked with lines) using the piezoelectric transducer (blue lines) and the piston (red lines) as source, are shown in Figs. 6.29(a), 6.29(b) and 6.29(c) as a function of frequency, respectively, and compared to measurement results (green lines). For $x = 180$ mm in Fig. 6.29(a), an agreement within 2 dB for the entire frequency range is shown between measurements and the simulated transducer, whereas the baffled piston model shows deviations in the frequency range 600 - 800 kHz. For $x = 200$ mm in Fig. 6.29(b), the same argument (agreement within 3.3 dB) as for Fig. 6.29(a) can be made. For $x = 220$ mm in Fig. 6.29(c), agreement within 0.8 dB for both simulation models to measurements can be shown up in the range 450 - 700 kHz, while the FEM transducer model follows the measurements above more closely than the baffled piston model.

The simulated pressure-to-pressure transfer function $|H_{PP}(x, 0, z_2, f)|$ for $f = 446$ kHz in Fig. 6.28 (marked with a horizontal line) using the piezoelectric transducer (blue lines) and the piston (red lines) as source, is shown in Fig. 6.30 as a function of $x-$position, and compared to measurement results (green lines). Agreement within 2 dB is shown for both models to measurements in the region

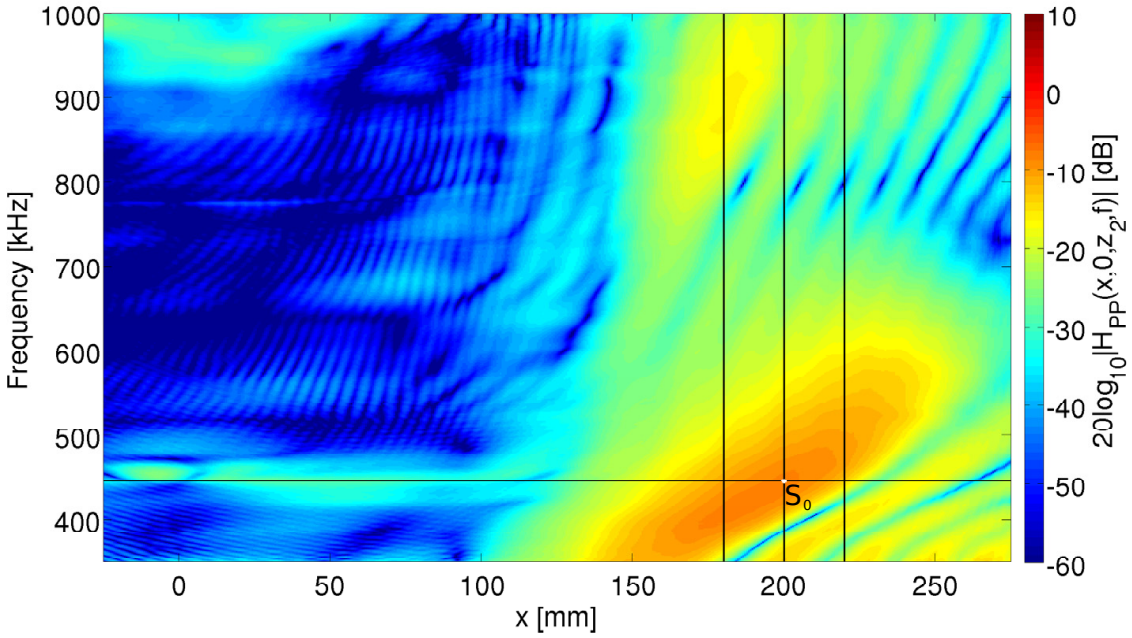

(a)

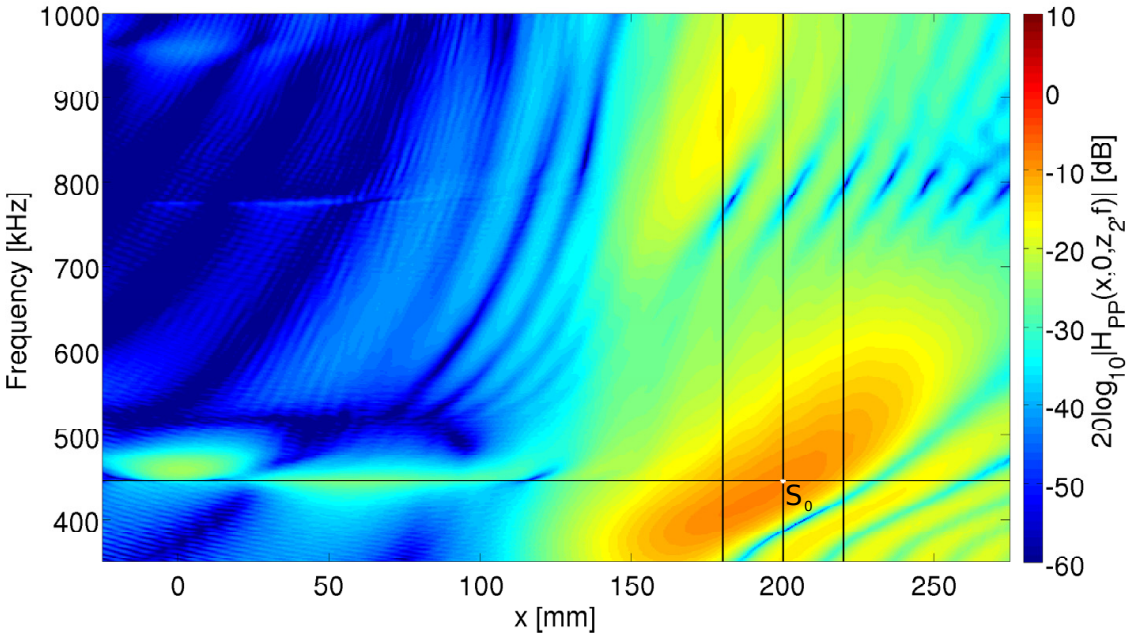

(b)

Fig 6.28. At $\theta = 25°$ beam incidence: Simulated magnitude of the pressure-to-pressure transfer function $|H_{PP}(x, 0, z_2, f)|$ using the hybrid FEM-ASM approach, for **a)** the piezoelectric transducer and **b)** the piston source. Solid lines indicate the $x-$distances and frequencies addressed in Figs. 6.29 and 6.30, respectively. The S_0 mode for a plane-wave incident angle $\theta_P = 25°$ is indicated at its respective frequency at $x = 200$ mm.

$x = 125 - 250$ mm (except minimum at $x = 230$ mm), while the FEM transducer model also shows agreement within 5.5 dB downwards to $x = 0$ mm.

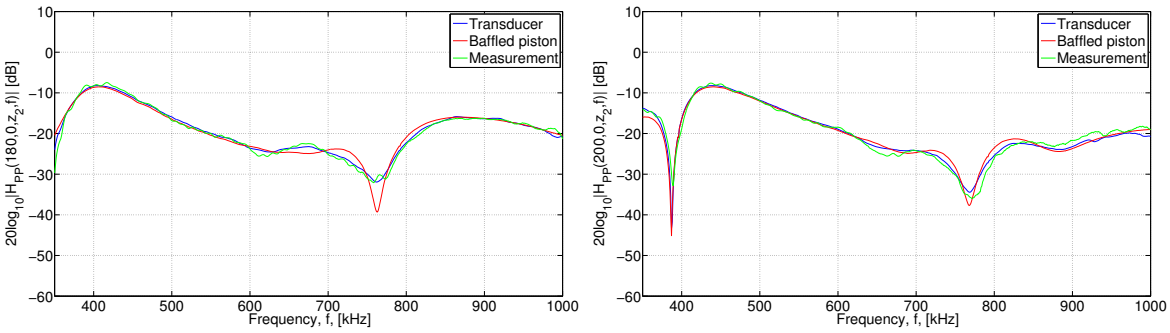

(a) (b)

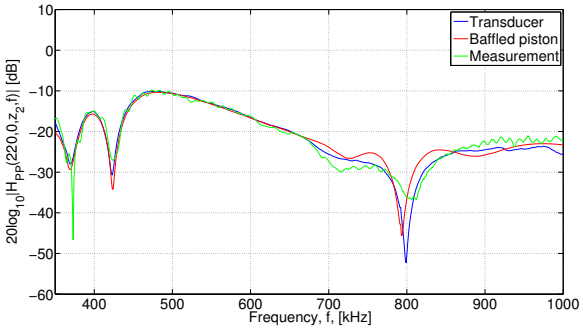

(c)

Fig 6.29. At $\theta = 25°$ beam incidence: Simulated magnitude of the pressure-to-pressure transfer function $|H_{PP}(x, 0, z_2, f)|$ using the hybrid FEM-ASM approach for the piezoelectric transducer (blue line) and piston (red line), in comparison with measurements (green line) for **a)** $x = 180$ mm, **b)** $x = 200$ mm and **c)** $x = 220$ mm. The frequency spectra at the three $x-$distances are indicated with solid lines in Fig. 6.28.

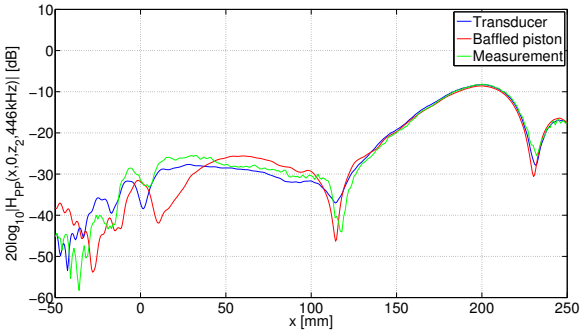

Fig 6.30. At $\theta = 25°$ beam incidence: Simulated magnitude of the pressure-to-pressure transfer function $|H_{PP}(x, 0, z_2, f)|$ using the hybrid FEM-ASM approach for the piezoelectric transducer (blue line) and baffled piston (red line), in comparison with measurements (green line) for $f = 446$ kHz.

6.3.7 $\theta = 30°$ beam incidence

In Figs. 6.31(a) and 6.31(b) the simulated $|H_{PP}(x, 0, z_2, f)|$ is shown for 30° beam incidence angle, as a function of frequency and $x-$position, at the receiver depth z_2, using the piezoelectric transducer and piston source, respectively. The frequency corresponding to the leaky Lamb mode S_0 for a plane-wave incident angle $\theta_P = 30°$ cf. Fig. 6.6 is 691.3 kHz, indicated at $x = 230$ mm in Fig. 6.31.

The simulated pressure-to-pressure transfer function $|H_{PP}(x, 0, z_2, f)|$ at $x = 200$ mm, $x = 230$ mm and $x = 260$ mm in Fig. 6.31 (marked with lines) using the piezoelectric transducer (blue lines) and the piston (red lines) as source, are shown in Figs. 6.32(a), 6.32(b) and 6.32(c) as a function of frequency, respectively, and compared to measurement results (green lines). For all these $x-$positions, an agreement within 5 dB between the two simulation models and measurement is shown for the entire frequency range.

The simulated pressure-to-pressure transfer function $|H_{PP}(x, 0, z_2, f)|$ for $f = 692$ kHz in Fig. 6.31 (marked with a horizontal line) using the piezoelectric transducer (blue lines) and the piston (red lines)

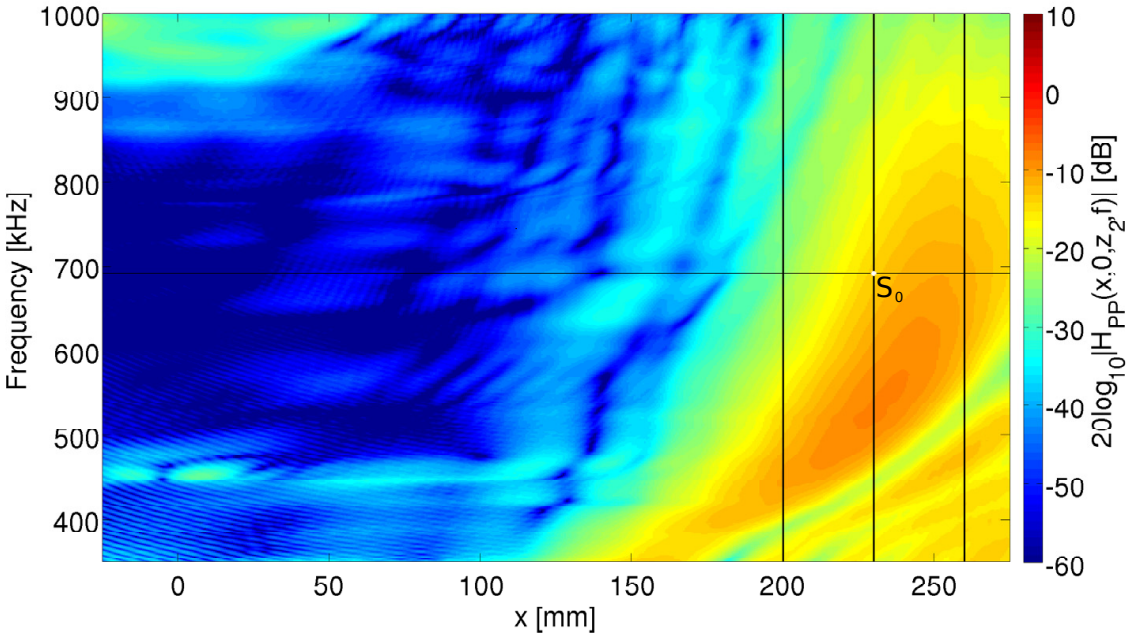

(a)

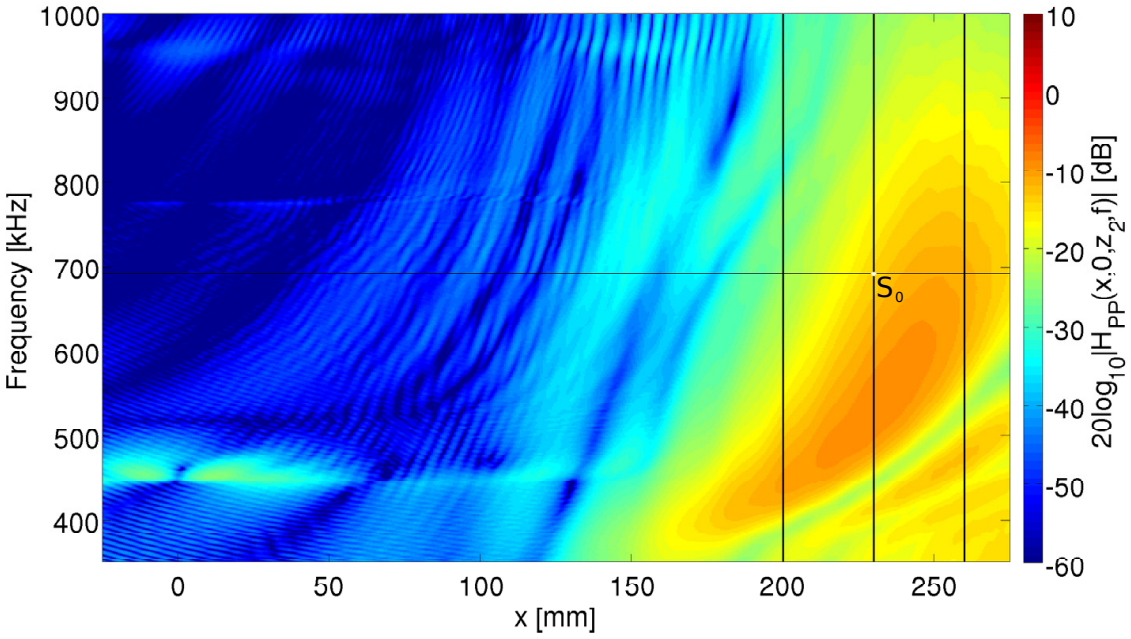

(b)

Fig 6.31. At $\theta = 30°$ beam incidence: Simulated magnitude of the pressure-to-pressure transfer function $|H_{PP}(x, 0, z_2, f)|$ using the hybrid FEM-ASM approach, for **a)** the piezoelectric transducer and **b)** the piston source. Solid lines indicate the $x-$distances and frequencies addressed in Figs. 6.32 and 6.33, respectively. The S_0 mode for a plane-wave incident angle $\theta_P = 30°$ is indicated at its respective frequency at $x = 230$ mm.

as source, is shown in Fig. 6.33 as a function of $x-$position, and compared to measurement results

(green lines). For the region $x = 190 - 250$ mm an agreement within 4 dB is shown for the FEM transducer model, whereas 8.6 dB for the baffled piston model. For positions $x = -50 - 190$ mm, noise is a dominant part of the measurements.

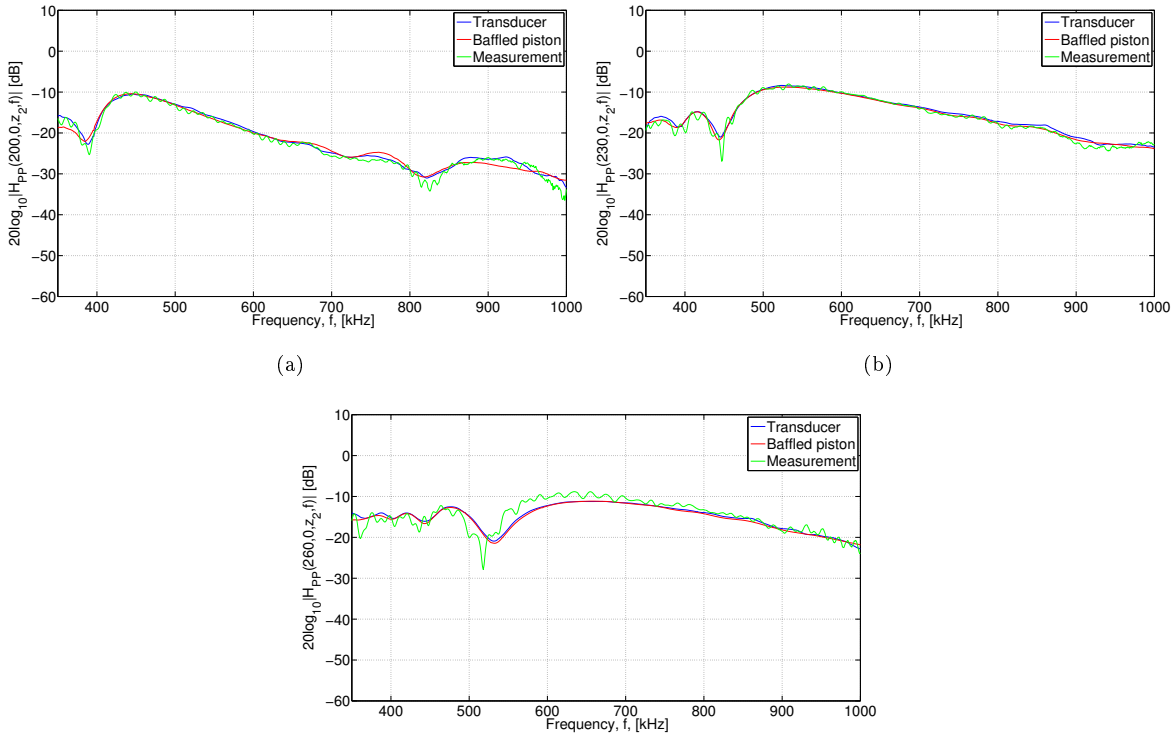

Fig 6.32. At $\theta = 30°$ beam incidence: Simulated magnitude of the pressure-to-pressure transfer function $|H_{PP}(x, 0, z_2, f)|$ using the hybrid FEM-ASM approach for the piezoelectric transducer (blue line) and piston (red line), in comparison with measurements (green line) for **a)** $x = 200$ mm, **b)** $x = 230$ mm and **c)** $x = 260$ mm. The frequency spectra at the three $x-$distances are indicated with solid lines in Fig. 6.31.

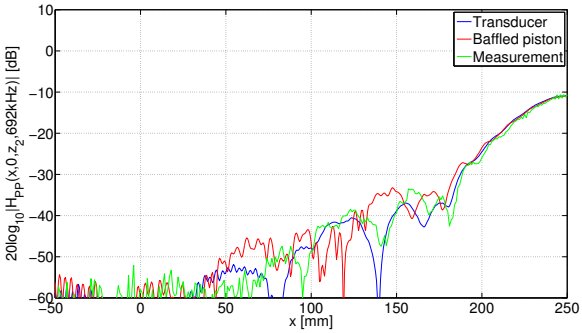

Fig 6.33. At $\theta = 30°$ beam incidence: Simulated magnitude of the pressure-to-pressure transfer function $|H_{PP}(x, 0, z_2, f)|$ using the hybrid FEM-ASM approach for the piezoelectric transducer (blue line) and baffled piston (red line), in comparison with measurements (green line) for $f = 692$ kHz.

6.4 Summary and discussion

In Sect. 6.2.1 the signal transmission through the plate, and excitation of leaky Lamb modes, are studied and discussed, based upon comparisons of plane waves and 3D beams. Fig. 6.7 shows a comparion of the plane-wave transmission coefficient $\mathscr{T}$ and the FEM calculated $|P_1(0,0,z_+2L,f)/P_0(0,0,z_0,f)|$ at normal beam incidence, which demonstrates the effect of accounting for a 3D beam in transmission simulations. This is in agreement with [91, 92], which observed and discussed 3D beam diffraction effects using a baffled piston model and $H_{PP}(x,y,z_2,f)$. Depending on the beam pattern of the source used and the behaviour of leaky Lamb modes as a function of frequency/incident angle, non-zero plane-wave components of the beam can excite leaky Lamb modes at small non-zero incident angles. Results using a directive beam can for that reason deviate from plane-wave results. Such effects can also apply for oblique beam incidence angles. Many works on material property determination or monitoring uses the plane-wave theory and discuss and/or suggests ways to minimize these beam effects, e.g. [65, 80, 77, 96].

In Sect. 6.3 the signal transmission through the plate, and excitation of leaky Lamb modes, are studied and discussed, based upon comparisons of the 3D beams using the simulated piezoelectric source transducer, the baffled piston model, and the measurement transducer, at different beam incidence angles. A similar study using the baffled piston model and measurements is reported in Lohne *et al.* [91]. They discussed the validity of the baffled piston model for describing the real beam pattern of the measurement transducer, concluding fairly good correspondence to measurements, but also highlighted that a finite element simulation of the beam from the measurement tranducer could be more accurate. A normalization method was used to compare simulations to measurements, in this thesis this normalization method is avoided by using a longer needle hydrophone in transmission measurements. Younghouse [70] showed transmission results as a function of $x-$position through an aluminum plate, comparing meaurement results to the baffled piston model.

Figs. 6.13, 6.16, 6.19, 6.22, 6.25, 6.28 and 6.31 show that the local maxima of transmission through the plate does not necessarily correspond to single plane-wave excitation of leaky Lamb modes, and show therefore the importance of using a more realistic 3D beam for transmission optimization with respect to bandwidth, signal level and waveform. In Figs. 6.17, 6.20, 6.23, 6.26, 6.29 and 6.32 the simulated pressure-to-pressure transfer function $|H_{PP}(x,y,z_2,f)|$ using the transducer and baffled piston models as sources, are compared to measurements, as a function of frequency for given $x-$positions. In Figs. 6.18, 6.21, 6.24, 6.27, 6.30 and 6.33 the simulated pressure-to-pressure transfer function $|H_{PP}(x,y,z_2,f)|$ using the transducer and the baffled piston models, are compared to measurements, as a function of $x-$position for given frequencies. For $x-$positions within the region covered by the source's main lobe, the piezoelectric transducer and baffled piston produce similar results, as expected from the comparison of beam patterns in Fig. 6.12. For $x-$positions on the edge/outside this region, there is a closer agreement between the simulated piezoelectric source transducer and measurement results, than with the simulated baffled piston source, since the first and higher order sidelobes of the FEM calculated transducer models the measurements more closely than the baffled piston source model. As the main lobe narrows as frequency increases, $x-$positions initially covered by the source's main lobe at low frequencies, are covered at higher frequencies by the first or higher order sidelobes.

The deviations between the FEM transducer vs. baffled piston model as source will then also increase.

For individual transducer configurations the baffled piston model can be adequate for studying signal transmission through the plate, depending on accuracy requirements. But, one has to measure the transducer's beam pattern over a wide frequency range to calculate the effective radii for a range of frequencies. This is both time consuming and laborious. In addition, by using the baffled piston model one does not gain simulation results on an absolute level, and no representation of pressure waveforms in the time domain, for a given input voltage signal to the measurement transducer. The signal transmission through the plate is extended to account for the signal transmission through the system, including the piezoelectric source transducer in Chap. 7.

Chapter 7

System approach including piezoelectric transducer modeling

7.1 Introduction

This chapter reports the results for the signal transmission through the measurement system, from input voltage to the piezoelectric source transducer, to transmitted pressure waveforms below the plate, using the FEM and hybrid FEM-ASM approaches, in comparison with measurement results. The effects of 3D diffracted beams through the plate, and the electroacoustical coupling in the piezoelectric source transducer, are studied with respect to optimization of signal level and bandwidth of the transmitted signals. The voltage-to-pressure transfer function, $H_{VP}(x, y, z_2, f)$ in Eq. (2.10), governing the signal transmission through the system (absolute scale), and transmitted pressure field distributions, $|P_t(x, y, z_2, f)|$ in Eq. (2.9) in the frequency domain, and pressure waveforms in the time domain, $p_t(x, y, z_2, f)$ in Eq. (2.12), are presented for given voltage excitation signal to the transducer and for different beam incidence angles between the transducer and the plate. The deviation in the pulse arrival time is given in fractions of the waveform's centre frequency wavelength.

7.2 Normal beam incidence

In Fig. 7.1 the hybrid FEM-ASM calculated $|H_{VP}(x, 0, z_2, f)|$ is shown for a 0° beam incidence angle, as a function of frequency and x-position, at the receiver depth $z_2 = 376.05$ mm, in relation to Fig. 6.13 where the relative transmission through the plate is shown. The frequencies corresponding to the leaky Lamb modes S_1, S_2, A_2 and A_3 for a plane-wave incident angle $\theta_P = 0°$ cf. Fig. 6.6 are 477.7 kHz, 517.5$*$ kHz, 774.5$*$ kHz and 955.4 kHz respectively, indicated at $x = 0$ mm in Fig. 7.1. The $*$ indicates a $\theta_P = 1°$ incidence angle with the steel plate. The maxima are in the vicinity of the leaky Lamb modes, and demonstrates regions in space and frequency where the transmission through the system is relatively high. The black vertical lines show $x-$positions where the simulations are compared to measurements as a function of frequency, and the black horizontal lines show specific frequencies where the simulations are compared to measurements as a function of $x-$position. Similar plots are shown in

[98, 95] for the piezoelectric transducer, and in [91, 92] for a piston generated beam pattern.

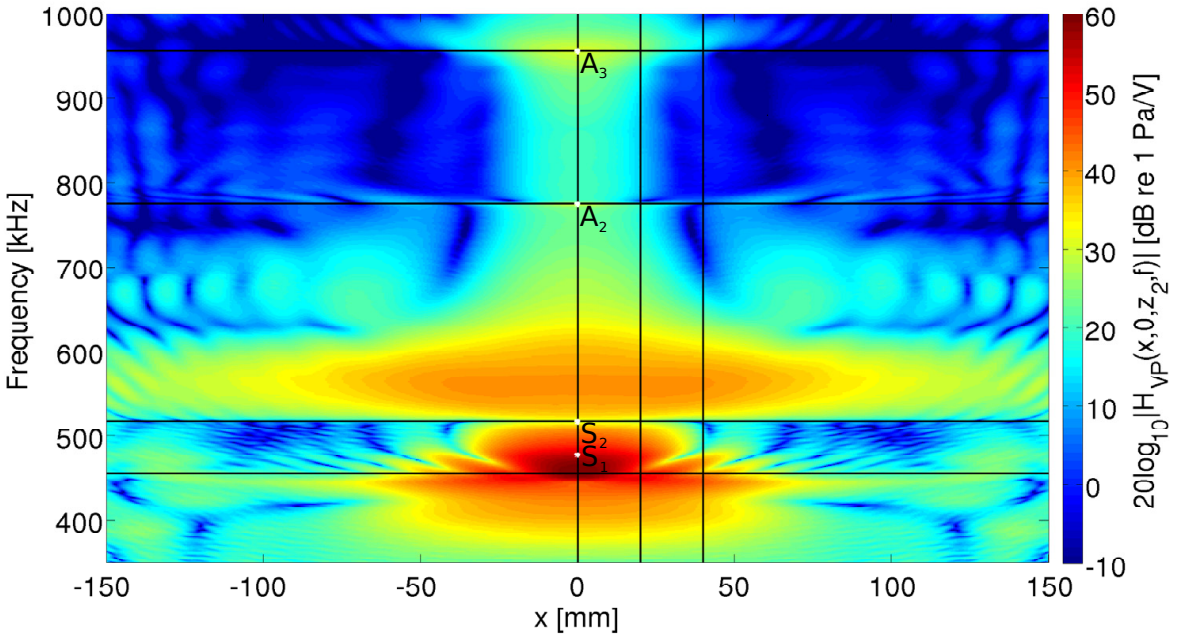

Fig 7.1. At normal beam incidence ($\theta = 0°$): Simulated magnitude of the voltage-to-pressure transfer function $|H_{VP}(x, 0, z_2, f)|$ using the hybrid FEM-ASM approach. Solid lines indicate the $x-$distances addressed in Fig. 7.2, and frequencies in Figs. 7.4, 7.5, 7.6 and 7.7. Leaky Lamb modes for a plane-wave incident angle $\theta_P = 0°$ are indicated at their respective frequencies at $x = 0$ mm.

The hybrid FEM-ASM simulated voltage-to-pressure transfer function $|H_{VP}(x, 0, z_2, f)|$ at $x = 0$ mm, $x = 20$ and $x = 40$ mm in Fig. 7.1 (marked with lines) are shown (blue lines) in Figs. 7.2(a), 7.2(b) and 7.2(c), respectively, as a function of frequency. The corresponding relative transmission through the plate are shown in Fig. 6.14. Comparisons are made with the transfer function calculated using the FEM approach (red lines) and measurements (green lines). The black vertical lines indicates frequencies where the transmitted waveforms are simulated and compared to measurements, cf. Figs. 7.4, 7.5, 7.6 and 7.7. For $x = 0$ mm in Fig. 7.2(a), an agreement within 1.8 dB to measurements is shown up to 900 kHz, except around the A_2 mode for the hybrid FEM-ASM approach. This is possibly due to improper frequency sampling (1 kHz) in the hybrid FEM-ASM approach. For $x = 20$ mm in Fig. 7.2(b) a similar agreement is shown. For $x = 40$ mm in Fig. 7.2(c), an agreement within 3.2 dB is shown, except at the minimum around 500 kHz and at higher frequencies. This position is situated outside the transducer's main lobe at these frequencies, and is influenced by the higher order sidelobes. In addition, accurate positioning of the needle hydrophone at higher frequencies is important, due to a highly directive transducer beam pattern (in relation to lower frequencies). An agreement within 1.2 dB between the FEM and hybrid FEM-ASM approaches is given.

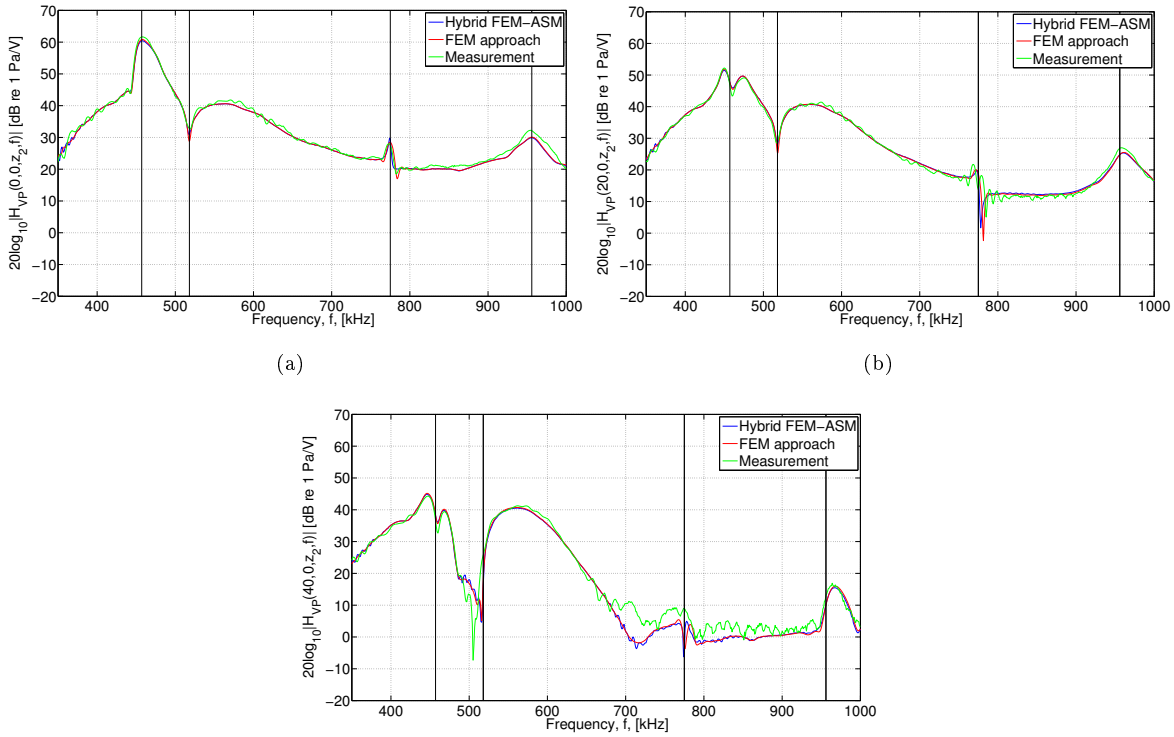

Fig 7.2. At normal beam incidence ($\theta = 0°$): Simulated magnitude of the voltage-to-pressure transfer function $|H_{VP}(x, 0, z_2, f)|$ using the hybrid FEM-ASM approach (blue line), in comparison with the FEM approach (red line) and measurements (green line) for **a)** $x = 0$ mm, **b)** $x = 20$ mm and **c)** $x = 40$ mm. The frequency spectra at the three $x-$distances are indicated with solid lines in Fig. 7.1.

Figs. 7.3(a), 7.3(b), 7.3(c) and 7.3(d) show the magnitude of the hybrid FEM-ASM simulated pressure field distribution $|P(x, 0, z, f)|$ at $f = 457$ kHz, $f = 518$ kHz, $f = 775$ kHz and $f = 956$ kHz as a function of $x-$ and $z-$ positions, respectively, near the leaky Lamb modes for $\theta_P = 0°$. The incident pressure field produced by, and propagated from, the piezoelectric transducer towards the plate, and the pressure field transmitted through the plate, is presented. The pressure field reflected by the plate's upper surface back towards the source is not displayed, since reflection's studies are not part of this work. Null regions are also present. Similar plots are reported in [78, 79] for a water-solid interface using the DPSM, showing the incident and reflected pressure fields, including null regions in accordance with the theory of Bertoni & Tamir [35]. These works showed qualitative agreement between the DPSM and measurement results, where quantitative agreement is shown in this thesis between the two approaches and experiments. For $f = 457$ kHz (near the S_1 mode), $f = 518$ kHz (near the S_2 mode) and $f = 775$ kHz (near the A_2 mode) in Figs. 7.3(a), 7.3(b) and 7.3(c), respectively, the plate causes a beam narrowing effect. This is most likely due to the lowpass filter effect $\mathscr{T}$ has in the frequency-wavenumber domain, cf. Sect. 4.3.1. But, for $f = 956$ kHz (near the A_3 mode), the plate causes a beam spreading effect.

Fig. 7.4(a) shows the hybrid FEM-ASM simulated transmitted pressure field distribution $|P_t(x, y, z_2, f)|$

at a frequency of 457 kHz as function of $x-$ and $y-$positions, for a constant $z = z_2$, close to the excitation frequency for plane-wave normal incidence of the S_1 at 477.6 kHz. Fig. 7.4(b) show the hybrid FEM-ASM (blue line) and FEM (red line) calculated $|H_{VP}(x, 0, z_2, 457\text{kHz})|$ as function of $x-$position, in comparison with measurements (green line), cf. Fig. 6.15 for the transmission through the plate. An agreement within 1.9 dB to measurement is shown up to $x = 50$ mm, and adequately thereafter. Negliable deviations between the two simulation approaches are shown. Recall that the FEM approach is axi-symmetric around the $z-$axis, therefore no results are shown for $x-$positions below $x = 0$. In Figs. 7.4(c), 7.4(d) and 7.4(e) the simulated sound pressure waveforms $p_t(x, y, z_2, t)$ with centre frequency $f = 457$ kHz are compared to measured waveforms, and simulated waveforms using the FEM approach, at three receiver positions '$*$' in Fig. 7.4(a), at $x = 0, 20, 40$ mm, respectively. Agreement within 1.55 dB between the two approaches and measurements in signal level and waveform are shown, as expected from Fig. 7.4(b). The deviations in the pulse arrival time between simulated and measured waveforms are 0.05, 0.14 and 0.1 for $x = 0, 20, 40$ mm, respectively. For $x = 0$ mm, due to the maximum in Fig. 7.4(a) at this position, the waveform has a wide bandwidth, and steadily increases to reach the maximum, whereas for $x = 20, 40$, the waveforms first oscillates at maximum, before they settle down at their respective amplitudes given by Fig. 7.4(a).

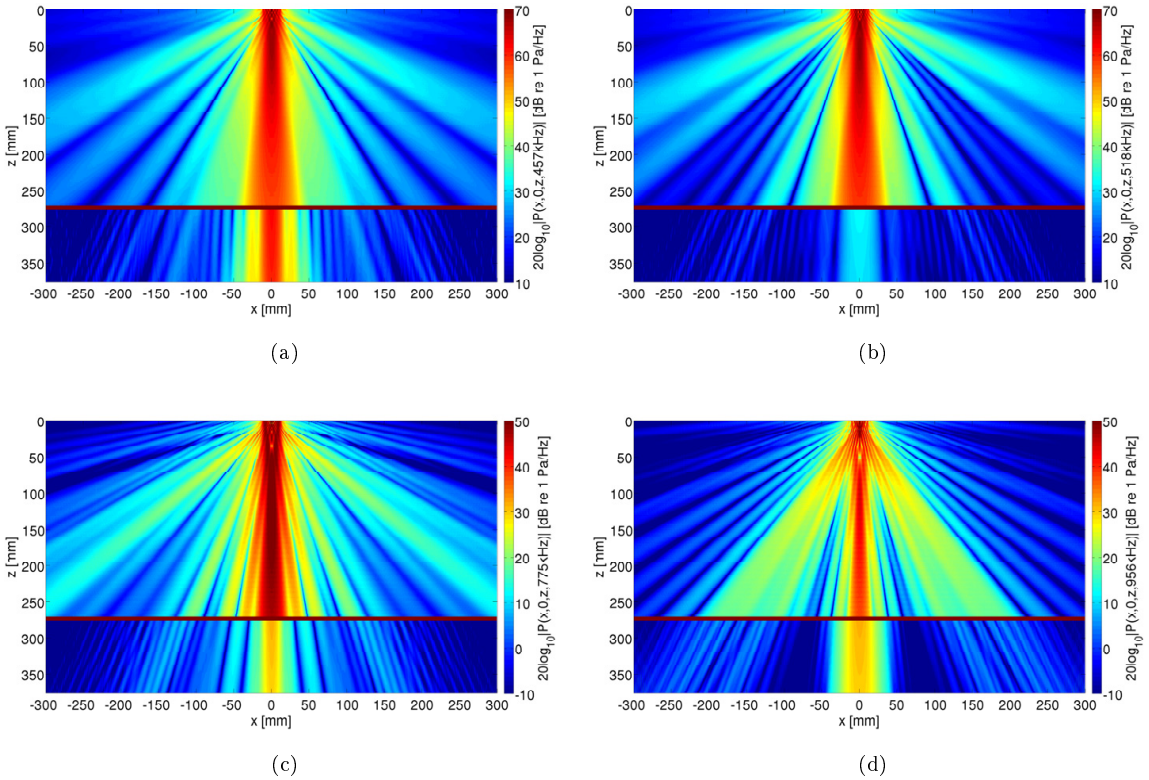

Fig 7.3. At normal beam incidence ($\theta = 0°$): Simulated magnitude of the transducer radiated pressure field distribution $|P(x, 0, z, f)|$, **a)** at $f = 457$kHz, **b)** at $f = 518$ kHz, **c)** at $f = 775$ kHz and **d)** at $f = 956$ kHz, using the hybrid FEM-ASM approach.

Fig. 7.5(a) shows the hybrid FEM-ASM simulated transmitted pressure field distribution $|P_t(x, y, z_2, f)|$

at a frequency of 518 kHz as function of $x-$ and $y-$positions, for a constant $z = z_2$, close to the excitation frequency for plane-wave normal incidence of the S_2 at 517.5 kHz. Fig. 7.5(b) shows the hybrid FEM-ASM (blue line) and FEM (red line) calculated $|H_{VP}(x, 0, z_2, 518\text{kHz})|$ as function of $x-$position, in comparison

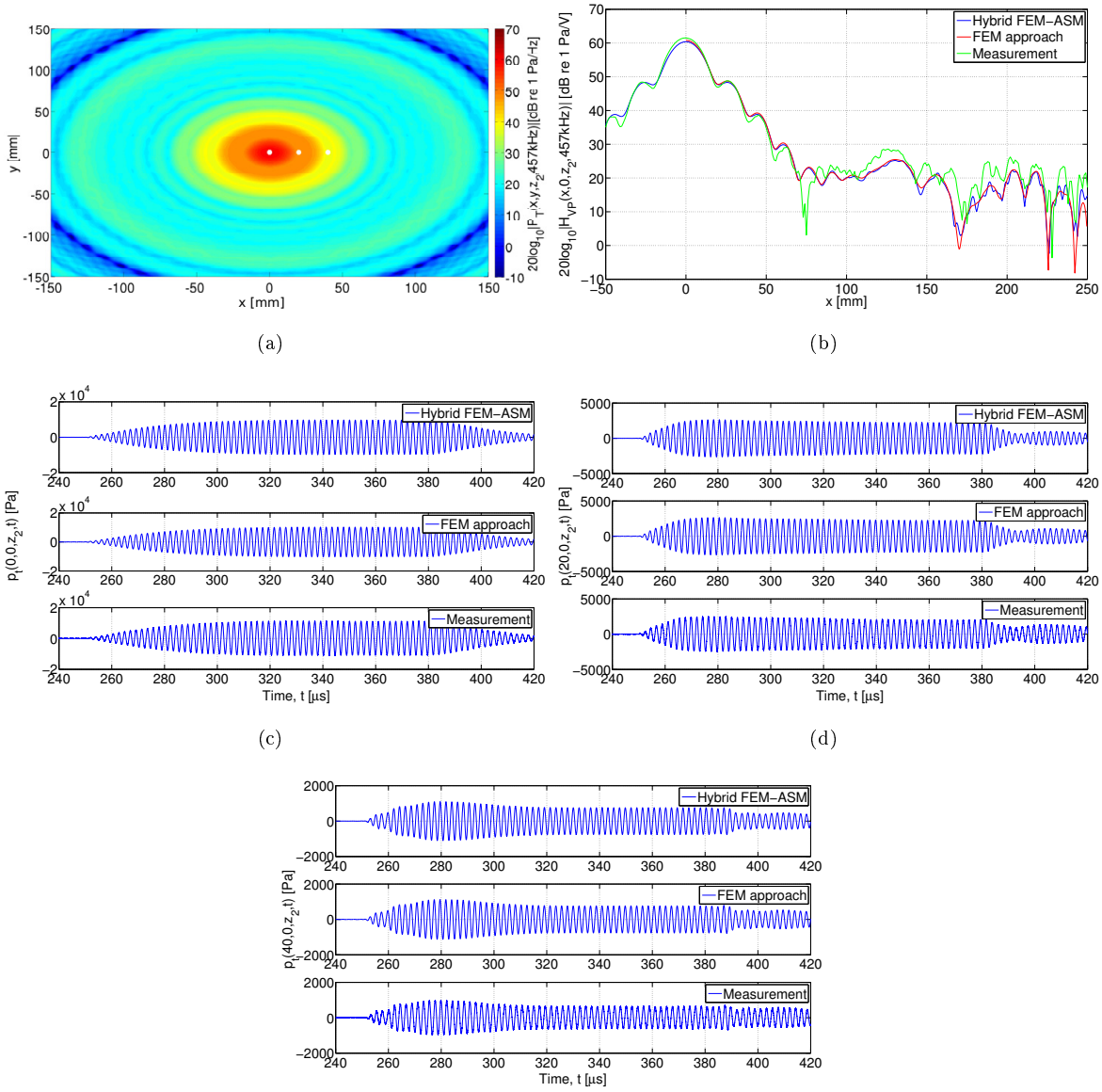

Fig 7.4. At normal beam incidence ($\theta = 0°$): Simulated magnitude of the transmitted pressure field distribution $|P_t(x, y, z_2, f)|$ at **a)** 457 kHz near the S_1 at 477.6 kHz. **b)** Simulated and measured $|P_t(x, 0, z_2, f)|$. Simulated and measured pressure waveforms $p_t(x, y, z_2, t)$ with centre frequency $f = 457$ kHz, at the receiver positions '$*$' in Fig. 7.4(a): **c)** at position $(0, 0, z_2)$, **d)** at position $(20, 0, z_2)$ and **e)** at position $(40, 0, z_2)$.

with measurements (green lines), cf. Fig. 6.15 for the transmission through the plate. An agreement within 1.8 dB between the hybrid FEM-ASM and measurements is shown in the region $x = -20 - 20$ mm, with a greater deviation to the FEM approach. In Figs. 7.5(c), 7.5(d) and 7.5(e) the simulated

sound pressure waveforms $p_t(x, y, z_2, t)$ with centre frequency $f = 518$ kHz are compared to measured waveforms, and simulated waveforms using the FEM approach, at three receiver positions '$*$' in Fig. 7.5(a) at $x = 0, 20, 40$ mm, respectively. Agreement within 1.8 dB between the hybrid approach and measurements in signal level and waveform are shown for $x = 0, 20$ mm, but the transmitted waveform at $x = 40$ is not simulated correctly. The deviations in the pulse arrival time between the simulated and measured waveforms are 0.05, 0.16 and 0.16 for $x = 0, 20, 40$ mm, respectively. Due to the minimum at this frequency in Figs. 7.1 and 7.2, the waveforms uses a relatively

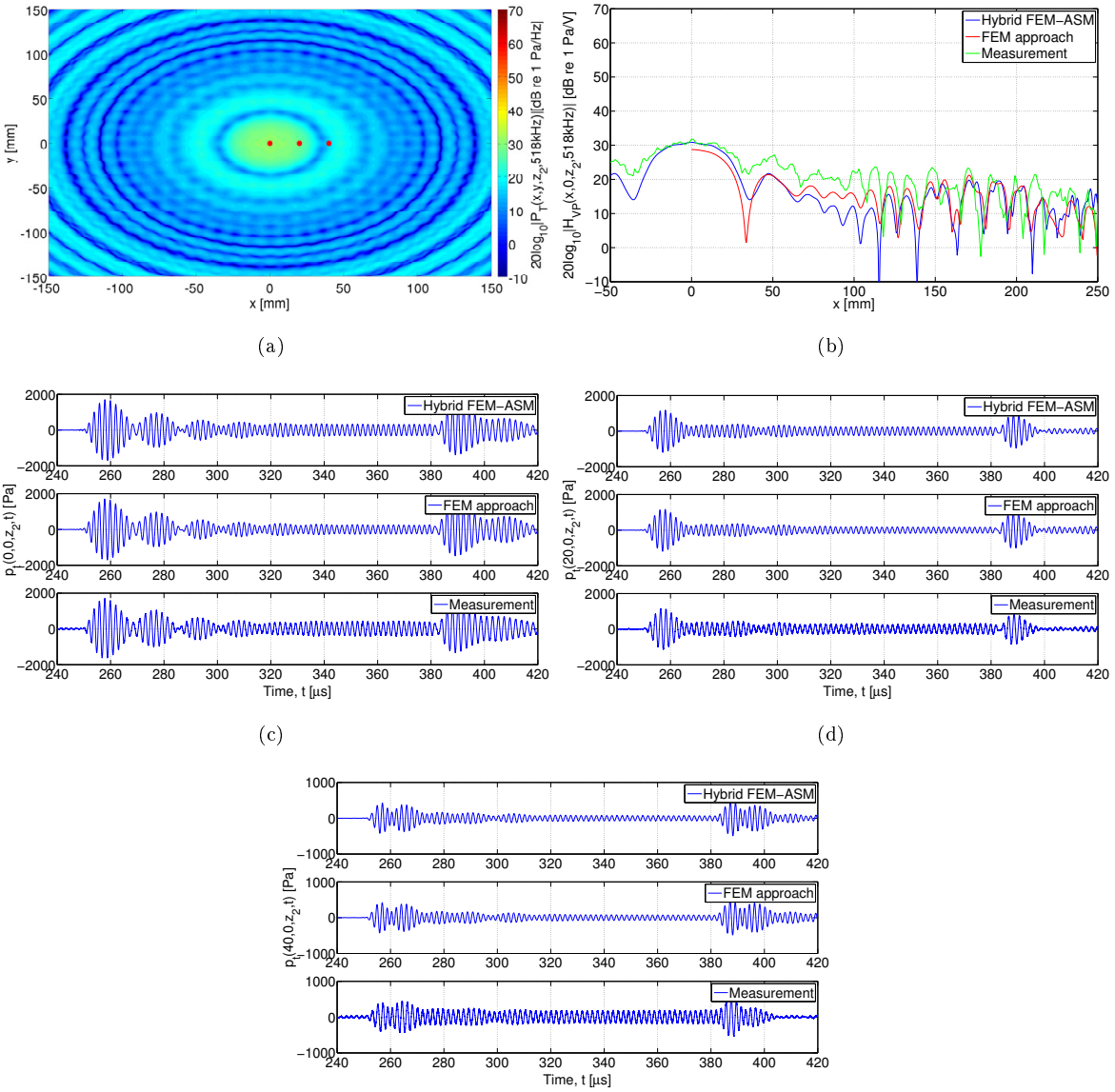

Fig 7.5. At normal beam incidence ($\theta = 0°$): Simulated magnitude of the transmitted pressure field distribution $|P_t(x, y, z_2, f)|$ at **a)** 518 kHz near the S_2 at 517.5 kHz. **b)** Simulated and measured $|P_t(x, 0, z_2, f)|$. Simulated and measured pressure waveforms $p_t(x, y, z_2, t)$ with centre frequency $f = 518$ kHz, at the receiver positions '$*$' in Fig. 7.5(a): **c)** at position $(0, 0, z_2)$, **d)** at position $(20, 0, z_2)$ and **e)** at position $(40, 0, z_2)$.

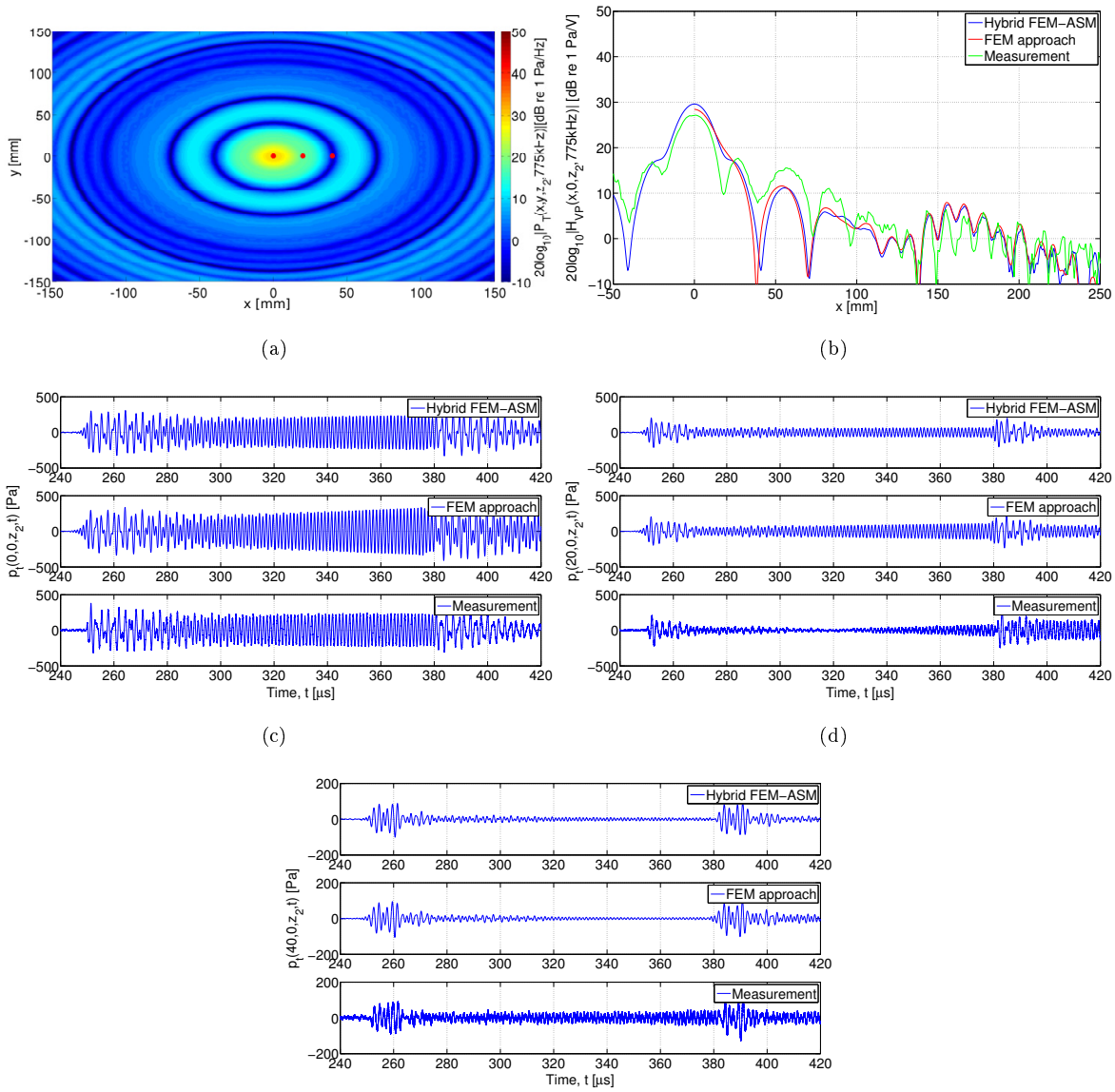

Fig 7.6. At normal beam incidence ($\theta = 0°$): Simulated magnitude of the transmitted pressure field distribution $|P_t(x, y, z_2, f)|$ at **a)** 775 kHz near the A_2 at 774.5 kHz. **b)** Simulated and measured $|P_t(x, 0, z_2, f)|$. Simulated and measured pressure waveforms $p_t(x, y, z_2, t)$ with centre frequency $f = 775$ kHz, at the receiver positions '$*$' in Fig. 7.6(a): **c)** at position $(0, 0, z_2)$, **d)** at position $(20, 0, z_2)$ and **e)** at position $(40, 0, z_2)$.

long time to settle down and reach a steady state, in relation to the waveforms in Fig. 7.4. Fig. 7.6(a) shows the hybrid FEM-ASM simulated transmitted pressure field distribution $|P_t(x, y, z_2, f)|$ at a frequency of 775 kHz as function of $x-$ and $y-$positions, for constant $z = z_2$, close to the excitation frequency for plane-wave normal incidence of the A_2 at 774.5 kHz. Fig. 7.6(b) shows the hybrid FEM-ASM (blue line) and FEM (red line) calculated $|H_{VP}(x, 0, z_2, 775\text{kHz})|$ as function of $x-$position, in comparison with measurements, cf. Fig. 6.15 for transmission through the plate. Deviations between the simulations and measurements are shown for the entire region, which is discussed under Fig. 7.2.

In Figs. 7.6(c), 7.6(d) and 7.6(e) the simulated sound pressure waveforms $p_t(x, y, z_2, t)$ with centre frequency $f = 775$ kHz are compared to measured waveforms, and simulated waveforms using the FEM approach, at three receiver positions '$*$' in Fig. 7.6(a) at $x = 0, 20, 40$ mm, respectively. Closer agreement between the two approaches and measurements in signal level and waveform is shown for $x = 0, 20$ mm, than for $x = 40$ mm, where the measured signal level show greater deviations to the simulated, as expected from Fig. 7.6(a).

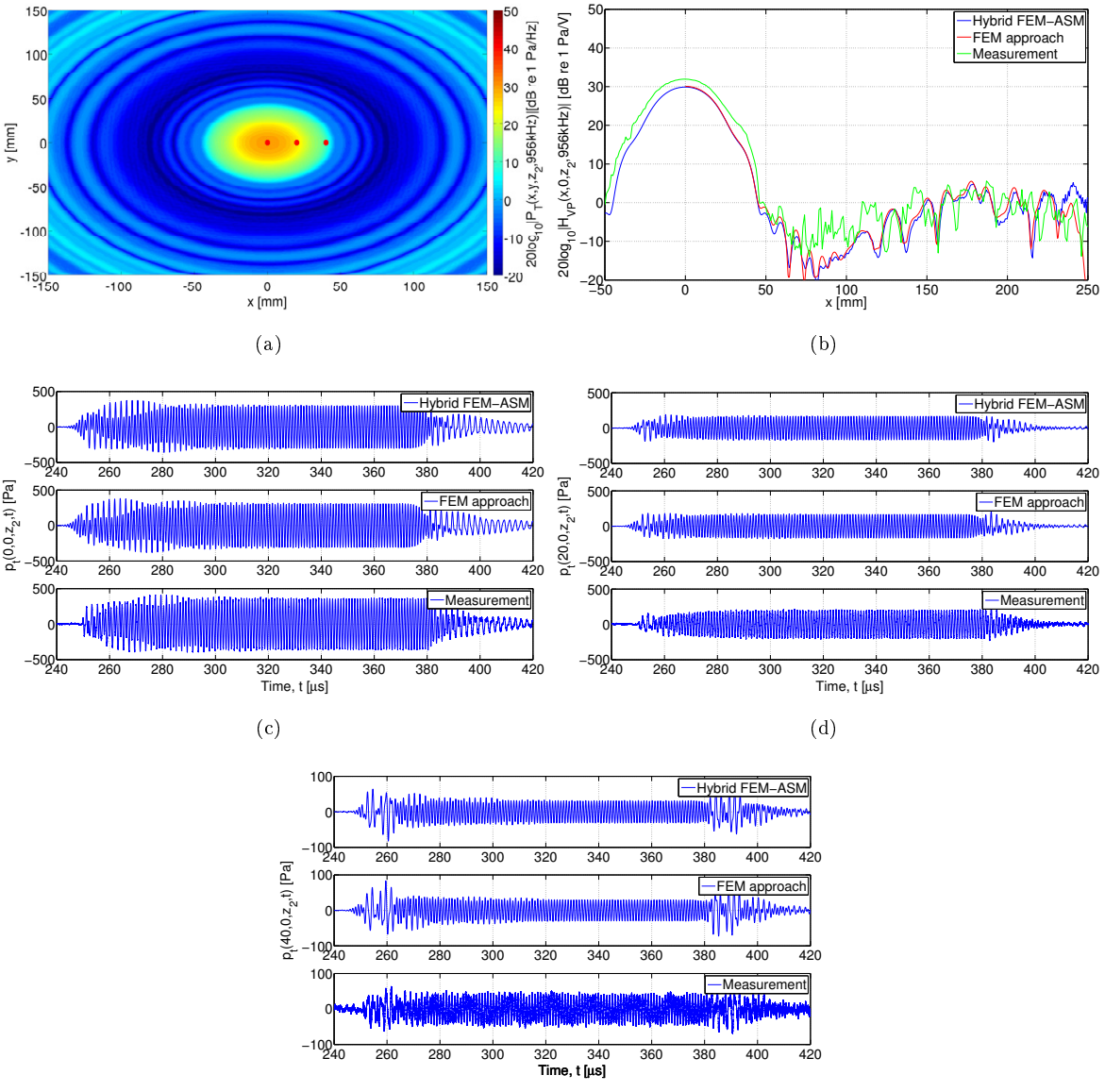

Fig 7.7. At normal beam incidence ($\theta = 0°$): Simulated magnitude of the transmitted pressure field distribution $|P_t(x, y, z_2, f)|$ at **a)** 956 kHz near the A_3 at 955.4 kHz. **b)** Simulated and measured $|P_t(x, 0, z_2, f)|$. Simulated and measured pressure waveforms $p_t(x, y, z_2, t)$ with centre frequency $f = 956$ kHz, at the receiver positions '$*$' in Fig. 7.7(a): **c)** at position $(0, 0, z_2)$, **d)** at position $(20, 0, z_2)$ and **e)** at position $(40, 0, z_2)$.

The deviations in the pulse arrival time are difficult to estimate, due to the different starting patterns

of the waveforms, they are 0.08, 0.23 and 0.93 for $x = 0, 20, 40$ mm, respectively. At $x = 0, 20$ mm, the FEM approach simulated waveforms does not reach a steady state, as the waveform steadily increases in this region. This will affect the calculation of $H_{VP}(x, y, z_2, f)$ in this frequency region. Fig. 7.7(a) shows the hybrid FEM-ASM simulated transmitted pressure field distribution $|P_t(x, y, z_2, f)|$ at a frequency of 956 kHz as function of $x-$ and $y-$positions, for constant $z = z_2$, close to the excitation frequency for plane-wave normal incidence of the A_3 at 955.4 kHz. Fig. 7.7(b) shows the hybrid FEM-ASM (blue line) and FEM (red line) calculated $|H_{VP}(x, 0, z_2, 956\text{kHz})|$ as function of $x-$position, in comparison with measurements (green line), cf. Fig. 6.15 for transmission through the plate. Agreement within 1.9 dB between simulations and mesurement is shown in the region $x = -50 - 50$ mm. Measurement noise is prominent for larger $x-$positions. In Figs. 7.7(c), 7.7(d) and 7.7(e) the simulated sound pressure waveforms $p_t(x, y, z_2, t)$ with centre frequency $f = 956$ kHz are compared to measured waveforms, and simulated waveforms using the FEM approach, at three receiver positions '$*$' in Fig. 7.7(a) at $x = 0, 20, 40$ mm. Agreement within 1.9 dB between the two approaches and measurements in signal level and waveform is shown for all positions, except the waveform at $x = 40$ mm. The deviations in the pulse arrival time between the simulated and measured waveforms are 3.44, 2.49 and 2.77 for $x = 0, 20, 40$ mm, respectively. The large deviations in the pulse arrival time for this frequency, in relation to the waveforms at lower frequencies shown earlier, can be explained by a too coarse element division at this frequency for FEM simulations, see Sect. 4.4 for FEM convergence tests. This will be further discussed in Sect. 7.9. As for the waveform near the S_1 mode in Fig. 7.4, the waveforms are broadbanded.

7.3 $\theta = 5^\circ$ beam incidence

In Fig. 7.8 the hybrid FEM-ASM calculated $|H_{VP}(x, 0, z_2, f)|$ is shown for a 5° beam incidence angle, as a function of frequency and x-position, at the receiver depth $z_2 = 376.05$ mm, in relation to Fig. 6.16, where the relative transmission through the plate is shown. The frequencies corresponding to the leaky Lamb modes S_1, S_2 and A_2 for a plane-wave incident angle $\theta_P = 5^\circ$ cf. Fig. 6.6 are 453.8 kHz, 581.1 kHz and 774.9 kHz, respectively, indicated at $x = 20$ mm in Fig. 7.8. The maxima are in the vicinity of the leaky Lamb modes, and demonstrates regions in space and frequency where the transmission through the system is relatively high. The black vertical lines show $x-$positions where the simulations are compared to measurements as a function of frequency, and the black horizontal lines show specific frequencies where the simulations are compared to measurements as a function of $x-$position. Similar plots are shown in [98, 95] for the piezoelectric transducer, and in [91, 92] for a piston generated beam pattern.

The hybrid FEM-ASM simulated voltage-to-pressure transfer function $|H_{VP}(x, 0, z_2, f)|$ at $x = 0$ mm, $x = 20$ mm, $x = 40$ mm and $x = 60$ mm in Fig. 7.8 (marked with lines) are shown (blue lines) in Fig. 7.9(a), 7.9(b), 7.9(c) and 7.9(d), respectively, as a function of frequency, and compared to measurement results (red lines). The corresponding relative transmission through the plate are shown in Fig. 6.17. The black vertical lines indicates frequencies where the transmitted waveforms are simulated and compared to measurements, cf. Figs. 7.11, 7.12 and 7.13. For $x = 0, 60$ mm in Figs.

7.9(a) and 7.9(d) respectively, an agreement within 1.8 dB to measurements is shown up to 750 kHz (near A_2 mode), but above this frequency there exists greater deviations. For $x = 20, 40$ mm in Figs. 7.9(b) and 7.9(c), an agreement within 3 dB to measurements is shown for the entire frequency range, except around the A_2 mode. The $x-$positions 0 mm and 60 mm are situated outside the transducer's main lobe at high frequencies, and is influenced by the higher order sidelobes. As the FEM calculated beam patterns show deviations to measurements beyond the main or first sidelobe, cf. Fig. 5.27, one expects greater deviations for the transmitted fields aswell.

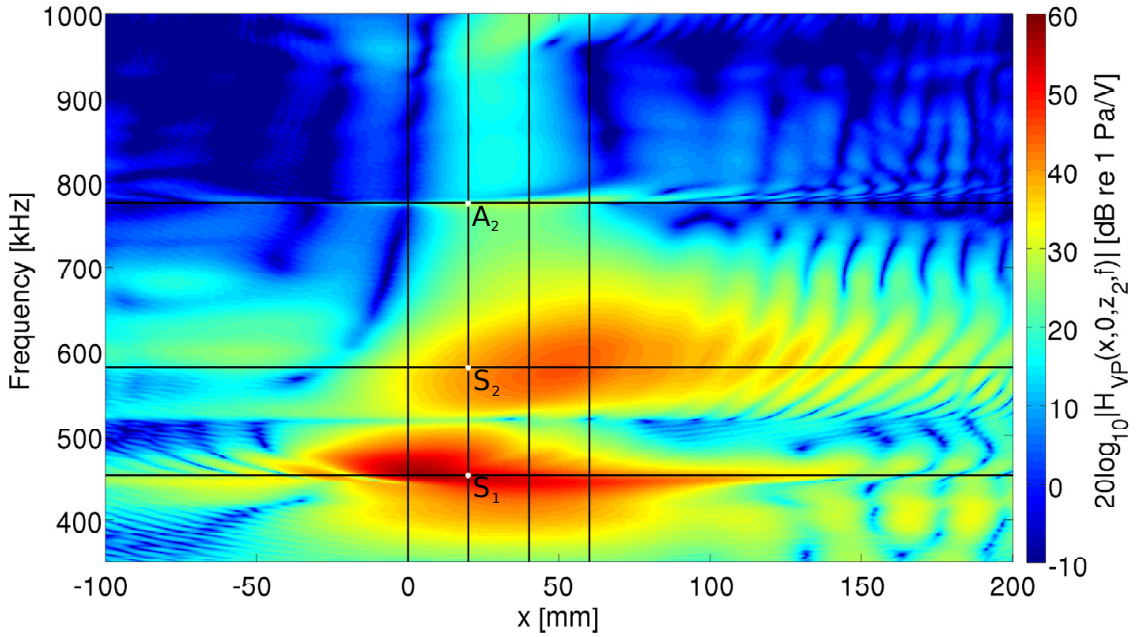

Fig 7.8. At $\theta = 5°$ beam incidence: Simulated magnitude of the voltage-to-pressure transfer function $|H_{VP}(x, 0, z_2, f)|$ using the hybrid FEM-ASM approach. Solid lines indicate the $x-$distances addressed in Fig. 7.9, and frequencies in Figs. 7.11, 7.12 and 7.13. Leaky Lamb modes for a plane-wave incident angle $\theta_P = 5°$ are indicated at their respective frequencies at $x = 20$ mm.

Figs. 7.10(a), 7.10(b) and 7.10(c) show the magnitude of the hybrid FEM-ASM simulated pressure field distribution $|P(x, 0, z, f)|$ at $f = 454$ kHz, $f = 581$ kHz and $f = 775$ kHz as a function of $x-$ and $z-$positions, respectively, near the leaky Lamb modes for $\theta_P = 5°$. The incident pressure field produced by, and propagated from, the piezoelectric transducer towards the plate, and the pressure field transmitted through the plate, is presented. For $f = 454$ kHz (near the S_1 mode) and $f = 775$ kHz (near the A_2 mode) in Figs. 7.10(a) and 7.10(c) respectively, the plate causes a beam displacement, in addition to a beam narrowing effect. While for $f = 581$ kHz (near the S_2 mode) in Fig. 7.10(b), the plate causes a beam narrowing effect. For all frequencies, an interference pattern can be seen below the plate, due to the superposition of a geometrically transmitted field and a leaky transmitted field due to the leaky guided wave motion inside the plate.

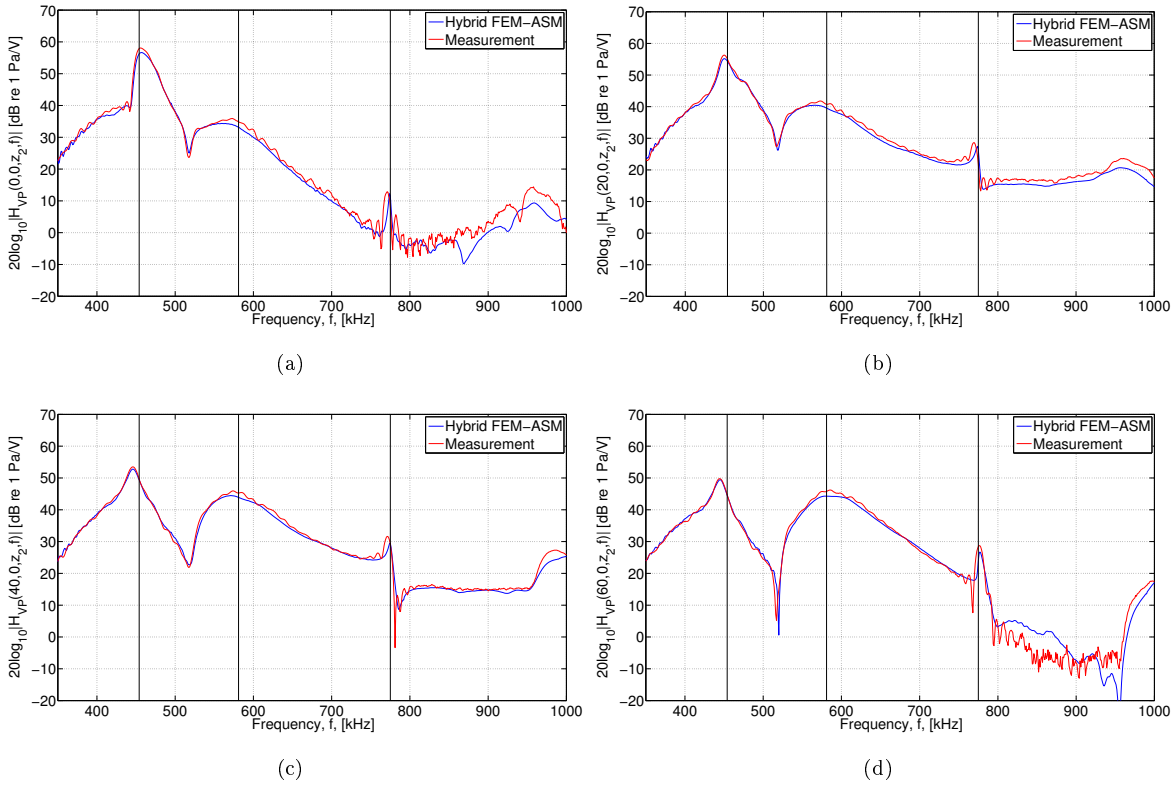

Fig 7.9. At $\theta = 5°$ beam incidence: Simulated magnitude of the voltage-to-pressure transfer function $|H_{VP}(x, 0, z_2, f)|$ using the hybrid FEM-ASM approach (blue line) in comparison with measurements (red line) for **a)** $x = 0$ mm, **b)** $x = 20$ mm, **c)** $x = 40$ mm and **d)** $x = 60$ mm. The frequency spectra at the four $x-$distances are indicated with solid lines in Fig. 7.8.

Fig. 7.11(a) shows the hybrid FEM-ASM simulated transmitted pressure field distribution $|P_t(x, y, z_2, f)|$ at a frequency of 454 kHz as a function of $x-$ and $y-$positions, for a constant $z = z_2$, close to the excitation frequency for a $\theta_P = 5°$ plane-wave incidence of the S_1 at 453.8 kHz. Fig. 7.11(b) shows the hybrid FEM-ASM (blue line) calculated $|H_{VP}(x, 0, z_2, 454\text{kHz})|$ as function of $x-$position, in comparison with measurements (red line), cf. Fig. 6.18 for the transmission through the plate. An agreement within 3.7 dB to measurement is shown for the entire region. In Figs. 7.11(c), 7.11(d), 7.11(e) and 7.11(f) the simulated sound pressure waveforms $p_t(x, y, z_2, t)$ with centre frequency $f = 454$ kHz are compared to measured waveforms at four receiver positions '$*$' in Fig. 7.11(a) at $x = 0, 20, 40, 60$ mm, respectively. Agreement within 1.4 dB between the simulations and measurements in signal level, bandwidth and waveform are shown, as expected from Fig.7.11(b). The deviations in the pulse arrival time between simulated and measured waveforms are 0.02, 0.02, 0.09 and 0.09 for $x = 0, 20, 40, 60$ mm, respectively.

Fig. 7.12(a) shows the hybrid FEM-ASM simulated transmitted pressure field distribution $|P_t(x, y, z_2, f)|$ at a frequency of 581 kHz as a function of $x-$ and $y-$positions, for a constant $z = z_2$, close to the excitation frequency for a $\theta_P = 5°$ plane-wave incidence of the S_2 at 581.1 kHz. The interference pattern present in Fig. 7.10(b) can be seen. Fig. 7.12(b) shows the hybrid FEM-ASM (blue line)

calculated $|H_{VP}(x, 0, z_2, 581\text{kHz})|$ as function of $x-$position, in comparison with measurements (red line), cf. Fig. 6.18 for the transmission through the plate. An agreement within 1.6 dB for the region $x = -10 - 50$ mm is shown, and the behaviour of the interference pattern is correctly simulated. In Figs. 7.12(c), 7.12(d), 7.12(e) and 7.12(f) the simulated sound pressure waveforms $p_t(x, y, z_2, t)$ with centre frequency $f = 581$ kHz are compared to measured waveforms at four receiver positions '$*$' in Fig. 7.12(a) at $x = 0, 20, 40, 60$ mm, respectively. The same conclusions as for the waveforms in Fig. 7.11 can be made. The deviations in the pulse arrival time between simulated and measured waveforms are 0.35, 0.4, 0.35 and 0.4 for $x = 0, 20, 40, 60$ mm, respectively. Fig. 7.13(a) shows the hybrid FEM-ASM simulated transmitted pressure field distribution $|P_t(x, y, z_2, f)|$ at a frequency of 775 kHz as a function of $x-$ and $y-$positions, for a constant $z = z_2$, close to the excitation frequency for a $\theta_P = 5°$ plane-wave incidence of the A_2 at 774.9 kHz. Fig. 7.13(b) shows the hybrid FEM-ASM (blue line) calculated $|H_{VP}(x, 0, z_2, 775\text{kHz})|$ as function of $x-$position, in comparison with measurements (red line), cf. Fig. 6.18 for transmission through the plate. In Figs. 7.13(c), 7.13(d), 7.13(e) and 7.13(f) the simulated sound pressure waveforms $p_t(x, y, z_2, t)$ with centre frequency $f = 775$ kHz are compared to measured waveforms at four receiver positions '$*$' in Fig. 7.13(a) at $x = 0, 20, 40, 60$ mm, respectively. Agreement within 1.7 dB between the simulations and measurements in bandwidth and waveform are shown, with some deviations in signal level, as expected from Fig. 7.13(b). For $x = 20, 40$ the signal level of the simulated waveforms increases, while the measurements decreases for $x = 20$, while

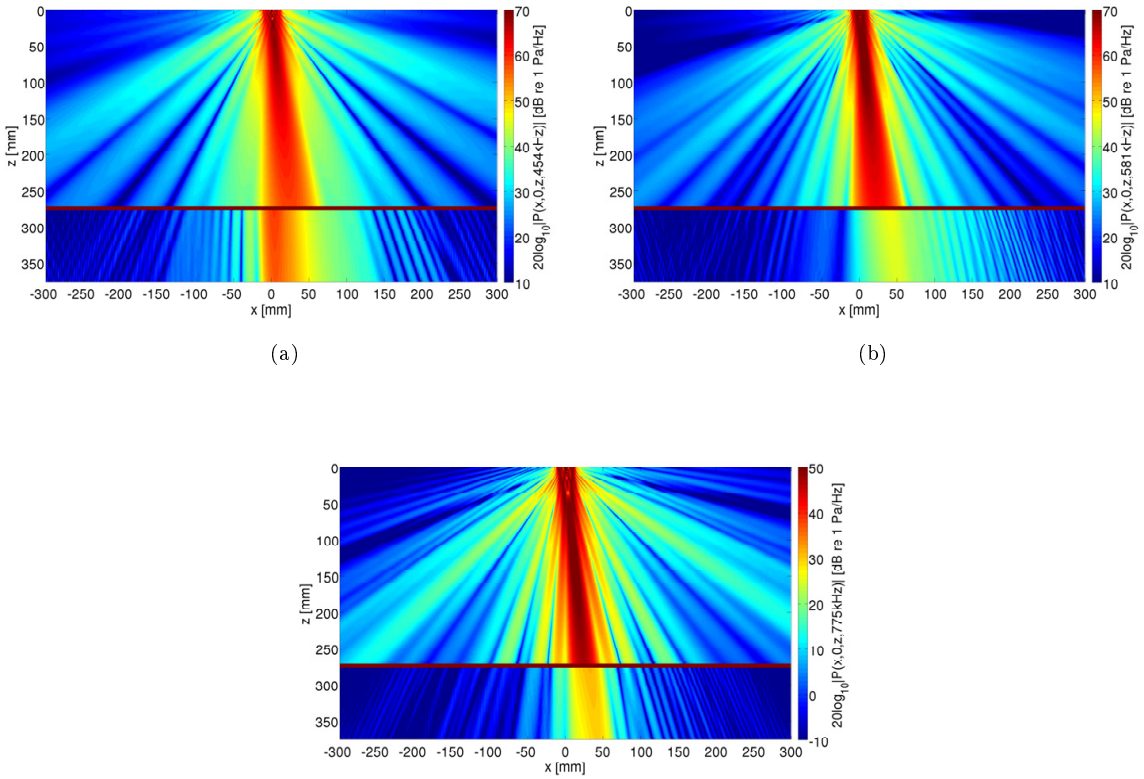

(a) (b)

(c)

Fig 7.10. At ($\theta = 5°$) beam incidence: Simulated magnitude of the pressure field distribution $|P(x, 0, z, f)|$, **a)** at $f = 454$ kHz, **b)** at $f = 581$ kHz and **c)** at $f = 775$ kHz, using the hybrid FEM-ASM approach.

increases at $x = 40, 60$ mm. This influences the calculations of the measurement results, which assumes a steady state region of each transmitted waveform. The measurement results in Fig. 7.13(f) are therefore calculated from the very beginning of the steady state region. To correct this, another method for determining $|P_t(x, y, z_2, f)|$ must be implemented. The deviations in the pulse arrival time between simulated and measured waveforms are 0.08, 1.47, 1.16 and 0.31 for $x = 0, 20, 40, 60$ mm, respectively.

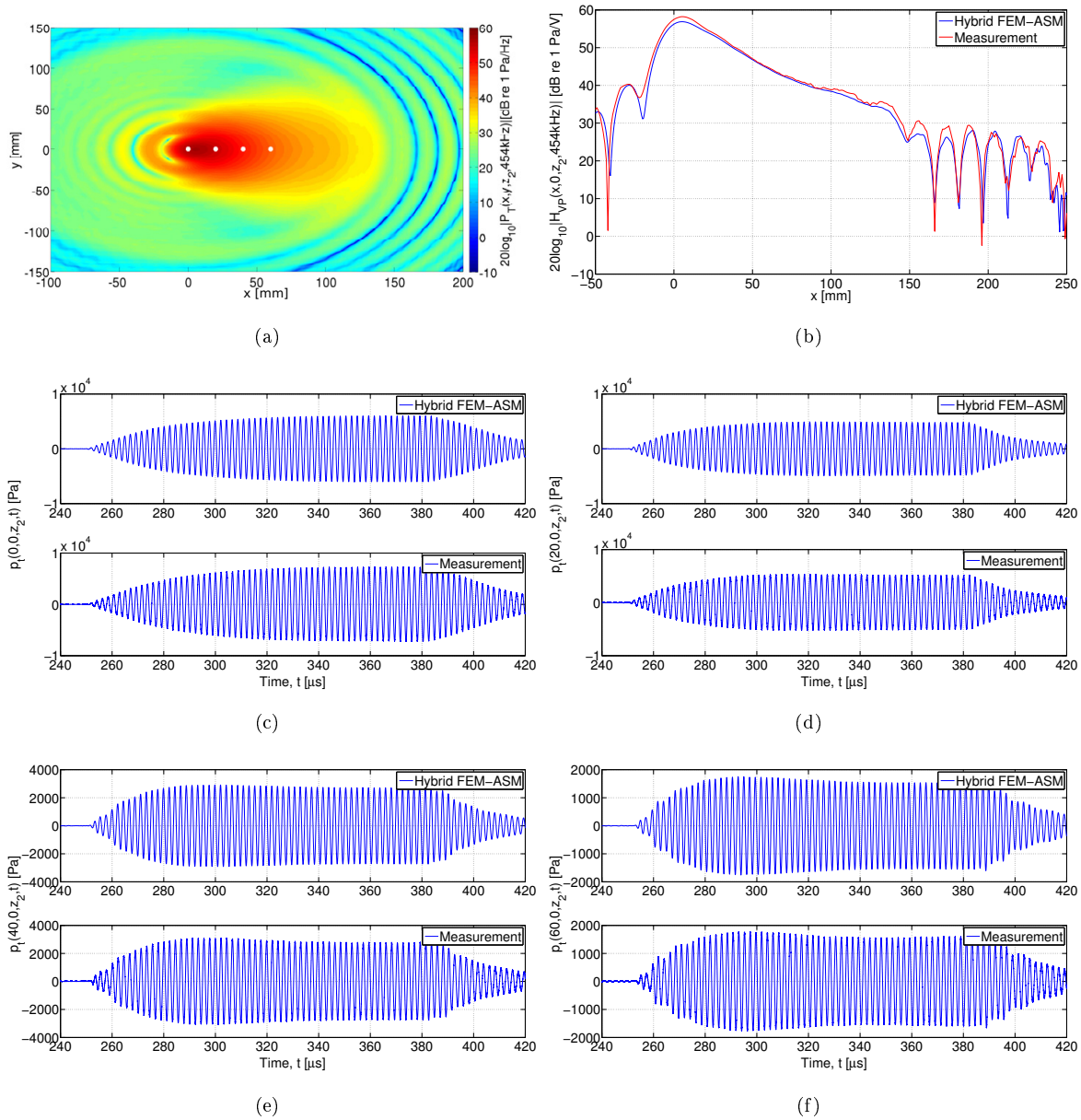

Fig 7.11. At $\theta = 5°$ beam incidence: Simulated magnitude of the transmitted pressure field distribution $|P_t(x, y, z_2, f)|$ at **a)** 454 kHz near the S_1 at 453.8 kHz. **b)** Simulated and measured $|P_t(x, 0, z_2, f)|$. Simulated and measured pressure waveforms $p_t(x, y, z_2, t)$ with centre frequency $f = 454$ kHz, at the receiver positions '$*$' in Fig. 7.11(a): **c)** at position $(0, 0, z_2)$, **d)** at position $(20, 0, z_2)$, **e)** at position $(40, 0, z_2)$ and **f)** at position $(60, 0, z_2)$.

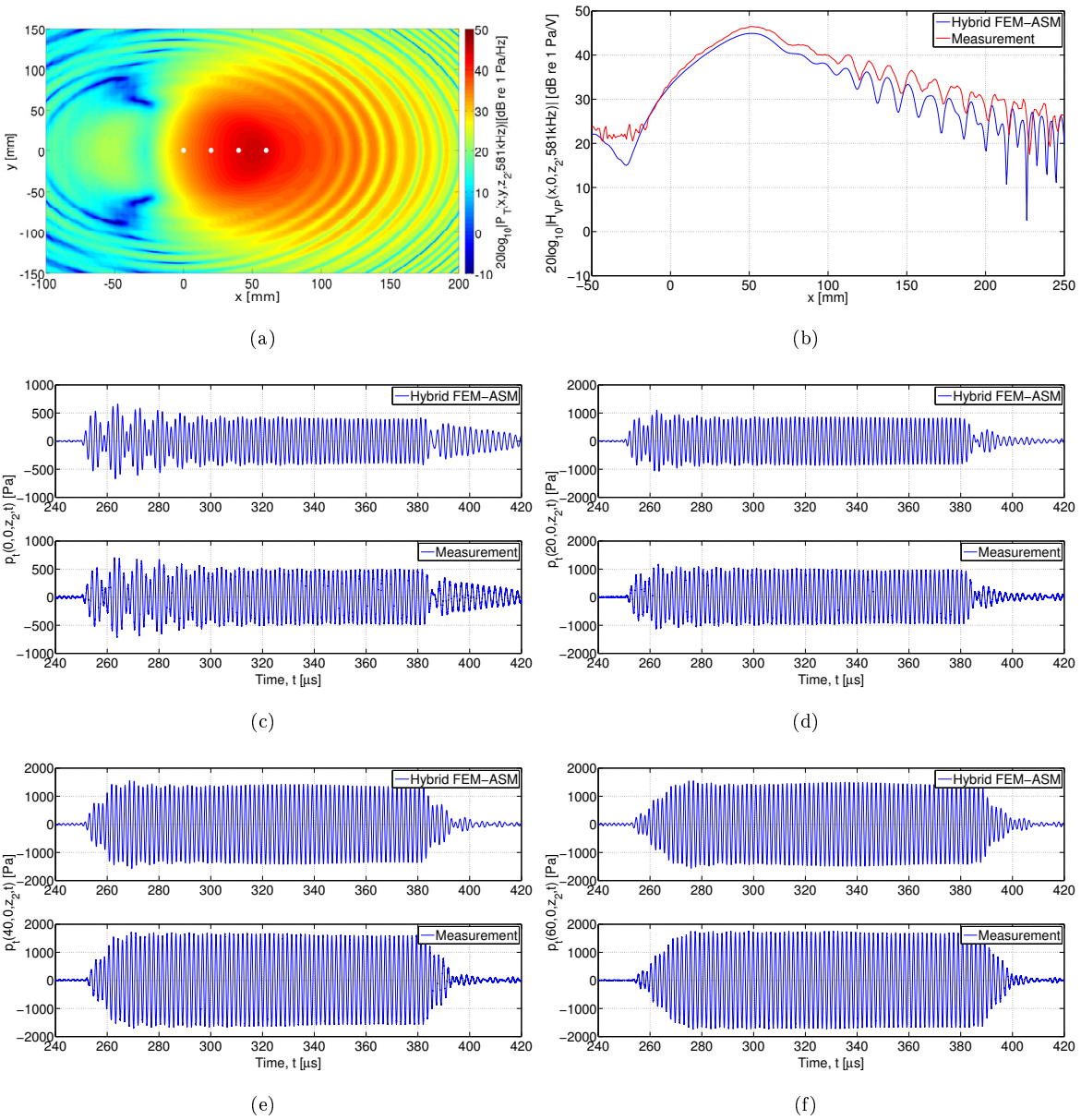

Fig 7.12. At $\theta = 5°$ beam incidence: Simulated magnitude of the transmitted pressure field distribution $|P_t(x, y, z_2, f)|$ at **a)** 581 kHz near the S_2 at 581.1 kHz. **b)** Simulated and measured $|P_t(x, 0, z_2, f)|$. Simulated and measured pressure waveforms $p_t(x, y, z_2, t)$ with centre frequency $f = 581$ kHz, at the receiver positions '$*$' in Fig. 7.12(a): **c)** at position $(0, 0, z_2)$, **d)** at position $(20, 0, z_2)$, **e)** at position $(40, 0, z_2)$ and **f)** at position $(60, 0, z_2)$.

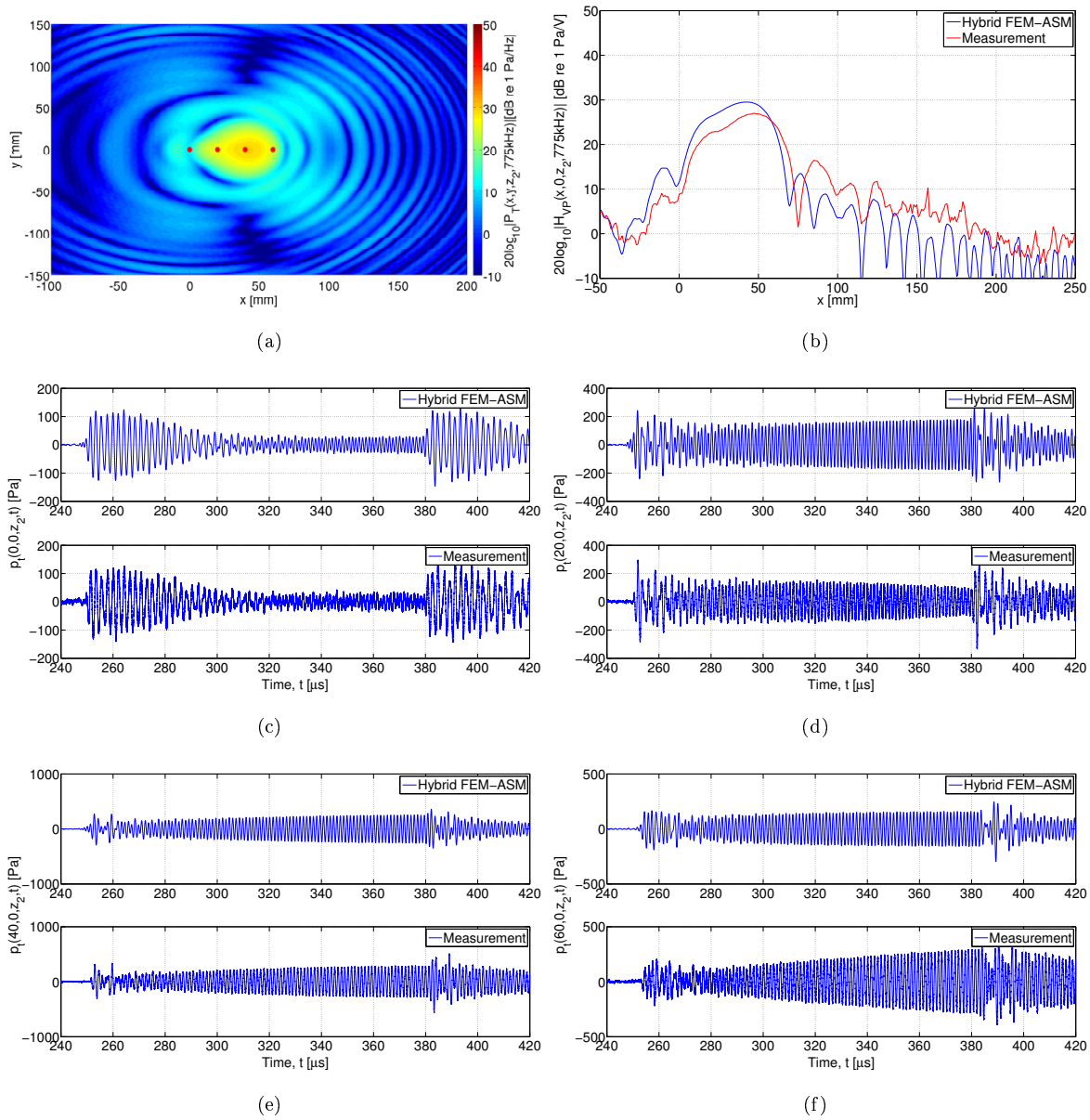

Fig 7.13. At $\theta = 5°$ beam incidence: Simulated magnitude of the transmitted pressure field distribution $|P_t(x, y, z_2, f)|$ at **a)** 775 kHz near the A_2 at 774.9 kHz. **b)** Simulated and measured $|P_t(x, 0, z_2, f)|$. Simulated and measured pressure waveforms $p_t(x, y, z_2, t)$ with centre frequency $f = 775$ kHz, at the receiver positions '$*$' in Fig. 7.13(a): **c)** at position $(0, 0, z_2)$, **d)** at position $(20, 0, z_2)$, **e)** at position $(40, 0, z_2)$ and **f)** at position $(60, 0, z_2)$.

7.4 $\theta = 10°$ beam incidence

In Fig. 7.14 the hybrid FEM-ASM calculated $|H_{VP}(x, 0, z_2, f)|$ is shown for a 10° beam incidence angle, as a function of frequency and x-position, at the receiver depth $z_2 = 376.05$ mm, in relation to Fig. 6.19. The frequencies corresponding to the leaky Lamb modes S_1, S_2 and A_2 for a plane-wave incident angle $\theta_P = 10°$ cf. Fig. 6.6 are 447.3 kHz, 738.6 kHz and 806.1 kHz, respectively, indicated at $x = 60$ mm in Fig. 7.14. The maxima are in the vicinity of the leaky Lamb modes, and demonstrates

regions in space and frequency where the transmission through the system is relatively high. The black vertical lines show $x-$positions where the simulations are compared to measurements as a function of frequency, and the black horizontal lines show specific frequencies where the simulations are compared to measurements as a function of $x-$position. Similar plots are shown in [95] for the piezoelectric transducer, and in [91, 92] for a piston generated beam pattern.

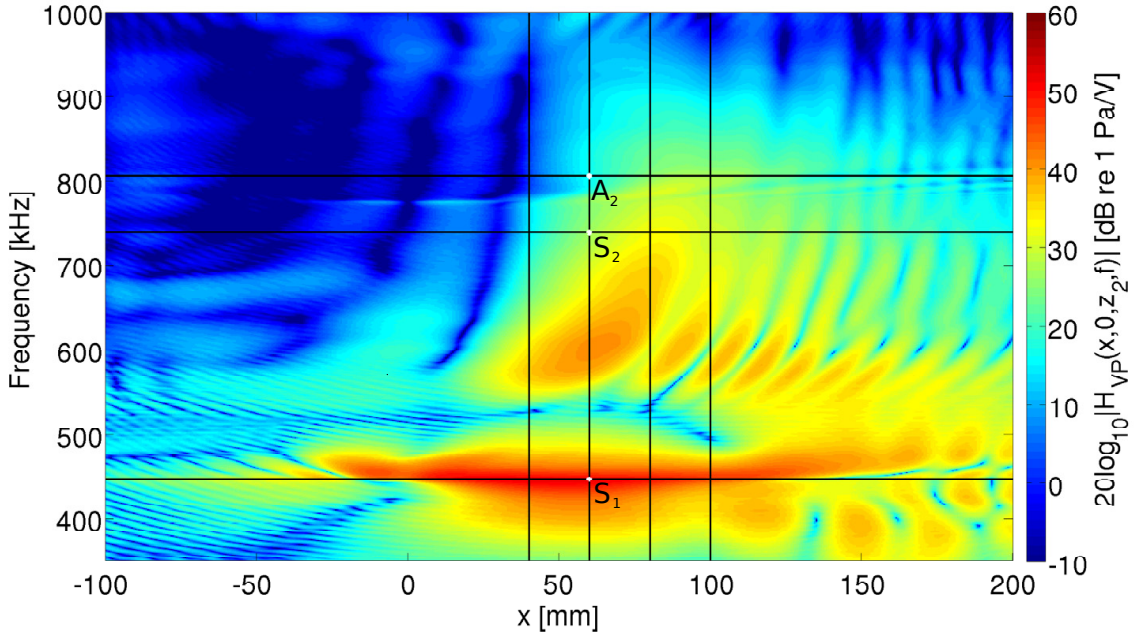

Fig 7.14. At $\theta = 10°$ beam incidence: Simulated magnitude of the voltage-to-pressure transfer function $|H_{VP}(x, 0, z_2, f)|$ using the hybrid FEM-ASM approach. Solid lines indicate the $x-$distances addressed in Fig. 7.15, and frequencies in Figs. 7.17, 7.18 and 7.19. Leaky Lamb modes for a plane-wave incident angle $\theta_P = 10°$ are indicated at their respective frequencies at $x = 60$ mm.

The hybrid FEM-ASM simulated voltage-to-pressure transfer function $|H_{VP}(x, 0, z_2, f)|$ at $x = 40$ mm, $x = 60$ mm, $x = 80$ mm and $x = 100$ mm in Fig. 7.14 (marked with lines) are shown (blue lines) in Fig. 7.15(a), 7.15(b), 7.15(c) and 7.15(d), respectively, as a function of frequency, and compared to measurement results (red lines). The corresponding relative transmission through the plate are shown in Fig. 6.20. The black vertical lines indicates frequencies where the transmitted waveforms are simulated and compared to measurements, cf. Figs. 7.17, 7.18 and 7.19. For all $x-$positions an agreement within 2 dB between simulations and measurements is shown for the entire frequency range, with some exceptions.

Figs. 7.16(a), 7.16(b) and 7.16(c) show the magnitude of the hybrid FEM-ASM simulated pressure field distribution $|P(x, 0, z, f)|$ at $f = 448$ kHz, $f = 739$ kHz and $f = 806$ kHz as a function of $x-$ and $z-$ positions, respectively, near the leaky Lamb modes for $\theta_P = 10°$. The incident pressure field produced by, and propagated from, the piezoelectric transducer towards the plate, and the pressure field transmitted through the plate, is presented. For $f = 448$ kHz (near the S_1 mode) in Fig. 7.16(a) the plate causes a beam displacement and beam narrowing effect. While for $f = 739$ kHz (near the S_2

mode) and $f = 806$ kHz (near the A_2 mode) in Figs. 7.16(b) and 7.16(c) respectively, the plate causes a beam narrowing effect only. An interference pattern is shown, as for a 5° beam incidence angle in Fig. 7.10, caused by the superposition of a geometrically transmitted field and a leaky field due to the leaky guided wave motion inside the plate. For all frequencies, some aliasing effects in the region $x = (-300) - (-200)$ mm can be experienced, this will be further discussed in Sect. 7.9.

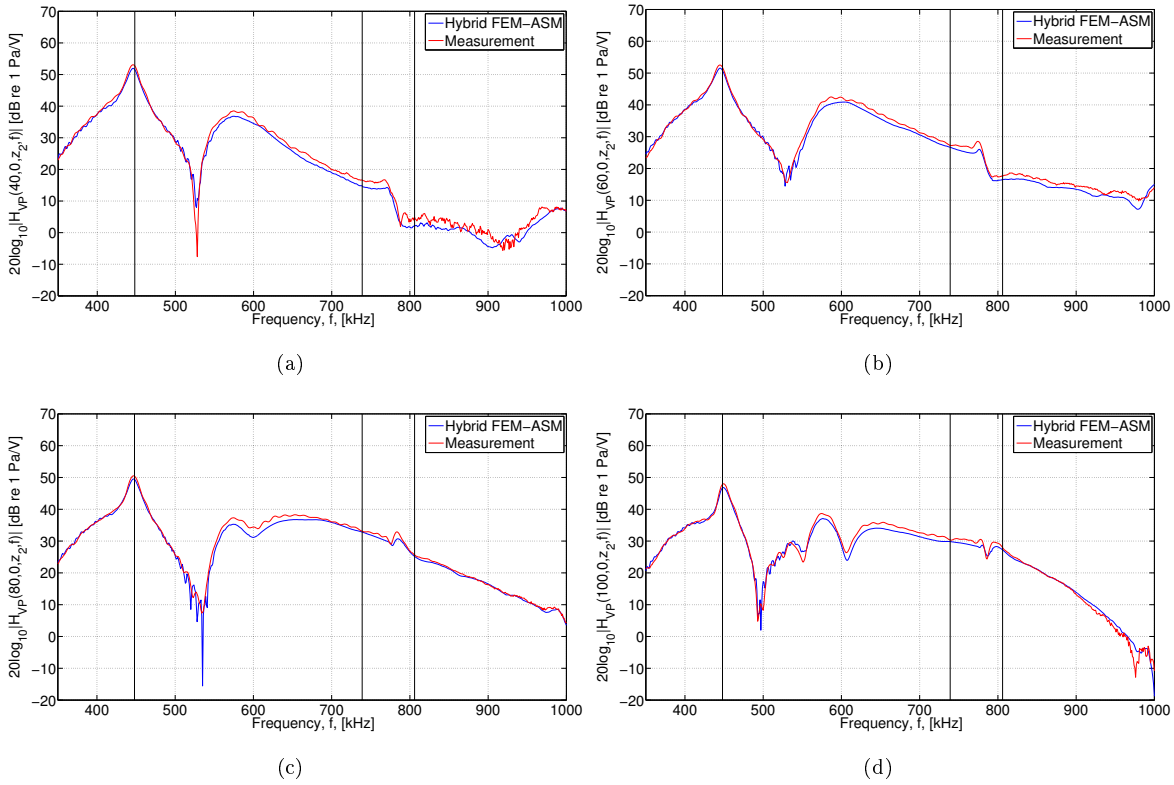

Fig 7.15. At $\theta = 10°$ beam incidence: Simulated magnitude of the voltage-to-pressure transfer function $|H_{VP}(x, 0, z_2, f)|$ using the hybrid FEM-ASM approach (blue line) in comparison with measurements (red line) for **a)** $x = 40$ mm, **b)** $x = 60$ mm, **c)** $x = 80$ mm and **d)** $x = 100$ mm. The frequency spectra at the four $x-$distances are indicated with solid lines in Fig. 7.14.

Fig. 7.17(a) shows the hybrid FEM-ASM simulated transmitted pressure field distribution $|P_t(x, y, z_2, f)|$ at a frequency of 448 kHz as a function of $x-$ and $y-$positions, for a constant $z = z_2$, close to the excitation frequency for a $\theta_P = 10°$ plane-wave incidence of the S_1 at 447.3 kHz. Fig. 7.17(b) shows the hybrid FEM-ASM (blue line) calculated $|H_{VP}(x, 0, z_2, 448\text{kHz})|$ as function of $x-$position, in comparison with measurements (red line), cf. Fig. 6.21 for transmission through the plate. An agreement within 2.4 dB between simulations and measurements is shown for up to $x = 130$ mm, at high $x-$positions the noise becomes a dominant part of the measurement results. In Figs. 7.17(c), 7.17(d), 7.17(e) and 7.17(e) the simulated sound pressure waveforms $p_t(x, y, z_2, t)$ with centre frequency $f = 448$ kHz are compared to measured waveforms at four receiver positions '$*$' in Fig. 7.17(a) at $x = 40, 60, 80, 100$ mm, respectively. Agreement within 1.2 dB between the simulated and measured waveforms in bandwidth, signal level and waveform is shown, as expected from Fig. 7.17(b). The deviations in the pulse arrival time between simulated and measured waveforms are 0.09, 0.05, 0.31 and 0.36 for $x = 40, 60, 80, 100$

mm, respectively.

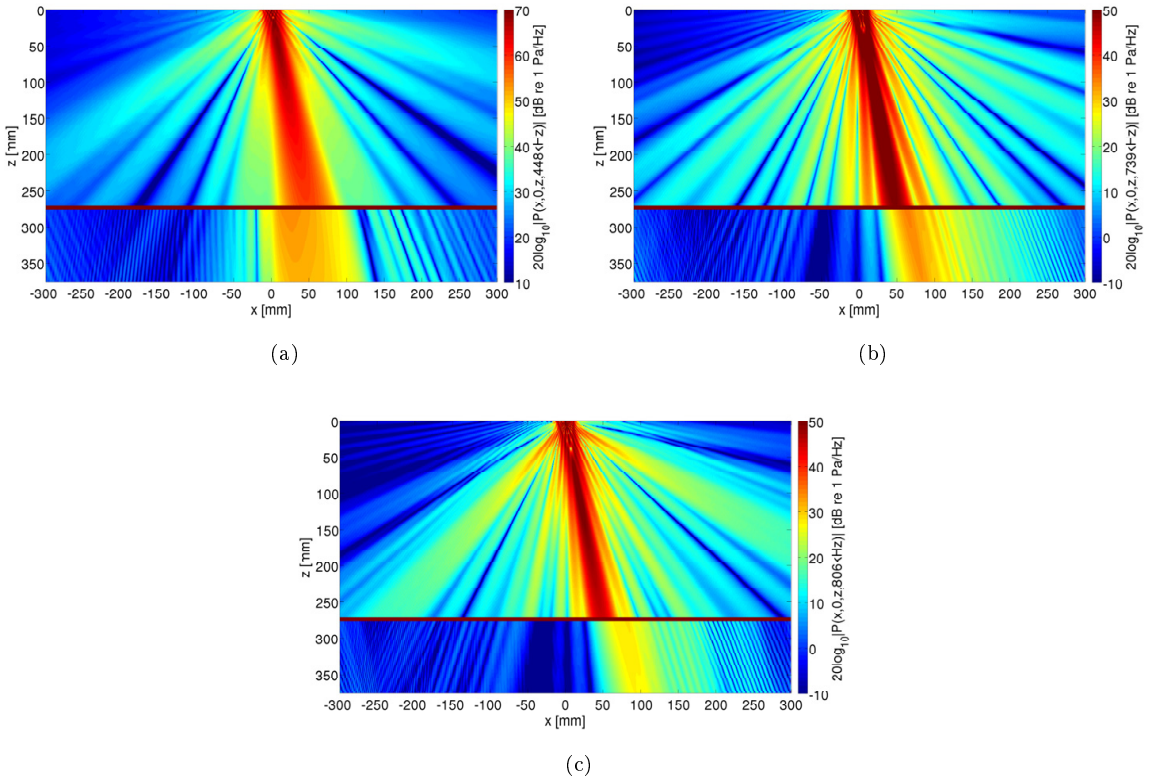

Fig 7.16. At ($\theta = 10°$) beam incidence: Simulated magnitude of the pressure field distribution $|P(x, 0, z, f)|$, **a)** at $f = 448$kHz, **b)** at $f = 739$ kHz and **c)** at $f = 806$ kHz, using the hybrid FEM-ASM approach.

Fig. 7.18(a) shows the hybrid FEM-ASM simulated transmitted pressure field distribution $|P_t(x, y, z_2, f)|$ at a frequency of 739 kHz as a function of $x-$ and $y-$positions, for a constant $z = z_2$, close to the excitation frequency for a $\theta_P = 10°$ plane-wave incidence of the S_2 at 738.6 kHz. Fig. 7.18(b) shows the hybrid FEM-ASM (blue line) calculated $|H_{VP}(x, 0, z_2, 739\text{kHz})|$ as function of $x-$position, in comparison with measurements (red line), cf. Fig. 6.21 for transmission through the plate. An agreement within 0.8 dB between simulations and measurements is shown in the region $x = 30 - 100$ mm, outside this region noise becomes a dominant part of the measurement results. Also, in this region the higher order sidelobes contributes to the overall transmission. Hence, greater deviations due to the deviations in the beam patterns in Fig. 5.27. In Figs. 7.18(c), 7.18(d), 7.18(e) and 7.18(e) the simulated sound pressure waveforms $p_t(x, y, z_2, t)$ with centre frequency $f = 739$ kHz are compared to measured waveforms at four receiver positions '$*$' in Fig. 7.18(a) at $x = 40, 60, 80, 100$ mm, respectively. Agreement within 0.8 dB between simulated and measured waveforms for bandwidth, signal level and waveform is shown. The deviations in the pulse arrival time between simulated and measured waveforms are 0.07, 0.07, 0.59 and 0.51 for $x = 40, 60, 80, 100$, respectively. Fig. 7.19(a) shows the hybrid FEM-ASM simulated transmitted pressure field distribution $|P_t(x, y, z_2, f)|$ at a frequency of 806 kHz as a function of $x-$ and $y-$positions, for a constant $z = z_2$, close to the excitation frequency for a $\theta_P = 10°$ plane-wave incidence of the A_2 at 806.1 kHz. Fig. 7.19(b) shows the hybrid FEM-ASM (blue line) calculated

$|H_{VP}(x, 0, z_2, 806\text{kHz})|$ as function of $x-$position, in comparison with measurements (red line). An agreement within 2.2 dB is shown in the region $x = 40 - 150$ mm, although for $x-$positions above

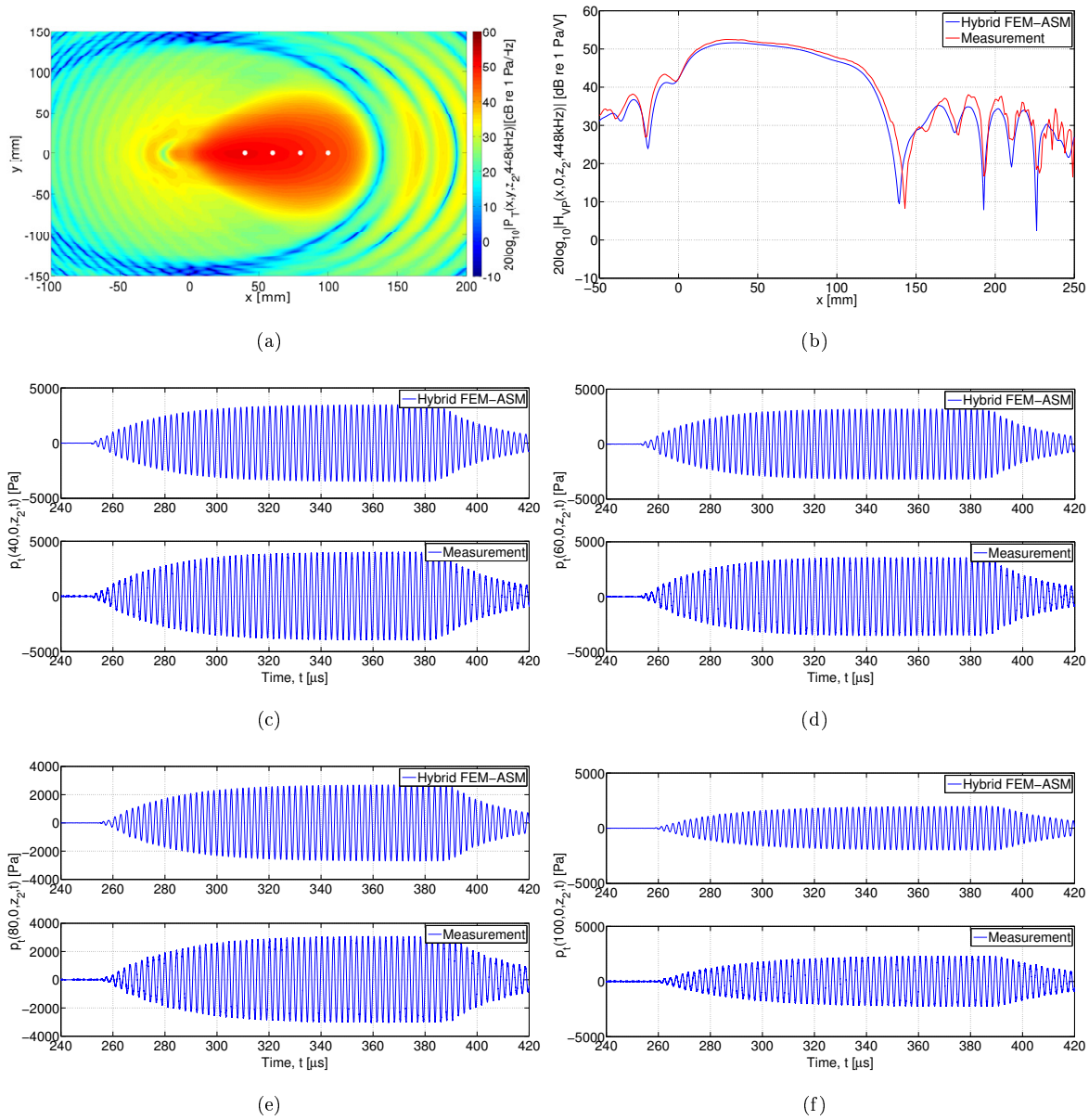

Fig 7.17. At $\theta = 10°$ beam incidence: Simulated magnitude of the transmitted pressure field distribution $|P_t(x, y, z_2, f)|$ at **a)** 448 kHz near the S_1 at 447.3 kHz. **b)** Simulated and measured $|P_t(x, 0, z_2, f)|$. Simulated and measured pressure waveforms $p_t(x, y, z_2, t)$ with centre frequency $f = 448$ kHz, at the receiver positions '$*$' in Fig. 7.17(a): **c)** at position $(40, 0, z_2)$, **d)** at position $(60, 0, z_2)$, **e)** at position $(80, 0, z_2)$ and **f)** at position $(100, 0, z_2)$.

150 mm, the simulations still follows the behaviour of the measured interference pattern. In Figs. 7.19(c), 7.19(d), 7.19(e) and 7.19(e) the simulated sound pressure waveforms $p_t(x, y, z_2, t)$ with centre frequency $f = 806$ kHz are compared to measured waveforms at four receiver positions '$*$' in Fig. 7.19(a) at $x = 40, 60, 80, 100$ mm, respectively. The same conclusion regarding waveform, bandwidth and signal level can be made as for Fig. 7.18, deviations within 1.3 dB. The deviations in the pulse arrival

time between simulated and measured waveforms are 0.16, 0.24, 0.72 and 0.64 for $x = 40, 60, 80, 100$, respectively. As for other waveforms at high frequencies, e.g. Fig. 7.7, the numerical errors in the simulated time arrival increases with frequency, as the FE element division decreases, cf. convergence tests in Sect. 4.4. Another reason for the deviations in the transient region of the pulses, is that the transfer function $H_{VP}(x, y, z_2, f)$ is only simulated up to 1.2 MHz. The transient region for high frequency (above 700-800 kHz) waveforms could be improved by extending the transfer function to

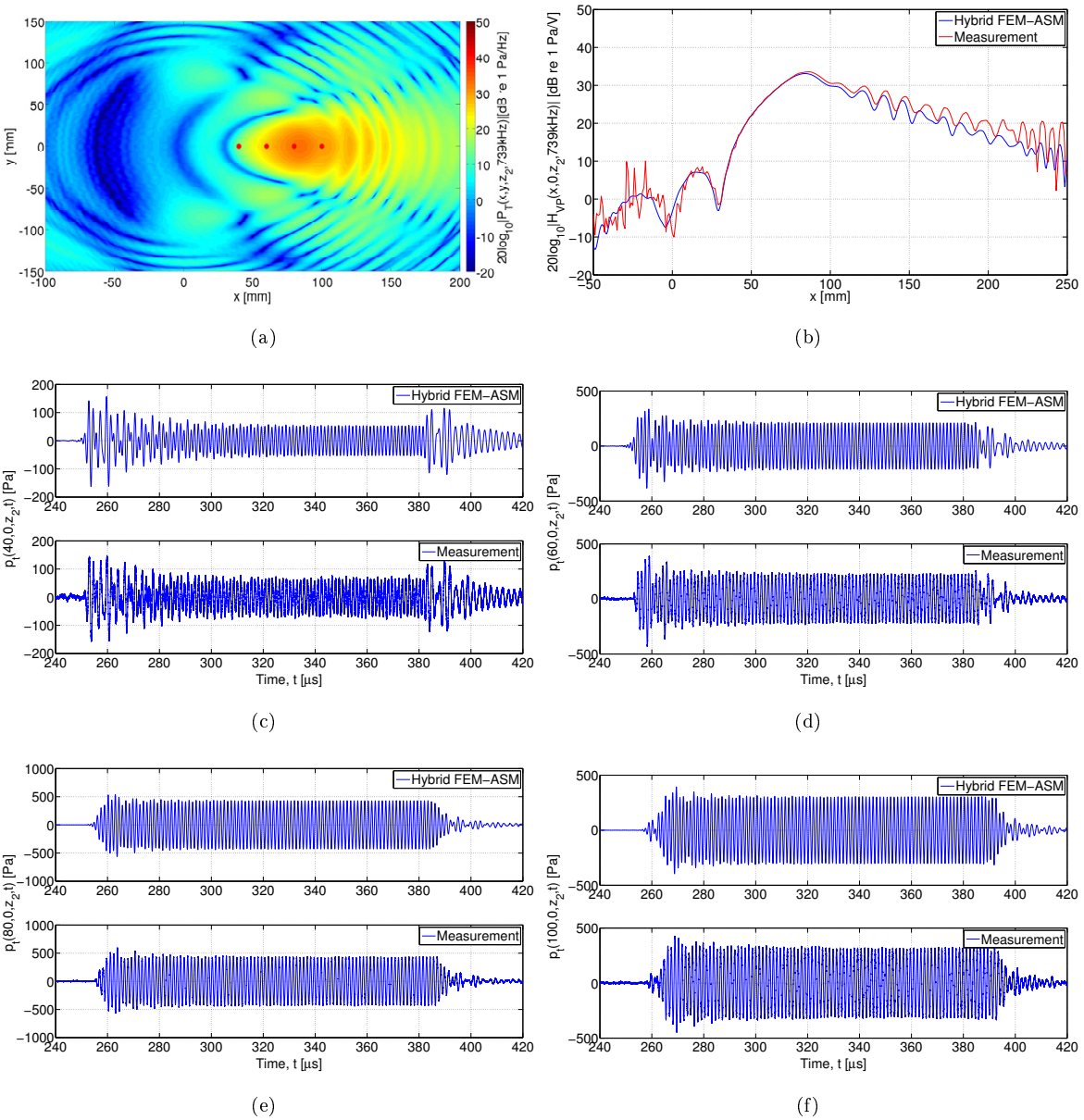

Fig 7.18. At $\theta = 10°$ beam incidence: Simulated magnitude of the transmitted pressure field distribution $|P_t(x, y, z_2, f)|$ at **a)** 739 kHz near the S_2 at 738.6 kHz. **b)** Simulated and measured $|P_t(x, 0, z_2, f)|$. Simulated and measured pressure waveforms $p_t(x, y, z_2, t)$ with centre frequency $f = 739$ kHz, at the receiver positions '$*$' in Fig. 7.18(a): **c)** at position $(40, 0, z_2)$, **d)** at position $(60, 0, z_2)$, **e)** at position $(80, 0, z_2)$ and **f)** at position $(100, 0, z_2)$.

higher frequencies beyond 1.2 MHz, and using a finer FE division. This is further discussed in Sect. 7.9.

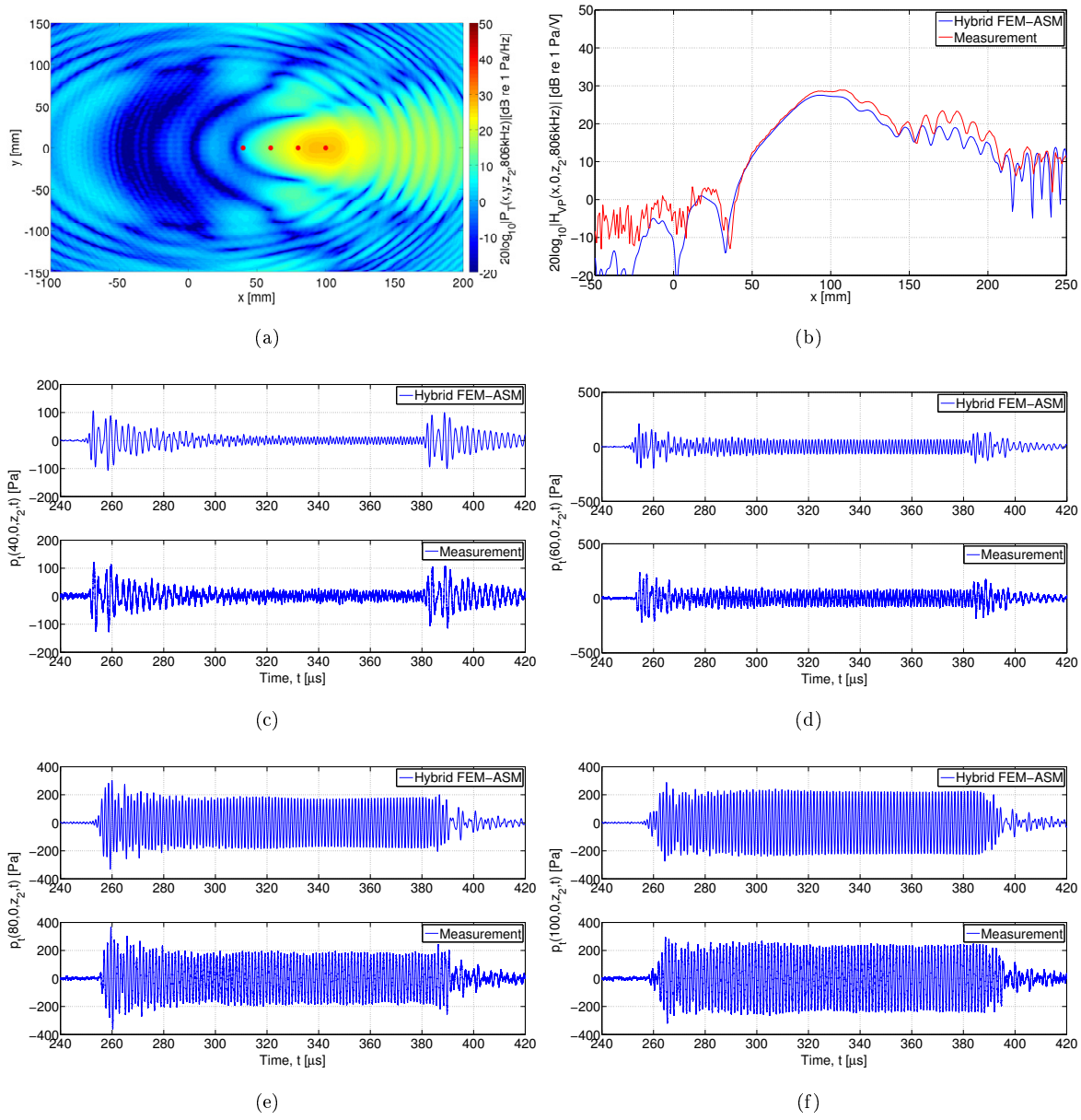

Fig 7.19. At $\theta = 10°$ beam incidence: Simulated magnitude of the transmitted pressure field distribution $|P_t(x, y, z_2, f)|$ at **a)** 806 kHz near the A_2 at 806.1 kHz. **b)** Simulated and measured $|P_t(x, 0, z_2, f)|$. Simulated and measured pressure waveforms $p_t(x, y, z_2, t)$ with centre frequency $f = 806$ kHz, at the receiver positions '$*$' in Fig. 7.19(a): **c)** at position $(40, 0, z_2)$, **d)** at position $(60, 0, z_2)$, **e)** at position $(80, 0, z_2)$ and **f)** at position $(100, 0, z_2)$.

7.5 $\theta = 15°$ beam incidence

In Fig. 7.20 the hybrid FEM-ASM simulated $|H_{VP}(x, 0, z_2, f)|$ is shown for a 15° beam incidence angle, as a function of frequency and x-position, at the receiver depth $z_2 = 376.05$ mm, in relation to Fig.

6.22. The frequencies corresponding to the leaky Lamb modes A_1 and S_1 for a plane-wave incident angle $\theta_P = 15°$ cf. Fig. 6.6 are 523.9 kHz and 631.9 kHz, respectively, indicated at $x = 120$ mm in Fig. 7.20. The maxima are in the vicinity of the leaky Lamb modes, and demonstrates regions in space and frequency where the transmission through the system is relatively high. The black vertical lines show $x-$positions where the simulations are compared to measurements as a function of frequency, and the black horizontal lines show specific frequencies where the simulations are compared to measurements as function of $x-$position. Similar plots are shown in [95] for the piezoelectric transducer, and in [91, 92] for a piston generated beam pattern.

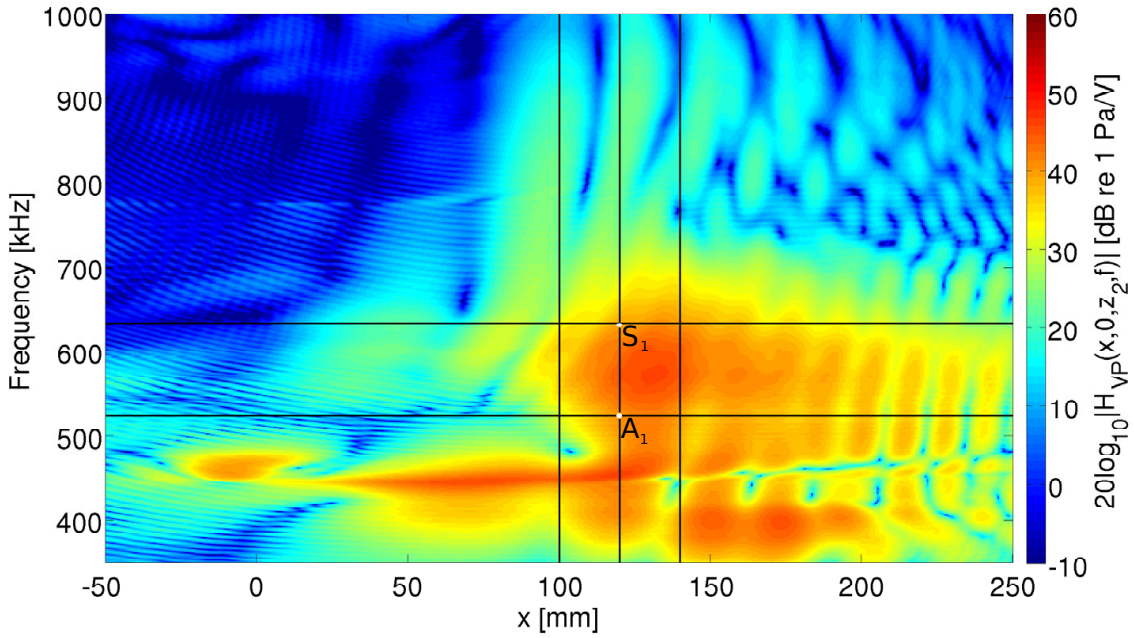

Fig 7.20. At $\theta = 15°$ beam incidence: Simulated magnitude of the voltage-to-pressure transfer function $|H_{VP}(x, 0, z_2, f)|$ using the hybrid FEM-ASM approach. Solid lines indicate the $x-$distances addressed in Fig. 7.21, and frequencies in Figs. 7.23 and 7.24. Leaky Lamb modes for a plane-wave incident angle $\theta_P = 15°$ are indicated at their respective frequencies at $x = 120$ mm.

The hybrid FEM-ASM simulated voltage-to-pressure transfer function $|H_{VP}(x, 0, z_2, f)|$ at $x = 100$ mm, $x = 120$ mm and $x = 140$ mm in Fig. 7.20 (marked with lines) are shown (blue lines) in Fig. 7.21(a), 7.21(b) and 7.21(c) , respectively, as a function of frequency, and compared to measurement results (red lines). The corresponding relative transmission through the plate are shown in Fig. 6.23. For all $x-$positions an agreement within 1.6 dB between simulations and measurements is shown for the entire frequency range, except at higher frequencies at $x = 140$ mm. For high frequencies, this $x-$position is not covered by the main lobe of the transducer.

Figs. 7.22(a) and 7.22(b) show the magnitude of the hybrid FEM-ASM simulated pressure field distribution $|P(x, 0, z, f)|$ at $f = 524$ kHz and $f = 634$ kHz as a function of $x-$ and $z-$positions, respectively, near the leaky Lamb modes for $\theta_P = 15°$. The incident pressure field produced by, and propagated from, the piezoelectric transducer towards the plate, and the pressure field transmitted through the

plate, is presented. For $f = 524$ kHz (near the A_1 mode) in Fig. 7.22(a), the plate causes a beam narrowing effect, in addition to an interference pattern discussed in Sect. 7.4. For $f = 634$ kHz (near the S_1 mode) in Fig. 7.22(b), the plate causes, in addition to the beam narrowing effect shown for $f = 524$ kHz, a beam displacement. As discussed earlier, aliasing effects in the region around -300 to -200 mm for the transmitted pressure are present. This is further discussed in Sect. 7.9. The

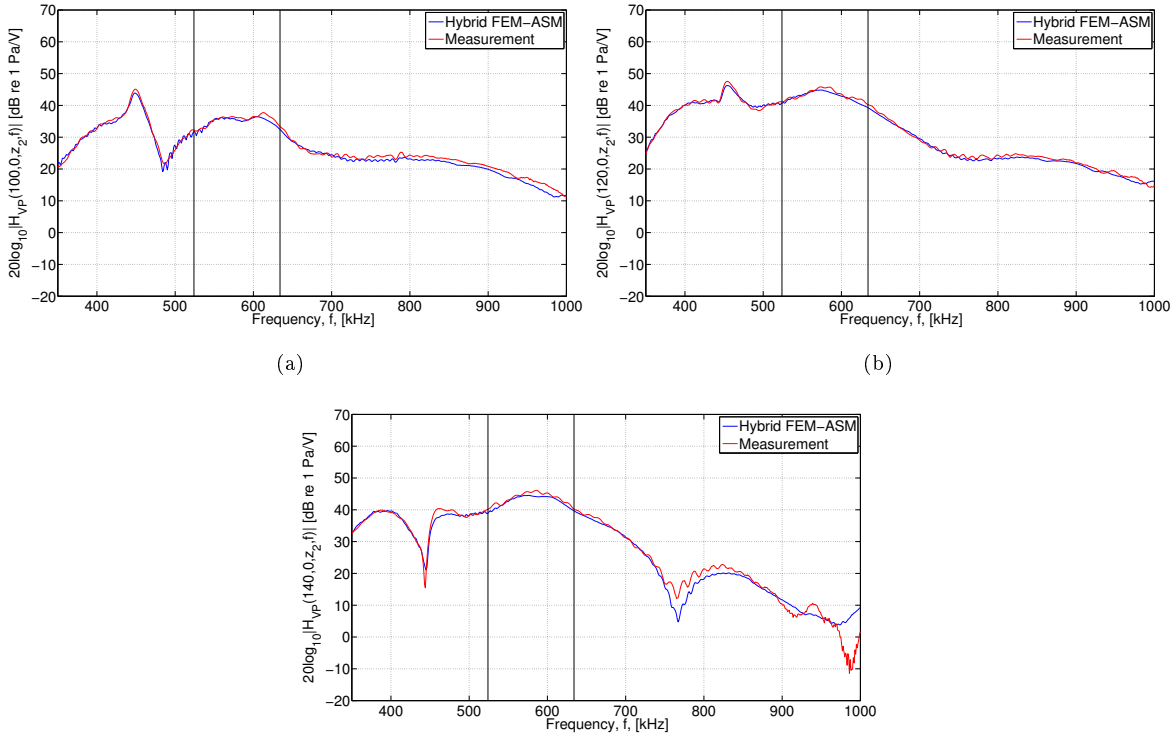

Fig 7.21. At $\theta = 15°$ beam incidence: Simulated magnitude of the voltage-to-pressure transfer function $|H_{VP}(x, 0, z_2, f)|$ using the hybrid FEM-ASM approach (blue line) in comparison with measurements (red line) for **a)** $x = 100$ mm, **b)** $x = 120$ mm **c)** $x = 140$ mm. The frequency spectra at the three $x-$distances are indicated with solid lines in Fig. 7.20.

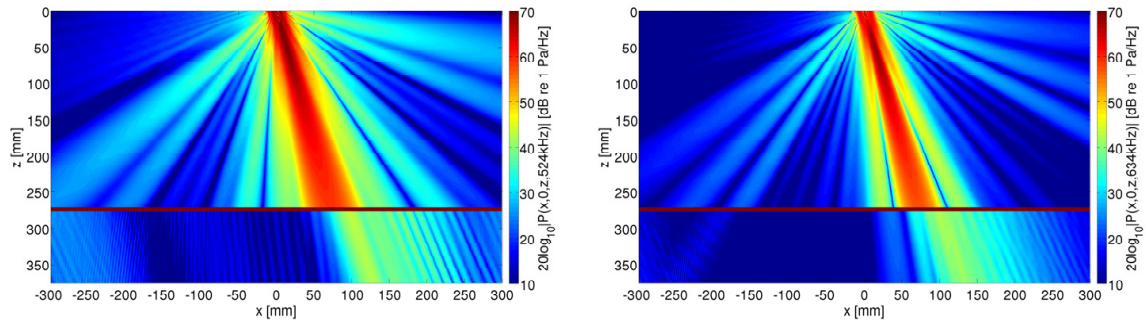

Fig 7.22. At ($\theta = 15°$) beam incidence: Simulated magnitude of the pressure field distribution $|P(x, 0, z, f)|$, **a)** at $f = 524$kHz and **b)** at $f = 634$ kHz, using the hybrid FEM-ASM approach.

step-by-step simulation process of the hybrid FEM-ASM approach is exemplified in Sect. 4.3.1.

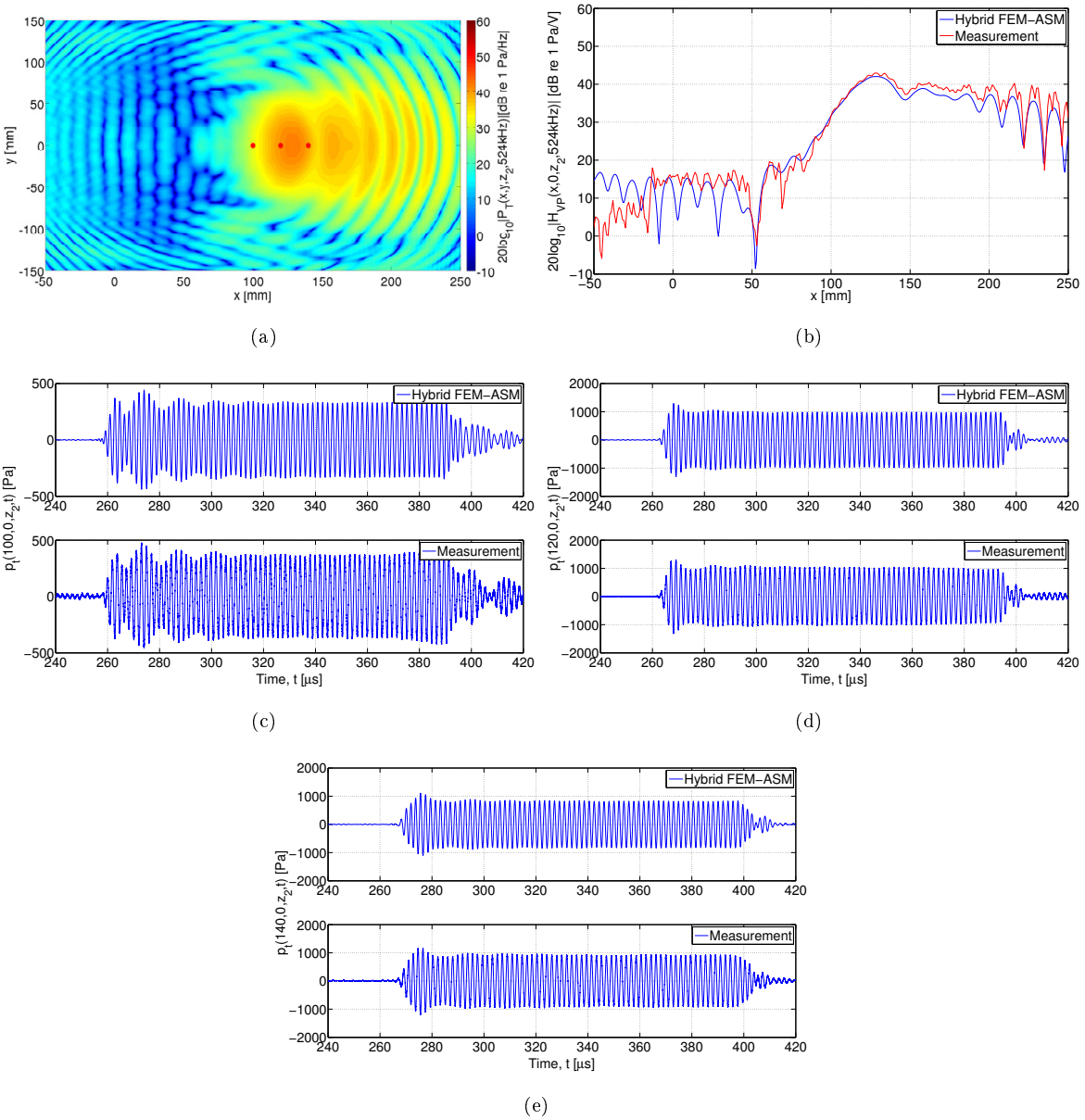

Fig 7.23. At $\theta = 15°$ beam incidence: Simulated magnitude of the transmitted pressure field distribution $|P_t(x, y, z_2, f)|$ at **a)** 524 kHz near the A_1 at 523.9 kHz. **b)** Simulated and measured $|P_t(x, 0, z_2, f)|$. Simulated and measured pressure waveforms $p_t(x, y, z_2, t)$ with centre frequency $f = 524$ kHz, at the receiver positions '$*$' in Fig. 7.23(a): **c)** at position $(100, 0, z_2)$, **d)** at position $(120, 0, z_2)$ and **e)** at position $(140, 0, z_2)$.

Fig. 7.23(a) shows the hybrid FEM-ASM simulated transmitted pressure field distribution $|P_t(x, y, z_2, f)|$ at a frequency of 524 kHz as a function of $x-$ and $y-$positions, for a constant $z = z_2$, close to the excitation frequency for a $\theta_P = 15°$ plane-wave incidence of the A_1 at 523.9 kHz. Here, the interference pattern present in Fig. 7.22(a) can be observed. Fig. 7.23(b) shows the hybrid FEM-ASM (blue line) calculated $|H_{VP}(x, 0, z_2, 524\text{kHz})|$ as function of $x-$position, in comparison with measurements (red

line), cf. Fig. 6.24 for transmission through the plate. An agreement within 4 dB is shown in the region $x = 70 - 250$ mm, but for $x-$positions below greater deviations are present. In this region, higher

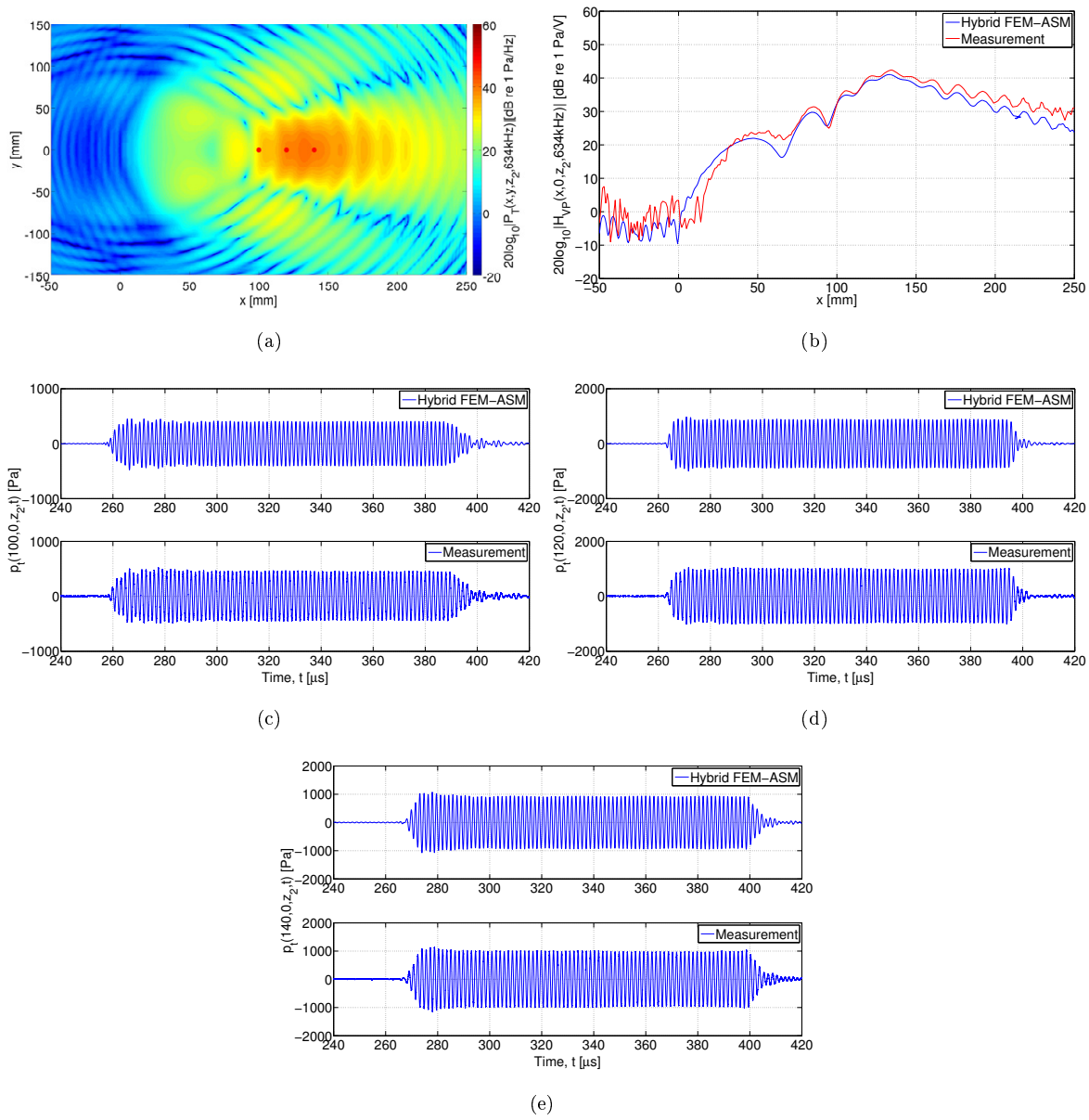

Fig 7.24. At $\theta = 15°$ beam incidence: Simulated magnitude of the transmitted pressure field distribution $|P_t(x, y, z_2, f)|$ at **a)** 634 kHz near the S_1 at 631.9 kHz. **b)** Simulated and measured $|P_t(x, 0, z_2, f)|$. Simulated and measured pressure waveforms $p_t(x, y, z_2, t)$ with centre frequency $f = 634$ kHz, at the receiver positions '$*$' in Fig. 7.24(a): **c)** at position $(100, 0, z_2)$, **d)** at position $(120, 0, z_2)$ and **e)** at position $(140, 0, z_2)$.

order sidelobes dominates the transmission through the plate, hence, deviations based upon the beam patterns in Fig. 5.27 affects the comparion. In Figs. 7.23(c), 7.23(d) and 7.23(e) the simulated sound pressure waveforms $p_t(x, y, z_2, t)$ with centre frequency $f = 524$ kHz are compared to measured waveforms at three receiver positions '$*$' in Fig. 7.23(a) at $x = 100, 120, 140$ mm, respectively. An agreement within 1.9 dB between simulated and measured waveforms for signal level, bandwidth and

waveform is shown for all $x-$positions. As is evident from Fig. 7.23(a), for these $x-$positions the transmission through the system is relatively high, hence the wide bandwidth of the signals. The deviations in the pulse arrival time between simulated and measured waveforms are 0.47, 0.52 and 0.68 for $x = 100, 120, 140$ mm, respectively. Fig. 7.24(a) shows the hybrid FEM-ASM simulated transmitted pressure field distribution $|P_t(x, y, z_2, f)|$ at a frequency of 634 kHz as a function of $x-$ and $y-$positions, for a constant $z = z_2$, close to the excitation frequency for a $\theta_P = 15°$ plane-wave incidence of the S_1 at 631.9 kHz. Fig. 7.24(b) shows the hybrid FEM-ASM (blue line) calculated $|H_{VP}(x, 0, z_2, 634\text{kHz})|$ as function of $x-$position, in comparison with measurements (red line), cf. Fig. 6.24 for transmission through the plate. An agreement within 6 dB is shown for the region $x = 50-200$, including the interference pattern at $x-$positions 150 mm and higher. In Figs. 7.24(c), 7.24(d) and 7.24(e) the simulated sound pressure waveforms $p_t(x, y, z_2, t)$ with centre frequency $f = 634$ kHz are compared to measured waveforms at three receiver positions '$*$' in Fig. 7.24(a) for $x = 100, 120, 140$ mm, respectively. The same conclusions as for $f = 524$ kHz in Fig. 7.23 can be made, deviations within 1.2 dB. The deviations in the pulse arrival time between simulated and measured waveforms are 0.5, 0.76 and 0.5 for $x = 100, 120, 140$ mm, respectively.

7.6 $\theta = 20°$ beam incidence

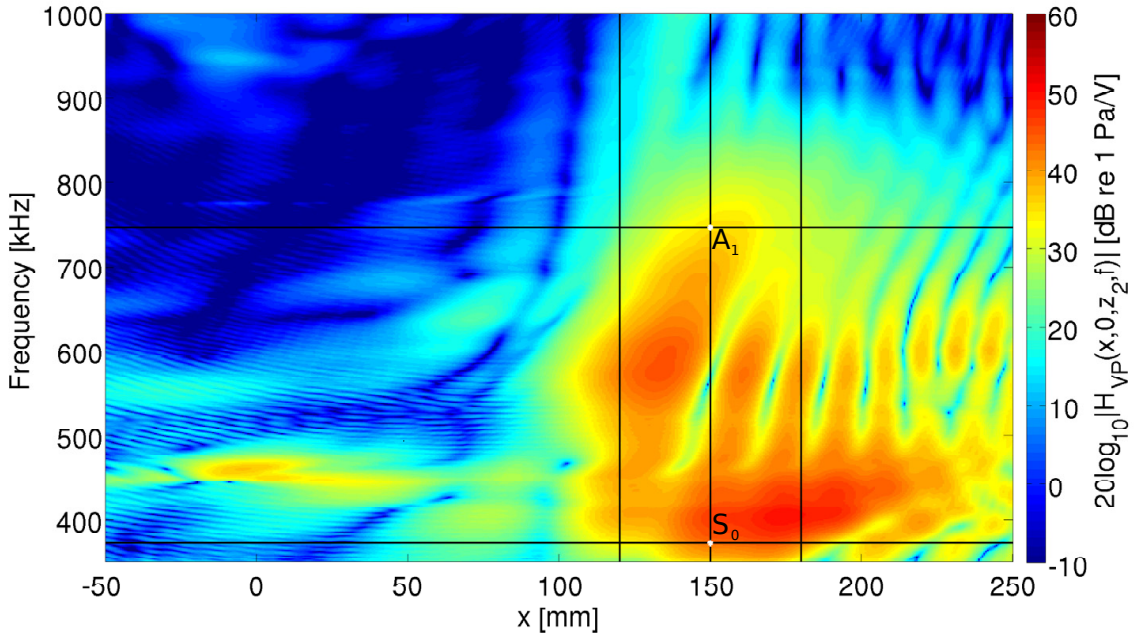

Fig 7.25. At $\theta = 20°$ beam incidence: Simulated magnitude of the voltage-to-pressure transfer function $|H_{VP}(x, 0, z_2, f)|$ using the hybrid FEM-ASM approach. Solid lines indicate the $x-$distances addressed in Fig. 7.26, and frequencies in Figs. 7.28 and 7.29. Leaky Lamb modes for a plane-wave incident angle $\theta_P = 20°$ are indicated at their respective frequencies at $x = 150$ mm.

In Fig. 7.25 the hybrid FEM-ASM calculated $|H_{VP}(x, 0, z_2, f)|$ is shown for a 20° beam incidence angle, as a function of frequency and x-position, at the receiver depth $z_2 = 376.05$ mm, in relation to

Fig. 6.25. The frequencies corresponding to the leaky Lamb modes S_0 and A_1 for a plane-wave incident angle $\theta_P = 20°$ cf. Fig. 6.6 are 372.6 kHz and 746.0 kHz, respectively, indicated at $x = 150$ mm in Fig. 7.25. The maxima are in the vicinity of the leaky Lamb modes, and demonstrates regions in space and frequency where the transmission through the system is relatively high. The black vertical lines show $x-$positions where the simulations are compared to measurements as a function of frequency, and the black horizontal lines show specific frequencies where the simulations are compared to measurements as function of $x-$position. Similar plots are shown in [95] for the piezoelectric transducer, and in [91, 92] for a piston generated beam pattern.

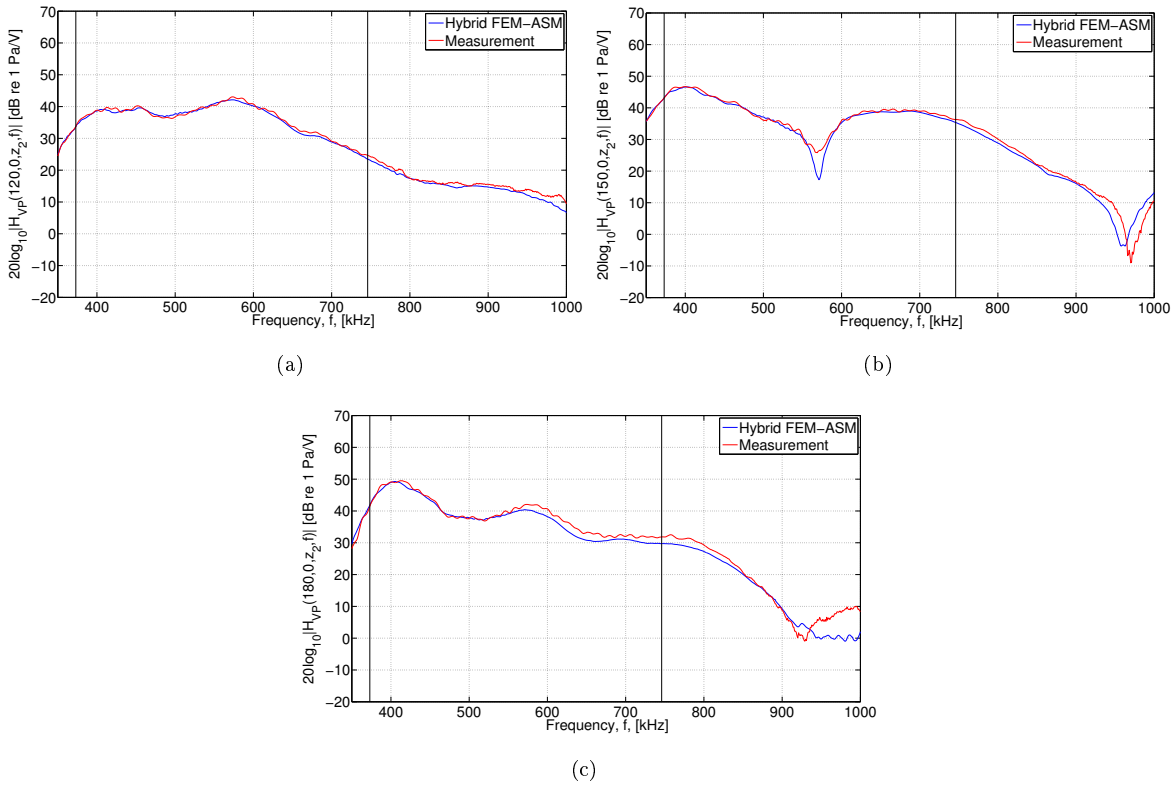

Fig 7.26. At $\theta = 20°$ beam incidence: Simulated magnitude of the voltage-to-pressure transfer function $|H_{VP}(x, 0, z_2, f)|$ using the hybrid FEM-ASM approach (blue line) in comparison with measurements (red line) for **a)** $x = 120$ mm, **b)** $x = 150$ mm **c)** $x = 180$ mm. The frequency spectra at the three $x-$distances are indicated with solid lines in Fig. 7.25.

The hybrid FEM-ASM simulated voltage-to-pressure transfer function $|H_{VP}(x, 0, z_2, f)|$ at $x = 120$ mm, $x = 150$ mm and $x = 180$ mm in Fig. 7.25 (marked with lines) are shown (blue lines) in Fig. 7.26(a), 7.26(b) and 7.26(c) , respectively, as a function of frequency, and compared to measurement results (red lines). The corresponding relative transmission through the plate are shown in Fig. 6.26. The black vertical lines indicates frequencies where the transmitted waveforms are simulated and compared to measurements, cf. Figs. 7.28 and 7.29. For all $x-$positions an agreement within 2.6 dB between measurements and simulations is shown for the entire frequency range, except at higher frequencies (above 900 kHz) and the minimum at 570 kHz for $x = 150$ mm. For $x = 150$ mm, the measured minimum around 960 kHz is shifted upwards in frequency in relation to simulations. As discussed earlier, alignment issues at high frequency due to the directive transducer can be problematic.

Figs. 7.27(a) and 7.27(b) show the magnitude of the hybrid FEM-ASM simulated pressure field distribution $|P(x,0,z,f)|$ at $f = 373$ kHz and $f = 746$ kHz as a function of $x-$ and $z-$positions, respectively, near the leaky Lamb modes for $\theta_P = 20°$. The incident pressure field produced by, and propagated from, the piezoelectric transducer towards the plate, and the pressure field transmitted through the plate, is presented. For $f = 373$ kHz (near the S_0 mode) and $f = 746$ kHz (near the A_1 mode) in Figs. 7.27(a) and 7.27(b), the plate causes a beam narrowing effect, in addition to a trailing leaky field (further discussed in Sect. 7.9. Aliasing effects as for e.g. Fig. 7.22(a) are present for both frequencies.

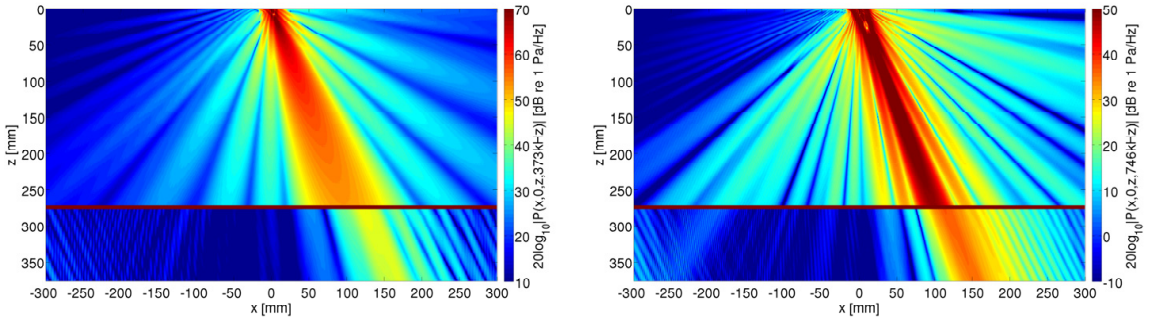

(a) (b)

Fig 7.27. At ($\theta = 20°$) beam incidence: Simulated magnitude of the pressure field distribution $|P(x,0,z,f)|$, **a)** at $f = 373$kHz and **b)** at $f = 746$ kHz, using the hybrid FEM-ASM approach.

Fig. 7.28(a) shows the hybrid FEM-ASM simulated transmitted pressure field distribution $|P_t(x,y,z_2,f)|$ at a frequency of 373 kHz as a function of $x-$ and $y-$positions, for a constant $z = z_2$, close to the excitation frequency for a $\theta_P = 20°$ plane-wave incidence of the S_0 at 372.6 kHz. Fig. 7.28(b) shows the hybrid FEM-ASM (blue line) calculated $|H_{VP}(x,0,z_2,373\text{kHz})|$ as function of $x-$position, in comparison with measurements (red line), cf. Fig. 6.27 for transmission through the plate. An agreement within 3.7 dB is shown in the region $x = 50 - 250$ mm, for $x-$positions below 50 mm, noise is a dominant part of the measurement results. In Figs. 7.28(c), 7.28(d) and 7.28(e) the simulated sound pressure waveforms $p_t(x,y,z_2,t)$ with centre frequency $f = 373$ kHz are compared to measured waveforms at three receiver positions '$*$' in Fig. 7.28(a) at $x = 120, 150, 180$ mm, respectively. Agreement within 0.1 dB is shown for waveform, bandwidth and signal level, as expected from Fig. 7.28(b). The deviations in the pulse arrival time between simulated and measured waveforms are 0.37, 0.04 and 0.30 for $x = 120, 150, 180$ mm, respectively. Fig. 7.29(a) shows the hybrid FEM-ASM simulated transmitted pressure field distribution $|P_t(x,y,z_2,f)|$ at a frequency of 746 kHz as a function of $x-$ and $y-$positions, for a constant $z = z_2$, close to the excitation frequency for a $\theta_P = 20°$ plane-wave incidence of the A_1 at 746.0 kHz. Fig. 7.29(b) shows the hybrid FEM-ASM (blue line) calculated $|H_{VP}(x,0,z_2,746\text{kHz})|$ as function of $x-$position, in comparison with measurements (red line), cf. Fig. 6.27 for transmission through the plate. Agreement within 4.1 dB is shown in the region $x = 75 - 250$ mm. The greater deviations for lower $x-$position is a combination of noise in measurement results, and the deviations in the simulated beam pattern to the measured beam pattern moving beyond the first sidelobe. In Figs. 7.29(c), 7.29(d) and 7.29(e) the simulated sound pressure waveforms $p_t(x,y,z_2,t)$ with centre frequency

$f = 746$ kHz are compared to measured waveforms at three receiver positions '$*$' in Fig. 7.29(a) at $x = 120, 150, 180$ mm, respectively. The same conclusions as for Fig. 7.28 can be made. The deviations in the pulse arrival time between the simulated and measured waveforms are 0.3, 0.04 and 0.52 for $x = 120, 150, 180$ mm, respectively. The transient regions for the simulated waveforms, especially at $x = 180$ mm deviates for the measured waveforms. Recall the discussion in Sect. 7.4 regarding higher frequency waveforms.

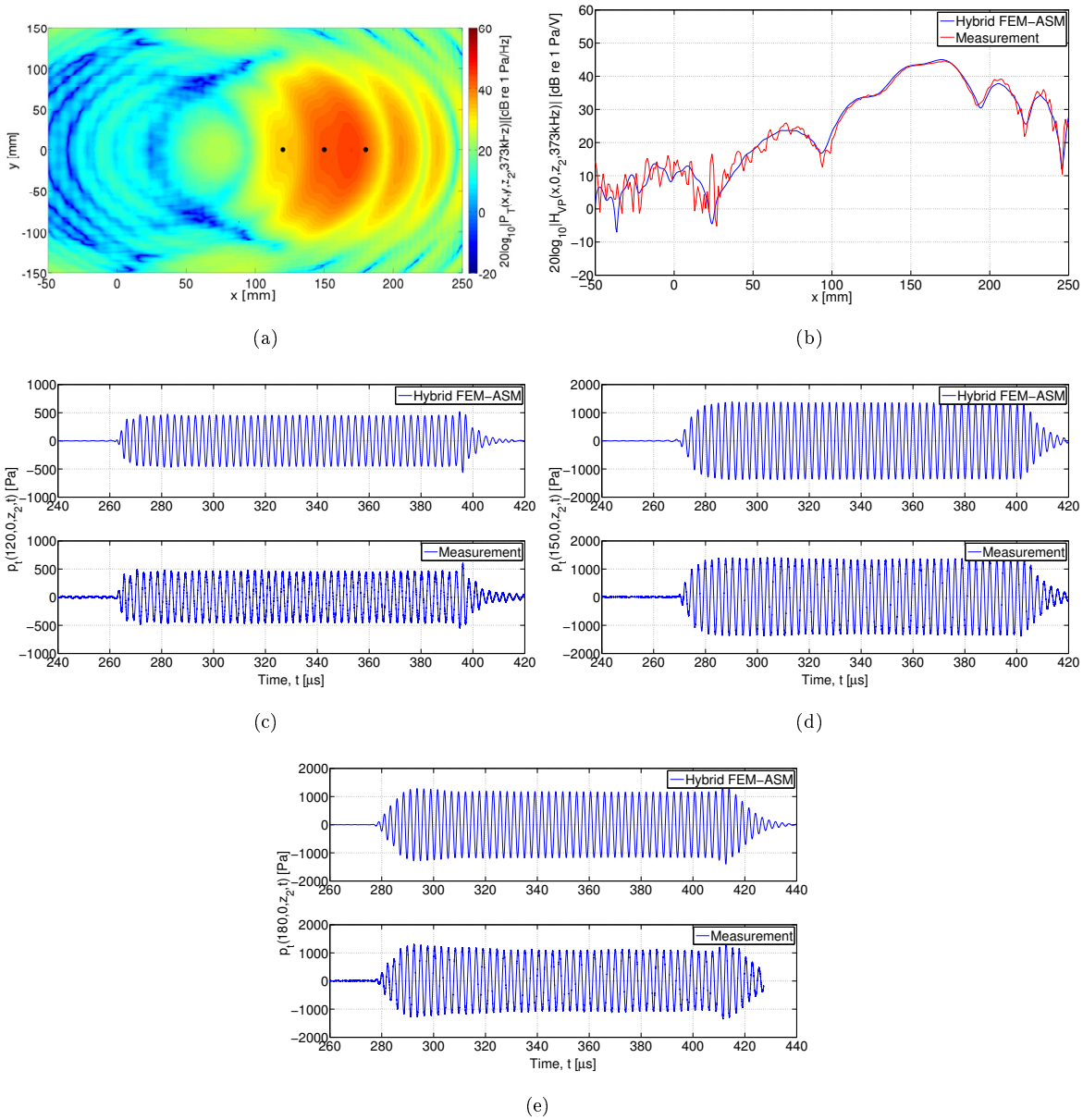

Fig 7.28. At $\theta = 20°$ beam incidence: Simulated magnitude of the transmitted pressure field distribution $|P_t(x, y, z_2, f)|$ at **a)** 373 kHz near the S_0 at 372.6 kHz. **b)** Simulated and measured $|P_t(x, 0, z_2, f)|$. Simulated and measured pressure waveforms $p_t(x, y, z_2, t)$ with centre frequency $f = 373$ kHz, at the receiver positions '$*$' in Fig. 7.28(a): **c)** at position $(120, 0, z_2)$, **d)** at position $(150, 0, z_2)$ and **e)** at position $(180, 0, z_2)$.

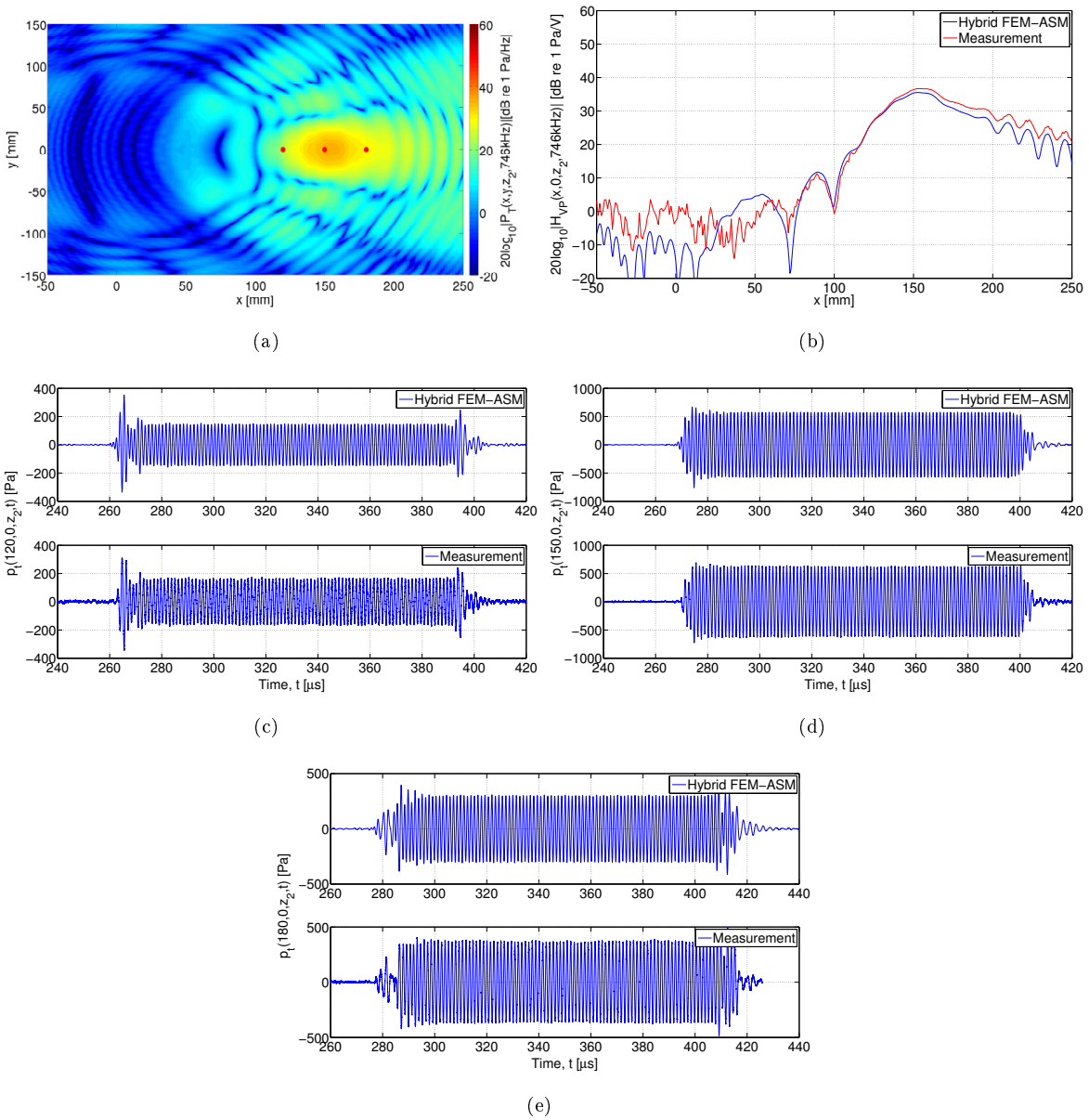

Fig 7.29. At $\theta = 20°$ beam incidence: Simulated magnitude of the transmitted pressure field distribution $|P_t(x, y, z_2, f)|$ at **a)** 746 kHz near the A_1 at 746.0 kHz. **b)** Simulated and measured $|P_t(x, 0, z_2, f)|$. Simulated and measured pressure waveforms $p_t(x, y, z_2, t)$ with centre frequency $f = 746$ kHz, at the receiver positions '$*$' in Fig. 7.29(a): **c)** at position $(120, 0, z_2)$, **d)** at position $(150, 0, z_2)$ and **e)** at position $(180, 0, z_2)$.

7.7 $\theta = 25°$ beam incidence

In Fig. 7.30 the hybrid FEM-ASM calculated $|H_{VP}(x, 0, z_2, f)|$ is shown for a 25° beam incidence angle, as a function of frequency and x-position, at the receiver depth $z_2 = 376.05$ mm, in relation to Fig. 6.28. The frequency corresponding to the leaky Lamb mode S_0 for a plane-wave incident angle $\theta_P = 25°$ cf. Fig. 6.6 is 446.0 kHz, indicated at $x = 200$ mm in Fig. 7.30. The maximum is in the vicinity of the leaky Lamb mode, and demonstrates regions in space and frequency where the

transmission through the system is relatively high. The black vertical lines show $x-$positions where the simulations are compared to measurements as a function of frequency, and the black horizontal line show the specific frequency where the simulations are compared to measurements as function of $x-$position. Similar plots are shown in [95] for the piezoelectric transducer, and in [91, 92] for a piston generated beam pattern.

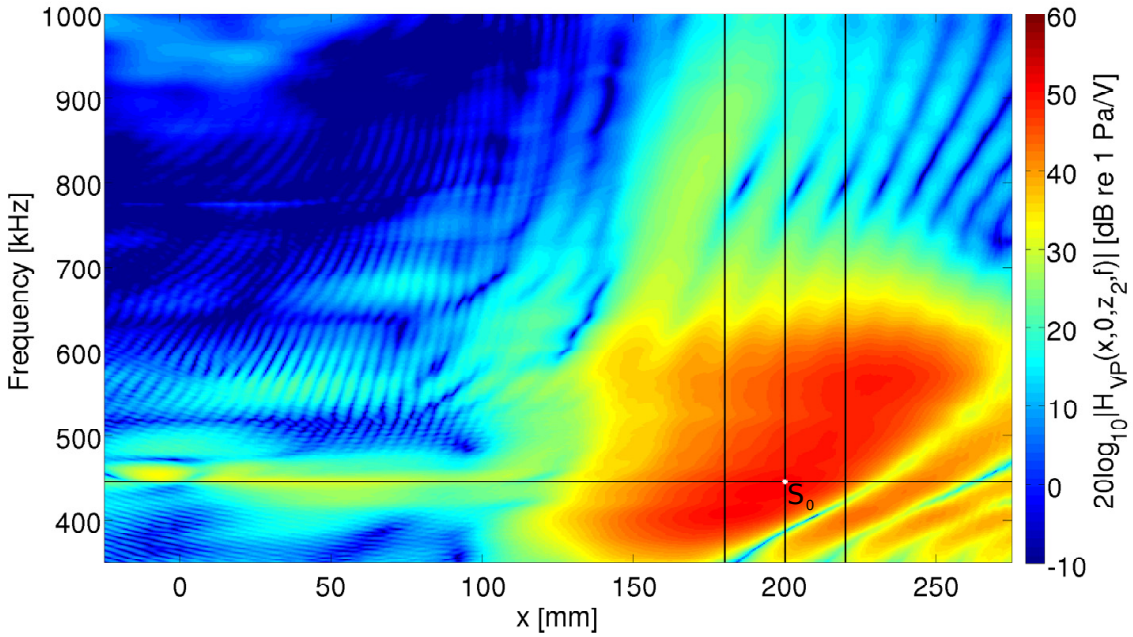

Fig 7.30. At $\theta = 25°$ beam incidence: Simulated magnitude of the voltage-to-pressure transfer function $|H_{VP}(x, 0, z_2, f)|$ using the hybrid FEM-ASM approach. Solid lines indicate the $x-$distances addressed in Fig. 7.31, and the frequency in Fig. 7.33. The leaky Lamb mode S_0 for a plane-wave incident angle $\theta_P = 25°$ is indicated at its respective frequency at $x = 200$ mm.

The hybrid FEM-ASM simulated voltage-to-pressure transfer function $|H_{VP}(x, 0, z_2, f)|$ at $x = 180$ mm, $x = 200$ mm and $x = 220$ mm in Fig. 7.30 (marked with lines) are shown (blue lines) in Fig. 7.31(a), 7.31(b) and 7.31(c), respectively, as a function of frequency, and compared to measurement results (red lines). The corresponding relative transmission through the plate are shown in Fig. 6.29. The black vertical line indicate the frequency where the transmitted waveforms are simulated and compared to measurements, cf. Fig. 7.33. For $x = 180, 200$ mm in Figs. 7.31(a) and 7.31(b), an agreement within 3.6 dB between measurements and simulations is shown, except at the minimum for $x = 200$ mm. For $x = 220$ mm in Fig. 7.31(c), an agreement within 2.8 dB is shown up to 750 kHz. At higher frequencies, the simulations deviates from the measurement results.

Fig. 7.32 shows the magnitude of the hybrid FEM-ASM simulated pressure field distribution $|P(x, 0, z, f)|$ at $f = 446$ kHz as a function of $x-$ and $z-$positions, near the leaky Lamb mode for $\theta_P = 25°$. The incident pressure field produced by, and propagated from, the piezoelectric transducer towards the plate, and the pressure field transmitted through the plate, is presented. The plate causes minimal beam displacement, but a trailing leaky field can be observed. As for other pressure field distributions

at non-zero beam incidence angles, aliasing effects in the region -300 to -200 mm is evident.

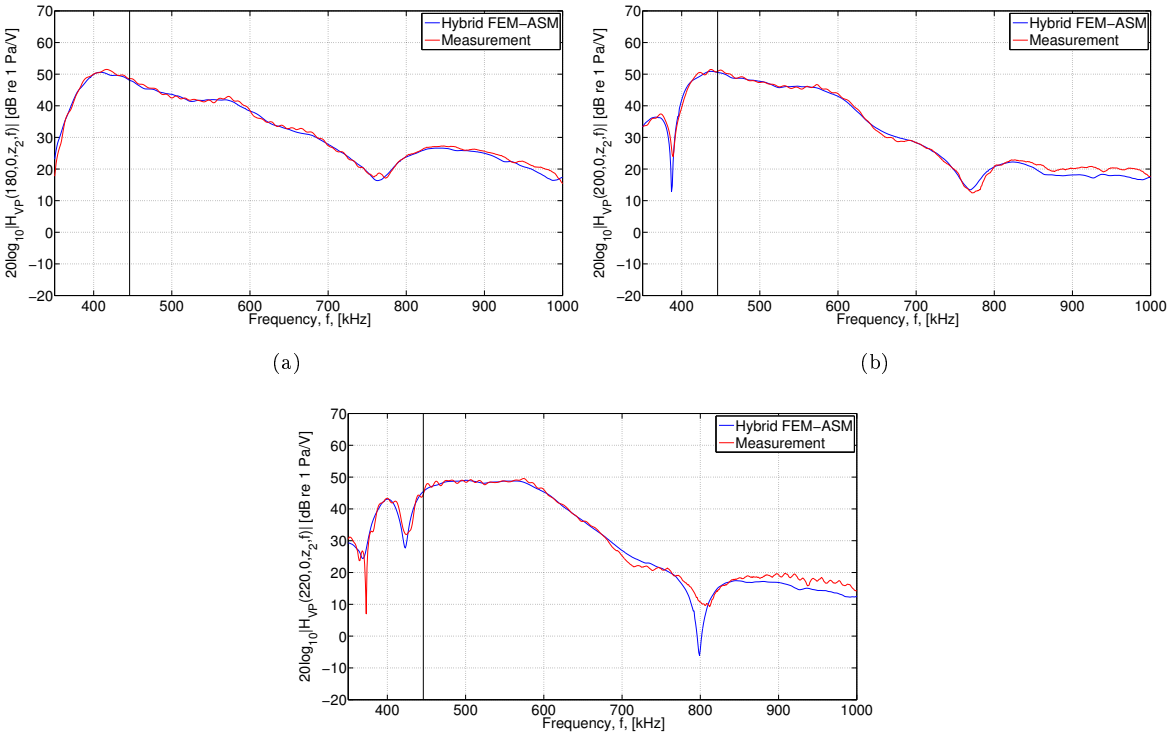

Fig 7.31. At $\theta = 25°$ beam incidence: Simulated magnitude of the voltage-to-pressure transfer function $|H_{VP}(x, 0, z_2, f)|$ using the hybrid FEM-ASM approach (blue line) in comparison with measurements (red line) for **a)** $x = 180$ mm, **b)** $x = 200$ mm **c)** $x = 220$ mm. The frequency spectra at the three $x-$distances are indicated with solid lines in Fig. 7.30.

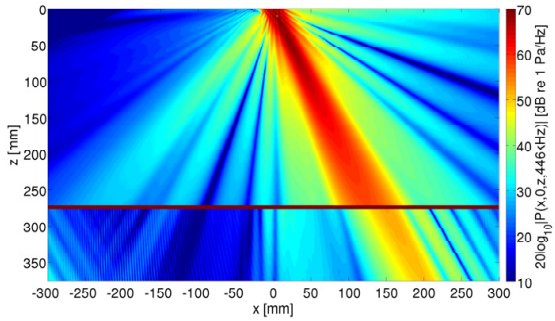

Fig 7.32. At ($\theta = 25°$) beam incidence: Simulated magnitude of the pressure field distribution $|P(x, 0, z, f)|$ at $f = 446$ kHz using the hybrid FEM-ASM approach.

Fig. 7.33(a) shows the hybrid FEM-ASM simulated transmitted pressure field distribution $|P_t(x, y, z_2, f)|$ at a frequency of 446 kHz as a function of $x-$ and $y-$positions, for a constant $z = z_2$, close to the excitation frequency for a $\theta_P = 25°$ plane-wave incidence of the S_0 at 446.0 kHz. Fig. 7.33(b) shows the hybrid FEM-ASM (blue line) calculated $|H_{VP}(x, 0, z_2, 446\text{kHz})|$ as function of $x-$position, in comparison with measurements (red line), cf. Fig. 6.30 for transmission through the plate. Agreement

within 1.1 dB is shown in the region $x = -130 - 230$ mm. In Figs. 7.33(c), 7.33(d) and 7.33(e) the simulated sound pressure waveforms $p_t(x, y, z_2, t)$ with centre frequency $f = 446$ kHz are compared to measured waveforms at three receiver positions '$*$' in Fig. 7.33(a) at $x = 180, 200, 220$ mm, respectively. An agreement within 0.6 dB is shown for waveform, signal level and bandwidth of the measured and simulated transmitted waveforms. Due to the relatively high transmission around this frequency and

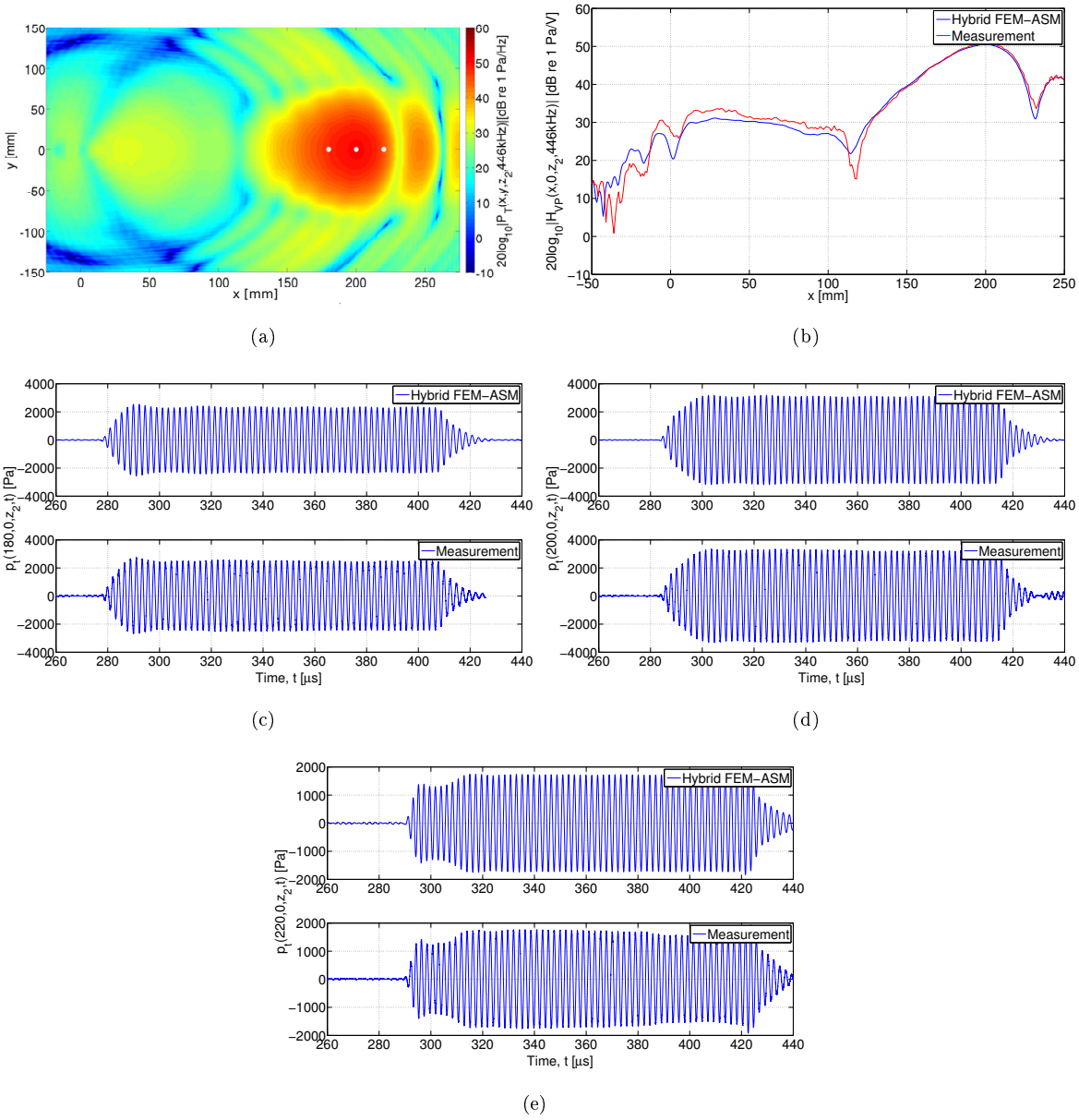

Fig 7.33. At $\theta = 25°$ beam incidence: Simulated magnitude of the transmitted pressure field distribution $|P_t(x, y, z_2, f)|$ at **a)** 446 kHz near the S_0 at 446.0 kHz. **b)** Simulated and measured $|P_t(x, 0, z_2, f)|$. Simulated and measured pressure waveforms $p_t(x, y, z_2, t)$ with centre frequency $f = 446$ kHz, at the receiver positions '$*$' in Fig. 7.33(a): **c)** at position $(180, 0, z_2)$, **d)** at position $(200, 0, z_2)$ and **e)** at position $(220, 0, z_2)$.

$x-$position, cf. Fig. 7.30, the waveforms have wide bandwidths. The deviations in the pulse arrival

time between the simulated and measured waveforms are 0.45, 0.31 and 0.49 for $x = 180, 200, 220$ mm, respectively.

7.8 $\theta = 30°$ beam incidence

In Fig. 7.34 the hybrid FEM-ASM calculated $|H_{VP}(x, 0, z_2, f)|$ is shown for a 30° beam incidence angle, as a function of frequency and x-position, at the receiver depth $z_2 = 376.05$ mm. The frequency corresponding to the leaky Lamb mode S_0 for a plane-wave incident angle $\theta_P = 30°$ cf. Fig. 6.6 is 691.3 kHz, indicated at $x = 230$ mm in Fig. 7.34. The maximum is in the vicinity of the leaky Lamb mode, and demonstrates regions in space and frequency where the transmission through the system is relatively high. The black vertical lines show $x-$positions where the simulations are compared to measurements as a function of frequency, and the black horizontal line show the specific frequency where the simulations are compared to measurements as function of $x-$position. Similar plots are shown in [95] for the piezoelectric transducer, and in [91, 92] for a piston generated beam pattern.

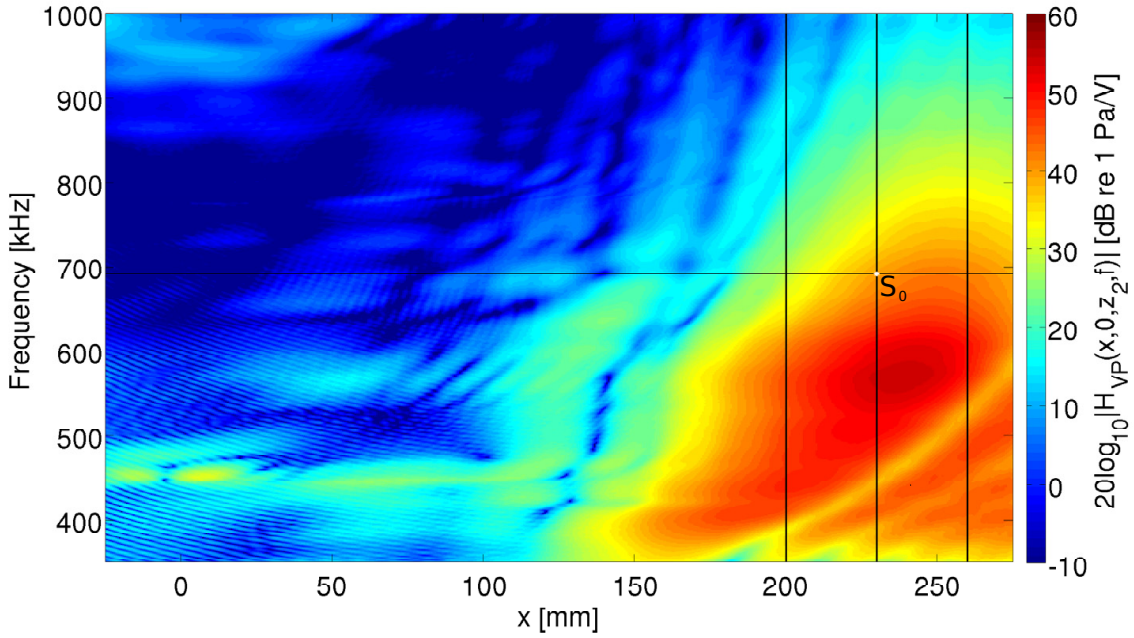

Fig 7.34. At $\theta = 30°$ beam incidence: Simulated magnitude of the voltage-to-pressure transfer function $|H_{VP}(x, 0, z_2, f)|$ using the hybrid FEM-ASM approach. Solid lines indicate the $x-$distances addressed in Fig. 7.35, and the frequency in Fig. 7.37. The leaky Lamb mode S_0 for a plane-wave incident angle $\theta_P = 30°$ is indicated at its respective frequency at $x = 230$ mm.

The hybrid FEM-ASM simulated voltage-to-pressure transfer function $|H_{VP}(x, 0, z_2, f)|$ at $x = 200$ mm, $x = 230$ mm and $x = 260$ mm in Fig. 7.34 (marked with lines) are shown (blue lines) in Fig. 7.35(a), 7.35(b) and 7.35(c), respectively, as a function of frequency, and compared to measurement results (red lines). The corresponding relative transmission through the plate are shown in Fig. 6.32. The black vertical line indicate the frequency where the transmitted waveforms are simulated and compared to measurements, cf. Fig. 7.37. For $x = 200, 230$ mm in Figs. 7.35(a) and 7.35(b), an

agreement within 1.5 dB between simulations and measurements is shown for the entire frequency range. For $x = 260$ mm in Fig. 7.35(c), an agreement within 3.4 dB is found, but the measurements fluctuates more than at $x = 200, 230$ mm. A possible reason for this is reflections for the sides of the measurement tank described in Chap. 3, where the needle hydrophone is positioned at the extremity of the tank for measurements at $\theta = 30°$ and $x = 260$ mm.

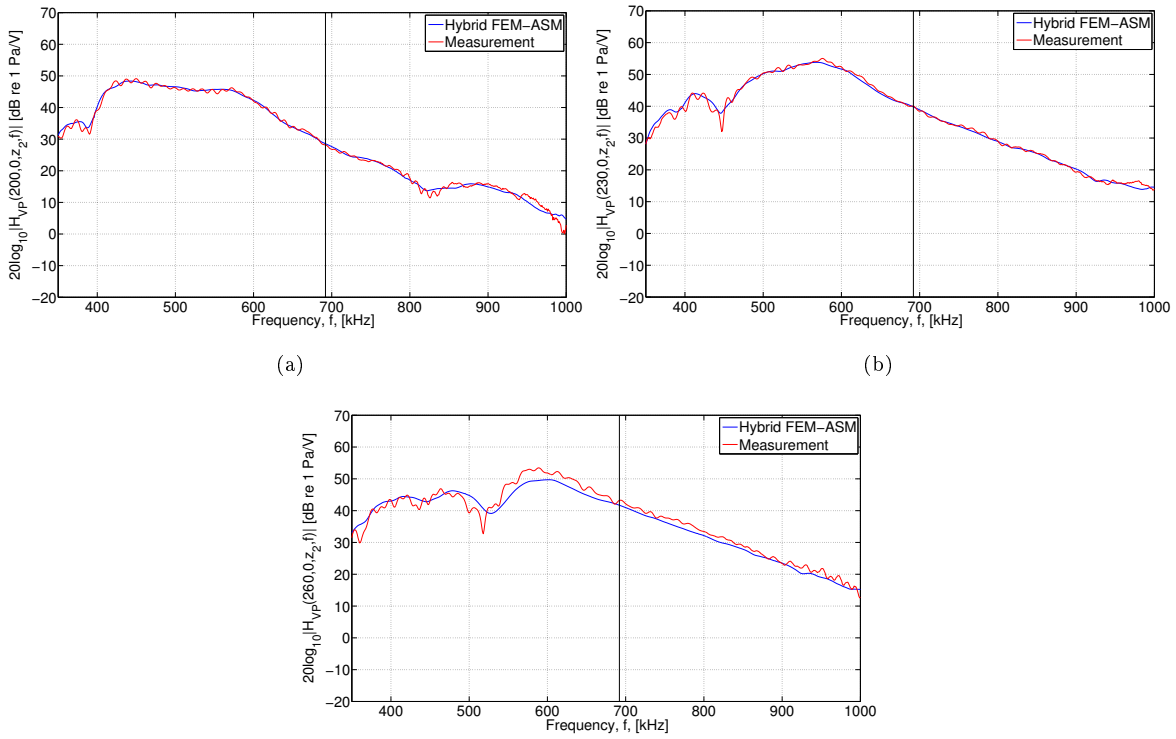

Fig 7.35. At $\theta = 30°$ beam incidence: Simulated magnitude of the voltage-to-pressure transfer function $|H_{VP}(x, 0, z_2, f)|$ using the hybrid FEM-ASM approach (blue line) in comparison with measurements (red line) for **a)** $x = 200$ mm, **b)** $x = 230$ mm **c)** $x = 260$ mm. The frequency spectra at the three $x-$distances are indicated with solid lines in Fig. 7.34.

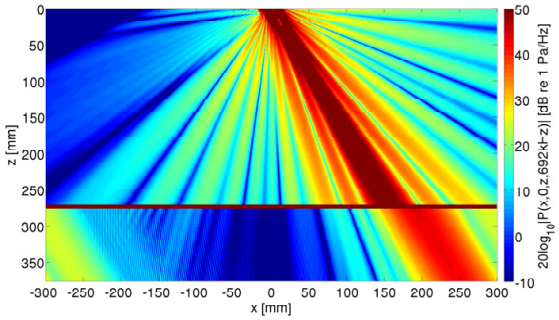

Fig 7.36. At ($\theta = 30°$) beam incidence: Simulated magnitude of the pressure field distribution $|P(x, 0, z, f)|$ at $f = 692$ kHz using the hybrid FEM-ASM approach.

Fig. 7.36 shows the magnitude of the hybrid FEM-ASM simulated pressure field distribution $|P(x, 0, z, f)|$

at $f = 692$ kHz as a function of $x-$ and $y-$positions, near the leaky Lamb mode for $\theta_P = 30°$. The incident pressure field produced by, and propagated from, the piezoelectric transducer towards the plate, and the pressure field transmitted through the plate, is presented. The plate causes a beam widening

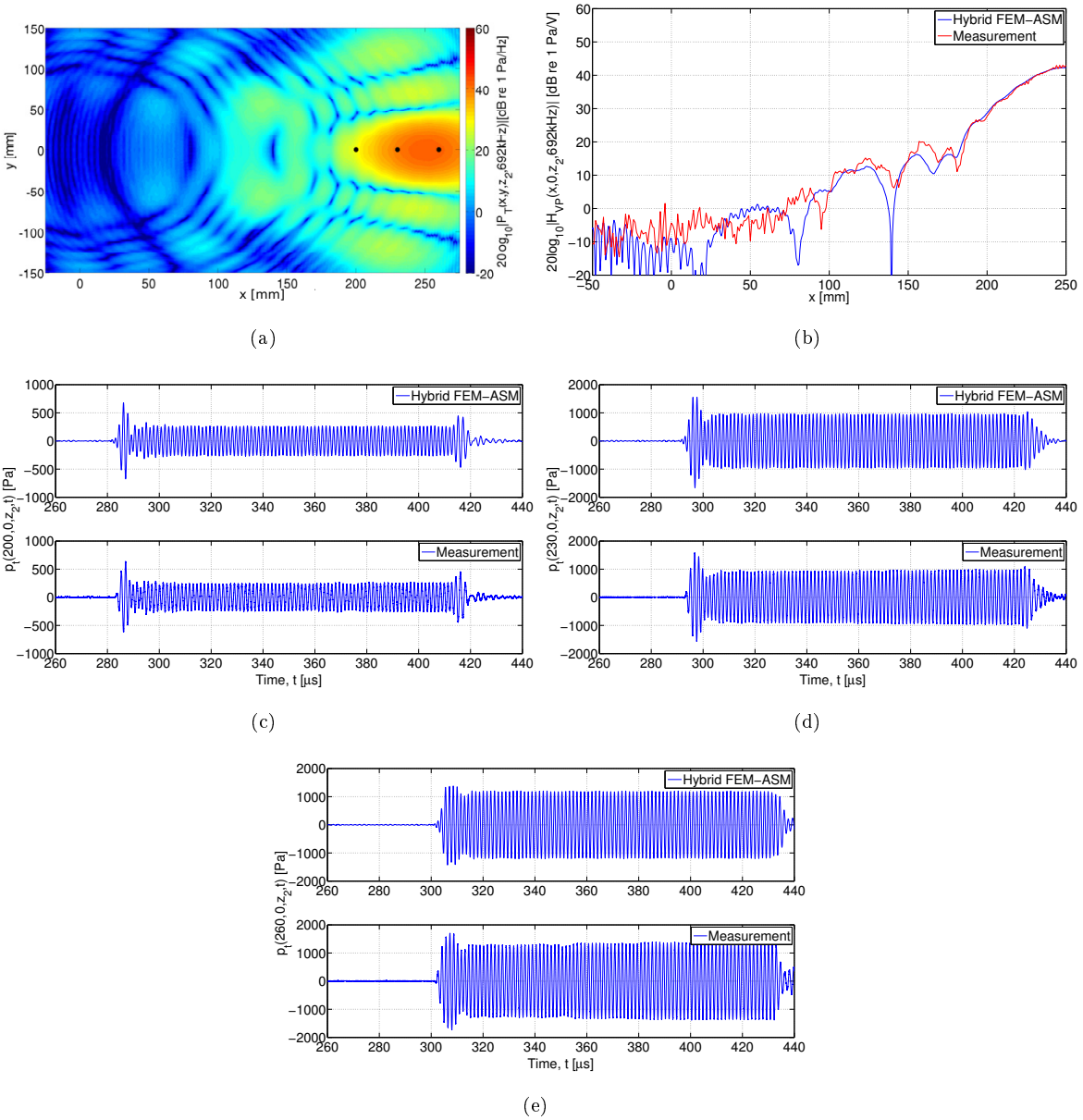

Fig 7.37. At $\theta = 30°$ beam incidence: Simulated magnitude of the transmitted pressure field distribution $|P_t(x, y, z_2, f)|$ at **a)** 692 kHz near the S_0 at 691.3 kHz. **b)** Simulated and measured $|P_t(x, 0, z_2, f)|$. Simulated and measured pressure waveforms $p_t(x, y, z_2, t)$ with centre frequency $f = 692$ kHz, at the receiver positions '$*$' in Fig. 7.37(a): **c)** at position $(200, 0, z_2)$, **d)** at position $(230, 0, z_2)$ and **e)** at position $(260, 0, z_2)$.

effect, which therefore is also a beam displacement effect. Aliasing effects are present for the transmitted pressure field in the region -300 to -200 mm, as for other non-zero pressure field distributions. Here, the aliasing effects are greater than for smaller beam incidence angles. The reason for this is

while the beam incidence angle increases, the energy distribution moves from $x = 0$ to the extremity of the grid used. Aliasing occurs when the frequency-wavenumber spectrum ends abruptly, as discussed in Sect. 4.2 for the FEM approach, but the discussion is also valied for this case.

Fig. 7.37(a) shows the hybrid FEM-ASM simulated transmitted pressure field distribution $|P_t(x, y, z_2, f)|$ at a frequency of 692 kHz as a function of $x-$ and $y-$positions, for a constant $z = z_2$, close to the excitation frequency for a $\theta_P = 30°$ plane-wave incidence of the S_0 at 691.3 kHz. Fig. 7.37(b) shows the hybrid FEM-ASM (blue line) calculated $|H_{VP}(x, 0, z_2, 692\text{kHz})|$ as function of $x-$position, in comparison with measurements (red line), cf. Fig. 6.33 for transmission through the plate. Agreement within 2.3 dB is shown in the region $x = 180 - 250$, where the main lobe gives the largest contribution to the overall transmission. As for $x-$positions below 150 mm, the higher order sidelobes contributes, therefore greater deviations, cf. Fig. 5.27. In Figs. 7.37(c), 7.37(d) and 7.37(e) the simulated sound pressure waveforms $p_t(x, y, z_2, t)$ with centre frequency $f = 692$ kHz are compared to measured waveforms at three receiver positions '$*$' in Fig. 7.37(a) at $x = 200, 230, 260$ mm, respectively. An agreement within 0.9 dB is shown for waveform, signal level and bandwidth of the measured and simulated transmitted waveforms. Due to the relatively high transmission around this frequency and $x-$position, cf. Fig. 7.34, the waveforms have wide bandwidths. The deviations in the pulse arrival time between the simulated and measured waveforms are 0.42, 0.28 and 0.04 for $x = 200, 230, 260$ mm, respectively.

7.9 Summary and discussion

In Figs. 7.1, 7.8, 7.14, 7.20, 7.25, 7.30 and 7.34 the voltage-to-pressure transfer function $|H_{VP}(x, 0, z_2, f)|$ is shown for different angles of beam incidence as function of frequency and $x-$position. The figures demonstrate regions in space and frequency where the transmission through the measurement system is relatively high. These regions need not necessarily correspond to single plane-wave excitation of leaky Lamb modes in the steel plate due to 3D beam diffraction effects. In Figs. 7.2, 7.9, 7.15, 7.21, 7.26, 7.31 and 7.35 the simulated voltage-to-pressure transfer functions are compared to measurement results for different $x-$positions as a function of frequency. In these figures, if lines are on top of each other, or in contact, a deviation within 0.5 dB is present. The measurement uncertainty in the NPL calibration of the needle hydrophone was 0.8 dB. Recall the discussion in Chap. 5 and Fig. 5.27, the FEM calculated beam patterns show deviations to measurement beyond the first sidelobe. So, at $x-$positions where the main contribution comes from either the source's main lobe or first sidelobe, an agreement within, or in the range of, the measurement uncertainty of the needle hydrophone is observed, in relation to moving to $x-$positions outside this region, where the contributions also comes from higher order sidelobes. As the main and first sidelobe narrow as the frequency increases, deviations to measurement results will also increase.

As mentioned in Chap. 6, a similar study by Lohne *et al.* [91, 92] showed qualitative comparisons between the baffled piston model and measurements (relative scale), since the electroacoustical coupling in the transducer is not included in the baffled piston model, and due to the normalization method used. A comparison on an absolute scale is made by Hosten and Biateau [85], where they measured

and simulated the particle velocity on the surface of an air-embedded plate using 2D FEM (for the plate). They simulated the transducer's beam by volume pressure excitation equal to the measured pressure (magnitude only) from the transducers. Masmoudi *et al.* [88, 97] extended this by using 3D FEM for the plate, where they assumed that the transducer's front surface radiated as an unbaffled and rigid piston. These works also used the measured efficieny (magnitude only) of the transducer to enable comparison of absolute amplitudes (predicted and measured), hence the phase response of the transducer is not taken into account. For all three works a more simplified beam pattern than can be achieved using FEM for the transducer was used. Time domain waveforms are not shown in these works.

In Fig. 7.3, 7.10, 7.16, 7.22, 7.27, 7.32 and 7.36 the hybrid FEM-ASM simulated pressure field distributions are shown for different angles of beam incidence at frequencies near to excitation frequencies of the leaky Lamb modes in the steel plate, as a function of $x-$ and $z-$positions. The incident pressure field produced, and propagated from, the piezoelectric source transducer towards the plate, and the pressure field transmitted through the plate is shown. Aliasing effects exists for the transmitted pressure fields, due to the use of bandlimited frequency-wavenumber spectra. These aliasing effects increases with the incident angle θ, due to an increasingly abrubt ending of the frequency-wavenumber spectra, cf. discussion in Sect. 4.2. These aliasing effects could be minimized by expanding the spatial domain, but this would again lead to larger FEM simulations in the hybrid FEM-ASM approach. The reflected pressure field from the plate's upper surface is not displayed, since reflection studies are not part of this thesis. As leaky guided waves in the plate are excited, the transmitted pressure fields are a superposition of a geometrically transmitted field and a trailing leaky field due to the leaky guided wave motion inside the plate. Similar plots are reported in [78, 79] for a water-solid interface using the DPSM, showing the incident and reflected pressure fields, including null regions in accordance with the theory of Bertoni & Tamir [35]. These works showed qualitative agreement between the DPSM and measurement results, where quantitative agreement is shown in this thesis between the two approaches and experiments. Similar plots are also shown in [84] for a large Gaussian acoustic beam.

Simulated pressure field distributions at the receiver depth z_2 and simulated pressure waveforms for frequencies near leaky Lamb modes are presented in Figs. 7.4, 7.5, 7.6, 7.7, 7.11, 7.12, 7.12, 7.17, 7.18, 7.19, 7.24, 7.24, 7.28, 7.29, 7.33 and 7.37 for different incidence beam angles and frequencies close to the excitation of leaky Lamb modes, as a function of $x-$ and $y-$positions, for a constant $z = z_2$. The simulated pressure fields distributions at the receiver depth are compared to measurements for $y = 0$. The simulated pressure waveforms are compared to measured waveforms, at different receiver positions and frequencies. Agreement within, or in the range of, the measurement uncertainty for the needle hydrophone, for waveform, signal level and bandwidth is shown. These parameters change quickly as function of $x-$position, for a given θ, f, and z_2. Time delay in the electronics, such as the phase response of the hydrophone, amplifier and cables have not been accounted for. In addition, the simulated waveforms use a sound velocity of 1485 m/s for the surrounding water, whereas for measured waveforms, the sound velocity in water can fluctutate over the time period where measurements are conducted, due to changes in the water temperature, cf. Sect. 5.2.4.1. The deviations in the pulse arrival time between the majority of the simulated and measured waveforms are within 0.8 fractions of

a wavelength. As frequency increases, the time delay between measured and simulated waveforms also increase. This is due to the element division in the FEM simulations. Such an effect would contribute to larger time deviations as frequency increases, as the element division for a given frequency decreases. A higher element division in FEM simulations would improve convergence of the FEM results, cf. discussion concerning phase convergence in Sect. 4.4, as the relative error using less than 5 elements per wavelength increases quickly beyond 46°, i.e. 0.12 fractions of a wavelength. Increasing the maximum frequency above 1.2 MHz in the FEM simulations would also increase accuracy of the simulations at high frequencies, as discussed in Sect. 4.2.

Lohne *et al.* [91, 92] showed comparison of pulsed piston-generated waveforms and measurements in the time-domain. They concluded that the simulated waveforms, both in signal level and bandwidth, followed the measured waveforms fairly. The results showed larger time-of-flight differences between measured and simulated waveforms than demonstrated using the FEM piezoelectric transducer model in this thesis. The transducer's phase response, hence the signal propagation through the transducer, is not taken into account using the baffled piston model, which is included in the FEM transducer model. This could partly explain some of the larger time-of-flight differences shown in [91]. [11, 12] showed comparisons of measured and simulated FEM-HIRM receiver voltage waveforms through a transit-time ultrasonic flowmeter. There, the focus was on accurate flowmetering, and not on optimization of the transmission through the plate/pipe and excitation of leaky Lamb modes.

Possible other experimental sources of errors are alignment of the transducer, steel plate and needle hydrophone, in addition to the conversion from voltage to pressure in transmitted pulsed waveforms. Also, the positioning of the needle hydrophone for transmission measurements is crucial, and will affect comparison in regions where large changes in the transmission occur over a relatively small region in space/frequency, and for measured pressure waveforms. The hydrophone is not rotated around its axis moving to different $x-$positions, hence the front face of the hydrophone is only orthogonal to transmitted waveforms at normal beam incidence.

Chapter 8

Conclusions and Outlook

Conclusions from the presented work and its overall findings are given in Sect. 8.1. In Sect. 8.2, suggestions for future investigations are made.

8.1 Conclusions and overall findings

This thesis reports an investigation of the three-dimensional signal propagation through a measurement system consisting of a piezoelectric source transducer and a water-embedded viscoelastic plate at normal and oblique angles of beam incidence. The signal transmission has been studied in terms of a FEM approach, hybrid FEM-ASM approach, and by measurements. Simulation models were developed to describe a realistic bounded beam from a finite dimensional piezoelectric transducer and its vibration, including its electro-acoustical coupling, its interaction with a fluid-embedded viscoelastic plate, and then those models were evaluated experimentally.

Since use of a commercial transducer does not provide sufficient information and control cencerning the transducer construction, dimensions, materials and material data involved, a piezoelectric transducer has been designed, constructed, characterized, and used for measurements and FEM simulations. This includes a more realistic theoretical and complete transducer description/model in relation to e.g. the baffled piston and Gaussian sources, especially with regard to the signal propagation (phase response) through the transducer.

By including the piezoelectric source transducer in the theoretical description, a quantitative description (absolute scale) of the signal chain, from electrical input voltage to the transducer - to the transmitted sound pressure through the plate is made. This makes it possible to understand and control larger parts of the real signal chain through the measurement system, including the signal propagation through the transducer, in relation to e.g. the baffled piston and Gaussian sources. Optimization of that signal path, in addition to its effect on the signal path through the plate, provides an improved accuracy and physical understanding, which is vital in the development, optimization and use of non-invasive ultrasonic methods and applications.

By utilizing the FEM to model the source transducer, a more realistic beam pattern, and its influence on leaky Lamb mode excitation in the plate has been realized, in contrast to earlier work which used transducer models such as the baffled piston source, Gaussian beams or DPSM, with a simplified description of the measurement transducer's beam pattern. The effects of using a baffled piston source model to approximate the incident free-field pressure radiated by the piezoelectric source transducer has been studied in terms of the pressure-to-pressure transfer function $H_{PP}(x, y, z_2, f)$. This transfer function governs the signal propagation through the steel plate and the water, including leaky Lamb mode excitation in the plate. Error estimation of the baffled piston model used as source can now be quantified, and prediction can be made under which circumstances a baffled piston model can be used in replacement of the FEM transducer in transmission simulations. The comparison could easily be extended to include comparison to other transducer beam models, such as e.g. Gaussian beams.

The 3D signal propagation in time and frequency domain (signal waveforms, signal spectra, and transfer functions), and results for the transducer fields, have been compared and discussed in relation to results using plane-waves and measurements. Results demonstrate regions in space and frequency, where the transmission through the measurement system (including the plate) is relatively high. These regions do not always correspond to single plane-wave excitation of leaky Lamb modes in the steel plate due to 3D beam diffraction effects. Such effects in relation to plane-wave theory have been discussed using the FEM approach at normal beam incidence, comparing the ratio $|P_1(0, 0, z_0 + 2L, f)/P_0(0, 0, z_0, f)|$ to the plane-wave pressure transmission coefficient. These beam diffraction effects can have a major impact on various ultrasonic methods and applications where one initially makes use of plane-waves to investigate or monitor material properties. In general, a combination of the source transducer's 3D beam pattern and the behaviour of the leaky Lamb modes in a plate with respect to frequency/incident angle, gives the transmitted pressure fields below the plate.

8.2 Future work

A logical continuation of the present work with respect to non-invasive ultrasonic technology would be to replace the needle hydrophone by a finite dimensional piezoelectric receiver transducer, and use and account for this in the simulations. The FEM approach can be extended to account for a finite receiver transducer, in addition to a second steel plate. The hybrid FEM-ASM approach can also be extended to account for a finite receiver transducer, using the output of the ASM at a given distance as input in a FEM receiver transducer simulation. Transferring from an immersion transducer technique for leaky Lamb mode excitation, to a wedge-transducer setup, will make it possible to also include the signal chain through a possible wedge.

One further important goal will be to obtain transit-time simulations at relevant high accuracies. Better information on the required materials constants is expected to improve the accuracy of the simulations. Phase calibration of the needle hydrophone, amplifier and cables would also be a valuable tool in that respect. Improvement of positioning and maintaining a steady temperature for measurements will also increase accuracy for time-of-flight comparisons.

Since the plane-wave pressure transmission coefficient is limited to an isotropic viscoelastic plate and plane-wave theory, extending the description of the steel plate by finite elements for an oblique angle of beam incidence would be advantageous. One possible approach is to create a FEM calculated transmission coefficient using a normal beam incidence in the FEM approach, to be substituted for the plane-wave transmission coefficient in the hybrid FEM-ASM approach. This can be achieved by subtracting information from the wavenumber-frequency spectrum of the incident and transmitted beam in the FEM approach, but for the moment these spectra (due to limitations in the computer) does not adequately represent all plane-wave components needed to calculate the plane-wave pressure transmission coefficient for given frequencies.

Bibliography

[1] F. Song, Y. Lu, D. Zhang, and Z. Zhu, "Time-frequency analysis of SH waves in an isotropic plate bordered with one elastic solid layer," *Chinese Science Bulletin*, vol. 51, no. 17, pp. 2041–2045, Sep. 2006.

[2] J. Ma, M. J. S. Lowe, and F. Simonetti, "Measurement of the properties of fluids inside pipes using guided longitudinal waves." *IEEE Transactions on Ultrasonics, Ferroelectrics and Frequency Control,*, vol. 54, no. 3, pp. 647–58, Mar. 2007.

[3] R. Kippersund, P. Lunde, and K. Frøysa, "Deposit detection using plate waves," in *Proceedings of the 32nd Scandinavian Symposium on Physical Acoustics*, Geilo, Norway, 8-11 February, 2009.

[4] ——, "Measurement of fluid viscosity in pipes using multimode ultrasonic guided wave attenuation," in *Proceedings of Baltic-Nordic Acoustic Meeting 2010*, Bergen, Norway, 10-12 May, 2010.

[5] Z. Su, L. Ye, and Y. Lu, "Guided Lamb waves for identification of damage in composite structures: A review," *Journal of Sound and Vibration*, vol. 295, no. 3-5, pp. 753–780, Aug. 2006.

[6] A. Løvstad, "Detection of localised corrosion in pipes using guided waves," Ph.D. dissertation, Department of Electronics and Telecommunications, Norwegian University of Science and Technology, Norway, 2012.

[7] Vacossin, Bruno and Potel, Catherine and Gatignol, Philippe and de Belleval, Jean-François, "Interaction of a monochromatic ultrasonic beam with a finite length defect at the interface between two anisotropic layers: Kirchhoff approximation and Fourier representation." *IEEE Transactions on Ultrasonics, Ferroelectrics, and Frequency control*, vol. 56, no. 10, pp. 2251–67, Oct. 2009.

[8] C. P. Nacera Bedrici, Philippe Gatignol, "A iterative method for the interaction between a bounded beam and an interface defect in solids, under Kirchhoff approximation," *Acta Acustica united with Acustica*, vol. 95, pp. 189–202, 2009.

[9] R. Carandente and P. Cawley, "The effect of complex defect profiles on the reflection of the fundamental torsional mode in pipes," *NDT & E International*, vol. 46, pp. 41–47, Mar. 2012.

[10] J. Ma and P. Cawley, "Low-frequency pulse echo reflection of the fundamental shear horizontal mode from part-thickness elliptical defects in plates." *The Journal of the Acoustical Society of America*, vol. 127, no. 6, pp. 3485–93, Jun. 2010.

[11] M. Bezdêk, A. Rieder, H. Landes, R. Lerch, and W. Drahm, "A Novel Boundary Integral Formulation for Acoustic Radiation in a Nonuniform Flow : Coupling to FEM and Applications," in *IEEE Ultrasonics Symposium*, 2005, pp. 771–774.

[12] M. Bezdêk, H. Landes, A. Rieder, R. Lerch, and S. Member, "A Coupled Finite-Element , Boundary-Integral Method for Simulating Ultrasonic Flowmeters," *IEEE Transactions on Ultrasonics, Ferroelectrics and Frequency Control*, vol. 54, no. 3, pp. 636–646, 2007.

[13] M. Bezdêk, *Numerical modeling of ultrasonic flowmeters.* VDM Verlag Dr. Müller GmbH & Co. KG, Saarbruken, Germany, 2008.

[14] J. Li and J. L. Rose, "Natural beam focusing of non-axisymmetric guided waves in large-diameter pipes." *Ultrasonics*, vol. 44, no. 1, pp. 35–45, Jan. 2006.

[15] K. F. Graff, *Wave motion in elastic solids*, Oxford University Press, London, England, 1975.

[16] J. D. Achenbach, *Wave propagation in elastic solids*, North-Holland Publishing, Amsterdam, Netherlands, 1973.

[17] A. Velichko and P. D. Wilcox, "Excitation and scattering of guided waves: relationships between solutions for plates and pipes." *The Journal of the Acoustical Society of America*, vol. 125, no. 6, pp. 3623–31, Jun. 2009.

[18] P. Norli, "Sound velocity cell for gas characterization," Ph.D. dissertation, University of Bergen, Norway, 2007.

[19] F. Wolf, T. Lahmer, L. Bahr, A. Hauck, A. Sutor, R. Lerch, and M. Kaltenbacher, "Finite element modeling of ultrasonic transducer by utilizing an inverse scheme for the determination of its material parameters," in *IEEE Ultrasonics Symposium*, 2008, pp. 784–787.

[20] M. Aanes, E. Storheim, M. Vestrheim, and P. Lunde, "Finite element analysis and measurements of ultrasonic piezoceramic transducers in air and water," in *Proceedings of the Baltic-Nordic Acoustic Meeting 2010*, Bergen, Norway, May 10-12, 2010.

[21] L. Rayleigh, "On the free vibrations of an infinite plate of homogeneous isotropic elastic matter," in *London Mathematical Society*, 1889, pp. 225–234.

[22] H. Lamb, "On the flexure of an elastic plate," in *London Mathematical Society*, 1889, pp. 70–91.

[23] ——, "On waves in an elastic plate," in *Royal Society of London*, 1917, pp. 114–128.

[24] H. Reissner, "Der senkrecthe und schäge Durchtritt einer in einem flüssigen Medium erzeugten ebenen Dilatations Welle durch eie in diesem Medium befindliche plan-parallelle feste Platte," *Helv. Phys. Acta*, vol. 11, pp. 140–155, 1938.

[25] F. Levi and N. Nath, "Zur Theorie des Durchgangs von Ultraschallwellen durch eine feste Platte," *Helv. Phys. Acta*, vol. 11, pp. 408–431, 1938.

[26] M. F. M. Osborne and S. D. Hart, "Transmission, reflection, and guiding of an exponential pulse by a steel plate in water. I. Theory," *The Journal of the Acoustical Society of America*, vol. 17, no. 1, pp. 1–18, Jul. 1945.

[27] A. Schoch, "Der schalldurchgang durch platten," *Acustica*, vol. 2, no. 1, pp. 1–17, 1952.

[28] F. H. Sanders, "Transmission of sound through thin plates," *Canadian Journal of Research*, vol. 17a, no. 9, pp. 179–193, 1939.

[29] M. F. M. Osborne and S. D. Hart, "Transmission, Reflection, and Guiding of an Exponential Pulse by a Steel Plate in Water. II. Experiment," *The Journal of the Acoustical Society of America*, vol. 18, no. 1, pp. 170–184, Jul. 1946.

[30] J. B. Smyth and R. B. Lindsay, "Transmission at Oblique Incidence Through a Solid Plate in Water," *The Journal of the Acoustical Society of America*, vol. 16, no. May 2013, pp. 20–25, 1944.

[31] R. D. Fay and O. V. Fortier, "Transmission of Sound through Steel Plates Immersed in Water," *The Journal of the Acoustical Society of America*, vol. 23, no. 3, pp. 339–346, May 1951.

[32] A. Schoch, "Schallreflexion, Schallbrechung und Schallbeugung," *Ergebnisse der Exakten Naturwissenschaften*, vol. 23, pp. 127–234, 1950.

[33] M. S. Weinstein, "On the Failure of Plane Wave Theory to Predict the Reflection of a Narrow Ultrasonic Beam," *The Journal of the Acoustical Society of America*, vol. 24, no. 3, pp. 284–287, May 1952.

[34] W. G. Neubauer, "Ultrasonic reflection of a bounded beam at Rayleigh and critical angles for a plane liquid-solid interface," *Journal of Applied Physics*, vol. 44, no. 1, pp. 48–54, 1973.

[35] H. Bertoni and T. Tamir, "Unified theory of Rayleigh-angle phenomena for acoustic beams at liquid-solid interfaces," *Applied Physics A: Materials Science & Processing*, vol. 2, no. 4, pp. 157–172, Oct. 1973.

[36] W. G. Neubauer and L. R. Dragonette, "Measurement of rayleigh phase velocity and estimates of shear speed by schlieren visualization," *Journal of Applied Physics*, vol. 45, no. 2, pp. 618–622, 1974.

[37] T. J. Plona, M. Behravesh and W. G. Mayer, "Rayleigh and Lamb waves at liquid-solid boundaries," *Ultrasonics*, 1975.

[38] Leslie E. Pitts, T. J. Plona and Walter G. Mayer, "Theoretical similarties of Rayleigh and Lamb modes of vibration," *The Journal of the Acoustical Society of America*, vol. 60, no. 2, pp. 374–377, 1976.

[39] M. A. Breazeale, L. Adler, and G. W. Scott, "Interaction of ultrasonic waves incident at the Rayleigh angle onto a liquid-solid interface," *Journal of Applied Physics*, vol. 48, pp. 530–537, 1977.

[40] T. J. Plona, L. E. Pitts, and W. G. Mayer, "Ultrasonic bounded beam reflection and transmission effects at a liquid/ solid-plate/liquid interface," *The Journal of the Acoustical Society of America*, vol. 59, no. 6, pp. 1324–1328, 1976.

[41] L. Pitts, T. Plona, and W. Mayer, "Theory of nonspecular reflection. Effects for an ultrasonic beam incident on a solid plate in a liquid," *IEEE Transactions on Sonics and Ultrasonics*, vol. 24, no. 2, pp. 101–108, 1977.

[42] R. Fiorito and H. Uberall, "Resonance theory of acoustic reflection and transmission through a fluid layer," *The Journal of the Acoustical Society of America*, vol. 65, no. 1, pp. 9–14, Jan. 1979.

[43] W. Madigosky and R. Fiorito, "Modal resonance analysis of acoustic transmission and reflection losses in viscoelastic plates," *The Journal of the Acoustical Society of America*, vol. 65, no. 5, pp. 1105–1115, 1979.

[44] T. D. K. Ngoc and W. G. Mayer, "Numerical integration method for reflected beam profiles near Rayleigh angle," *The Journal of the Acoustical Society of America*, no. May 2013, pp. 1149–1152, 1980.

[45] K. W. Ng, T. D. K. Ngoc, J. A. McClure, and W. G. Mayer, "Nonspecular transmission effects for ultrasonic beams incident on a solid plate in liquid," *Acustica*, vol. 48, pp. 168–173, 1981.

[46] J. M. Claeys and O. Leroy, "Reflection and transmission of bounded sound beams on half-spaces and through plates," *The Journal of the Acoustical Society of America*, vol. 72, no. 2, pp. 585–590, 1982.

[47] J. Pott and J. G. Harris, "Scattering of an acoustic Gaussian beam from a fluid-solid interface," *The Journal of the Acoustical Society of America*, vol. 76, no. May 2013, pp. 1829–1838, 1984.

[48] H. Schmidt and F. B. Jensen, "A full wave solution for propagation in multilayererd viscoelastic media with application to gaussian beam reflection at fluid-solid interfaces," *The Journal of the Acoustical Society of America*, vol. 77, pp. 813–825, 1985.

[49] M. Rousseau and P. Gatignol, "Asymptotic analysis of nonspecular effects for the reflection and the transmission of a Gaussian acoustic beam incident on a solid plate," *The Journal of the Acoustical Society of America*, vol. 80, pp. 325–332, 1986.

[50] K. W. Ng, T. D. K. Ngoc, I. Molinero and M. de Billy, "Measurement of the profile of an ultrasonic beam non-specularly reflected from a solid plate," *Ultrasonics*, vol. 26, pp. 44–46, 1988.

[51] T. Kundu, "On the nonspecular reflection of bounded acoustic beams," *The Journal of the Acoustical Society of America*, vol. 83, no. 1, pp. 18–24, 1988.

[52] P. Lunde, "Interference effects in sound fields transmitted at fluid-fluid and fluid-solid interfaces," in *Proceedings of the 14th Scandinavian Symposium on Physical Acoustics*, Ustaoset, Norway, 27-30 January, 1991.

[53] P. Lunde and M. Vestrheim, "Sound propagation from a seismic source array - the simulation model CAPROS," Christian Michelsen Institute, Bergen, Norway, Tech. Rep. CMI Report 851403-3, 1986 (In Norwegian).

[54] S. Zeroug and L. B. Felsen, "Nonspecular reflection of beams from liquid-solid interfaces," *Journal of nondestructive evaluation*, vol. 11, pp. 263–278, 1992.

[55] M. R. Theodore E. Matikas and P. Gatignol, "Theoretical analysis for the reflection of a focused ultrasonic beam from a fluid-solid interface," *The Journal of the Acoustical Society of America*, vol. 93, no. 3, pp. 1407–1416, 1993.

[56] K. V. D. Abeele and O. Leroy, "On the influence of frequency and width of an ultrasonic bounded beam in the investigation of materials: Study in terms of heterogeneous plane waves," *The Journal of the Acoustical Society of America*, vol. 93, p. 2699, 1993.

[57] M. Deschamps and P. Chev'ee, "Reflection and transmission of a transient bounded beam by a dispersive and orthotropic plate," *Acta Acustica*, vol. 1, pp. 3–14, 1993.

[58] D. E. Chimenti, J.-G. Zhang, S. Zeroug and L. B. Felsen, "Interaction of acoustic beams with fluid-loaded elastic structures," *The Journal of the Acoustical Society of America*, vol. 95, no. January, pp. 45–59, 1994.

[59] S. Zeroug and L. B. Felsen, "Nonspecular reflection of two-and three-dimensional acoustic beams from fluid-immersed plane-layered elastic structures," *The Journal of the Acoustical Society of America*, vol. 95, no. June, pp. 3075–3089, 1994.

[60] M. J. Anderson, P. R. Martin and C. M. Fortunko, "Resonant transmission of a three-dimensional acoustic sound beam through a solid plate in air: Theory and measurement," *The Journal of the Acoustical Society of America*, vol. 98, no. 5, pp. 2628–2638, 1995.

[61] S. Zeroug and F. E. Stanke, "Ultrasonic pulsed beam interaction with a fluid-loaded elastic plate : Theory," *The Journal of the Acoustical Society of America*, vol. 100, no. November 1995, pp. 1339–1348, 1996.

[62] O. I. Lobkis, A. Safaeinilli and D.E. Chimenti, "Precision ultrasonic reflection studies in fluid-coupled plates," *The Journal of the Acoustical Society of America*, vol. 99, no. 5, pp. 2727–2736, 1996.

[63] O. I. Lobkis, A. Safaeinilli and D. E. Chimenti, "Effects of diffraction and experimental geometry on acoustic beam reflection from a fluid-loaded plate: a 3-D analysis," *Ultrasonics*, vol. 34, pp. 477–481, 1996.

[64] M. Castaings and P. Cawley, "The generation, propagation, and detection of Lamb waves in plates using air-coupled ultrasonic transducers," *The Journal of the Acoustical Society of America*, vol. 100, no. 5, p. 3070, 1996.

[65] P. Cawley and B. Hosten, "The use of large ultrasonic transducers to improve transmission coefficient measurements on viscoelastic anisotropic plates," *The Journal of the Acoustical Society of America*, vol. 101, no. May 2013, pp. 1373–1379, 1997.

[66] E. Moulin, J. Assaad, C. Delebarre, M. Houy, V. Cedex, and D. Osmont, "Modeling of Lamb waves generated by integrated transducers in composite plates using a coupled finite element-normal modes expansion method," *The Journal of the Acoustical Society of America*, vol. 107, pp. 87–94, 1999.

[67] E. Moulin, J. Assaad, C. Delebarre, S. Grondel, and D. Balageas, "Modeling of integrated Lamb waves generation systems using a coupled finite element-normal modes expansion method," *Ultrasonics*, vol. 38, pp. 522–6, 2000.

[68] B. J. Landsberger, "Second harmonic generation in sound beams reflected from and transmitted through immersed elastic solids," Ph.D. dissertation, University of Texas at Austin, USA, 1997.

[69] B. J. Landsberger and M. F. Hamilton, "Second-harmonic generation in sound beams reflected from, and transmitted through, immersed elastic solids," *The Journal of the Acoustical Society of America*, vol. 109, no. 2, pp. 488–500, Feb. 2001.

[70] S. J. Younghouse, "Irradiation of an elastic plate by a finite-amplitude sound beam with applications to nondestructive evaluation," Ph.D. dissertation, University of Austin, Texas, USA, 2002.

[71] O. L. J. Vandeputte and G. Shkerdin, "Influence of planar cracks in plates on reflected and transmitted fields of gaussian acoustic beams," *The Journal of the Acoustical Society of America*, vol. 114, no. 2, pp. 634–643, 2003.

[72] O. L. Sigfried Vanaverbeke and G. Shkerdin, "Interaction of a bounded ultrasonic beam with a thin inclusion inside a plate," *The Journal of the Acoustical Society of America*, vol. 114, no. 2, pp. 601–610, 2003.

[73] L. Duquenne, E. Moulin, J. Assaad, and S. Grondel, "Transient modeling of Lamb waves generated in viscoelastic materials by surface bonded piezoelectric transducers," *The Journal of the Acoustical Society of America*, vol. 116, p. 133, 2004.

[74] C. Potel, S. Baly, J. de Belleval, M. Lowe, and P. Gatignol, "Deviation of a monochromatic lamb wave beam in anisotropic multilayered media: Asymptotic analysis, numerical and experimental results," *IEEE Transactions on Ultrasonics, Ferroelectrics, and Frequency control*, vol. 52, no. 6, pp. 987–1001, 2005.

[75] N.F. Declercq, R. Briers, J. Degrieck and O. Leroy, "The history and properties of ultrasonic inhomogeneous waves." *IEEE transactions on Ultrasonics, Ferroelectrics, and Frequency control*, vol. 52, no. 5, pp. 776–791, 2005.

[76] R. Kazys, A. Demcenko, E. Zukauskas, and L. Mazeika, "Air-coupled ultrasonic investigation of multilayered composite materials." *Ultrasonics*, vol. 44, pp. 819–822, Dec. 2006.

[77] Y. Bouzidi and D. R. Schmitt, "A large ultrasonic bounded acoustic pulse transducer for acoustic transmission goniometry: Modeling and calibration," *The Journal of the Acoustical Society of America*, vol. 119, no. 1, pp. 54–64, 2006.

[78] S. Banerjee and T. Kundu, "Ultrasonic field modeling in plates immersed in fluid," *International Journal of Solids and Structures*, vol. 44, no. 18-19, pp. 6013–6029, Sep. 2007.

[79] S. Banerjee, T. Kundu and N. A. Alnuaimi, "DPSM technique for ultrasonic field modelling near fluid-solid interface," *Ultrasonics*, vol. 46, pp. 235–250, 2007.

[80] J. Jocker and D. Smeulders, "Minimization of finite beam effects in the determination of reflection and transmission coefficients of an elastic layer," *Ultrasonics*, vol. 46, no. 1, pp. 42–50, Mar. 2007.

[81] E. Lamkanfi, N. F. Declercq, W. v. Paepegem, and J. Degrieck, "Finite element analysis of transmission of leaky rayleigh waves at the extremity of a fluid-loaded thick plate," *Journal of Applied Physics*, vol. 101, pp. 114 907–1–10, 2007.

[82] M. Bezdêk and B. R. Tittmann, "Dispersion Analysis of a Three-Layered Waveguide with Finite Element and Matrix Methods," *Acta Acustica united with Acustica*, vol. 94, no. 5, pp. 792–806, Sep. 2008.

[83] S. Das, C. M. Dao, S. Banerjee, and T. Kundu, "DPSM modeling for studying interaction between bounded ultrasonic beams and corrugated plates with experimental verification." *IEEE transactions on Ultrasonics, Ferroelectrics, and Frequency control*, vol. 54, no. 9, pp. 1860–72, 2007.

[84] Y. Bouzidi and D. Schmitt, "Quantitative modeling of reflected ultrasonic bounded beams and a new estimate of the schoch shift," *IEEE Transactions on Ultrasonics, Ferroelectrics, and Frequency control*, vol. 55, no. 12, pp. 2661–2673, 2008.

[85] B. Hosten and C. Biateau, "Finite element simulation of the generation and detection by air-coupled transducers of guided waves in viscoelastic and anisotropic materials." *The Journal of the Acoustical Society of America*, vol. 123, no. 4, pp. 1963–71, 2008.

[86] W. Ke, M. Castaings, and C. Bacon, "3D finite element simulations of an air-coupled ultrasonic NDT system," *NDT & E International*, vol. 42, no. 6, pp. 524–533, Sep. 2009.

[87] C. M. Dao, S. Das, S. Banerjee, and T. Kundu, "Wave propagation in a fluid wedge over a solid half-space - mesh-free analysis with expermental verification," *International Journal of Solids and Structures*, vol. 46, pp. 2486–2492, 2009.

[88] M. Masmoudi, B. Hosten and C. Biateau, "Analytical and finite element methods for studying the influence of the air-coupled transducer characteristics on the purity of guided waves generated in solids," *Review of Quantitative Nondestructive Evaluation*, vol. 29, pp. 1887–1894, 2010.

[89] S. Delrue, K. Van Den Abeele, E. Blomme, J. Deveugele, P. Lust, and O. B. Matar, "Two-dimensional simulation of the single-sided air-coupled ultrasonic pitch-catch technique for non-destructive testing." *Ultrasonics*, vol. 50, no. 2, pp. 188–96, Mar. 2010.

[90] K. D. Lohne, M. Vestrheim, and P. Lunde, "Ultrasonic signal transmission in plates - Study of a steel plate immersed in water," in *Proceedings of the 31st Scandinavian Symposium on Physical Acoustics*, Geilo, Norway, 27-30 January, 2008.

[91] K. D. Lohne, P. Lunde, and M. Vestrheim, "Measurements and 3D simulations of ultrasonic directive beam transmission through a water-immersed steel plate," in *Proceedings of the 34th Scandinavian Symposium on Physical Acoustics*, Geilo, Norway, 30 January - 2 February, 2011.

[92] K. D. Lohne, Ph.D. dissertation, University of Bergen, Department of Physics and Technology, Bergen, Norway [in progress].

[93] M. Aanes, K. D. Lohne, P. Lunde, and M. Vestrheim, "Finite element analysis of acoustic beam interactions with a plate at normal incidence. Comparison with a 3D angular spectrum method and measurements," in *Proceedings of the 34th Scandinavian Symposium on Physical Acoustics*, no. February, Geilo, Norway, January 30 - February 2, 2011.

[94] ——, "Normal incidence ultrasonic beam transmission through a water-immersed plate using a piezoelectric transducer. Finite element modeling, angular spectrum method and measurements," in *Proceedings of the International Congress on Sound Vibration*, Vilnius, Lithuania, 08-12 July, 2012.

[95] ——, "Ultrasonic beam transmission through a water-immersed plate at oblique incidence using a piezoelectric source transducer . Finite element - angular spectrum modeling and measurements," in *IEEE International Ultrasonics Symposium Proceedings*, (October 7-10) 2012, pp. 1972–1977.

[96] G. Waag, L. Hoff and P. Norli, "Model for thickness measurements of steel plates using half-wave resonances," in *IEEE International Ultrasonics Symposium Proceedings*, 2012.

[97] M. Masmoudi and M. Castaings, "Three-dimensional hybrid model for predicting air-coupled generation of guided waves in composite material plates." *Ultrasonics*, vol. 52, no. 1, pp. 81–92, Jan. 2012.

[98] M. Aanes, P. Lunde, and M. Vestrheim, "Ultrasonic beam transmission through a steel plate at oblique incidence. Uniform piston vs. piezoelectric transducer." in *Proceedings of the 36th Scandinavian Symposium on Physical Acoustics*, no. February, Geilo, Norway, February 3 - 6, 2013.

[99] M. Rahman, *Applications of Fourier Transforms to Generalized Functions*. Southampton, England: WIT Press, 2011.

[100] E. Williams, *Fourier Acoustics*, Academic Press, London, England, 1999.

[101] L. M. Brekhovskikh, *Waves in layered media*, Academic Press, New York, USA, 1960.

[102] D. E. Chimenti and A. H. Nayfeh, "Ultrasonic Reflection and Guided Waves in Fluid-Coupled Composite Laminates," *Journal of Nondestructive Evaluation*, vol. 9, no. 2, pp. 51–69, 1990.

[103] J. Kocbach, "Finite Element Modeling of Ultrasonic Piezoelectric Transducers," Ph.D. dissertation, Department of Physics, University of Bergen, Norway, 2000.

[104] N. Guo, "The vibration characteristics of piezoelectric discs," Ph.D. dissertation, Department of Mechanical Engineering, Imperial College of Science, Technology and Medicine, London, England, 1989.

[105] R. H. C. Martine Naillon and F. Besnier, "Analysis of piezoelectric structures by a finite element method," *Acta Electronica*, vol. 25, no. 4, pp. 341–362, 1983.

[106] J. Kocbach, P. Lunde, and M. Vestrheim, "FE Simulations of Piezoceramic Disks with a Front Layer of Varying Thickness," in *IEEE Ultrasonic Symposium*, 1999.

[107] ——, "FEMP - Finite Element Modeling of Piezoelectric Structures. Theory and Verification for Piezoceramics Disks," Department of Physics, University of Bergen, Norway, Tech. Rep. 1999-07, 1999.

[108] J. Kocbach, P. Lunde, M. Vestrheim, and R. A. Kippersund, "Finite element modeling of ultrasonic piezoelectric transducers. Extension of FEMP to 3D analysis," CMR-06-A10046-RA-01, Christian Michelsen Research, Bergen, Norway, Tech. Rep., 2006.

[109] J. Kocbach, P. Lunde, and M. Vestrheim, "Resonance Frequency Spectra with Convergence Tests of Piezoceramic Disks using the Finite Element Method," *Acta Acustica united with Acustica*, vol. 87, pp. 271–285, 2001.

[110] M. Aanes and M. Vestrheim, "Finite Element Studies of Permittivity Constants in Piezoceramic Disks," in *Proceedings of the 32nd Scandinavian Symposium on Physical Acoustics*, Finse, Norway, (February 8-11) 2009.

[111] R. Fardal, "Endelig element analyse av elektriske egenskaper til piezoelektriske skiver," Master's thesis, Department of Physics, University of Bergen, 2002 [in Norwegian].

[112] R. A. Kippersund, J. Kocbach, and P. Lunde, "Simulation of guided waves in a fluid loaded elastic plate," in *Proc. of 31st Scandinavian Symposium on Physical Acoustics*, 27-30 January, Geilo, Norway, 2008.

[113] J. Kocbach, R. A. Kippersund, and P. Lunde, "Time Domain Finite Element Modeling of SH-mode propagation in elastic plates with deposits," in *Proceedings of the 33rd Scandinavian Symposium on Physical Acoustics*, Geilo, Norway, 2010.

[114] K. D. Lohne, "Undersøkelse og utnyttelse av svingemoder i ultralyd transduserkonstruksjoner," Master's thesis, Department of Physics and Technology, University of Bergen, Norway, 2005 [in Norwegian].

[115] V. Knappskog, "Radiellmode svingninger i piezoelektriske ultralydtransdusere for luft. Målinger og endelig element analyser," Master's thesis, Department of Physics and Technology, University of Bergen, Norway, 2007.

[116] R. Holland, "Representation of Dielectric, Elastic, and Piezoelectric Losses by Complex Coefficients," *IEEE Transactions on Sonics and Ultrasonics*, vol. 14, no. 1, pp. 18–20, 1967.

[117] J.-P. Berenger, "A perfectly matched layer for the absorption of electromagnetic waves," *Journal of Computational Physics*, vol. 114, no. 2, pp. 185–200, Oct. 1994.

[118] A. Bermúdez, L. Hervella-Nieto, A. Prieto, and R. Rodriguez, "An optimal perfectly matched layer with unbounded absorbing function for time-harmonic acoustic scattering problems," *Journal of Computational Physics*, vol. 223, no. 2, pp. 469–488, May 2007.

[119] M. Kaltenbacher and R. Lerch, "Perfectly Matched Layer Technique for the Numerical Computation of Wave Propagation Phenomena," in *IEEE Ultrasonics Symposium*, 2007, pp. 183–186.

[120] I. A. Viktorov, *Rayleigh and Lamb waves. Physical theory and applications*, Plenum Press, New York, USA, 1967.

[121] B. A. Auld, *Acoustic Fields and Waves in Solids, 2 Vol.*, Krieger Publishing Company, Malabar, Florida, USA, 1990.

[122] J. Rose, *Ultrasonic waves in solid media*. Cambridge University Press, United Kingdom, 1999.

[123] *HP 33120A User's guide Edition 6, March 2002, Publications number 33120-90006, Agilent Technologies, Inc. 1994-2002.*

[124] *Precision Acoustic Ltd, Hampton Farm Business Park, Higher Bockhampton, Dorchester, Dorset, U.K.*

[125] *Datasheet for Femto HVA-10M-60-F voltage amplifier, FEMTO Messtechnik Gmbh, Berlin, Germany, 2013.*

[126] *Operation manual for HK 3202 filter, Krohn-Hite, Brockton, MA, USA, 2013.*

[127] *Digital Phosphor Oscilloscopes User Manual DPO3000 series, Tektronix, Inc. Beaverton, OR. USA, 2013.*

[128] *Precision Rotation Stage PRS-110, PiMicos GmbH, Eschbach, Germany, 2009.*

[129] *404XE T07 Linear Positioning Tables Catalog 8087, Parker Automation, USA, 2006.*

[130] *Linear Motor Stage LMS-100, PiMicos GmbH, Eschbach, Germany, 2009.*

[131] *404XE T09 Linear Positioning Tables Catalog 8087, Parker Automation, USA, 2006.*

[132] *EK-i/EW-i Series Instruction manual, A&D Company Limited, Tokyo, Japan, 2013.*

[133] *Kobra/Mauser caliper, Germany.*

[134] *TESA SA, Rue du Bugnon 38, Switzerland, 2013.*

[135] *Olympus V301 immersion transducer, 48 Woerd Avenue Waltham, MA, 02453, US, 2013.*

[136] J. Wu, "Determination of velocity and attenuation of shear waves using ultrasonic spectroscopy," *The Journal of the Acoustical Society of America*, vol. 99, no. 5, pp. 2871–2875, 1996.

[137] *National Physical Laboratory, Hampton Road, Teddington, Middlesex, TW111 0LW, England.*

[138] *ANSI S1.20 - Procedures for calibration of underwater electroacoustic transducers*, Std., 1988.

[139] L. L. Foldy and H. Primakoff, "A general theory of passive linear electroacoustic transducers and the electroacoustic reciprocity theorem." *The Journal of the Acoustical Society of America*, vol. 17, no. 2, pp. 109–120, 1945.

[140] *Operation and service manual Model 4192A LF impedance analyzer, Yokogawa-Hewlett-Packard Ltd, Tokyo, Japan, 1982*, 1981.

[141] L. E. Kinsler, A. R. Frey, A. B. Coppens, and J. V. Sanders, *Fundamentals of Acoustics*, 4th ed. Wiley, Dec. 1999.

[142] M. Aanes, "Undersøkelser av piezokeramiske skiver. Målinger og endelig element analyser." Master's thesis, University of Bergen, Department of Physics and Technology, Bergen, Norway [in Norwegian], 2009.

[143] M. Vestrheim and R. Fardal, "Methods for determining constants of piezoelectric ceramic materials. using synthetic data for studying basic accuracies," in *Proceedings of the 25th Scandinavian Symposium on Physical Acoustics*, Ustaoset, Norway, January 27 - 30, 2002.

[144] ——, "Basic accuracy of measurement methods for material constants of piezoelectric ceramics," in *Proceedings of the Baltic-Nordic Acoustic Meeting 2002*, Copenhagen, Denmark, August 26 - 28, 2002.

[145] *High accuracy digimatic micrometer, Mitutoyo Europe GmbH, 41469 Neuss, Germany, 2013.*

[146] *Meggit Ferroperm Piezoceramics, High quality components and materials fo the electronics industry, Hejreskovvej 18A, DK-3490 Kvistgård, Denmark, 2013.*

[147] *Eccosorb MF114, Laird Technologies - Emerson & Cuming Microwave Products, 28 York Avenue, Randolph, MA 02369, USA, 2013.*

[148] *HCP70, Divinycell International AB, DIAB Group, Norra Sofieroleden 8, 31232 Laholm, Sweden, 2013.*

[149] E. Storheim, M. Aanes, M. Vestrheim, and P. Lunde, "Ultrasonic piezoceramic transducers for air , - finite element analysis and measurements," in *Proceedings of the 33rd Scandinavian Symposium on Physical Acoustics*, Geilo, Norway, February 7-10, 2010.

[150] M. Aanes, J. Kocbach, and M. Vestrheim, "Modal and direct harmonic solution methods in FE modeling of piezoceramic disks," in *Proceedings of the 33rd Scandinavian Symposium on Physical Acoustics*, Geilo, Norway, February 7-10, 2010.

[151] Ø. S. Amundsen, "Material constants determination for piezoelectric disks, and influence on source sensivitiy. measurements and simulations." Master's thesis, Department of Physics and Technology, University of Bergen, Norway, 2011.

[152] Ø. S. Amundsen, M. Aanes, J. Kocbach, and M. Vestrheim, "Generalized permittivity and source sensitivity of piezoelectric ceramic disks," in *Proceedings of the 34th Scandinavian Symposium on Physical Acoustics*, Geilo, Norway, January 30 - February 2, 2011.

[153] *ANSI/IEEE standard 176-1987, "IEEE Standard on Piezoelectricity", Published by the institute of Electrical and Electronics Engineers, Inc. New York, USA*, Std., 1988.

[154] T. Lahmer, M. Kaltenbacher, B. Kaltenbacher, R. Lerch, and E. Leder, "FEM-Based determination of real and complex elastic, dielectric, and piezoelectric moduli in piezoceramic materials," *IEEE Transactions on Ultrasonics, Ferroelectrics and Frequency Control*,, vol. 55, no. 2, pp. 465–475, 2008.

[155] S. Rupitsch, F. Wolf, A. Sutor, and R. Lerch, "Estimation of material parameters for piezoelectric actuators using electrical and mechanical quantities," in *IEEE Ultrasonics Symposium*, 2009, pp. 1–4.

[156] S. Sherrit, N. Gauthier, H. D. Wiederick, and B. K. Mukherjee, "Accurate evaluation of the real and imaginary material constants for a piezoelectric resonator in the radial mode," *Ferroelectrics*, vol. 119, no. 1, p. 17, 1991.

[157] S. Sherrit, H. D. Wiederick, and B. K. Mukherjee, "A polynomial fit for calculating the electromechanical coupling constants of piezoelectric materials using the method described by Onoe et al." *The Journal of the Acoustical Society of America*, vol. 91, no. 3, pp. 1770–1771, Mar. 1992.

[158] *Morgan TechnicalCeramics - Electro Ceramics, Bursledon Road, Thornhull, Southapton, SO19 7TG, England.*

[159] G. Kossoff, "The effects of backing and matching on the performance of piezoelectric ceramic transducers," *IEEE Transactions on sonics and ultrasonics*, vol. 13, pp. 20–30, 1966.

[160] *Guide to dynamic measurements of piezoelectric ceramics with high electromechanical coupling*, International Electrotechnical Commission, 1976.

[161] *Loctite, Henkel Norden AB, branch office Oslo, Østensjøveien 14, NO-0661 OSLO, Norway, 2013.*

[162] *MG Chemicals, 9347 - 193rd Street, Surrey, B.C., Canada V4N 4E7, 2013.*

[163] J. P. Sessarego, J. Sagèloli, C. Gazanhes and H. Überall, "The splitting of dispersion curves for plates fluid-loaded on both sides," *The Journal of the Acoustical Society of America*, vol. 101, pp. 1246–1248, 1997.

[164] M. Deschamps and O. Poncelet, "Transient lamb waves: Comparison between theory and experiment," *The Journal of the Acoustical Society of America*, vol. 107, no. 6, pp. 3120–3129, 2000.

[165] R.D. Doherty, D.A. Hughes, F.J. Humphreys, J.J. Jonas, D. Juul Jensen, M.E. Kassner, W.E. King, T.R. McNelley, H.J. McQueen and A.D. Rollet, "Current issues in recrystallization: a review," *Materials Science and Engineering A*, vol. 238, pp. 219–274, 1997.

[166] D. F. Ball and D. Shewring, "Some problems in the use of Lamb waves for the inspection of cold-rolled steel sheet and coil," *Non-Destructive Testing*, vol. 6, no. 3, pp. 138–145, 1973.

[167] A. Moro, C. Farina, and F. Rossi, "Measurement of ultrasonic wave velocity in steel for various structures and degrees of cold-working," *NDT International*, vol. 13, no. 4, pp. 169–175, 1980.

Appendix A

FEM baffled piston project-file

```
if ~isempty(read.piston)
  r=read.piston(1,1,:);
  elr=read.piston(1,2,:);
  elfluid=read.piston(1,3,:);
  matnumfluid=read.piston(1,4,:);
  pistonvalue=read.piston(1,5,:);
  zPlate=read.piston(1,6,:);
  avstandPlate=read.piston(1,7,:);
  avstandNedre=read.piston(1,8,:);
  rPlate=read.piston(1,9,:);
  matnumPlate=read.piston(1,10,:);
  elplate=read.piston(1,11,:);

  for s=1:size(r,3)
 pmllag(s) = 20e-3;
     bakpiston(s) = 50e-3;
     glob.pmlsigma_star_vec=0;
     read.points(:,:,s)=[ 1 0 0;
2 r(s) 0;
3 0 1e-5;
4 r(s) 1e-5;
5 0 -avstandPlate(s);
6 r(s) -avstandPlate(s);
7 0 -avstandPlate(s)-zPlate(s);
8 r(s) -avstandPlate(s)-zPlate(s);
9 0 -avstandPlate(s)-zPlate(s)-avstandNedre(s);
10 r(s) -avstandPlate(s)-zPlate(s)-avstandNedre(s);
11 rPlate(s) 0;
12 rPlate(s) -avstandPlate(s);
13 rPlate(s) -avstandPlate(s)-zPlate(s);
14 rPlate(s) -avstandPlate(s)-zPlate(s)-avstandNedre(s);
                15 0 bakpiston(s);
                16 r(s) bakpiston(s);
                17 rPlate(s) bakpiston(s);
                18 rPlate(s) 1e-5];

     read.areas(:,:,s)=[ 1,1,2,4,3,1001,1001,0,0;
3,5,6,2,1,elfluid(s),elfluid(s),0,0;
3,7,8,6,5,elfluid(s),elfluid(s),0,0;
3,8,13,12,6,elfluid(s),elfluid(s),0,0;
3,6,12,11,2,elfluid(s),elfluid(s),0,0;
3,9,10,8,7,elfluid(s),elfluid(s),0,0;
3,10,14,13,8,elfluid(s),elfluid(s),0,0;
```

```
                %3,3,4,16,15,elfluid(s),elfluid(s),0,0;
                %3,4,18,17,16,elfluid(s),elfluid(s),0,0;
                %3,2,11,18,4,elfluid(s),elfluid(s),0,0];
];

     matnumelast=6; % Just choose elastic material. Not important which material!
     read.materials(:,:,s)=[ 1 glob.globvariables.mechanic matnumelast;
2 glob.globvariables.mechanic matnumelast;
                           3 glob.globvariables.fluid matnumfluid(s)];

     read.restraints(:,:,s)=[-1 r(s)+1e-9 -1e-9 1e-9 glob.free.dz pistonvalue(s)];

     read.dof(:,:,s)=[ %% PML
-1 1 -avstandPlate(s)-zPlate(s)-avstandNedre(s)-1e-9 -avstandPlate(s)-zPlate(s)-avstandNedre(s)+1e-9 glob.free.vp;
                -1 1 bakpiston(s)-1e-9 bakpiston(s)+1e-9 glob.free.vp;
%% Bare fluid
rPlate(s)-1e-9 rPlate(s)+1e-9 -1 1 glob.free.vp];
%rPlate(s)-1e-9 rPlate(s)+1e-9 -avstandPlate(s) 0 glob.free.vp;
%rPlate(s)-1e-9 rPlate(s)+1e-9 -avstandPlate(s)-zPlate(s)-avstandNedre(s) -avstandPlate(s)-zPlate(s) glob.free.vp;];

% Creating decreasing Qm for plate outside fluid region
% Eksponentiell neddempning av Qm til Qmin i (retning (enten +-(r,z) (-1,1,-2,2),rmin,rmax,zmin,zmax,Qmin,Qm) - naturlige logaritme --
% se mer i k_calc_mechanic.m
%glob.lossvariation=1;
%glob.lossvarvecs{s} = [1,rPlate(s)-pmllag(s),rPlate(s)+staalvakum(s),-avstandPlate(s),-avstandPlate(s)-zPlate(s),Qmin(s),Qm(s)];

% PML for mange regioner (ikke symmetrisk boks som er default)
% Default glob.pmlform er symmetrisk boks, her er den definert som "manyregions". Dermed kan du legge pmllag vilkaarlig i 2.5d.
% glob.pmlregions{k} = [retning pml(enten +-(r,z) (-1,1,-2,2),rmin,rmax,zmin,zmax]; -- se mer i k_calc_pml.m
glob.pmlform=glob.globvariables.manyregions;
glob.pmlregions={1,2};  % region 4 er for testing av bare fluid (bytt ut 1 og 2 med 4)
%glob.pmlregions{1}=[1,rPlate(s)-pmllag(s),rPlate(s),-avstandPlate(s),0];
%glob.pmlregions{2}=[1,rPlate(s)-pmllag(s),rPlate(s),-avstandPlate(s)-zPlate(s)-avstandNedre(s),-avstandPlate(s)-zPlate(s)];
glob.pmlregions{1}=[-2,0,rPlate(s),-avstandPlate(s)-zPlate(s)-avstandNedre(s),-avstandPlate(s)-zPlate(s)-avstandNedre(s)+pmllag(s)];
% For testing av bare fluid
glob.pmlregions{2}=[1,rPlate(s)-pmllag(s),rPlate(s),-avstandPlate(s)-zPlate(s)-avstandNedre(s),bakpiston(s)];
        %glob.pmlregions{3}=[2,0,rPlate(s),bakpiston(s)-pmllag(s),bakpiston(s)];

f=(read.directharmonicanalysis(1)+read.directharmonicanalysis(3))/2;
glob.pmlomega_vec=2*pi*f;
glob.pmlfluid=1;
  end
end
```

Appendix B

FEM piezoelectric transducer project-file

```
if ~isempty(read.transducerlimplate)
  rp=read.transducerlimplate(1,1,:); % Radius of piezo disk
  tp=read.transducerlimplate(1,2,:); % Thickness of piezo disk
  rfr=read.transducerlimplate(1,3,:); % Radius of front layer
  tfr=read.transducerlimplate(1,4,:); % Thickness of front layer
  tb=read.transducerlimplate(1,5,:); % Thickness of backing layer
  tc=read.transducerlimplate(1,6,:); % Thickness of steel casing - back end
  matnump=read.transducerlimplate(1,7,:);
  matnumfr=read.transducerlimplate(1,8,:);
  matnumb=read.transducerlimplate(1,9,:);
  matnumc=read.transducerlimplate(1,10,:);
  rPlate=read.transducerlimplate(1,11,:); % Radius of steel plate
  tBAK=read.transducerlimplate(1,12,:); % Distance from back of transducer to end of fluid region
  avstandPlate=read.transducerlimplate(1,13,:); % Distance between the transducer and the steel plate (front to front)
  tPlate=read.transducerlimplate(1,14,:); % Thickness of steel plate
  tFRONT=read.transducerlimplate(1,15,:); % Distance from lower surface of the steel plate to end of fluid region
  tlim = read.transducerlimplate(1,16,:);

  % INPUT FOR AIR LAYER AT THE BACK OF THE TRANSDUCER
  tair = 10.42e-3; % Depth of cone of air in backing layer
  rbair = 4.01e-3; % Radius of cone of air in backing layer
  tb = tb-tair;
  tc2 = 2.83e-3; % Casing thickness - sides
  elp = 3; % Elements per wavelength in piezo disk
  elfr = 3; % Elements per wavelength in front layer
  elc = 3; % Elements per wavelength in casing
  elf = 3; % Elements per wavelength in water
  elb = 3; % Elements per wavelength in backing layer
  matnumf = 444;  % Material number for water
  staalvakum = 200e-3; % Steel plate radius in vacuum
  PMLlag = 30e-3; % Fluid PML thickness
  glob.pmlsigma_star_vec=0;     % Damping function to fluid PML
  Qm = 1000;  % "Decreasing Qm" from Qm
  Qmin = 0.001; % to Qmin
  matnumcasing = 5;
  %%%%%%%%%%%%%%%%%%%%%%%%%%%
  rair = rfr-rbair;
  rc = rfr+tc2;
  matdatalim = 560;
```

```
  for s=1:size(rp,3)
    read.points(:,:,s)=[1 0 0;
2 rair(s) 0;
3 rp(s) 0;
4 rfr(s) 0;
5 rc(s) 0;
6 rPlate(s) 0;
7 0 tfr(s)+tlim(s);
8 rair(s) tfr(s)+tlim(s);
9 rp(s) tfr(s)+tlim(s);
10 rfr(s) tfr(s)+tlim(s);
11 rc(s) tfr(s)+tlim(s);
12 rPlate(s) tfr(s)+tlim(s);
13 0 tfr(s)+tp(s)+tlim(s);
14 rair(s) tfr(s)+tp(s)+tlim(s);
15 rp(s) tfr(s)+tp(s)+tlim(s);
16 rfr(s) tfr(s)+tp(s)+tlim(s);
17 rc(s) tfr(s)+tp(s)+tlim(s);
18 rPlate(s) tfr(s)+tp(s)+tlim(s);
19 0 tfr(s)+tp(s)+tb(s)+tlim(s);
20 rair(s) tfr(s)+tp(s)+tb(s)+tlim(s);
21 rp(s) tfr(s)+tp(s)+tb(s)+tlim(s);
22 rfr(s) tfr(s)+tp(s)+tb(s)+tlim(s);
23 rc(s) tfr(s)+tp(s)+tb(s)+tlim(s);
24 rPlate(s) tfr(s)+tp(s)+tb(s)+tlim(s);
25 0 tfr(s)+tp(s)+tb(s)+tair(s)+tlim(s);
26 rair(s) tfr(s)+tp(s)+tb(s)+tair(s)+tlim(s);
27 rp(s) tfr(s)+tp(s)+tb(s)+tair(s)+tlim(s);
28 rfr(s) tfr(s)+tp(s)+tb(s)+tair(s)+tlim(s);
29 rc(s) tfr(s)+tp(s)+tb(s)+tair(s)+tlim(s);
30 rPlate(s) tfr(s)+tp(s)+tb(s)+tair(s)+tlim(s);
31 0 tfr(s)+tp(s)+tb(s)+tair(s)+tc(s)+tlim(s);
32 rair(s) tfr(s)+tp(s)+tb(s)+tair(s)+tc(s)+tlim(s);
33 rp(s) tfr(s)+tp(s)+tb(s)+tair(s)+tc(s)+tlim(s);
34 rfr(s) tfr(s)+tp(s)+tb(s)+tair(s)+tc(s)+tlim(s);
35 rc(s) tfr(s)+tp(s)+tb(s)+tair(s)+tc(s)+tlim(s);
36 rPlate(s) tfr(s)+tp(s)+tb(s)+tair(s)+tc(s)+tlim(s);
37 0 tfr(s)+tp(s)+tb(s)+tair(s)+tc(s)+tBAK(s)+tlim(s);
38 rair(s) tfr(s)+tp(s)+tb(s)+tair(s)+tc(s)+tBAK(s)+tlim(s);
39 rp(s) tfr(s)+tp(s)+tb(s)+tair(s)+tc(s)+tBAK(s)+tlim(s);
40 rfr(s) tfr(s)+tp(s)+tb(s)+tair(s)+tc(s)+tBAK(s)+tlim(s);
41 rc(s) tfr(s)+tp(s)+tb(s)+tair(s)+tc(s)+tBAK(s)+tlim(s);
42 rPlate(s) tfr(s)+tp(s)+tb(s)+tair(s)+tc(s)+tBAK(s)+tlim(s);
43 0 -avstandPlate(s);
44 rair(s) -avstandPlate(s);
45 rp(s) -avstandPlate(s);
46 rfr(s) -avstandPlate(s);
47 rc(s) -avstandPlate(s);
48 rPlate(s) -avstandPlate(s);
49 rPlate(s)+staalvakum(s) -avstandPlate(s);
50 0 -avstandPlate(s)-tPlate(s);
51 rair(s) -avstandPlate(s)-tPlate(s);
52 rp(s) -avstandPlate(s)-tPlate(s);
53 rfr(s) -avstandPlate(s)-tPlate(s);
54 rc(s) -avstandPlate(s)-tPlate(s);
55 rPlate(s) -avstandPlate(s)-tPlate(s);
56 rPlate(s)+staalvakum(s) -avstandPlate(s)-tPlate(s);
57 0 -avstandPlate(s)-tPlate(s)-tFRONT(s);
58 rair(s) -avstandPlate(s)-tPlate(s)-tFRONT(s);
59 rp(s) -avstandPlate(s)-tPlate(s)-tFRONT(s);
60 rfr(s) -avstandPlate(s)-tPlate(s)-tFRONT(s);
```

```
61 rc(s) -avstandPlate(s)-tPlate(s)-tFRONT(s);
62 rPlate(s) -avstandPlate(s)-tPlate(s)-tFRONT(s);
63 0 tfr(s);
64 rair(s) tfr(s);
65 rp(s) tfr(s);
66 rfr(s) tfr(s);
67 rc(s) tfr(s);
68 rPlate(s) tfr(s)];

    read.areas(:,:,s)=[ 1 1 2 64 63 elp(s) elfr(s) 0 0;
1 2 3 65 64 elp(s) elfr(s) 0 0;
1 3 4 66 65 elp(s) elfr(s) 0 0;
2 4 5 67 66 elp(s) elc(s) 0 0;
3 5 6 68 67 elp(s) elf(s) 0 0;
7 63 64 8 7 elp(s) elfr(s) 0 0;
            7 64 65 9 8 elp(s) elfr(s) 0 0;
            7 65 66 10 9 elp(s) elfr(s) 0 0;
            2 66 67 11 10 elp(s) elc(s) 0 0;
            3 67 68 12 11 elp(s) elf(s) 0 0;
            4 7 8 14 13 elp(s) elp(s) 0 0;
4 8 9 15 14 elp(s) elp(s) 0 0;
5 9 10 16 15 elp(s) elb(s) 0 0;
2 10 11 17 16 elp(s) elc(s) 0 0;
3 11 12 18 17 elp(s) elf(s) 0 0;
5 13 14 20 19 elp(s) elb(s) 0 0;
5 14 15 21 20 elp(s) elb(s) 0 0;
5 15 16 22 21 elp(s) elb(s) 0 0;
2 16 17 23 22 elp(s) elc(s) 0 0;
3 17 18 24 23 elp(s) elf(s) 0 0;
5 20 21 27 26 elp(s) elb(s) 0 0;
5 21 22 28 27 elp(s) elb(s) 0 0;
2 22 23 29 28 elp(s) elc(s) 0 0;
3 23 24 30 29 elp(s) elf(s) 0 0;
2 25 26 32 31 elp(s) elc(s) 0 0;
2 26 27 33 32 elp(s) elc(s) 0 0;
2 27 28 34 33 elp(s) elc(s) 0 0;
2 28 29 35 34 elp(s) elc(s) 0 0;
3 29 30 36 35 elp(s) elc(s) 0 0;
3 31 32 38 37 elp(s) elf(s) 0 0;
3 32 33 39 38 elp(s) elf(s) 0 0;
3 33 34 40 39 elp(s) elf(s) 0 0;
3 34 35 41 40 elp(s) elf(s) 0 0;
3 35 36 42 41 elp(s) elf(s) 0 0; %%
3 2 1 43 44 elp(s) elf(s) 0 0;
3 3 2 44 45 elp(s) elf(s) 0 0;
3 4 3 45 46 elp(s) elf(s) 0 0;
3 5 4 46 47 elp(s) elf(s) 0 0;
3 6 5 47 48 elp(s) elf(s) 0 0;
%3 44 43 50 51 elp(s) elc(s) 0 0; %6
%3 45 44 51 52 elp(s) elc(s) 0 0; %6
%3 46 45 52 53 elp(s) elc(s) 0 0, %6
%3 47 46 53 54 elp(s) elc(s) 0 0; %6
%3 48 47 54 55 elp(s) elc(s) 0 0; %6
%3 49 48 55 56 elp(s) elc(s) 0 0; %6
3 44 43 57 58 elp(s) elf(s) 0 0; % endret
3 45 44 58 59 elp(s) elf(s) 0 0; % endret
3 46 45 59 60 elp(s) elf(s) 0 0; % endret
3 47 46 60 61 elp(s) elf(s) 0 0; % endret
3 48 47 61 62 elp(s) elf(s) 0 0; % endret
];

    read.materials(:,:,s)=[ 1 glob.globvariables.mechanic matnumfr(s);
```

```
2 glob.globvariables.mechanic matnumcasing(s);
3 glob.globvariables.fluid matnumf(s);
4 glob.globvariables.piezo matnump(s);
5 glob.globvariables.mechanic matnumb(s);
6 glob.globvariables.mechanic matnumc(s);
7 glob.globvariables.mechanic matdatalim(s)];

    read.restraints(:,:,s)=[-1e-9 rp(s)+1e-9 tfr(s)+tp(s)+tlim(s)-1e-9 tfr(s)+tp(s)+tlim(s)+1e-9 glob.free.ep 1];
    read.dof(:,:,s)=[ -1e-9 rp(s)+1e-9 tfr(s)+tlim(s)-1e-9 tfr(s)+tlim(s)+1e-9 glob.free.ep;
-1 1 tfr(s)+tp(s)+tb(s)+tair(s)+tc(s)+tBAK(s)+tlim(s)-1e-9 tfr(s)+tp(s)+tb(s)+tair(s)+tc(s)+tBAK(s)+tlim(s)+1e-9 glob.free.vp;
-1 1 -avstandPlate(s)-tPlate(s)-tFRONT(s)+1e-9 -avstandPlate(s)-tPlate(s)-tFRONT(s)-1e-9 glob.free.vp;
rPlate(s)-1e-9 rPlate(s)+1e-9 -1 1 glob.free.vp;
];

   % Creating decreasing Qm for plate outside fluid region
   % Eksponentiell neddempning av Qm til Qmin i (retning (enten +-(r,z) (-1,1,-2,2),rmin,rmax,zmin,zmax,Qmin,Qm) - naturlige logaritme --
   % se mer i k_calc_mechanic.m
   glob.lossvariation=1;
   glob.lossvarvecs{s} = [1,rPlate(s)-PMLlag(s),rPlate(s)+staalvakum(s),-avstandPlate(s),-avstandPlate(s)-tPlate(s),Qmin(s),Qm(s)];

   % PML for mange regioner (ikke symmetrisk boks som er default)
   % Default glob.pmlform er symmetrisk boks, her er den definert som "manyregions". Dermed kan du legge pmllag vilkaarlig i 2.5d.
   % glob.pmlregions{k} = [retning pml(enten +-(r,z) (-1,1,-2,2),rmin,rmax,zmin,zmax]; -- se mer i k_calc_pml.m
   glob.pmlform=glob.globvariables.manyregions;
   glob.pmlregions={1,2,3};
   glob.pmlregions{1}=[2,0,rPlate(s),tfr(s)+tp(s)+tb(s)+tair(s)+tc(s)+tBAK(s)+tlim(s)-PMLlag(s),tfr(s)+tp(s)+tb(s)+tair(s)+tc(s)+tBAK(s)+tlim(s)];
   glob.pmlregions{2}=[1,rPlate(s)-PMLlag(s),rPlate(s),-avstandPlate(s)-tPlate(s)-tFRONT(s),tfr(s)+tp(s)+tb(s)+tair(s)+tc(s)+tBAK(s)];
%   glob.pmlregions{3}=[1,rPlate(s)-PMLlag(s),rPlate(s),-avstandPlate(s)-tPlate(s)-tFRONT(s),-avstandPlate(s)-tPlate(s)];
   glob.pmlregions{3}=[-2,0,rPlate(s),-avstandPlate(s)-tPlate(s)-tFRONT(s),-avstandPlate(s)-tPlate(s)-tFRONT(s)+PMLlag(s)];

   %f=(read.directharmonicanalysis(1)+read.directharmonicanalysis(3))/2;
   f = 750e3;
   glob.pmlomega_vec=2*pi*f;
   glob.pmlfluid=1;
  end
end
```

Appendix C

FEM approach project-file

```
if ~isempty(read.transducerlimplate)
  rp=read.transducerlimplate(1,1,:); % Radius of piezo disk
  tp=read.transducerlimplate(1,2,:); % Thickness of piezo disk
  rfr=read.transducerlimplate(1,3,:); % Radius of front layer
  tfr=read.transducerlimplate(1,4,:); % Thickness of front layer
  tb=read.transducerlimplate(1,5,:); % Thickness of backing layer
  tc=read.transducerlimplate(1,6,:); % Thickness of steel casing - back end
  matnump=read.transducerlimplate(1,7,:);
  matnumfr=read.transducerlimplate(1,8,:);
  matnumb=read.transducerlimplate(1,9,:);
  matnumc=read.transducerlimplate(1,10,:);
  rPlate=read.transducerlimplate(1,11,:); % Radius of steel plate
  tBAK=read.transducerlimplate(1,12,:); % Distance from back of transducer to end of fluid region
  avstandPlate=read.transducerlimplate(1,13,:); % Distance between the transducer and the steel plate (front to front)
  tPlate=read.transducerlimplate(1,14,:); % Thickness of steel plate
  tFRONT=read.transducerlimplate(1,15,:); % Distance from lower surface of the steel plate to end of fluid region
  tlim = read.transducerlimplate(1,16,:);

  % INPUT FOR AIR LAYER AT THE BACK OF THE TRANSDUCER
  tair = 10.42e-3; % Depth of cone of air in backing layer
  rbair = 4.01e-3; % Radius of cone of air in backing layer
  tb = tb-tair;
  tc2 = 2.83e-3; % Casing thickness - sides
  elp = 3; % Elements per wavelength in piezo disk
  elfr = 3; % Elements per wavelength in front layer
  elc = 3; % Elements per wavelength in casing
  elf = 3; % Elements per wavelength in water
  elb = 3; % Elements per wavelength in backing layer
  matnumf = 444; % Material number for water
  staalvakum = 200e-3; % Steel plate radius in vacuum
  PMLlag = 30e-3; % Fluid PML thickness
  glob.pmlsigma_star_vec=0;     % Damping function to fluid PML
  Qm = 1000;  % "Decreasing Qm" from Qm
  Qmin = 0.001; % to Qmin
  matnumcasing = 5;
  %%%%%%%%%%%%%%%%%%%%%%%%%%%%
  rair = rfr-rbair;
  rc = rfr+tc2;
  matdatalim = 560;

  for s=1:size(rp,3)
    read.points(:,:,s)=[1 0 0;
2 rair(s) 0;
```

```
3 rp(s) 0;
4 rfr(s) 0;
5 rc(s) 0;
6 rPlate(s) 0;
7 0 tfr(s)+tlim(s);
8 rair(s) tfr(s)+tlim(s);
9 rp(s) tfr(s)+tlim(s);
10 rfr(s) tfr(s)+tlim(s);
11 rc(s) tfr(s)+tlim(s);
12 rPlate(s) tfr(s)+tlim(s);
13 0 tfr(s)+tp(s)+tlim(s);
14 rair(s) tfr(s)+tp(s)+tlim(s);
15 rp(s) tfr(s)+tp(s)+tlim(s);
16 rfr(s) tfr(s)+tp(s)+tlim(s);
17 rc(s) tfr(s)+tp(s)+tlim(s);
18 rPlate(s) tfr(s)+tp(s)+tlim(s);
19 0 tfr(s)+tp(s)+tb(s)+tlim(s);
20 rair(s) tfr(s)+tp(s)+tb(s)+tlim(s);
21 rp(s) tfr(s)+tp(s)+tb(s)+tlim(s);
22 rfr(s) tfr(s)+tp(s)+tb(s)+tlim(s);
23 rc(s) tfr(s)+tp(s)+tb(s)+tlim(s);
24 rPlate(s) tfr(s)+tp(s)+tb(s)+tlim(s);
25 0 tfr(s)+tp(s)+tb(s)+tair(s)+tlim(s);
26 rair(s) tfr(s)+tp(s)+tb(s)+tair(s)+tlim(s);
27 rp(s) tfr(s)+tp(s)+tb(s)+tair(s)+tlim(s);
28 rfr(s) tfr(s)+tp(s)+tb(s)+tair(s)+tlim(s);
29 rc(s) tfr(s)+tp(s)+tb(s)+tair(s)+tlim(s);
30 rPlate(s) tfr(s)+tp(s)+tb(s)+tair(s)+tlim(s);
31 0 tfr(s)+tp(s)+tb(s)+tair(s)+tc(s)+tlim(s);
32 rair(s) tfr(s)+tp(s)+tb(s)+tair(s)+tc(s)+tlim(s);
33 rp(s) tfr(s)+tp(s)+tb(s)+tair(s)+tc(s)+tlim(s);
34 rfr(s) tfr(s)+tp(s)+tb(s)+tair(s)+tc(s)+tlim(s);
35 rc(s) tfr(s)+tp(s)+tb(s)+tair(s)+tc(s)+tlim(s);
36 rPlate(s) tfr(s)+tp(s)+tb(s)+tair(s)+tc(s)+tlim(s);
37 0 tfr(s)+tp(s)+tb(s)+tair(s)+tc(s)+tBAK(s)+tlim(s);
38 rair(s) tfr(s)+tp(s)+tb(s)+tair(s)+tc(s)+tBAK(s)+tlim(s);
39 rp(s) tfr(s)+tp(s)+tb(s)+tair(s)+tc(s)+tBAK(s)+tlim(s);
40 rfr(s) tfr(s)+tp(s)+tb(s)+tair(s)+tc(s)+tBAK(s)+tlim(s);
41 rc(s) tfr(s)+tp(s)+tb(s)+tair(s)+tc(s)+tBAK(s)+tlim(s);
42 rPlate(s) tfr(s)+tp(s)+tb(s)+tair(s)+tc(s)+tBAK(s)+tlim(s);
43 0 -avstandPlate(s);
44 rair(s) -avstandPlate(s);
45 rp(s) -avstandPlate(s);
46 rfr(s) -avstandPlate(s);
47 rc(s) -avstandPlate(s);
48 rPlate(s) -avstandPlate(s);
49 rPlate(s)+staalvakum(s) -avstandPlate(s);
50 0 -avstandPlate(s)-tPlate(s);
51 rair(s) -avstandPlate(s)-tPlate(s);
52 rp(s) -avstandPlate(s)-tPlate(s);
53 rfr(s) -avstandPlate(s)-tPlate(s);
54 rc(s) -avstandPlate(s)-tPlate(s);
55 rPlate(s) -avstandPlate(s)-tPlate(s);
56 rPlate(s)+staalvakum(s) -avstandPlate(s)-tPlate(s);

57 0 -avstandPlate(s)-tPlate(s)-tFRONT(s);
58 rair(s) -avstandPlate(s)-tPlate(s)-tFRONT(s);
59 rp(s) -avstandPlate(s)-tPlate(s)-tFRONT(s);
60 rfr(s) -avstandPlate(s)-tPlate(s)-tFRONT(s);
61 rc(s) -avstandPlate(s)-tPlate(s)-tFRONT(s);
62 rPlate(s) -avstandPlate(s)-tPlate(s)-tFRONT(s);
63 0 tfr(s);
```

```
64 rair(s) tfr(s);
65 rp(s) tfr(s);
66 rfr(s) tfr(s);
67 rc(s) tfr(s);
68 rPlate(s) tfr(s)];

    read.areas(:,:,s)=[ 1 1 2 64 63 elp(s) elfr(s) 0 0;
1 2 3 65 64 elp(s) elfr(s) 0 0;
1 3 4 66 65 elp(s) elfr(s) 0 0;
2 4 5 67 66 elp(s) elc(s) 0 0;
3 5 6 68 67 elp(s) elf(s) 0 0;
7 63 64 8 7 elp(s) elfr(s) 0 0;
            7 64 65 9 8 elp(s) elfr(s) 0 0;
            7 65 66 10 9 elp(s) elfr(s) 0 0;
            2 66 67 11 10 elp(s) elc(s) 0 0;
            3 67 68 12 11 elp(s) elf(s) 0 0;
            4 7 8 14 13 elp(s) elp(s) 0 0;
4 8 9 15 14 elp(s) elp(s) 0 0;
5 9 10 16 15 elp(s) elb(s) 0 0;
2 10 11 17 16 elp(s) elc(s) 0 0;
3 11 12 18 17 elp(s) elf(s) 0 0;
5 13 14 20 19 elp(s) elb(s) 0 0;
5 14 15 21 20 elp(s) elb(s) 0 0;
5 15 16 22 21 elp(s) elb(s) 0 0;
2 16 17 23 22 elp(s) elc(s) 0 0;
3 17 18 24 23 elp(s) elf(s) 0 0;
5 20 21 27 26 elp(s) elb(s) 0 0;
5 21 22 28 27 elp(s) elb(s) 0 0;
2 22 23 29 28 elp(s) elc(s) 0 0;
3 23 24 30 29 elp(s) elf(s) 0 0;
2 25 26 32 31 elp(s) elc(s) 0 0;
2 26 27 33 32 elp(s) elc(s) 0 0;
2 27 28 34 33 elp(s) elc(s) 0 0;
2 28 29 35 34 elp(s) elc(s) 0 0;
3 29 30 36 35 elp(s) elc(s) 0 0;
3 31 32 38 37 elp(s) elf(s) 0 0;
3 32 33 39 38 elp(s) elf(s) 0 0;
3 33 34 40 39 elp(s) elf(s) 0 0;
3 34 35 41 40 elp(s) elf(s) 0 0;
3 35 36 42 41 elp(s) elf(s) 0 0; %%
3 2 1 43 44 elp(s) elf(s) 0 0;
3 3 2 44 45 elp(s) elf(s) 0 0;
3 4 3 45 46 elp(s) elf(s) 0 0;
3 5 4 46 47 elp(s) elf(s) 0 0;
3 6 5 47 48 elp(s) elf(s) 0 0;
6 44 43 50 51 elp(s) elc(s) 0 0; %6
6 45 44 51 52 elp(s) elc(s) 0 0; %6
6 46 45 52 53 elp(s) elc(s) 0 0, %6
6 47 46 53 54 elp(s) elc(s) 0 0; %6
6 48 47 54 55 elp(s) elc(s) 0 0; %6
6 49 48 55 56 elp(s) elc(s) 0 0; %6 -- 2 er samme som 6
3 51 50 57 58 elp(s) elf(s) 0 0;
3 52 51 58 59 elp(s) elf(s) 0 0;
3 53 52 59 60 elp(s) elf(s) 0 0;
3 54 53 60 61 elp(s) elf(s) 0 0;
3 55 54 61 62 elp(s) elf(s) 0 0;
];

    read.materials(:,:,s)=[ 1 glob.globvariables.mechanic matnumfr(s);
2 glob.globvariables.mechanic matnumcasing(s);
3 glob.globvariables.fluid matnumf(s);
4 glob.globvariables.piezo matnump(s);
```

```
5 glob.globvariables.mechanic matnumb(s);
6 glob.globvariables.mechanic matnumc(s);
7 glob.globvariables.mechanic matdatalim(s)];

    read.restraints(:,:,s)=[-1e-9 rp(s)+1e-9 tfr(s)+tp(s)+tlim(s)-1e-9 tfr(s)+tp(s)+tlim(s)+1e-9 glob.free.ep 1];
    read.dof(:,:,s)=[ -1e-9 rp(s)+1e-9 tfr(s)+tlim(s)-1e-9 tfr(s)+tlim(s)+1e-9 glob.free.ep;
-1e-9 1 tfr(s)+tp(s)+tb(s)+tair(s)+tc(s)+tBAK(s)+tlim(s)-1e-9 tfr(s)+tp(s)+tb(s)+tair(s)+tc(s)+tBAK(s)+tlim(s)+1e-9 glob.free.vp;
-1e-9 1 -avstandPlate(s)-tPlate(s)-tFRONT(s)+1e-9 -avstandPlate(s)-tPlate(s)-tFRONT(s)-1e-9 glob.free.vp;
rPlate(s)-1e-9 rPlate(s)+1e-9 -1 -avstandPlate(s)-tPlate(s) glob.free.vp;
rPlate(s)-1e-9 rPlate(s)+1e-9 -avstandPlate(s) 1 glob.free.vp;
];

   % Creating decreasing Qm for plate outside fluid region
   % Eksponentiell neddempning av Qm til Qmin i (retning (enten +-(r,z) (-1,1,-2,2),rmin,rmax,zmin,zmax,Qmin,Qm) - naturlige logaritme --
   % se mer i k_calc_mechanic.m
   glob.lossvariation=1;
   glob.lossvarvecs{s} = [1,rPlate(s)-PMLlag(s),rPlate(s)+staalvakum(s),-avstandPlate(s),-avstandPlate(s)-tPlate(s),Qmin(s),Qm(s)];

   % PML for mange regioner (ikke symmetrisk boks som er default)
   % Default glob.pmlform er symmetrisk boks, her er den definert som "manyregions". Dermed kan du legge pmllag vilkaarlig i 2.5d.
   % glob.pmlregions{k} = [retning pml(enten +-(r,z) (-1,1,-2,2),rmin,rmax,zmin,zmax]; -- se mer i k_calc_pml.m
   glob.pmlform=glob.globvariables.manyregions;
   glob.pmlregions={1,2,3,4};
   glob.pmlregions{1}=[2,0,rPlate(s),tfr(s)+tp(s)+tb(s)+tair(s)+tc(s)+tBAK(s)+tlim(s)-PMLlag(s),tfr(s)+tp(s)+tb(s)+tair(s)+tc(s)+tBAK(s)+tlim(s)];
   glob.pmlregions{2}=[1,rPlate(s)-PMLlag(s),rPlate(s),-avstandPlate(s),tfr(s)+tp(s)+tb(s)+tair(s)+tc(s)+tBAK(s)];
   glob.pmlregions{3}=[1,rPlate(s)-PMLlag(s),rPlate(s),-avstandPlate(s)-tPlate(s)-tFRONT(s),-avstandPlate(s)-tPlate(s)];
   glob.pmlregions{4}=[-2,0,rPlate(s),-avstandPlate(s)-tPlate(s)-tFRONT(s),-avstandPlate(s)-tPlate(s)-tFRONT(s)+PMLlag(s)];

   %f=(read.directharmonicanalysis(1)+read.directharmonicanalysis(3))/2;
   f = 750e3;
   glob.pmlomega_vec=2*pi*f;
   glob.pmlfluid=1;
  end
end
```

Appendix D

Calculation of FEM incident fields

```
%%%%%%%%%%%%%%%%%%%%%%%%%%%%%%%%%%%%%%%%%%%%%%%%%%%%%%%%%%%%%%%%%%%%%%%%%%%%%%%
% Hybrid FEM-ASM
%
% This routine calculates the sound pressure from the transducer in a plane
% parallell to the steel plate. The user can specify the distance from the
% transducer to the plane, the (x,y) grid of the plane in addition to the
% incident angle the transducer shall have towards the plane (e.g. steel
% plate). The front surface of the transducer is located at the origin
% (x,y,z) = (0,0,0). Then, this pressure field can be further processed
% using ASM.
%
% INPUT NEEDED: grid (x,y) of the plane, distance to plane, incident angle
%               FE simulation of the transducer.
% OUTPUT PROVIDED: sound pressure in grid (X,Y) at the given distance.
%
% @author, Magne Aanes
% STARTED: 16.02.2012
% UPDATED: 11.12.2012
%-------------------------------------------------------------------------
%clear all
%load piston_result.mat
%load piston_plate_stor_result.mat

disp(' ')
disp('-------------------------')
disp('-----Hybrid FEM-ASM-----')
disp('-------------------------')
disp(' ')

% Importing coordinate system from FE simulation
r_akse = result.nearfieldpressure_r{1,1}; % r-coordinate to each node
z_akse = result.nearfieldpressure_z{1,1}; % z-coordinate to each node
frekvens = result.nearfieldpressure_f{1,1};
%[a,b] = find(frekvens==956e3);
%frekvens = frekvens(b);

% Sound field grid in (x,y)
x_0 = 300e-3;  % -x_0 < x > x_0
y_0 = 300e-3;  % -y_o < y > y_0
z_0 = -270e-3; % z-coordinate to the plane parallell to the steel plate

% Incident angle to the transducer towards the steel plate
%theta_inc = 0;%input('Incident angle [deg]: ');
```

```
% Number of points to use in the (x,y) grid for each direction
N_fft = 2^10;

% Creating the x-coordinates
qx = [-N_fft/2:1:N_fft/2-1];
Lx = 2*x_0;
XX = qx*Lx/N_fft;

% Creating the y-coordinates
qy = [-N_fft/2:1:N_fft/2-1];
Ly = 2*y_0;
YY = qy*Ly/N_fft;

% Creating the z-coordinates
ZZ = z_0*ones(1,length(YY));

% Coordinate transformation to (x',y',z') to be able to "simulate" an
% incident angle towards the plane.
XXm = cos(deg2rad(theta_inc))*XX + sin(deg2rad(theta_inc))*ZZ;
%XXm = cos(deg2rad(theta_inc))*XX - sin(deg2rad(theta_inc))*ZZ;
YYm = YY;
ZZm = -sin(deg2rad(theta_inc))*XX + cos(deg2rad(theta_inc))*ZZ;
%ZZm = sin(deg2rad(theta_inc))*XX + cos(deg2rad(theta_inc))*ZZ;

% Meshing grid in (x,y)
[X,Y] = meshgrid(XX,-YY);
% Meshing grid in (x',y')
[Xm,Ym] = meshgrid(XXm,-YYm);
% Creating corresponding z-coordinates for each grid point above
ZZm = repmat(ZZm,N_fft,1);
% Converting (x',y') to polar coordinates (THETA,R)
[THETA,R] = cart2pol(Xm,Ym);

if min(min(ZZm)) < z_akse(1)
   disp('WARNING!!! Not enough information to calculate this incident angle!!!')
   break
end

% Interpolating the sound pressure over (x',y') for each frequency
for f = 1:length(frekvens)
   % Extracting the sound pressure in every node in the FE simulation
   P = result.nearfieldpressure{1}(:,f);
   % Interpolating the sound pressure 'P' in coordinates (r_akse,z_akse)
   % over (R,ZZm) using 'griddata' with triangle-based cubic interpolation
   [Ri,Zi,Pi] = griddata(r_akse,z_akse,P,R,ZZm,'linear');
   disp(['Frequency: ' num2str(frekvens(f)/1000) ' kHz'])
   % Saving the sound pressure for each frequency to individual files for
   % import to an ASM.
   fil = ['p_TRANSDUCER_DEG_' num2str(theta_inc) '_' num2str(frekvens(f)/1000) '_OK.mat'];
   p = Pi;
   save(fil,'p','X','Y');
end
```

Appendix E

ASM approach

```
% Angular spectrum method for transmission/reflection through a visco-
% elastic isotropic solid in vacuum or immersed in a single fluid using raw
% data from FEMP 5.

% HYBRID FEM-ASM

% @author, Magne Aanes
% STARTED: 17.04.2012
% UPDATED: 10.10.2013

disp(' ')
disp('------------------------')
disp('-----------ASM----------')
disp('------------------------')
disp(' ')

%%%%%%%%%%%%%%%%%%%%%%%%%%%%%%%%%%%%%%%%%%%%%%%%%%%%%%%%%%%%%%%%%%%%%%%%%%%%%%%%
clear all
%%%%%%%%%%%%%%%%%%%%%%%%%%%%%%%%%%%%%%%%%%%%%%%%%%%%%%%%%%%%%%%%%%%%%%%%%%%%%%%%
% Sweeping frequencies in kHz
freq = 300:1:1100;
%freq = 600;
% Incident angle of the transducer
theta_inc = 0;
% Distance from the steel plate to the receiver (for transmitted)
zT = 100e-3;
% Distance from the steel plate to the receiver (for reflected)
zR = 100e-3;
%%%%%%%%%%%%%%%%%%%%%%%%%%%%%%%%%%%%%%%%%%%%%%%%%%%%%%%%%%%%%%%%%%%%%%%%%%%%%%%%
%--------------------------------INPUT DATA--------------------------------%
% MATERIAL PROPERTIES FOR FLUID, layer 1 and 3.
cl = 1485;      % longitudinal velocity
rhoF = 1000;    % density of fluid

% MATERIAL PROPERTIES FOR VISCOELASTIC SOLID, layer 2
cL = 5780;      % longitudinal velocity
cS = 3130;      % shear velocity
QL = 1e3;       % loss factor for cL
QS = 500;       % loss factor for cS
rhoS = 8000;    % density of viscoelastic solid
t = 6.05e-3;    % thickness of viscoelatic solid

%%%%%%%%%%%%%%%%%%%%%%%%%%%%%%%%%%%%%%%%%%%%%%%%%%%%%%%%%%%%%%%%%%%%%%%%%%%%%%%%
```

```
%#########################################################################%
%------------------------------FLUID LAYER------------------------------%
% Possibility to include loss in the fluid, not used as of now. NOT TESTED!
% Including loss by defining complex sound velocity
%Ql = 10e3;      % loss factor for cl
%cl = cl*(1+i./Ql);

%#########################################################################%
%------------------------------SOLID LAYER------------------------------%
% Including loss by defining complex sound velocities.
cL = cL*(1+i./QL);
cS = cS*(1+i./QS);
% Half thickness of the elastic plate
L = t/2;

disp(['Simulation for incident angle [deg] of: ' num2str(theta_inc)]);
disp('Starting sweep of frequencies...')
for cc = 1:length(freq)
    % Loading the pressure field at (X,Y,Z_0) from FE simulations
    try
fil = ['p_PISTON_DEG_' num2str(theta_inc) '_' num2str(freq(cc)) '_OK.mat'];
load(fil);
    catch
fil = ['p_TRANSDUCER_DEG_' num2str(theta_inc) '_' num2str(freq(cc)) '_OK.mat'];
load(fil);
    end
    disp(['Frequency: ' num2str(freq(cc)) ' kHz']);
    % Angular frequency
    w = 2*pi*freq(cc)*1e3;
    % Need only to calculate kx & ky one time, since the X,Y grid is the
    % same for all frequencies.
    if cc == 1
        %#################################################################%
        % Horizontal spatial frequencies in rads/meter in x- and y-direction.
        Nx = size(X,2);Ny = size(Y,2);
        x0 = abs(min(min(X)));y0 = abs(max(max(Y)));
        kx = 2*pi/(2*x0)*(-Nx/2:1:Nx/2-1);
        ky = 2*pi/(2*y0)*(-Ny/2:1:Ny/2-1);
        [KX,KY] = meshgrid(kx,-ky);
        eta = sqrt(KX.^2+KY.^2);
        %#################################################################%
    end
    % Wavenumber for longitudinal waves in fluid.
    hF = w/cl;
    %dum_hF_rx = +(hF >= abs(KX));
    %dum_hF_ry = +(hF >= abs(KY));
    %dum_hF_R = dum_hF_rx.*dum_hF_ry;
    dum_hF_R = +(hF >= eta);
    dum_hF_E = abs(dum_hF_R-1);
    % Vertical wavenumber for longitudinal waves.
    hFz = dum_hF_R.*sqrt(hF^2-KX.^2-KY.^2)+dum_hF_E.*i.*sqrt(KX.^2+KY.^2-hF^2);
    %#################################################################%
    % Wavenumber for longitudinal waves in solid.
    h = w/cL;
    %dum_h_rx = +(h >= abs(KX));
    %dum_h_ry = +(h >= abs(KY));
    %dum_h_R = dum_h_rx.*dum_h_ry;
    dum_h_R = +(h >= eta);
    dum_h_E = abs(dum_h_R-1);
    % Vertical wavenumber for longitudinal waves.
    hz = dum_h_R.*sqrt(h^2-KX.^2-KY.^2)+dum_h_E.*i.*sqrt(KX.^2+KY.^2-h^2);
    %#################################################################%
```

```
    % Wavenumber for shear waves in solid.
    k = w/cS;
    %dum_k_rx = +(k >= abs(KX));
    %dum_k_ry = +(k >= abs(KY));
    %dum_k_R = dum_k_rx.*dum_k_ry;
    dum_k_R = +(k >= eta);
    dum_k_E = abs(dum_k_R-1);
    % Vertical wavenumber for longitudinal waves.
    kz = dum_k_R.*sqrt(k^2-KX.^2-KY.^2)+dum_k_E.*i.*sqrt(KX.^2+KY.^2-k^2);
    %#########################################################################%
    % Reflection and transmission coeff. to an elastic plate immersed in a
    % single fluid, following Jocker 2007. He assumes an exp(iwt), as is
    % used in FEMP 5 and must be used to correctly handled raw data from
    % FEMP 5.
    %A1 = (k^2-2.*eta.^2).^2;
    A1 = (2.*eta.^2-k^2).^2;
    A2 = tan(hz.*L);
    A3 = 4.*eta.^2.*kz.*hz;
    A4 = tan(kz.*L);
    A = A1.*A2+A3.*A4;
    S2 = cot(hz.*L);
    S4 = cot(kz.*L);
    S = A1.*S2+A3.*S4;
    YY = (rhoF/rhoS)*k^4.*(hz./hFz);

    R = (A.*S-YY.^2)./((S+i.*YY).*(A-i.*YY));   % reflection coeff.
    T = (-i.*YY.*(S+A))./((S+i.*YY).*(A-i.*YY)); % transmission coeff.
    %#########################################################################%
    %%%%%%%%%%%%%%%% 2-D discrete Fourier transform. fft(fft(p).').' %%%%%%%%%
    % Pressure in (X,Y,Z_0) in spatial angular frequency domain.
    % p(h_x,h_y,Z_0,w)
    Pfk = ifftshift(ifft(ifft(p*length(p)).').');
    %#########################################################################%
    % Propagation term for transmitted/reflected beam following Younghouse
    % (he assumes an exp(iwt)).
    prop_termT = dum_hF_R.*exp(-i*hFz.*zT)+dum_hF_E.*exp(-abs(hFz).*zT);
    prop_termR = dum_hF_R.*exp(-i*hFz.*zR)+dum_hF_E.*exp(-abs(hFz).*zR);
    prop_termT(isnan(prop_termT)) = 0;
    prop_termR(isnan(prop_termR)) = 0;

    % Transmitted beam through the plate.
    Pfk_T1 = Pfk.*T;

    % Reflected beam from the plate.
    Pfk_R1 = Pfk.*R;

    % Transmitted/reflected beam propagated to distance zT/zR respectively.
    Pfk_T = Pfk_T1.*prop_termT;
    Pfk_R = Pfk_R1.*prop_termR;
    %#########################################################################%
    %%%%%%%%% INVERSE 2-D discrete Fourier transform. fft(fft(p).').' %%%%%%%%%
    p_T = fft(fft((Pfk_T/length(Pfk_T))).').';
    p_R = fft(fft((Pfk_R/length(Pfk_R))).').';
    P =   fft(fft((Pfk/length(Pfk))).').';
    %#########################################################################%
    result.p{cc} = p_T;
end

result.f = freq;
result.X = X;
result.Y = Y;
```

```
filnavn = ['result_' num2str(theta_inc) 'deg2'];
save (filnavn,'result','-v7.3')
disp('Done!');
```

#####

```
% ASM postprocess
% @author, Magne Aanes

% STARTED: 15.01.2013
% UPDATED: 15.01.2013

%load result_0deg.mat

% Pressure to be extracted at (x,y) for transfer function calculation
x = 00e-3;
y = 0e-3;
theta_inc = 0;
f1 = 457;
f2 = 518;
f3 = 775;
f4 = 956;

X = result.X;
Y = result.Y;

% Extracting the pressure at (x,y) for further transfer function
% calculation.
aa = find(abs(X(1,:)-x) < 0.3e-3);
bb = find(abs(Y(:,1)-y) < 1e-4);

if x == 0
mkdir(pwd,'transmittert lydfelt')
end
for i = 1:length(result.f)
PP(i,:) = result.p{i}(bb,aa);
if x == 0
TLL(i,:) = result.p{i}(bb,:);
        if i == 1
   TLL(1,:) = 0;
end
if isnan(TLL(i,:))
TLL(i,:) = TLL(i-1,:);
end
if result.f(i) == f1 || result.f(i) == f2 || result.f(i) == f3 || result.f(i) == f4
        filnavn2 = ['lydfelt_' num2str(theta_inc) 'deg_f_' num2str(result.f(i))];
p = result.p{i};
save(filnavn2,'p','X','Y');
movefile([filnavn2 '.mat'],[pwd '\transmittert lydfelt'])
disp([num2str(result.f(i)) ' kHz'])
end
end
% MUST BE FIXED! WHY NAN?
if i == 1
    PP(1) = 0;
end
if isnan(PP(i))
PP(i) = PP(i-1);
end
end

if x == 0
```

```
freq = result.f;
save(['TLL_' num2str(theta_inc) 'deg'],'TLL','X','Y','freq')
end

% For further post processing with 'fft_analysis.m', converting to a column matrix
% Important to use .' NOT ' to compute the matrix, since .' computes the column matrix with
% real/imag intact, and ' computes the complex conjugate transpose, giving real/-imag.
P2 = PP.';
f = result.f*1000;
filnavn = ['P2_' num2str(theta_inc) 'deg_x=' num2str(x*1000) '_y=' num2str(y*1000)'];
save(filnavn,'P2','f')
disp('Done!');
```

Appendix F

Time domain signal calculation

```
% FOURIER TRANSFORMATION USING FFT
% Creating a sine burst in time domain, using FFT to represent the signal
% in the frequency domain. Multiplying the signal with the wanted transfer
% function calculated using e.q. finite element or analytical. At the end
% using IFFT to do an inverse DFT in order to return to time domain for
% analysis.
%
% !!! TIPS !!!
% The FE result-file to be loaded must use the same frequency range as for
% the FFT. This means that you have to controll 'Fs' and 'N' to get the
% wanted frequency step. In addition a 'Fs' larger than the highest
% frequency in the FE result-file must also be used.
%
% It is possible to use a frequency vector or a single frequency.
%
% @author, Magne Aanes, UiB
%
% STARTED: 05.05.2011
% UPDATED: 11.12.2012

clear all
disp(' ')
disp(' ------------------------------------------------')
disp('| Fourier transformation -- ADD-ON to FEMP 5 |')
disp(' ------------------------------------------------')
disp(' ')
disp('CHOOSE THE METHOD FOR CALCULATING THE AMPLITUDE OF THE PULSE:');
option = input('[1 = FFT] OR [2 = MAXMIN]: ');
disp(' ');
disp('!!!WARNING!!! Use only Thevenin circuit when transducer is included')
disp(' ');
elLOAD = input(['Use Thevenin circuit to calculate electrical load of the transducer [1 = OK]' ...
    '[ENTER = NO]: ']);
soundfield = input('Calculate the sound pressure field [1 = OK] [ENTER = NO]: ');
disp(' ');
if isempty(soundfield)
    option2 = input('Save and display reduction of frequency spectra [1 = OK] [ENTER = NO]: ');
    disp(' ');
    else option2 = 0;
end
option3 = input('Butterworth filter [1 = OK] [ENTER = NO]: ');
%------------------------------ USER ----------------------------------%
%----------------------------------------------------------------------%
```

```
% Please use the DIALOG BOX for changes!
freq = (300e3:500:1150e3);      % centre frequencies of bursts
freq = 956e3;
ant_peri = 125;%59,68,101,125    % number of periods
A = 10;                          % amplitude of sine bursts [e.g. in V]

tPlate = 6.05e-3;                % steel plate thickness
Fs = 4e7;                        % sample frequency
N = 8e4;                         % N-point FFT

z1 = 0.270;                      % distance between transducer and plate

z = 0.270;                       % distance to source [in m]
z = z+tPlate+0.100;
rhof = 1000;                     % density of fluid
cf = 1485;                       % compressional sound velocity of fluid
a = 30.44e-3/2;                  % radius of source [in m]

% Number of periods where a transient of the pulse is experienced
transient_begin = 40;           % number of periods in the beginning of the main pulse
transient_end = 20;             % number of periods in the end of the main pulse

% Butterworth low pass filter
Fc = 20e3;                       % cut-off frequency (-3 dB)
order = 5;                       % filter order

disp(' ');
disp('------------------------------------------------');
disp('!!!REMEMBER TO LOAD FEMP-RESULT FILE CORRECTLY!!!');
disp('------------------------------------------------');

%FEMP-result file to load
%load FEM_q1000_KDL_1.239MHz.mat
load PT_tot_0mm.mat
load PT_tot_20mm.mat
load PT_tot_40mm.mat
%load PTr_tot.mat
%load P2_0deg_x=0_y=0.mat
% Frequency 'FEM_f'
% Distance 'FEM_r'
% Pressure 'FEM_p'.
% These 3 can either be a vector or a scalar.
FEM_f = f;
% To calculate only on-axis pressure
if isempty(soundfield)
    FEM_sp = P2;
    FEM_rad = 1;
else
    FEM_sp = p;
    FEM_rad = r;
end
% Possibility to load input admittance to the transducer
if elLOAD
    Yt = Y;
end
%##########################################################################%
%##########################################################################%

% %------------------------------ DIALOG BOX -----------------------------%
% %-----------------------------------------------------------------------%
% disp(' ');
% disp('DIALOG BOX opened for input variables:');
```

```
% disp(' ');
% dlg_title = 'Fourier transformation';
% prompt = {'Min frequency [Hz]','Step frequency [Hz]','Max frequency [Hz]',...
%     'Number of periods of the bursts','Amplitude of sine bursts [V]','Sample frequency [Hz]',...
%     'N-point FFT','Distance to source [m]','Density of fluid [kg/m^3]',...
%     'Sound velocity of fluid [m/s]','Radius of source [m]',...
%     'Number of periods of beginning transient of main pulse',...
%     'Number of periods of end transient of main pulse'};
% options.Resize='on';
% options.WindowStyle='normal';
% options.Interpreter='tex';
% if length(freq) == 1
%     freq_step = freq;
% else
%     freq_step = freq(2)-freq(1);
% end
% def = {num2str(freq(1)),num2str(freq_step),num2str(freq(end)),...
%     num2str(ant_peri),num2str(A),num2str(Fs),num2str(N),num2str(z),num2str(rhof),...
%     num2str(cf),num2str(a),num2str(transient_begin),num2str(transient_end)};
% answer = inputdlg(prompt,dlg_title,1,def,options);
% if isempty(answer)
%     disp('EXITING THE PROGRAM!');
%     clear all
%     break;
% end
%
% fmin = str2num(answer{1});
% fstep = str2num(answer{2});
% fmax = str2num(answer{3});
% freq = (fmin:fstep:fmax);
% ant_peri = str2num(answer{4});
% A = str2num(answer{5});
% Fs = str2num(answer{6});
% N = str2num(answer{7});
% z = str2num(answer{8});
% rhof = str2num(answer{9});
% cf = str2num(answer{10});
% a = str2num(answer{11});
% transient_begin = str2num(answer{12});
% transient_end = str2num(answer{13});
%#########################################################################%
%#########################################################################%
%------------------------------ FFT ------------------------------------%
%-------------------------------------------------------------------------%
Ts = 1/Fs;      % sample time
fres = Fs/N;
disp(['The frequency resolution is ' num2str(fres) ' Hz'])
disp(['The time resolution is ' num2str(Ts) ' s'])
if (fres ~= (FEM_f(2)-FEM_f(1)))
    disp('WARNING!!! The frequency resolution for the FE simulation and the sweep frequency is not the same!')
    break
end

%--------------------- BUTTERWORTH LOW PASS FILTER ----------------------%
%-------------------------------------------------------------------------%
if option3 == 1
    % Cut-off frequency of Fc (normalized to Fs/2) in order to run 'butter'
    Fc = Fc/(Fs/2);
    % Creating a Butterworth low pass filter of Nth order with cutoff Fc. 'BB'
    % and 'AA' gives the zeros and poles in H = BB/AA
    [BB,AA] = butter(order,Fc);
    % Converts the transfer function representation to an second-order section
```

```
    % representation. sos is a matrix with BBs and AAs like below.
    [sos,gB] = tf2sos(BB,AA);
    Bs = sos(:,1:3);
    As = sos(:,4:6);
    [nsec,temp] = size(sos);
    Butterworth = gB*[1,zeros(1,N-1)];
    % Filters the data in 'Butterworth' with vectors 'Bs' and 'As'.
    % Implementation of the standard difference equation.
    for aa = 1:nsec
        Butterworth = filter(Bs(aa,:),As(aa,:),Butterworth);
    end
    %plot(Imp) % Plot impulse response to make sure it has decayed to zero
    Butterworth = fft(Butterworth);
    BWF = fftshift(Butterworth);
end
%########################################################################%
%########################################################################%


% Calculating the FFT for each frequency defined in 'freq'
disp(' ')
disp('STARTING...');
for jj = 1:length(freq)
    if length(freq) > 1
        if jj == ceil(length(freq)/4)
            disp('25% completed')
        else if jj == ceil(length(freq)/2)
                disp('50% completed')
            else if jj == ceil(length(freq)*(3/4))
                    disp('75% completed')
                end
            end
        end
    end
    tstop(jj) = ant_peri*1/freq(jj);         % Get the time after 'ant_peri' of burst
    t = (0:Ts:tstop(jj));                   % time vector for constructing the signal

    % Be aware that N must be larger than length(y), if not, fft(y,N) will
    % truncate and be false.
    if N<length(t)
        disp('!!!WARNING!!! N is smaller than the length of your signal')
        break;
    end

    % Sine burst with centre frequency freq
    y = A*sin(2*pi.*freq(jj).*t);

    % From time domain to frequency domain. In Matlab the fft command must be
    % scaled with the length of the signal 'y'. In addition the fftshift shifts
    % the zero-frequency component to the center of the spectrum.
    Fhat = fft(y,N)/length(y);
    Fhat = fftshift(Fhat);

     % The option to use a BWF
    if option3 == 1
        Fhat = Fhat.*BWF;
    end

    % Frequency and time vector
    if mod(N,2) == 0
        kk = -N/2:N/2-1; % N even
    else
```

```
    kk = -(N-1)/2:(N-1)/2; % N odd
end
fr = kk.*Fs/N;
tt = (0:1/Fs:(length(Fhat)-1)/Fs);

%#########################################################################%
%#########################################################################%

%------------------------ TRANSFER FUNCTIONS -----------------------------%
%-------------------------------------------------------------------------%
% Transfer functions to be multiplied are included in this section.

% PHYS373: Plane wave model --> transfer functions
k = (2*pi.*fr/cf);
Hp = exp(-i.*k*z)*rhof*cf; % particle velocity to pressure (on-axis)
%Hp = exp(-i.*k*z)*rhof*cf.*(i*2*pi.*fr); % displacement to pressure (on-axis)
Fhat_Hp = Fhat.*Hp;
t_Hp = z/cf;

% UNIFORMLY VIBRATING CIRCULAR PISTON SOURCE MOUNTED IN A RIGID BAFFLE OF
% INFINITE EXTENT

% PHYS373: Far field propagation --> transfer functions
Hf = i*2*pi.*fr*rhof*a^2/(2*z).*exp(-i.*k*z); % particle velocity to pressure (on-axis)
%Hf = i*2*pi.*fr*rhof*a^2/(2*z).*exp(-i.*k*z).*(i*2*pi.*fr); % displacement to pressure (on-axis)
Fhat_Hf = Fhat.*Hf;

%%%%%%%%%%%%%%%%%%%%%%%%%%%%%%%%%%%%%%%%%%%%%%%%%%%%%%%%%%%%%%%%%%%%%%%%%%%

%% FINITE ELEMENT
% On-axis pressure/amplitude -> transfer function X to pressure
% Sensitivity/amplitude -> transfer function X to pressure
% Nearfieldpressure/amplitude -> transfer function X to pressure

% Transfer function --> X to pressure
% Remember that A is the amplitude of the sine burst.
for mm = 1:length(FEM_rad)
    Hfe = FEM_sp(mm,:);%./(i*2*pi.*freq);
    % Finding start and stop frequencies from FEMP-result, to add zeros
    % where it's needed.
    [aa,bb] = find(fr==FEM_f(end));
    [cc,dd] = find(fr==-fr(bb));
    if FEM_f(1) == 0
        % Shall not flip the DC component, therefore (2:end).
        Hfe = [conj(fliplr(Hfe(2:end))) Hfe];
        Hfe = [zeros(1,dd-1) Hfe zeros(1,length(fr)-bb)];
        % Thevinin model to simulate the load of the signal generator.
        if elLOAD
            % Impedance to the signal generator
            Z_gen = 50;
            Zt = 1./Yt;
            Zthev = Zt./(Zt+Z_gen);
            % Fixing NaN problem.
            Zthev(1) = 0;
            Hzt = [conj(fliplr(Zthev(2:end))) Zthev];
            Hzt = [zeros(1,dd-1) Hzt zeros(1,length(fr)-bb)];
        end
    else
        % No DC component, flip the entire thing!
        [ee,ff] = find(fr==FEM_f(1));
        [gg,hh] = find(fr==-fr(ff));
        Hfe = [zeros(1,dd-1) conj(fliplr(Hfe)) zeros(1,ff-hh-1) Hfe zeros(1,length(fr)-bb)];
```

```
    % Thevenin model to simulate the load of the signal generator
    if elLOAD
        % Impedance to the signal generator
        Z_gen = 50;
        Zt = 1./Yt;
        Zthev = Zt./(Zt+Z_gen);
        Hzt = [zeros(1,dd-1) conj(fliplr(Zthev)) zeros(1,ff-hh-1) Zthev zeros(1,length(fr)-bb)];
    end
end
% Calculating the transfer function Hzt (ThÃ©vinin model)
if elLOAD
    Fhat = Fhat.*Hzt;
end
Fhat_Hfe = Fhat.*Hfe;
%##########################################################################%
%##########################################################################%
%------------------------------ IFFT ----------------------------------%
%--------------------------------------------------------------------------%
% From frequency domain to time domain
% To scale corretly we multiply by length(y) since we divided by the
% length(y) when we did the fft
F_y = ifft(ifftshift(Fhat*length(y)));
F_Hp = ifft(ifftshift(Fhat_Hp*length(y)));
F_Hf = ifft(ifftshift(Fhat_Hf*length(y)));
F_Hfe = ifft(ifftshift(Fhat_Hfe*length(y)));

%##########################################################################%
%##########################################################################%

%--------------------- POST PROCESSING & VALIDATION ----------------------%
%--------------------------------------------------------------------------%
% Post processing and validation tools for analysis are added here.

%% SPECTRUM REDUCTION
% Using envelope.m in order to get the envelope of the spectrum for
% analysis.
% Check to verify that the sinc function of the input sine burst
% has fallen to a minimum required value at the start and stop
% frequencies of the FE simulation in order to produce a correct
% frequency spectrum.
% Calculating also the frequency spectrum reduction of transfer
% functions.
if option2 == 1
    transfer = {'Fhat','Fhat_Hp','Fhat_Hf','Fhat_Hfe'};
    for c = 1:length(transfer)
        [CC,ans] = envelope(fr,abs(eval(transfer{c})));
        CC_at_start = CC(find(fr==FEM_f(1)));
        CC_at_stop = CC(find(fr==FEM_f(end)));
        % If the number is "not a number" the neareast frequency
        % with a finite number is used.
        if isnan(CC_at_stop)
            CCd = ~isnan(CC);
            [ab,cd] = find(CCd);
            CC_at_stop = CC(cd(end));
        end
        reductSTART(c) = 20*log10(max(CC)/CC_at_start);
        reductSTOP(c) = 20*log10(max(CC)/CC_at_stop);
    end
    % Saving information for every frequency of the above calculation
    % Arranged: 1 row --> Fhat, 2 row --> Fhat_Hp, 3 row --> Fhat_Hf
    % and 4 row --> Fhat_Hfe
    redSTART(:,jj) = reductSTART;
```

```
    redSTOP(:,jj) = reductSTOP;
    if length(freq)==1
        disp(['Recuction of sine burst at FE start frequency [in dB]: ' num2str(reductSTART(1))]);
        disp(['Reduction of sine burst at FE stop frequency [in dB]: ' num2str(reductSTOP(1))]);
        disp('-----------------------------------------------------------------')
        disp(['Recuction of Fhat_Hp at FE start frequency [in dB]: ' num2str(reductSTART(2))]);
        disp(['Reduction of Fhat_Hp at FE stop frequency [in dB]: ' num2str(reductSTOP(2))]);
        disp('-----------------------------------------------------------------')
        disp(['Recuction of Fhat_Hf at FE start frequency [in dB]: ' num2str(reductSTART(3))]);
        disp(['Reduction of Fhat_Hf at FE stop frequency [in dB]: ' num2str(reductSTOP(3))]);
        disp('-----------------------------------------------------------------')
        disp(['Recuction of Fhat_Hfe at FE start frequency [in dB]: ' num2str(reductSTART(4))]);
        disp(['Reduction of Fhat_Hfe at FE stop frequency [in dB]: ' num2str(reductSTOP(4))]);
        disp('-----------------------------------------------------------------')
    end
end
%%%%%%%%%%%%%%%%%%%%%%%%%%%%%%%%%%%%%%%%%%%%%%%%%%%%%%%%%%%%%%%%%%%%%%%%%%%%

%% LOCATING THE MAIN PULSE AND FINDING THE AMPLITUDE IN STEADY STATE
% FINDING THE AMPLITUDE OF THE MAIN PULSE
% First we must find the steady state region, before maxmin or fft
% Steady-state region uses t_Hp to find the start of the pulse!
if ant_peri < transient_begin+transient_end
    disp('!!!WARNING!!! NO STEADY STATE OF PULSE CAN BE DETERMINED!!!');
    break;
end
tSTART = t_Hp+transient_begin/freq(jj);
out = abs(tt-tSTART) < abs(Ts);
[X,Y] = find(out==1);
tSTART = tt(Y(1));
tSTOP = t_Hp+(ant_peri-transient_end)/freq(jj);
out = abs(tt-tSTOP) < abs(Ts);
[XX,YY] = find(out==1);
tSTOP = tt(YY(1));
if option == 1 % FFT
    F_MAIN = fft(F_Hfe(Y:YY),N)/length(F_Hfe(Y:YY));
    F_MAIN = fftshift(F_MAIN);
    [a,b] = max(abs(F_MAIN));
    MAG_MAIN(mm,jj) = 2*abs(F_MAIN(b)); % peak2peak amplitude
end
if option == 2 % MAXMIN
    F_MAIN = F_Hfe(Y:YY);
    cMAX = 1;
    cMIN = 1;
    % Finding the maxs and mins of the F_MAIN vector and collecting them in
    % vectors 'maks' and 'mini' for further analysis
    for cc = 2:length(F_MAIN)-1
        if F_MAIN(cc-1) < F_MAIN(cc) && F_MAIN(cc+1) < F_MAIN(cc)
            maks(cMAX) = F_MAIN(cc);
            cMAX = cMAX+1;
        else if F_MAIN(cc-1) > F_MAIN(cc) && F_MAIN(cc+1) > F_MAIN(cc)
                mini(cMIN) = F_MAIN(cc);
                cMIN = cMIN + 1;
            end
        end
    end
    % Make sure that vectors 'maks' and 'mini' have equal lengths
    if length(maks) ~= length(mini)
        if length(maks) > length(mini)
            maks = maks(1:length(mini));
        else if length(maks) < length(mini)
                mini = mini(1:length(maks));
```

```
                    end
                end
            end
            MAG_MAIN(mm,jj) = sum(maks+abs(mini))/length(mini); % peak2peak amplitude
        end
    end
end
% Check that the burst ends before the signal is reflected at the plate
for kk = 1:length(tstop)
    if tstop(kk) >= z1/cf
        check(kk) = 0;
    else
        check(kk) = 1;
    end
end
[check1,ind] = find(check,1);  % Finds the first 1, or first frequency where the burst ends
% before the signal is reflected
if length(freq)>1
    disp('!!!WARNING!!!')
    disp(['Every burst before ' num2str(freq(ind)) ' Hz does not end before the burst is reflected at the plate surface!'])
else
    if check == 0
        disp('!!!WARNING!!!')
        disp(['The burst at ' num2str(freq) ' Hz does not end before the burst is reflected at the plate surface!'])
    end
end
disp('COMPLETED!')

if soundfield == 1
    disp(' ')
    disp('Calculating the sound pressure field...')
    % Defining angles
    theta = linspace(0,2*pi,length(r));
    disp('Converting from cylindrical coordinates to cartesian...')
    % Meshing a grid
    [THETA,R] = meshgrid(theta,r);
    % Converting to cartesian coordinates
    [X,Y] = pol2cart(THETA,R);
    disp('Done!')
    % Calculating the pressure along the r-axis.
    PPP = cell(size(freq));
    for f = 1:length(freq)
        p(:,f) = MAG_MAIN(:,f);
        % Since axisymmetrical, the pressure is symmetrical around the z-axis
        for dthet = 1:length(theta)
            PP(:,dthet) = p(:,f);
        end
        PPP{f} = PP;
        if f == ceil(length(freq)/4)
            disp('25 % completed...')
        else if f == ceil(length(freq)/2)
                disp('50 % completed...')
            else if f == ceil(length(freq)*3/4)
                    disp('75 % completed...')
                end
            end
        end
    end
    save FFT_P2_SP.mat freq MAG_MAIN r PPP X Y
    disp('Done!')
else save FFT_P2.mat freq MAG_MAIN
end
```

Appendix G

Various program codes for the measurement setup

Various program codes for the measurement setup are listed below. Permission from relevant co-authors is given.

```
% Routine to calculate peak-to-peak amplitude using FFT
% Halvor Hobaek, modified by Magne Aanes april 2010
function [v1,v2,serie1,serie2] = fftamplitude(resultatV1,fv1,resultatV2,fv2,grense1,grense2...
   ,grense3,grense4,tidsskala1,tidsskala2)
for m = 1:length(fv1)
    dt1 = tidsskala1/length(resultatV1{1,m})*10;
    T1 = 1/fv1(m);
    pp1 = T1/dt1;
    DN1 = floor((grense2-grense1)/pp1);
    N1 = floor(DN1*pp1);
    serie1 = grense1:grense1+N1;
    fs1 = fft(resultatV1{1,m}(serie1))/length(serie1)*2;
    fs1 = fftshift(fs1);
    [a,b] = max(abs(fs1));
    v1(m) = 2*abs(fs1(b));% SPENNING I PEAK2PEAK
    if m == ceil(length(fv1)/2)
        disp('25% completed');
    end
end
disp('50% completed');
if fv2 ~= 0
    for k = 1:length(fv2)
        dt2 = tidsskala2/length(resultatV2{1,k})*10;
        T2 = 1/fv2(k);
        pp2 = T2/dt2;
        DN2 = floor((grense4-grense3)/pp2);
        N2 = floor(DN2*pp2);
        serie2 = grense3:grense3+N2;
        fs2 = fft(resultatV2{1,k}(serie2))/length(serie2)*2;
        fs2 = fftshift(fs2);
        [aa,bb] = max(abs(fs2));
        v2(k) = 2*abs(fs2(bb));% SPENNING I PEAK2PEAK
        if k == ceil(length(fv2)/2)
            disp('75% completed');
        end
    end
```

```
else
    v2 = 0;
    serie2 = 0;
end
end
%%%%%%%%%%%%%%%%%%%%%%%%%%%%%%%%%%%%%%%%%%%%%%%%%%%%%%%%%%%%%%%%%%%%%%%%%%%%%%%%%%%%%%%%%%%%%%%%

% Frequency response of the HK 3202 filter,
% Used as a bandpass filter - 20 kHz to 2 MHz
% @author, Magne Aanes, 22.09.2011

function [HK_ref] = frekresponsHK(f)
% Measurement frequencies
fr = [100000,110000,120000,130000,140000,150000,160000,170000,180000,190000,200000,210000,220000,...
230000,240000,250000,260000,270000,280000,290000,300000,310000,320000,330000,340000,350000,360000,...
370000,380000,390000,400000,410000,420000,430000,440000,450000,460000,470000,480000,490000,500000,...
510000,520000,530000,540000,550000,560000,570000,580000,590000,600000,610000,620000,630000,640000,...
650000,660000,670000,680000,690000,700000,710000,720000,730000,740000,750000,760000,770000,780000,...
790000,800000,810000,820000,830000,840000,850000,860000,870000,880000,890000,900000,910000,920000,...
930000,940000,950000,960000,970000,980000,990000,1000000,1010000,1020000,1030000,1040000,1050000,...
1060000,1070000,1080000,1090000,1100000,1110000,1120000,1130000,1140000,1150000,1160000,1170000,...
1180000,1190000,1200000,1210000,1220000,1230000,1240000,1250000,1260000,1270000,1280000,1290000,...
1300000,1310000,1320000,1330000,1340000,1350000,1360000,1370000,1380000,1390000,1400000,1410000,...
1420000,1430000,1440000,1450000,1460000,1470000,1480000,1490000,1500000];
% Voltage out of filter (p2p)
HK = [1.89815740322123,1.92873083818361,1.95336881941598,1.97316157387699,1.99015206784505,2.00411740251144,...
2.01290807114181,2.02252602437783,2.03194475639046,2.04005235145225,2.04686459061708,2.05331468959520,2.05918052121350,...
2.06448881875557,2.06977708469002,2.07417167946944,2.07813053384716,2.08141992975389,2.08453072100330,2.08735129500222,...
2.09064029006953,2.09365176309648,2.09269586791321,2.09492691210165,2.09740904108479,2.09914004232902,2.10129523634651,...
2.10241448879628,2.10353159918450,2.10524556101876,2.10584720437715,2.10605274023387,2.10705730578532,2.10739952719187,...
2.10729239521700,2.10713365267900,2.10610269610551,2.10188357975474,2.10210572325542,2.10123292933098,2.10011683350218,...
2.09960990442605,2.09816821316199,2.09685568572899,2.09575579583769,2.09465802327442,2.09319186588965,2.09103320086925,...
2.08944333852575,2.08764703635882,2.08617415358091,2.08462262220898,2.08251844055760,2.08027778388965,2.07867681227726,...
2.07672651218456,2.07449208996783,2.07222063297409,2.06976252138390,2.06747388447342,2.06413251743233,2.06145060070353,...
2.05882571025035,2.05624747391985,2.05358088245313,2.05032156173946,2.04721480061956,2.04470493388936,2.04191784983454,...
2.03945890329554,2.03620206565054,2.03307694476910,2.02970074452694,2.02680817756840,2.02316438428378,2.02012716567419,...
2.01667358293956,2.01326104438806,2.00928017154085,2.00608869922460,2.00250015824930,1.99993553333333,1.99612518393362,...
1.99253583980407,1.98825987418586,1.98488464719847,1.98088161856625,1.97735574120827,1.97251022703901,1.96899322035048,...
1.96504267175709,1.96122510312408,1.96086146786233,1.95660673705674,1.95238157369340,1.94838564794585,1.94354829169392,...
1.93913984641265,1.93473595997899,1.92993629064445,1.92513099561255,1.92123902534167,1.91765574341443,1.91295127279374,...
1.90899212181378,1.90397718626617,1.89875151439848,1.89414485460304,1.89266995370215,1.88756564852459,1.88319838077207,...
1.87881375997534,1.87455009353038,1.86963132535586,1.86403279482595,1.85916358010046,1.85377934122101,1.84904551335195,...
1.84416236097935,1.83975546735543,1.83530023103576,1.83012970004957,1.82479907179603,1.82206595489330,1.81671234466812,...
1.81135175216276,1.80601771957717,1.80188457672097,1.79740730975252,1.79213386367607,1.78728481041618,1.78479717984203,...
1.77909014828480,1.77370848975682,1.76790995802517,1.76304129699747,1.75882601888896,1.75395663500320,1.74817006905680,...
1.74233645729959,1.73696680161402];
% Voltage out of the generator (p2p)
v1 = 2;
HK_1 = HK./2;
HK_ref = interp1(fr,HK_1,f,'spline');
end
%%%%%%%%%%%%%%%%%%%%%%%%%%%%%%%%%%%%%%%%%%%%%%%%%%%%%%%%%%%%%%%%%%%%%%%%%%%%%%%%%%%%%%%%%%%%%%%%

function [M_ref] = frekresponsPA_MIN(f)
%#############
%
% Frequency response of a 1 mm PVDF needle hydrophone with submersible
% preamplifier and DC coupler from Percision Acoustics with NPL
% calibration.
%
% My own calibration of the hydrophone!
% This is the end-of-cable loaded sensitivity!
```

```
% DCC terminated with 50 ohm before high impedance amplifier!
%
% Hydrophone serial number 1820 (cone length = 100 mm)
% Preamplifier serial number PA110078
% DC coupler serial number DCPS223
%
% Date of calibration: 19.12.2011
%
% ##########
% @author, Magne Aanes (PhD candidate)

% Frequency range
fr = [100000,105000,110000,115000,120000,125000,130000,135000,140000,145000,...
150000,155000,160000,165000,170000,175000,180000,185000,190000,195000,200000,...
205000,210000,215000,220000,225000,230000,235000,240000,245000,250000,255000,...
260000,265000,270000,275000,280000,285000,290000,295000,300000,305000,310000,...
315000,320000,325000,330000,335000,340000,345000,350000,355000,360000,365000,...
370000,375000,380000,385000,390000,395000,400000,405000,410000,415000,420000,...
425000,430000,435000,440000,445000,450000,455000,460000,465000,470000,475000,...
480000,485000,490000,495000,500000,505000,510000,515000,520000,525000,530000,...
535000,540000,545000,550000,555000,560000,565000,570000,575000,580000,585000,...
590000,595000,600000,605000,610000,615000,620000,625000,630000,635000,640000,...
645000,650000,655000,660000,665000,670000,675000,680000,685000,690000,695000,...
700000,705000,710000,715000,720000,725000,730000,735000,740000,745000,750000,...
755000,760000,765000,770000,775000,780000,785000,790000,795000,800000,805000,...
810000,815000,820000,825000,830000,835000,840000,845000,850000,855000,860000,...
865000,870000,875000,880000,885000,890000,895000,900000,905000,910000,915000,...
920000,925000,930000,935000,940000,945000,950000,955000,960000,965000,970000,...
975000,980000,985000,990000,995000,1000000,1005000,1010000,1015000,1020000,...
1025000,1030000,1035000,1040000,1045000,1050000,1055000,1060000,1065000,1070000,...
1075000,1080000,1085000,1090000,1095000,1100000,1105000,1110000,1115000,1120000,...
1125000,1130000,1135000,1140000,1145000,1150000,1155000,1160000,1165000,1170000,...
1175000,1180000,1185000,1190000,1195000,1200000,1205000,1210000,1215000,1220000,...
1225000,1230000,1235000,1240000,1245000,1250000,1255000,1260000,1265000,1270000,...
1275000,1280000,1285000,1290000,1295000,1300000,1305000,1310000,1315000,1320000,...
1325000,1330000,1335000,1340000,1345000,1350000,1355000,1360000,1365000,1370000,...
1375000,1380000,1385000,1390000,1395000,1400000,1405000,1410000,1415000,1420000,...
1425000,1430000,1435000,1440000,1445000,1450000,1455000,1460000,1465000,1470000,...
1475000,1480000,1485000,1490000,1495000,1500000];

% End-of-cable free-field loaded sensitivity of the hydrophone with
% submersible preamplifier was measured using the 3-way transducer method.
% 2xV301 transducers used for this calibration.
Mr = [[2.76091345645997e-07,2.75421523193422e-07,3.16243463297973e-07,3.11487072661680e-07,...
3.03623021562325e-07,3.14454833695198e-07,3.16755059464921e-07,3.12838949582926e-07,3.18661564614097e-07,...
3.05550491223325e-07,3.64361135962019e-07,3.81926251326734e-07,3.76686493181816e-07,3.71838088943900e-07,...
3.68074165890078e-07,3.83533797784435e-07,4.03113003131974e-07,4.03542115958275e-07,3.97681308849417e-07,...
3.99282364998118e-07,3.98900079719884e-07,3.97699764435349e-07,3.98997922519259e-07,4.00354883590101e-07,...
4.08598101373321e-07,4.11210285210782e-07,4.16031235965742e-07,4.27268862341550e-07,4.31280427591582e-07,...
4.35477376199615e-07,4.32549796750957e-07,4.39016618118537e-07,4.58086670243405e-07,4.67128512701699e-07,...
4.72086768538730e-07,4.82403067832842e-07,4.83318049143168e-07,4.79989844873704e-07,4.78094080936171e-07,...
4.78154667501315e-07,4.86127255885192e-07,4.90469078572423e-07,4.93792175401778e-07,5.01443643693584e-07,...
5.05560382587869e-07,5.06967604456015e-07,5.11275684820825e-07,5.17589189519650e-07,5.21755815638895e-07,...
5.25797598184856e-07,5.26841269404257e-07,5.27573525541725e-07,5.26861729054782e-07,5.31710473255266e-07,...
5.39176548496288e-07,5.45922628986755e-07,5.51869241780812e-07,5.56523043822461e-07,5.61302331883916e-07,...
5.63891989352595e-07,5.72972930988710e-07,5.78431912330580e-07,5.83548837209076e-07,5.87118638018870e-07,...
5.89726519960340e-07,5.93813173808333e-07,5.99272268504966e-07,6.04097859425462e-07,6.06830652344201e-07,...
6.09778110893800e-07,6.15890841983134e-07,6.19637396794305e-07,6.23794905918278e-07,6.29350862095580e-07,...
6.33419231106831e-07,6.36592890010718e-07,6.40137499755651e-07,6.44645790453476e-07,6.49006956184417e-07,...
6.54283372137286e-07,6.59157111360917e-07,6.62153659291096e-07,6.65687594245454e-07,6.68161603617548e-07,...
6.68583986552830e-07,6.70957586121654e-07,6.75816090459039e-07,6.82432212970228e-07,6.87056724177234e-07,...
6.90073232048095e-07,6.90966653395120e-07,6.90569967967553e-07,6.92318762655037e-07,6.95993394543202e-07,...
```

```
7.00407126085292e-07,7.04171490282558e-07,7.06083815107289e-07,7.09520869071188e-07,7.13409890336911e-07,...
7.18861010138570e-07,7.24540184425074e-07,7.30544688931713e-07,7.35572359748979e-07,7.37335524222054e-07,...
7.38211869000691e-07,7.39665043986315e-07,7.42661762927014e-07,7.45981618931322e-07,7.47828063995749e-07,...
7.48334680277360e-07,7.37421123930218e-07,7.36063404995771e-07,7.33155285415006e-07,7.31327312969360e-07,...
7.32326547179410e-07,7.31027746945021e-07,7.27540539130840e-07,7.26965503349350e-07,7.28524505224955e-07,...
7.29711972997135e-07,7.31856170956545e-07,7.35399429923127e-07,7.38097174186245e-07,7.39327754754062e-07,...
7.38051244117940e-07,7.33864168378220e-07,7.32509675521098e-07,7.33749112682955e-07,7.37068376337002e-07,...
7.42689089167171e-07,7.45551054731415e-07,7.44262295122714e-07,7.39505541000156e-07,7.34505911130450e-07,...
7.30934360411520e-07,7.26594349583124e-07,7.22403895734720e-07,7.16559204254364e-07,7.09268087795336e-07,...
7.00766500888909e-07,6.93985453330685e-07,6.89160390024992e-07,6.90270479717488e-07,6.92155267588744e-07,...
6.95032256832094e-07,6.97984601546282e-07,6.99867304887416e-07,7.01441912579486e-07,7.03691937629746e-07,...
7.11087350231957e-07,7.02180591574316e-07,7.11976687129642e-07,7.28201541882973e-07,7.31612378894755e-07,...
7.36618384439645e-07,7.42750386203334e-07,7.50590926538649e-07,7.60150161425968e-07,7.70653808219418e-07,...
7.75938144667102e-07,7.71153088636672e-07,7.75962109249487e-07,7.78323994787633e-07,7.78912520129838e-07,...
7.79689264881613e-07,7.78463656420448e-07,7.77526529522518e-07,7.75937941453780e-07,7.76785030651611e-07,...
7.79863883218558e-07,7.86162722031940e-07,7.92942331288838e-07,7.97916110378814e-07,8.01419669812515e-07,...
8.03116927328679e-07,8.04943067008664e-07,8.07544069501249e-07,8.08503097076701e-07,8.08649727055833e-07,...
8.08266589536351e-07,8.04215665262388e-07,8.04021155606195e-07,8.06023413776108e-07,8.10847246054877e-07,...
8.12857228770046e-07,8.17196734194048e-07,8.17884692438086e-07,8.19448321664221e-07,8.26565666820093e-07,...
8.36667844324382e-07,8.49457809243306e-07,8.51182843740821e-07,8.54033666430174e-07,8.55501280321430e-07,...
8.59176170775880e-07,8.62541825719085e-07,8.62793017797866e-07,8.68211337223638e-07,8.68008350642363e-07,...
8.68540774104594e-07,8.70109985403806e-07,8.79427894155075e-07,8.24391237787265e-07,7.77727545478631e-07,...
7.35703433817644e-07,6.94987751384647e-07,6.63822448768573e-07,6.45943657447942e-07,6.36041656036990e-07,...
6.38558046229674e-07,6.45028527493031e-07,6.58078630042246e-07,6.75739204944177e-07,7.13839095570644e-07,...
7.43750611925665e-07,8.00225888489881e-07,8.43616574621657e-07,8.86584910867210e-07,8.80260907972616e-07,...
8.76498492232071e-07,8.77096797804935e-07,8.69469283192916e-07,8.80190727873579e-07,8.82139034287977e-07,...
8.83895748619141e-07,8.81346019272906e-07,8.81986807307602e-07,8.83213892342342e-07,8.78438963243795e-07,...
8.79246730916659e-07,8.62426151666629e-07,8.56928795439361e-07,8.50129496133516e-07,8.46531148595368e-07,...
8.44536076658198e-07,8.44878888767139e-07,8.46289027905807e-07,8.43137116885640e-07,8.36863132201161e-07,...
8.32216505566977e-07,8.25051328072354e-07,8.21753176558422e-07,8.26119865949769e-07,8.23908535742162e-07,...
8.23893474689699e-07,8.21902847902860e-07,8.21259636118640e-07,8.20740483428052e-07,8.20399119694938e-07,...
8.20822043432679e-07,8.28116538925632e-07,8.29161419760123e-07,8.26868598101934e-07,8.24239512150485e-07,...
8.23799676865008e-07,8.27600880844856e-07,8.33548995172697e-07,8.37953111468078e-07,8.37530438094176e-07,...
8.33403773290846e-07,8.12326409131759e-07,8.10266967460775e-07,8.12494369324493e-07,8.18127315573633e-07,...
8.21210288354246e-07,8.20667791176934e-07,8.17175419221940e-07,8.13440220048933e-07,8.10909911400541e-07,...
8.10103531159447e-07,8.09999707627059e-07,8.10664646272352e-07,8.08409069553990e-07,8.05588925631147e-07,...
8.02762999265310e-07,8.01488805090309e-07,8.03264328390172e-07,8.03624847730191e-07,8.02316346598973e-07,...
7.98184507187390e-07,7.93543431386231e-07];

% Interpolated using the frequency range specified by user!
M_ref = interp1(fr,Mr,f,'spline');
end
%%%%%%%%%%%%%%%%%%%%%%%%%%%%%%%%%%%%%%%%%%%%%%%%%%%%%%%%%%%%%%%%%%%%%%%%%%%%%%%%%%%%%%%%%%%%%%%%%%%%%%%%%%%%

function [M_ref] = frekresponsPA_NPL(f)
% ##########
%
% Frequency response of a 1 mm PVDF needle hydrophone with submersible
% preamplifier and DC coupler from Percision Acoustics with NPL
% calibration.
%
% Hydrophone serial number 1820 (cone length = 100 mm)
% Preamplifier serial number PA110078
% DC coupler serial number DCPS223
%
% Date of calibration: 28 November - 1 December 2011
%
% ##########
% Delivered UiB: 13 December 2011
% @author, Magne Aanes (PhD candidate)

% Frequency range
```

```
fr = [100:10:1000]*1e3;

% End-of-cable free-field loaded sensitivity of the hydrophone with
% submersible preamplifier was determined by the comparison calibration
% method, in conformance with IEC 60565: 2006 (BS EN 60565: 2007), using an
% NPL reference standard hydrophone. The hydrophone under test was
% terminated with a 50 Ohm load. More information in calibration sheet.
% dB re 1V/ÂţPa
Mv_dB = -[249.4,249.0,249.2,248.5,249.0,248.2,248.6,248.2,248.5,248.0,247.4,248.1,...
    247.6,247.1,247.8,247.8,246.6,246.1,246.4,246.3,246.2,246.0,245.9,245.9,245.6,...
    245.5,245.5,245.2,245.0,244.9,244.8,244.8,244.8,244.6,244.4,244.4,244.3,244.3,...
    244.0,243.9,244.0,243.9,243.7,243.7,243.7,243.6,243.3,243.4,243.4,243.3,243.1,...
    243.0,243.0,243.0,242.7,242.8,243.0,243.0,243.0,242.9,243.0,243.0,243.0,243.0,...
    243.0,243.0,243.0,243.1,243.3,243.4,243.6,243.6,243.7,243.7,243.5,243.4,243.3,...
    243.2,243.0,243.0,242.7,242.5,242.6,242.7,242.7,242.6,242.8,242.7,242.6,242.7,...
    242.7];

% Uncertainty, confidence of approximately 95 %, k = 2.
Mv_dB_k2 = [ones(1,70)*0.7 ones(1,length(Mv_dB)-70)*0.8];
Mv_50ohm_k2 = 10.^(Mv_dB_k2./20);
upper_limit = Mv_50ohm_k2;
lower_limit = 1-(upper_limit-1);

% End-of-cable free_field loaded sensitivity (mV/MPa) ~ terminated with 50 ohm
Mv_50ohm = 10.^(Mv_dB./20)/1e-6*1e3/1e-6;

% Open-ended free-field loaded sensitvity (mV/MPa) ~ terminated with 1 MOhm
Mv_1Mohm = Mv_50ohm/(50/(50+50));

% End-of-cable loaded sensitivity to be used! DCC terminated with 50 ohm
% and then connected to the HVA.
M = Mv_50ohm/1e3*1e-6;
M_ref = interp1(fr,M,f,'spline');
end
%%%%%%%%%%%%%%%%%%%%%%%%%%%%%%%%%%%%%%%%%%%%%%%%%%%%%%%%%%%%%%%%%%%%%%%%%%%%%%%%%%%%%%%%%%%%%%%%

%%%%%%%%%%%%%%%%%%%%%%%%%%%%%%%%%%%%%%%%%%%%%%%%%%%
% Skript som setter opp Micos-motorer.
% Fungerer paa Matlab/Windows.
% Espen Storheim, 08/07-2009
% Magne Aanes, 28/04-2011 - Modifisert
%%%%%%%%%%%%%%%%%%%%%%%%%%%%%%%%%%%%%%%%%%%%%%%%%%%

% Skriptet setter opp et haandtak for den aktuelle porten og
% gjor dette til ein global variabel. Da kan den brukes av
% alle skript og funksjoner uten at en slipper aa deklarere
% den paa nytt.

global s1
s1 = serial('COM1','BaudRate',115200);
fopen(s1)

fprintf(s1,'1 init');
% Setter konstanter i PID-en paa LMS110
% Fra PI-MiCos : PID(400,2,4000)
%PID(800,1.5,8000);
PID(1000,1,10000);

% Setter hastighet og akselerasjon
fprintf(s1,'4 1 sna'); % 2
fprintf(s1,'5 1 snv'); % 10
```

```
% Setter hastighet og akselerasjon til rotasjonsmotor
fprintf(s1,'100 2 sna');
fprintf(s1,'1 2 snv');

% Finner utgangspunktet
%fprintf(s1,'1 ncal');
%fprintf(s1,'2 ncal');
%%%%%%%%%%%%%%%%%%%%%%%%%%%%%%%%%%%%%%%%%%%%%%%%%%%%%%%%%%%%%%%%%%%%%%%%%%%%%%%%%%%%%%%%%%%%%%%%

%%%%%%%%%%%%%%%%%%%%%%%%%%%%%%%%%%%%%%%%%%%%%%%%%%%%%%%%%%%%%%%%
% Skript som initialeserer Parker-motorene som Kjersti brukte.
% Basert paa motorinitiering.m av Halvor Hobaek.
% Denne versjonen er tilpassa Matlab/Windows.
% Espen Storheim, 08/07-2009.
% Magne Aanes, 28.04.2011 - modifisert
%%%%%%%%%%%%%%%%%%%%%%%%%%%%%%%%%%%%%%%%%%%%%%%%%%%%%%%%%%%%%%%%

% Oppsett av seriellporten. Deklarerar handtaket globalt slik at
% det kan nyttast inni funksjonar, t.d. Parkerstep.m.
global s2;
s2 = serial('COM3','Terminator','CR');

% Oppstart av motorane.
fopen(s2);
fprintf(s2,'#1');
%disp('Dersom resultatet nedanfor er 3 er alt i orden.')
idn = fscanf(s2);

% Killer motor nr. 1 paa grunn av nokre smaa men ukjente problem.
fprintf(s2,'1K');
fscanf(s2);

% Startar motor nr. 1.
fprintf(s2,'1ON');
fscanf(s2);

% Startar motor nr. 2.
fprintf(s2,'2ON');
fscanf(s2);

% Set grensene til motorane. Desse er trulig relatert til dei elektriske
% sensorane som er montert.
fprintf(s2,'1LIMITS(0,0,0)');
fscanf(s2);
fprintf(s2,'2LIMITS(0,0,0)');
fscanf(s2);

% Generelle kommentarar til koden:
% Det viktigaste i forbindelse med desse motorane er aa settje terminatoren
% til CR og aa sende kommandoen #1. Denne koden er berre verifisert paa Matlab
% 2006 under Windows XP.
%%%%%%%%%%%%%%%%%%%%%%%%%%%%%%%%%%%%%%%%%%%%%%%%%%%%%%%%%%%%%%%%%%%%%%%%%%%%%%%%%%%%%%%%%%%%%%%%

%%%%%%%%%%%%%%%%%%%%%%%%%%%%%%%%%%%%%%%%%%%%%%%%%%%
% Skript som styrer Micos-motorer.
% Fungerer paa Matlab/Windows.   %
% Espen Storheim, 08/07-2009   %
% Magne Aanes, 28.04.2011 - modifisert
%%%%%%%%%%%%%%%%%%%%%%%%%%%%%%%%%%%%%%%%%%%%%%%%%%%

% a = 1: lineaer
% a = 2: rotasjon
```

```
function Micosstep(g,a,m)

% KORT FORKLARING:
% Dette skriptet styrar Micos DT-80 (2008/04) rotasjonsmotoren som finns
% paa akustikklaben. Argument som trengs er lista nedanfor.
%
% g er antal grader (positiv eller negativ), Mp vaere en streng + X.0 i mm
% a er aksen (1),
% m = 0 -> relativ royrsle,
% m = 1 -> absolutt royrsle.

% Standardinnstillingar dersom ein berre oppgir vinkelen i argumentet til skriptet:
if (nargin < 3)
    a = 1;  % Akse 1 er default.
    m = 0;  % Relativ step (r) er default.
else
end

global s1   % Brukar handtaket fraa Micosinitialisering.m.

% Setter bevegelsestype (absolutt eller relativ).
if (m==0)
    cmd = [num2str(g) ' ' num2str(a) ' nr'];
else (m==1)
    cmd = [num2str(g) ' ' num2str(a) ' nm'];
end

fprintf(s1,cmd)

% Maa vente til motor staar i ro
% Sjekker hvortid motor er ferdig med aa kjore
tall = 1;
while tall == 1
    beveger_seg = MotorSend(s1,[num2str(a) ' nst']);
    tall = str2num(beveger_seg);
    if tall == 0
        break;
    end
end
end
%%%%%%%%%%%%%%%%%%%%%%%%%%%%%%%%%%%%%%%%%%%%%%%%%%%%%%%%%%%%%%%%%%%%%%%%%%%%%%%%%%%%%%%%%%%%%%%%%

%%%%%%%%%%%%%%%%%%%%%%%%%%%%%%%%%%%%%%%%%%%%%%%%%%%%%%%%%%%%%%%%%%%%%%%%%%%%%%%
% Skript som kjorer motorane ein gitt distanse, her konvertert til mm. Input
% i denne funksjonen er distanse og motor nummer. Dette forutset at skriptet
% Parkerinitiering.m er brukt i forkant slik at motorane er klar til bruk.
% Espen Storheim, 08/07-2009.
% Magne Aanes, 28.04.2011 - modifisert
%%%%%%%%%%%%%%%%%%%%%%%%%%%%%%%%%%%%%%%%%%%%%%%%%%%%%%%%%%%%%%%%%%%%%%%%%%%%%%%

% n = 1: langs tank
% n = 2: paa tvers av tank
% d = avstand i mm, n = akse
function Parkerstep(d,n)
global s2

% Konverterar distanse til antal step.

if (nargin ==1)
n = 1;
else
end
```

```
% Konverterar distanse til antal step.
a1 = 1.250e-3;
a2 = 1.250e-3;

if (n == 1)
    d = d/a1;
else
    d = d/a2;
end
% Klargjer motoren.
cmd = [num2str(n) ’D’ num2str(d)];
fprintf(s2,cmd);
fscanf(s2);

% Kjorar steget.
fprintf(s2,[num2str(n) ’G’]);
fscanf(s2);

% Sjekker hvortid motor er ferdig med aa kjore
beveger_seg = 1;
while beveger_seg == 1
    midlertidig = MotorSend(s2,[num2str(n) ’R(MV)’]);
    midlertidig = fscanf(s2);
    beveger_seg = str2num(midlertidig(3:end));
    if beveger_seg == 0
        break;
    end
end
end
%%%%%%%%%%%%%%%%%%%%%%%%%%%%%%%%%%%%%%%%%%%%%%%%%%%%%%%%%%%%%%%%%%%%%%%%%%%%%%%%%%%%%%%%%%%%%%%%

% PID-constants for Micos stages
function PID(p,i,d)

global s1;
fprintf(s1,[num2str(p) ’ 1 1 setsp’]);
fprintf(s1,’1 1 getsp’);
P = fscanf(s1);

fprintf(s1,[num2str(i) ’ 2 1 setsp’]);
fprintf(s1,’2 1 getsp’);
I = fscanf(s1);

fprintf(s1,[num2str(d) ’ 3 1 setsp’]);
fprintf(s1,’3 1 getsp’);
D = fscanf(s1);

% disp([’P-ledd = ’,P]);
% disp([’I-ledd = ’,I]);
% disp([’D-ledd = ’,D]);
%%%%%%%%%%%%%%%%%%%%%%%%%%%%%%%%%%%%%%%%%%%%%%%%%%%%%%%%%%%%%%%%%%%%%%%%%%%%%%%%%%%%%%%%%%%%%%%%

% [x wf timeDiv] = adjustAmplitude(ch,instrument,meas)
% Adjusts voltage scaling and gathers acoustic data.
% Rune Hauge & Eivind Mosland, 2012
% Mod. Magne Aanes, for aa fungere med mitt oppsett

function [x wf timeDiv] = adjustAmplitude(ch,ud_skop,meas2,samples)
% Magne Aanes, 11.01.2013, endringer til bruk i min kode!
instrument = [];
instrument.scope = ud_skop;
```

```
meas = [];
meas.wait_scaling = meas2;

% Stop aquisition.
fprintf(instrument.scope,'ACQ:STATE STOP');
% Wait to ensure that the scope wipes its memory.
pause(1)
% Start aquisition.
fprintf(instrument.scope,'ACQ:STATE RUN');
% Wait for averaging.
pause(meas.wait_scaling)

% Read waveform.
[x wf timeDiv] = DPOLes(ch,samples,instrument.scope);
maxV = max(wf);

% Get current scaling.
Scaling = str2num(query(instrument.scope,['CH',num2str(ch),':SCA?']));

% The divs of interest for acoustic measurements are: 10e-3, 20e-3,
% 50e-3, 100e-3, 200e-3, 500e-3
%verticalScalings = [1e-3 2e-3 5e-3 10e-3, 20e-3, 50e-3, 100e-3, 200e-3, 500e-3 1 2];
verticalScalings = [2e-3 5e-3 10e-3, 20e-3, 50e-3, 100e-3, 200e-3, 500e-3 1 2];
%verticalScalings = [10e-3];
ind = find(Scaling==verticalScalings);
if ind == 0
    ind = 1;
    fprintf(instrument.scope,['CH',num2str(ch),':SCA ',10e-3]);
end

scrnRows = 5;
% scrnRows = 4;

% Adjust vertical scaling and measure until no clipping.
finished = 0;
while ~finished
    %disp(['Current volt/div: ',num2str(verticalScalings(ind))])
    if maxV >= scrnRows*verticalScalings(ind)
        Scaling = verticalScalings(ind+1);
        fprintf(instrument.scope,['CH',num2str(ch),':SCA ',num2str(Scaling)]);
        ind = ind +1;

        % Wait for averaging to finish.
        pause(meas.wait_scaling)

        %disp('Measuring')
        [x wf timeDiv] = DPOLes(ch,samples,instrument.scope);
        maxV = max(wf);

    elseif ind ~= 1 && maxV < scrnRows*verticalScalings(ind-1)
        %disp('Decreasing scaling')
        Scaling = verticalScalings(ind-1);
        fprintf(instrument.scope,['CH',num2str(ch),':SCA ',num2str(Scaling)]);
        ind = ind -1;

        % Wait for averaging to finish.
        pause(meas.wait_scaling)

        %disp('Measuring')
        [x wf timeDiv] = DPOLes(ch,samples,instrument.scope);
        maxV = max(wf);
    else
```

```
        finished = 1;
    end
end
end
%%%%%%%%%%%%%%%%%%%%%%%%%%%%%%%%%%%%%%%%%%%%%%%%%%%%%%%%%%%%%%%%%%%%%%%%%%%%%%%%%%%%%%%%%%%%%%%%%%%

% Skript som kommuniserer med Tektronix DPO3012
% 8-bit unsigned characters. Windows version.
% Modifisert Magne Aanes, 20.07.2011 for aa fungere med Matlab Instrument
% Control Toolbox.
function [x,wf,tidsskala] = DPOLes(ch,samples,DPO)

fprintf(DPO,'SAV:WAVE:GATI NON');
fprintf(DPO,['SAV:WAVE CH' num2str(ch) ',REF1']);
fprintf(DPO,'DAT:SOU REF1');
fprintf(DPO,'DAT:START 1');
fprintf(DPO,['DAT:STOP ' num2str(samples)]);
fprintf(DPO,'CURV?');
pause(1);
ydata = binblockread(DPO,'int8');
fscanf(DPO); % reading trailing terminating character

fprintf(DPO,'HOR:SCA?');
tidsskala = str2num(fscanf(DPO));

fprintf(DPO,'WFMO:XZE?'); % time coordinate of the first point
xze = str2num(fscanf(DPO));

fprintf(DPO,'WFMO:XIN?'); % horizontal point spacing in unites
xin = str2num(fscanf(DPO));

fprintf(DPO,'WFMO:YMU?'); % vertical scale factor per digitizing level in units
YMU = str2num(fscanf(DPO));

fprintf(DPO,'WFMO:YZE?'); % vertical offset
YZE = str2num(fscanf(DPO));

x = xze:xin:(xze+(length(ydata)-1)*xin); % time vector
wf = (ydata*YMU) + YZE; % scaling the waveform (wf)
end
%%%%%%%%%%%%%%%%%%%%%%%%%%%%%%%%%%%%%%%%%%%%%%%%%%%%%%%%%%%%%%%%%%%%%%%%%%%%%%%%%%%%%%%%%%%%%%%%%%%

%% Program for akustiske maalinger i vanntank
% Magne Aanes, juli 2011
% Programmet kjorer gjennom spesifisert frekvensomraade
% og henter ut data fra valgfritt skop
% Bruk 'instrreset' hvis programmet bryter for det avsluttes skikkelig
%%--------------------------------BRUKER---------------------------------%%
% Frekvensomraadet en onsker aa undersoke
fstart = 350e3;
fstep = 1e3;
fstop = 1000e3;

burst_rate = 50; % Tid(i Hz) mellom hver burst
voltinn = 10; % Spenning paa innsignal fra generatoren(pk)
samples = 100e3; % antall samples paa skop
ch=1; % Lese fra kanal 1 paa skop
average =  256; % antall midling paa skop
meas = 1; % Tid for midling

%%----------------------------------------------------------------------%%
%%----------------------------------------------------------------------%%
```

```
fprintf(ud_signal,[’BM:INT:RATE ’ num2str(burst_rate)]);
fprintf(ud_signal,[’VOLT ’ num2str(voltinn)]);

fprintf(ud_skop,’ACQ:MOD AVE’);
fprintf(ud_skop,[’ACQ:NUMAV ’ num2str(average)]);
fprintf(ud_skop,[’HOR:RECO ’ num2str(samples)]);
fprintf(ud_skop,’DAT:START 1’);
fprintf(ud_skop,[’DAT:STOP ’ num2str(samples)]);
fprintf(ud_skop,’TRIG:A:TYP EDG;A:EDGE:AUX’);
fprintf(ud_skop,’TRIG:A:TYP EDG’);

resultat = {};
frekvens = [];
f = fstart;
i = 1;
% Avstand til forste kant paa PA hydrofon er 26 mm --> 18 pulser ved 500 kHz
%t = 30e-6;
% Avstand til stang - 170 mm --> 225Âţs
%t = 225e-6;
% Pulslengde lang, 60 pulser ved 500 kHz
t = 130e-6;

disp(’Commencing measurements’)
    %% Innhenting av data fra skop og sweeping av frekvensomraadet
while f <= fstop;
    disp(f)
    fprintf(ud_signal,[’BM:NCYC ’, num2str(ceil(f*t))]);
    fprintf(ud_signal,[’FREQ ’, num2str(f)]);
    pause(2);
    [tid{1},resultat{i},tidsskala] = adjustAmplitude(ch,ud_skop,meas,samples);
    frekvens(i) = f;
    ant_peri(i) = ceil(f*t);
    f = f + fstep;
    i = i + 1;
end

disp(’Done!’);
disp(’Saving data to file...’);
save elektrisk.mat tid resultat frekvens tidsskala ant_peri
disp(’Done!’);
%%%%%%%%%%%%%%%%%%%%%%%%%%%%%%%%%%%%%%%%%%%%%%%%%%%%%%%%%%%%%%%%%%%%%%%%%%%%%%%%%%%%%%%%%%%%%%%%

addpaths;
%% BRUKER
disp(’Source sensitivity using hydrophone!’);
disp(’Commencing calculation of source sensitivity’);
d = 0.9068; % Avstand mellom lydkilde og hydrofon (i m)
amp_faktor = 45.74; % [dB] Forsterkning i HVA-10M-60-F
delta_amp = 20.24;  % [dB] delta mellom 40/60 dB. (mÃělt ved 500kHz)
temperatur = 19; % Temperatur (i C)

% Steady-state omrÃěde for spenning inn pÃě sendertransduser (v1)
grense1 = 35000;
grense2 = 45000;

% Steady-state omrÃěde for spenning ut fra forsterker (v2)
grense3 = 40000;
grense4 = 50000;

disp(’Loading measurement data...’);
%% PROGRAM
load elektrisk_pNo2_20Vpp.mat
```

```
resultatV1 = resultat;
fv1 = frekvens;
tidsskala1 = tidsskala;
load akustisk_pNo2--PA_20Vpp.mat
resultatV2 = resultat;
fv2 = frekvens;
tidsskala2 = tidsskala;

disp('Done!');
disp('Method for calculating voltage amplitude:');
valg2 = input('[FFT = 1] [MAXMIN = 2]');
disp('Calculating voltage amplitudes...');
if valg2 == 1
    % FFT-metode fra Halvor for Ãě finne amplitude, modifisert
    [v1,v2,serie1,serie2] = fftamplitude(resultatV1,fv1,resultatV2,fv2,grense1,grense2,grense3...
        ,grense4,tidsskala1,tidsskala2);
    disp('Done!');
else if valg2 == 2
        % %%---MAKS PEAK-PEAK AV SPENNING UT OG INN---%%
        [v1,v2] = maxmin(resultatV1,fv1,resultatV2,fv2,grense1,grense2,grense3,grense4);
    end
    disp('Done!');
end

if length(fv1)>length(fv2)
    f = fv2;
else f = fv1;
end

disp('');
valg1 = input('End-of-cable free field loaded sensitivity by [1]-UiB or [2]-NPL: ');
% End-of-cable free field loaded sensitivity! DCC terminated with 50 ohm
% before high impedance amplifier.
if valg1 == 1
    [M_ref] = frekresponsPA_MIN(f);
else if valg1 == 2
        [M_ref] = frekresponsPA_NPL(f);
    end
end
amp = 10^((amp_faktor+delta_amp)/20);
V = v2/amp; %v2 er i peak2peak
% Korrigerer for forsterkning i HK-filteret
V = V./frekresponsHK(f);
% Trykk ved hydrofon (peak2peak)
p = V./M_ref;

disp('Calculating source sensitivity at 1 m...');
% Trykk ved 1 m
d0 = 1;
p_1m = p*d/d0;
% KildefÃÿlsomhet Sv
Sv=p_1m./v1;
% KildefÃÿlsomheten gitt i dB re 1V/Pa
Svlg = 20*log10(abs(Sv));
save akustiskSVhyd.mat f Sv Svlg
disp('Done!');
%%%%%%%%%%%%%%%%%%%%%%%%%%%%%%%%%%%%%%%%%%%%%%%%%%%%%%%%%%%%%%%%%%%%%%%%%%%%%%%%%%%%%%%%%%%%%%%%

%% Program for akustiske maalinger i vanntank
% Magne Aanes, jan 2012
% Direktivitetsmaalinger
```

```
addpaths;
%%--------------------------------BRUKER---------------------------------%%
% Frekvensen en onsker aa undersoke
f = 575e3;

burst_rate = 50; % Tid(i Hz) mellom hver burst
voltinn = 10; % Spenning paa innsignal fra generatoren(pk)
samples = 100e3; % antall samples paa skop
ch=1; % Lese fra kanal 1 paa skop
average = 64; % antall midling paa skop

% Vinkler i grader
vstart = -45;
vstep = 1;
vstop = 45;

% Avstand = 270 mm, f = 575 kHz
vertikal_v = [-45,-35,-25,-15,-10,-7,-6,6,7,10,15,25,35,45];
vertikal = [20,50,20,50,100,200,500,200,100,50,20,50,20]*1e-3;
%%-----------------------------------------------------------------------%%
%%-----------------------------------------------------------------------%%

% Initalisering av HP 33120A
ud_signal = gpib('agilent',7,12);   % GPIB-kanal 12
fopen(ud_signal);
fprintf(ud_signal,['BM:INT:RATE ' num2str(burst_rate)]);
fprintf(ud_signal,['VOLT ' num2str(voltinn)]);

% Initalisering av Tektronix DPO3012
ud_skop = gpib('agilent',7,1,'InputBufferSize',samples,'OutputBufferSize',samples);
fopen(ud_skop);
fprintf(ud_skop,'ACQ:MOD AVE');
fprintf(ud_skop,['ACQ:NUMAV ' num2str(average)]);
fprintf(ud_skop,['HOR:RECO ' num2str(samples)]);
fprintf(ud_skop,'DAT:START 1');
fprintf(ud_skop,['DAT:STOP ' num2str(samples)]);
fprintf(ud_skop,'TRIG:A:TYP EDG;A:EDGE:AUX');
fprintf(ud_skop,'TRIG:A:TYP EDG');
% Pulslengde lang, 60 pulser ved 500 kHz
t = 130e-6;
fprintf(ud_signal,['BM:NCYC ', num2str(ceil(f*t))]);
fprintf(ud_signal,['FREQ ', num2str(f)]);

resultat = {};
i = 1;
v = vstart;
vinkel = [];
ant_peri = ceil(f*t);

disp('Commencing measurements')
    %% Innhenting av data fra skop og sweeping av frekvensomraadet
while v <= vstop;
    disp(v)
    for k = 1:length(vertikal_v)
        if v == vertikal_v(k)
            fprintf(ud_skop,['CH' num2str(ch) ':SCA ' num2str(vertikal(k))]);
            fprintf(ud_skop,['REF' num2str(ch) ':SCA ' num2str(vertikal(k))]);
            pause(5)
        end
    end
    pause(10)
    [tid{1},resultat{i},tidsskala] = DPOLes(ch,samples,ud_skop);
```

```
    vinkel(i) = v;
    v = v + vstep;
    i = i + 1;
    Micosstep(vstep,2,0)
end

disp('Done!');
disp('Saving data to file...');
save elektrisk.mat tid resultat vinkel tidsskala ant_peri
disp('Done!');
%%%%%%%%%%%%%%%%%%%%%%%%%%%%%%%%%%%%%%%%%%%%%%%%%%%%%%%%%%%%%%%%%%%%%%%%%%%%%%%%%%%%%%%%%%%%%%%%

%%--------------------------------BRUKER---------------------------------%%
% Kjor mainSV for aa sette frekvens og slikt!
%
start_x = -250;
step_x = -1;
stop_x = -300;

start_y = 0;
step_y = -0;
stop_y = -0;

x_akse = [start_x:step_x:stop_x];
if start_y == 0 && stop_y == 0
    y_akse = 1;
else
    y_akse = [start_y:step_y:stop_y];
end
xx = start_x;yy = start_y;
ii = 1;
ch=1;
meas=1;
samples=100e3;
resultat={};

while ii <= length(x_akse)*length(y_akse)
    % Styrer motor
    disp(['x = ' num2str(xx) ' :: y = ' num2str(yy)])
    [tid{1},resultat{ii},tidsskala] = adjustAmplitude(ch,ud_skop,meas,samples);
    xx = xx + step_x;
    ii = ii + 1;
    if start_y == 0 && stop_y == 0
        Micosstep(step_x,1,0);
        pause(3)
    else
        if xx > stop_x && yy > stop_y
            Parkerstep(step_y,2);
            pause(10)
            instrreset
            Parkerinitiering
            Micosinitialisering
            init_mainSV
            pause(5)
            Micosstep(-(abs(stop_x)+abs(start_x)),1,0);
            % Vente for 100 mm distanse
            pause(60)
            yy = yy + step_y;
            xx = start_x;
        else
            Micosstep(step_x,1,0);
            pause(3)
```

```
        end
    end
end

disp('Done!');
disp('Saving data to file...');
save elektrisk.mat tid resultat tidsskala x_akse y_akse
disp('Done!');
%%%%%%%%%%%%%%%%%%%%%%%%%%%%%%%%%%%%%%%%%%%%%%%%%%%%%%%%%%%%%%%%%%%%%%%%%%%%%%%%%%%%%%%%%%%%%%%%

% 3-transducers resiprocity calibration of the PA 1 mm needle hydrophone
% @author, Magne Aanes

% STARTED: 05.10.2011
% UPDATED: 19.12.2011

% Method: see pp. 7.26-28 in PHYS 272
% Assumes:
% Free field
% Far field
% Spherical waves
% V301 nr. 654055 transducer is reciprocal

% Source S: V301 nr. 654220
% Receiver R: PA 1 mm needle hydrophone
% Transducer T: V301 nr. 654055

% All sensitivities are given with respect to voltage
%%
d0 = 1;
rho = 1000;
temperatur = 19.0;   % Celsius, beregnet cl = 1485.9 m/s.
amp_faktor = 45.74;  % [dB] Forsterkning i HVA-10M-60-F
delta_amp = 20.24; % [dB] Forsterkning i HVA-10M-60-F. Delta fra 40 til 60 dB.

% a) Source S --> Receiver R
% Voltage Vs1 into source S [20 Vpp]
load elektrisk_Vs1.mat
Vs1 = v1;
clear v1
% Voltage Vsr out of receiver R using source S (terminated with 50 ohm)
load akustisk_Vsr_50ohm.mat
% Distance between source S and receiver R [in m]
d1 = 0.9109;
% Corrects for the amplification in HVA
Vsr = v1/(10^((amp_faktor+delta_amp)/20));
% Corrects for the amplification in HK-filter
Vsr = Vsr./frekresponsHK(f);
clear v1

% b) Source S --> transducer T
% Voltage Vs2 into source S [2 Vpp]
load elektrisk_Vs2.mat
Vs2 = v1;
clear v1
% Input admittance to source S
load Z_V301_654220.mat
Y = g+i.*b;
ZtS = 1./Y;
clear fr g b
% Current Is2
Is2 = Vs2./ZtS;
```

```
% Voltage Vst out of transducer T using source S (terminated with 1 Mohm)
load akustisk_Vst.mat
% Distance between source S and transducer T [in m]
d2 = 1.167;
% Corrects for the amplification in HVA
Vst = v1/(10^((amp_faktor)/20));
% Corrects for the amplification in HK-filter
Vst = Vst./frekresponsHK(f);
clear v1

% c) Transducer T --> Receiver R
% Voltage Vt into transducer T [20 Vpp]
load elektrisk_Vt1.mat
Vt1 = v1;
clear v1
% Voltage Vtr out of receiver R using transducer T (terminated with 50 ohm)
load akustisk_Vtr_50ohm.mat
% Distance between transducer T and receiver R [in m]
d3 = 0.9123;
% Corrects for the amplification in HVA
Vtr = v1/(10^((amp_faktor+delta_amp)/20));
% Corrects for the amplification in HK-filter
Vtr = Vtr./frekresponsHK(f);
clear v1
% Input admittance to transducer T
load Z_V301_654055.mat
Y = g+i.*b;
ZtT = 1./Y;
clear fr g b
% Resiprocity factor for transducer T
J = 2*d0./(rho*f);

checkResiprocity = input('Control that transducer T is resiprocal?[1=OK]: ');
if checkResiprocity == 1
    % d) Transducer T --> Source S
    disp('Reciprosity check!')
    % Voltage Vt2 into transducer T [2 Vpp]
    load elektrisk_Vt2.mat
    Vt2 = v1;
    clear v1
    % Current It2
    It2 = Vt2./ZtT;
    % Voltage Vts out of source S using transducer T (terminated with 1 Mohm)
    load akustisk_Vts.mat
    % Distance between transducer T and source S [in m]
    d4 = 1.167;
    % Corrects for the amplification in HVA
    Vts = v1*sqrt(2)/(10^(amp_faktor/20));
    % Corrects for the amplification in HK-filter
    Vts = Vts./frekresponsHK(f);
    clear v1
    figure
    plot(f/1000,abs(Vst./Is2)./abs(Vts./It2),'Linewidth',2)
    set(gca,'Fontsize',30);xlabel('Frequency, f [kHz]');ylabel('Ratio of fractions')
    xlim([100 1000])
    ylim([0.9 1.05])
    grid on;box on;
end

%% Receiver sensitivity with respect to voltage
% 1. Measurement a,b,c,d) terminated with 1 Mohm --> free field open curcuit
% 2. Measurement a,b) terminated with 50 ohm,
```

```
%                c,d) terminated with 1 Mohm,
%    End-of-cable free field loaded (as in the NPL calibration)
Mr = abs(sqrt((Vs2./Vs1).*(Vsr./Vst).*J.*ZtT.*(d1/d2).*(Vtr./Vt1)*(d3/d0)));
% I mV/MPa:
Mr_korr = Mr*1e3/1e-6;
%%%%%%%%%%%%%%%%%%%%%%%%%%%%%%%%%%%%%%%%%%%%%%%%%%%%%%%%%%%%%%%%%%%%%%%%%%%%%%%%%%%%%%%%%%%%%%%

% 2-transducers resiprocity calibration of the PA 1 mm needle hydrophone
% @author, Magne Aanes

% STARTED: 05.09.2011
% UPDATED: 09.02.2012

%%
% Source S: V301 nr. 654220
% Receiver R: PA 1 mm needle hydrophone
% Transducer T: V301 nr. 654055

d0 = 1;
rho = 1000;
temperatur = 19.0;   % Celsius, beregnet cl = 1485.9 m/s.
amp_faktor = 45.74;  % [dB] Forsterkning i HVA-10M-60-F
delta_amp = 20.24; % [dB] Forsterkning i HVA-10M-60-F. Delta fra 40 til 60 dB.

% a) Source S --> transducer T
% Voltage Vs2 into source S [2 Vpp]
load elektrisk_Vs2.mat
Vs2 = v1;
clear v1
% Input admittance to source S
load Z_V301_654220.mat
Y = g+i.*b;
ZtS = 1./Y;
clear fr g b
% Current Is2
Is2 = Vs2./ZtS;
% Voltage Vst out of transducer T using source S (terminated with 1 Mohm)
load akustisk_Vst.mat
% Distance between source S and transducer T [in m]
d1 = 1.167;
% Corrects for the amplification in HVA
Vst = v1/(10^((amp_faktor)/20));
% Corrects for the amplification in HK-filter
Vst = Vst./frekresponsHK(f);
clear v1

% Resiprocity factor for transducer T
J = 2*d0./(rho*f);

% Source sensitivity to source S
Sv = sqrt((Vst./Vs2).*(d1/d0).*(1./(ZtS.*J)));

% b) Source S --> Receiver R
% Voltage Vs1 into source S [20 Vpp]
load elektrisk_Vs1.mat
Vs1 = v1;
clear v1
% Voltage Vsr out of receiver R using source S (terminated with 50 ohm)
load akustisk_Vsr_50ohm.mat
% Distance between source S and receiver R [in m]
d2 = 0.9109;
% Corrects for the amplification in HVA
```

```
Vsr = v1/(10^((amp_faktor+delta_amp)/20));
% Corrects for the amplification in HK-filter
Vsr = Vsr./frekresponsHK(f);
clear v1

% Pressure at hydrophone
pH = Sv.*Vs1*d0/d2;
% End-of-cable loaded sensitivity
Mr = abs(Vsr./pH);
% I mV/MPa:
Mr_korr = Mr*1e3/1e-6;
%%%%%%%%%%%%%%%%%%%%%%%%%%%%%%%%%%%%%%%%%%%%%%%%%%%%%%%%%%%%%%%%%%%%%%%%%%%%%%%%%%%%%%%%%%%%%%%%%%%%

% Transmission measurement calculations
warning('off');
%% BRUKER
d1 = 270e-3; % Avstand mellom lydkilde og staalplate
d2 = 100e-3; % Avstand mellom staalplate og hydrofon

temperatur = 19.7;   % Celsius, beregnet cl = 1485.9 m/s.
amp_faktor = 45.74;  % [dB] Forsterkning i HVA-10M-60-F
delta_amp = 20.24; % [dB] Forsterkning i HVA-10M-60-F. Delta fra 40 til 60 dB.

% Steady-state omraade for maaling uten plate
grense1 = 55000;
grense2 = 65000;

% Steady-state omraade for maaling med plate
grense3 = 75000;
grense4 = 85000;

% Steady-state omraade for elektrisk
grense5 = 60000;
grense6 = 70000;

disp('Loading measurement data...');
%% PROGRAM
load akustisk_pNo3_20Vpp_270mm.mat
resultatV1 = resultat;
fv1 = frekvens;
tidsskala1 = tidsskala;
clear resultat frekvens tidsskala
navn = '0deg_x0';
load(navn,'-mat')
resultatV2 = resultat;
fv2 = frekvens;
tidsskala2 = tidsskala;
clear resultat frekvens tidsskala
load elektrisk_pNo3_20Vpp.mat
resultatV3 = resultat(1,:);
fv3 = frekvens;
tidsskala3 = tidsskala;
clear resultat frekvens tidsskala

disp('Done!');
f = fv2;
disp('Calculating voltage amplitudes...');
% FFT-metode fra Halvor for aa finne amplitude, modifisert av Magne Aanes
[v1,v2,serie1,serie2] = fftamplitude(resultatV1,fv1,resultatV2,fv2,grense1,grense2,grense3...
,grense4,tidsskala1,tidsskala2);

% FFT-metode fra Halvor for aa finne amplitude, modifisert av Magne Aanes
```

```
[e1,e2,Eserie1,Eserie2] = fftamplitude(resultatV3,fv3,0,0,grense5,grense6,0,...
        0,tidsskala3,0);
disp('Done!');

v1 = v1(1:2:end);
e1 = e1(1:2:end);

valg1 = input('End-of-cable free field loaded sensitivity by [1]-UiB or [2]-NPL: ');
% End-of-cable free field loaded sensitivity! DCC terminated with 50 ohm
% before high impedance amplifier.
if valg1 == 1
    [M_ref] = frekresponsPA_MIN(f);
else if valg1 == 2
        [M_ref] = frekresponsPA_NPL(f);
    end
end
amp = 10^(amp_faktor/20);
V1 = v1/amp; %v1 er i peak2peak
V2 = v2/amp;
% Korrigerer for forsterkning i HK-filteret
V1 = V1./frekresponsHK(f);
V2 = V2./frekresponsHK(f);
% Trykk ved hydrofon (peak2peak)
P1 = V1./M_ref;
P2 = V2./M_ref;

Hpp = 20*log10(abs(P2./P1));
HVp = 20*log10(abs(P2./e1));
navn2 = [navn '_resultat'];
save(navn2,'f','P1','P2','e1','HVp','v2','v1','e1','Hpp')
%%%%%%%%%%%%%%%%%%%%%%%%%%%%%%%%%%%%%%%%%%%%%%%%%%%%%%%%%%%%%%%%%%%%%%%%%%%%%%%%%%%%%%%%%%%%%%%
```